J/ψ PRODUCTION AS A FUNCTION OF CHARGED PARTICLE MULTIPLICITY IN PP COLLISION AT 2.76 TeV AND 5.02 TeV WITH ALICE DETECTOR AT LHC

THESIS

SUBMITTED FOR THE AWARD OF THE DEGREE OF

Doctor of Philosophy
In
Physics

BY
ANISA KHATUN

DEPARTMENT OF PHYSICS
ALIGARH MUSLIM UNIVERSITY
ALIGARH-202002
INDIA

2020

CANDIDATE'S DECLARATION

I, **Anisa Khatun**, Department of Physics, A.M.U., Aligarh, certify that the work embodied in this Ph.D thesis is my own bonafied work carried out by me under the supervision of **Prof. Shakeel Ahmad** and co-supervision of **Prof. Sukalyan Chattopadhyay**, at Aligarh Muslim University, Aligarh. The matter embodied in this Ph.D thesis has not been submitted for the award of any other degree.

I declare that I have faithfully acknowledge, given credit to and referred to the research workers wherever their works have been cited in the text and the body of the thesis. I further certify that I have not willfully lifted up some other's work, para, text, data, result, etc. reported in the journals, books, magazines, reports, dissertations, thesis, etc., or available at web-sites and included them in this Ph.D. thesis and cited as my own work.

Date: **(Signature of the candidate)**

ANISA KHATUN

Certificate from the Supervisor/Co-supervisor

This is to certify that the above statement made by the candidate is correct to the best of my/our knowledge.

Signature of the Co-supervisor:

Prof. Sukalyan Chattopadhyay
HENPP Division
Saha Institute of Nuclear Physics
Kolkata - 700 064, West Bengal, India.

Signature of the Supervisor

Prof. Shakeel Ahmad
Department of Physics
Aligarh Muslim University
Aligarh - 202 002, U.P, India.

(Signature of the Chairman of the Department with seal)

COURSE WORK/COMPREHENSIVE EXAMINATION/PRE-SUBMISSION SEMINAR COMPLETION CERTIFICATE

This is to certify that Ms. Anisa Khatun, Department of Physics, A.M.U., Aligarh has satisfactorily completed the course work/comprehensive examination and pre-submission seminar requirement which is part of her Ph.D. programme.

Date: (Signature of the Chairman of the Department)

COPYRIGHT TRANSFER CERTIFICATE

Title of the Thesis: J/ψ production as a function of charged-particle multiplicity in pp collision at 2.76 TeV and 5.02 TeV with ALICE detector at LHC.

Candidate's Name: Anisa Khatun

Copyright Transfer

The undersigned hereby assign to the Aligarh Muslim University, Aligarh copyright that may exist in and for the above thesis submitted for the award of the Ph.D degree.

Anisa Khatun
Signature of Candidate

Note: However, the author may reproduce or authorize others to reproduce material extracted verbatim from the thesis or derivative of the thesis for author's personal use provide that the source and the University's copyright notice are indicated.

Dedicated
To
My Abba & Maa

Life need not be easy, provided only
that it is not empty

— Lise Meitner

Acknowledgments

First of all, I thank Almighty Allah for blessing me with health, vision and life. I am grateful to Allah for making me able to finish this course and guiding my heart in my despair and hope.

I wish to express my sincere gratitude to my supervisor Prof. Shakeel Ahmad for taking me under his supervision and introducing me to the world of experimental high energy physics. He taught me during masters and course work program. I am thankful to him for teaching programming languages and data analysis. He provided me with several opportunities to attend national/international conferences, schools and all the facilities that were required to carry out this project. He supported me to work independently and at the same time guided me with appropriate advises and fruitful suggestions to accomplish doctoral work.

My greatest gratitude to late Prof. Muhammad Irfan for showing me the path to the ALICE experiment and strong motivation which helped me to choose this field in the first place. I truly appreciate his genuine kindness and pray for his soul may rest in peace.

I have been fortunate to be a part of the ALICE collaboration which lead me to meet amazing people around the world. First and foremost, I awe my heartfelt appreciation towards my co-supervisor Prof. Sukalyan Chattopadhyay, without his persistent encouragement, guidance, help and motivation, this work could not have been possible. I am indebted to him for having faith in me and for being one of my source of inspiration.

My cordial gratitude to Dr. Tinku-Sarkar Sinha, who is one of the first people, I started working within the collaboration. I am grateful for her guidance during the beginning of the analysis work, moral support and positive attitude, which helped me finish this task. I wish my sincere thanks to Dr. Indranil Das for his exceptional advice and pushing my boundaries to work hard. I have learnt a lot about academia from him and consider myself lucky to be able to work with him.

I want to express my special thanks to Dr. Gines Martinez Garcia for his valuable suggestions regarding multiplicity analysis. I am genuinely thankful to Dr. Philippe Pilot and Dr. Roberta Arnaldi for their guidance and helpful pieces of advice throughout the time of the physics analysis. I sincerely thank Dr. Hugo Pereira Da Costa and Dr. Torsten Dahms for their extensive academic help, suggestions and for being

patient with me, especially during the times of physics results approvals. I am grateful to all the PWG-DQ colleagues who were always there for co-operation whenever I approached them and physics discussion during the group meetings.

I am grateful to all of those with whom I have had the pleasure to work during the thesis work in one way or another. I like to express my cordial gratitude to Dr. Raghunath Sahoo for his generous professionalism and letting me work at his lab for the phenomenological study.

I like to extend my words of gratitude towards my collaborators Dhananjaya Thakur, Mohammad Tarhini, Stephen George Weber, Benjamin Auderier and Suman Deb, for their academic support. It was a great experience to be able to work with them. Their spontaneous co-operation and immediate sense of teamwork helped me in a significant way in the fulfilment of this research work. I would like to thank my seniors Dr. Biswarup Paul, Dr. Hushnud and Dr. Sourav Dey for always being there for me in the hour of need and their kind support in both academic and personal level. I also like to thank Tasnuva Chowdhary, Yanchun Ding and Jana Crkovska, for their academic correspondences.

I hold an immense sense of gratitude for my lab mates of Room No. 249 at SINP. My warm regards and appreciation to my beloved friends Shamik Ghosh, Suvankar Roy Chowdhury, Kuntal Mondal, Biswarup Das, Kalyanmoy Chatterjee, Swagata Mukherjee, Souvik Priyam Adhya, Saswati Nandan, Rajarshi Mukherjee, Wadut Shaikh, Jhuma Ghosh, Arghya Mukherjee, Pritam Palit, Gourab Saha, Md Samsul Islam, Arindam Das, Debabrata Bhowmik for their affection, friendship, creating joyful and healthy work environment and never letting me feel like an outsider whenever I visited 249.

Moving back to Aligarh Muslim University at Department of Physics, my sincere regards to former Chairman Prof. Rahimullah Khan, Prof. M. Afzal Ansari, Prof. Tauheed Ahmad, present Chairperson Prof. Bhanu Prakash Singh for extending their academic support and providing me necessary facilities in my academic endeavours. My special thanks to Dr. Raktim Abir for his insightful suggestions regarding thesis writing, moral support and helpful advice. My sincere gratitude to Prof. Afzal Ahmad for taking the time to check the manuscripts and all the corrections of the thesis. My heartfelt appreciation towards his genuine efforts for his valuable suggestions, which helped me to improve the quality of this thesis. I also like to thank Prof. Mohammad Sajjad Athar for his inspirational classes during course work and always showing us the passion for physics. I thank Dr. Mohammad Rafi Alam for his encouraging words. My heartiest gratitude to Prof. Shabbir Ahmad and Prof. Isar Ahmad Rizvi for their unconditional support and encouragement during my thesis submission process. I take this opportunity to acknowledge all my teachers at the Department of Physics who taught me during B.Sc., M.Sc. and post-M.Sc program.

I would like to show my gratitude to Mrs. Amera Shakeel Ahmad for her kind advice

and moral supports. I thank my ALICE collaborators at AMU, Dr. Danish Azmi, Dr. Mohd. Mohshin Khan, Dr Nazeer Ahmad, Dr. Tahir Hussain for their academic acquaintances.

I am thankful to all non-teaching staff of the Physics Department, Mr. Naseem Ahmad Khan, Mr. Musharraf Ali, Mr. Maaz Moonis, Mr. Ashish Jacob, Mr. Zulfkar Ahmad and Ms. Amna Afridi, for their support in every technical and official situation.

Time to thank my colleagues Shaista Khan, Dr. Anuj Chandra, Bushra Ali, Mohammad Nadeem and Meeran Zuberi for their persistent co-operation in professional and personal level during this long period of ups and downs. It has been a great pleasure to be among them who have always shown their best interests in mind for me and brighten my days in the hardest time of my life.

I am blessed with the most beautiful and understanding parents in the world. I take this opportunity to express my gratefulness to my father Md. Rejaul Karim, who is my first teacher, and the reason behind my love for physics. My mother, Amina Khatun, set an example for me of being a robust independent human being. Their unconditional love, guidance, patience and encouragement helped me to accomplish this task. I want to mention my younger sibling Mushahid Karim for always being there for me and listening to my rants. I thank my childhood friends gang Juhi, Shuely, Dona, Samima and Preeti (JNSDSP) for their unconditional support and affection, which helped me to get through in thick and thin. I am also thankful to my close friends Asma Amjad Gaznavi, Faiza Akbar and Lubna Bhat for always standing by my side. I also like to thank my dearest friend Omveer Singh and my cousin Asif for showing their love, support and encouragement. I am thankful to Tabassum Naz, Mariyah Siddiqah, Muntazir Gul, Atika Fatima, Naheed Wasim and Farhana Zaidi. My sincere gratitude to them for their academic and personal advice, and for helping me with thesis correction and always being affectionate and kind towards me. I am thankful to my friend Geetika Jain, Preeti Dhankar and Bharati Naik for their genuine affection and helpful advice. I thank my friend Naseema, Nisha, Naushaba, Shabina, Tanzeel, Asfia, Sana, Minhal, Wahida and my present hostel roommate Akansha for making my hostel life memorable.

Besides, several people have knowingly and unknowingly helped me in the successful completion of this work; I acknowledge all of them.

- Anisa Khatun

Abstract

Production of charmonia (bound states of c and $\bar{c}$ quarks) and bottomia (bound states of b and $\bar{b}$) in heavy-ion collisions is considered as an ideal probe to explore the possibility of the Quark-Gluon Plasma (QGP) formation in the laboratory. The J/ψ suppression is one of the major key to probe the presence of primordial condition of earlier universe. The quarkonium measurements in the hadron-hadron collisions provide an essential tool to test the Quantum Chromo-Dynamics (QCD), as it contains the full energy regime studied by perturbative QCD to the lattice QCD. The studies involving multiplicity of charged-particles produced in high energy collisions is taken as a simple yet important variable for understanding the collision dynamics. The multiplicity measurement is useful in studying the general properties of particles collisions.

The quarkonium production as a function of charged-particle multiplicity in proton-proton and proton-nucleus collisions is considered as an interesting observable to comprehend multi-parton interactions and to explore the presence of collective behaviour (fluid like) in small systems. Such studies can play an important role in understanding the production mechanism of soft scale processes and its relation with heavy quarks produced in the hard processes. The multiplicity dependence study of hard probes also provides important ground to look for the contribution of jets (hard p_T particles) in the underlying events, which are mainly dominated by the soft probes like pion, kaon. The self-normalized quarkonium yield as a function of self-normalized charged-particle multiplicity is a good observable where most of the efficiency corrections cancel out in the normalization process. In this way, the results become independent of the experiments from where it has been carried out and a comparative study is possible among the various experiments. Similarly, the evolution of the first moment of the mean transverse momentum of J/ψ ($\langle p_T^{J/\psi} \rangle$) as a function of multiplicity provides information about the collective nature of the collision system.

The multiplicity dependence of J/ψ production has been previously studied in pp collisions at $\sqrt{s}$ = 7 and 13 TeV and p-Pb collisions at $\sqrt{s_{\rm NN}}$ = 5.02 TeV at forward and mid-rapidity using the ALICE detector. A similar study was previously carried out for open charm (e.g. D mesons) particles. An increase of the relative J/ψ yields with the relative charged-particle multiplicity has been reported. The mean transverse momentum of the J/ψ as a function of relative charged-particle pseudo-rapidity density were reported in p-Pb and Pb-p collisions at $\sqrt{s_{\rm NN}}$ = 5.02 TeV. The increasing trend of mean transverse momentum of J/ψ at low multiplicity with saturation towards high multiplicity was observed.

Therefore, in this thesis, the study of J/ψ production as a function of charged-particles has been carried out in pp collisions at $\sqrt{s}$ = 2.76 and 5.02 TeV with the data from the ALICE detector at LHC. The findings have been compared with the results obtained in pp collisions at $\sqrt{s}$ = 7 and 13 TeV at forward and mid-rapidity to explore the energy and rapidity dependence of the correlation between soft and hard physics processes. The results are also compared with the theoretical model calculations. An extensive study with PYTHIA8 events generator has been done to explain the experimental data.

The measurement of the inclusive production cross-section of J/ψ has been performed for consistency. The relative J/ψ yield has been measured as function of relative $dN_{ch}/d\eta$ in pp collisions at $\sqrt{s}$ = 2.76 and 5.02 TeV at forward rapidity. The estimation of charged-particles multiplicity using the various approaches in pp collisions at $\sqrt{s}$ = 2.76 and 5.02 TeV have been reported. The analysis is carried out for inelastic>0 event class. The new analysis techniques were used to calculate the efficiency correction factors related to the events. The charged-particle multiplicity ($dN_{ch}/d\eta$) increases as a function of the center of mass (CM) energies. The results of integrated charged-particle pseudo-rapidity ($\langle dN_{ch}/d\eta \rangle$) is consistent with the independent analysis reported by ALICE collaboration. The J/ψ yield scales with multiplicity linearly at both the CM energies. The comparison study reveals that the process is independent of the CM energy and largely depends on the rapidity. All the theoretical models e.g. higher fock states, percolation, PYTHIA8 etc., describe the data qualitatively, however, models provide best description at low multiplicity while more investigations are needed for high multiplicity.

The evolution of $\langle p_T^{J/\psi} \rangle$ as a function of self-normalised $dN_{ch}/d\eta$ in pp collisions at $\sqrt{s}$ = 5.02 TeV has been reported. The experimental results have been compared with other available results from ALICE to investigate the energy, rapidity and collision system dependencies. An increase of $\langle p_T^{J/\psi} \rangle$ has been observed at low multiplicity, while at high multiplicity a saturation is observed. The observed trend is found to be independent of the energy and collision system. However, the rate of the growth of $\langle p_T^{J/\psi} \rangle$ varies between the collision systems. The comparison of $\langle p_T^{J/\psi} \rangle$ results with the PYTHIA8 model calculation shows well description of the data.

An extensive calculation of multiplicity dependence of J/ψ production has been carried out using 4C tune PYTHIA8.2 model. The double differential study in terms of event shapes and multiplicity has been performed in pp collisions at $\sqrt{s}$ = 5.02 and 13 TeV at mid and forward rapidities. The thermodynamic properties of J/ψ production has also been studied using non-extensive Tsallis distribution. The finding reveals that at mid-rapidity there is more contribution of jet in the J/ψ production while at forward rapidity it is more isotropic in nature. The non-extensive Tsallis temperature provides indication of collectiveness in the small system like pp collisions.

The conventional way to investigate the QGP formation is well established with the heavy-ion collisions where pp collisions data are mainly used as a baseline. The

formation of hot and dense fireball consisting of hadronic and (or) partonic matter is most likely to happen in heavy-ion collisions. To check for such thermalised medium formation, a systematic analysis of the experimental data on heavy-ion collisions at AGS and SPS energies, available in the laboratory has been carried out to study the correlations and event-by-event fluctuations. The main motivation behind such studies is that the fluctuations in physical observables in heavy-ion collisions serve as an indicator for the possible phase transition and QGP formation. There are some events, produced in ^{32}S-AgBr and ^{32}S-Gold collisions at 200 A GeV/c which indicate the presence of narrow phase space regions. Analysis of densely such events has been carried out separately which indicates the presence of dominant cluster or jet-like phenomena in one dimensional η and ϕ and two dimensional $\eta - \phi$ space. The study of intermittent pattern in term of scaled factorial moments suggests that it may seem serve as an tool to select a special class of events having high density phase regions for further analysis to search for the signals of some exotic states like disoriented chiral condensate (DCC) or QGP. In context to data at RHIC and LHC energies, it may be remarked that by applying the d_{ik} cuts, used in the present study, rare events with large particle density in narrow phase space bins may be identified for further studies; analysis of such an individual event would be statistically reliable because of its high multiplicity. The findings reveals that the identification of large dynamical fluctuations may possible if particle density fluctuations are studied using selection of events with densely populated narrow regions or spikes. Formation of jet-like structure in multi-hadronic final states or clusters in the selected spiky events has also been investigated and compared with the predictions of a multi phase transport (AMPT) and independent emission hypothesis models by carrying out Monte Carlo simulation. The findings suggest that clustering or jet-like algorithm adopted in the present study may also serve as an important tool for triggering different classes of events.

Furthermore, the possibility of occurrence of long range correlations has been investigated by analyzing the experimental data in ^{16}O-AgBr and ^{32}S-AgBr collisions at 200A GeV/c and the results are compared with the AMPT model predictions. The results show that the observed forward-backward (F-B) multiplicity correlations are mainly of short-range in nature. The range of F-B correlations increases with increasing projectile mass. The observed extended range of F-B correlations might be due to overall multiplicity fluctuations arising because of nuclear geometry. The findings are not sufficient for making any definite conclusions regarding the presence of long-range correlations.

In addition, event-by-event fluctuations of hadronic patterns have been searched in terms of voids by analyzing the experimental data on 4.5, 14.5 and 60A GeV/c ^{16}O-AgBr collisions. Two lowest moments of event-by-event fluctuations of voids, $< G_q >$ and S_q as function of phase space bin width show power-law behaviour. The findings reveal that scaling exponent estimated from the observed power-law behavior of the voids may be used to characterize the various aspects of hadronic phase transition. The results also reject occurrence of second order quark-hadron phase transition at the projectile energies considered.

Contents

List of Figures

List of Tables

Chapter 1

Introduction

The biggest scientific challenge today is to understand how the universe was formed and evolved to its present state. The most acceptable theory so far, which helps us to understand the creation of the universe, is the Big-Bang theory. The theory predicts that the microsecond universe was in the form of a plasma of quarks and gluons (QGP). The primary objective of ultra-relativistic colliders (RHIC in BNL and LHC at CERN) is to recreate QGP in the laboratory and felicitate the study of this matter and its evolution.

The current understanding of the early universe is best described within the framework of Standard Model. So we start with a short introduction to the Standard Model and a description of QGP. Then we proceed with the QGP signatures and its relation with pp collisions. Later the connection between the hard probes and soft probes, *e.g.* charged-particles multiplicity, are discussed with some motivation from available experimental results. We conclude this chapter by introducing the theoretical model predictions (mainly PYTHIA) that are related to the experimental results.

1.1 The Standard Model

The Standard Model (SM) summaries all the basic building blocks and three fundamental interactions of nature [1]. It consists of six quarks, six leptons and mediators

of three forces and the Higgs boson.[1]. The elementary particles are attributed masses and quantum numbers, such as the spin (S), the electric charge (Q), the baryon number (B), the lepton number (L), the color charge. The electron (e), the muon (μ), the tau (τ) and their corresponding neutrinos (ν_e, ν_μ, ν_τ) are the leptons. There are three generations of leptons (e,ν_e), (μ,ν_μ), (τ,ν_τ) which carry an electric charge (except for neutrinos) and interact via strong, electromagnetic and weak interactions. There are six flavours of quarks namely, up (u), down (d), strange (s), charm (c), top (t) and bottom (b). In a similar manner to the leptons, there are three generations of quarks (u,d), (s,c), (b,t). The quarks have a fractional electric charge and a color charge, and they interact via all the three forces of the SM. The quarks can not be found in an isolated state as they always form colorless particles. These generations of particles follow a mass hierarchy from low mass to higher mass as we go from first to the third generation. The first-generation particles are the most stable one, and everyday matters are composed of them. The third and second-generation particles are massive ones which decay into their lower generation particles to become stable. The details of the SM is summarized in Figure 1-1. All the particles in the SM have their partner 'anti-particles' which carry the same mass but opposite quantum numbers.

The SM is a very successful model. Various experiments with incredible precision have confirmed its accurate predictions, *e.g.* the magnetic moment (or g-value) of the electron, existence of $W^{\pm}$ and Z^0 vector gauge bosons, the gluons, the charm and top quarks as well as the Higgs boson. The SM is incomplete until today. Since it can only unify three primary forces (strong, electromagnetic and weak forces) and is unable to explain the fourth fundamental interaction, the gravity. However, we will focus on the scale of the strong interaction (which hold the quarks together) where the effect of gravity is negligible and goes to physics beyond Standard Model.

The fundamental constituents of the matter are broadly categorized in two main groups based on their spin, *i.e.* fermions with half-integral spin and bosons with integral spin. All the quarks and leptons are fermions while the mediating charge carriers (photon, $W^{\pm}$ and Z^0, gluons) are the bosons. The interaction between par-

[1]In addition there is a hypothesized graviton.

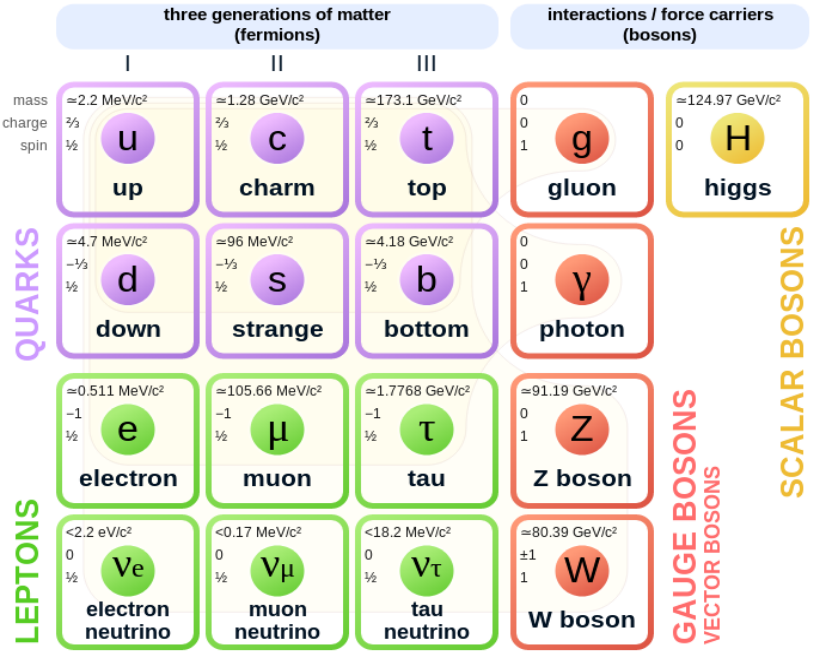

Figure 1-1: The Standard Model of particles [2].

ticles are described by the Quantum Field Theory, which uses the gauge symmetry SU(3)× SU(2)× U(1) [3]. The photon is responsible for the electromagnetic interaction, which is described by the Quantum Electrodynamics (QED) and represented by gauge group symmetry $U(1)^2$. This is the most common interaction between two particles having an electric charge. The $W^{\pm}$ and Z^0 bosons give rise to the weak interaction (*e.g.* radioactive decay of the atom) which is represented by the SU(2) group. The weak and electromagnetic interactions unify and together they are governed by the electroweak theory. The theory includes the Higgs mechanism, which explains the mass of all the particles [4]. When a particle interacts through the Higgs field it gains mass. The discovery of Higgs boson is reported by the ATLAS [5] and the CMS [6] experiments in 2012 at CERN. The gluon is a mediator for the strong interaction which occur between particles with color charges. The theory to explain the strong interaction is the Quantum Chromo Dynamics (QCD). The basic properties of the strong interaction are discussed in the following section.

[2]It is an abelian gauge symmetry means there is only one type of charge and mediating particle photon is mass and charge less allow to interact for an infinite range.

1.1.1 The Quantum Chromo Dynamics and Hadrons

As mentioned in the previous section, the theory of strong interaction is QCD which is analogous to the QED [7]. The QCD is represented by the non-abelian SU(3) gauge symmetry, which means the quarks carry three distinct color charges red, green and blue and three corresponding anti-color charges [8]. The mediator gluon also carry a color charge (anti-color) which allows them to interact with other gluons[3] and quarks. The strength of the strong force increases with the distance, unlike QED, where the electric field decreases with distance. Due to the self-interaction of gluons, the force between two quarks increases with an increase in distance between them. The strength of the strong interaction is described by the strong coupling constant ($\alpha_s \approx 1$), which depends on the momentum transferred in the interaction (Q^2) by Equation 1.1.

$$\alpha_s(Q^2) = \frac{4\pi}{\beta ln(Q^2/\Lambda^2_{QCD})} \tag{1.1}$$

where $\beta = 11n_c - \frac{2}{3}n_f$ is the first-order corrections in the expansion of the QCD coupling; n_c and n_f corresponds to the number of colors and quark flavours, respectively. The Λ_{QCD} (≈ 200 MeV) is the QCD energy scale. It can be seen from Figure 1-2 that at very high Q^2 (high energy) and short distance, the α_s decreases which allows the quarks and gluons to interact very weakly in this domain. This phenomenon is known as asymptotic freedom [9]. That means at asymptotically high energy, the quarks will behave like free particles. On the other hand, when Q^2 is low, the α_s becomes stronger holding the quarks together inside colorless hadrons (strongly interacting particles) like protons and neutrons. This feature is known as confinement [10].

In nature free quark has not been observed (so far till now 2020) due to this color confinement. The process of formation of hadrons is called hadronisation. As we try to separate a quark and an anti-quark, the force becomes so strong that the string between them which holds the potential energy breaks up and results in a new pair of quarks and anti-quarks. Since quarks are fermions and no two quarks

[3]That is why QCD is a non-abelian gauge theory and applicable within Fermi range.

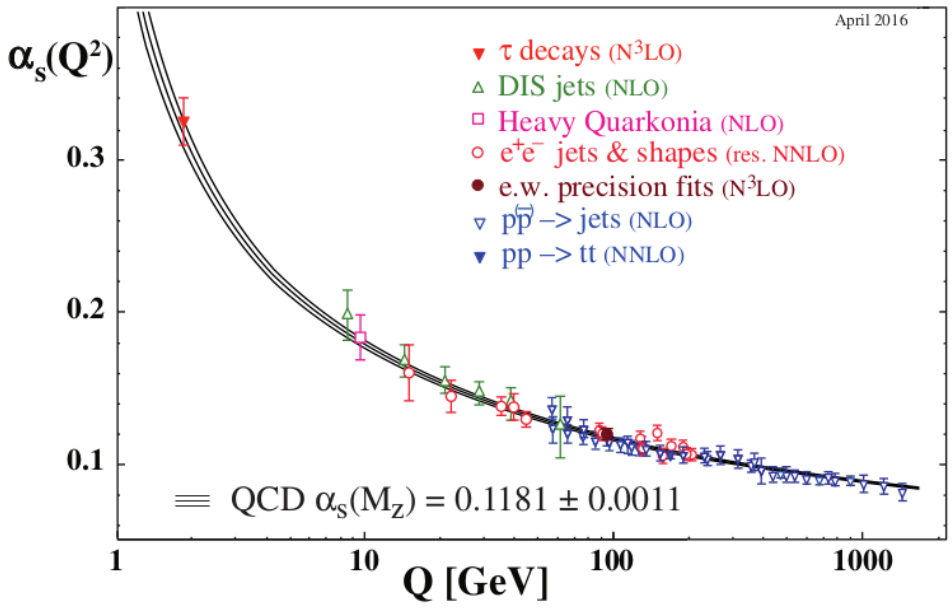

Figure 1-2: The measurements of running coupling constant as a function of transfer momentum [2].

with the same quantum numbers can exist in the same state. It allows them to be bound together in color neutral group of three quarks (qqq) known as baryons and a quark-anti-quark ($q\bar{q}$) is called the meson. Theoretically, there are other possible color neutral combinations of quark states formed exotic hadrons like tetraquarks ($q\bar{q}q\bar{q}$), pentaquarks ($qqqq\bar{q}$) and hexaquarks ($qqqqqq$). Recently the existence of tetra and pentaquarks are reported by Belle[11] and LHCb experiments [12]. Particles can also be composed only of gluons, without valence quarks. Such hypothetical particles are called glueballs. No experimental evidence for glueballs and hexaquarks have been found so far. The QCD has effectively been able to describe the physical behaviour of hadrons, and it's structure in various energy scales [10]. The perturbative QCD (pQCD) approach is applied to hadrons to probe their small-distance quark-gluon structure. When the interaction is governed by high-momentum transfers, Q $\gg \Lambda_{QCD}$, the processes are termed as hard processes or hard QCD [13]. The pQCD is not applicable in low momentum transfer regime (when α_s is significant) which are known as soft QCD processes. The most effective non-perturbative approach is

the Lattice QCD (lQCD) which has been a very successful method in describing the thermodynamic properties of QCD matter [14]. There are effective field theories for exceptional cases where pQCD and lQCD are not applicable. The detail of soft and hard processes will be discussed further since the significant aspect of this thesis work is to investigate the correlation between hard and soft processes in hadronic collisions.

1.1.2 The QCD matter and phase diagram

QCD predicts a phase transition above a critical temperature T_c from ordinary hadronic matter to a phase of deconfined quarks and gluons. At very high densities, the nuclear matter would exist as a quark-soup instead of a dense hadronic system. This new state of deconfined QCD matter is known as the QGP [15]. It is expected that the universe would have existed in a QGP state with zero net baryon density ($\mu_B = 0$) during the first few microseconds after the Big-Bang. It is possible that neutron stars, which have a low temperature but high net baryon number, might contain a QGP at their core.

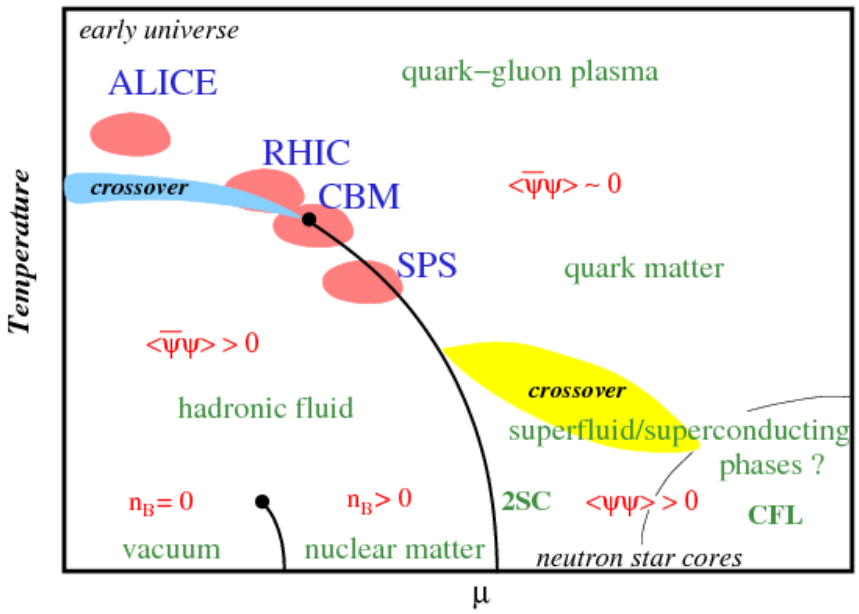

Figure 1-3: The schematic diagram of different phases of QCD. This figure is taken from [16].

The different regions of QCD phase are shown as a function of temperature (T)

and net baryon density in Figure 1-3. At LHC, the ALICE experiment is dedicated to studying the region of QCD phase transition where the temperature is high and $\mu_B \to 0$. This regime has been extensively studied by lQCD models [17]. A cross over of first-order phase transition is expected around $180 \leq T_c \leq 200$ MeV according to lQCD calculations [18]. The QGP system is also likely to restore the QCD Lagrangian symmetry of color under the helicity transformations of the quarks in the absence of quark masses, namely, the chiral symmetry ($\langle\bar{\psi}\psi\rangle = 0$). The restoration of chiral symmetry means the light quarks (u, d, s) are expected to appear as nearly mass less particles compared to their larger constituent quark masses when confined inside hadrons. The transition from hadronic matter to QGP state is still a topic of debate. Various experimental facilities such as STAR and RHIC as well as ALICE at CERN are dedicated for investigating different part of QCD phase-space (T, μ_B) at different collision energies using ultra-relativistic heavy-ion collisions. In the heavy-ion collision Section 1.3.1 we will discuss more about QGP and it's experimental observable.

1.2 The quarkonium resonances

Quarkonia are the mesonic resonance particles comprise of bound states of a massive quark-anti-quark pair. Heavy quarkonium system is an excellent probe to test all the regimes of QCD and allows to study the interplay between pQCD and nonperturbative QCD which are not fully understood. The quarkonia provide experimental ground to perform these QCD calculations through the investigation of correlation of soft and hard processes [19]. The heavy quarkonia are also significant probe to investigate the presence of QGP. The quarkonia are formed in the hadron collisions in initial hard scattering processes and experiences full evolution of the collisions medium. In the presence of nuclear matter, they may experience hadronisation, fragmentation or both. As a consequence the suppression and regeneration mechanism of quarkonia provide the signature of the QGP [20, 21, 22]. The charmonia *i.e.* bound state of $c\bar{c}$ and bottomonia *i.e.* $b\bar{b}$, are the best examples of heavy quarkonia. The bound state of top quarks $t\bar{t}$ has not been observed yet, because of its large mass and small

lifetime. The quarkonia resonances are short-lived and are found in different mass states which is due to the hyperfine splitting of the angular momentum state of the quark pair. The focus will remain on the first excited state of charmonium, the J/ψ meson, which is the main probe used in this thesis work. The different resonance states of charmonium, which are experimentally observed with their hadronic decay modes, are shown in Figure 1-4.

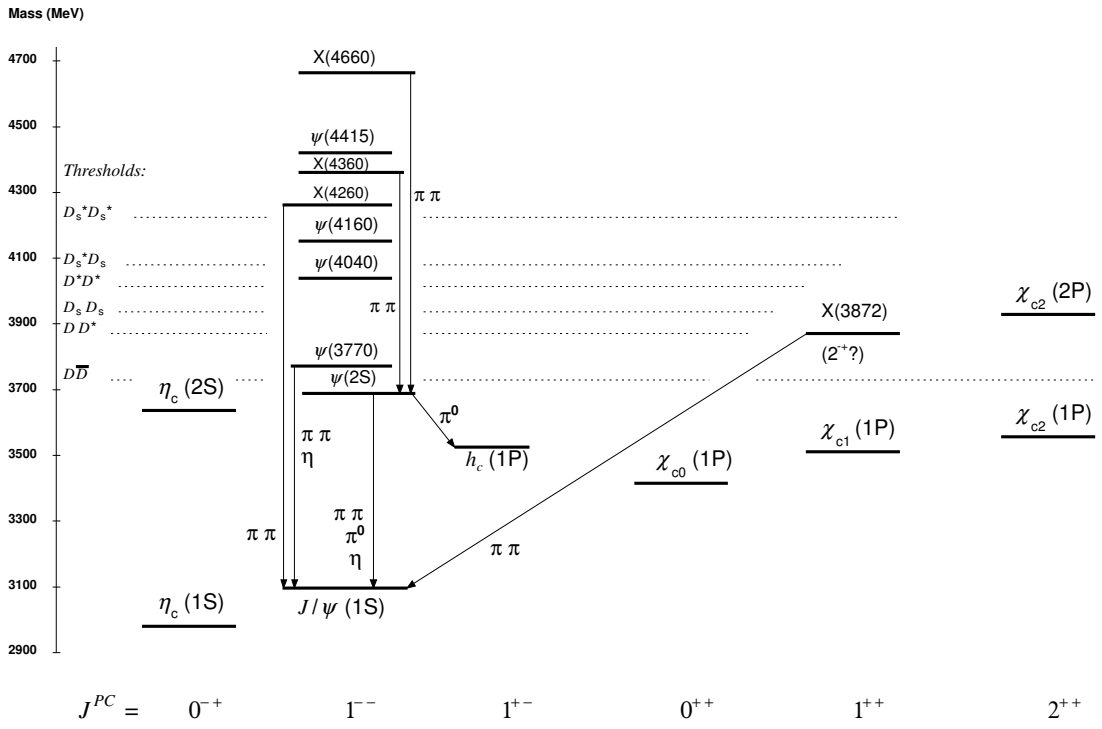

Figure 1-4: The charmonium spectroscopy with their hadronic transition. Similar plot for bottomonium spectroscopy can be found here [2]. The x-axis shows the mass of the resonance states and in the y-axis their spin, parity and charge-conjugation are listed.

The quark model had been established after the discovery of the J/ψ, followed by the excited state $\psi(2S)$ in 1974 [23, 24]. Two groups independently discovered J/ψ at the same time. One from Brookhaven National Laboratory (BNL) discovered at a fixed target experiment Alternating-Gradient Synchrotron (AGS) by hitting a proton beam on beryllium target in the electron-positron channel [24]. Another group from the Stanford Linear Accelerator Center (SLAC) observed a sharp resonance in an electron-positron annihilation experiment in the SPEAR collider in hadronic and dilepton

channel [23]. The discovery of J/ψ played a significant role in accelerating the field of particle physics known as the November revolution. The perceived value of mass and width of J/ψ is $m_{J/\psi} = 3096.900 \pm 0.006$ GeV/c^2 and $\Gamma_{J/\psi} = 92.9 \pm 2.8$ keV/c^2 [2]. The J/ψ is a vector meson[4] ($J^{PC} = 1^{--}$), with J the total spin, P the parity quantum number ($P = (-1)^{L+1}$) and C the charge conjugation quantum number ($C = (-1)^{L+S}$). It has a long lifetime ($\sim 10^{-20}$ sec) compared to the other strongly interacting particles ($\sim 10^{-23}$). This phenomenon was explained by the Okubo, Zweig and Iizuka, *i.e.* OZI suppression rule. As per the OZI rule, the strong decays of charmonium into three pions is suppressed more than decaying into lightest open charm D° mesons pair. But the mass of the charmonium is below the threshold of twice of the D° ($2\times m_{D^0} \approx 3730$ GeV/c^2). Hence this decay mode is forbidden. This suppression of hadronic decays made a window for significant electromagnetic decays into leptonic pair ($\ell^+ + \ell^-$) via a virtual photon. The dilepton decay modes with their branching ratios are [2]: $\mathrm{BR}_{J/\psi \to e^+e^-} = (5.971 \pm 0.032)\%$ and $\mathrm{BR}_{J/\psi \to \mu^+\mu^-} = (5.961 \pm 0.033)\%$. In Figure 1-5 J/$\psi$ signal is reconstructed via its dilepton decay modes. The

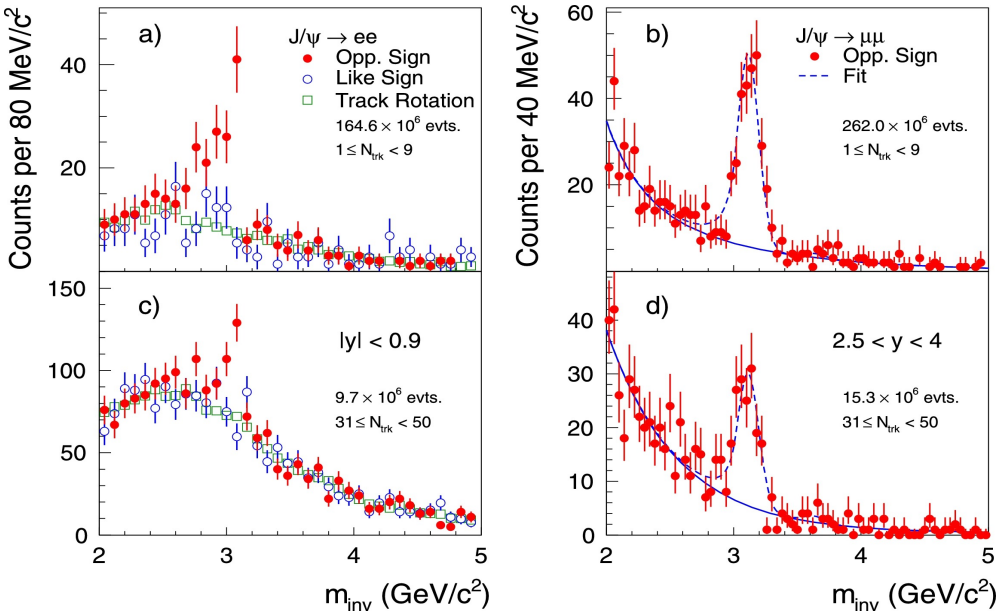

Figure 1-5: The invariant mass of di-electron and di-muon showing J/ψ signal around 3.1 GeV/c^2 measured by ALICE [25].

quarkonium resonances are formed in hadronic collisions via initial hard scattering

[4]Total spin 1 and odd parity makes them vector meson

processes as mentioned in the Section 1.1.1. The J/ψ can be produced directly from the hadronisation of the $c\bar{c}$. The higher mass resonances such as $\psi(2S) \rightarrow J/\psi + X$ and $\chi_c \rightarrow J/\psi + X$ can decay into J/ψ, this process is known as 'feed down effect'. The J/ψ, which are produced either by direct production or by the feed down effect, are known as prompt J/ψ. The J/ψ are also formed from the weak decays of B quark mesons feed down (B $\rightarrow J/\psi + X$). These type of J/ψ are called non-prompt J/ψ. In hadronic collisions, the major fraction of J/ψ is produced via direct production, *i.e.* 60% prompt J/ψ with 10-30% from χ_c and 8% from $\psi(2S)$ feed down [26, 27, 28]. The contribution of non-prompt J/ψ is about 10% and the production of non-prompt J/ψ increases with transverse momentum (p_T). The combination of prompt and non-prompt J/ψ is called inclusive production. In Figure 1-6 the signal of inclusive, prompt and non-prompt J/ψ and its variation with p_{T} is depicted. It also shows the fraction of J/ψ produced from B-hadronic decay measurements in ALICE, compared with other experiments at LHC and CDF at the Tevatron at different collision energies and systems [29].

1.2.1 Theoretical overview of J/ψ production

The quarkonia production involves both pQCD and non-perturbative QCD scales. The mass of the heavy quarks are substantially more than the typical energy and the momentum of the quarks inside quarkonium [30]. Hence the pQCD is applicable to calculate heavy quarks production cross-section where $Q \geq 2m_q >> \Lambda_{QCD}$. On the other hand, the hadronisation process is non-perturbative, which involves energy scales of the order of the binding energy of the quarkonium. Heavy quarks can be treated by the non-relativistic approach because of their large masses. There are various theoretical models available to describe charmonia production mechanism. Most of the models consider factorization of the pair production(high momentum) and hadronisation (low momentum). An excellent overview about models description of J/ψ production can be found in reference [31]. In the following sections, a brief description of the theoretical models are given.

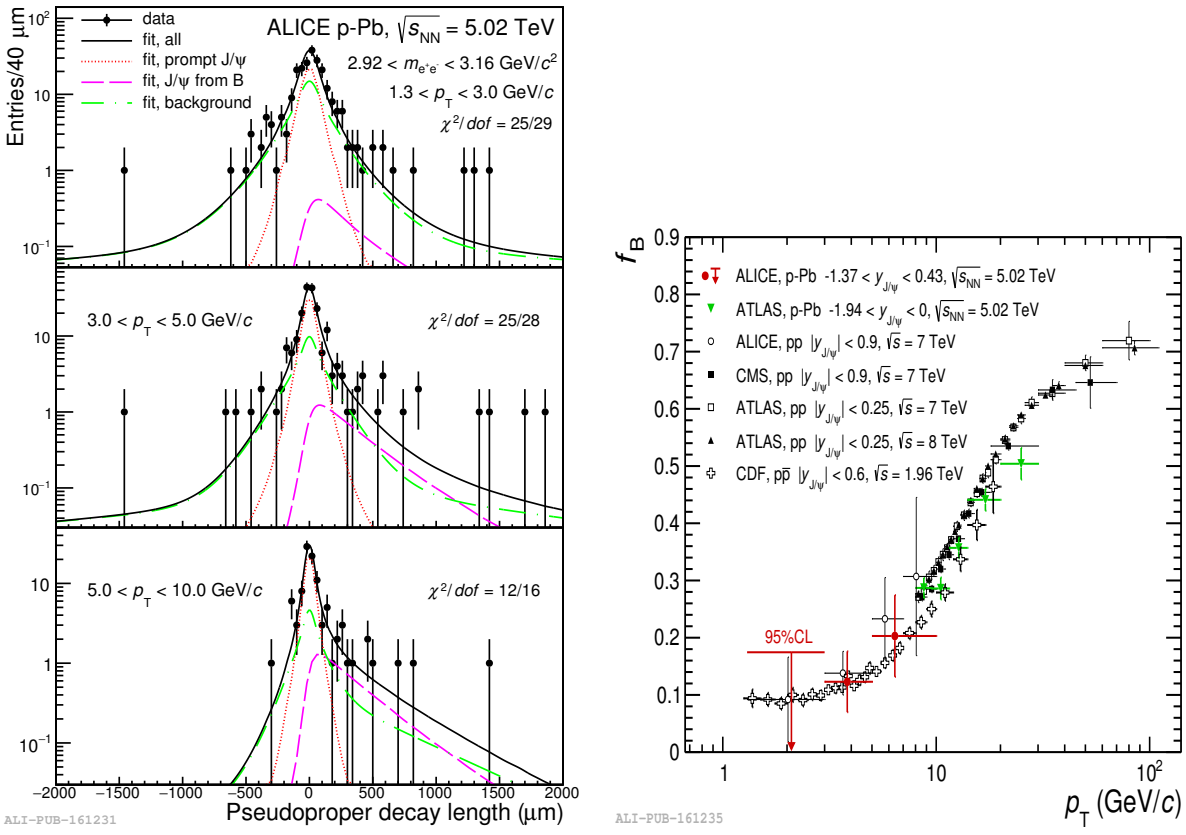

Figure 1-6: The J/ψ signal from various sources and contribution of B-hadronic feed down [29].

Color Evaporation Model (CEM)

The Color-Evaporation Model (CEM) is a phenomenological approach that commonly describes the quarkonia production cross-sections [32]. According to CEM, the hadronisation removes the correlation between the q$\bar{q}$ pair by the exchange of soft gluons with the color field in the collision. That is why the name of the model is "color evaporation" model. The production cross-section of a quarkonium state is given by summing over all the quantum state of quarkonium, where necessary lower and upper bound are, the required mass to form quarkonium state $2M_c$ and mass of open charm pair, $2M_D$. Hence, the total production cross-section is given by

$$\sigma_{q\bar{q}} = F_{q\bar{q}} \int_{2M_c}^{2M_D} \frac{d\sigma_{q\bar{q}}}{dm_{q\bar{q}}} dm_{q\bar{q}} \tag{1.2}$$

where the $F_{q\bar{q}} = 1/9$ represents the statistical probability that the pair hadronizes

into a color neutral state of quarkonium. The CME model calculation can be done at Leading Order (LO) in perturbation theory or at Next-to Leading Order (NLO) framework to account for the p_T dependence. This model well describes the data for the energy dependence and p_T distribution of the cross-section [33]. However, the CEM model fails to predict the J/ψ spin-alignment or polarization and also discrepancies are found in the description of p_T spectra. The J/ψ cross-section at forward rapidity are compared with the CEM as a function of energy, where the model roughly estimates the ALICE data [34]. The recent development of the CEM model is named as Improved Color Evaporation Model(ICEM) [35]. The comparison of experimental data from LHC with ICEM can be found in reference [36].

Color Singlet Model (CSM)

The Color Singlet Model (CSM) was the earliest model to describe the quarkonium production using pQCD [37, 38]. It takes into account the correlation between the production of the bound state to the $q\bar{q}$ production. Unlike CEM, this model explicitly considers the quantum state of $q\bar{q}$ pair. That means the $q\bar{q}$ are produced in a color-singlet state and the quantum numbers are conserved after the quarkonium production. The probability for a $q\bar{q}$ to transform to quarkonium is proportional to the radial wave function at the origin (r = 0) for S-wave states. The hadronic cross-section given by the model is

$$\sigma_{J/\psi+X} = \int_0^\infty dM \frac{d\sigma_{c\bar{c}[^3S_1]+X}}{dM} \psi_{J\psi}(r=0) \tag{1.3}$$

The wave function $\psi_{J/\psi}$ can be derived using the effective potential model calculation [39]. The J/ψ production mechanism via gluon fusion at the LO process in CSM model is illustrated in Figure 1-7 (a). The only inputs required in the model are the $|\psi(0)|^2$ and its derivatives that can be extracted from data of decay processes. The CSM, thus, has no free parameter [40]. The CSM manages to describe the charmonium and bottomium production cross-section as a function of $\sqrt{s}$ in LO framework at lower collision energies [41, 42] but fails to explain the $\psi(2S)$ production cross-

sections at higher energies and at high p_T [43]. However, the CSM provides a better description of the data if the computation at higher orders in the α_s expansion is included. The data comparison with CSM for J/ψ production at $\sqrt{s}$ = 7 TeV at forward rapidity measured by ALICE is shown in Figure 1-8, [44].

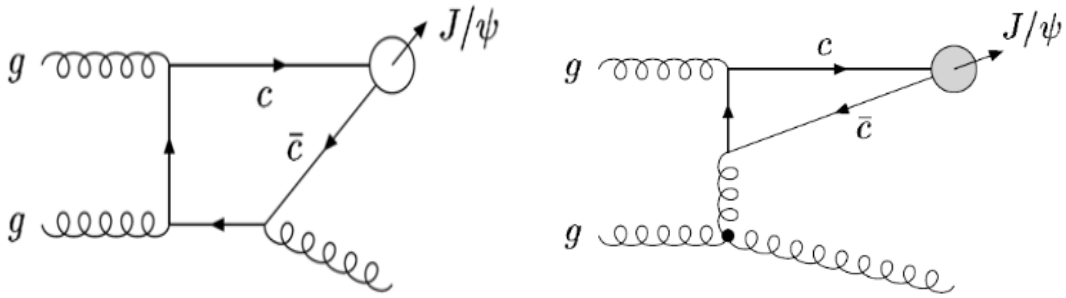

(a) (b)

Figure 1-7: (a) The J/ψ production Feynman diagram of the leading order color-singlet sub process via gluon fusion of the initial state partons. (b) Color octet contribution via gluon splitting [45].

Color Octet Model (COM) and Non-Relativistic QCD (NRQCD)

The Color Octet Model (COM) is incorporated in the Non-Relativistic Quantum Chromo Dynamics (NRQCD) framework and corrects the shortcomings of the CSM approach [45]. Figure 1-7 (b) shows the example of J/ψ production of LO COM contribution by Feynman diagram. The factorization of energy scales hierarchy, $M_Q << M_Q v << M_q v^2$ is implemented in NRQCD framework, where the term M_Q distance range for creation. The quarkonia production in NRQCD is calculated as follows. The creation of the pair in a hard scattering at short distances, which is calculated perturbatively as an expansion in the α_s and the non-perturbative part, the evolution of the pair into quarkonium state, is given by the Long Distance Matrix Element (LDME) which estimated by comparison with experimental data. The NRQCD has been able to describe the production cross-section of J/ψ as a function of p_T at higher energies.

The results of inclusive production cross-sections of J/ψ and $\psi(2S)$ are calculated

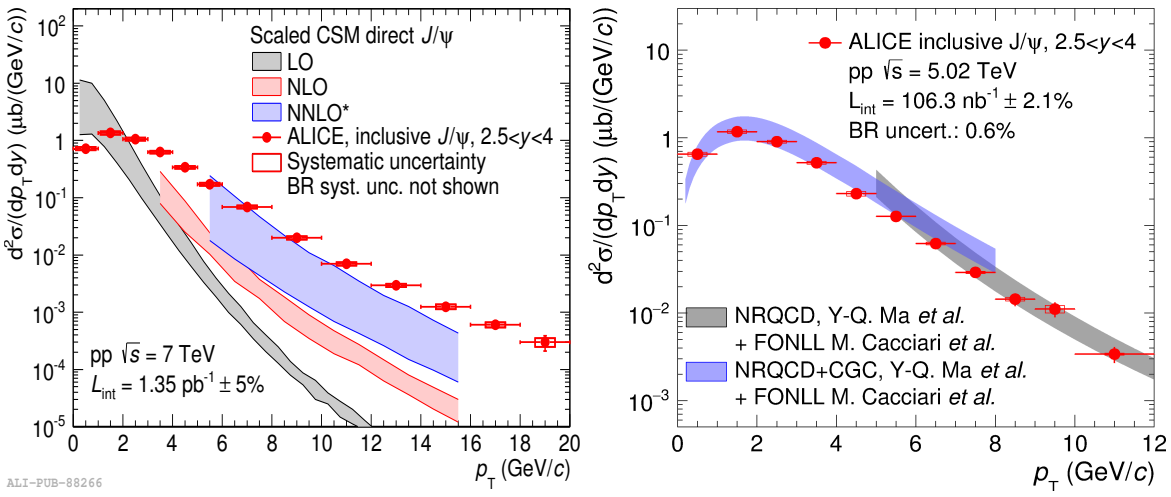

(a) (b)

Figure 1-8: (a) The J/ψ production cross section as a function of p_T at forward rapidity in pp collisions at $\sqrt{s}$ = 7 TeV, compared to predictions from the CSM at leading order (LO), next-to-leading order (NLO), and NLO with leading p_T next-to-next-to-leading order contributions (NNLO*) [44]. (b) The J/ψ production cross section as a function of p_T at forward rapidity in pp collisions at $\sqrt{s}$ = 5.02 TeV compared with NRQCD models [34].

within LO NRQCD framework at LHC energies and are reported in reference [46]. The results show a good description of the data at various energies and rapidity regions for $p_T > 4$. In Figure 1-8, the comparison of p_T dependence of J/ψ production from the ALICE experiment is shown at $\sqrt{s}$ = 5.02 TeV with two NRQCD based models [34]. The FNOLL model is used to account for the feed down contributions from the B-meson at high p_T values [47, 48]. Another one, combined with The Color Glass Condensate (CGC) model [49], is used to describe the production at low p_T values. It can be summarized that currently none of the theoretical models can describe all the experimental observations simultaneously.

1.3 Hadronic collisions

The simplest and the most common of hadronic collision is the proton-proton (pp) collision. A simple system is expected to be formed in pp collisions which allows to study the properties of QCD and investigate the nuclear matter as well as opens a

window for unknown physics[5]. It also provides directions for more complex processes in proton-nucleus (p-Pb) and nucleus-nucleus (Pb-Pb) collisions [50]. In pp collisions, the constituent quarks and gluons (partons) of protons interaction classified as head-on collisions assuming that protons are point like particles. It involves both hard and soft processes that are described in Section 1.1.1. Heavy quarks and jet productions represent hard processes where energy scale is > 1 GeV. The underlying events (UE) activity, initial and final state soft radiation, soft parton scattering, total cross-section, hadronic decay rates and properties described by non-perturbative QCD are examples of the soft process. Figure 1-9 describes a typical inelastic pp collision which involves both soft and hard processes.

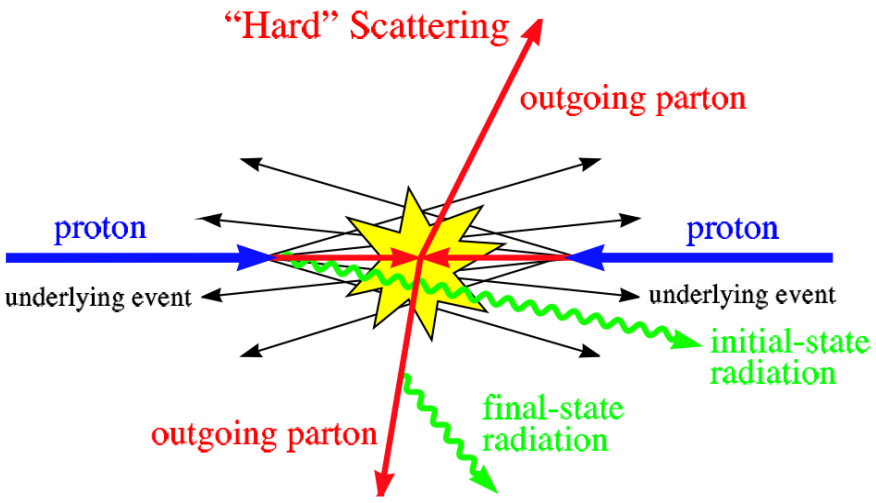

Figure 1-9: Schematic representation of a pp collision [51].

The global properties of interactions in pp collisions are characterized in terms of diffractive and non-diffractive processes. The interactions in which the vacuum quantum numbers are exchanged between interacting colorless particles (known as pomerons) are defined as diffractive interactions. According to Regge theory, the diffraction occurs via the number of pomeron exchanges in the pp collisions [52]. Diffractive processes can be classified depending on either one (single diffractive) or both (double diffractive) incoming protons dissociate into final state particles. The different classes of diffractive pp processes are shown in Figure 1-10. The diffraction interaction can

[5]Speaking in terms of relativistic high energy scales at particle collider

also be classified in terms of rapidity-gap topology. The total cross-section of pp collisions in terms of these diffractive events can be found in these references [53, 54, 55]. The diffraction processes make up about 25% of the inelastic pp cross-section, and about 70% processes are non-diffractive in nature [54]. The partonic interactions are non-diffractive interactions which are again comprised of underlying events and hard scattering processes. The combination of the double diffractive and non-diffractive inelastic process are termed as non-single diffractive (NSD) process.

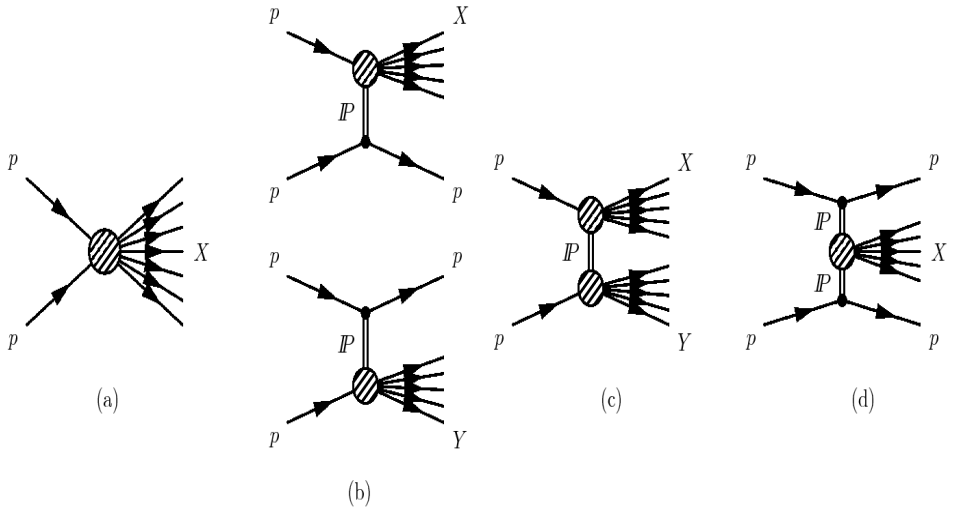

Figure 1-10: Different processes in a inelastic pp collisions. a) non-diffractive process b) single diffractive c) double diffractive d) central diffractive process [55].

The information of the initial parton structure of the pp collisions is described in terms of the parton distribution functions (PDF). The PDF is the probability density to find a parton in a proton with a fraction x of the total momentum at an energy scale Q^2 ($f(x,Q^2)$). The PDFs can characterize the hadronic bound states where hadronic processes are factorized in partonic processes. The PDFs can not be calculated using pQCD, and they strongly depend on Q^2 at low x. The production of heavy flavour, *i.e.* J/ψ, is dominated by gluon fusion in relativistic collisions[56]. The gluon distribution strongly increases with energy at low x. The strong interaction weakens as a consequence of the increase of gluon density until getting saturated as a result of the self-interaction of gluons in QCD. The saturation can be studied through the CGC model [49]. The PDFs are independent of the specific process. Thus, the

$\sqrt{s}$	x_1	x_2
5.02	$1.1 \times 10^{-5} < x < 5.1 \times 10^{-5}$	$7.5 \times 10^{-3} < x < 3.4 \times 10^{-2}$
13	$4.4 \times 10^{-6} < x < 2.0 \times 10^{-5}$	$2.3 \times 10^{-3} < x < 1.3 \times 10^{-2}$

Table 1.1: The momentum fractions for forward J/ψ at the LHC

PDFs are determined by fitting the data from Deep Inelastic Scattering (DIS) of electron off proton (ep) and are used to predict hadronic processes [57]. An example of proton PDFs, relevant to low p_T J/ψ production at an energy scale of $Q^2 = 10$ GeV^2, measured with H1 experiment at HERA, is shown in Figure 1-11. The momentum fractions of the two incoming hadrons, x_1 and x_2 at a given rapidity and centre of mass energy $\sqrt{s}$ can be written as

$$x_{1,2} = \frac{M_{J/\psi}}{\sqrt{s}} e^{\pm y} \tag{1.4}$$

Therefore, different kinematic regions of the PDFs can be explored by measuring it at different rapidity regions. The typical values of x, for J/ψ at forward rapidity region ($2.5 < y < 4.0$) in pp collisions, accessible in ALICE experiment are listed in Table 1.1.

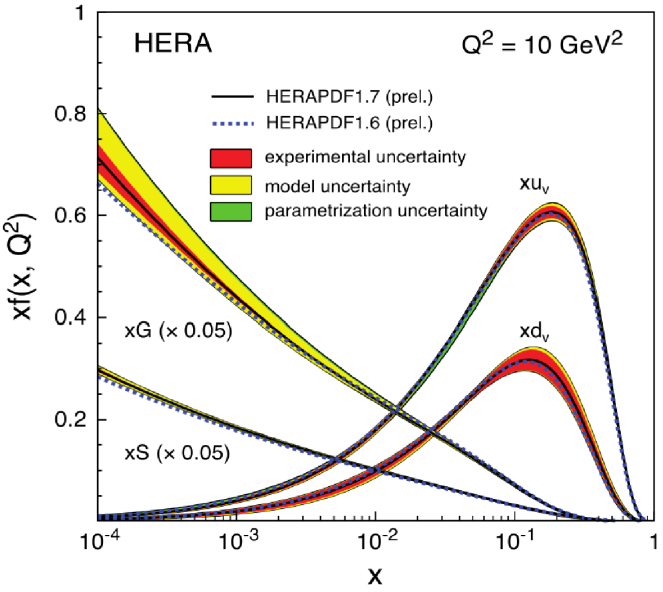

Figure 1-11: Parton distribution functions for valence quarks, sea quarks and gluons at HERA [58].

At ultra-relativistic energies, the proton can be treated as an extended object composed of partons. In this case, the perpendicular distance between the centres of the two protons is defined as the impact parameter, 'b'. Hence, the geometry of pp collisions depends on b as well as the parton distributions of the two incoming protons.

The particles in pp collisions can also be produced due to Multiple Parton Interaction (MPI) process. MPI is defined as multiple parton interactions occurring in a single pp collision. MPI can have a significant contribution in the heavy quarks productions along with the charged- particles. The MPI and its contributions to soft and hard processes will be discussed in detail in Section 1.5.2. The pp collisions are well described by the Monte Carlo event generators such as PYTHIA [59], EPOS3 [60] etc. The QCD inspired models which include soft and hard processes, MPI, as well as the diffractive process, are implemented in PYTHIA8. An overview of these theoretical models is given in Section 1.5.

1.3.1 Heavy-ion collisions and QGP signatures

To create QGP at high energy density, one need more number of colliding particles. Such conditions can be created experimentally in ultra-relativistic heavy-ion collisions. The conditions of the collisions depend on the initial geometry of the colliding nuclei and their degree of overlap. The degree of overlap or centrality is determined by the impact parameter b. Hence, b = 0, would correspond the most central collisions and $0 < b < r_1 + r_2$ (r_1 and r_2 are the radius of the either nuclei) represents the peripheral collisions. The collision centrality and number of participating nuclei can be estimated using the Glauber model formalism [61].

In experiments, the impact parameter and the numbers of participants and binary collisions can not be directly measured. These parameters are calculated by carrying out Monte Carlo simulation and comparing the findings with the data. The Glauber model is employed in mapping the number of charged-particles produced by defining centrality classes in both measured and calculated distributions [62]. The collision centrality classes, in experiments are determined by taking the basic assumption that

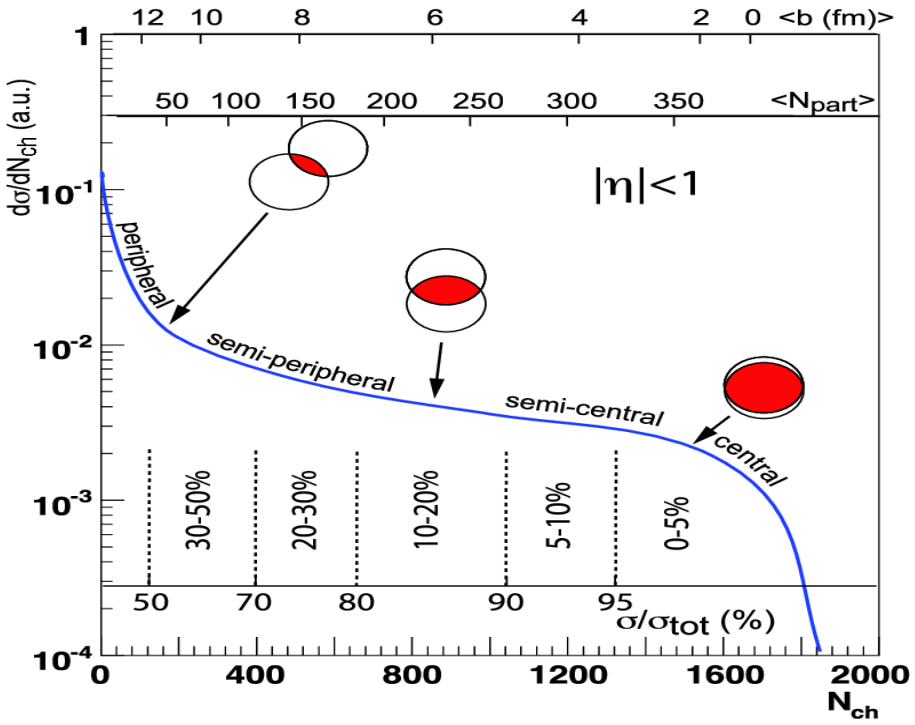

Figure 1-12: A cartoon example of the correlation between the number of participating nucleons in a heavy-ion collision, their cross section and the impact parameter, b, defining the centrality classes [63]. These plotted distributions and various values are illustrative, not actual experimental measurements.

the b is monotonically related to the charged-particles multiplicity and production cross-section of the interacting nuclei in an interval of pseudorapidity (η). The large b represents less number of charged-particles multiplicity and a large number of spectator nucleons, while the small b corresponds to central collisions with high multiplicity and a low number of spectators[6]. Figure 1-12 depicts illustration of heavy-ion collisions in terms of centrality classes at the mid-rapidity region. In the following section, we will discuss more about the charged-particles multiplicity.

The thermal models describe the QGP medium, and its subsequent expansion can be studied in terms of relativistic hydrodynamics [64]. After the QGP is created, the system expands and cools to the critical temperature and the energy density becomes low enough for the transition back to the hadronic phase of confined quarks and gluons. The QGP is extremely short-lived ($\tau \sim 20$ fm/c) and can not be detected

[6]Spectators are the nucleons that do not participate in the collisions.

directly. Therefore, only via tracing back the final state of particles observed by the detectors of the experiments, we can know about the system of the earlier times. In general, there is no unique signal which proves the existence of QGP, and rather there are a variety of probes to characterize the produced system in experiments. The probe of several signatures simultaneously may indicate the formation of the QGP [65]. The probes are broadly categorized into two groups, analogous to QCD processes (hard and soft) as follows:

- **Hard probes** or the early signatures are originated in the initial stage of a collision due to high momentum transfer as a result of hard scattering processes. Examples of such probes are electroweak bosons (γ, $W^{\pm}$, Z^0) decaying into leptons, jet quenching, heavy quarkonia production. The photons that are directly emitted from the QGP system are known as thermal photons, and these weakly interacting photons provide information about the initial temperature of the QGP medium [66, 67]. The $W^{\pm}$ and Z^0 bosons also interact weakly with the QGP medium since they are colorless. Hence, production of $W^{\pm}$ and Z^0 bosons are treated as an ideal probe to study cold nuclear matter effects in heavy-ion collisions [68]. The results of $W^{\pm}$ and Z^0 production at central rapidity can be found in these references [69, 70, 71] and Z^0 production measurement at forward rapidity is done by ALICE [72]. High p_T parton pairs that are produced from a single hard scattering in early stage of a collision which results in a shower of collimated hadrons, known as jets. These jets suffer energy loss while passing through QGP medium. Thus, their yield is modified with respect to the yield without QGP medium. This phenomenon is known as jet quenching which is regarded as another important probe for QGP [73]. We have already discussed about quarkonia being a major probe to QGP in Section 1.2.

- **Soft probes** are described by soft QCD process. Soft probes may originate during all stages of collisions and provide information on the collective effects. The anisotropic flow of charged-particles [74], event-by-event fluctuations and correlations among charged-particles [75], modification of particle yield and ra-

tios [76] are the examples of soft probes. The correlations and fluctuations observables have been introduced in Section 1.3.3, since the study of these soft probes in heavy-ion collisions are also part of this thesis.

1.3.2 Importance of charged-particles multiplicity study

The term multiplicity is a general term for the number of particles emitted in a collision. The charged-particles multiplicity is a global observable which provides information about the initial energy density, geometrical information such as impact parameter and number of participant nucleons and binary nucleon-nucleon collisions in the system, as discussed in the previous section. Events passing a minimum set of requirements in inelastic pp collisions are known as minimum bias events[7]. These events are dominated by soft multiple scattering process. At LHC energies, the charged-particles multiplicities are generally obtained from these minimum bias events in certain rapidity regions. Theoretically, the calculation of charged-particles multiplicity is more complex, and pQCD is not applicable here since soft processes dominate the particle production. It can also have a significant contribution from hard scattering. Thus, its measurement can help to explore both soft and hard probes. The multiple soft collisions change only the excited states of the nucleons, which in turn produce particles the moment they leave the interaction region. As a consequence, the appropriate scaling of the multiplicity of soft processes is assumed to be the number of participating nucleons. On the other hand, in hard processes, the number of particles produced is assumed to scale with the number of binary collisions [77].

The probability $P(N_{ch})$ for producing N_{ch} charged-particles $i.e.$ multiplicity distribution, in the final state can be described by the KNO scaling named after Z. Koba, H.B. Nielsen and P. Olesen [78]. KNO scaling states that multiplicity distribution when normalized by its average value $(P(N_{ch})/\langle N_{ch}\rangle)$ is independent of the collision energy which is again based on Feynman scaling [79]. According to Feynman scaling for asymptotically large energies, the mean number of charged particles increase logarithmically with collision energy $i.e.$ $\langle N_{ch}\rangle \propto ln\sqrt{s}$. This also leads to the con-

[7]More specific definition of minimum bias event is given in chapter two.

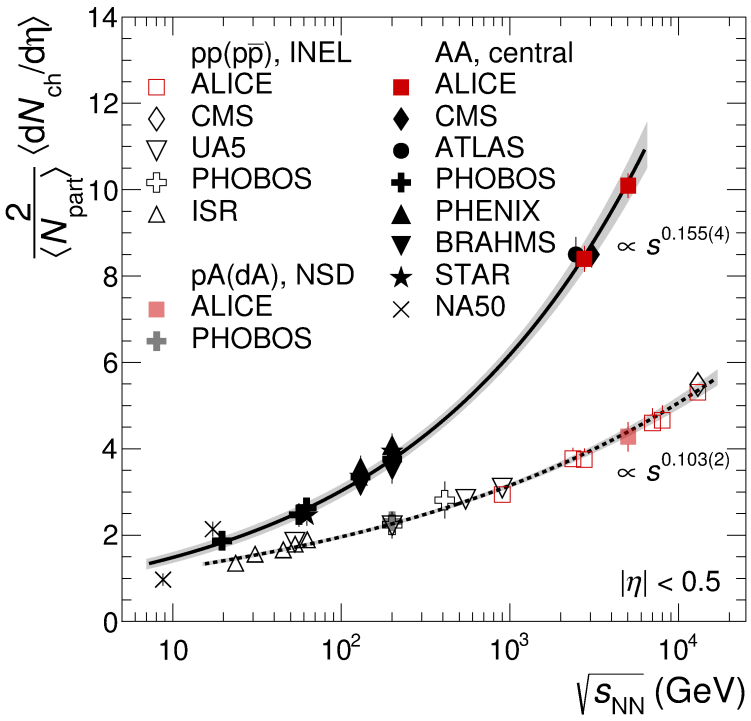

Figure 1-13: Energy dependence of average charged-particles density normalised by the mean number of participating nucleon pairs $\frac{2}{\langle N_{part}\rangle}\langle N_{ch}/d\eta\rangle$ at various colliding systems and event classes measured by various experiments. Comparison with power law functions represented by solid and dashed lines [80].

clusion that charged-particles density around mid-rapidity is independent of energy, *i.e.* dN_{ch}/dy = constant. Considering the fact that maximum available rapidity in a collision also increases logarithmically with $\sqrt{s}$. Experimentally it has been observed that both Feynman scaling and KNO scaling are violated at energies greater than $\sqrt{s}$ = 200 GeV. The deviation of KNO scaling also depends on the η intervals and type of collisions (inelastic, NSD, diffractive, etc.) [81]. The Negative Binomial Distribution (NBD) describes well the shape of the multiplicity distribution at lower collision energies in full phase space up to $\sqrt{s}$ = 540 GeV. At higher energies sum of two NBDs gives reasonable fit for larger η intervals. Such violation are attributed to the presence of semi hard gluon radiation or mini jets and MPI [77].

An alternative approach to describe the energy dependence of multiplicity distributions is parameterization with power-law functions. The power-law parameterization well describes the data from ISR to LHC energies. The results from ALICE

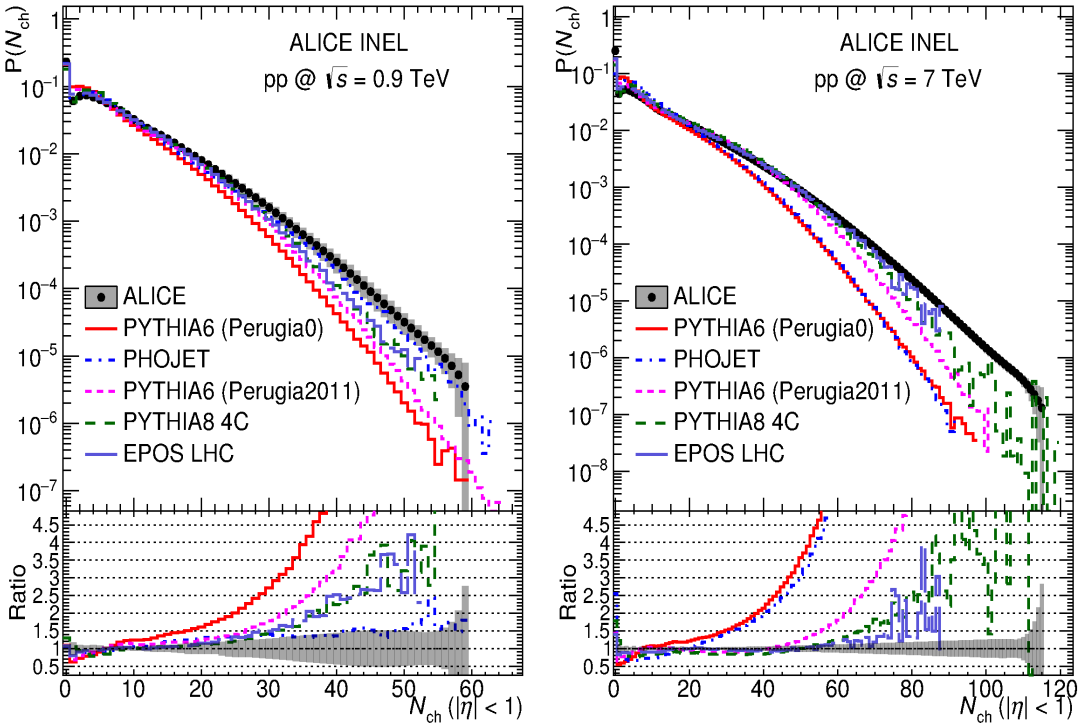

Figure 1-14: Model comparison of charged particles distribution [82].

collaboration show a clear indication that $dN_{ch}/d\eta$ increases faster in Pb-Pb than in pp collisions, (Figure 1-13) and the high multiplicity pp collisions are comparable with the central collisions(Au-Au) at RHIC [80]. Hence, high multiplicity pp collisions at LHC can be useful for studying nuclear matter properties for a medium with similar $dN_{ch}/d\eta$ but very different volumes.

At ultra-relativistic energies (LHC energies) the sea quarks dominates in the low x-region as $x = 2p_{\mathrm{T}}/\sqrt{s}$ which results in large number of MPI [59]. In this case, the QCD inspired models that consider the presence of MPI describes well the charged-particles multiplicity distributions and their energy dependencies. The probability distribution of charged-particles multiplicity measured by ALICE in pp collisions at $\sqrt{s} = 0.9$ and 7 TeV for inelastic events and comparison with model predictions from different MC event generators is shown in Figure 1-14. Detail of charged-particles measurement by ALICE can be found in reference [82].

1.3.3 Study of correlation and fluctuations of the charged particles

The particle correlations and event-by-event fluctuations allow the study of the properties of the matter in that medium. Fluctuations are important for the study of the perturbations of a thermodynamic system. When a system undergoes a phase transition, various thermodynamic quantities show varying degree of fluctuations. Hence, to investigate the of phase transition, the measurement of particle number, energy and charge fluctuations become relevant. The first-order phase transition results in large amounts of energy liberation in the system in localized space which leads to explosions. These localized explosions cause large fluctuations in the production of matter and energy as a function of the rapidity. Therefore, event-by-event fluctuation of the transverse energy per unit rapidity can be used as an important tool for providing possible signatures of plasma formation.

1.3.4 Collectivity in small systems

The experimental data of heavy-ion collisions have shown several essential features which indicate the formation of strongly interacting QCD matter in the collision system or QGP [83, 84, 85, 86]. The consistent measurement of jet quenching, anisotropic and radial flow, quarkonia suppression and regeneration, strangeness enhancement, etc., have established the possible existence of a collective medium produced in these collisions. Especially, at LHC with Pb-Pb collisions at $\sqrt{s_{NN}}$ = 2.76 TeV and 5.02 TeV (also Xe-Xe at $\sqrt{s_{NN}}$ = 5.02 TeV) it was possible to reach at such high energies where a large number of particles (high multiplicities) and hard probes can be created in a medium on event-by-event basis. The pp systems have a much smaller volume compared to the Pb-Pb systems, and they have been frequently used in heavy-ion physics for normalisation as QGP is not expected to be formed. We have already discussed in the previous section that the energy density reached in high multiplicity pp events at LHC is comparable to the Cu-Cu central collisions or Au-Au peripheral collisions at $\sqrt{s}$ = 200 GeV, and hence one can wonder about the possibility to obtain

a system similar to heavy-ion collisions.

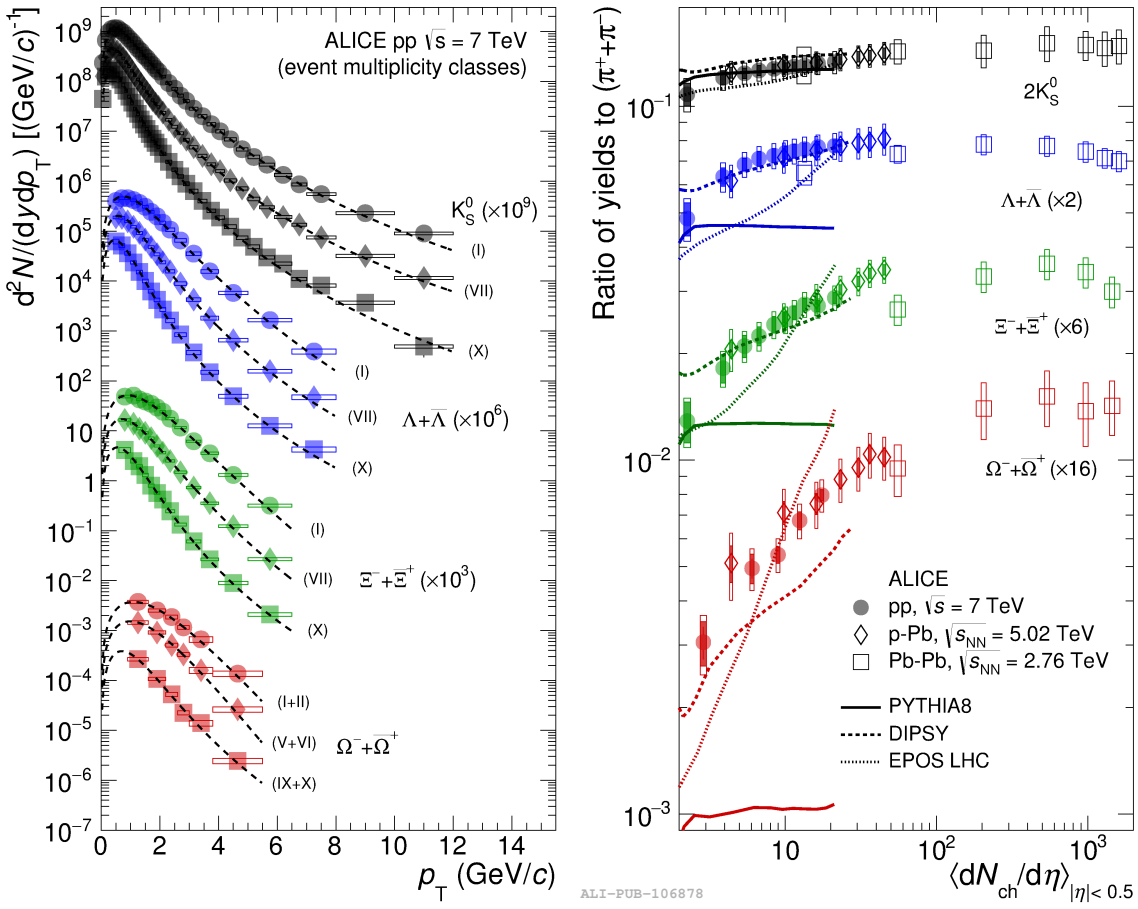

(a) (b)

Figure 1-15: (a) p_T spectra of strange hadrons at different event multiplicity classes. (b) The relative yields of strange particles compared to charged pions as a function of $dN_{ch}/d\eta$ [87].

In recent years, search for collectivity in small systems at LHC energies has become an active area of research in the of high energy particle physics. The experimental evidence of enhancement of strange and multi-strange particles as a function of multiplicity in high multiplicity pp collisions has been reported by ALICE collaboration [87]. The enhancement of strange quark is a typical signature of QGP formation in Heavy-ion collisions. In heavy-ion collisions, in the presence of the QGP medium, the strange quark-anti-quark production is more frequent than in pp collision system due to the fact that coupling of gluon to strange, and gluon to light quarks is similar. The formation of light quarks (u,d) lessened as per Pauli blocking in the central rapidity

region and $s\bar{s}$ annihilation is less frequent. Therefore, enhancement of strange particles is expected and treated as a probe for QGP formation. In Figure 1-15 strikingly, a similar feature has been observed in high multiplicity pp collisions.

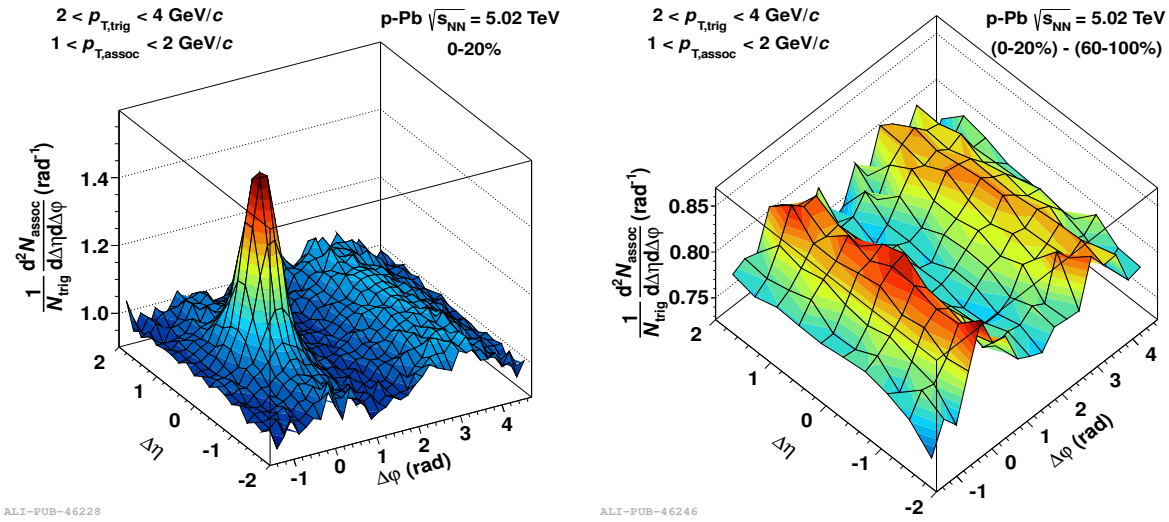

Figure 1-16: Two-particle correlations as function of pseudorapidity and azimuthal angle [92].

Another observation of collective features in small systems is the emergence of azimuthal correlations that extend in long rapidity range or near side ridge effects are reported in pp collisions at $\sqrt{s} = 7$ and 13 TeV by CMS [88, 89] and at $\sqrt{s} = 13$ TeV by ATLAS [90] experiments. The measurements also shown "double-side ridge" effect in p-Pb collisions at $\sqrt{s_{NN}} = 5.02$ TeV by ALICE and CMS [91, 92]. Figure 1-16 shows two-particle correlations along $\delta\eta$ and azimuthal angle $\delta\phi$ of high multiplicity events and subtraction of two-particle correlations in high and low multiplicity events measured in p-Pb collisions $\sqrt{s_{NN}} = 5.02$ TeV. The similar type of near side ($\delta\eta = 0$) and away side ($\delta\phi = \pi$) ridge is observed in heavy-ion collisions which are interpreted as the outcome of the hydrodynamic expansion of the hot dense medium.

Along with these results, elliptical and triangular flow patterns of charged particles produced in proton-gold (p+Au), deuteron-gold (d+Au), and helium-gold (^{3}He+Au) collisions at $\sqrt{s_{NN}} = 200$ GeV is reported by PHENIX Collaboration [93]. A strong multiplicity dependence of average transverse momentum, $\langle p_T \rangle$, which is attributed to radial flow has been observed as well. The observation of collective behaviour in

small systems similar to heavy-ion collisions has led to the questions about their origins. Whether a medium is formed in high multiplicity pp collisions events remain an open question. Another possibility may be to explain these experimental observations without the formation of a deconfined medium. Such alternative theoretical interpretations of these collective phenomena are explained in references [94, 95, 96, 97, 98]. Hence, it is crucial to understand these collective phenomena in small systems at high particle multiplicity.

1.4 Quarkonia and Heavy flavour measurement as a function of multiplicity

In the previous section, some interesting results have been discussed that indicate the collectivity in small systems. In the same direction, the study multiplicity dependencies of hard probes can provide more insight into this area of research. It has been known since 1990 that contribution of MPI is important in describing the phenomena related to pp collisions at high energies. The multiplicity dependence of quarkonia and heavy flavour production will help us to understand the correlation between soft processes, produced bulk multiplicity, and hard processes *e.g.* quarkonium production in hadron-ion and hadron-hadron collisions [99]. Relative yield and relative mean transverse momentum of quarkonium as a function of self-normalised charged-particles pseudorapidity density is a convenient observable to study because the self-normalisation cancels out various corrections and scaling properties (x-axis is the KNO variable $dN_{ch}/d\eta$) make it possible to compare among different collision systems, centre of mass (CM) energies, rapidity regions and quark contents.

Various tests have been performed by ALICE, CMS and STAR experiments on this topic in recent time. In this section, the experimental observations will be discussed. The dependence of the J/ψ yield as a function of multiplicity was investigated in pp collisions at $\sqrt{s} = 7$ TeV in forward rapidity ($2.5 < y < 4.0$) and mid-rapidity ($|y| < 0.9$) regions [25]. The non-prompt J/ψ along with D mesons (D°, D^{+}, D^{*+})

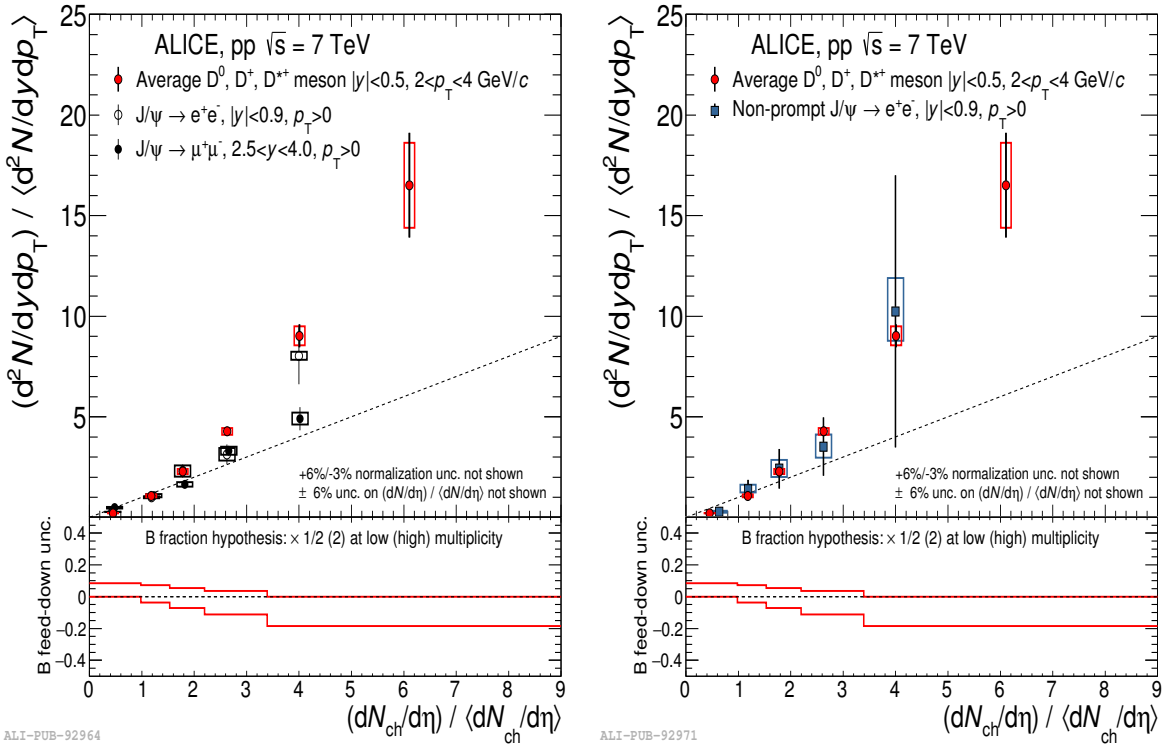

(a) (b)

Figure 1-17: (a) Relative inclusive J/ψ and D meson yield as function of relative charged-particles multiplicity in pp collisions at $\sqrt{s} = 7$ TeV at mid- and forward rapidities. (b) Non-prompt J/ψ and prompt D meson yield vs multiplicity at mid-rapidity [100].

yield as a function of multiplicity were measured at mid-rapidity [100]. These ALICE studies showed an increase of the relative the J/ψ production and the D mesons with increasing relative charged-particles multiplicity, as shown in Figure 1-17. These measurements are done in two ways. At mid-rapidity, both observables particle yield and $dN_{ch}/d\eta$ are measured at same rapidity region while at forward rapidity measurement, $dN_{ch}/d\eta$ computed in mid-rapidity ($|\eta| < 1$) and J/ψ yield is determined at forward-rapidity. A stronger than linear increment is observed at mid-rapidity. The fact that both D and J/ψ production increase as a function of multiplicity suggests that this is related to charm production rather than to a specific hadronisation process.

The results from STAR collaboration in pp collisions at lower collision energies at $\sqrt{s} = 200$ and 500 GeV also show similar increasing trend of relative yield J/ψ

as a function of charged-particle multiplicity [101, 102]. The measurement is done by calculating J/ψ for integrated p_T and $p_T < 1.4$ and $p_T < 4$ GeV/c. The results show with an increase of transverse momentum the increment of yield becomes more stronger. The results are in good agreement with PYTHIA8 and percolation model calculations (discussed in Section 1.5). Figure 1-18 shows multiplicity dependence of J/ψ yield at $\sqrt{s} = 200$ GeV, PYTHIA8 model comparison EPOS3 model calculations of D° mesons.

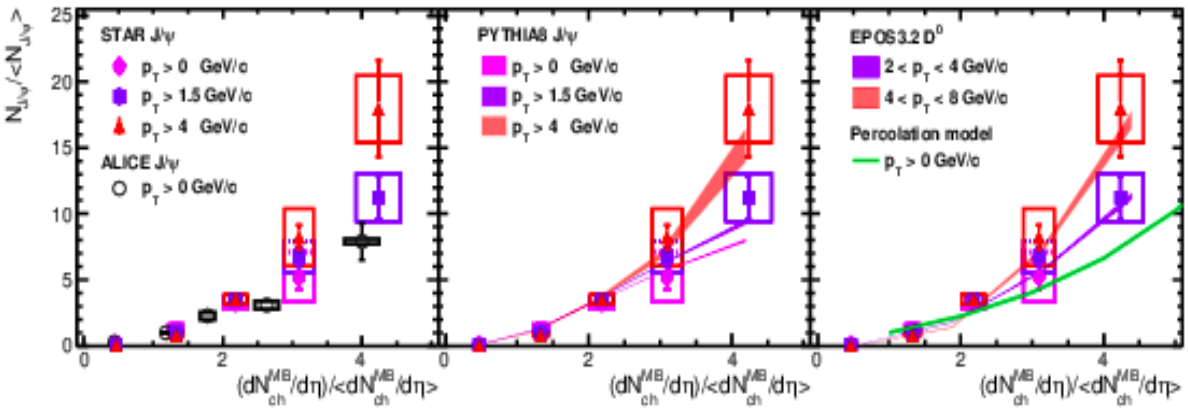

Figure 1-18: Relative J/ψ yield as a function of event multiplicity in three p_T regions in pp collisions at $\sqrt{s} = 200$ GeV [101].

The multiplicity dependence of J/ψ has also been studied in p-Pb collisions with ALICE detector at $\sqrt{s_{\rm NN}} = 5.02$ TeV in forward ($2.03 < y_{\rm cms} < 3.53$), backward ($-4.46 < y_{\rm cms} < -2.96$) and mid-rapidity ($-1.37 < y_{\rm cms} < 0.43$) regions, as shown in Figure 1-19 [103]. An increment of relative J/ψ yield is observed in all three rapidity regions at low multiplicities. The forward rapidity region shows saturation towards higher multiplicities.

The ratio of the yields at forward and backward rapidities $R_{\rm FB}$ as a function of multiplicity is shown in Figure 1-20 (a). The figure shows a clear suppression of the J/ψ yield at forward rapidity with respect to backward rapidity and the suppression increases with increasing charged-particles multiplicity, which is consistent with the calculation with gluon shadowing. The relative average transverse momentum ($\langle p_{\rm T} \rangle$) of J/$\psi$ as a function of charged-particles density is reported for forward and backward rapidities in Figure 1-20 (b), the same trend is observed for the two rapidity

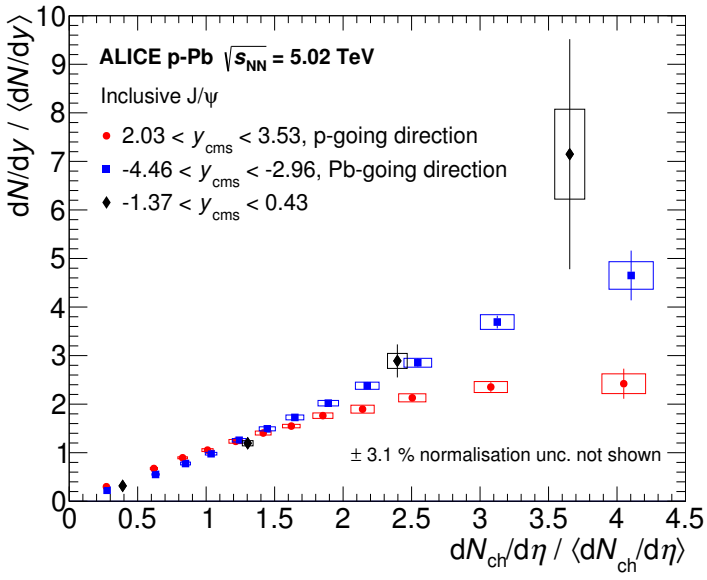

Figure 1-19: Relative inclusive J/ψ yield as a function of relative charged-particles multiplicity in three rapidity regions in p-Pb collisions at $\sqrt{s_{\rm NN}}$ = 5.02 TeV.

ranges [103]. The dashed lines represent the $\langle p_T \rangle$ of charged-hadrons as a function of multiplicity in the mid-rapidity region.

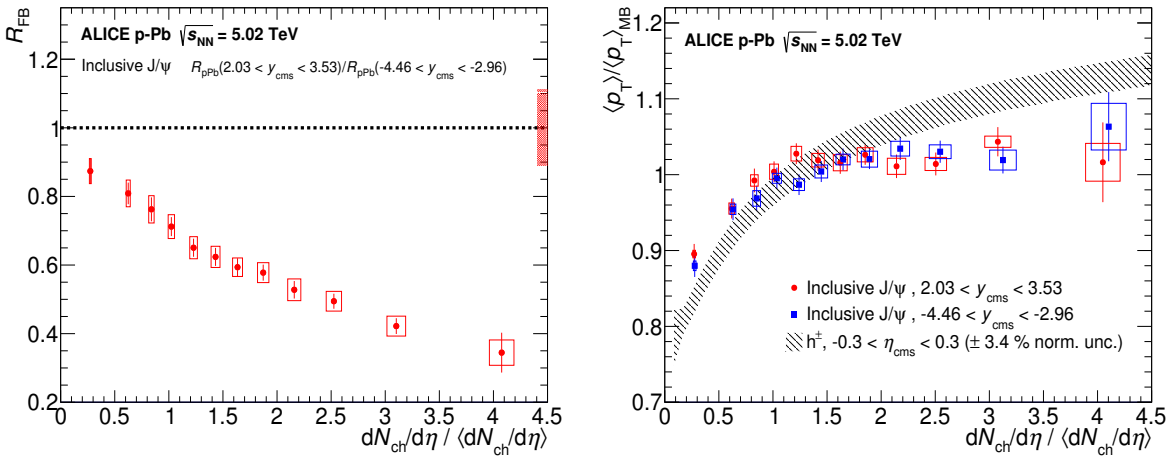

(a) (b)

Figure 1-20: (a) The ratio $R_{\rm FB}$ of inclusive J/ψ in p-Pb collisions at $\sqrt{s_{\rm NN}}$ = 5.02 TeV as a function of multiplicity. (b) Relative $p_{\rm T}$ for J/ψ as function of relative charged-particles multiplicity for forward and backward rapidity.

In ALICE with Run2 data, the same study has been carried out in pp collisions at $\sqrt{s}$ = 13 TeV in the mid-rapidity region and compared with the previous results

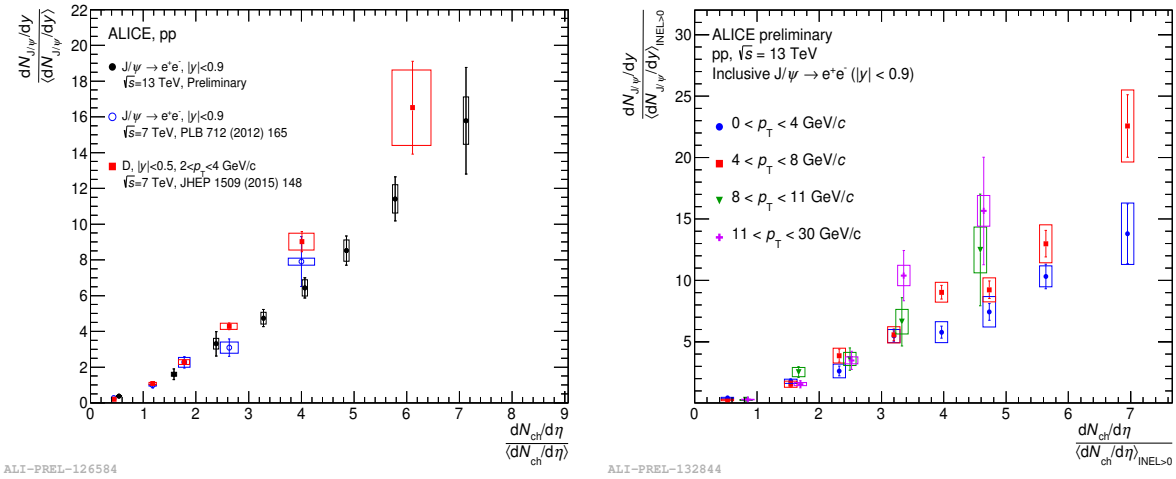

(a) (b)

Figure 1-21: (a) Comparison of relative J/ψ yield at $\sqrt{s} = 7$ TeV, 13 TeV and D mesons yield at $\sqrt{s} = 7$ TeV as function of relative charged-particles multiplicity in pp collisions. (b) Normalised J/ψ yield as a function of relative charged-particles multiplicity in pp collisions at $\sqrt{s} = 13$ TeV with EMCAL in four different p_{T} bins.

obtained by ALICE in pp collisions and is shown in Figure 1-21 (a) [104]. The multiplicity range is much larger, spanning twice the range than explored in the previous study. The observed trend is similar but the slope is significantly larger than unity. The EMCAL triggered events allow to study high p_{T} as well as high multiplicity events. ALICE measured the J/ψ normalized yield as a function of the normalized charged-particles multiplicity up to $p_{\mathrm{T}} = 30$ GeV. The p_{T} window is divided in four p_{T} bins, as shown in Figure 1-21 (b). This analysis indicates stronger than a linear increase of J/ψ yield as a function of multiplicity with increasing transverse momentum. Results obtained using PYTHIA8.2 event generator agree with experimental data in the defined p_{T} intervals. The relative J/ψ yield increases steeply with multiplicity in pp at 13 TeV, and the effect is stronger for high p_{T}. The larger statistics collected in Run-2 at LHC allowed us to extend the measurement to larger charged-particles multiplicities and to higher p_{T}. The experimental results are qualitatively described by the existing theoretical models. It will be interesting to explore the energy dependence of the self-normalised J/ψ yield as a function of charged-particles multiplicity over a wider $\sqrt{s}$ range.

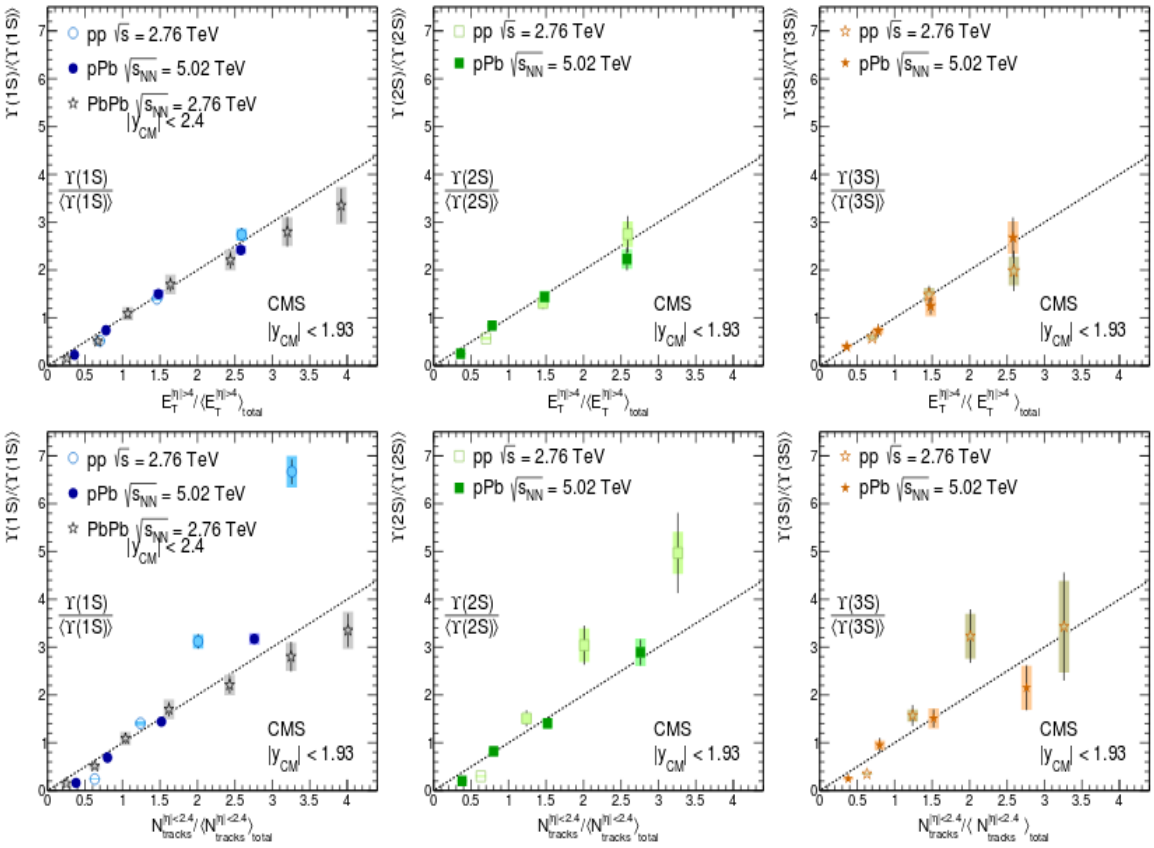

Figure 1-22: Event activity of $\Upsilon(1S)$, $\Upsilon(2S)$, $\Upsilon(3S)$ yield as a function of multiplicity and transverse energy [105].

In Figure 1-22 the dependence of event activity of Υ production as well as it's resonance states are shown in pp (Pb-Pb) collisions at $\sqrt{s}$ ($\sqrt{s_{\rm NN}}$) = 2.76 TeV, p-Pb collisions at $\sqrt{s_{\rm NN}}$ = 5.02 TeV, measured by CMS experiment [105]. The results are compared with the results of Pb-Pb collisions at $\sqrt{s_{\rm NN}}$ = 2.76 TeV. The bottomonia states are measured at centre of mass rapidity ($|y_{\rm cms}| < 1.93$) in each case and for x-axis two different estimators have been calculated. One is charged-particles multiplicity at mid-rapidity ($|\eta| < 2.4$) and another is transverse energy at forward rapidity ($4 < \eta < 5.2$). A consistent linear increment can be seen in all three states if a η gap is introduced irrespective of the collision systems. In the case of pp, while yield and estimators are measured at the mid-rapidity, a stronger than the linear increment is observed. The results also show that the ratio of yield of higher states to the ground state decreases as a function of multiplicity in pp and p-Pb collisions. Due to large

statistical uncertainties the Pb-Pb results are not significant.

Moving on to the light flavour sector, in ALICE, the multiplicity dependence study has been performed for high- p_T charged-hadrons in pp collisions at $\sqrt{s} = 5.02$ and 13 TeV [106]. The multiplicity is estimated by taking the signal combination of V0C and V0A (V0M) detector in ALICE as well as tracklet multiplicity[8]. From Figure 1-23 (a) it is observed that stronger than the linear increment of charged-hadrons irrespective of the estimators and $\sqrt{s}$. Figure 1-23 (b) gives the motivation for the study of mean transverse momentum as function of event multiplicity in pp collisions. The ALICE measurement shows $\langle p_T \rangle$ of charged-particles as function of N_{ch} in pp collisions at $\sqrt{s}$ = 0.9, 2.76 and 7 TeV, in p-Pb collisions at 5.02 TeV and Pb-Pb collision at 2.76 TeV at mid-rapidity, $|\eta| < 0.3$ as a function of charged-particles multiplicity [107]. An increase of $\langle p_T \rangle$ as a function multiplicity as well as $\sqrt{s}$ is observed in pp collisions. The $\langle p_T \rangle$ at higher multiplicity in p-Pb and Pb-Pb collisions exhibits a saturation which is similar to the case of J/ψ.

Therefore, all these experimental observations present strong motivation to investigate the multiplicity dependence study of hard probes more precisely. In ALICE such studies have been performed at the currently available collision energies namely, pp collisions at $\sqrt{s} = 2.76$, 5.02 (this work) and 13 TeV and in p-Pb collisions at $\sqrt{s_{\rm NN}} = 8.16$ TeV.

1.5 Theoretical model predictions

Several theoretical models have been employed to explain the increasing trend of yield with multiplicity. The theoretical model calculations of multiplicity dependence of J/ψ productions have been carried out in pp collisions at $\sqrt{s} = 13$ TeV in the mid-rapidity region and compared with the results obtained by ALICE in pp collisions (shown in Figure 1-24 [104]). These results have been compared to the predictions from theoretical models (Figure 1-24) by Ferreiro [108], EPOS3 by Werner et al [60], PYTHIA8 [59], Kopeliovich [109]. All models predict a J/ψ enhancement with mul-

[8]Definitions of these estimators and detector description are given in chapter two

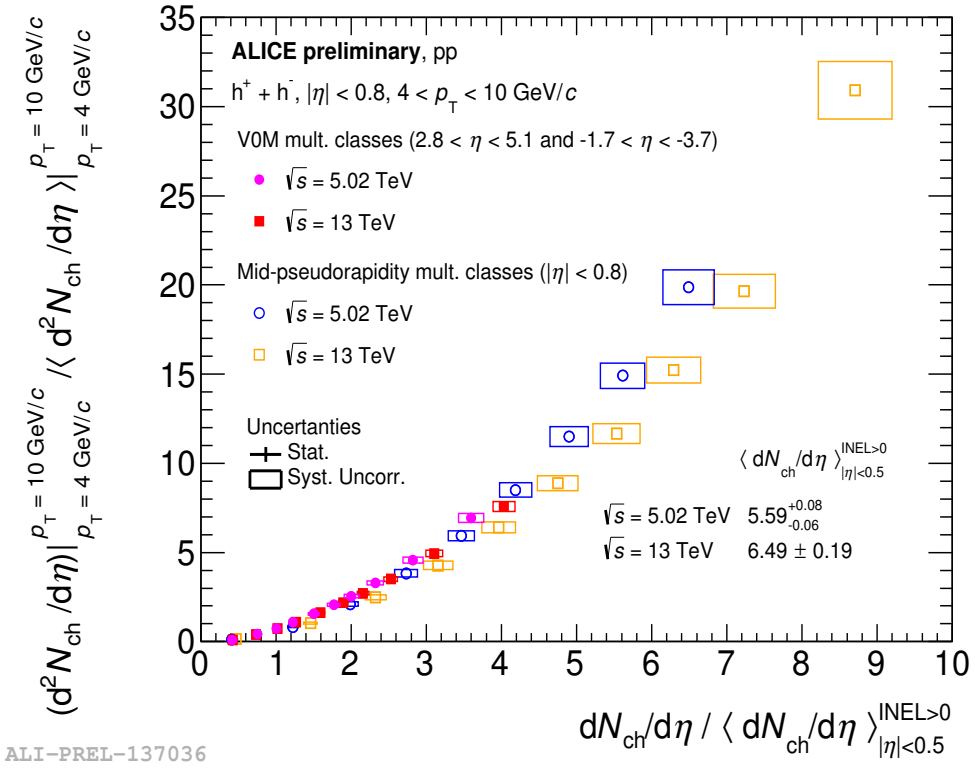

(a)

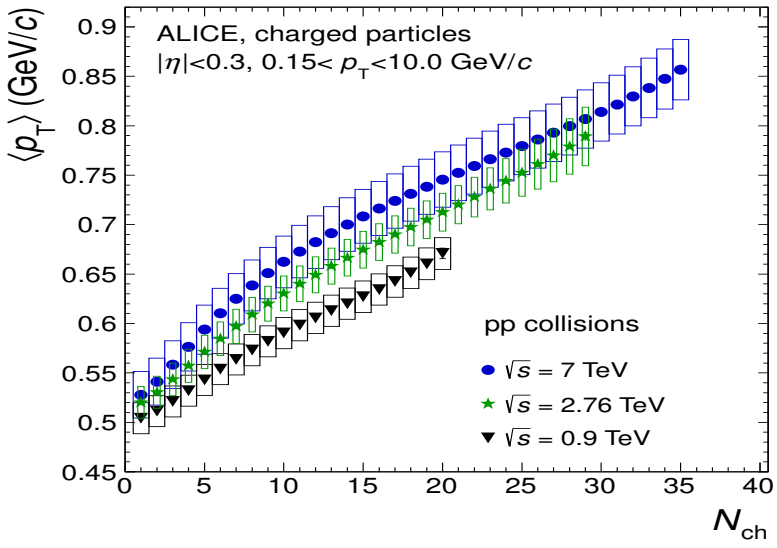

(b)

Figure 1-23: (a) Relative charged-hadron yield at $\sqrt{s} = 5.02$ and 13 TeV as function of V0M and tracklet multiplicity in pp collisions [106]. (b) $\langle p_T \rangle$ of charged-particles as function of multiplicity in pp collisions at $\sqrt{s} = 0.9$, 2.76 and 7 TeV [107].

tiplicity. However, at higher multiplicity values, the models show different trends. EPOS3 model is in fair agreement with the data. PYTHIA8 results under estimate the data at higher multiplicity region. Figure 1-25 shows the data comparison of PYTHIA8 model for charged-hadrons at mid-rapidity ($|\eta| < 0.8$) for three p_T regions for the same collision energy. At high p_T steeper increment is observed as a function of multiplicity similar to heavy flavour particles. PYTHIA8 describes well the data in lower multiplicity region in all cases, it overestimates the data towards higher multiplicity, and deviation gets stronger at high p_T.

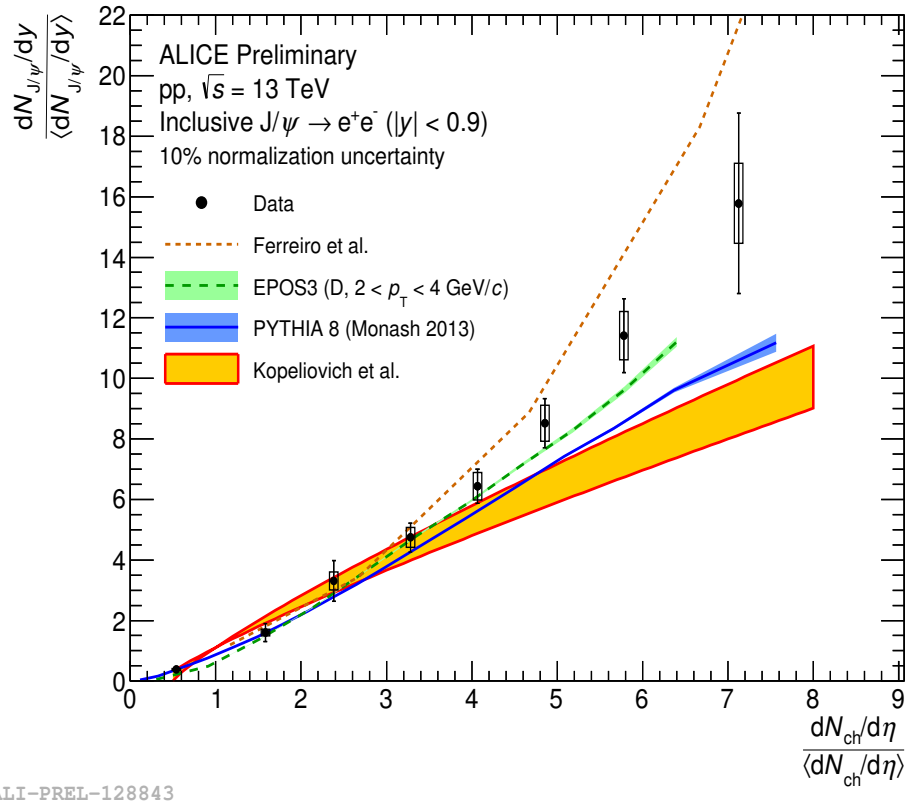

Figure 1-24: Dependence of relative J/ψ as a function of multiplicity in pp collisions at $\sqrt{s} = 13$ TeV compared with theoretical models [8].

Figure 1-26 represents the comparison of open charm yield as a function of multiplicity with PYTHIA8, percolation model, EPOS3 with and without hydrodynamic expansion in four p_T intervals. At lower p_T interval and lower multiplicity regions, all the models well describe the data while at high multiplicity only percolation model gives fair descriptions. The models underestimate the data as we go towards high p_T

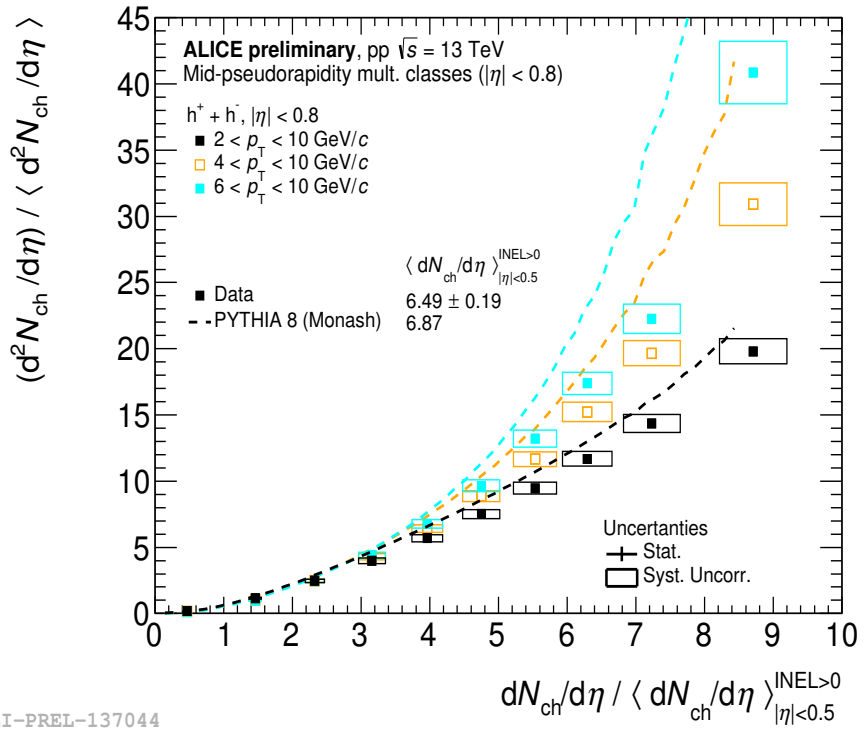

Figure 1-25: The multiplicity dependence of charged-hadrons in pp collisions at $\sqrt{s} = 13$ TeV compared to PYTHIA8 model prediction [106]

intervals. It can also be interpreted from these measurements that the hydrodynamic features are necessary for a better description of the data in multiplicity dependence study.

In connection with model prediction, the results have been discussed from CDF collaboration in p$\bar{p}$ collisions at $\sqrt{s} = 1.96$ TeV [110]. The $\langle p_T \rangle$ of total particles was measured at mid-rapidity ($|\eta| < 1$) and the data were compared with various tunes of PYTHIA6. The PYTHIA6 results with MPI and tuned with $p_T = 0$ and 1.5 GeV/c showed good agreement with data at lower multiplicities. On the other hand, the multiplicity dependence of the $\langle p_T \rangle$ without MPI increases faster as a function of multiplicity. ALICE results of $\langle p_T \rangle$ of charged-hadrons have also been compared with various models [107]. In pp collisions, the PYTHIA8 is tuned with and without color re-connection (CR) mechanism (will discuss later in Section 1.5.2) along with MPI [111, 112]. Thus, model predictions are in good agreement with the data. In

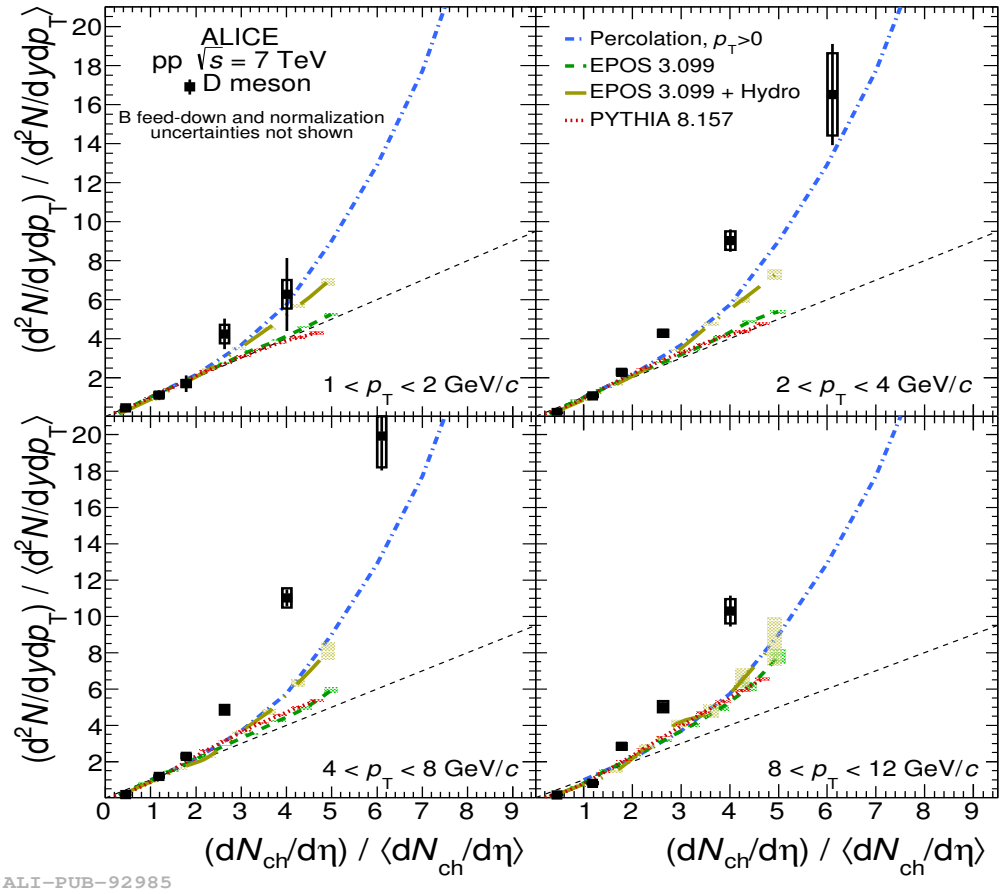

Figure 1-26: The multiplicity dependence of average D mesons in pp collisions at $\sqrt{s} = 7$ TeV compared to different models [100]

p-Pb collisions, the calculation with MPI and CR mechanism fail to describe the data. Only the EPOS model, which includes collective flow parametrization gives fair agreement to data [113]. The observed saturation of the $\langle p_T \rangle$ in p-Pb and Pb-Pb collisions towards high multiplicity can be interpreted as re-distribution of the spectrum due to re-scattering of constituents nucleons due to a locally thermalized medium which shows collective hydrodynamic behaviour. No model prediction could give a satisfactory description of the data in Pb-Pb collisions.

It is intriguing to observe if these theories hold true for $\langle p_T \rangle$ of J/ψ in pp collisions or not. We have discussed $\langle p_T \rangle$ of J/ψ in p-Pb collisions and a theoretical investigation will provide more insight to understand the evolution of $\langle p_T \rangle$ as a function of event activity. The models that have been used in the present thesis are briefly described

in the following sections.

1.5.1 The PYTHIA model

PYTHIA is one of the most widely used general-purpose event generators for pp collisions. It was first released in 1978. This QCD inspired MC event generator also works for leptons, hadrons and recently added heavy-ion (pA, AA) collisions. It includes diverse physics processes at different stages of the collisions specially programmed to simulate physics mechanisms that can occur in high-energy particle collisions at LHC. A sketch of the complex physics mechanisms involved in pp collisions is shown in Figure 1-27. PYTHIA is in continuous development mode, updating new features from time to time. PYTHIA6 was written in FORTRAN. PYTHIA8 is the improvised version of PYTHIA6, written in C++ programming language. A detailed description of PYTHIA6 can be found in reference [114] and the recent developments in physics processes are given in reference [115]. A large number of hard and soft processes are available in PYTHIA, for example, hard QCD processes 2→2, open charm and bottomia production, electroweak processes, such as photon collision, single and pair weak bosons production, charmonia and bottomia production via color singlet and color octet mechanism, singly and pair top productions as well as Higgs and SUSY (super symmetric particles) mechanisms etc. In the soft process part, it includes the total cross-section in hadronic collisions, including elastic, diffractive and non-diffractive topologies and so forth.

- **Parton Distribution Functions** : We have discussed PDFs in Section 1.3. There are total sixteen sets of PDFs for protons, a few for pion, pomerons and leptons are available in PYTHIA8. The PYTHIA is based on LO framework, where the PDFs can be interpreted as the number density of partons. The moderate-x regions and for the hard interactions the LO PDFs are suitable while for MPI and underlying events the NLO PDFs are used. The PDFs studies based on PYTHIA are reported in reference [117].

- **Parton showers** : In hard processes, due to large momentum transfer, the

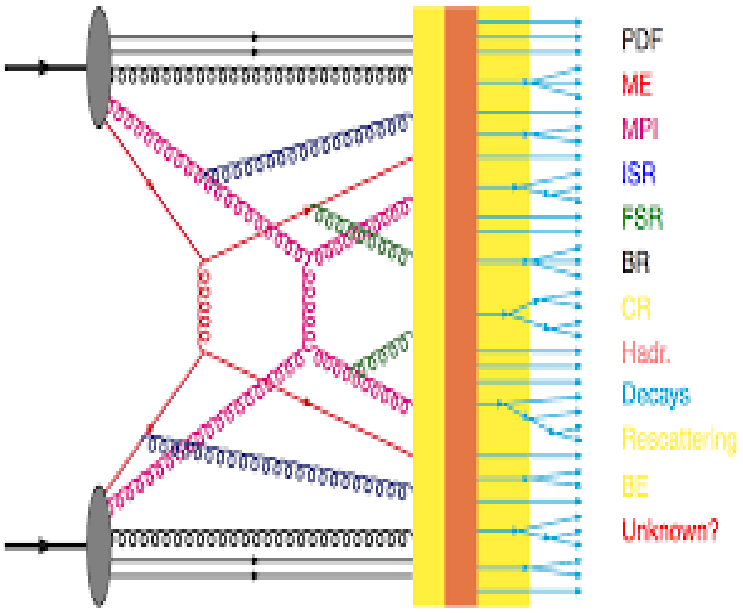

Figure 1-27: The layout of a typical pp collision in PYTHIA [116].

partons, as well as any new particles with color, are highly accelerated. This acceleration results in radiation of virtual gluons, which can themselves emit further gluons (radiation) or produce $q\bar{q}$ pairs. This leads to the formation of parton showers. The parton showers are based on space like Initial State Radiation (ISR) and time like Final State Radiation (FSR) algorithms [118, 119]. The final-state parton showers trigger the process of hadronisation. The parton showers of the incoming hadrons may undergo multiple interactions which produce the underlying events.

- **Multi Partonic Interaction** : The MPI process is a hallmark for PYTHIA. The idea of multiple interactions is to view the hadrons as bunches of partons arising from a single pp collision. More detail is given in Section 1.5.2.

- **Beam remnants** : Each incoming parton may leave behind a beam remnant after going through several hard scattering processes. The beam remnants contain partons with flavours given by the lost valence quarks and require sea quarks for the overall flavour conservation. The gluons also may be present in the remnant as an origin of the remaining sea-quark pairs. Hence, beam remnants are used to distinguish between valence and sea quarks and to obtain a consistent set

of flavours after the perturbative evolution is finished. They may also produce color singlets by reducing total color charge via the gluon initiators [115].

- **Color reconnection** : The color reconnection (CR) mechanism is sub-process of hadronisation associated with a parton shower, MPI and beam remnants. According to CR, a minimum number of hadrons share the transverse momentum of the partons, $i.e.$ the total string length between the partons become as small as possible. Hence, the total multiplicity reduces because of the reconnected strings [120]. The details of various model implementations of CR is described in the updated PYTHIA8.2 manual [115].

- **Hadronisation** : The formation of final state color-neutral hadrons or hadronisation process in PYTHIA is based on the Lund string fragmentation framework [121]. At parton shower level the perturbative QCD is not applicable. The non-perturbative lattice QCD is useful to explain the scenario. In the string model, the q and $\bar{q}$ move apart very fast after being produced each carrying half of the total energy at the centre of mass frame. The gluonic string connected with the $q\bar{q}$ stretched, and the potential energy stored in the string increases. When the potential energy becomes the order of the hadron mass, the string breaks and a new pair of $q\bar{q}$ is produced. This process continues till the invariant mass of these strings are large enough to produce $q\bar{q}$ pairs. Thus, this process leaves only on-shell hadrons with small strings. The string breaking process is favourable for light quarks because of their low p_T relative to the string axis. The heavy quarks are less likely to be produced because of their large mass. The hadronisation mechanism can be neglected for quarkonia production in PYTHIA. A cluster model has been proposed for heavy quarks and quarkonium states [119].

- **Resonances and particle decays** : The resonances have a lifetime shorter than the hadronisation scale, and they decay along with the hard process. So the total cross-section is dependent on resonance decay channels. On the other hand, particle decays take place after hadronisation and any change in the decay channels does not affect the total cross-sections. In PYTHIA, the low mass res-

onances and quarkonium are treated as particles rather than resonances. This way the decay of $J/\psi \to \mu^+ + \mu^-$ does not affect cross-section of the hard process $gg \to \mathrm{J}/\psi + \mathrm{g}$. The J/$\psi$ can also be produced from parton showers, string fragmentation and particle decay, such as $g \to b\bar{b}$, $\bar{b} \to B$, $B \to J/\psi$. One has to be very careful in choosing the physics process as any bias in the hard process level affect the production mechanism of the desired particle [115].

In PYTHIA various physics components are governed by a set of parameters which are determined by comparing them with experimental data. These sets of parameters are known as tunes. The first tune was based on RHIC and LEP data before the LHC era. Most recent tune in PYTHIA8 is Monash. It is the default tune in PYTHIA since 2013 [122]. However, in this thesis work, we have used PYTHIA8.2 with 4C tune [123] for theoretical model comparison which is widely used for LHC data. In this tune, the MPI and the CR have been included or excluded and the corresponding numerical data have been compared with experimental data to observe therein effects at LHC energies.

1.5.2 MPI study with PYTHIA

In order to explore the high multiplicity events, the small systems and the emergence of collectivity in small systems, it is mandatory to understand the initial state and the relation between the soft and the hard component of events. The MPI directly influnces the charged-particles multiplicity of an event. Thus, the multiplicity dependence of the J/ψ production will also be affected by the MPI. The contribution of MPI in the hard processes is not well understood yet. But the rise of the J/ψ yield in pp collisions as a function of multiplicity could be explained in terms of MPI study.

In Figure 1-28 multiplicity distribution of charged-particles is shown for pp collisions at $\sqrt{s} = 5.02$ TeV for $|\eta| < 1$. The multiplicity distribution is well described by PYTHIA when MPI and CR are included (Table 1.2). The simulation without MPI underestimates the data. On the the other hand, switiching off CR overestimates the data. The charged-particle density is computed at experimental energies and com-

pared with data for inelastic > 0 events (Table 1.2). The inelastic > 0 event class is defined as at least one charged-particles within $|\eta| < 1$. Figure 1-28 also shows that PYTHIA results are in good agreement to the data at $\sqrt{s} = 5.02$ TeV. However, at lower centre of mass energies, the present PYTHIA tune fails to describe the data. It's worth mentioning that data and the PYTHIA results can not be compared di-

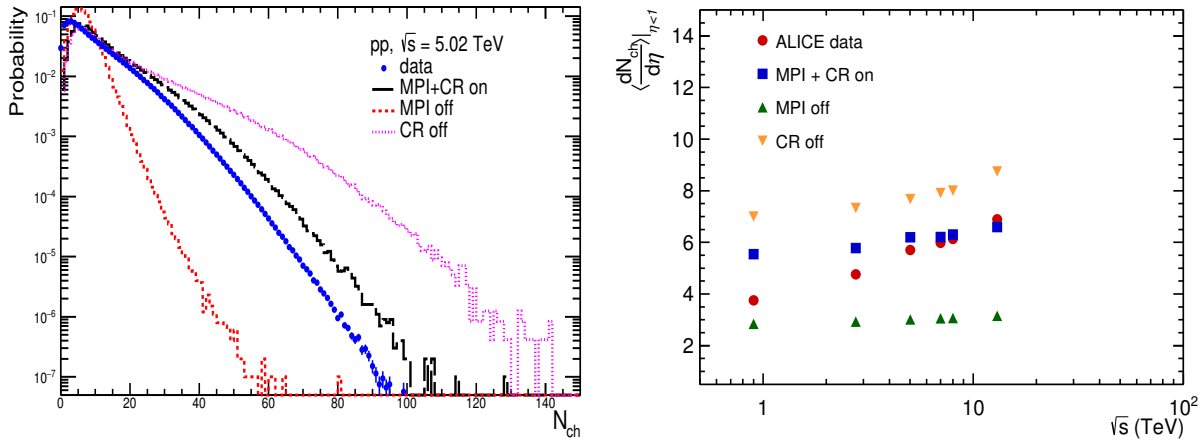

(a) (b)

Figure 1-28: (a) Charged-particle multiplicity distribution comparison between data and PYTHIA. (b) The charged-particles pseudo-rapidity density as a function of $\sqrt{s}$ compared to PYTHIA8 results. Experimental data points are taken from reference [82] for this thesis.

rectly as in PYTHIA, the detector efficiency is not taken into account. These rough estimations have been performed to highlight the importance of MPI along with CR. There is a correlation between MPI and CR effects in the charged-particles multiplicity. This correlation is also reported in this reference [77]. The detailed simulation study with PYTHIA model is presented in chapter 6.

1.5.3 Percolation model

The percolation string model was proposed to address the increase of the relative J/ψ yield as a function of self-normalised charged-particle multiplicity in pp collisions which was observed by the ALICE experiment [108, 124]. The model is given by E. G. Ferreiro and C. Pajares, and is based on the assumption that the color ropes, the

$\sqrt{s}$	$dN_{ch}/d\eta$			
	$Data$	$MPI + CR$ on	$MPI\ off$	$CR\ off$
0.9	3.75	5.54	2.84	7.00
2.76	4.76	5.78	2.93	7.33
5.02	5.70	6.20	3.01	7.67
7	5.98	6.21	3.06	7.91
8	6.13	6.30	3.07	8.01
13	6.89	6.59	3.15	8.75

Table 1.2: The comparison $dN_{ch}/d\eta$ ($|\eta| < 1$) with PYTHIA8 4C tune in pp collisions at the LHC energies.

flux tube or the string with non-negligible transverse size, are the source of particle production. The number of produced strings N_s gives the number of parton-parton collisions. The strings can interact and overlap at higher densities mainly for the soft particles production. The hard probes like J/ψ are proportional to the number of collisions and thus, as per this model $N_{J/\psi} \propto N_s$. The soft particle production in a rapidity region is governed by the number of participants in the collisions and the reduction in the number of soft particles at high CM energies may be due to parton saturation or string interaction. Hence, the charged-particles multiplicity is related to the number of strings by the following definition

$$\frac{dN_{ch}}{d\eta} = F(\rho) N_s \mu_1 \tag{1.5}$$

where $F(\rho) = \sqrt{1 - e^{-\rho}}/\rho$ is the damping factor introduced by the string interaction and μ_1 represents the multiplicity of the strings in given η range. $\rho = \frac{N_s \sigma_0}{\sigma}$ is the string density; σ_0 represents the transverse area of a string while σ denotes the transverse area of the collision. At small N_s, the string density is small, which leads to the decrease of $F(\rho)$ thereby affecting the soft particle production. Thus, at low multiplicity, the linear dependence of hard probe yield (both proportional to N_s) is observed due to limited parton-parton interaction. While at high multiplicity, $i.e.$ at high string density, the effect of $F(\rho)$ is significant along with an increase in σ. This leads to a quadratic increase at higher multiplicities as observed in Figure 1-24 and 1-26.

1.5.4 Higher Fock states model

The model, proposed by B. Z. Kopeliovich, H. J. Pirner, I. K. Potashnikova, K.Reygers and I. Schmidt is based on the analogy between high multiplicity pp and p-A collisions [109]. Larger hadron multiplicities as compared to the mean value in collisions can be reached at high energy due to the enhanced number of gluons in hadron-nucleus collisions. In this case, due to the higher number of nuclei, gluons overlap in the longitudinal direction at low x-region. Thus, the nucleus act as a single source of gluon similar to the contribution of higher Fock components in a single nucleon. Because of these increasing number of gluons, the relative J/ψ production rate is enhanced. Since a gluon rich environment is abundant for a large number of production of heavy flavour particles. This model also gives the linear increment of hard probes as a function of soft probes (Figure 1-24).

1.5.5 EPOS3 model

The energy conserving quantum mechanical multiple scattering approach, based on the parton ladders, the off-shell remnant, and the splitting of parton ladders is known as EPOS. It is a real (one event at LHC = one event at EPOS) event generator [125]. In EPOS, the MPI is based on combining the pQCD with Gribov-Regge theory [52] which gives the quantum treatment for MPI. EPOS also includes hydrodynamical approach and is able to describe radial flow in heavy-ion collisions at LHC energies [113]. The latest version of this event generator is EPOS3 [60]. In EPOS3, the initial interactions splits into a core and a corona part depending on the momentum and density of the string fragments. The hard particles in the corona escape due to higher momentum whereas the soft particles in the core are treated with a viscous hydrodynamic expansion. The production of heavy quarks and prompt photons mechanism have been implemented and same treatment is applied for pp, p-A and A-A collisions [126]. From Figure 1-24 and 1-26, it can be concluded that EPOS3 well describes the ALICE data.

1.5.6 AMPT

A Multi Phase Transport (AMPT) is MC generator generally used for heavy-ion collisions at relativistic energies. This model is given by Che-Ming Ko, Bao-An Li, Zi-Wei Lin, Subrata Pal, and Bin Zhang [127, 128] which includes both initial partonic and final hadronic interactions, and the transition between these two phases of matter. AMPT unifies four main features with the aim to provide kinematic description of all essential stages of p-A and A-A collisions. The collision energy range of AMPT is $\sqrt{s_{\rm NN}}$ = 5 to 5500 GeV. The initial conditions which are generated by the Heavy Ion Jet Interaction Generator (HIJING) model, partonic interactions which are treated by Zhang's Parton Cascade (ZPC) model, the conversion from the partonic to the hadronic matter, and hadronic interactions are modelled by A Relativistic Transport (ART) model. The formation of thermalized medium and reach equilibrium state do not necessarily hold for every heavy-ion collisions. Due to the finite size and energy, the medium produced in a heavy-ion collision may not reach the full chemical and thermal equilibrium state. AMPT model is used to describe such dynamic systems. The HIJING model includes mini jets and soft strings, then ZPC describes scattering among the partons followed by Lund string fragmentation to reach hadronisation. The ART model is included later to describe the scattering among the resulting hadrons. The extended ART includes hadron cascade and secondary interactions for light flavour resonance particles. The AMPT model successfully able to describe the data from SPS, RHIC and LHC [129, 130, 131]. Two versions of AMPT models are available, default and string melting. In default version the hadronisation occurs via Lund string fragmentation and quark coalescence performs the hadronisation in the string melting process [131, 132]. This model has been used to compare the results from experimental data in chapter 7.

1.5.7 Structure and purpose of this thesis

The J/ψ production as a function of the global observable, *i.e.* charged-particle multiplicity, may provide an insight to the interplay between the soft and hard processes.

The evolution of mean transverse momentum is another observable in this connection which might indicate about collectivity in small systems. Therefore, the study of charmonia production as a function of charged-particles multiplicity is carried out in pp collisions at $\sqrt{s}$ = 2.76 and 5.02 TeV with the data collected from the ALICE detector at LHC. In addition, the soft probes, like forward-backward multiplicity correlations and event-by-event fluctuations in heavy-ion collisions have been studied using the data taken from the experiments performed by of EMU01 collaboration.

In chapter 2, the ALICE detector and the experimental set-up and data samples are described extensively.

Chapter 3 deals with the analysis of charged-particles multiplicity using the various approaches in pp collisions at $\sqrt{s}$ =2.76 and 5.02 TeV. The analysis is carried out for inelastic $>$ 0 event class. The new analysis techniques, used to calculate the efficiency corrections for events, have been described.

Chapter 4 presents the J/ψ yield measurement in pp collisions at $\sqrt{s}$ = 2.76 and 5.02 TeV at forward rapidity. The measurement of the production cross-section is also reported for consistency purpose.

Chapter 5 gives the detail of measurements of the mean transverse momentum of J/ψ production in pp collisions at $\sqrt{s}$ = 5.02 TeV. The experimental results are also compared with other available results from ALICE to investigate the energy, rapidity and collision system dependencies.

In chapter 6, the results of J/ψ production yield and $\langle p_T^{J/\psi} \rangle$ as a function of multiplicity are compared with various model predictions. An extensive model calculation of multiplicity dependence of J/ψ production is carried out using PYTHIA8.2. This model calculation study has been extended further in terms of event shapes and non-extensive thermodynamics in pp collisions at $\sqrt{s}$ = 5.02 and 13 TeV.

Chapter 7 deals with the study of correlation and fluctuations using experimental data in heavy-ion collisions. The results are compared with AMPT model predictions.

Chapter 8, is devoted for summary and further scope of research in this field.

Bibliography

[1] D. Griffiths, "Introduction to Elementary Particles", (2008), Wiley-VCH, ISBN-13: 978-0-471-60386-3.

[2] M. Tanabashi et al., Particle Data Group Collaboration, "Review of Particle Physics", Phys. Rev. D98 (2018) 030001.

[3] M. E. Peskin, "An Introduction to Quantum Field Theory", (1995), Perseus Books, ISBN-0: 201-50397-2.

[4] P. W. Higgs, "Broken Symmetries Massless Particles and Gauge Fields", Phys. Lett. 12 (1964) 132.

[5] G. Aad et al., ATLAS Collaboration, "Observation of a New Particle in the Search for the Standard Model Higgs Boson with the ATLAS Detector at the LHC", Phys. Lett. B716 (2012) 1.

[6] S. Chatrchyan et al., CMS Collaboration, "Observation of a New Boson at a Mass of 125 GeV with the CMS Experiment at the LHC", Phys. Lett. B716 (2012) 30.

[7] P. Z. Skands, "Introduction to QCD", (2017), World Scientific, ISBN: 978-981-4525-21-3.

[8] F. Muheim, "QCD-Quantum Chromodynamics", Lecture notes, https://www2.ph.ed.ac.uk/∼muheim/teaching/np3/lect-qcd.pdf

[9] The Royal Swedish Academy of Sciences, Press release, 5 October (2004), https://www.nobelprize.org/prizes/physics/2004/press-release/

[10] F. Wilczek,"QCD Made Simple", Physics Today 53 (2000) 8.

[11] S. K. Choi et al., Belle Collaboration, "Observation of a Resonance-like Structure in the $\pi^+ - \psi'$ Mass Distribution in Exclusive $B \to K\pi^+ - \psi'$ Decays", Phys. Rev. Lett. 100 (2008) 142001.

[12] R. Aaij et al., LHCb Collaboration, "Observation of J/ψp Resonances Consistent with Pentaquark States in $\Lambda_b^0 \to J/\psi K^- p$ Decays", Phys. Rev. Lett. 115 (2015) 072001.

[13] Y. L. Dokshitzer, "Perturbative QCD for Beginners", (2002), Springer, Dordrecht, ISBN: 978-1-4020-1036-1.

[14] R. Gupta, "Introduction to Lattice QCD", Lect. Notes (1997) 150.

[15] S. Sarkar et al., "The Physics of the Quark-Gluon Plasma", Lect. Notes Phys. 785 (2010) 1.

[16] N. Haque, "Some Applications of Hard Thermal Loop Perturbation Theory in Quark Gluon Plasma", Doctoral thesis (2014), arXiv:1407.2473 [hep-ph].

[17] Z. Fodor et al., "Critical Point of QCD at Finite T and mu, Lattice Results for Physical Quark Masses", J. High Energy Phys. 04 (2004) 050.

[18] A. Bazavov et al., "Equation of state and QCD transition at Finite Temperature", Phys. Rev. D80 (2009) 014504.

[19] N. Brambilla et al., "Heavy quarkonium: Progress, Puzzles and Opportunities", Eur. Phys. J. C71 (2011) 1534.

[20] T. Matsui et al., "J/ψ Suppression by Quark-Gluon Plasma Formation", Phys. Lett. B178 (1986) 416.

[21] R. Thews et al., "Enhanced J/ψ Production in Deconfined Quark Matter", Phys. Rev. C63 (2001) 054905.

[22] P. Braun-Munzinger et al., "(Non)Thermal Aspects of Charmonium Production and a New Look at J/ψ Suppression", Phys. Lett. B490 (2000) 196.

[23] J. E. Augustin et al., SLAC-SP-017 Collaboration, "Discovery of a Narrow Resonance in e^+e^- Annihilation", Phys. Rev. Lett. 33 (1974) 1406; Adv. Exp. Phys. 5, (1976) 141.

[24] J. J. Aubert et al., E598 Collaboration, "Experimental Observation of a Heavy Particle J", Phys. Rev. Lett. 33 (1974) 1404.

[25] B. Abelev et al., ALICE Collaboration, "J/ψ Production as a Function of Charged Particle Multiplicity in pp Collisions at $\sqrt{s}$ = 7 TeV", Phys. Lett. B712 (2012) 165.

[26] Y. Lemoigne et al., "Measurement of Hadronic Production of the $\chi_1^{++}(3507)$ and the $\chi_2^{++}(3553)$ Through Their Radiative Decay to J/ψ", Phys. Lett. B113 (1982) 509.

[27] L. Antoniazzi et al., "Measurement of J/ψ and ψ' Production in 300 GeV Proton, Anti-Proton and $\pi^{\pm}$ Interactions with Nuclei", Phys. Rev. D46 (1992) 4828.

[28] L. Antoniazzi et al., "Production of J/ψ via ψ' and χ Decay in 300 GeV/c Proton and $\pi^{\pm}$-Nucleon Interactions", Phys. Rev. Lett. 70 (1993) 383.

[29] S. Acharya et al., ALICE Collaboration, "Prompt and Non-Prompt J/ψ Production and Nuclear Modification at Mid-Rapidity in p-Pb Collisions at $\sqrt{s_{\rm NN}}$ = 5.02 TeV", Eur. Phys. J. C78 (2018) 466.

[30] E. Braaten, "Introduction to the NRQCD Factorization Approach to Heavy Quarkonium", arXiv:hep-ph/9702225.

[31] A. Andronic et al.,"Heavy-Flavour and Quarkonium Production in the LHC era: From Proton-Proton to Heavy-Ion Collisions", Eur. Phys. J. C76 (2016) 107.

[32] H. Fritzsch, "Producing heavy quark flavors in hadronic collisions: A test of quantum chromodynamics", Phys. Lett. B67 (1977) 217.

[33] J. F. Amundson et al., "Quantitative Tests of Colour Evaporation: Charmonium Production", Phys. Lett. B390 (1997) 323.

[34] S. Acharya et al., ALICE Collaboration, "Energy Dependence of Forward-Rapidity J/ψ and ψ(2S) Production in pp Collisions at the LHC", Eur. Phys. J. C77 (2017) 392.

[35] Y. Q. Ma et al., "Quarkonium Production in an Improved Colour Evaporation Model", Phys. Rev. D94 (2016) 114029.

[36] V. Cheung et al., "Production and Polarization of Prompt J/ψ in the Improved Colour Evaporation Model Using the k_T-Factorization Approach", Phys. Rev. D98 (2018) 114029.

[37] C. H. Chang, "Hadronic Production of J/ψ Associated With a Gluon", Nucl. Phys. B172 (1980) 425.

[38] R. Baier et al., "Hadronic Production of J/ψ and Υ: Transverse Momentum Distributions", Phys. Lett. B102 (1981) 364.

[39] A. Pineda, "Heavy Quarkonium and Non relativistic Effective Field Theories", Nucl. Phys. B (Proc. Suppl.) 86 (2000) 517.

[40] C. Chao-Hsi, "Hadronic Production of J/ψ Associated with a Gluon", Nucl. Phys. B172 (1980) 425.

[41] R. Baier et al., "Hadronic Collisions: A Quarkonium Factory", Z. Phys. C19 (1983) 251.

[42] G. A. Schuler,"Quarkonium Production and Decays", arXiv:hep-ph/9403387.

[43] F. Abe et al.,"J/ψ and ψ(2S) Production in pp Collisions at $\sqrt{s}$ = 1.8 TeV", Phys. Rev. Lett. 79 (1997) 572.

[44] B. Abelev et al., ALICE Collaboration, "Measurement of Quarkonium Production at Forward Rapidity in pp Collisions at $\sqrt{s} = 7$ TeV", Eur. Phys. J. C74 (2014) 2974.

[45] M. Kramer, "Quarkonium Production at High-Energy Colliders", Prog. Part. Nucl. Phys. 47 (2001) 141.

[46] B. Paul et al., "Systematic Study of Charmonium Production in pp Collisions at the LHC Energies", J. Phys. G42 (2015) 065101.

[47] M. Cacciari et al., "The p_T Spectrum in Heavy-Flavour Hadroproduction", J. High Energy Phys. 7 (1998) 9805.

[48] M. Cacciari et al., "The p_T Spectrum in Heavy-Flavour Photoproduction", J. High Energy Phys. 103 (2001) 006.

[49] E. Iancu et al., "The Colour Glass Condensate and High-Energy Scattering in QCD", arXiv:hep-ph/0303204.

[50] F. H. Sawy et al., "Dynamic Characteristics of Proton-Proton Collisions", arXiv:1507.03156 [hep-ph].

[51] E. Halkiadakis, "Introduction to the LHC Experiments", arXiv:1004.5564 [hep-ex].

[52] P. D. B. Collins, "An Introduction to Regge Theory and High-Energy Physics", (2009), Cambridge Univ. Press, ISBN: 9780521110358.

[53] B. Abelev et al., ALICE Collaboration, "Measurement of Inelastic, Single- and Double-Diffraction Cross-Sections in Proton-Proton Collisions at the LHC with ALICE", Eur. Phys. J. C73 (2013) 2456.

[54] G. Aad et al., ATLAS Collaboration, "Measurement of the Inelastic Proton-Proton Cross-Section at $\sqrt{s} = 7$ TeV with the ATLAS Detector", Nat. Commun. 2 (2011) 463.

[55] V. Khachatryan et al., CMS Collaboration, "Measurement of Diffraction Dissociation Cross-Sections in pp Collisions at $\sqrt{s} = 7$ TeV", Phys. Rev. D92 (2015) 012003.

[56] A. Adare et al., PHENIX Collaboration, "Heavy-Flavor Electron-Muon Correlations in p+p and d+Au Collisions at $\sqrt{s_{\mathrm{NN}}} = 200$ GeV", Phys. Rev. C 89 (2014) 034915.

[57] R. Placakyte, "Parton Distribution Functions", arXiv:1111.5452 [hep-ph].

[58] F. D. Aaron et al., H1 Collaboration, "Inclusive Deep Inelastic Scattering at High Q2 with Longitudinally Polarised Lepton Beams at HERA", J. High Energy Phys. 9 (2012) 061.

[59] T. Sjostrand et al.,"A Brief Introduction to PYTHIA 8.1", Comput. Phys. Commun. 178 (2008) 852.

[60] K. Werner et al., "Analyzing Radial Flow Features in p-Pb and p-p Collisions at Several TeV by Studying Identified-Particle Production with the Event Generator EPOS3", Phys. Rev. C89 (2014) 064903.

[61] M. L. Miller et al., "Glauber Modeling in High Energy Nuclear Collisions", Ann. Rev. Nucl. Part. Sci. 57 (2007) 205.

[62] B. Abelev et al., ALICE Collaboration, "Centrality Determination of Pb-Pb Collisions at $\sqrt{s_{\rm NN}} = 2.76$ TeV with ALICE", Phys. Rev. C88 (2013) 044909.

[63] B. Betz, "Jet Propagation and Mach-Cone Formation in (3+1)-dimensional Ideal Hydrodynamics", Doctoral Thesis (2009), arXiv:0910.4114 [nucl-th].

[64] J. Y. Ollitrault, "Anisotropy as a Signature of Transverse Collective Flow", Phys. Rev. D46 (1992) 229.

[65] C. Y. Wong, "Introduction to High-Energy Heavy-Ion Collisions", (1995), Singapore: World Scientific, ISBN: 9789810202637.

[66] A. Adare et al., "Detailed Measurement of the e^+e^- Pair Continuum in p+p and Au+Au Collisions at $\sqrt{s_{\rm NN}} = 200$ GeV and Implications for Direct Photon Production", Phys. Rev. C81 (2010) 034911.

[67] Martin Wilde, ALICE Collaboration, "Measurement of Direct Photons in pp and Pb-Pb Collisions with ALICE", Nucl. Phys. A904 (2013) 573.

[68] Z. Conesa del Valle, "Vector Bosons in Heavy-Ion Collisions at the LHC", Eur. Phys. J. C61 (2009) 729.

[69] G. Aad et al., ATLAS Collaboration, "Measurement of Z boson Production in Pb+Pb Collisions at $\sqrt{s_{\rm NN}} = 2.76$ TeV with the ATLAS Detector", Phys. Rev. Lett. 110 (2013) 022301.

[70] S. Chatrchyan et al., CMS Collaboration, "Study of Z production in Pb-Pb and pp collisions at $\sqrt{s_{\rm NN}} = 2.76$ TeV in the dimuon and dielectron decay channels", J. High Energy Phys. 03 (2015) 022.

[71] V. Khachatryan et al., CMS Collaboration, "Study of W Boson Production in p-Pb Collisions at $\sqrt{s_{\rm NN}}$ =5.02 TeV", Phys. Lett. B750 (2015) 565.

[72] S. Acharya et al., ALICE Collaboration, "Measurement of Z^0-Boson Production at Large Rapidities in Pb-Pb Collisions at $\sqrt{s_{\rm NN}} = 5.02$ TeV", Phys. Lett. B780 (2018) 372.

[73] S. Chatrchyan et al., "Jet Momentum Dependence of Jet Quenching in Pb-Pb Collisions at $\sqrt{s_{\rm NN}} = 2.76$ TeV", Phys. Lett. B712 (2012) 176.

[74] K. Aamodt et al., ALICE Collaboration, "Higher Harmonic Anisotropic Flow Measurements of Charged Particles in Pb-Pb Collisions at $\sqrt{s_{\rm NN}}$ =2.76 TeV", Phys. Rev. Lett. 107 (2011) 032301.

[75] M. Arslandok, ALICE Collaboration, "Event-by-Event Identified Particle Ratio Fluctuations in Pb-Pb Collisions with ALICE using the Identity Method", Nucl. Phys. A956 (2016) 870.

[76] P. Braun-Munzinger et al., "Particle Production in Heavy-Ion Collisions", arXiv:nucl-th/0304013.

[77] J. F. Grosse-Oetringhaus et al., "Charged-Particle Multiplicity in Proton-Proton Collisions", arXiv:0912.0023 [hep-ex].

[78] Z. Koba et al., "Scaling of Multiplicity Distributions in High-Energy Hadron Collisions", Nucl. Phys. B40 (1972) 317.

[79] R. P. Feynman, "Very High-Energy Collisions of Hadrons", Phys. Rev. Lett. 23 (1969) 1415.

[80] J. Adam et al., ALICE Collaboration, "Centrality Dependence of the Charged-Particle Multiplicity Density at Mid-Rapidity in Pb-Pb Collisions at $\sqrt{s_{\rm NN}}$ = 5.02 TeV", Phys. Rev. Lett. 116 (2016) 222302.

[81] R. E. Ansorge et al., "Charged-Particle Multiplicity Distributions at 200 and 900 GeV C.M. Energy", Z. Phys. C43 (1989) 357.

[82] J. Adam et al., ALICE Collaboration, "Charged-particle Multiplicities in Proton-Proton Collisions at $\sqrt{s}$ = 0.9 to 8 TeV", Eur. Phys. J. C77 (2017) 33.

[83] I. Arsene et al., BRAHMS Collaboration, "Quark Gluon Plasma and Color Glass Condensate at RHIC? The Perspective from the BRAHMS Experiment", Nucl. Phys. A757 (2005) 1.

[84] B. B. Back et al., "The PHOBOS Perspective on Discoveries at RHIC", Nucl. Phys. A757 (2005) 28.

[85] J. Adams et al., "Experimental and Theoretical Challenges in the Search for the Quark Gluon Plasma: The STAR Collaboration's Critical Assessment of the Evidence from RHIC Collisions", Nucl. Phys. A757 (2005) 102.

[86] K. Adcox et al., "Formation of Dense Partonic Matter in Relativistic Nucleus-Nucleus Collisions at RHIC: Experimental Evaluation by the PHENIX Collaboration", Nucl. Phys. A757 (2005) 184.

[87] J. Adam et al., ALICE Collaboration, "Enhanced Production of Multi-Strange Hadrons in High-Multiplicity Proton-Proton Collisions", Nature Phys. 13 (2017) 535.

[88] V. Khachatryan et al., "Observation of Long-Range Near-Side Angular Correlations in Proton-Proton Collisions at the LHC", J. High Energy Phys. 09 (2010) 091.

[89] V. Khachatryan et al.,"Measurement of Long-Range Near-Side Two-Particle Angular Correlations in pp Collisions at $\sqrt{s}$ = 13 TeV", Phys. Rev. Lett. 116 (2016) 172302.

[90] G. Aad et al., "Observation of Long-Range Elliptic Azimuthal Anisotropies in $\sqrt{s}$ = 13 and 2.76 TeV pp Collisions with the ATLAS Detector", Phys. Rev. Lett. 116 (2016) 172301.

[91] S. Chatrchyan, et al.,"Observation of Long-Range Near-Side Angular Correlations in Proton-Lead Collisions at the LHC", Phys. Lett. B718 (2013) 795.

[92] B. Abelev et al., ALICE Collaboration, "Long-Range Angular Correlations on the Near and Away Side in p-Pb Collisions at $\sqrt{s}$ = 5.02 TeV", Phys. Lett. B719 (2013) 29.

[93] C. Aidala et al., PHENIX Collaboration, "Creation of Quark-Gluon Plasma Droplets with Three Distinct Geometries", Nature Phys. 15 (2019) 214.

[94] B. Blok et al., "Collectivity from Interference", J. High Energy Phys. 12 (2017) 074.

[95] A. Dumitru et al., "The Ridge in Proton-Proton Collisions at the LHC", Phys. Lett., B697 (2011) 21.

[96] A. Ortiz Velasquez et al., "Colour Reconnection and Flowlike Patterns in pp Collisions", Phys. Rev. Lett., 111(4) (2013) 042001.

[97] C. Bierlich. "Rope Hadronization and Strange Particle Production", Eur. Phys. J. Web Conf. Ser. 171 (2018) 14003.

[98] C. Bierlich et al., "A Shoving Model for Collectivity in Hadronic Collisions", (2016), arXiv:1612.05132 [hep-ph]

[99] S.Porteboeuf et al., "J/ψ Yield vs. Multiplicity in Proton-Proton Collisions at the LHC", Nucl. Phys. B (Proc. Suppl.) 214 (2011) 181.

[100] J. Adam et al., ALICE Collaboration, "Measurement of Charm and Beauty Production at Central Rapidity Versus Charged-Particle Multiplicity in Proton-Proton Collisions at $\sqrt{s}$ =7 TeV", J. High Energy Phys. 09 (2015) 148.

[101] J. Adam et al., STAR Collaboration, "J/ψ Production Cross-Section and its Dependence on Charged-Particle Multiplicity in p+p Collisions at $\sqrt{s}$ = 200 GeV.", Phys. Lett. B786 (2018) 87.

[102] B. Trzeciak et al., "J/ψ and $\psi(2S)$ Measurement in p+p Collisions $\sqrt{s}$ = 200 and 500 GeV with the STAR Experiment", J. Phys. Conf. Ser. 668 (2016) 012093.

[103] D. Adamova et al., ALICE Collaboration, "J/ψ Production As a Function of Charged-Particle Pseudorapidity Density in p-Pb Collisions at $\sqrt{s_{NN}}$ =5.02 TeV", Phys. Lett. B776 (2018) 91.

[104] S. G. Weber, ALICE Collaboration, "Measurement of J/ψ Production As a Function of Event Multiplicity in pp Collisions at $\sqrt{s}$ =13 TeV with ALICE", Nucl. Phys. A967 (2017) 333.

[105] S. Chatrchyan et al., CMS Collaboration, "Event Activity Dependence of Y(nS) Production in $\sqrt{s_{NN}}$ = 5.02 TeV p-Pb and $\sqrt{s}$ = 2.76 TeV pp Collisions", J. High Energy Phys. 04 (2014) 103.

[106] S. A. Iga Buitron, "Energy and Multiplicity Dependence of Charged-Particle Production in pp and p-pb Collisions with ALICE at the LHC", Talk at the Initial Stages Conference 2017, (2017).

[107] B. Abelev et al., ALICE Collaboration,"Multiplicity Dependence of the Average Transverse Momentum in pp, p-Pb and Pb-Pb Collisions at the LHC", Phys. Lett. B727 (2013) 371.

[108] E. G. Ferreiro et al., "High Multiplicity pp Events and J/ψ Production at LHC", Phys. Rev. C86 (2012) 034903.

[109] B. Z. Kopeliovich et al., "J/ψ in High-Multiplicity pp Collisions: Lessons from p-A", Phys. Rev. D88 (2013) 116002.

[110] T. Aaltonen, et al., "Measurement of Particle Production and Inclusive Differential Cross Sections in $p\bar{p}$ Collisions at $\sqrt{s}$ =1.96 TeV", Phys. Rev. D79 (2009) 112005.

[111] P. Z. Skands, "Tuning Monte Carlo Generators: The Perugia Tunes", Phys. Rev. D82 (2010) 074018.

[112] A. Ortiz Velasquez et al., "Color Reconnection and Flow like Patterns in pp Collisions", Phys. Rev. Lett. 111 (2013) 042001.

[113] T. Pierog et al., "EPOS LHC : Test of Collective Hadronization with LHC Data", Phys. Rev. C92 (2015) 034906.

[114] T. Sjostrand et al., "PYTHIA 6.4 Physics and Manual", J. High Energy Phys. 05 (2006) 026.

[115] T. Sjostrand et al., "An Introduction to PYTHIA 8.2", Comput. Phys. Commun. 191 (2015) 159.

[116] http://home.thep.lu.se/ torbjorn/talks/cern18cosmic.pdf

[117] T. Kasemets et al., "A Comparison of New MC-Adapted Parton Densities", Eur. Phys. J. C69 (2010) 19.

[118] T. Sjostrand et al., "Transverse-Momentum-Ordered Showers and Interleaved Multiple Interactions", Eur. Phys. J. C39 (2005) 129.

[119] B. Webber, "Parton Shower Monte Carlo Event Generators", Scholarpedia 6 (2011) 10662.

[120] A. Buckley et al., MCnet Collaboration, "General-Purpose Event Generators for LHC Physics", Phys. Rept. 504 (2011) 145.

[121] B. Andersson et al., "Parton Fragmentation and String Dynamics", Phys. Rept. 97 (1983) 31.

[122] P. Skands et al., "Tuning PYTHIA 8.1:The Monash 2013 Tune", arXiv:1404.5630 [hep-ph].

[123] R. Corke et al., "Interleaved Parton Showers and Tuning Prospects", J. High Energy Phys. 1103 (2011) 032.

[124] E. G. Ferreiro et al., "Open Charm Production in High Multiplicity Proton-Proton Events at the LHC", (2015), arXiv:1501.03381 [hep-ph].

[125] H. J. Drescher et al., "Parton Based Gribov-Regge Theory", Phys. Rept., 350 (2001) 93.

[126] B Guiot et. al., "Hard Probes and the Event Generator EPOS", J. Phys. Conf. Ser. 589 (2015) 012008.

[127] http://myweb.ecu.edu/linz/ampt/

[128] Z. W. Lin et al., "Evolution of Transverse Flow and Effective Temperatures in the Parton Phase from a Multiphase Transport Model", Phys. Rev. C90 (2014) 014904.

[129] Z. W. Lin et al., "A Multi-Phase Transport Model for Relativistic Heavy Ion Collisions", Phys. Rev. C72 (2005) 064901.

[130] Z. W. Lin et al., "Charged Particle Rapidity Distributions at Relativistic Energies", Phys. Rev. C64 (2001) 011902.

[131] B. Zhang et al., "Multiphase transport model for relativistic nuclear collisions", Phys. Rev. C61 (2000) 067901.

[132] Z.W. Lin et al., "Partonic Effects on Pion Interferometry at the Relativistic Heavy-Ion Collider", Phys. Rev. Lett. 89 (2002) 152301.

Chapter 2

Experimental set up and Data samples

The source of data for the present research work is A Large Ion Collider Experiment (ALICE) that is described in this chapter. Before we learn about ALICE, a brief description of the world's largest particle accelerator Large Hadron Collider (LHC) is given. In addition, a guide to the data taking procedure and data sample is explained.

2.1 LHC experiments at CERN

2.1.1 The CERN accelerator complex

The LHC is the most powerful general-purpose accelerator, located at CERN[1] in Geneva, Switzerland. The reconstruction of the LHC was inaugurated in 2001 underground Swiss-French border replacing the Large Electron Proton (LEP) Collider [1, 2]. The LHC machine was built inside a 26.7 km long tunnel with an average depth of about 100 m under the ground. In November 2009, the LHC produced the first proton-proton collisions at $\sqrt{s}$ = 900 GeV and have recently, achieved collision energy $\sqrt{s}$ = 13 TeV and have reached the integrated luminosity of about 51 fb^{-1} in 2017 [2].

[1]The Conseil Européen pour la Recherche Nucléaire or the European Organization for Nuclear Research was established in 1951.

[2]The luminosity for a particle accelerator experiment is defined by $\mathscr{L} = fnN^2/A$; where n is the number of bunches in both beams, N is the number of particles per bunch, A gives the cross-sectional area of the beams, and f is the revolution frequency. The frequency of interactions can be estimated

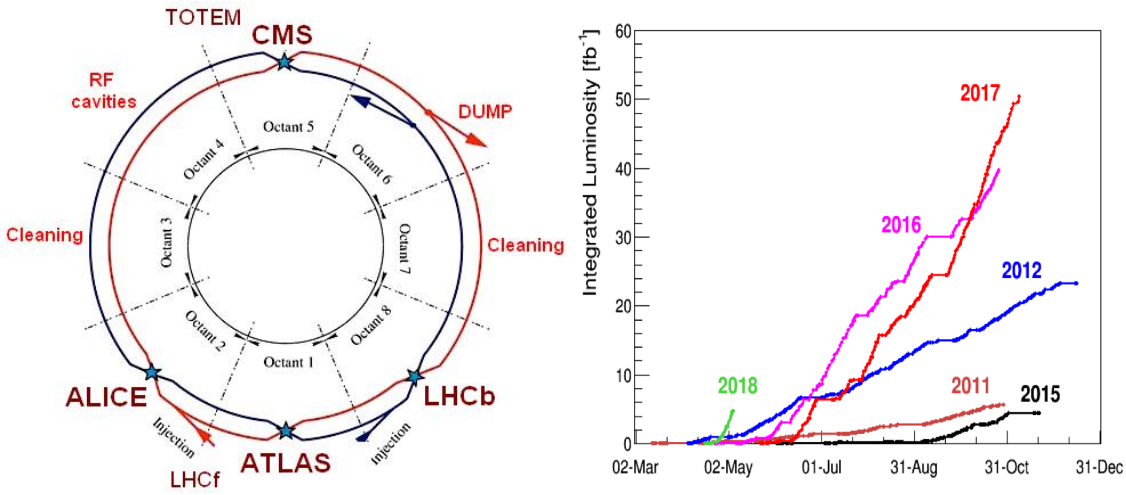

(a) (b)

Figure 2-1: (a) Schematic diagram of LHC [3]. (b) Integrated luminosity achieved by LHC [4].

The layout of the LHC ring and the luminosity recorded by the LHC is shown in Figure 2-1. The LHC is a circular collider (synchrotron) surrounded by superconducting magnets with several radio-frequency cavities to accelerate the particles on their way to collisions. The protons are taken from the hydrogen atoms by stripping of their electrons. Then the protons are injected into the PS Booster (PSB) at an energy of 50 MeV from Linac2. The protons are accelerated by PSB up to 1.4 GeV energy. The beam is then passed to the Proton Synchrotron (PS) which accelerates them to 25 GeV. These protons are then sent to the Super Proton Synchrotron (SPS) where they gain an energy of about 450 GeV. Thereafter, they are transferred to the LHC. The protons are injected as bunches into two rings in the opposite directions at LHC. The beams circulate for several hours inside the LHC beam pipes under normal operating conditions, after losing energy in the collisions the beams are then dumped. In the meantime, next bunches are prepared for collisions. The accelerator complex similarly accelerates ions-ions and proton-ions. Recently, LHC had Xenon ions (Xe-Xe) collisions in addition to the traditional Lead ion (Pb-Pb) collisions. Finally, the particles are made to collide in four interaction points (IP). The beam1 is

by the definition $dN/dt = \mathscr{L}\sigma$, using the corresponding cross-section σ and the luminosity.

injected near IP2 and beam2 is injected near IP8 opposite to IP2. The filling scheme determines the timing and bunches that are to collide in each IP. The LHC is not a perfect circular collider. It is made of eight segments of arc and eight intersections. The set of 1232 superconducting dipole magnets keep the beam on track through the curved tunnel. So far at the end of the Run2 program (2015 - 2018), the LHC has recorded the data with pp collisions at $\sqrt{s}$ = 0.9, 2.76, 5.02, 7, 8 and 13 TeV, with Pb-Pb collisions at $\sqrt{s_{\mathrm{NN}}}$ = 2.76 and 5.02, 5.44 TeV, with p-Pb at $\sqrt{s_{\mathrm{NN}}}$ = 5.02 and 8.16 TeV respectively. The CERN accelerator experimental setup is shown in Figure 2-2. This huge experimental set up at CERN costs about 15 billion dollars which made LHC the costliest experiment in the world [5, 6].

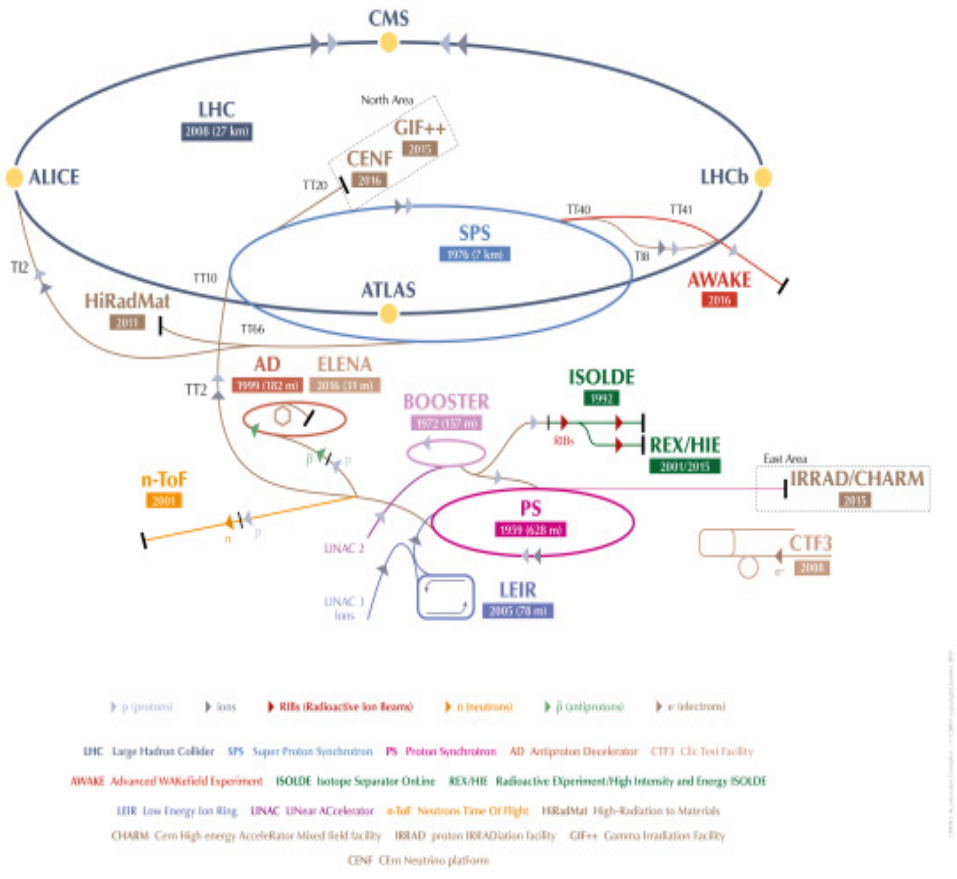

Figure 2-2: Layout of CERN accelerator complex [7].

2.1.2 Experiments at LHC

There are seven experiments at LHC namely ATLAS (IP1), ALICE (IP2), CMS (IP5), LHCb (IP8), TOTEM, LHCf, and MoEDAL. These experiments are dedicated to various physics purposes as described in the following section.

1. ATLAS [8] (A ToroidaL AparatuS) is a multi purpose detector covering a wide range of physics goals. The 46 m long, 25 m high, 25 m wide gigantic detector weighs 7000 tons and consists of 100 million sensors. The detector is mainly designed for searching new particles. ATLAS is now searching for extra dimensions and supersymmetric particles along with dark matter candidate particles. ATLAS detector discovered Higgs boson along with CMS.

2. ALICE [9] (A Large Ion Collider Experiment) is dedicated to study heavy-ion collisions. The main goal of this detector is to understand the primordial nature of the universe right after Big Bang. The detail of the ALICE experiment has been discussed in the following sections.

3. CMS [10] (Compact Muon Solenoid) is also a multi-purpose detector that has similar physics motivations as ATLAS. But it is different in design and construction. The detector is a multi-layered cylinder surrounded by a superconducting solenoid magnet (4T).

4. LHCb [11] (Large Hadron Collider beauty) is designed to look into matter-antimatter asymmetry by studying CP violation and heavy flavour particles, in particular, B mesons. It is a 21 m long, 10 m high and 13 m wide detector, situated in the beam direction. LHCb catches low angle particles in the forward directions.

5. TOTEM [12] (TOTal Elastic and diffractive cross-section Measurement) is situated near CMS and shares the same interaction point (IP5). TOTEM measures the elastic, the diffractive and the total cross-sections.

6. LHCf [13] (Large Hadron Collider forward experiment) measures particles in the beam direction to study the ultra-relativistic high energy particles (similar to those found in cosmic rays) produced in the collisions. It is placed near the ATLAS detector.

7. MoEDAL [14] (MOnopole and Exotics Detector At the LHC) consists of an array of scintillator detectors, was built around the collision point near LHCb. It searches for the hypothetical highly ionizing particles like monopoles.

2.2 A Large Ion Collider Experiment at LHC

The ALICE detector is mainly dedicated to studying QCD matter created in extreme high temperature ($\sim$ 170 MeV) and densities ($\sim$ 1 GeV/c^3) due to high energy heavy-ion collisions at LHC [9]. ALICE detector is designed in such a way that it can cope with the highest particle multiplicity environment created in heavy-ion collisions (8000 particles per unit rapidity at mid-rapidity). The detector has a very unique feature of measuring particle tracks and particle identification over a wide p_{T} range from 100 MeV/c to 100GeV/c. The summary of physics topics covered by ALICE and performance of its various subdetectors in measuring different observable can be found in references [15, 16, 17]. The latest ALICE physics results are given in references [18] and [19].

ALICE has been positioned in such a way that its origin is at the beam interaction point which is defined as a global coordinate system of ALICE. The coordinate system follows the right-handed orthogonal Cartesian system. As shown in Figure 2-3, the x-axis is perpendicular to the IP and is pointed to the LHC ring center. The y-axis pointed upwards w.r.t beam axis. The z-axis is parallel to the beam axis. The positive and negative sides of the z-axis are named as A and C sides of the detector. The muon spectrometer is placed at the C-side of the detector. Similarly, the I, O and U, D are the positive and negative sides of the x and y-axis respectively.

ALICE has in total 19 sub-detectors, categorized in mainly three broader parts. First, the central barrel detectors, which cover a rapidity range $|\eta| < 0.9$, are surround

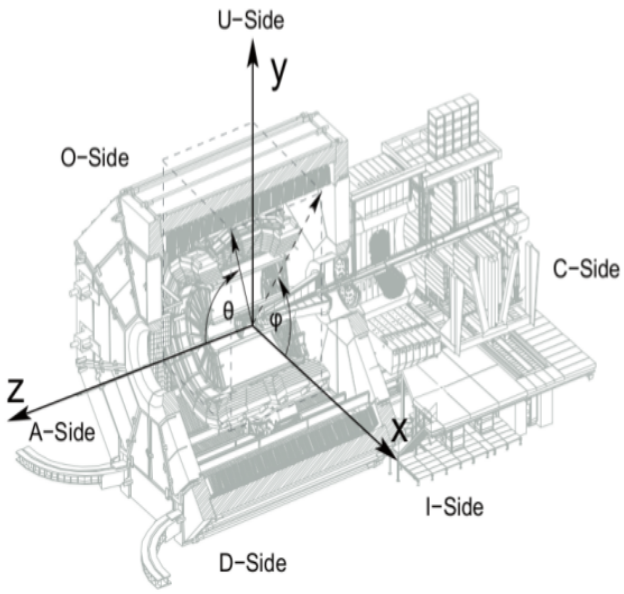

Figure 2-3: Depiction of the ALICE global coordinate system [19].

by a solenoid magnet (magnetic field $B = 0.5$ T). These subsystems are dedicated for tracking and identification of charged-particles namely, Inner Tracking System (ITS) [20, 21], Time Projection Chamber (TPC) [22], Transition Radiation Detector (TRD) [23], Time of Flight (TOF) [24] and High-Momentum Particle Identification Detector (HMPID) [25]. The subsystems, dedicated for photons detection are PHOton Spectrometer (PHOS) [26] and ElectroMagnetic CALorimeter (EMCAL) [27]. Then, there are global detectors, Forward Multiplicity Detector (FMD) [28], Photon Multiplicity Detector (PMD) [29], VZERO [30], TZERO [31], and Zero Degree Calorimeter (ZDC) [32]. They participate in the trigger generation, event characterization (centrality, event plane, etc.) and beam luminosity measurements. The Muon Spectrometer is responsible for muon tracking and triggering in the forward rapidity range ($2.5 < y < 4$). Finally, the detector is covered at the top by arrays of scintillators which act as a trigger for cosmic rays, ALICE COsmic Ray DEtector (ACORDE) [33].

The ALICE detector subsystems are shown in Figure 2-4. The focus of this chapter will be on the detectors which have served as a data source for this thesis. The detailed characteristic of the data source subsystems are described in the following subsections.

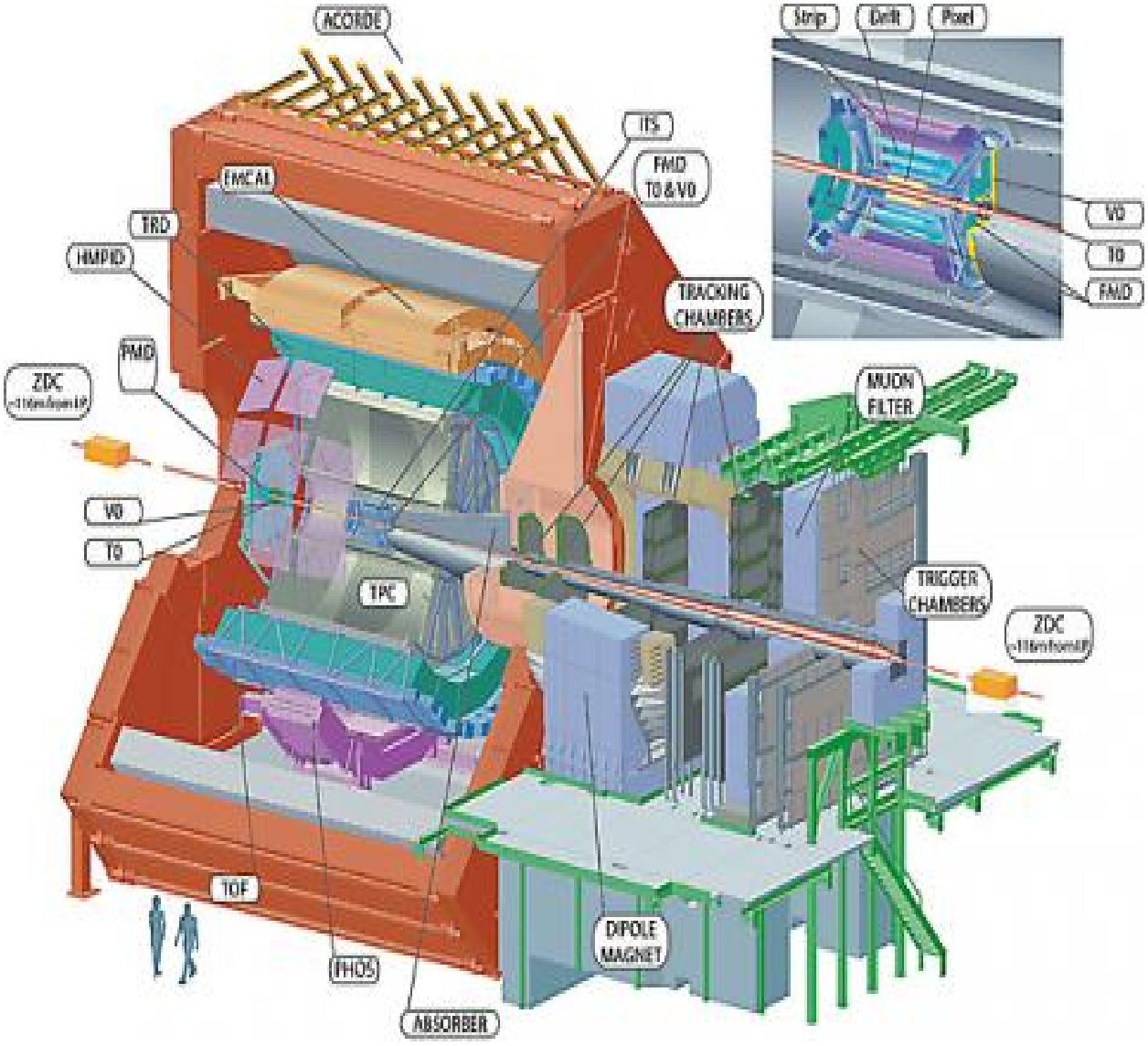

Figure 2-4: Schematic diagram of the ALICE detector and it's various subsystems [19].

2.2.1 Inner Tracking System (ITS)

The ITS is situated closest to the IP and is made of three cylindrical layers of silicon detectors [20]. The layers of ITS are designed for efficient track reconstruction and vertex resolution. The outer radius is chosen in such a way that it matches the track of the TPC. The silicon detectors are very fast detectors with features like high granularity and excellent spatial precision, and are optimized for high particle multiplicity measurement. ITS covers the mid-rapidity region with $|\eta| < 0.9$ for all vertices which are located within the length of IP i.e about $\pm$ 10.6 cm along the beam

axis.

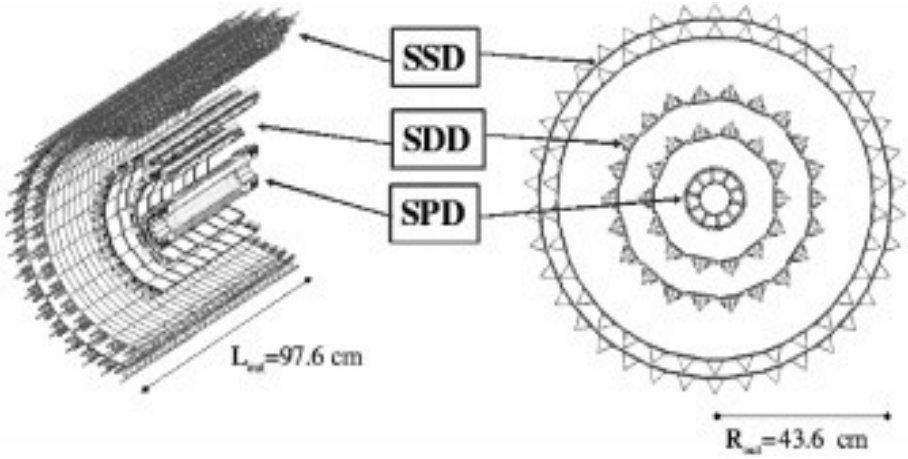

Figure 2-5: The layout of the Inner Tracking System [21].

The two innermost layers of ITS are called Silicon Pixel Detector (SPD). SPD can deal with a high particle rate, 80 particles per cm^2 (about 1 kHz). The following two layers are Silicon Drift Detector (SDD) which can handle particle up to $7/cm^2$. The outermost two layers are called Silicon Strip Detector, equipped with a double-sided silicon micro strip that can handle particle rate below $1/cm^2$. The dimensions of these layers are listed in Table 2.1 and the schematic view of the ITS is depicted in Figure 2-5.

$Layers$	$Type$	$r(cm)$	$\lvert\eta\rvert$	$\pm\ z(cm)$
$1, 2$	$Pixel$	$3.9, 7.6$	$2.0, 1.4$	14.1
$3, 4$	$Drift$	$15.0, 23.9$	0.9	$22, 2, 29.7$
$5, 6$	$Strip$	$38, 43$	1.0	$43.1, 48.9$

Table 2.1: Dimensions of various layers of ITS [20].

The main physics goal of ITS [21] is to reconstruct the primary vertex positions of the collisions with an accuracy better than 100 μm and with a momentum estimation of the particle tracks. It also estimates the secondary vertices coming from hyperons (Σ, Λ, Ξ, Ω) and heavy-quark (open-charm D or open-beauty B) decays. The particle identification is done by ITS through the measurement of the specific energy loss (dE/dx) in the medium and by the tracking mechanism. ITS can identify particles with p_{T} below 100 MeV/c and reconstruct the particles which pass through the dead

regions of the TPC. One of the basic functions of ITS is to improve the momentum and mass resolution. The mass resolution of any track depends on momentum resolution and the mass resolution of the resonance mesons (ρ, ω and ϕ) has to match with the natural width of the resonances to establish the expected chiral symmetry. It can also measure the heavy flavour states with better momentum resolution, which allows the estimation of the signal-to-background ratio of heavy quarkonia suppression, such as J/ψ and Υ in a better way.

The details of SPD layers is presented here, as it is responsible to form so-called 'tracklet' and thus, to measure the charged-particle multiplicity. The two layers of SPD consist of a total of 60 layers around the beam pipe in the z-direction, and each of them is formed by 4 ladders. The ladders are a two-dimensional matrix of silicon pixel detector sensors of 256×160 cells connected to 5 ALICE readout chips. The SPD is made of a total of 1200 ALICE readout chips and about 9.8×10^6 pixel cells. The whole structure is mounted on carbon-fibre sectors for cooling purposes.

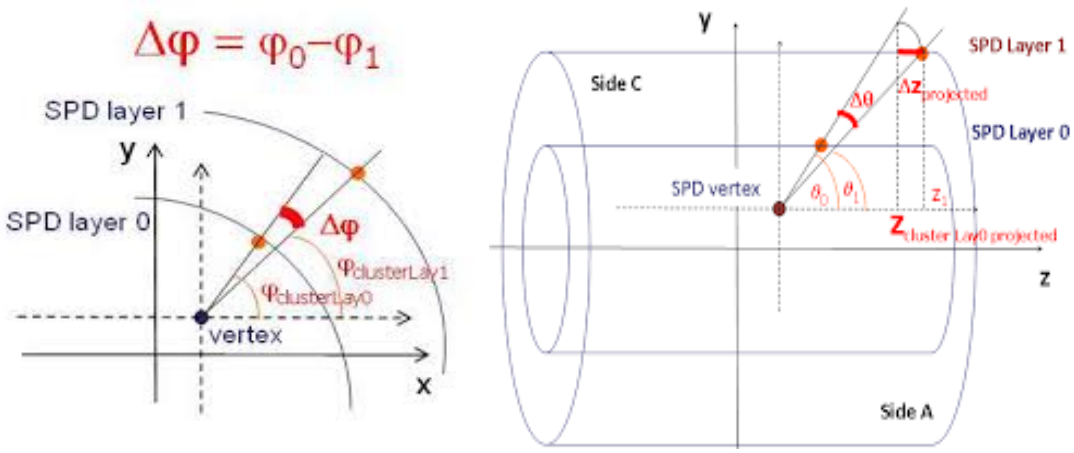

(a) (b)

Figure 2-6: Sketch of tracklet algorithm defined by using SPD layers. (a) View of the transverse plane of the detector for $\Delta\phi$ computation. (b) View of the $z-y$ plane for Δz projection [34].

The SPD vertex are reconstructed using two algorithms [35]. First, the 3D vertexer, which reconstructs the x, y, z coordinates of the IP. Second is 1D vertexer which reconstructs the z coordinates of the IP when 3D vertexer fails. The schematic view

of SPD tracklet formation is illustrated in Figure 2-6. A cluster is formed by one or more particles hit on the adjacent pixels. The tracklets are made up by correlating the SPD vertex with the clusters and SPD vertex is used as a origin. The difference in the azimuthal angles ($\Delta\phi$) and polar angles ($\Delta\theta$) are calculated between the clusters at inner and outer layer of the SPD, respectively. Based on an iterative process the tracklets are formed by matching of a pair of hits in the inner layer to the outer layer of SPD. Only those candidates are selected which satisfy criteria of $\Delta\theta = 0.08$ rad (corresponding to $p_T = 35$ MeV/c) and $\Delta\theta = 0.025$ rad. The efficiency of primary charged-particles traclet reconstruction is 98% and background that are reconstructed using secondary charged-particles clusters and combinatorics.

2.2.2 The V0 detector

The V0 [30] detector is made of two scintillator arrays (V0A and V0C) placed asymmetrically on either side of the interaction point. The V0A and V0C arrays are segmented in four rings in the radial direction, and each ring consists of eight sections in the azimuthal direction Figure 2-7.

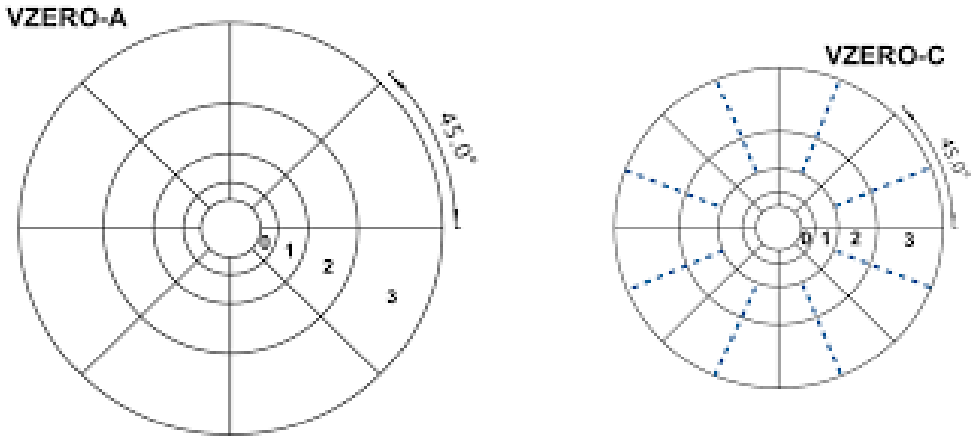

Figure 2-7: The view V0A and V0C scintillator arrays [9]

The V0 detector provides information for the minimum-bias trigger (L0 trigger) of the ALICE. The detector is also used to measure charged particles, reject beam-gas interactions by the time difference between the two arrays, and acts as a pre-trigger

for the TRD. The V0A is situated at 3.29 m from the interaction point, on the side opposite to the muon spectrometer. The V0C is attached to the front face of the front absorber of the muon spectrometer, placed at -0.88 m from the IP. The counter V0A covers pseudo-rapidity range $2.8 < \eta < 5.1$ and V0C covers $-3.7 < \eta < -1.7$. The V0 detector also provides the centrality trigger in Pb-Pb collisions and acts as a centrality indicator. It provides a validation signal for the muon trigger to filter background in pp mode. The V0 is also used for the measurement of luminosity.

2.2.3 The Time 0 detector (T0)

The T0 [31] is another forward detector of ALICE, which is mainly used for triggering purpose. The detector is made of two arrays of Cherenkov counters. There are 12 counters per array and each of them is based on a photomultiplier tube (PMT) optically coupled to a 45 mm long quartz radiator. The arrays are named as T0A and T0C, located asymmetrically on either side (A and C side) of the interaction point.

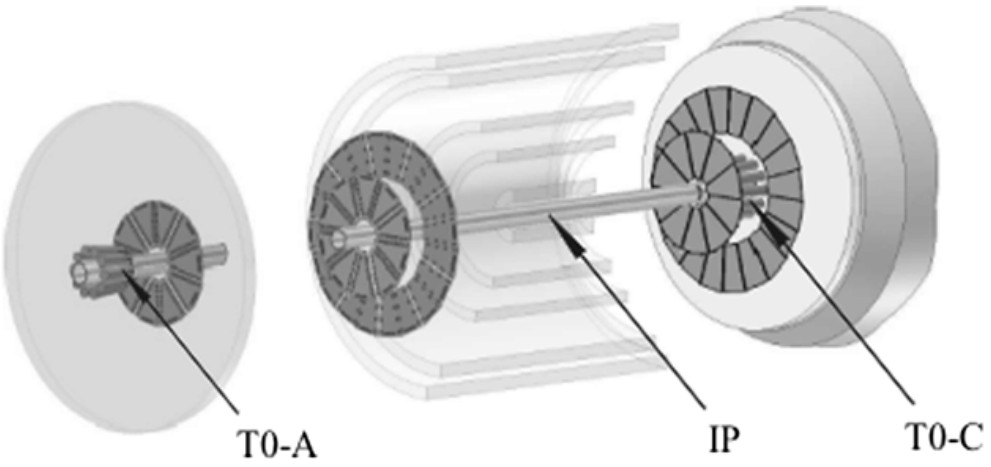

Figure 2-8: The illustrative view of T0A and T0C cherenkov counters are shown with respect to the central region of the ALICE. The T0A is located on the extreme leff, behind V0A and the fifth ring of FMD. The T0C is surrounded by two rings of FMD and V0C [31].

The distance of T0C from the IP is 70 cm while on the opposite side T0A is placed at a distance of about 3.6 m from the IP (Figure 2-8). The pseudorapidity ranges are covered by T0C is $2.9 < \eta < 3.3$ and T0A of $-5 < \eta < -4.5$. The T0 detector

provides the event time with a precision of 50 ps, which is required for precise vertex position determination. The detector is designed to deliver an early (prior to L0 trigger) wake-up signal to TRD and it also gives a precise start signal to the TOF detector for particle identification. Along with the V0 detector, the T0 is also used for the luminosity measurement of ALICE.

2.3 The Muon Spectrometer (MS)

The Muon Spectrometer [36, 37] is dedicated to study the production of quarkonia (J/ψ, ψ(2S), Υ(1S), Υ(2S), Υ(3S)) and low mass vector mesons (ρ, ω, ϕ) through their dimuon ($\mu^+\mu^-$) decay channel in the beam direction. It is also used to study the heavy flavor hadrons (D and B mesons) production and the $W^{\pm}$ and Z bosons via a single muon decay channel. The spectrometer is optimized to reconstruct the tracks of the opposite charge muons in order to measure their momentum and the angle between them which are required for the invariant mass calculation of the muon pair. The measurement of all the quarkonia states allows a direct comparison of their production rate and relative suppression as a function of different kinematic parameters such as transverse momentum (p_{T}), rapidity, collision centrality as well as multiplicity. The spectrometer has a mass resolution of 70 MeV/c^2 in the J/ψ mass region and 140 MeV/c^2 in the Υ mass region. The Muon Spectrometer is a unique apparatus at the LHC to measure charmonia production down to zero transverse momentum. The spectrometer is located from $\sim$ 90 cm to $\sim$ 1720 cm along with the negative z-direction with respect to beamline and covers pseudorapidity range -4. $\leq \eta \leq$ -2.5. The angular acceptance of the spectrometer is 171° to 178° and azimuthal coverage is 2π. It consists of the following components: Front absorber, small angle absorber, dipole magnet, ten tracking stations, muon absorber, and four trigger stations. The detailed schematic view of the spectrometer is shown in Figure 2-9 and the different components are described in the following subsections.

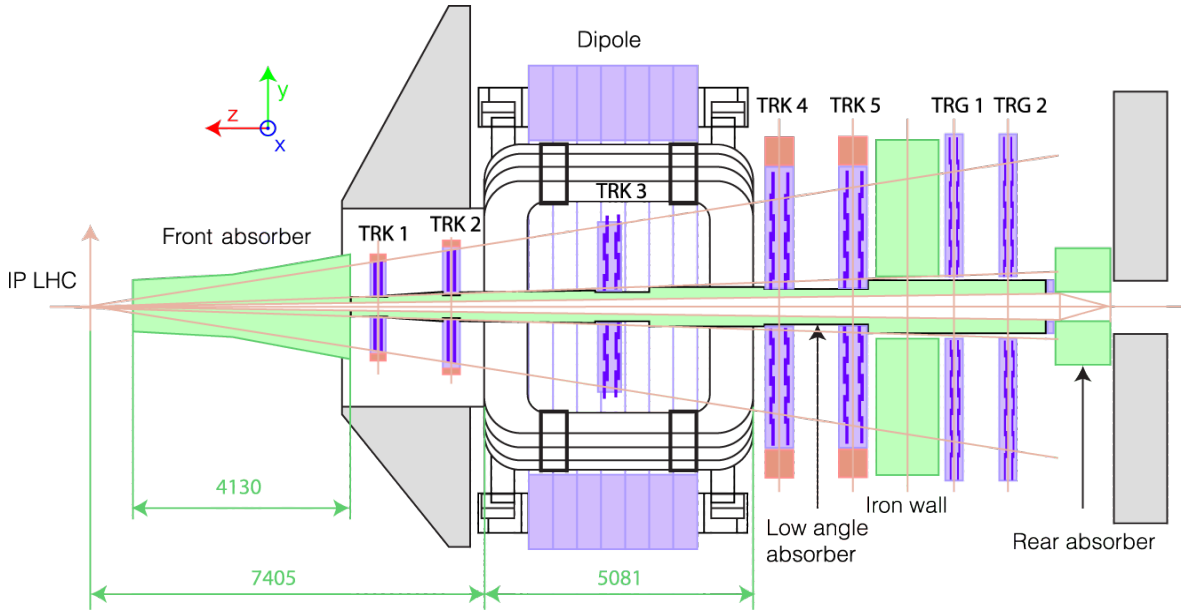

Figure 2-9: The layout view of Muon Spectrometer along with its's various components [36].

2.3.1 Front absorber

The front absorber is composed of a 4.13 m long central cone located inside the central barrel solenoid magnet, 90 cm away from the IP. The front absorber is designed to reduce the forward flux of primary hadrons from nucleus-nucleus collisions by a factor 100 and to decrease the decay muon background by limiting the free path for primary $\pi, K \rightarrow \mu$ decay. The front absorber layout is shown in Figure 2-10. The main ingredients of the absorber are graphite, concrete, Lead, polyCH$_2$, tungsten and steel of radiation lengths 13.87, 11.27, 0.05, 46.47, 0.37 and 1.76 cm respectively. Constituent material, radius, depth, and position have been chosen to satisfy the requirement to prevent the recoil particles to reach the TPC as well as to minimize the invariant mass resolution deterioration of the spectrometer due to straggling and multi-scattering. Due to this reason, upper limits on the amount of material ($\sim 10\lambda$ in mean free path and $\sim 60\ X_0$ radiation length) are imposed. The low atomic mass (Z) components, such as carbon, are located close to the interaction point (IP) to reduce the multiple scattering, whereas high Z components are placed close to the spectrometer.

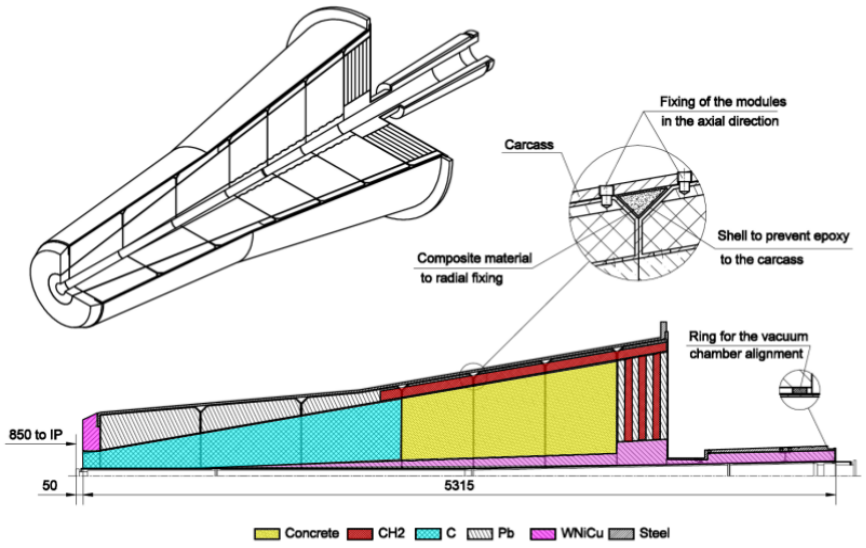

Figure 2-10: The layout of the front absorber of the Muon Spectrometer [36].

2.3.2 Small angle absorber

The small angle absorber, alternatively known as a 'beam shield', covers the beam pipe along the spectrometer length. It is designed to protect the tracking detectors from particles produced at very small angles and from secondary particles generated in the beam pipe due to the beam gas interaction. The outer part of the small angle absorber is shielded by a 4 cm thick stainless steel. The section nearest to the IP is made of tungsten, while the farthest from the IP is made of lead. The small angle absorber ends with an iron plug of 1.1 m in diameter and 1 m thick, which prevents the background particles to reach the trigger detectors.

2.3.3 Dipole magnet

The Dipole magnet of the Muon Spectrometer is located about 10 m away from the IP. The third Muon Tracking station is located in the center of the dipole magnet. The magnet provides the bending power necessary to measure the muon momenta by the muon tracking detectors. The integrated magnetic field of the dipole is 3 Tm. The muon dipole magnet is the world's largest warm dipole magnet. It has a weight

of 850 tons, 5 m in length, 7 m in width and 9 m in height. The magnet is used as a support for the front absorber and beam shield as well. The angular acceptance of the dipole is $171^\circ < \theta < 178^\circ$ and is designed to provide a horizontal magnetic field perpendicular to the beam axis. The polarity of the magnetic field can be reversed.

2.3.4 Tracking Stations

The muon tracking system (MCH) of the Muon Spectrometer is responsible for muon trajectory reconstruction [38]. The dimension of MCH is $\sim$ 1000 cm long starting from $\sim$ 500 cm of the interaction point (IP). The MCH consists of five tracking stations and each of the stations is composed of pair of muon tracking chambers. The design of the tracking system is shown in Figure 2-11.

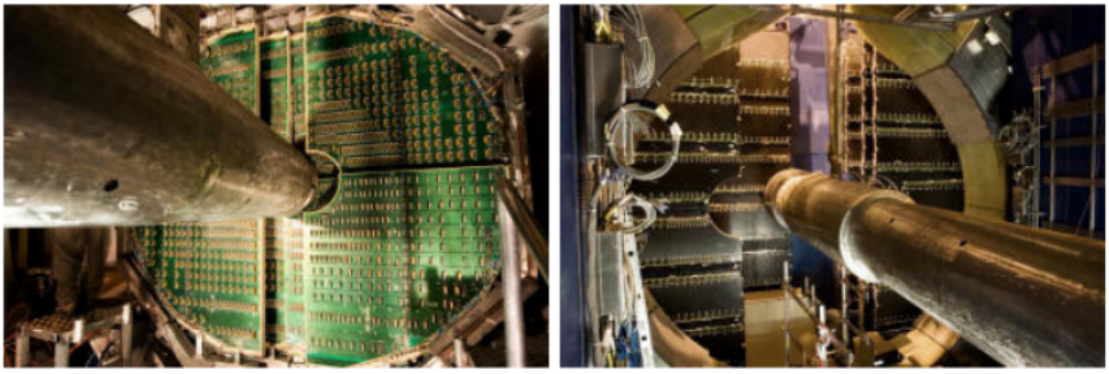

Figure 2-11: The picture of tracking chamber: quadrant shape on the right and slat shape on the left [9].

The first two stations are placed in front of the muon dipole magnet at a distance of 5.4 m and 6.8 m respectively from the IP and the third station is placed inside the dipole magnet (at a distance 9.7 m from IP). The third and fourth tracking stations are situated at 12.6 m and 14.2 m from the IP. The tracking system covers a total area of about 100 m^2. The dimuon tracking chamber is designed to cope with high particle flux in the forward rapidity direction and to achieve a spatial resolution of about 100 μm, which are the required criteria to distinguish the invariant mass of the resonance family (Υ invariant mass). These conditions are satisfied by Cathode

Pad Chambers (CPC) of the muon tracker. They are made of the segmented cathode with anode wires in between, operated with a gas mixture of Ar/CO_2 (80%/20%).

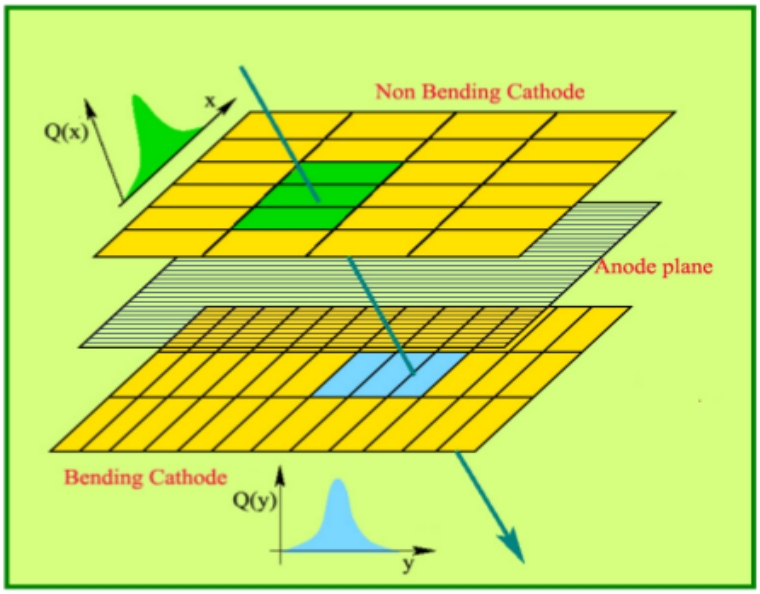

Figure 2-12: The working principle of MWPC [39].

The working principle of CPC is shown in Figure 2-12, which is used to determine the position of a particle passing through the detector. When a charge particle traverses the active gas volume of the detector, it produces ionization (electron-ion pair) along its trajectories. The primary electrons move towards the nearest anode wire, where avalanche takes place. The induced charge on the cathode planes is sampled by specific geometric shape pads. The relative values the absolute positions of the pads in a charge cluster and the corresponding induced charges are used to determine the position of the charged particle passing through the detector. The pad occupancy should be kept below 5%, in order to keep the number of overlapping clusters[3] to be less than 1%. Therefore, a large segmentation of the readout pads is needed. Small pads of dimension 4.2×6 mm^2 are needed for the first station close to the beam pipe, due to the expectation of the highest charged particle multiplicity rate. As the hit density decreases with the distance from the beam, larger pads are adequate

[3] A cluster is formed by combining two dimensional hit information on the CPC. More detail can be found here [9]

at larger radii. These criteria are fulfilled by using the total number of channels of about 1 million. The material budget is kept less than 3% of the radiation length to minimize the multiple scattering of the muons in the chambers. Two different designs have been adopted because of the different sizes of the stations (ranging from a few square meters for station 1 to more than 30 m^2 for station 5). The readout electronics are distributed on the quadrant surface of the first two stations. A slat architecture has been chosen for the remaining three stations. The electronics are implemented on the top and bottom sides of the slats, which have the maximum size of 40 $\times$ 280 cm^2. Thus, the dead zones on the detector are covered by overlapping the slats.

2.3.5 Muon Filter

The muon filter consists of a 1.2 m thick iron wall that is placed at 15 m from the IP, between the last tracking station and the first trigger station. The iron wall reduces the background on the trigger stations by absorbing pions and low momentum muons. It also stops energetic hadrons and secondary particles that escape the absorber. The front absorber and the muon filter enhance the performance of the trigger station by stopping muons with momentum less than 4 GeV/c.

2.3.6 Trigger stations

The physics motivation behind the muon trigger system is to obtain unlike sign muon pairs from the decay of quarkonia resonances, single muons from heavy flavours and like sign muon pairs for combinatorial background studies. A large number of background muons reach the trigger stations in spite of the momentum selection by the spectrometer and shielding by the absorbers. The majority of the background is due to the low momentum muons coming from pion and kaon decays. A simple trigger selection based on the presence of two muons is not sufficient. Thus, to minimize the probability of triggering on these background events, a selection criterion on each muon p_{T} value is applied according to the physics interest.

The muon trigger (MTRG) system consists of two stations MT1 and MT2, located

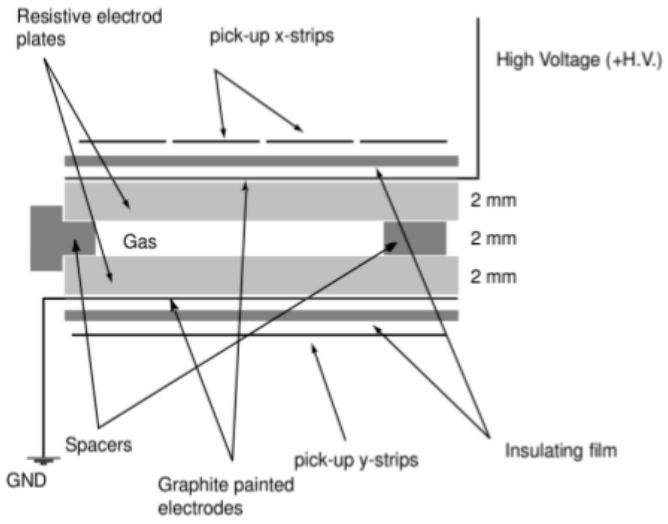

Figure 2-13: The layout of a Resistive Plate Chamber [9].

at a distance of 16 m and 17 m from the IP respectively. As depicted in Figure 2-13, each trigger station is made of two parallel Resistive Plate Chambers (RPC) planes. The first and second trigger stations cover 6.12×5.44 m^2 and 6.50×5.78 m^2 active area, respectively. The RPCs are positioned on a mechanical structure in two parallel plates, which allows the superposition of active and dead areas of the trigger system to avoid the inactive zones. A 2 mm gas volume separates the two high resistivity Bakelite plates which are coated with graphite and one is connected to high voltage and the other is grounded. The RPC follows the principle of the gas detector, where the active gas material is flushed through the resistive electrode plates. The graphite electrodes and aluminium strips, placed at the outside of the chamber are covered by an insulating film. The strips work to read on the signals produced by the RPC. The pitch of the strips is also governed by the momentum resolution required for the p_{T} selection criteria. The total number of readout channels is about 21000. Trigger chambers are optimized for good timing properties and a prompt time gate of 20 ns on the trigger electronics which are used to reject soft-background (mainly electrons leaking out of the absorber) and has widely spread time structure.

The working principle of momentum measurement for the trigger decision is shown

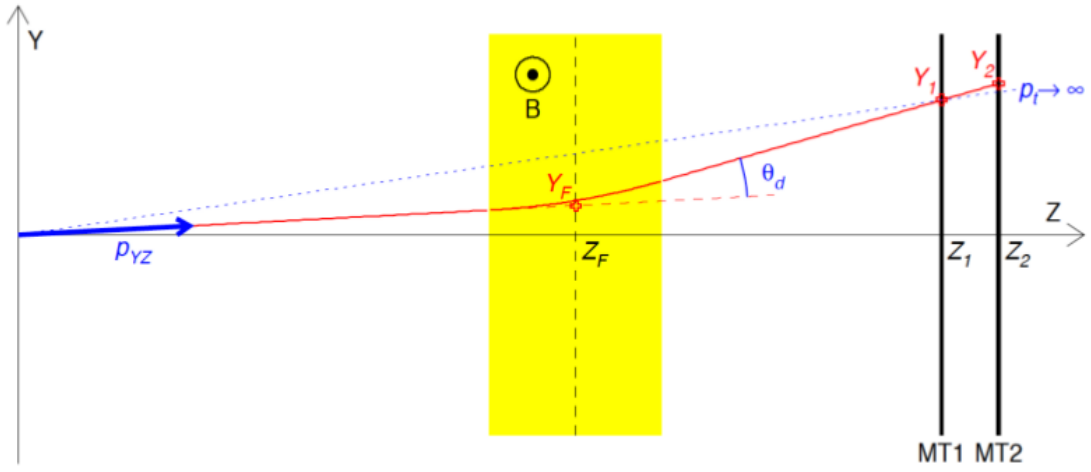

Figure 2-14: The muon trigger principle for muon track selection [9].

in Figure 2-14. The algorithm is based on the measurement of the deviation of the measured track from the muon track with infinite momentum so that we can estimate muon tracks with $p_{\mathrm{T}} \geq p_{\mathrm{T}}^{threshold}$. The track position ($\mathrm{X}_1$, Y_1, Z_1) on the first trigger station (MT1) are measured and projected as a straight line in to the second trigger station (MT2). During this process p_{T} is assumed to be 'infinite' (no deviation of track in the presence of magnetic field) which pass through the interaction vertex. The direction of the tracks are reconstructed using the positions of the hit coordinates in the MT1 and MT2. Then the deviation of measured tracks with respect to the straight line is estimated on the (Y, Z) plane that has to be smaller than a certain value, which corresponds to the threshold value of the p_{T}.

2.3.7 Muon track reconstruction

The muon track reconstruction is briefly discussed in this section. The muon track candidates are formed by tracking algorithm which combines the clusters from each MCH. The muon track reconstruction is done in the MCH and matched with a track in the MTR [40]. The tracking stations 4 and 5 are subjected to lower track density than the stations 1 to 3 since they are situated far from the IP as described in Section 2.3.4. So the reconstruction process is started by taking all possible combinations

of clusters in Station 4 or 5 and the hit position, momentum direction and impact parameter at IP are computed. By assuming that the tracks are originated in the vertex and taking into account the average magnetic field of the dipole, the momentum is estimated. All parameters are computed with their uncertainties. The candidates that pass certain criteria on momentum and impact parameter are selected. Then the track candidates are extrapolated from Station 4 to Station 5 or opposite, after that the track parameters are recomputed. The track selection criteria are such that at least one cluster is required in the other station, candidates sharing identical combinations of clusters are removed and those which do not pass the condition on momentum and impact parameters are not considered as well. In stations 1, 2 and 3, the same process is repeated consecutively. The track reconstruction is treated as successful if at least one cluster per station is compatible with the track. The track is duplicated to consider all options in the case of several clusters per chamber. The tracks which share one or more clusters are rejected. The tracks are formed by considering the candidates with the largest amount of clusters or with the best fit in case of an equal number of clusters. Furthermore, the reconstructed track is matched with the trigger track. Finally, the reconstructed tracks are extrapolated to the vertex which is measured with the ITS. The reconstructed track parameters are corrected for energy loss and multiple scattering in the front absorber.

2.3.8 Beam shield

The beam shield is placed at the back of the trigger chambers which provides an additional shielding from beam gas interactions produced in the LHC beam pipe in the LHC tunnel. It is made of high Z tungsten-lead composite embedded in a 4 cm thick stainless steel envelope, which surrounds the beam pipe along the Muon Spectrometer. The beam shield is extended to fully cover the LHC tunnel aperture.

2.3.9 Detector Readout

The front-end electronics of the muon tracking stations are composed of a 16-channel chip Multiplexed ANAlog Signal processor (MANAS) chips. A MANU board has four MANAS chips connected to 12-bit Analog to Digital Converters (ADCs), which are read out by the Multiple Automated Readout Computer (MARC) chip. There are about 16,850 MANU cards to read the 1,076,224 channels of the tracking system. The MANU cards are arranged in bus patches and each patch connected to read out by a Translator board. The data are transferred from the translator board to the Concentrator Read Out Cluster Unit System (CROCUS). There are 20 numbers of CROCUS, two per tracking chamber. The CROCUS is designed for taking data from the chambers, then transporting them to the Data Acquisition System (DAQ). The CROCUS is also responsible for the calibration of the front-end electronics and dispatching of the trigger signals. The topmost readout element of the detector (i.e. CROCUS for dimuon tracking chambers) is connected to the DAQ by the Detector Data Link (DDL). The readout mechanism is shown in Figure 2-15.

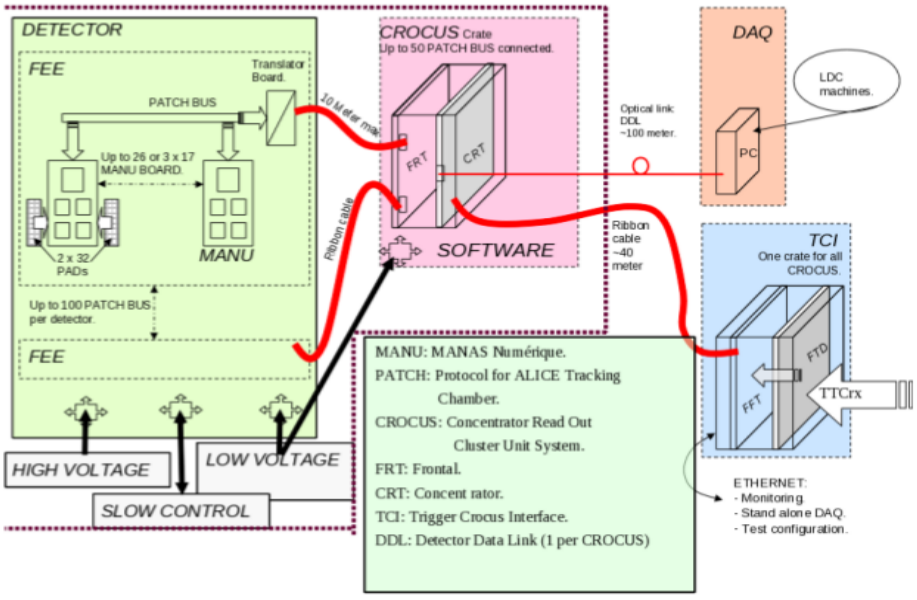

Figure 2-15: The read out flow chart of the MWPC [39].

The trigger front-end electronics (FEE) provides a time resolution of 2 ns, which is necessary for the identification of the bunch crossing. The dimuon trigger participates in the ALICE L0 trigger. The Indian Collaboration, Saha Institute of Nuclear Physics and Aligarh Muslim University have been in charge of design, fabrication, installation and commission of the second tracking station and design, fabrication and testing of the MANAS chips for all the five stations of the Muon Spectrometer.

2.4 Data taking overview in ALICE

The data taking in ALICE is a very complex procedure and is out of the scope of this thesis. The ALICE experiment requires continuous monitoring of the ongoing operation at the ALICE Run Control Room (ARC, experimental site) which is provided by the shift crew, composed by the ALICE collaboration members. We will briefly discuss the salient features of the ALICE experiment.

2.4.1 Detector Control System (DCS)

The Detector Control System (DCS) ensures safety and control operation of the various ALICE detector during data taking [41]. The DCS provides the detector configuration, remote control, monitoring the status and check for errors during the ongoing experiment. It can also recover possible failures to maximize the number of operational readout channels at any time as well as measures and stores all parameters necessary for the offline data analysis. To connect the detector modules to their sub-detectors and devices a tree-like software architecture has been adapted. The basic building blocks of the control hierarchy are called Control Units which model the behaviour and communication between components for example LV and HV supplies. The DCS is based on Finite-State Machines (FSMs) to model the functionality and behaviour of the components.

The various external services needed for the operation of the experiment such as gas, cooling, electricity, safety are also taken care by DCS along with the controlling of all sub-detector equipment. The DCS performs an important task of the handshaking

with LHC control during the beam injection and beam dumping to ensure the safety of the subdetectors.

2.4.2 Data Quality Monitoring (DQM)

The Data Quality Monitoring (DQM) is another online control system that monitors the quality of the data being recorded to ensure the acquisition of high-quality data [42]. The DQM shifter inspects the data online by detector group defined algorithms and the visualization of the monitoring results while they are being collected. The monitoring histograms have been defined by each detector and are provided by some processes called "agents", which are written in the AMORE (Automatic MOnitoRing Environment) framework. To check the behaviour of the detector, data taking configuration, fix problems online, to save precious time of data-taking, it is very important to have quick and efficient feedback about data quality monitoring. An important task of a DQM shifter is to report the problems during data taking and keep a summary of the observations in the electronic logbook that makes the monitoring results available through a web browser. Since 2012, the DQM also controls the offline systems and provides registration, transfer, and replication of the raw data.

2.4.3 Experiment Control System (ECS)

The Experiment Control System (ECS) allows shifter to operate the data acquisition, the central trigger, and the high level trigger systems [43]. The ECS provides a framework for a unified view of all the online systems and a central point from where the experiment operations can be controlled. The ALICE experiment runs either as a whole (during the physics production) or as a set of independent detectors (for installation and commissioning). The ECS does this task to permit all the features necessary to split the experiment into partitions containing one or more detectors, which can be operated independently or all together. The Detector Control Agent (DCA) is connected with all necessary online systems (DCS, CTP, and HLT). It is the

central control point of the experiment and provides an overall view of the experiment using the Partition Control Agent (PCA) which are connected to individual DCAs. The priority logic and communication between the control agents, based on the control of objects located in a remote Activity Domain, are implemented via Finite-State Machines (FSMs). FSM allows the DCA or PCA, depending on the owner of the control of the detector, to control a sub-detector.

2.4.4 ALICE trigger system

The goal of any trigger system is to sort out event samples which are enriched with physics processes and reject those events that are not of interest and at the same time to make efficient use of the available detectors [9]. The ALICE trigger system can be categorized into two main parts, the Central Trigger Processor (CTP) and High Level Trigger (HLT), which is mainly implemented as a software trigger. The CTP is a hardware trigger set up, which is placed in the experimental cavern. The CTP generates the trigger decision using the information from various detector signals and the LHC bunch filling scheme (see Section 2.1.1). One of the main tasks of the CTP is to select events with different features at rates that can be scaled down according to physics requirements and to cope with the limited Data Acquisition (DAQ) system bandwidth. It also takes care of pile-up protection, checks on the ready status of different detectors and read-out memories, trigger priority, and finally synchronization with the machine clock cycle ($\sim$ 25 ns). The signal from a triggering detector to the CTP is defined as a "trigger input" and "trigger signal" is the signal from the CTP send to the read-out electronics of the detector. The signal is sent by CTP send to the detector Local Trigger Unit (LTU) which is the interface between the detector read-out and the CTP. The difference in event processing speed of the detectors led to the design of a 3-level ALICE trigger system as follows:

- Level 0 (L0) is the first and the fastest trigger level where trigger inputs arrive from the interaction to the CTP in about 1.2 μs. The L0 is also known as L0b and L0a, where a and b corresponds to "after the CTP" and "before the CTP",

respectively. The V0, T0, SPD, EMCAL, PHOS and MTR detectors provide signals to the L0 trigger level. The CTP decision for L0b and L0a levels are stored in the so called scalers.

- Level 1 (L1) is the second level trigger with the latency of about 6.5 μs. The L1 trigger inputs to the CTP are given by the TRD, ZDC, and EMCAL. This delay in L1 trigger input is caused by the computation time in the TRD and EMCAL and the propagation times in the ZDC. An event is rejected if the L1 trigger signal does not arrive on time to the readout detectors.

- Level 2 (L2) trigger is delivered after 100 μs from the interaction. This latency corresponds to the drift time of electrons in the TPC. The event is stored after passing the L2 level. The L2 trigger is also responsible for compressing the TPC data without loss of physical information. In Run1 data, all events with L1 were accepted by L2.

Another feature of the ALICE trigger system is to configure groups of detectors that participate in the readout of any given event which is defined by the trigger clusters. A trigger class[4] is made of the logical AND and OR of different trigger inputs and CTP vetoes (in which the CTP does not generate the L0 signals, e.g. the trigger input does not match with a bunch crossing or the downscaling of certain trigger classes to allocate more DAQ bandwidth to rare events). Thus, the trigger cluster ensures coincidence among the participating detectors. The CTP sends independent trigger signals to each trigger cluster so that if a slow detector is processing an event, another fast detector can process other events, simultaneously. The CTP is complemented by the HLT which can take more refined trigger decisions than the CTP. The HLT combines and processes already read-out data from the major detectors and accepts or rejects events based on an online analysis of the output from the large input stream. This includes the compression of the data volume by an order of magnitude to fit the available storage bandwidth. During Run 1 and 2, HLT was used for TPC alone.

[4]These definition will help us to understand the data sample that have been used in this analysis.

2.4.5 Data acquisition (DAQ)

The ALICE Data AcQusition system (DAQ) controls the dataflow from the detector up to the data storage [44]. The DAQ was designed to handle large interaction rates and a large amount of data (1.25 GB/s). It also includes software packages for raw data integrity and system performance monitoring. The DAQ dataflow starts at the detector FEE. Data from the sub detectors is received by Detector Data Links (DDLs) on Local Data Concentrators (LDCs) that build the event fragments from the FEE into sub-events. Then sub-event information is shipped to the Global Data Collector computers (GDC), which build the events combining the information of various LDCs. Eventually, the data is stored in the Global Data Storage Servers (GDS). Finally, the data are sent to the CERN computing centre. The data are replicated to CASTOR disk then copied to the CASTOR tape finally transferred to Tier1 computing centres and made available for the offline reconstruction. The data transfer scheme is shown in Figure 2-16.

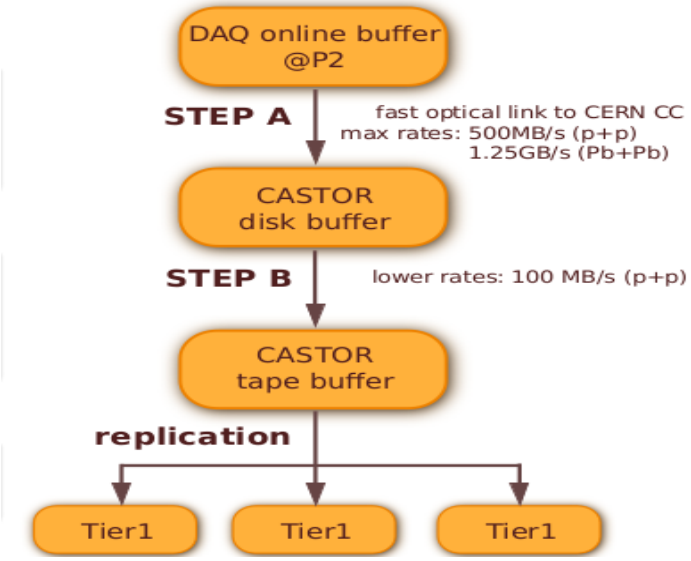

Figure 2-16: The raw data transfer flow-chart [42].

2.4.6 Data Reconstruction

The data reconstruction is done by ALICE offline framework software AliROOT [19]. ALiROOT is based on an object-oriented ROOT framework [45] (mostly written in C++ programming language with some parts in FORTRAN, now PYTHON is being implemented). The high-precision alignment and calibration of data are done during the first time reconstruction. Then the first reconstructed (known as pass1), detector alignment and calibration data are stored in the Offline Condition Data Base (OCDB) together with scalers and information on the magnetic field. The information filed in the OCDB can be accessed in all reconstruction, analysis, and simulation of the data. The first set of Event Summary Data (ESD) is produced using the data reconstruction information. The quality assurance (QA) analysis is performed on ESD data and is filtered into the first Analysis Object Data (AOD) files, which contain reduced information essential for a specific type of analysis. Both ESD and AOD undergo several cycles of reconstruction called passes and results of each reconstruction pass are stored in the successive pass. The second pass is processed by tuning the feedback derived from the first pass (including analysis).

2.5 Data Sample

The data analysis in the present thesis have been carried out using ALICE data in pp collisions at $\sqrt{s}$ = 2.76 TeV and 5.02 TeV. The data at $\sqrt{s}$ = 2.76 TeV was collected in March 2011 during the LHC Run1 phase and in November 2015 the data at $\sqrt{s}$ = 5.02 TeV were collected at LHC Run2 Phase. The data periods[5] are LHC11a and LHC15n for the two collision energies.

The present analysis uses the reconstructed AOD and the data was passed through standard quality checks (Quality Assurance (QA)). The runs are selected that are good for muon analyses which are listed in the Run Condition Table of MONALISA[6] web page. The runs for the data set of both the collision energies is listed in the

[5]The naming convention follows LHC+year+letter
[6]ALICE GRID monitoring facility

Appendix A.1. The details about the data conditions and the result of the QA can be found here [46], [47].

The analysis was done considering data mainly from the fast detector cluster muon trigger and muon tracking chamber including SPD, T0, V0, AD. The Minimum Bias (MB) trigger mainly involves V0, T0 and SPD detector signal. The various trigger classes, which were considered during the data analysis are as follows:

- CINT1-B-NOPF-ALLNORTD is a MB trigger class, which is defined by a coincidence of signals either one of the V0 detectors with the SPD i.e. V0A |V0C|SPD. ALLNOTRD cluster includes a coincidence of signal from SPD, SDD, SSD, TPC, TOF, HMPID, PHOS, PMD, MUON-TRK, MUON-TRG, T0, V0, ZDC and EMCal except for TRD signal.

- CINT1-B-NOPF-ALL-FASTNORTD is MB trigger class with V0A|V0C|SPD condition and FASTNOTRD satisfy signal from fast detector cluster SPD, SSD, TPC, TOF, HMPID, V0, ZDC and T0 except for TRD.

- CMUS1-B-NOPF-MUON is a single muon trigger class that satisfies coincidence of signals either V0A or V0C or SPD with unlike sign muon pair of low p_{T} threshold of 1 GeV/c in the Muon Spectrometer. The muon trigger cluster is a rare trigger cluster that involves signal from SPD, MUON-TRK, MUON-TRG, T0, V0, and ZDC.

- CINT7-B-NOPF-MUFAST is a MB trigger class which is defined by a coincidence of signals between two sides of V0 detector V0A and V0C. MUFAST represents the fast detector cluster contains signal from SPD, MUON-TRK, MUON-TRG, T0, V0, and AD.

- CMUL7-B-NOPF-MUFAST is an, unlike sign dimuon trigger class that satisfies a coincidence of signals in V0A and V0C and muon pair satisfying the low p_{T} threshold of 0.5 GeV/c in the Muon Spectrometer.

- CMSL7-B-NOPF-MUFAST is a single muon trigger class with a coincidence of

signals in V0A and V0C systems and of a muon satisfying the low p_{T} threshold of 0.5 GeV/c in the Muon Spectrometer.

- CINT7-B-NOPF-CENTNOTRD is also a MB trigger class with coincidence of signal of V0A&V0C and CENTNOTRD trigger class includes signals from SPD, SDD, SSD, TPC, TOF, HMPID, PHOS, CPV, FMD, T0, V0, EMCal, AD and PMD.

- C0TVX-B-NOPF-CENTNOTRD is a MB trigger class which is given by a coincidence of signals in T0A and T0C and also fulfills a condition with T0 vertex within $|z| < 30$ cm from IP.

The trigger classes were named in such a way that they include name of the trigger input (e.g. 0MUL, 0MSL, etc are basically L0 input where "0" is replaced by "C".), followed by LHC bunch crossing mask which provides information about interaction (beam-beam, beam-gas, satellite, etc.), then a future past protection rejects events with multiple collisions from different bunch crossings (NOPF means future past protection is not applied) and in the end trigger cluster (group of detectors to be read out if the trigger conditions are satisfied). A physics selection (PS) criteria is applied on the events before they pass through the respective triggers [48]. PS prevents backgrounds and poor quality events. The PS consists of a timing condition on V0, ZDC signals and the correlation between SPD tracklet and cluster checks. The number of PS selected trigger events that were analysed during this work with their corresponding reconstructed pass are listed in Tables 2.2 and 2.3.

The J/ψ multiplicity results for pp collisions at $\sqrt{s} = 2.76$ TeV have been analyzed using the pass4_without_SDD (AOD113) data set from the LHC11a period. However, since the previous publication of J/ψ cross-section has been performed with Pass2_with_SDD (AOD052) data-set by ALICE [49], it has been also used in the present study for cross-checking. The production of J/ψ as a function of charged particle multiplicity has been studied for pp collisions at $\sqrt{s} = 5.02$ TeV from the LHC15n period. CINT7 trigger classes that are listed in the table are the rare trigger

Period = LHC11a	pp$\sqrt{s}$ = 2.76 TeV	Total Runs = 18
Trigger Name	Trigger Counts	
	pass2_withSDD	pass4_without_SDD
CINT1-B-NOPF-ALLNORTD	-	2.69×10^7
CINT1-B-NOPF-ALL-FASTNORTD	-	7.06×10^7
CMUS1-B-NOPF-MUON	7.05×10^6	8.8×10^6

Table 2.2: Events passing the above triggers are used in this analysis.

Period = LHC15n	pp$\sqrt{s}$ = 5.02 TeV	Total Runs = 25
Trigger Name	Trigger Counts	
	muon_calo_pass1	muon_calo_pass2
CINT7-B-NOPF-MUFAST	0.015×10^6	0.54×10^6
CMUL7-B-NOPF-MUFAST	1.19×10^6	1.17×10^6
CMSL7-B-NOPF-MUFAST	3.48×10^6	3.42×10^6
C0TVX-B-NOPF-CENTNOTRD	7.46×10^6	7.34×10^6
General pass2/AOD183		
CINT7-B-NOPF-CENTNOTRD		2.43×10^6
Central Analysis: muon_calo_pass2 (AOD174)		
CINT7		1.061×10^8

Table 2.3: CMUL7 and CINT7 Trigger events are the main events used for analysis, remaining triggers are for calculating normalization factor.

events (MB trigger downscaled). Hence all the CINT7 events are analysed instead of any particular trigger class. Similarly, for $\sqrt{s}$ = 2.76 TeV, CINT1 events are used.

2.5.1 Monte Carlo data selection

The MC production used for the calculation of charged particle multiplicity in pp collisions at $\sqrt{s}$ = 2.76 TeV and $\sqrt{s}$ = 5.02 TeV are evaluated using the Monte-Carlo data-set as shown in Table 2.4:

Energy	Data	MC	Events($\times 10^7$)
2.76 LHC11a	pass2-with-SDD	LHC11b10a	2.59
	pass4-without-SDD	LHC12f1a (PYTHIA8)	2.70
		LHC12f1b (PHOJET)	2.48
5.02 LHC15n	muon-calo-pass2	LHC16h8a (PYTHIA8)	5.15
		LHC16h8b(PYTHIA6)	5.23

Table 2.4: MC periods used in the analysis.

Bibliography

[1] T. S. Pettersson et al., "The Large Hadron Collider : Conceptual Design", CERN-AC-95-05 LHC (1995).

[2] O. S. Bruning et al., "LHC Design Report Volume I+II+III", CERN-2004-003-V-1, CERN-2004-003-V-2, CERN-2004-003-V-3 (2004).

[3] LHC Layout: Taking a Closure Look at LHC, https://www.lhc-closer.es/taking-a-closer-look-at-lhc/0.lhc-layout

[4] Luminosity: Taking a Closure Look at LHC, https://www.lhc-closer.es/taking-a-closer-look-at-lhc/0.luminosity

[5] The LHC Faq Guide, https://cds.cern.ch/record/2255762/files/CERN-Brochure-2017-002-Eng.pdf

[6] The Large Hadron Collider Unique Scientific Insight The LHC, https://cds.cern.ch/record/1278169/files/CERN-Brochure-2010-006-Eng.pdf

[7] The CERN Accelerator Complex, https://cds.cern.ch/record/2197559

[8] G. Aad et al., ATLAS Collaboration, "The ATLAS experiment at the cern large hadron collider", JINST 3 (2008) S08004.

[9] K. Aamodt et al., ALICE Collaboration, "The ALICE experiment at the CERN LHC", JINST 3 (2008) S08002.

[10] S. Chatrchyan et al., CMS Collaboration, "The CMS experiment at the CERN LHC", JINST 3 (2008) S08004.

[11] A Augusto Alves et al., LHCb Collaboration, "The LHCb experiment at the CERN LHC", JINST 3 (2008) S08005.

[12] TOTEM Collaboration, "TOTEM Technical Proposal", CERN/LHCC 99-7 (1999).

[13] LHCf Collaboration, "Technical Proposal for the CERN LHCf Experiment", CERN/LHCC 2005-032 (2005).

[14] MoEDAL Collaboration, "Technical Design Report of the MoEDAL Experiment", CERN-LHCC-2009-006, MoEDAL-TDR-001.

[15] F. Carminati et al., "ALICE: Physics Performance Report, Volume I", J. Phys. G30 (2004) 1517.

[16] B. Alessandro et al., "ALICE: Physics Performance Report, Volume II", J. Phys. G32 (2006) 1295.

[17] B. Abelev et al., ALICE Collaboration, "Performance of the ALICE Experiment at the CERN LHC", Int. J. Mod. Phys. A29 (2014) 1430044.

[18] http://aliceinfo.cern.ch/ArtSubmission/publications

[19] http://aliweb.cern.ch/

[20] ALICE Collaboration, "ALICE Technical Design Report of the Inner Tracking System (ITS)", CERN-LHCC-99-12, (1999).

[21] K. Aamodt et al., "Alignment of the ALICE Inner Tracking System with Cosmic-Ray Tracks", JINST 5 (2010) 03003.

[22] ALICE Collaboration, "ALICE: Technical Design Report of the Time Projection Chamber", CERN-OPEN-2000-183; CERN-LHCC-2000-001, (2000).

[23] ALICE Collaboration, "ALICE Transition-Radiation Detector: Technical Design Report", ALICE-TDR-9 ; CERN-LHCC-2001-021, (2001).

[24] ALICE Collaboration, "ALICE Technical Design Report of the Time-of-Flight System (TOF)", CERN-LHCC-2000-012, (2000).

[25] ALICE Collaboration, "ALICE Technical Design Report of the High Momentum Particle Identification Detector", CERN-LHCC-98-19, (1998).

[26] ALICE Collaboration, "ALICE Technical Design Report of the Photon Spectrometer (PHOS)", CERN-LHCC-99-04, (1999).

[27] ALICE Collaboration, "ALICE Electromagnetic Calorimeter Technical Design Report", CERN-LHCC-2008-014 ; ALICE-TDR-14, (2008).

[28] ALICE Collaboration, "ALICE FMD Techanical Design Report", CERN-LHCC 2004-025 2004.

[29] ALICE Collaboration, "ALICE Technical Design Report: Photon multiplicity Detector (PMD)", CERN-LHCC-99-32 ; CERN-OPEN-2000-184, (1999).

[30] ALICE Collaboration, "Performance of the ALICE VZERO System", JINST 8 (2013) P10016, CERN-PH-EP-2013-082.

[31] ALICE Collaboration, "ALICE Technical Design Report on Forward Detectors: FMD, T0 and V0", CERN-LHCC-2004-025 ; ALICE-TDR-011, (2004).

[32] ALICE Collaboration, "ALICE Technical Design Report of the Zero Degree Calorimeter (ZDC)", CERN-LHCC-99-05, (1999).

[33] A.Fernandez et al., "ACORDE- A Cosmic Ray Detector for ALICE", arxiv:physics/0612051, (2006) 305.

[34] D. Elia, et al., "The Pixel Detector Based Tracklet Reconstruction Algorithm in ALICE", https://cdsweb.cern.ch/record/1225500/ , (2009).

[35] E. Bruna et al., "Vertex Reconstruction for Proton-Proton Collisions in ALICE", https://cds.cern.ch/record/1225497/, (2010).

[36] ALICE Collaboration, "ALICE Technical Design Report of the Dimuon Forward Spectrometer", CERN-LHCC-99-22, 1999.

[37] ALICE Collaboration, "Addendum to the ALICE Technical Design Report of the Dimuon Forward Spectrometer", CERN-LHCC 2000-046, 200.

[38] https://twiki.cern.ch/twiki/bin/view/ALICE/MuonTracking

[39] http://www.saha.ac.in/web/henppd-introduction-detector working

[40] ALICE Collaboration, "Numerical Simulations and Offline Reconstruction of the Muon Spectrometer of ALICE", ALICE-INT-2009-044.

[41] ALICE Collaboration, "Trigger, Data Acquisition, High-Level Trigger and Control System Technical Design Report", CERN-LHCC, 2003-062 2003.

[42] A. Telesca et al., "The ALICE Data Quality Monitoring System", Real Time Conference (RT), 2010 17th IEEE-NPSS, May (2010).

[43] F. Carena et al., "THE ALICE EXPERIMENT CONTROL SYSTEM", 10th ICALEPCS Int. Conf. on Accelerator & Large Expt. Physics Control Systems. Geneva, 10 - 14 Oct (2005).

[44] ALICE Collaboration, "ALICE Trigger Data-Acquisition High-Level Trigger and Control System: Technical Design Report", ALICE-TDR-10 ; CERN-LHCC-2003-062, (2004).

[45] http://root.cern.ch

[46] https://twiki.cern.ch/twiki/bin/view/ALICE/MuonppQA2011

[47] https://twiki.cern.ch/twiki/bin/view/ALICE/MuonppQA2015

[48] https://twiki.cern.ch/twiki/bin/view/ALICE/AliDPGtoolsPhysSel

[49] B. Abelev et al., ALICE Collaboration, "Inclusive J/ψ Production in pp Collisions at $\sqrt{s} = 2.76$ TeV", Phys. Lett. B718 (2012) 295306.

Chapter 3

Measurement of charged-particle pseudo-rapidity density

In this chapter, we shall address the analysis of the charged-particles multiplicity estimation at $\sqrt{s} = 2.76$ and 5.02 TeV. The differential measurement of charged-particle pseudo-rapidity density ($\mathrm{d}N_{\mathrm{ch}}/\mathrm{d}\eta$) is necessary to explore the multiplicity dependence of hard probes. The value of $\mathrm{d}N_{\mathrm{ch}}/\mathrm{d}\eta$ can be calculated by taking the average number of charged-particles in a given pseudo-rapidity (η) interval. The charged-particle multiplicity (N_{ch}) gives the number of charged-particles produced in the pp collisions or the frequency distribution of the charged-particles in a given collision. The primary charged-particles are defined as the particles produced in the collisions, which includes products of strong, electromagnetic and weak decays of charm and beauty particles. These primary charged-particles do not include the feed-down particles from weak decays of strange particles and other sources, e.g, the particles produced due to photon conversions and secondary hadronic interactions with the detector materials. These are known as secondary charged-particles. In this present work, charged-particles have been estimated in terms of tracklets, using the SPD detector. The tracklets are selected based on the algorithm described in the previous chapter [1, 2]. The charged-particles detection is sensitive to the acceptance and efficiency of the detectors. Hence, the precise measurements can be done only after taking into account the necessary detector acceptance criteria, vertex measurements and so forth. Furthermore, the charged-particles are selected such that at least one charged-particle is produced within $|\eta| < 1$ (i.e. inelastic > 0 event class). Hence, $\mathrm{d}N_{\mathrm{ch}}/\mathrm{d}\eta$ are

corrected with global efficiency factor using MC. The SPD data are corrected using the method described in references [3, 4]. The event averaged $\mathrm{d}N_{\mathrm{ch}}/\mathrm{d}\eta$ measurements are presented in these references [3, 4]. The $\mathrm{d}N_{\mathrm{ch}}/\mathrm{d}\eta$ has been computed by calculating N_{ch} on event-by-event basis with the procedure reported earlier [5, 6]. The $\mathrm{d}N_{\mathrm{ch}}/\mathrm{d}\eta$ has also been extimated using central ALICE framework method described in references [4, 7, 8]. Therefore, the calculation of $\mathrm{d}N_{\mathrm{ch}}/\mathrm{d}\eta$ has been performed using various approaches to check for the consistency.

3.1 SPD status during run condition

The whole SPD detector is not fully functional during data taking due to various reasons e.g, the SPD pixels or modules were inactive during data taking. The reason can be due to dead pixels which do not provide any signal or noisy pixels which provide signal even without a particle hit. In addition, some modules were switched off due to lack of proper cooling. The overall effect of these dead regions resulted in decreasing the SPD acceptance. In Figure 3-1, the module map of the inner and outer layer of SPD as a function of z-vertex (z_v) and the azimuthal angle (ϕ) in pp collisions for LHC11a ($\sqrt{s}$=2.76 TeV) and LHC15n ($\sqrt{s}$=5.02 TeV) periods, are shown. These blue channels represent the active modules during data taking while the gap depicts the dead regions. The number of dead zones can vary with run, which means the SPD status has to be checked for each run to ensure stability. It has been observed that the SPD active modules were stable during the whole period of LHC11a and LHC15n, since we got the same map for each run over the whole periods.

The Figure 3-2 represents the number of SPD tracklets as a function of z_v and ϕ at LHC11a and LHC15 periods. The effect of the inactive SPD modules corresponding to the module maps is clearly visible in terms of the reduced number of tracklets in the ϕ regions for the respective data set. Furthermore, it can also be noted that the overall SPD acceptance in LHC15n is much improved as compared to LHC11a.

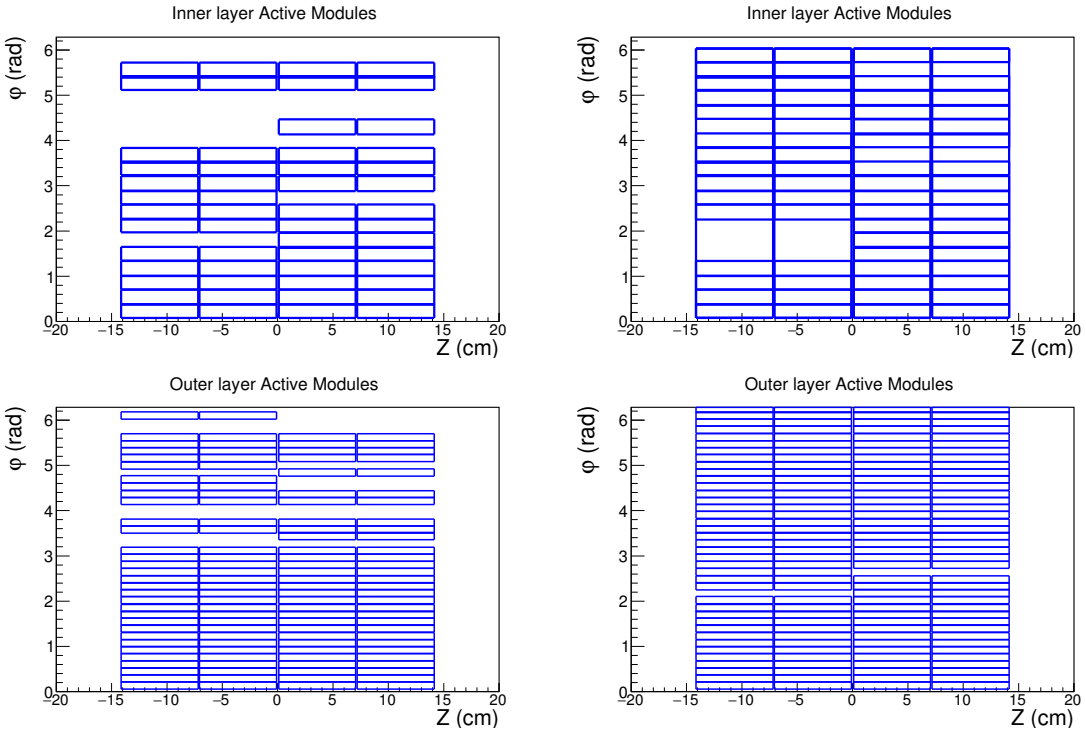

(a) LHC11a (b) LHC15n

Figure 3-1: The inner and outer layer of active module of SPD during various runs for LHC11a and LHC15n periods as function of z-vertex and ϕ.

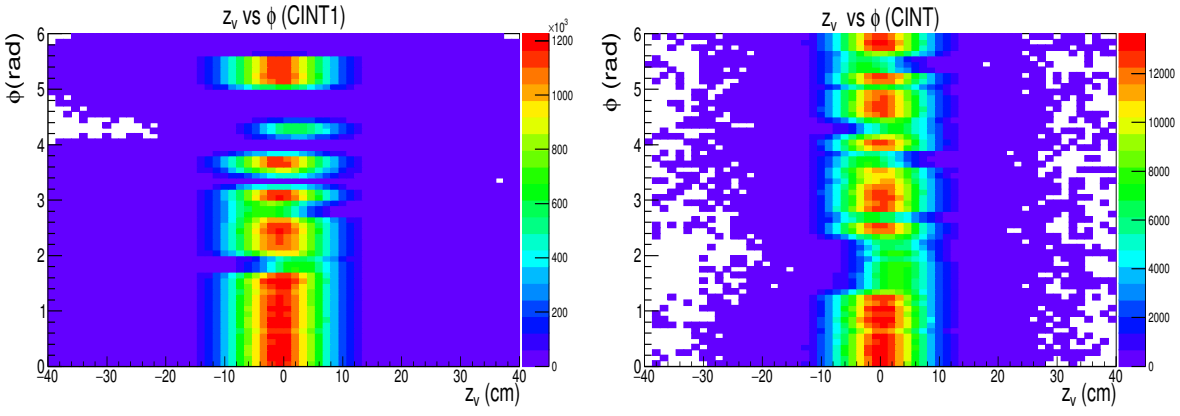

(a) LHC11a (b) LHC15n

Figure 3-2: The number of reconstructed SPD tracklets for LHC11a and LHC15n periods as function of z-vertex and ϕ.

3.2 Event selection for multiplicity analysis

A tracklet is a part of a charged-particle track. The particle hits on the two layers of SPD and was reconstructed along with the z_v of SPD to form a tracklet. Therefore, it is essential to estimate the accurate position of SPD vertex for multiplicity analysis. A set of vertex selection conditions have been tested to check the quality of vertex and applied in the present study. The primary vertex was chosen as the one with the most significant number of SPD tracklets contributing to the vertex measurement.

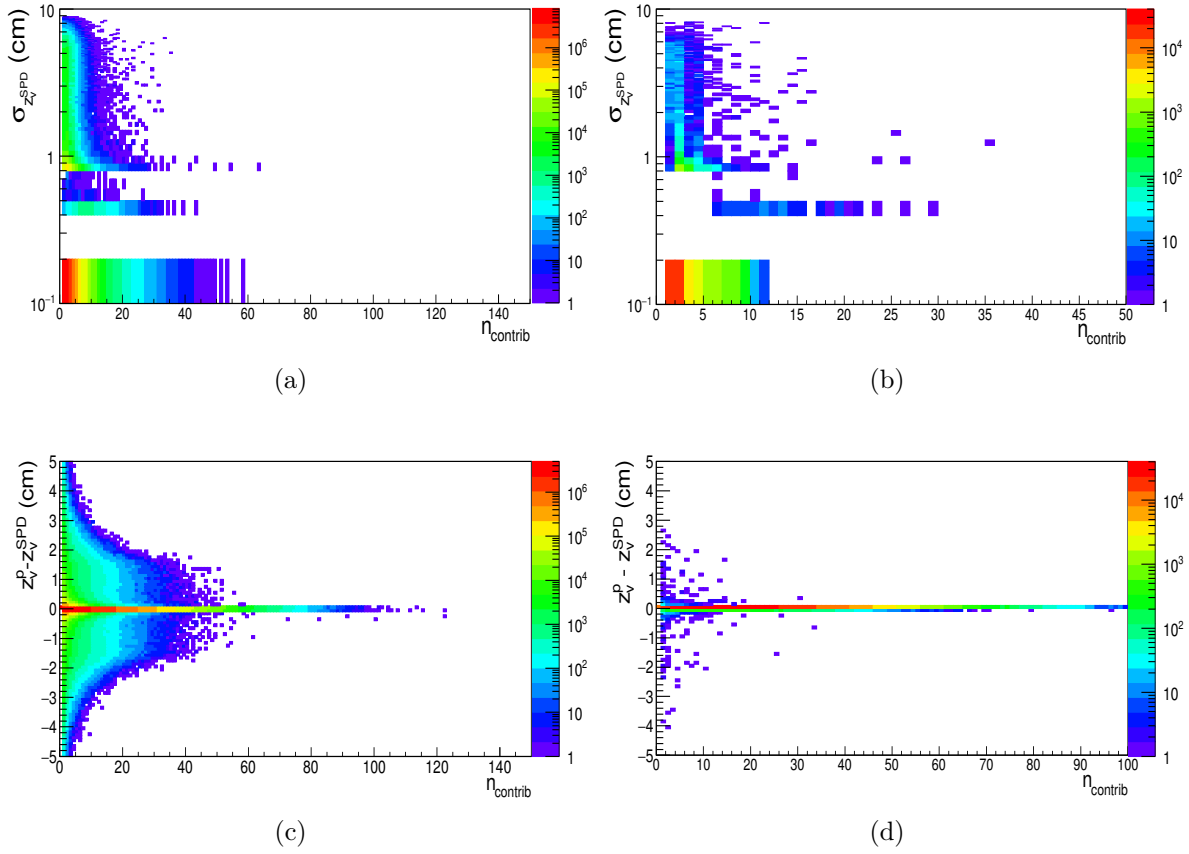

Figure 3-3: (a) This figure represents the SPD vertex resolution with respect to the number of CINT7 contributors. (c) Difference between SPD z_v and primary z_v as function of number of CINT7 contributors. (b) SPD z_v resolution with respect to the number of CMUL7 contributors. (d) Difference between SPD z_v and primary z_v as function of number of CMUL7 contributors

In general, when the information of TPC, ITS or both are available, the primary

vertex (=ITS+TPC vertex) can be reconstructed using the tracks from these detectors. Here, we are not dealing with TPC information (MUFAST cluster). In principle, the primary vertex and SPD vertex should be the same as there is no other detector available which contributes to track reconstruction. The vertex selection conditions from two different trigger cluster MUFAST & CENTNOTRD as well as for the whole MB (V0 and) aka CINT7, along with CMUL7 events, are tested and applied for this purpose. A vertex selection is applied to accept events with SPD z_v resolution better than 0.25 cm. This vertex selection condition results in a reduction of CINT7 (CMUL7) trigger events by 1.08% (0.377%). As the number of contributors increases, the difference between primary and SPD z_v decreases (Figure 3-3). In the case of pp collisions, the primary and SPD z_v should be at the same position. Therefore, in this analysis, the check $|z_v^{SPD} - z_v^p| > 0.5$ has been confirmed. A reduction of 0.01% (CINT7) and 0.0069% (CMUL7) has been observed due to this selection. This is very small and shown in Figure 3-4 (a) and (b). The slight difference in z_v between SPD and primary vertex might be caused due to the presence of EMCAL in the trigger cluster for data taking. It is also crucial for the events to be

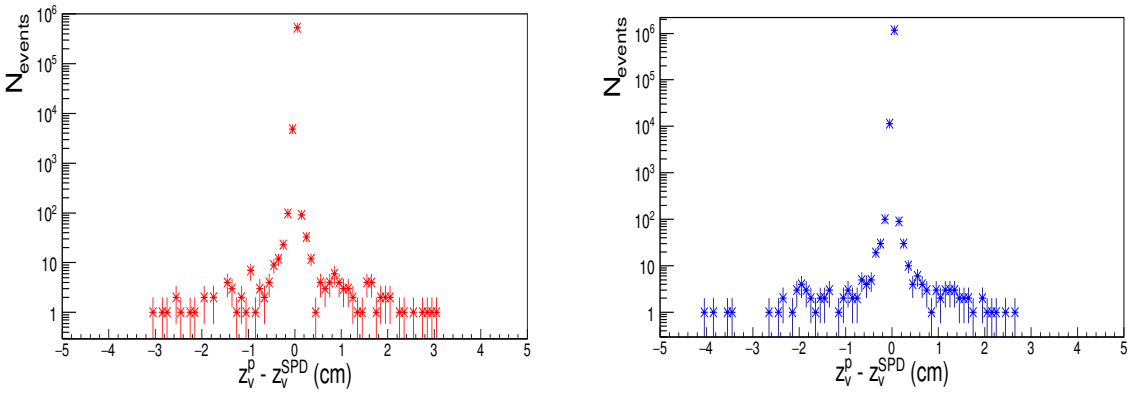

(a) CINT7 (b) CMUL7

Figure 3-4: The number of events with $|z_v^{SPD} - z_v^p| > 0.5$ cm for CINT7 from MUFAST (a) and CMUL7 (b).

selected within the good acceptance of SPD for tracklet determination. Furthermore, the vertex position is tested within 20 cm and 10 cm (Figure 3-5 (a) and (b). The condition $|z_v^{SPD}| \leq 10$ cm is harder than above mentioned cuts and removes 6.95%

(CINT7) and 6.68% (CMUL7) events. The MB events from CENTNOTRD trigger

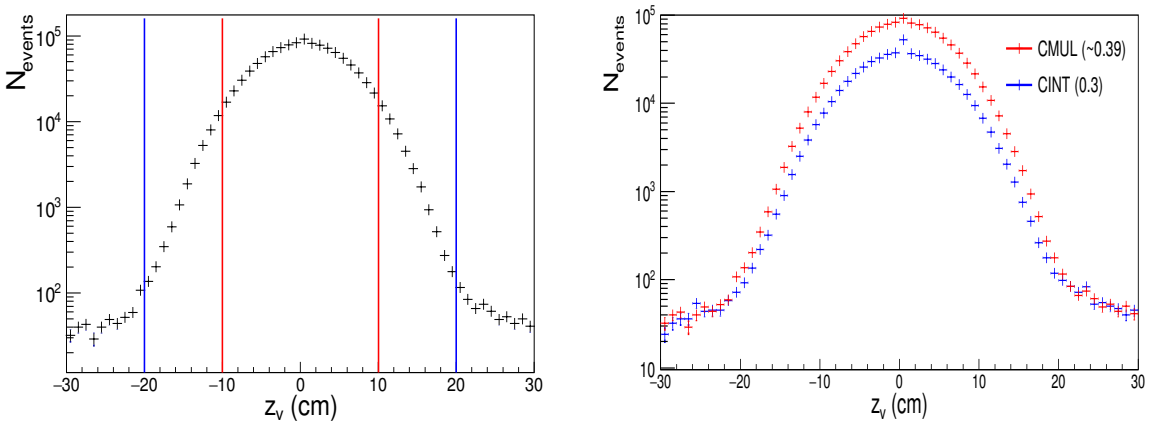

(a) (b)

Figure 3-5: (a) SPD z_v distribution for LHC15n period. The red line represents $|z_v| \leq 10$ cm and blue line represents $|z_v| \leq 20$ cm. (b) SPD z_v distribution for both CINT7 and CMUL7.

.

cluster were also tested for this analysis to determine whether they can be used as a replacement for MUFAST triggers. The difference between primary and SPD z_v is more prominent (1.84%) in the CENTNOTRD as TPC is present in the cluster. z_v^{SPD} resolution is better in CENTNOTRD events (0.747%) and contributors are also larger within $|z_v| \leq 10$ cm (2.963%). CENTNOTRD trigger events have been found to be good candidates for multiplicity analysis but are not present for all 25 runs selected for this study. Finally the whole MB (CINT7) events are analyzed to see the vertex QA effects in the large statistics. The condition $|z_v^{SPD} - z_v^p| > 0.5$ cm, rejects 0.731% events. The z_v resolution better than 0.25 cm is also in a good agreement, only 0.976% events do not pass the criteria. Events, which are not within SPD z_v acceptance (within 10 cm) are 6.148%. Events which do not have reconstructed SPD vertex are 0.254%.

The similar event selection criteria are also checked at 2.76 TeV data set for events from two trigger clusters FASTNOTRD and MUON. The presence of TPC in the FASTNOTRD cluster introduces the difference in the primary and SPD z_v and rejects events 1.622%. In the MUON cluster events this effect is negligible 0.00162%.

It was observed that the difference between primary and SPD z_v is almost negligible. Thus, it is natural to assume the z_v^{SPD} as z_v. The analyzed events are tested to pass the physics selection (PS) condition as described in the Section 2.5. The pile-up rejection tag is enabled in the PS for MB and CMUL7 events at 5.02 TeV. The details of pile-up study is described in the dedicated Section 4.2.1 in the next chapter. The pile-up tag from PS was not activated for RUN-1 data sets i.e. 2.76 TeV energy data. In this case, pile-up rejection is enabled from AOD event class. In order to calculate inclusive J/ψ cross-section, only those events have been selected which satisfy the PS cut along with necessary trigger conditions. However, for multiplicity analysis the additional event selection cuts and Vertex Quality Assurance (VQA) conditions are applied, which are summarized below :

a. Events with a reconstructed SPD vertex are retained.

b. Events in which SPD vertex has number of contributor ≥ 1 are kept.

c. Events with vertex reconstructed with the SPD resolution better than 0.25 cm.

d. Difference between primary and SPD z_v is not more than 0.5 cm. This cut is only tested, not applied during analysis.

e. Events with SPD z_v within 10 cm are considered.

f. -1 $\leq \eta \leq$ 1 on SPD tracklets. At least one charged-particle are selected within full SPD acceptance.

Total number of events, that are rejected due to these event selection cuts are 10.54% (CINT7-B-MUFAST), 7.73% (CMUL7) and 9.87% MB at 2.76 TeV, the pile-up selection cut rejected is about 0.677% events in FASTNOTRD and 1.794% in events MUON cluster, respectively. The combination of all the event cuts removes 24.54% (16.21%) for MB (MUON) events respectively. A set of criteria are applied to select events from MC as well. The charged-particles are selected from simulation within η and SPD acceptance. The event selection criteria for reconstructed SPD tracklets in

MC are similar to that of data. The conditions applied on generated charged-particles are as follows :

1. Charge $\neq 0$
2. Physical primary
3. -1 $\leq \eta \leq$ 1
4. z vertex within 10 cm

3.3 Multiplicity measurement

The events are selected which satisfy the multiplicity analysis conditions that are summarized in Section 3.2 for both MB and muon triggers. After the event and trigger selection, the distributions of number of tracklets are plotted for MB and muon triggers events at both the CM energies.

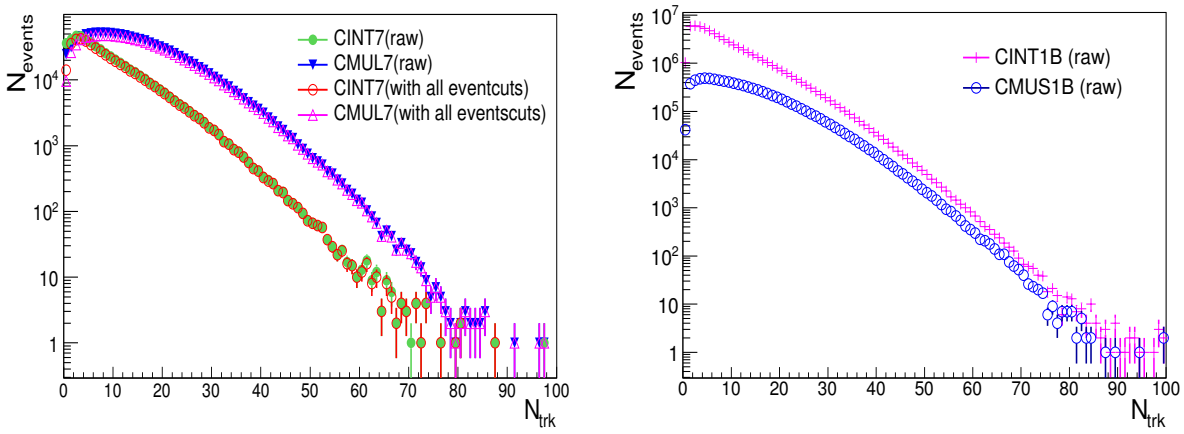

(a) LHC15n period.

(b) LHC11a period.

Figure 3-6: (a) and (b) Event-by-event raw multiplicity distribution of MB and muon events for both the CM energies. (a) The multiplicity distribution after vertex corrections is also shown for both type of events at $\sqrt{s}$ = 5.02 TeV.

In Figure 3-6, the multiplicity distribution as a function of number of SPD tracklets ($N_{\rm trk}$) are shown with and without applying the event selection conditions. It can be seen from these tracklet distribution plots that the VQA conditions have negligible

effect on the SPD tracklets. These small difference can be taken into account during efficiency corrections. As mentioned in Section 3.2, the position of z_v plays an important role in the multiplicity analysis. Therefore, event-by-event mean multiplicity distribution ($\langle N_{trk} \rangle$) was checked as a function of z_v position for both the energies.

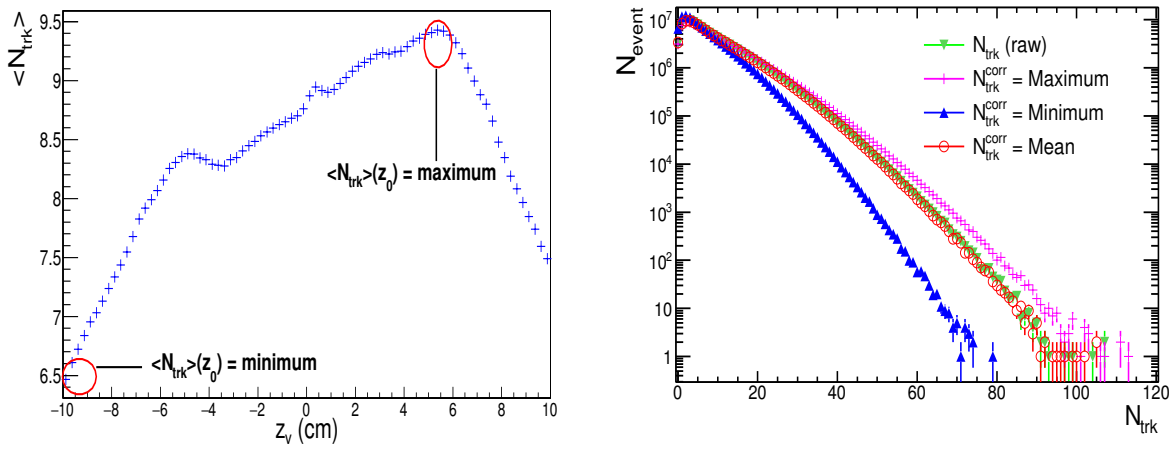

(a) (b)

Figure 3-7: (a) Example of event-by-event raw mean tracklet distribution as a function of z_v, the red circles show the minimum and maximum reference value, respectively. (b) The $N_{\rm trk}$ distribution after the corrections with three reference values (maximum, minimum and mean).

It can be seen from Figure 3-7 that the $\langle N_{trk} \rangle$ distribution at all the z_v position is not continuous, i.e SPD efficiency is not same all over the z_v. The reason of inhomogeneous tracklets distribution can be due to the inactive module of SPD layers. To take into account these acceptance losses, the $N_{\rm trk}$ are corrected using a data driven method, described in the following section.

3.3.1 SPD tracklets correction

To get a flat distribution of $\langle N_{trk} \rangle$ as a function of z_v position, a data driven method has been applied. Previously this method was used to estimate multiplicity for pp $\sqrt{s} = 7$ TeV [5]. This method has also been used for p-Pb & Pb-p $\sqrt{s_{\rm NN}} = 5.02$ [6]. The correction will be applied on MC also to get the corrected $N_{\rm trk}$ which is necessary

to compute the charged-particle multiplicity. The correction is given by

$$\Delta N = N_{tr}(z)\frac{\langle N_{tr}\rangle(z_0 - \langle N_{tr}\rangle(z)}{\langle N_{tr}\rangle(z)} \tag{3.1}$$

where, $\langle N_{tr}(z)\rangle$ is event averaged number of tracklets at a given z_v. $\langle N_{tr}(z_0)\rangle$ is the reference value. It can be taken as maximum (highest SPD efficiency), minimum (lowest SPD efficiency) or mean (average SPD efficiency) in order to get equal distribution of tracklets over z_v (Figure 3-7). The correction is generated randomly with a Poisson distribution centered at ΔN. The corrected tracklets is defined as

$$N_{tr}^{corr}(z) = N_{tr}(z) + \Delta N_{rand} \tag{3.2}$$

where ΔN_{rand} can be taken as positive or negative depending on the reference value $\langle N_{tr}(z_0)\rangle$ (minimum or maximum) as compared to the event averaged values. $N_{tr}^{corr}(z)$ represents the corrected number of SPD tracklets in a given z_v position. The tracklets were corrected by taking the maximum, minimum and mean values as references. The reference values were taken from CINT7 profile histogram. All CINT7 events for the LHC15n period, were considered for this correction. After the correction, the distribution $\langle N_{trk}^{corr}\rangle$ as a function of z_v is flat as can be seen from the Figure 3-8.

The probability distribution of the raw tracklets and the corrected tracklets from minimum bias at both energies are shown in Figure 3-9 (a). In Figure 3-9 (b) tracklets are normalized by mean number of the tracklets from respective energies. It can be seen from the Figure 3-8 that the corrected tracklets distribution has changed with respect to the raw tracklets as well as by the choice of reference value. In order to obtain the homogeneous efficiency of SPD, the tracklets are added (subtracted). The corrected tracklets with maximum reference value are closer to the original tracklets than the corrected tracklets, with the minimum reference. The distribution pattern of all self normalized (corrected, raw) tracklets are similar and the corrected tracklets with maximum reference matches with the raw ones. Thus, in the present analysis maximum reference is taken for the correction procedure.

The data sample is divided into six sub-samples of N_{trk}^{corr} bins for multiplicity analysis.

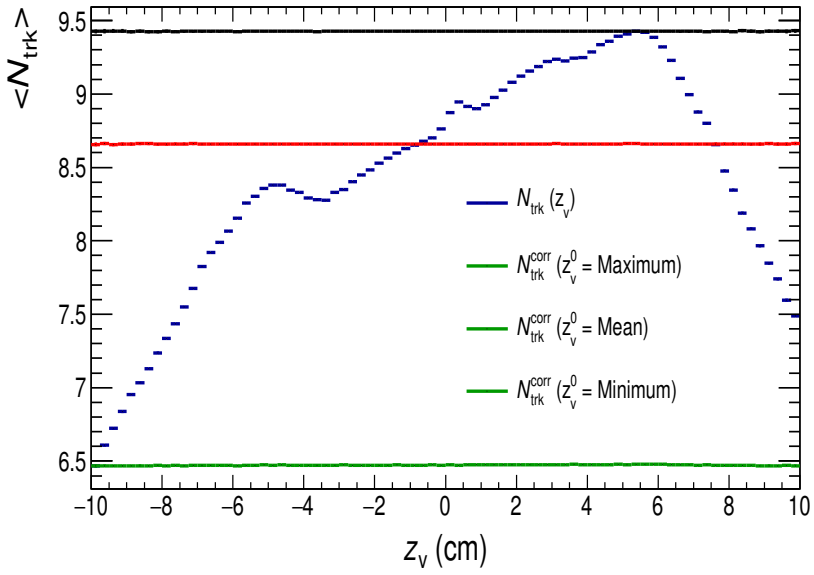

(a) CINT7.

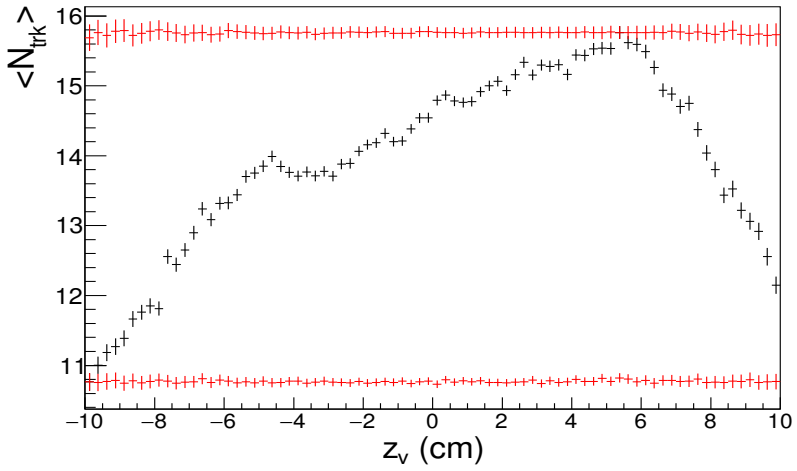

(b) CMUL7.

Figure 3-8: The example of event-by-event corrected mean tracklet distribution over z_v for MB and Muon events at 5.02 TeV.

The $\langle N_{trk}^{corr} \rangle$ are computed in each corresponding multiplicity bins. Thus, three sets of N_{trk}^{corr} are calculated in each multiplicity bin corresponding to the maximum and minimum $\langle N_{tr}(z_0) \rangle$ reference values. The relative N_{trk}^{corr} are also computed by normalizing in each multiplicity bin with the integrated $\langle N_{trk}^{corr} \rangle$. A similar approach is taken for the analysis of 2.76 TeV data. The event averaged value of $\langle N_{trk}^{corr,i} \rangle$ in each

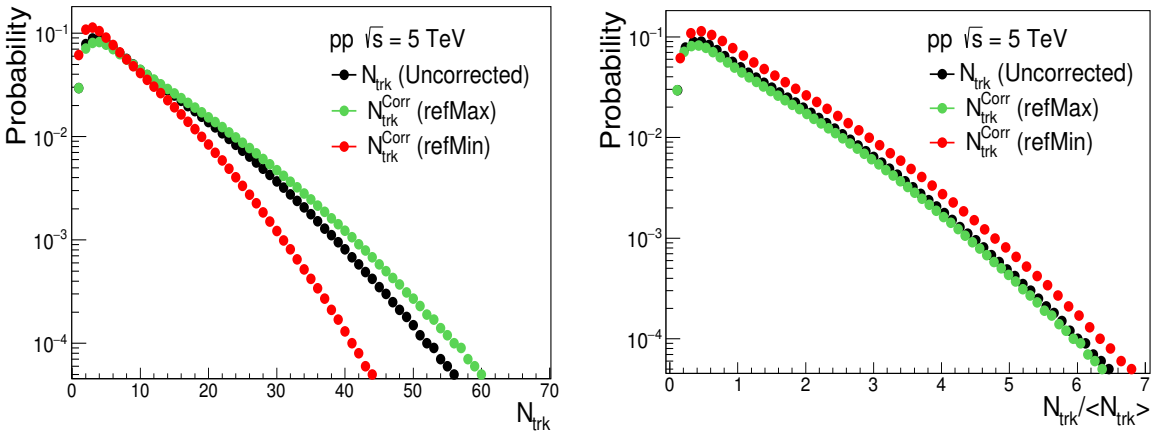

(a) (b)

Figure 3-9: (a) Probability distributions of tracklets before and after tracklet correction. (b) Self normalized probability distributions at pp 5.02 TeV.

corrected multiplicity bin is listed in Tables 3.1 and 3.2 for the respective energies.

$N_{trk}^{corr,i} = bin$	$< N_{trk}^{corr,i} > (max)$ $(\pm\text{stat.})\times10^{-2}$	$\frac{<N_{trk}^{corr,i}>}{<N_{trk}^{corr}>}(max)$ $(\pm\text{stat.})\times10^{-2}$	$< N_{trk}^{corr,i} > (min)$ $(\pm\text{stat.})\times10^{-2}$	$\frac{<N_{trk}^{corr,i}>}{<N_{trk}^{corr}>}(min)$ $(\pm\text{stat.})\times10^{-2}$
$1-4$	2.40 ± 0.02	0.37 ± 0.01	2.42 ± 0.02	0.51 ± 0.01
$5-8$	6.30 ± 0.03	0.98 ± 0.01	5.73 ± 0.03	1.21 ± 0.02
$9-12$	10.31 ± 0.04	1.60 ± 0.02	10.36 ± 0.04	2.18 ± 0.03
$13-16$	14.3 ± 0.05	2.22 ± 0.03	14.35 ± 0.06	3.03 ± 0.04
$17-100$	21.60 ± 0.25	3.36 ± 0.6	20.61 ± 0.31	4.349 ± 0.10
Integrated	6.43 ± 0.10		4.74 ± 0.10	

Table 3.1: $N_{trk}^{corr,i}$ values in pp collisions at $\sqrt{s}$ = 2.76 TeV.

$N_{trk}^{corr,i} = bin$	$< N_{trk}^{corr,i} > (max)$ $(\pm\text{stat.})\times10^{-2}$	$\frac{<N_{trk}^{corr,i}>}{<N_{trk}^{corr}>}(max)$ $(\pm\text{stat.})\times10^{-2}$	$< N_{trk}^{corr,i} > (min)$ $(\pm\text{stat.})\times10^{-2}$	$\frac{<N_{trk}^{corr,i}>}{<N_{trk}^{corr}>}(min)$ $(\pm\text{stat.})\times10^{-2}$
$1-7$	3.81 ± 0.03	0.40 ± 0.03	3.22 ± 0.02	0.50 ± 0.03
$8-12$	9.80 ± 0.03	1.04 ± 0.10	9.70 ± 0.03	1.50 ± 0.10
$13-18$	15.20 ± 0.04	1.61 ± 0.10	15.03 ± 0.10	2.32 ± 0.20
$19-29$	22.90 ± 0.10	2.43 ± 0.30	22.30 ± 0.10	3.43 ± 0.40
$30-48$	35.20 ± 0.25	3.73 ± 1.00	33.65 ± 0.50	5.20 ± 3.00
$49-100$	54.32 ± 1.30	5.76 ± 7.75	52.31 ± 5.10	8.08 ± 4.10
Integrated	9.43 ± 0.10		6.47 ± 0.10	

Table 3.2: $N_{trk}^{corr,i}$ values in pp collisions at $\sqrt{s} = 5.02TeV$.

It can be seen from Figure 3-10 that the corrected tracklets are in exact proportion

to the charged-particles from MC. Hence,

$$\frac{N_{tr}}{\langle N_{tr}\rangle} \propto \frac{dN_{ch}/d\eta}{\langle dN_{ch}/d\eta\rangle} \tag{3.3}$$

So relative tracklets can be used in place of relative charged-particle density and relative yield of J/ψ can be plotted as a function of relative tracklets multiplicity. However, the relative charged-particle density has to be estimated from MC to take into account global efficiency corrections.

3.3.2 Charged-particle multiplicity estimation

The number of charged particles are estimated using the MC event generator. The charged-particles are selected for inelastic > 0 event class i.e.$INEL > 0$. The events selection cuts along with additional conditions mentioned in Section 3.2 are applied to the MC events. The reconstructed tracklets from MC are corrected in a similar manner as data, using the data driven method as discussed in the previous section.

Here, the z_v equalization is done by taking reference value $\langle N_{tr}(z_0)\rangle$ maximum from data and MC $\langle N_{tr}(z)\rangle$ distributions or profiles. Thus, four combinations of profiles are analyzed. It can be observed from Figure 3-10 that the generated charged-particle distribution and the mean tracklet distribution agree well with each other. The distributions of the generated charged-particles N_{ch}^{gen} (MC-true value), the raw reconstructed N_{tr} and the corrected N_{tr}^{corr} tracklets are shown in Figure 3-11.

The correlation of reconstructed tracklets to the generated charged-particles are shown in Figure 3-12. The charged-particles estimation method is different from what is used in central ALICE framework. The $N_{\rm ch}$ are estimated using three different methods as described in the following sections. In each method, the global efficiency was determined from MC by comparing the N_{tr}^{corr} with the true N_{ch}^{gen}. But first the sources of systematic uncertainty will be discussed as they are common in all methods.

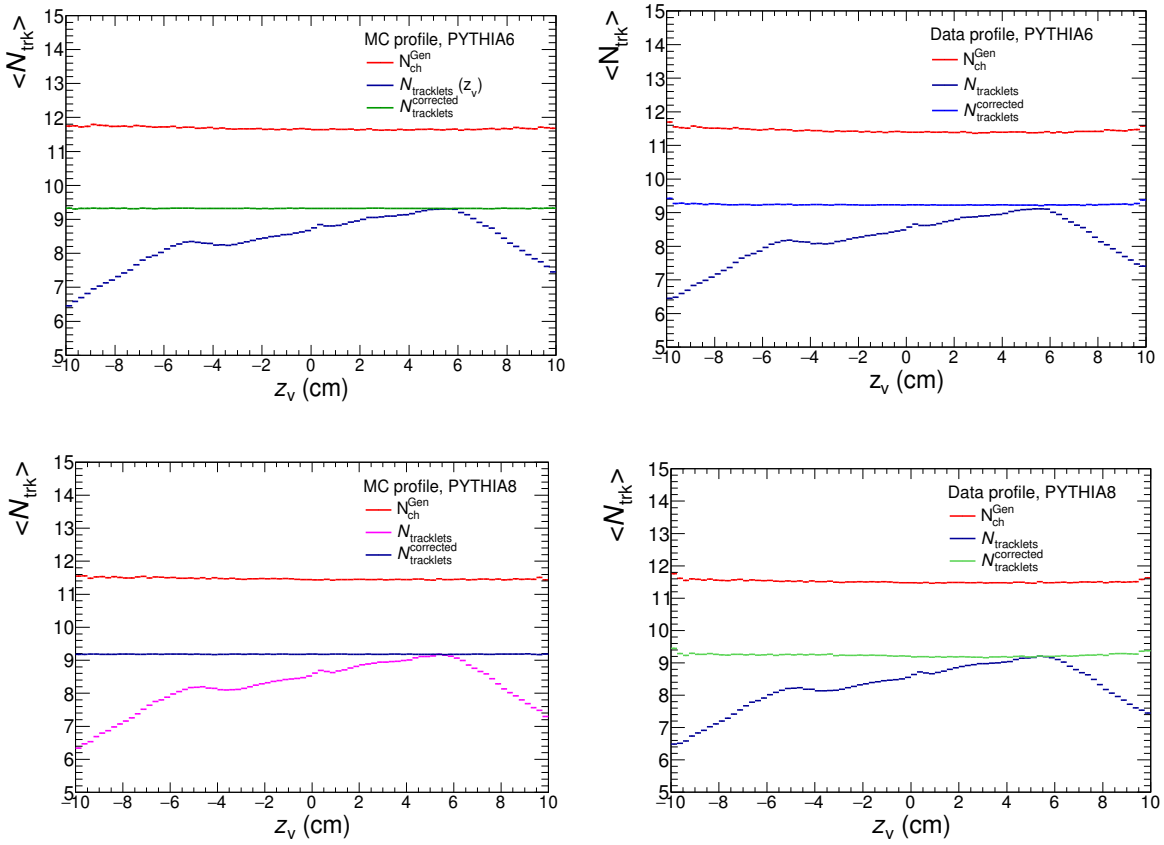

Figure 3-10: Generated, raw and corrected reconstructed mean tracklet distribution as a function of z_v for the four combinations of reference values from two sets of MC.

3.3.3 Source of systematic uncertainty

The N_{ch}^{gen} is not fully homogeneous with z_v. The reconstructed N_{tr}^{corr} was corrected and equalized as function of z_v but any correction to MC-true values were not applied. This may give rise to fluctuations on the global efficiency calculations. The segments of z_v are considered to account for this uncertainty. Two sets of MC event generators were used for both the energies namely PYTHIA8 (LHC16h8a) and PYTHIA6 (LHC16h8b) at 5.02 TeV and PYTHIA8 (LHC12f1a) and PHOJET (LHC12f1b) at 2.76 TeV. The differences in the two event generators were taken into account. Furthermore, as discussed earlier, reconstructed N_{tr} were corrected using profile histograms from both data and MC. These reference values are not identical in each case. This may cause deviation in $N_{\rm ch}$ estimation. Hence, the following aspects are

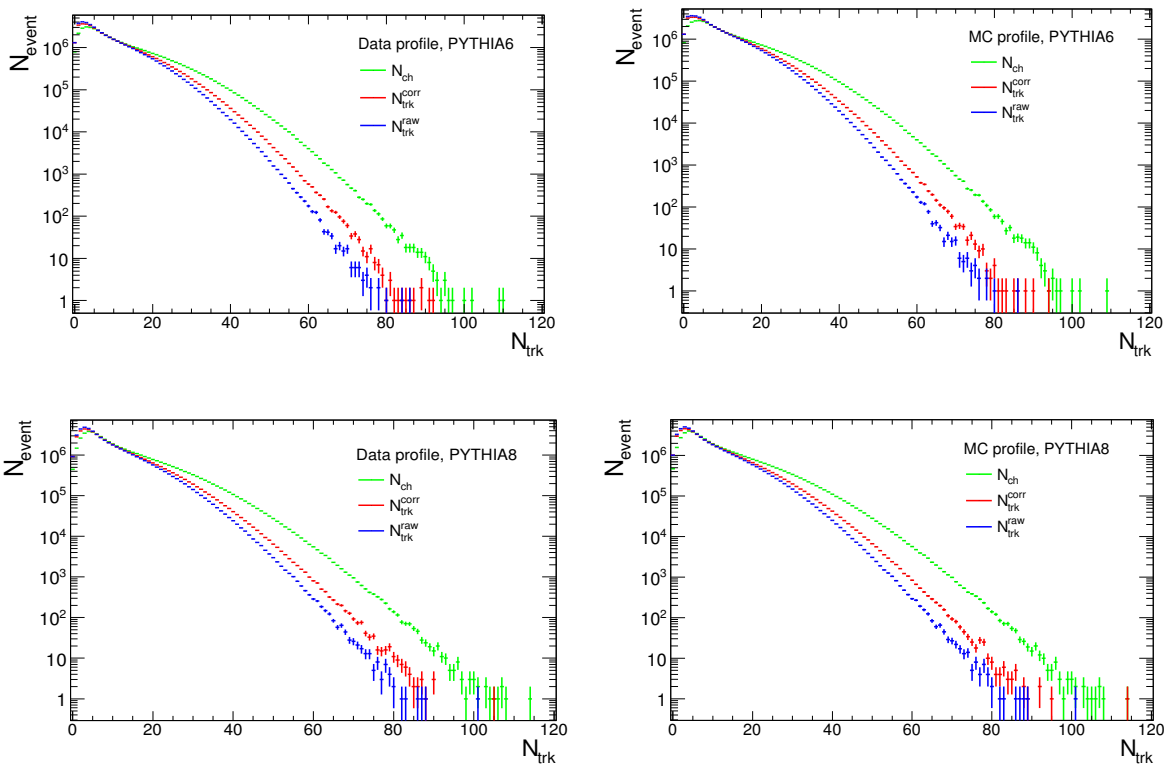

Figure 3-11: N_{ch}^{gen}, N_{tr}^{corr} and N_{tr} distribution for both MC period and for data and MC Profile.

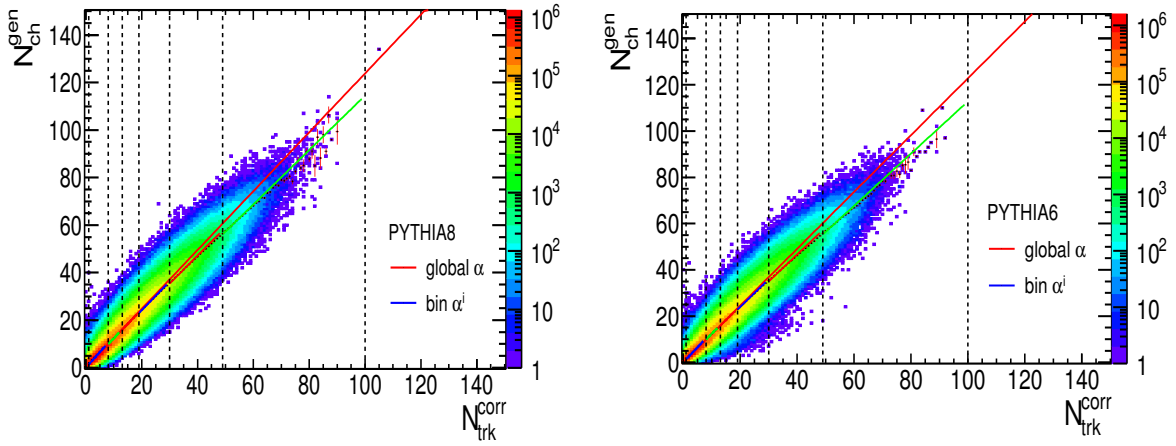

(a) LHC16h8a (b) LHC16h8b

Figure 3-12: Generated particles to corrected reconstructed tracklets correlation. Example of global α and α^i fit.

taken as a source of systematic uncertainties in the computation of mean number of charged-particle, $\langle N_{ch} \rangle$.

- To check the consistency of equalization over z_v, the z_v interval was divided into 5 segments and the deviation is taken as systematic. $-10 < z_v < 10$
  $-10 < z_v < -5$
  $-5 < z_v < -1$
  $-1 < z_v < 1$
  $1 < z_v < 5$
  $5 < z_v < 10$
- Dependency on MC generator: PYTHIA6 and PYTHIA8.
- Data and MC Profile for $N_{\rm ch}$ estimation.
- The uncertainty due to non-linearity.

Combining all the tests a total of 24 tests were performed to calculate charged-particle density. In the same way event averaged charged-particles in the multiplicity bins were also computed. The arithmetic mean of $N_{\rm ch}$ of all the tests and the average of their statistical errors were considered. The standard deviation from the mean value is taken as a systematic uncertainty.

3.3.4 $N_{\rm ch}$ estimation with α

To estimate the charged-particle density, corrected reconstructed tracklets $N_{\rm trk}^{\rm corr}$, from MC have been used to calculate the SPD acceptance efficiency from the $N_{\rm ch} - N_{\rm trk}^{\rm corr}$ correlation plot as given in Figure 3-12. In principle each N_{tr}^{corr} should have a linear dependence on $N_{\rm ch}$. But in reality we observe a deviation as a function of multiplicity. The mean charged-particles $\langle N_{\rm ch}^{\rm i} \rangle$ in the multiplicity bin are calculated by the definition:

$$\langle N_{ch}^{i} \rangle = \alpha . \langle N_{tr}^{corr,i} \rangle \tag{3.4}$$

where α is the global SPD acceptance efficiency calculated for the integrated multiplicity distribution. The deviation between the $N_{\rm ch}$ and $N_{\rm trk}^{\rm corr}$ is also given by α. The $\Delta\eta$ (=2) is the total η acceptance of SPD.

In the same manner, the SPD acceptance efficiencies (α^i) are extracted in tracklets bins to compute $\langle N^{\rm i}_{\rm ch}\rangle$ in each multiplicity segment as follows :

$$\langle N^i_{ch}\rangle = \alpha^i.\langle N^{corr,i}_{tr}\rangle \tag{3.5}$$

Quantities α and α^i were extracted from $N_{\rm ch} - N^{\rm corr}_{\rm trk}$ correlation plot by fitting with four linear fit functions shown in Figure 3-13 (a). The four linear functions were first-order, second-order polynomial functions and setting the constant of the first order polynomial to 0 and 1. Then, $\langle N^i_{ch}\rangle$ were computed using Equations 3.4 and 3.5. The results are plotted bin by bin and compared to the MC-true, shown in Figures 3-14 and 3-15. A clear deviation from linearity may be noticed in Figure 3-13 (a). The second-order polynomial function gives the best χ^2 value in case of global α. But this function can not describe well the $N_{\rm ch}$ in the multiplicity bins, as shown in Figure 3-15.

The integrated $\langle dN_{ch}/d\eta\rangle$ was estimated using the $\langle N_{ch}\rangle$ computed with α factor using Equation 3.4. It gives higher systematic uncertainty 4.628% shown in Figure 3-13 (b). It can be seen from the figure that none of the α fit result gives close value to the MC-true value of $\langle dN_{ch}/d\eta\rangle$.

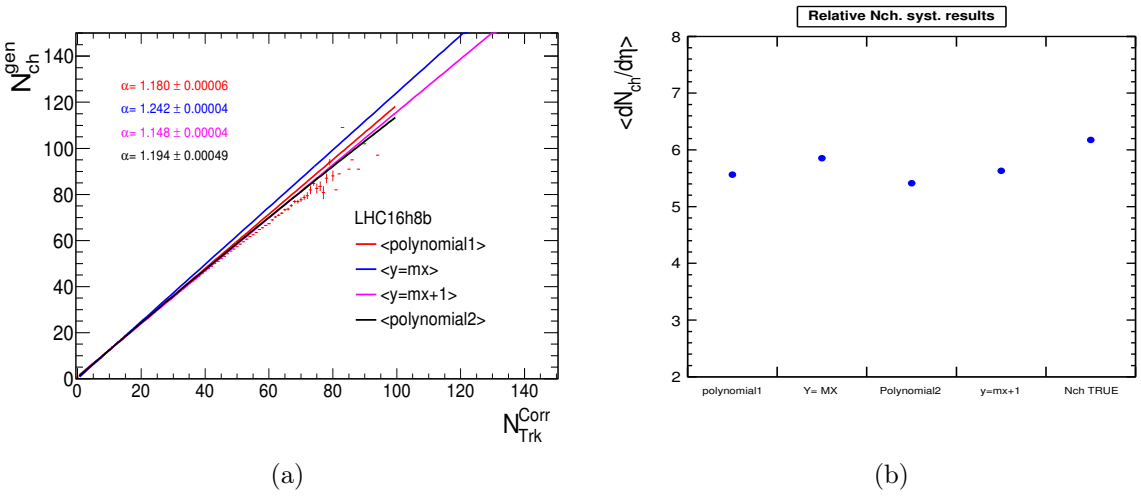

(a) (b)

Figure 3-13: (a) Extraction of α with different fit functions. (b) Integrated charged particle density calculated with α extracted from different fit functions.

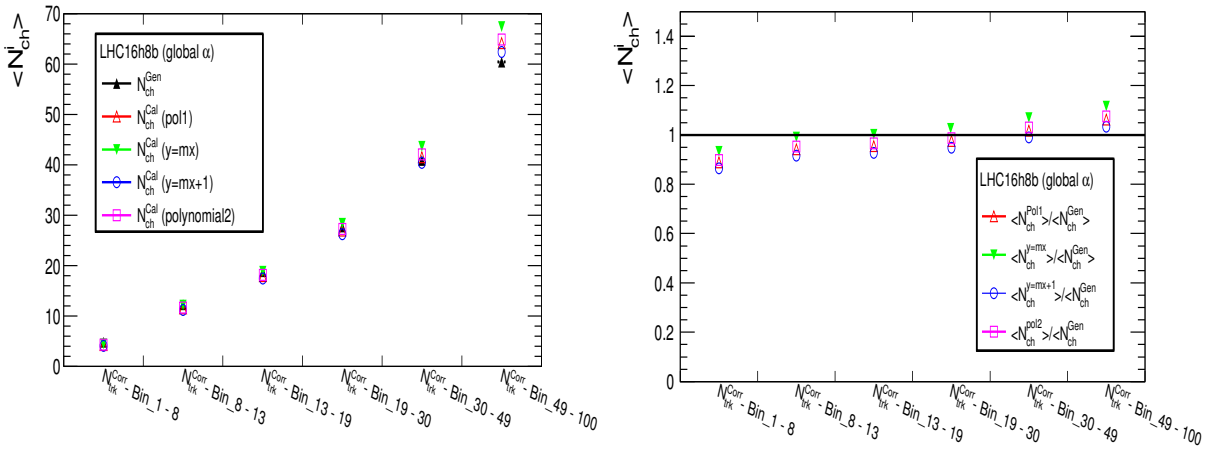

Figure 3-14: Comparison of $\langle N_{\rm ch}^{\rm i} \rangle$ estimated with global α with MC-true.

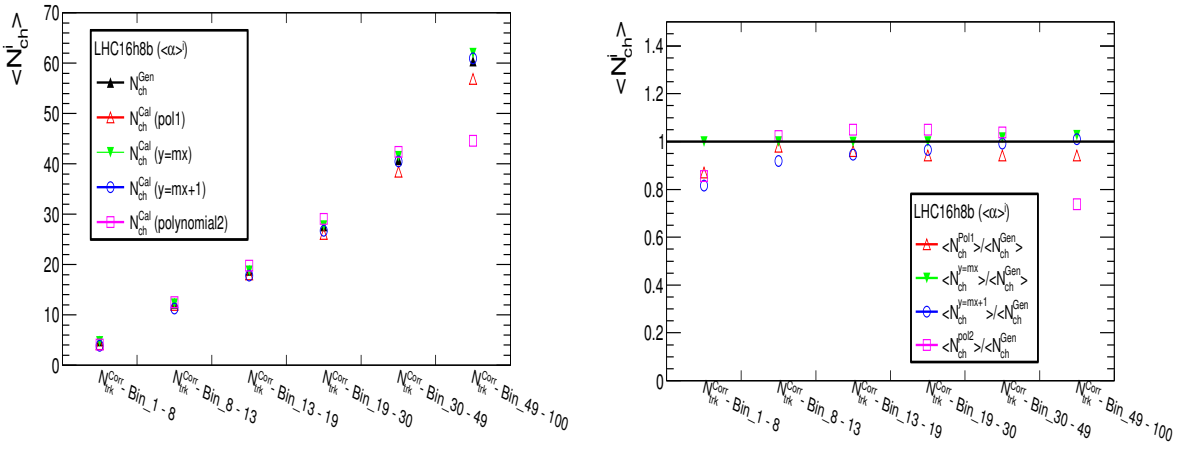

Figure 3-15: Comparison of $\langle N_{\rm ch}^{\rm i} \rangle$ estimated with bin by bin α^i with MC-true.

The $\langle N_{\rm ch}^{\rm i} \rangle$ were computed using Equations 3.4 and 3.5. The source of systematic uncertainties were the same as mentioned in the previous section. The systematic uncertainty obtained for α computation for integrated multiplicity is shown in Figure 3-16. The charged-particle multiplicity has been estimated using these computed α values by multiplying them with the $N_{\rm trk}^{\rm corr}$ from data for both integrated and differential multiplicities. The values of α factors and estimated $\langle N_{\rm ch} \rangle$ for corresponding multiplicity bins are listed in Tables 3.3 and 3.4 for both the energies. It is clear from the table that the α values are not constant against multiplicity. Hence, the correlation between $N_{\rm ch} - N_{\rm trk}^{\rm corr}$ is not linear. This non-linearity can be measured by comparing the global α with the bin by bin value.

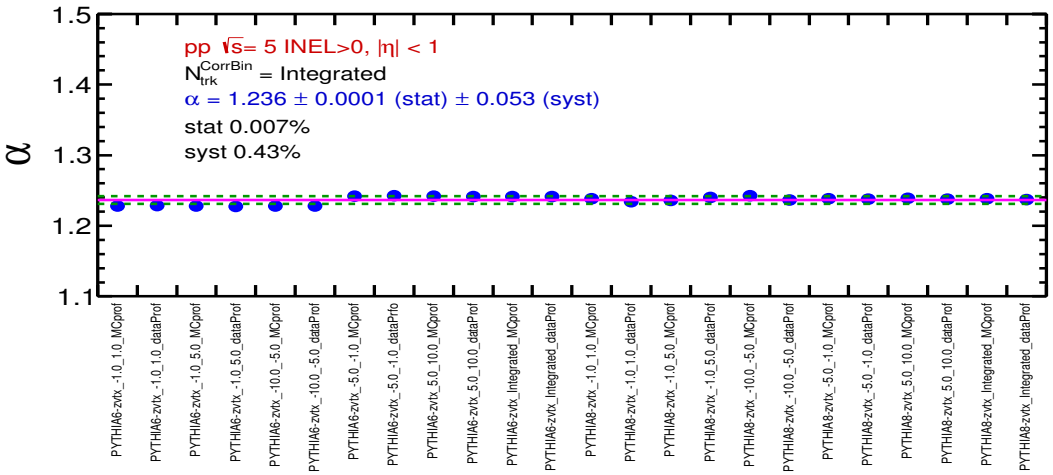

Figure 3-16: Systematic uncertainty of global α value.

$N_{trk}^{corr}bin$	α	$\langle N_{ch}\rangle(\alpha - fit)$	$\langle N_{ch}\rangle(\alpha^i - fit)$
	$\pm$stat. $\times 10^{-2} \pm$ syst. $\times 10^{-1}$		
$1-7$	$1.32 \pm 0.02 \pm 0.24$	$4.71 \pm 0.08 \pm 0.20$	$5.04 \pm 0.08 \pm 0.93$
$8-12$	$1.24 \pm 0.02 \pm 0.06$	$12.10 \pm 0.19 \pm 0.52$	$12.16 \pm 0.19 \pm 0.63$
$13-18$	$1.23 \pm 0.02 \pm 0.06$	$18.79 \pm 0.28 \pm 0.81$	$18.67 \pm 0.28 \pm 0.85$
$19-29$	$1.21 \pm 0.02 \pm 0.10$	$28.27 \pm 0.38 \pm 1.22$	$27.57 \pm 0.38 \pm 2.21$
$30-48$	$1.17 \pm 0.02 \pm 0.17$	$43.52 \pm 0.92 \pm 1.87$	$41.34 \pm 0.92 \pm 5.84$
$49-100$	$1.14 \pm 0.11 \pm 0.26$	$67.17 \pm 6.12 \pm 2.89$	$61.89 \pm 6.12 \pm 1.40$
Integrated	$1.24 \pm 0.01 \pm 0.05$	$11.65 \pm 0.10 \pm 0.50$	–

Table 3.3: α and corresponding $\langle N_{\rm ch}\rangle$ values in pp at $\sqrt{s} = 5.02$ TeV

$N_{trk}^{corr}bin$	α	$\langle N_{ch}\rangle(\alpha - fit)$	$\langle N_{ch}\rangle(\alpha^i - fit)$
	$\pm$stat. $\times 10^{-2} \pm$ syst. $\times 10^{-1}$		
$1-4$	$1.79 \pm 0.05 \pm 0.43$	$3.72 \pm 0.06 \pm 0.11$	$4.32 \pm 0.12 \pm 1.04$
$5-8$	$1.54 \pm 0.04 \pm 0.05$	$9.77 \pm 0.13 \pm 0.30$	$9.71 \pm 0.24 \pm 0.33$
$9-12$	$1.49 \pm 0.04 \pm 0.11$	$15.99 \pm 0.22 \pm 0.49$	$15.45 \pm 0.44 \pm 1.10$
$13-16$	$1.47 \pm 0.05 \pm 0.18$	$22.18 \pm 0.30 \pm 0.67$	$21.01 \pm 0.75 \pm 2.64$
$17-100$	$1.42 \pm 0.05 \pm 0.30$	$33.51 \pm 0.58 \pm 1.02$	$30.79 \pm 1.11 \pm 6.59$
Integrated	$1.55 \pm 0.02 \pm 0.50$	$9.97 \pm 0.18 \pm 0.30$	–

Table 3.4: α and corresponding $\langle N_{\rm ch}\rangle$ values in pp at $\sqrt{s} = 2.76$ TeV

Deviation of α value between integrated multiplicity (global) and in multiplicity bins is 0.52% (minimum) - 7.85% (maximum) at $\sqrt{s} = 5.02$ TeV and deviation in $\langle N_{\rm ch}\rangle$ due to non-linearity is 0.2% to 8.29%. Rest of the control plots for systematic uncertainty are listed in Appendices A.2.1 and A.2.2. Similarly, in pp collisions at $\sqrt{s} = 2.76$ TeV, the difference between global and differential α is 0.628%(minimum) - 16% (maximum) and the difference in $\langle N_{\rm ch}\rangle$ due to the non-linearity at 2.76 TeV is 0.67%(minimum)-

8.11%(maximum). Note that, the use of global α factor to compute $\langle N_{\rm ch}\rangle$ is strongly biased and fails to describe the non-linearities coming from tracklet to charged-particle correlation. The deviation from linearity is higher towards higher multiplicity bins. The systematic uncertainty obtained by this method is quite large. Next we shall discuss somewhat more sophisticated method for $\langle N_{\rm ch}\rangle$ estimation.

3.3.5 Ad-hoc-polynomial method

An alternative method to compute $\langle N_{\rm ch}^{\rm i}\rangle$ is suggested by Philippe Pillot [9]. This method takes into account the non-linearity coming from $N_{\rm ch} - N_{\rm trk}^{\rm corr}$ correlations. The average charged-particles are calculated by the formula :

$$\langle N_{ch}\rangle^{i} = \frac{\sum N^{i}_{events} \times f(N^{corr,i}_{tr})}{\sum N^{i}_{events}} \tag{3.6}$$

where N^{i}_{events} and $N^{corr,i}_{tr}$ are the number of events and corrected tracklets in the multiplicity bin taken from the data. Hence, the $\langle N_{\rm ch}^{\rm i}\rangle$ are re-weighted to match the data. The $N_{ch} - N^{corr}_{trk}$ correlations fitted using parameterization of f, in the range $0 \rightarrow \infty$. Hence f is the ad-hoc polynomial function as described below :

$$\begin{aligned} f(x) &= ax^{c} + b \quad \text{when} \qquad x < x_0 \\ f(x) &= a'x^{c'} + b' \quad \text{when} \qquad x >= X_0 \end{aligned} \tag{3.7}$$

where

$$\begin{aligned} a' &= (ac/c')x_0^{(c-c')} \\ b' &= (a - ac)/c' * x_0^{c} + b \end{aligned} \tag{3.8}$$

where x is the number of tracklets. The fitting plots of $N_{ch} - N^{corr}_{trk}$ correlations with ad-hoc polynomial as well as second-order polynomial functions are shown in the Appendix A.2.3. The charged-particle pseudo-rapidity densities in the multiplicity

bins are calculated by:

$$\langle dN_{ch}/d\eta \rangle^i = \frac{\langle N_{ch} \rangle^i}{\Delta\eta} \tag{3.9}$$

where $\Delta\eta$ is the range of the pseudo-rapidity taken as 2.

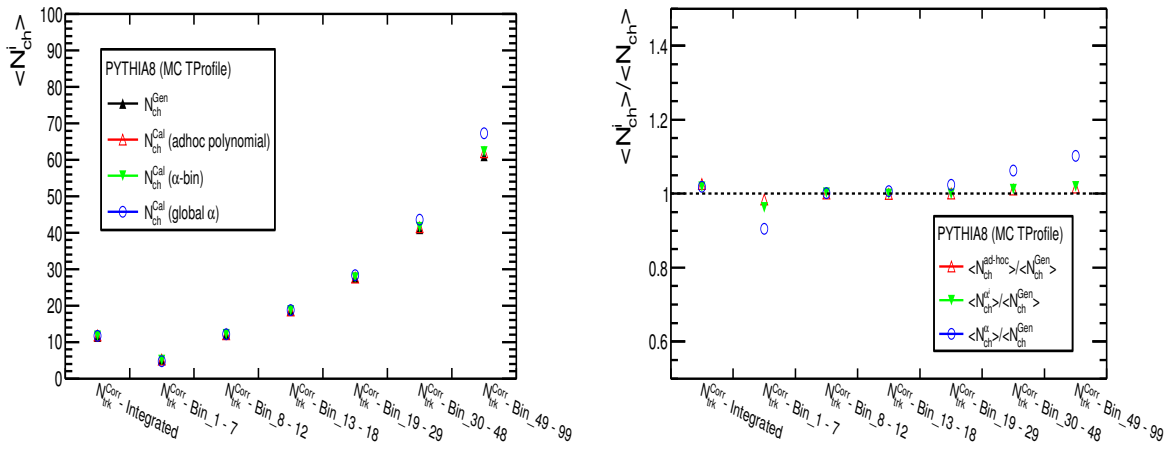

(a) (b)

Figure 3-17: (a) Comparison of $\langle N^i_{ch} \rangle$ computed using ad-hoc polynomial function as well as α factor with MC-true. (b) The comparison of ratio of $\langle N^i_{ch} \rangle$ computed using three method to MC-true.

The $\langle N^{\rm i}_{\rm ch} \rangle$ was calculated using Equations 3.4 and 3.5 and Equation 3.6 and compared to the true MC value. The comparison study helps us to conclude that $N_{\rm ch}$ calculation with ad-hoc polynomial fit gives least systematic uncertainty 0.3% at 5.02 TeV. Figure 3-17 shows that the value of $\langle N_{\rm ch} \rangle$ computed with ad-hoc polynomial are closer to the true MC value. Hence, it was taken as the central value. The $N_{\rm ch}$ calculated with α factor sums up 3.192% of uncertainty. The fluctuation of true MC in z_v bin was also computed to check the stability of $N_{\rm ch}$ over z_v, which has 0.355% uncertainty. Similar study has been done for the five z_v bins, mentioned in Section 3.3.3. The systematic uncertainty for integrated $\langle N_{\rm ch} \rangle$ is shown in Figure 3-18. Similarly, at 2.76 TeV, $\langle N_{\rm ch} \rangle$ are computed and the systematic uncertainty in each multiplicity bin were obtained from the previously mentioned twenty-four tests. An overall systematic uncertainty for $\langle N_{\rm ch} \rangle$ is 0.86% (minimum)-2.56% (maximum) is obtained.

The $\langle {\rm d}N_{\rm ch}/{\rm d}\eta \rangle^i$ is calculated in the same manner as the integrated $\langle {\rm d}N_{\rm ch}/{\rm d}\eta \rangle$ using

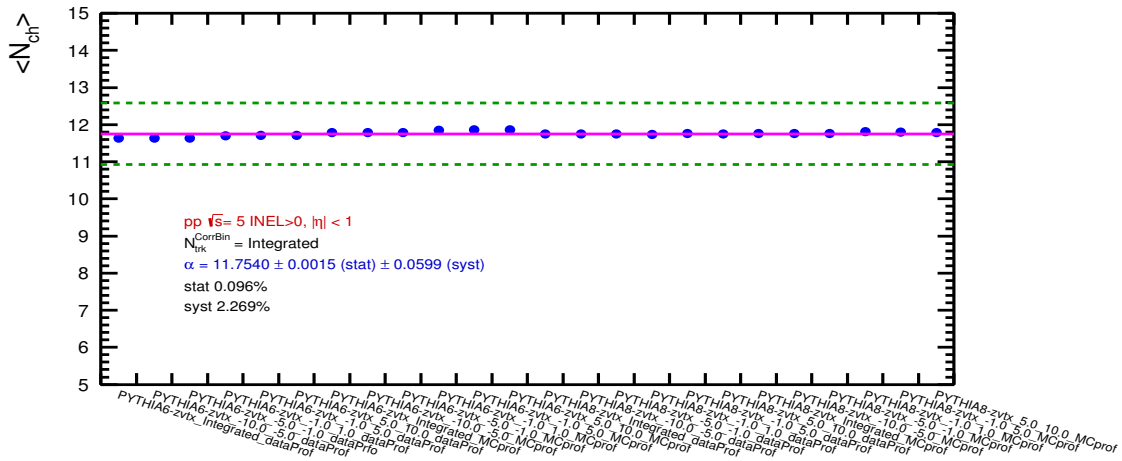

Figure 3-18: Integrated charged-particle systematic uncertainty calculated using ad-hoc polynomial method at $\sqrt{s} = 5.02$ TeV. The labels of the x-axis represent the various tests performed to calculate the systematic uncertainty.

$\sqrt{s} = 5.02$ TeV		$\sqrt{s} = 2.76$ TeV	
$N_{trk}^{corr} bin$	$< N_{ch} >$	$N_{trk}^{corr} bin$	$< N_{ch} >$
	$\pm$stat. $\times 10^{-2} \pm$ syst. $\times 10^{-1}$		
$1-7$	$5.12 \pm 0.04 \pm 1.10$	$1-4$	$10.01 \pm 0.12 \pm 0.60$
$8-12$	$12.13 \pm 0.08 \pm 0.71$	$5-8$	$4.46 \pm 0.07 \pm 1.14$
$13-18$	$18.66 \pm 0.10 \pm 0.88$	$9-12$	$9.72 \pm 0.09 \pm 0.26$
$19-29$	$27.57 \pm 0.14 \pm 2.16$	$13-16$	$15.38 \pm 0.18 \pm 1.32$
$30-48$	$41.28 \pm 0.34 \pm 5.88$	$17-100$	$21.01 \pm 0.28 \pm 2.83$
$49-100$	$61.60 \pm 1.51 \pm 13.81$		$30.67 \pm 0.44 \pm 7.26$
Integrated	$11.75 \pm 0.15 \pm 0.59$	Integrated	$10.01 \pm 0.12 \pm 0.59$

Table 3.5: The $\langle N_{\rm ch} \rangle$ computed using ad-hoc polynomial in pp collisions at $\sqrt{s} = 5.02$ and 2.76 TeV.

Equation 3.9. The final values obtained from $\langle N_{\rm ch} \rangle$ study using the ad-hoc polynomial method have been summarized in Table 3.5. The plots corresponding to the systematic uncertainties are listed in Appendices A.2.4 and A.2.5. The maximum charged-particle multiplicity is ∼31 and ∼61 at 2.76 and 5.02 TeV, respectively. It is also observed that the statistical errors increase consistently with increase of multiplicity. It can also be concluded from Tables 3.4 and 3.5 that the $\langle N_{\rm ch} \rangle$ values computed with the bin by bin α factor and ad-hoc polynomial method, are comparable. This is expected as the ad-hoc polynomial method is an extended version of the bin by bin α computation using a second-order polynomial.

3.3.6 $N_{\rm ch}$ estimation with multiplicity class

In this section, we have cross-checked the ALICE central framework results of charged-particle density in percentile bin using multiplicity class with our present data-driven method. The SPD tracklets are chosen as estimator in the multiplicity class. The charged-particles are estimated using multiplicity class in percentile bin in $-0.5 < \eta < 0.5$ range.

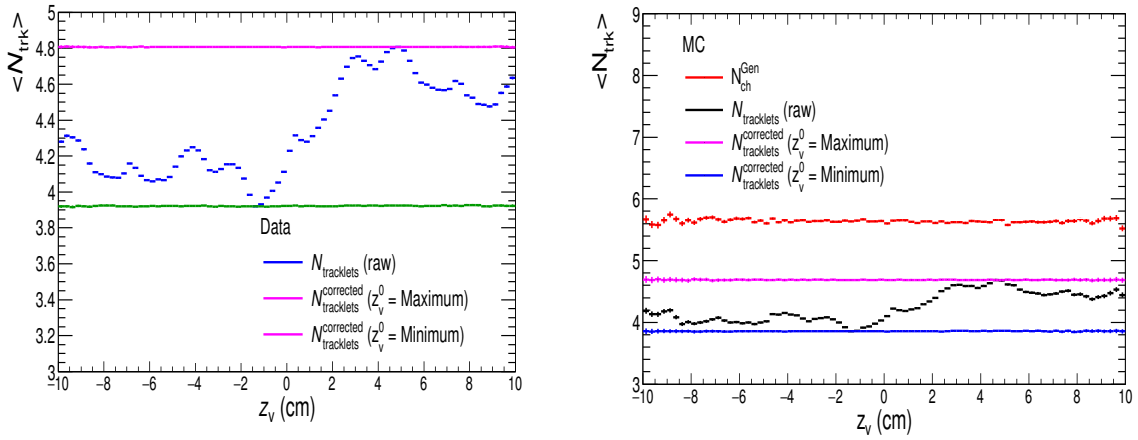

(a) Data. (b) MC.

Figure 3-19: Event-by-event corrected mean tracklet distribution over z_v for MC and Data sets at 5.02 TeV.

The same data set of LHC15n period has been analyzed. For MC anchored to the run 244351 with PYTHIA8 generator has also been analyzed to compute charged-particle multiplicity. All the events cut are the same as mentioned in Section 3.2. The SPD tracklets are corrected employing data driven method using the $\langle N_{tracklet} \rangle$ (z_v) reference maximum and minimum in both MC and data sets. This correction method has been discussed in Section 3.3.1. It can be seen from Figures 3-19 that the z_v equalization of corrected tracklets is flat in case of minimum and maximum references. In case of MC the corrected mean tracklets distribution are in proportion to the mean charged-particles as a function of z_v. The SPD tracklets were projected in the percentile bins. The raw and corrected tracklets were distributed in 10 percentile bins. This is shown in Figures 3-20 and 3-21, respectively. One can easily notice

that the shape of the distribution remains unchanged after the corrections. The distribution of tracklets in each of the individual percentile bins are consistent for data and MC sets.

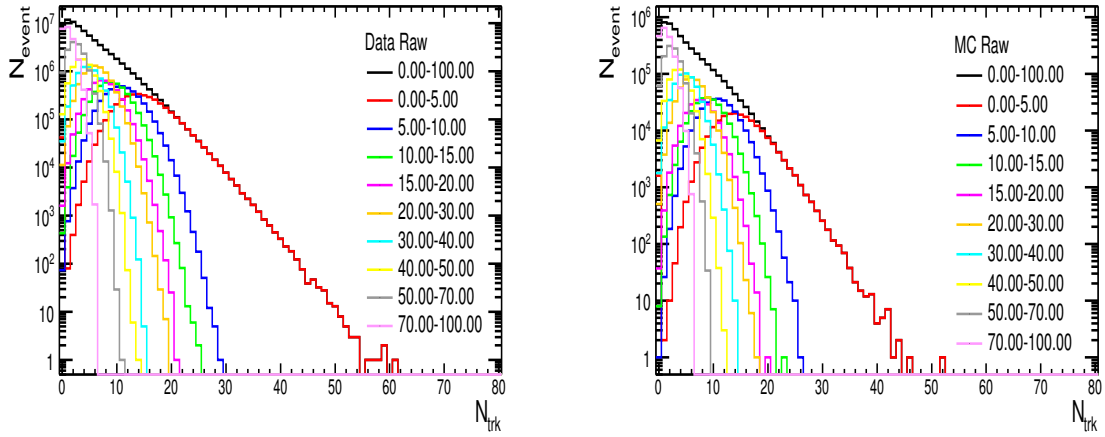

(a) Data. (b) MC.

Figure 3-20: Raw tracklets distribution in percentile bins in pp collisions at 5.02 TeV.

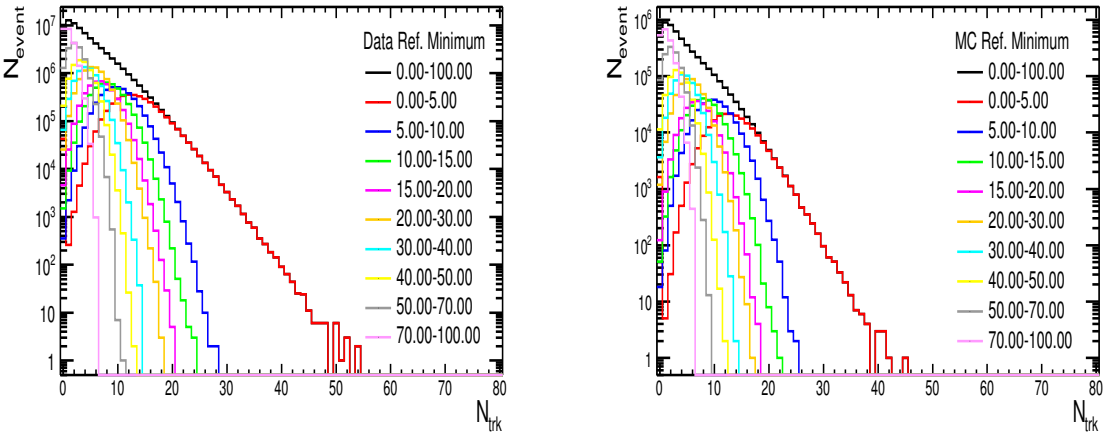

(a) Data. (b) MC.

Figure 3-21: Corrected tracklets (Ref. minimum) distribution in percentile bins in pp collisions at 5.02 TeV.

The $\langle N_{\rm ch} \rangle$ has been calculated employing the ad-hoc polynomial function and using Equation 3.6. In this case N^{i}_{events} and $N^{corr,i}_{tr}$ have been taken in percentile bins from

$Percentilebin(\%)$	$\langle \mathrm{d}N_{\mathrm{ch}}/\mathrm{d}\eta\rangle^{i}(\lvert\eta\rvert < 0.5)$
$0-1$	$25.16 \pm 0.40 - 0.31$
$1-5$	$17.86 \pm 0.24 - 0.20$
$5-10$	$13.82 \pm 0.20 - 0.19$
$10-15$	$11.46 \pm 0.17 - 0.17$
$15-20$	$9.83 \pm 0.16 - 0.15$
$20-30$	$8.02 \pm 0.14 - 0.13$
$30-40$	$6.23 \pm 0.12 - 0.11$
$40-50$	$4.84 \pm 0.09 - 0.08$
$50-70$	$3.34 \pm 0.06 - 0.05$
$70-100$	$1.61 \pm 0.04 - 0.03$

Table 3.6: The charged-particle density in percentile bins in pp collisions at $\sqrt{s} = 5.02$ TeV [8, 10].

data and MC. In this study the computed integrated $\langle \mathrm{d}N_{\mathrm{ch}}/\mathrm{d}\eta\rangle$ value is 5.61 ± 0.053 in pseudo-rapidity range $-0.5 < \eta < 0.5$. The obtained results are very close to the ALICE result with a marginal difference of 0.40%. The results is corrected for minimum bias trigger efficiency for $INEL > 0$ event class [8, 10]. The charged-particle density in percentile bin provided by central ALICE measurement (MM-group) are listed in Table 3.6. The $\langle \mathrm{d}N_{\mathrm{ch}}/\mathrm{d}\eta\rangle^{i}$ are computed in the respective percentile bins using data-driven method and compared to the results from MM-group.

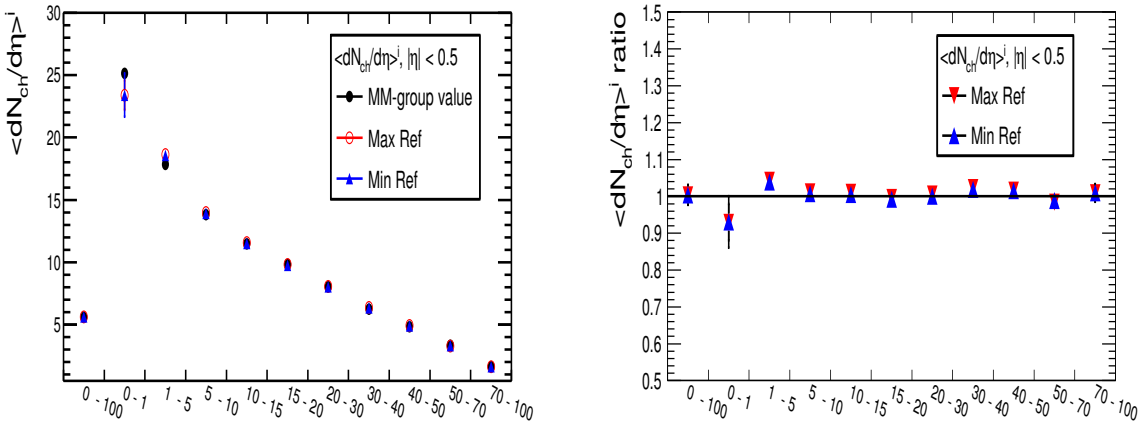

(a) Ref Maximum.

(b) Ref Minimum.

Figure 3-22: $\langle \mathrm{d}N_{\mathrm{ch}}/\mathrm{d}\eta\rangle^{i}$ comparison between data-driven method using z_v profile maximum, minimum and MM-group [8, 10].

It is observed from the Figure 3-22 that the difference in charged-particle pseudo-rapidity density is very small $\sim 1\%$ in integrated and in the percentile bins. The

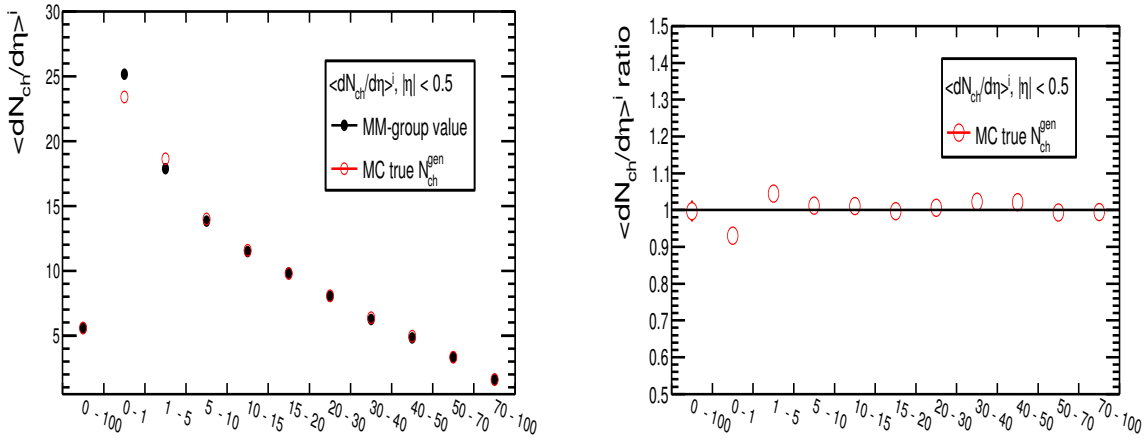

Figure 3-23: $\langle \mathrm{d}N_{\mathrm{ch}}/\mathrm{d}\eta \rangle^i$ comparison between MC-True and MM-group [8, 10].

first two percentile bins have large differences $\sim$ 7% and $\sim$ 4% in both the cases. The trend is similar for both maximum and minimum normalization. However, the results with minimum normalization gives better agreement with MM-group results. The $\langle \mathrm{d}N_{\mathrm{ch}}/\mathrm{d}\eta \rangle^i$ has been computed in percentile bin using the MC-true N_{ch}^{gen} and compared to the results of MM-group as shown in Figure 3-23. The results are in fair agreement with a little difference of $\sim$ 1% to $\sim$ 2%.

3.4 Efficiency correction

3.4.1 Event selection efficiency

The minimum bias trigger efficiency (ϵ_{MB}) was estimated in order to correct the J/ψ yields and tracklets. The efficiency corrections has been done in a similar manner for the 2.76 and 5.02 TeV data. The definition of MB at both the energies were different i.e. KINT7 corresponds to V0(AND) at 5.02 TeV and KINT1 corresponds to V0(OR 1 hit on SPD) at 2.76 TeV. The efficiency corrections will be addressed at 5.02 TeV. In the present analysis the events are selected for inelastic > 0 event class ($INEL > 0$). The ϵ_{MB} was computed from the two sets of MC, PYTHIA8 and

PYTHIA6, respectively, and is defined as follows:

$$\epsilon_{MB} = \frac{N_{ch} distribution with MB(PS + NoEventcuts)}{N_{ch} distribution without MB(PS + NoEventcuts)} \tag{3.10}$$

where all the events pass the physics selection condition. ϵ_{MB} may vary with multiplicity and to check the stability, ϵ^{i}_{MB} was also computed in the multiplicity bins using the following equation:

$$\epsilon^{i}_{MB} = \frac{N^{i}_{ch} distribution with MB(PS + NoEventcuts)}{N^{i}_{ch} distribution without MB(PS + NoEventcuts)} \tag{3.11}$$

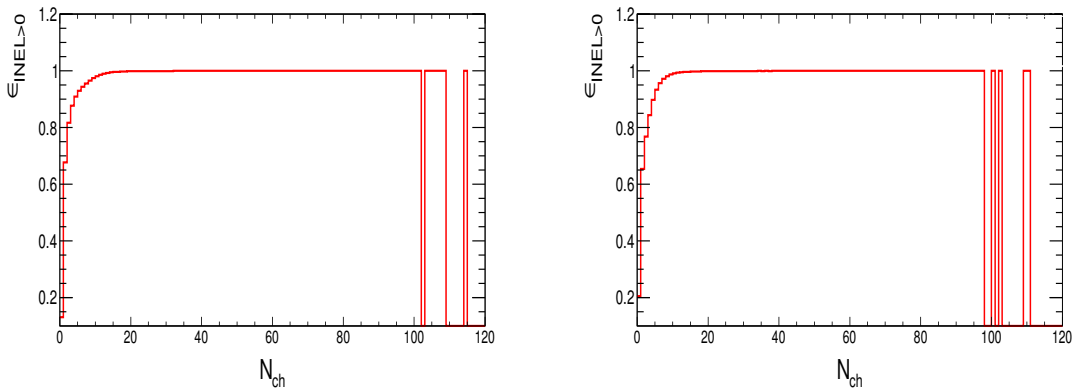

(a) PYTHIA8 (b) PYTHIA6

Figure 3-24: ϵ_{MB} for INEL > 0 as a function of multiplicity for both MC period.

The ϵ^{i}_{MB} is stable over the entire multiplicity range except for lower multiplicity region. The values are listed in the Table 3.7 and 3.8 for PYTHIA8 and PYTHIA6 MC at pp 5.02 TeV.

The integrated minimum bias trigger efficiency for V0 (AND) i.e. KINT7 trigger is very small in both MC generators for INEL$>$ 0 class. The fraction of events rejected due this selection are 6.26% (PYTHIA8) and 8.10% (PYTHIA6). The $N_{\rm ch}$ distribution is plotted for both the MC periods with and without KINT7 trigger as shown in Figure 3-24. As it can be seen from the Table 3.7 and Figure 3-24 that the values of ϵ_{MB} is almost unity in all the multiplicity bins except the first one having minimum multiplicity. Hence, for higher multiplicity bins ϵ_{MB} is taken as

$MultiplicityBin$	$EventswithKINT7$	$EventswithoutKINT7$	$\epsilon_{MB} \times 10^{-2}$
$Integrated$	$5.29e+07$	$5.65e+07$	0.94 ± 0.01
$1-7$	$2.57e+07$	$2.77e+07$	0.93 ± 0.02
$8-12$	$6.46e+06$	$6.46e+06$	0.99 ± 0.05
$13-18$	$4.57e+06$	$4.57e+06$	0.99 ± 0.07
$19-29$	$3.73e+06$	$3.73e+06$	1.00 ± 0.07
$30-48$	$0.95e+06$	$0.96e+06$	1.00 ± 0.01
$49-100$	$0.03e+06$	$0.03e+06$	0.997 ± 0.08

Table 3.7: Events with, without MB trigger and INEL > 0 ϵ_{MB} for PYTHIA8.

$MultiplicityBin$	$EventswithKINT7$	$EventswithoutKINT7$	$\epsilon_{MB} \times 10^{-2}$
$Integrated$	$4.95e+07$	$5.39e+07$	0.91 ± 0.01
$1-7$	$2.23e+07$	$2.44e+07$	0.92 ± 0.03
$8-12$	$5.94e+06$	$5.96e+06$	0.99 ± 0.06
$13-18$	$4.46e+06$	$4.46e+06$	1.00 ± 0.07
$19-29$	$3.66e+06$	$3.66e+06$	0.99 ± 0.07
$30-48$	$0.88e+06$	$0.88e+06$	0.99 ± 0.01
$49-100$	$0.02+06$	$0.02e+06$	1.00 ± 0.09

Table 3.8: Events with, without MB trigger and $INEL > 0$ ϵ_{MB} for PYTHIA6.

1. The ϵ_{MB} for first multiplicity bin has to be taken into account. The corrections to minimum bias trigger efficiency is computed as $\epsilon_{INEL>0} = 0.94$ (PYTHIA8) and 0.92 (PYTHIA6) for integrated multiplicity at 5.02 TeV. This is consistent with the reported value V0(AND) INEL> 0 [8]. Similarly, the $\epsilon_{INEL>0}$ computed at 2.76 TeV is 0.99 for both PYTHIA8 and PHOJET MC events.

3.4.2 Vertex selection efficiency

The fraction of events rejected by the vertex QA selection mentioned in Section 3.2 was also taken into account. The efficiency factor in this case ($\epsilon^{MB}_{vtx,QA}$) is defined as:

$$\epsilon^{MB}_{vtx,QA} = \frac{IntegratedN_{MB}(withvertexQA)}{IntegratedN_{MB}(withoutvertexQA)} \tag{3.12}$$

The $\epsilon^{MB}_{vtx,QA}$ was also checked for muon events (CMUL7). The ratio of number of MB events as well as muon (CMUL7) with and without vertex selection cuts are shown in Figure 3-25. The value of $\epsilon^{MB}_{vtx,QA}$ was found to be 0.96% in the present analysis for integrated multiplicity at 5.02 TeV. This value for pp 2.76 TeV was 0.85%. It can be noted that vertex quality of SPD was poor during RUN-1 data taking as compared

to RUN-2. Hence large number of events are rejected due to this selection criteria. However, vertex quality is consistent for muon trigger events and we obtained 95% efficiency at both energies due to vertex QA selection.

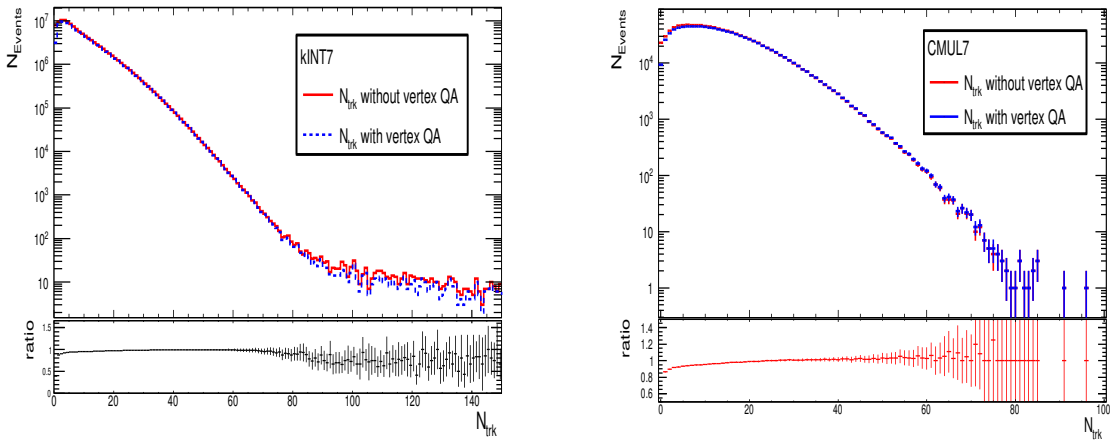

(a) MB events

(b) MUON events

Figure 3-25: Distribution of MB and Muon events with and without vertex QA cuts.

3.4.3 Vertex QA efficiency for $N_{\rm ch}$

Finally, the vertex QA efficiency has been computed as a ratio of charged-particles with and without vertex QA cuts for $INEL > 0$ events class. It is defined as:

$$\epsilon^{MB}_{vtx,QA}(MC, INEL > 0) = \frac{N_{events}(withN_{ch} > 0 + vertexQA)}{N_{events}(withN_{ch} > 0 + withoutvertexQA)} \tag{3.13}$$

The $\epsilon^{Nch}_{vtx,QA}$ was computed at both the CM energies for their respective MC periods. The results of vertex QA efficiency are listed in Table 3.9.

	$\epsilon_{vtx,QA}\sqrt{s}$=5.02 TeV	$\epsilon_{vtx,QA}\sqrt{s}$=2.76 TeV
N_{MB}	$0.96 \pm 0.01 \times 10^{-2}$	$0.85 \pm 0.02 \times 10^{-2}$
N_{CMUL}	$0.95 \pm 1.10 \times 10^{-2}$	$0.95 \pm 0.05 \times 10^{-2}$
$N_{ch}(MC1)$	$0.99 \pm 0.02 \times 10^{-2}$	$0.97 \pm 0.02 \times 10^{-2}$
$N_{ch}(MC2)$	$0.98 \pm 0.02 \times 10^{-2}$	$0.96 \pm 0.02 \times 10^{-2}$

Table 3.9: $\epsilon_{vtx,QA}$ factor for various components.

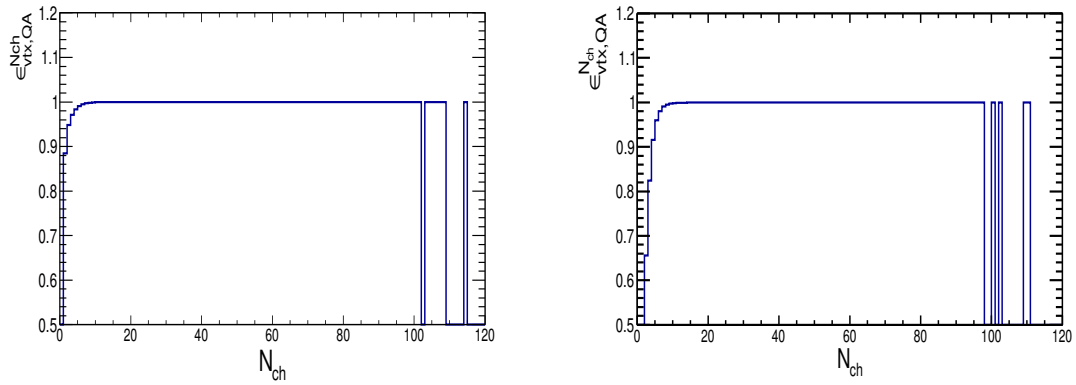

(a) PYTHIA8 (b) PYTHIA6

Figure 3-26: $\epsilon^{Nch}_{vtx,QA}$ as function of multiplicity for both MC generators.

The event selection efficiency for MB will be applied to correct calculated $N_{\rm ch}$ from N^{Corr}_{trk} as well as the relative J/ψ yield. The vertex QA efficiency are taken into account for integrated multiplicity estimation. Since, the effects of vertex QA efficiencies are negligible in individual multiplicity bins and hence, the efficiency correction factors are considered as unity.

3.4.4 Corrections for $INEL = 0$

In addition the correction due to $N_{trk} = 0$ events has been computed to look for possible contamination due to the events corresponds to $INEL = 0$. The efficiency corrections corresponds to $N_{trk} = 0$ or the contamination from $INEL = 0$ events can be considered in the following way:

$$\frac{N_{events}(withN_{ch} = 0 + kINT7)}{N_{events}(withN_{ch} \geq 0 + kINT7)} \tag{3.14}$$

The correction factors obtained were 0.047(PYTHIA6) and 0.024(PYTHIA8). The contamination for $INEL = 0$ in data was computed as: (1-0.047)/0.96 = 0.992 (PYTHIA6) and (1-0.024)/0.96 = 1.02 (PYTHIA8) respectively, where $\epsilon^{MB}_{vtx,QA} = 0.96$ for the data. The $INEL = 0$ contamination at 2.76 TeV is larger and are found to be 0.122 (PHOJET) and 0.124 (PYTHIA8) and the corresponding contamination in

data, are (1-0.122)/0.85 = 1.03 in each case. Similarly, the vertex QA correction can be done for $INEL = 0$ charged-particles, using the following definition:

$$\frac{N_{events}(withN_{ch} = 0 + kINT7 + vtx, QA)}{N_{events}(withN_{ch} \geq 0 + kINT7 + vtx, QA)} \tag{3.15}$$

A negligible contamination is observed in this case i.e. 0.019 (PYTHI6) and 0.009 (PYTHIA8) at 5.02 TeV. The corrections for charged-particles due to $INEL = 0$ are (1-0.019)/0.98 = 0.998 (PYTHIA6) and (1-0.009)/0.987 = 1.002 (PYTHI8). The vertex QA efficiency for $INEL = 0$ events at 2.76 TeV are 1.02 (PYTHIA8) and 1.02 (PHOJET).

3.4.5 Efficiency corrections for the first bin

The minimum bias trigger efficiency for $INEL > 0$ for the first bin are 0.902 (PYTHIA8) and 0.874 (PYTHIA6) respectively at 5.02 TeV. The value of ϵ^{i}_{MB} for first bin ($N^{\rm corr}_{\rm trk}$ = 1-7) is used to correct the relative yield using Equation 3.11. The $\langle N_{\rm ch}\rangle$ is also needed to be corrected in this bin. The correction for $\langle N_{\rm ch}\rangle$ can be done in the following two ways:

- If we use $N_{ch} = 1$, correction for the first bin comes out to be (0.889*5.122 + 0.111*1)/5.122 = 0.91. By assuming that the correction is 1 for events with and without trigger, we get final value (0.91+1)/2 = 0.95. The corrections (1/0.95) = 1.05 is to be applied for charged-particle density of the first bin.

- Alternatively, efficiency corrections for $\langle N_{\rm ch}\rangle$ in the first bin:

$$\epsilon^{MB}_{INEL>0} = \frac{\langle N_{ch}\rangle(N^{Corr}_{trk}[1,7] + INEL > 0 + PS(kINT7) + vtxQA + vtxrange)}{\langle N_{ch}\rangle(N^{Corr}_{trk}[1,7] + INEL > 0 + vtxQA + vtxrange)} \tag{3.16}$$

The obtained results for PYTHIA6 is 1.0628 and for PYTHIA8 is 1.0358 respectively. Final correction for $\langle N_{\rm ch}\rangle$ is 1.05, which is consistent with previous method value. The correction for first bin (1-4) at 2.76 TeV is 1.002 for both the MC estimators.

3.4.6 Event selection uncertainty

The systematic uncertainty due to the various events selection cuts described in Section 3.4.1 will be summarized here. There are contributions from vertex selection and trigger selection for inelastic > 0 events class. The vertex selection efficiency correction term from data is a contributory factor. The inelastic> 0 events class with V0(AND) trigger with good vertex events were considered for the present AOD sample. The corrections regarding z-vertex position i.e. events rejected due to $z_v < 10$ cm has not been included, since this selection criteria is same for both MB and J/ψ and the corrections cancel out in the self-normalizing process. The corrections regarding contamination due to events corresponds to $N_{trk} = 0$ has to be considered as well. Corrections for the first multiplicity bin is also taken into account in both yield calculation and $\langle N_{\rm ch} \rangle$ estimation.

The ϵ_{MB} has been computed for PYTHIA6 and PYTHIA8 MC periods at 5.02 TeV and PYTHIA8 and PHOJET at 2.76 TeV data. The average efficiency value is used as final value in this analysis. The deviation in the two MC values with respect to average value are taken as systematic uncertainty due to event selection.

Hence, $\epsilon_{INEL>0}$ i.e. the number of generated events selected for $N_{\rm ch} > 0$ and after passing of V0(AND) trigger, equal to 0.93 has been used with 1% systematic uncertainty in pp collisions at $\sqrt{s} = 5.02$ TeV for integrated multiplicity. The $\epsilon_{INEL>0}$ correction for first multiplicity bin, which is applied to correct J/ψ yield is 0.889 with 1.4% uncertainty. The $INEL > 0$ minimum bias trigger efficiency factor to correct $\langle N_{\rm ch} \rangle$ is 1.05 with 1.34% uncertainty. Similarly, $\epsilon_{INEL>0}$ after passing of V0 (OR 1 hit on SPD) trigger is 0.99% and 1% systematic uncertainty was assigned due this selection at 2.76 TeV. It has also been observed that the corrections for the first multiplicity bin is negligible at 2.76 TeV. Hence, it was taken as unity.

The efficiency corrections due to $INEL = 0$ is 1.04 with 1% systematic at 5.02 TeV. Similarly, the obtained value for 2.76 TeV is 1.14(1/1-0.122) with 1% systematic uncertainty. The contamination from $INEL = 0$ events in the first bin is small compared to the precision of the measurement. Besides this affects both the yield

and the $\langle N_{\rm ch}\rangle$ in the same way (Equation 4.23 in the next chapter), so it can be safely neglected for the first bin at 5.02 TeV. The correction is not applied for the fraction of events that do not pass the vertex QA in the first bin because of the assumption that it affects in the same way to events with or without a J/ψ. But conservatively this fraction ($\sim$ 1%) has been added in the systematic uncertainties on the yield in the first bin.

3.5 Results

The value obtained for charged-particle pseudo-rapidity density $\langle {\rm d}N_{\rm ch}/{\rm d}\eta\rangle$ is $5.64 \pm 0.02(stat.) \pm 0.03(syst.)$ in pseudo-rapidity range $-1 < \eta < 1$ in pp collision at $\sqrt{s}$ = 5.02 TeV . The computed result is corrected with vertex QA efficiency. The reported result of $\langle {\rm d}N_{\rm ch}/{\rm d}\eta\rangle$ is $5.70 \pm 0.06 - 0.08(syst)$ in $-1.0 < \eta < 1.0$ range [10]. Result obtained in the present study has difference of 1.% from ALICE result [10]. The integrated value of $N_{\rm ch}$ reported by this independent analysis is $11.39 \pm 0.12 - 0.16$ [10]. This value was used to compute relative charged-particle densities in multiplicity bins. Similarly, the integrated $\langle {\rm d}N_{\rm ch}/{\rm d}\eta\rangle$ is extrapolated for $INEL > 0$ event class within $|\eta| > 1$ from the ALICE results at 2.76 TeV is $4.841 \pm 0.074 - 0.085$ [4]. The obtained integrated $\langle {\rm d}N_{\rm ch}/{\rm d}\eta\rangle$ value for the same event class and η range is $4.85 \pm 0.001(stat.) \pm 0.03(syst.)$. We notice that, the corrections have been taken into account for event selection efficiency for $INEL = 0$ and the results of the present analysis are in a good agreement with the results from ALICE central framework. However, to be consistent with all the ALICE results and since $\langle {\rm d}N_{\rm ch}/{\rm d}\eta\rangle$ is a global observable, the centralized integrated $\langle {\rm d}N_{\rm ch}/{\rm d}\eta\rangle$ has been used to compute self-normalised charged-particle density in multiplicity bins. The $\langle N_{\rm ch}\rangle$ values obtained by ad-hoc polynomial method were taken as central results and the deviation in $\langle N_{\rm ch}\rangle$ computed using first and second method are taken as a systematic uncertainty due to non-linearity.

The average $\langle {\rm d}N_{\rm ch}/{\rm d}\eta\rangle$ for integrated multiplicity and $\langle dN^{i}_{ch}\rangle/d\eta/\langle dN_{ch}/d\eta\rangle$ in

$\sqrt{s}$ = 5.02 TeV		$\sqrt{s}$ = 2.76 TeV	
$N_{trk}^{corr,i}$	$< dN_{ch}^{i} > /d\eta/\langle dN_{ch}/d\eta \rangle$	$N_{trk}^{corr,i}$	$< dN_{ch}^{i} > /d\eta/\langle dN_{ch}/d\eta \rangle$
$1-7$	$0.43 \pm 0.04 - 0.03$	$1-4$	$0.46 \pm 0.04 - 0.03$
$8-12$	$1.07 \pm 0.08 - 0.07$	$5-8$	$1.00 \pm 0.08 - 0.08$
$13-18$	$1.64 \pm 0.12 - 0.11$	$9-12$	$1.59 \pm 0.13 - 0.13$
$19-29$	$2.42 \pm 0.17 - 0.17$	$13-16$	$2.17 \pm 0.18 - 0.18$
$30-48$	$3.62 \pm 0.26 - 0.26$	$17-100$	$3.17 \pm 0.27 - 0.27$
$49-100$	$5.41 \pm 0.40 - 0.40$		
Integrated	$5.64 \pm 0.02 \pm 0.03$	*Integrated*	$4.85 \pm 0.001 \pm 0.03$

Table 3.10: The differential charged-particle density for both the CM energies. The statistical error is too small ($\sim 10^{-4}$), hence not shown for the multiplicity bins.

differential case are summarized in the Table 3.10 at 5.02 and 2.76 TeV. The relative multiplicity reaches up to $\sim$6 at 5.02 TeV and $\sim$ 3 at 2.76 TeV. The evolution of relative J/ψ yield will be studied as a function of these estimated $\langle dN_{ch}^{i} \rangle / d\eta / \langle dN_{ch}/d\eta \rangle$ for both energies in the next chapter.

Bibliography

[1] E. Bruna et al., "Vertex Reconstruction for Proton-Proton Collisions in ALICE", Public Documents, https://cds.cern.ch/record/1225497.

[2] D. Elia et al., "The pixel Detector Based Tracklet Reconstruction Algorithm in ALICE", Public Documents, https://cdsweb.cern.ch/record/1225500.

[3] J. F. Grosse-Oetringhaus et al., "Charged-Particle Multiplicity in Proton-Proton Collisions", J. Phys. G37 (2010) 083001.

[4] J. Adam et al., ALICE Collaboration, "Charged-particle Multiplicities in Proton-Proton Collisions at $\sqrt{s}$ = 0.9 to 8 TeV", Eur. Phys. J. C77 (2017) 33.

[5] B. Abelev et al., ALICE Collaboration, "J/ψ Production as a Function of Charged Particle Multiplicity in pp Collisions at $\sqrt{s}$ = 7 TeV", Phys. Lett. B712 (2012) 165.

[6] D. Adamová et al., ALICE Collaboration, "J/ψ Production as a Function of Charged-Particle Pseudorapidity Density in p-Pb Collisions at $\sqrt{s_{NN}}$ =5.02 TeV", Phys. Lett. B776 (2018) 91.

[7] J. Adam et al., ALICE Collaboration, "Pseudorapidity and Transverse-Momentum Distributions of Charged Particles in Proton-Proton Collisions at $\sqrt{s}$ =13 TeV", Phys. Lett. B753 (2016) 319.

[8] S. Acharya et al., Alice Collaboration. ALICE Collaboration,"Energy and Multiplicity Dependence Study of Charged-Particle Pseudorapidity-Density Distribution in pp Collisions at $\sqrt{s}$ = 5.02, 7 and 13 TeV", In preparation.

[9] P. Pillot, "Closure Tests for Multiplicity Studies", PWGDQ−Quarkonia2mumupresentation.

[10] "Reference Multiplicity ALICE twiki.", https://twiki.cern.ch/twiki/bin/viewauth/ALICE/ReferenceMult-Minimum-Bias-pp-at-5-02-TeV.

Chapter 4

J/ψ yield measurement

In this chapter, the J/ψ yield measurement will be addressed in pp collisions at $\sqrt{s}$ = 2.76 and 5.02 TeV. The inclusive J/ψ production measurement in pp collisions has been performed in ALICE at 2.76 TeV [1] and 5.02 TeV [2]. The aim of the analysis is to check the consistency of the main observables (e.g. Number of dimuon trigger events, J/ψ, luminosity etc,) with the previous analysis and cross-check the results at 5.02 TeV. Since the same data sample has been used for multiplicity analyses, this analysis served as ground work for further study of J/ψ. In this chapter, the evolution of the relative J/ψ production is presented as a function of charged-particles pseudo-rapidity density. The J/ψ productions have been studied via their dimuon decay channel at forward rapidity ($-4 < y < -2.5$) for integrated transverse momentum (p_{T}). The dimuon events were detected in the MS detector of ALICE. CMUL7-B-NOPF-MUFAST trigger events at $\sqrt{s}$ = 5.02 TeV and CMUS1-B-NOPF-MUON trigger events have been analysed at $\sqrt{s}$ = 2.76 TeV. The detailed description of the dimuon trigger events that have been used in this analysis are given in Section 2.5. The events which passed the physics selection criteria and the dimuon trigger were analysed for J/ψ production cross-section measurements. The dimuon events which satisfied the event selection criteria as mentioned in Section 3.2 were used for multiplicity dependence study. The opposite sign muons were measured as a function of the corrected tracklet bins. The tracklets were corrected for detector efficiency of SPD. The study was performed by taking the $N_{trk}(z_v(0))$ reference as

maximum. However, the choice of reference value minimum has also been checked. The normalization factor calculations were done to get the equivalent number of minimum bias (MB) events from muon events in both inclusive J/ψ production study and multiplicity analysis. Furthermore, the contamination due to pile-up events were calculated and corrected.

4.1 J/ψ measurement

The muon track reconstruction is described in Section 2.3.7. The following conditions were applied on the reconstructed muon tracks :

1. The track reconstructed in the tracking chambers must match a trigger track reconstructed in the trigger system, above the low p_{T} trigger threshold of 0.5 GeV/c. This selection criterion rejects most of the hadrons escaping or produced in the front absorber and reduce the contribution at low p_{T} from pion and kaon decays.

2. Each muon track must be in the pseudo-rapidity range - 4 $\leq \eta \leq$ - 2.5. This selection criterion removes particles induced by beam gas interaction at edge of the detector and ensures detector's acceptance.

3. The transverse radius coordinate of the track, at the end of the hadron absorber, must be in the range 17.6 $\leq R_{\mathrm{abs}} \leq$ 89.5 (cm). This condition improves the mass resolution by rejecting the tracks crossing the high density material around the beam pipe. This selection criteria helps to reduce events with multiple coulomb scattering in high z materials of the absorber.

4. The two muons should be oppositely charged.

5. Finally, a cut of rapidity range 2.5 $\leq$ y $\leq$ 4.0 on the dimuon pairs was applied to cope with the spectrometer acceptance.

4.1.1 Signal extraction

The J/ψ signal was extracted by fitting the invariant mass distribution of dimuon pairs with combination of several signal and background functions. The signal extraction in pp collisions at $\sqrt{s}$ = 5.02 TeV energy was done using extended crystal ball (CB2) and NA60 functions as a signal. The variable width Gaussian (VWG) and ratio of first and second order polynomial functions were used for background estimation. It has seven parameters. In pp collisions at $\sqrt{s}$ = 2.76 TeV data the crystal ball (CB) and extended crystal ball (CB2) functions were used for signal extraction. The double exponential, VWG and ratio of first order polynomial to the second order polynomial were used for background estimation (Appendix B.1). The CB2 function consists of a Gaussian core with two power law tails. The two tail parameters represent asymmetric tails of the J/ψ signal. Similarly, CB consists of a Gaussian core portion and a power-law tail at low mass defined by the parameters α and n. The low mass tail originates due to the non Gaussian fluctuations due to energy loss processes. The NA60 function adopted for charmonia in NA50 and NA60 experiments. It has eight tail parameters (α^L, P_1^L, P_2^L, P_3^L, α^L, P_1^R, P_2^R, P_3^R) and two Gaussian parameters ($\bar{x}$, σ). During fitting, all the parameters are kept free except the tail parameters. The fits are executed in the invariant mass ranges (2.0, 5.0) GeV/c^2 and (1.7, 4.8) GeV/c^2. Mass of ψ(2S) is assumed to be connected to the mass of J/ψ by the following relation:

$$m_{\psi(2S)} = m_{J/\psi} + \left(m^{PDG}_{\psi(2S)} - m^{PDG}_{J/\psi}\right). \tag{4.1}$$

where, $m^{PDG}_{J/\psi}$ and $m^{PDG}_{\psi(2S)}$ are the masses of J/ψ and ψ(2S), respectively, from Particle Data Group (PDG) [3]. The width of ψ(2S) is fixed to the J/ψ such as:

$$\sigma_{\psi(2S)} = \sigma_{J/\psi}.\frac{m_{\psi(2S)}}{m_{J/\psi}}. \tag{4.2}$$

$$\sigma_{\psi(2S)} = \sigma_{J/\psi}.\frac{\sigma^{MC}_{\psi(2S)}}{\sigma^{MC}_{J/\psi}}. \tag{4.3}$$

where $\sigma^{MC}_{\psi(2S)}$ and $\sigma^{MC}_{J/\psi}$ are widths of $\psi(2S)$ and J/ψ, respectively, were extracted from the realistic MC simulation. All the fits were performed within three sigma confidence limit. The MC simulation which uses the input from the data (here data runs), is known as the realistic MC simulation.

4.1.2 Tail parameter

To know the energy straggling and the multiple coulomb scattering effects of the front absorber on the decay muons, the tail parameters of dimuon mass distribution are needed to be extracted. The tail parameters have been estimated from a realistic MC simulation anchored to 25 runs for pp collisions at $\sqrt{s}$ = 5.02 TeV. The signal extraction was done by fitting with CB2 and NA60 functions and all the parameters were kept free while fitting. The tail parameters determined by this method have been compared with the tail parameters [2].

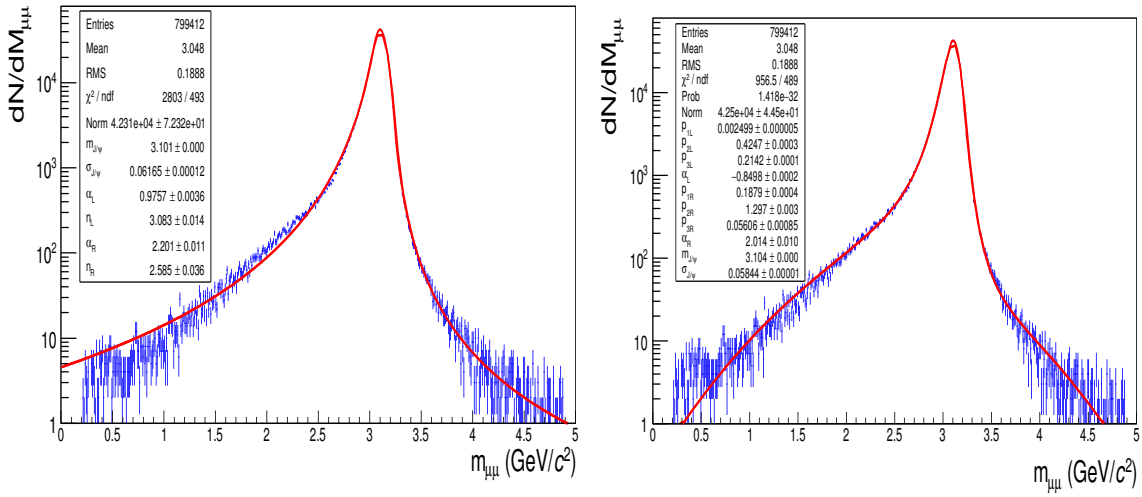

(a) CB2 function (b) NA60 function

Figure 4-1: Invariant mass spectrum of J/ψ from MC simulation fitted with two different signal functions.

The results of tail parameters are in good agreement with the ALICE results for both CB2 and NA60 functions. The values for tail parameters from the present analysis and from the pp collisions at $\sqrt{s}$ = 5.02 TeV analysis as function of p_{T} at forward rapidity are listed in Tables B.1 and B.2 as given in Appendix B.2. The quality of the fit to the MC shapes for J/ψ with CB2 and NA60 functions is shown in Figure 4-1. On the basis of χ^2 test, NA60 function gives slightly better result than CB2 on simulated spectrum. Both the functions have been used for signal extraction to calculate systematic uncertainty. Different sets of tail parameters were used to obtain systematic uncertainty.

4.2 Comparison of inclusive J/ψ yield in pp collisions at $\sqrt{s}$ = 5.02 TeV

The inclusive J/ψ yield as a function of p_{T} and rapidity has been calculated for comparison and cross-checking of previous analysis. The even and opposite sign dimuons were selected using the methods described in Section 4.1. A selection condition of $0 < p_{\mathrm{T}} < 12$ GeV/c was applied on the dimuon pairs to obtain maximum statistics of J/ψ and remove the fluctuations at the high-p_{T} values. The invariant mass distributions after passing these selection criteria are shown in Figure 4-2. A typical example of J/ψ signal extraction is illustrated in Figure 4-3. The fittings were done using techniques described in Section 4.1.1. Along with the tail parameters obtained in the present analysis, the tail parameters of 5.02 TeV and 13 TeV were also considered. The combination of two signal functions, two background functions, three sets of tail parameters and two sets of invariant mass ranges lead to a total of 20 fits. The average of these fits is taken as the final result and the root mean square (rms) value gives the systematic uncertainty.

The total number of J/ψ in this analysis are calculated as 8642 $\pm$ 123(stat.) $\pm$ 265(syst.) which is consistent with analysis of pp collisions at $\sqrt{s}$ = 5.02 TeV, where number of J/ψ reported as 8649 $\pm$ 123(stat.) $\pm$ 297(syst.) [2].

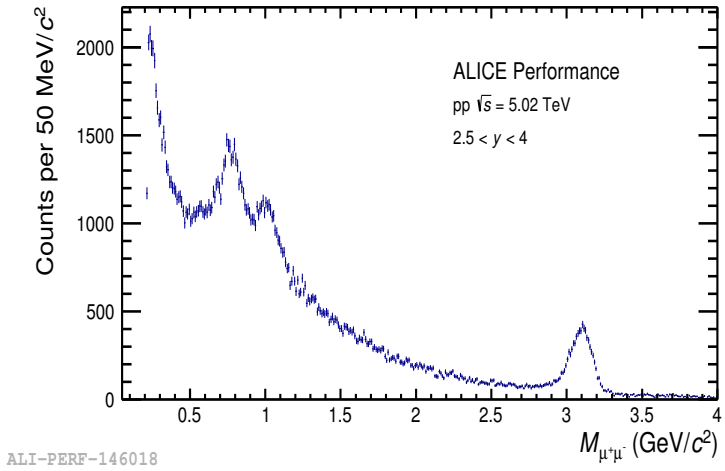

Figure 4-2: Invariant mass of dimuon in pp collisions at $\sqrt{s} = 5.02$ TeV.

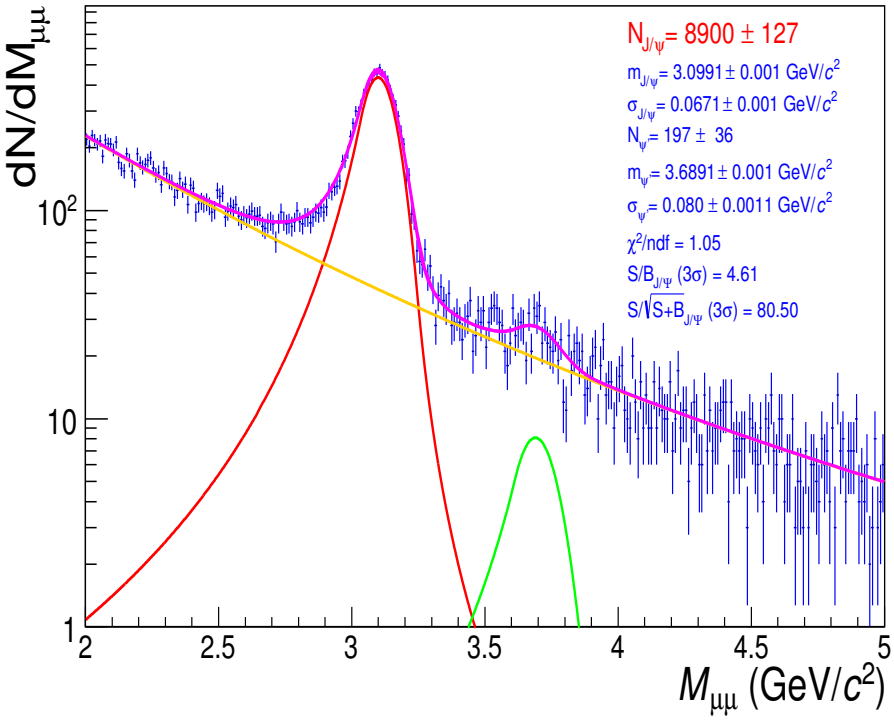

Figure 4-3: An example of signal extraction in integrated p_{T} and rapidity bin fitted with CB2+VWG. The blue points are data points. The red and green lines represent the J/ψ and $\psi(2S)$ signals. The yellow line represents the background and the magenta line shows the total function.

4.2.1 Pile-up correction factor calculation

The pile-up events can be of two types. The in-bunch pile-up which may arise due to several collisions in the given bunch-crossing. Another type of pile-up is out-of-bunch

pile-up where tracks from neighbouring bunch-crossings can be attached to current event. In order to estimate proper MB events, the pile-up events should be removed. To estimate the in-bunch pile-up rate which rejects the several collisions in a given bunch crossing, the following formula has been used.

$$PU^i = \frac{\mu^i}{1 - \exp^{\mu^i}} \tag{4.4}$$

where

$$\mu^i = -ln\left(1 - \frac{F^{MB,i}_{purity} \times L0b^i_{MB}}{D^i \times N^i_{colliding} \times f_{LHC}}\right) \tag{4.5}$$

where

- i denotes the run numbers.
- $L0b^i_{MB}$ is the level 0 minimum bias (MB) trigger scalar input.
- D^i is the run duration.
- $N^i_{colliding}$ is number of colliding bunches.
- $f_{LHC} = 11.245$ kHz is the LHC frequency.
- $F^{MB,i}_{purity}$ minimum bias efficiency calculated as the ratio of physics selected events to the total number of events (section 2.5).

$F^{MB,i}_{purity}$ for a given minimum bias trigger events can be written as :

$$F^{MB,i}_{purity} = \frac{N^i_{MB}(PS)}{N^i_{MB}(ALL)} \tag{4.6}$$

where $N^i_{MB}(PS)$ is the number of MB events after physics selection and $N^i_{MB}(ALL)$ denotes the raw number of MB events without physics selection for each run.

The efficiency of CINT7 trigger events was calculated as 97% and C0TVX minimum bias trigger efficiency is taken as 100%. The run by run pile-up correction factor for both MB CINT7 and C0TVX has been calculated using Equation 4.4 and

is shown in Figure 4-4. The average pile-up correction factor for both MB is computed as $P.U^{C0TVX} = 1.00482 \pm 0.000684$ and $P.U^{CINT7} = 1.01148 \pm 0.000284$, respectively.

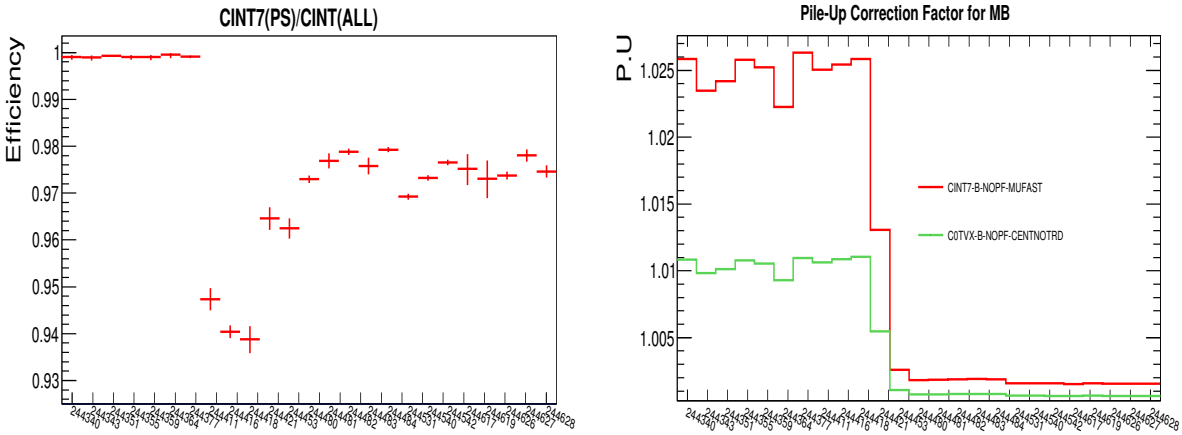

(a) Minimum Bias efficiency of CINT7.

(b) Plile-Up Correction factor.

Figure 4-4: Run by Run efficiency for CINT7 and pile-up correction factor for both MB trigger events.

4.2.2 Normalization Factor (F_{Norm})

The yield of J/ψ as well as the relative yield of J/ψ with respect to the total yield, the equivalent number of minimum bias events are to be estimated. The equivalent number of minimum bias events is defined as

$$N^{eq}_{MB} = \sum_{run=i} F^{i}_{norm} \times N^{i}_{MUL} \tag{4.7}$$

There are several methods to calculate normalization factor. In the present analysis two methods have been used, which are defined as follows :

Online scalar method

The level 0 scalar inputs of MB triggers and muon trigger events stored in OCDB and the normalization factor can be defined as

$$F^{scaler,i}_{norm} = PU^{i} \times \frac{F^{MB}_{purity} L0b^{i}_{MB}}{F^{MUL}_{purity} L0b^{i}_{MUL}} \tag{4.8}$$

where $L0b^i_{MUL}$ is the level 0 unlike sign muon trigger scalar input and F^{MUL}_{purity} is the efficiency of Muon trigger events. The F_{Norm} estimated as the weighted average over runs is 4727.72 ± 4.23 with CINT7 MB and 1960.16 ± 1.689 with C0TVX. The difference in F^i_{Norm} between the two trigger events arises due to the different number of statistics.

Two step offline method

As the statistics of scaled MB events (CINT7) is very low, this method has been used by using intermediate triggers expressed as

$$F^{Offline,i}_{norm} = PU^i \times \frac{MB^i}{MB\&0MSL^i} \times \frac{MSL^i}{MSL\&0MUL^i} \tag{4.9}$$

where MSL is the single muon trigger events (CMSL7) passed physics selection condition; $MSL\&0MUL^i$ is sub-sample of MSL trigger events also containing a 0MUL input; CINT7 with physics selection is taken as MB; $MB\&0MSL^i$ is the sub-sample of MB containing also 0MUL inputs.

The F_{Norm} varies with runs, In order to get the correct estimation for the whole period weighted average corresponding to Run-by-Run factor is computed by the equation:

$$F^{Offline}_{norm} = \frac{\sum_{i=1}^{n_{runs}} F^{Offline,i}_{norm}.N^i_{CMUL7}}{\sum_{i=1}^{n_{runs}} N^i_{CMUL7}} \tag{4.10}$$

Finally, $F^{Offline}_{norm}$ computed by this method using Equation 4.9 is 4766.07 ± 60.69.

4.2.3 J/ψ production cross-section

The F_{Norm} factor calculated with CINT7, C0TVX triggers and also with offline and online methods are shown in Figure 4-5. Run by run CMUL7 cross-section was calculated using the different F_{Norm} factors estimated by various methods, using the

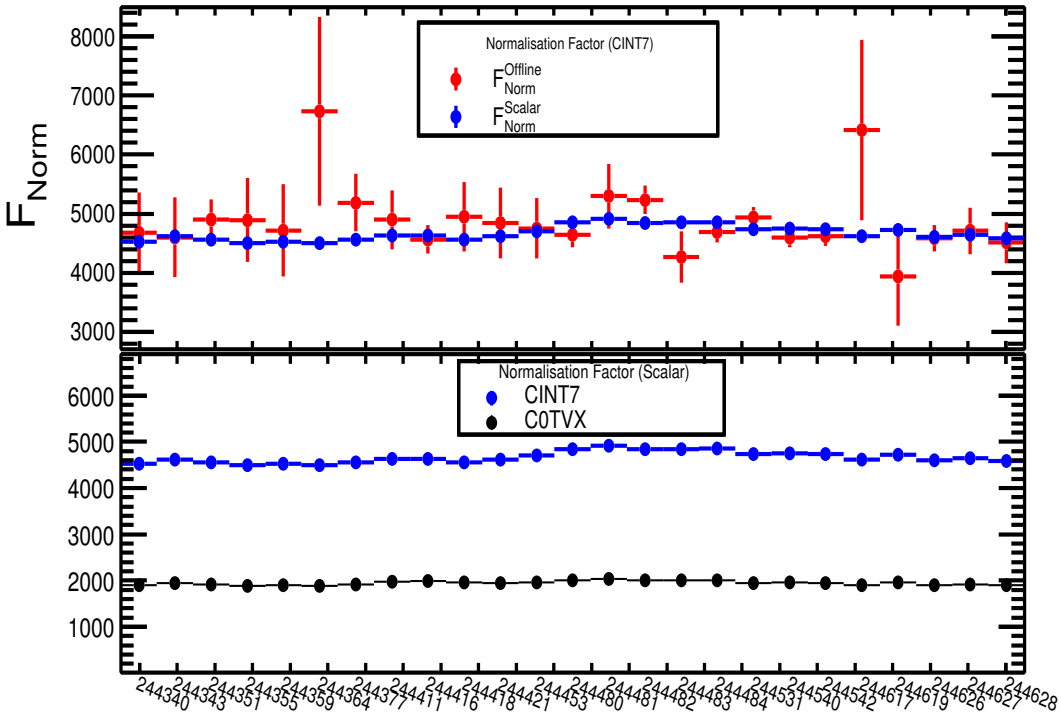

Figure 4-5: Run by Run F_{Norm} factor calculated by scalar and offline method with both MB trigger events.

expression :

$$\sigma^{i}_{MUL} = \frac{\sigma_{VdM}}{F^{i}_{Norm}} \tag{4.11}$$

where the value of σ_{VdM} was either V0 or T0 cross-section measured with Van der Meer (VdM) scan. The VdM values were given by $\sigma^{V0}_{VdM} = 51.17 \pm 1.18$ mb and $\sigma^{T0}_{VdM} = 21.55 \pm 0.45$ mb [2].

The CMUL7 cross sections computed by both online and offline methods are in good agreement. The F_{Norm} computed by the scalar method with C0TVX trigger has been used for J/ψ production calculation. To calculate the cross-section we also need to compute luminosity for the present data sample which is given by :

$$\mathcal{L}_{\rm int} = \frac{N^{tot}_{MUL} \times F_{Norm}}{\sigma_{VdM}} \tag{4.12}$$

where $N^{tot}_{MUL} = 1168507$ is the total number of CMUL7 events (passed only physics

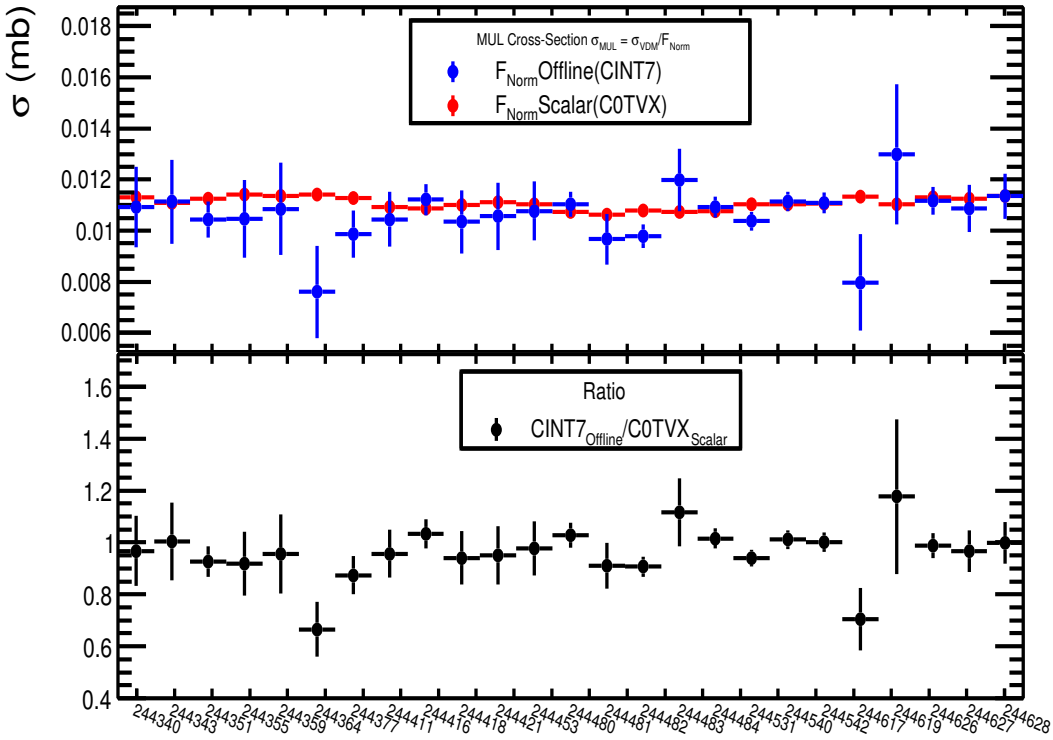

Figure 4-6: Run by Run CMUL7 cross-section calculated by scalar and offline method with both MB trigger events.

selection condition) at $\sqrt{s}$ =5.02 TeV. The integrated luminosity computed for the present data sample with T0 and V0 cross-section are as follows :

- $\mathcal{L}_{\rm int}(T0) = 106.286 \pm 0.091(stat.) \pm 2.258(syst.) nb^{-1}$ (with F^{scaler}_{Norm} for C0TVX)
- $\mathcal{L}_{\rm int}(V0) = 107.96 \pm 0.096(stat.) nb^{-1}$ (with F^{scaler}_{Norm} for CINT7)
- $\mathcal{L}_{\rm int}(V0) = 108.84 \pm 0.138(stat.) nb^{-1}$ (with $F^{offline}_{Norm}$)

Finally J/ψ production cross-section is given by :

$$\sigma^{pp}_{J/\psi} = \frac{N_{J/\psi}}{BR_{J/\psi\to\mu^+\mu^-} \times A \times \varepsilon \times \mathcal{L}_{\rm int}} \tag{4.13}$$

- N_ψ is the number of J/ψ obtained from the signal extraction (Section 4.2);
- A$\times\epsilon = 0.2435 \pm 0.0003$ is the acceptance and efficiency correction factor of J/ψ taken from the reference [2].

- BR($\psi \to \mu^+\mu^-$) is the branching ratio of J/ψ in dimuon decay channel ($J/\psi \to \mu^+\mu^-$). For J/ψ the branching ratio is (5.93 $\pm$ 0.06)% ;
- $\mathcal{L}_{\rm int}$ is the integrated luminosity.

The production cross-section computed in this analysis is $\sigma^{pp}_{J/\psi} = 5.602 \pm 0.084$ (stat.) $\pm$ 0.282 (syst.) μb . This value is consistent with the results from [2] $\sigma^{pp}_{J/\psi} = 5.61 \pm$ 0.08(stat.) $\pm$ 0.28(syst.) μb (0.14% difference) and with the interpolated cross section $\sigma^{pp}_{J/\psi} = 5.28 \pm 0.40$(stat.) $\pm$ 0.11(syst.) μb (5.75% difference).

4.3 Comparison of inclusive J/ψ yield in pp collisions at $\sqrt{s} = 2.76$ TeV

The J/ψ production cross-section has been calculated and compared with earlier publication [1]. The total number of CMSU1B events reported were 8.8 million using reconstructed $pass2 - with - SDD$ data set from AOD in this analysis [1]. We have analysed the same data set as well as reconstructed $pass4 - without - SDD$ data from AOD.

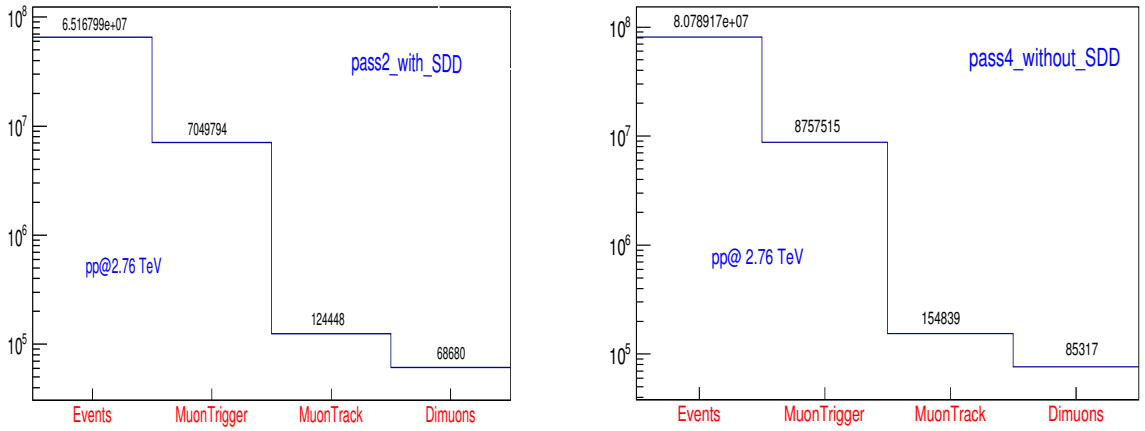

(a) Event counter for pass2.

(b) Event counter for pass4.

Figure 4-7: Number of events after passing each track cuts in both pass2 (a) and pass4 (b) reconstructed AOD.

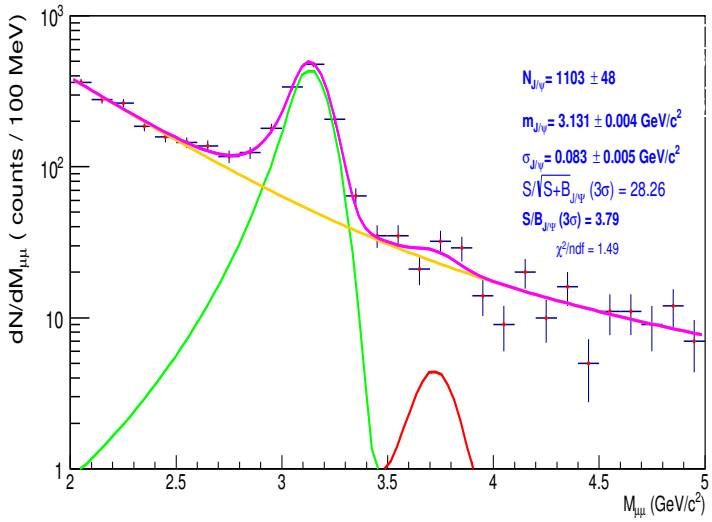

(a) pass2

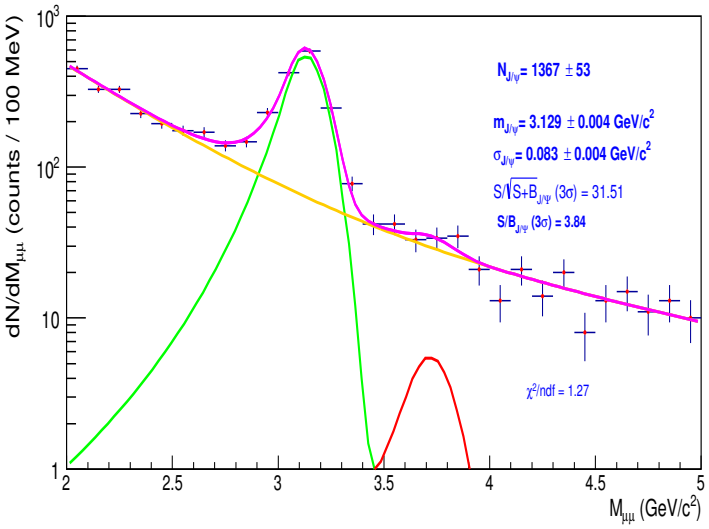

(b) pass4

Figure 4-8: J/ψ signal extraction for pass2 (a) and pass4 (b) reconstructed AOD.

The number of events after passing each muon track selection conditions are shown in Figure 4-7. A clear discrepancy (19.86%) in CMUS1B events between two passes (pass2 & pass4) can be seen from Figure 4-7. The run by run analysis of CMUS1B are also performed. The same trigger events are not reproducible using pass2 reconstructed data. This may be due to the malfunction of the data storage. This

difference in trigger counts reflects the J/ψ counts difference in Figure 4-8.

The number of J/ψ reported in previous study is $N_{J/\psi} = 1364 \pm 53$ (stat.) [1]. The number of J/ψ was obtained with pass2 (pass4) $N_{J/\psi} = 1103 \pm 48$ (stat.) with 19.13% discrepancy. $N_{J/\psi}$ in pass4 data is consistent with the reported result. The integrated luminosity ($\mathcal{L}_{\rm int}$) for the muon channel at 2.76 TeV is 19.9 nb^{-1}. The J/ψ production cross-section, $\sigma^{pp}_{J/\psi}$ can be computed using Equation 4.13 and it is 3.33 μb, which is within $\pm 1\sigma$ of the reported value [1].

Therefore, the pass4 data-set has been used for multiplicity analysis in pp collisions at $\sqrt{s} = 2.76$ TeV. The cross-check analysis of inclusive J/ψ production cross-section results are in good agreement with the previous results reported by ALICE in pp collisions at $\sqrt{s} = 2.76$ and 5.02 TeV. The multiplicity dependence analyses have been carried out with these two data sets in the following sections.

4.4 Multiplicity dependence study of J/ψ yield

The muon trigger events were selected by passing through the event selection criteria for multiplicity study, that are mentioned in Section 3.2 for the two data sets. The events were selected for the inelastic event class > 0 or $INEL > 0$ class. The SPD tracklets were corrected using data-driven method mentioned in the previous chapter using reference $\langle N_{\rm trk} \rangle$ $z_v(0)$ = maximum. The choice of reference value was same as charged-particle multiplicity. The multiplicity bins were chosen such that it excludes the bin $N_{trk} = 0$ to avoid the edge effects. The CMUL7 events were selected including pile-up rejection (physics selection), and thus, certain number of CMUL7 events were rejected at 5.02 TeV. The pile-up removal condition within physics selection was not available during LHC11a period at 2.76 TeV. Hence, the pile-up rejections were applied within SPD tracklet selection. The contamination due to the pile-up and the corresponding corrections will be discussed in Section 4.5.1. The selected muon events pass through the track selection criteria mentioned in Section 4.1. The only differences in track selection in pp collisions at $\sqrt{s} = 2.76$ TeV are at least one muon track (at $\sqrt{s}$ =5.02 TeV both muon tracks) in the tracking chambers matches with

trigger tracks above the 0.5 GeV/c p_{T} threshold. The $-4 < \eta < -2.5$ condition on each muon track was also not applied at 2.76 TeV. Other than that similar procedure was adapted for J/ψ yield calculation at both the energies. A total of 1003475 CMUL7 and 7342226 CMUS1 events were analysed at $\sqrt{s}$ = 5.02 and 2.76 TeV, respectively.

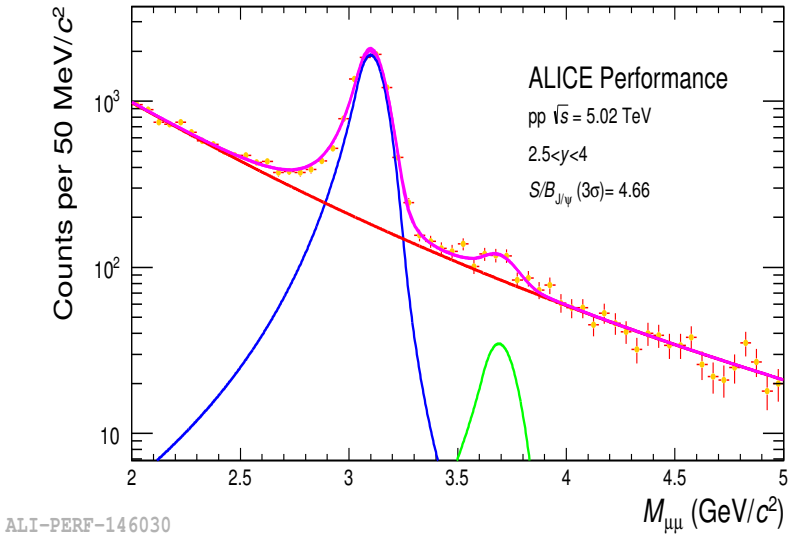

(a)

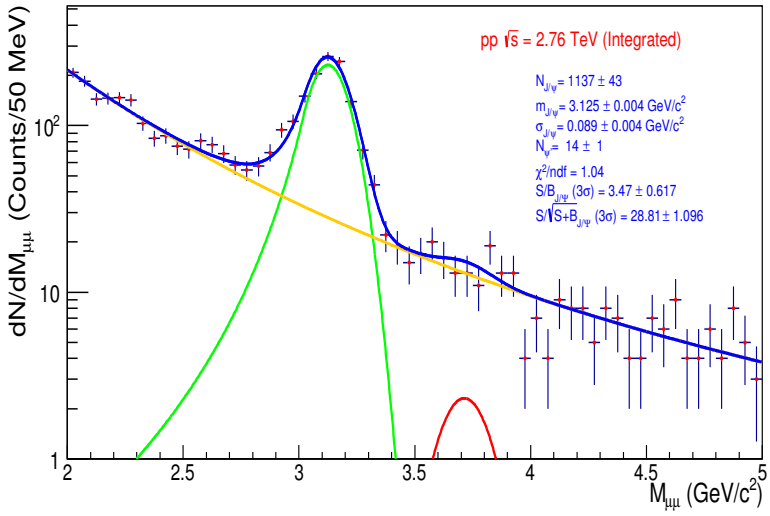

(b)

Figure 4-9: Example of J/ψ signal extractions for integrated multiplicity at (a) $\sqrt{s}$ = 5.02 TeV and (b) $\sqrt{s}$ = 2.76 TeV.

The signal has been extracted for integrated multiplicity and integrated p_{T}. The ex-

ample of J/ψ signal extraction as function of integrated p_{T} and multiplicity is shown in Figure 4-9. The number of J/ψ has been calculated using the fitting methods as mentioned in Section 4.1.1. J/ψ signals were extracted in two invariant mass ranges of dimuon, (2.0, 5.0) GeV/c^2 and (1.7, 4.8) GeV/c^2. In case of pp collisions at $\sqrt{s}$ = 5.02 TeV, CB2 and NA60 were used as signal functions and VWG and ratio of polynomial one to polynomial two were used to fit the background. Fitting with Variable width Gaussian background gives proper shape and the fits are also converged. Log likelihood method in Root is used in fit procedure. The signal extractions were also done using tail parameter of 13 TeV. The fit was performed using 13 TeV tail parameters with the combination of CB2, VWG and ratio of polynomial one to polynomial two. A weight factor of 4 was applied while taking average of these fits. Therefore, we ended up with 12 tests after using two sets of tail parameters, two invariant mass ranges, two signal and two background functions. The tail parameter used in this case was taken from the pp 5.02 TeV cross-section analysis [2]. The arithmetic mean of all these fits and there corresponding statistical errors were taken as a final result for number of J/ψ and it's statistical error. The rms value of these tests were taken as systematic uncertainty.

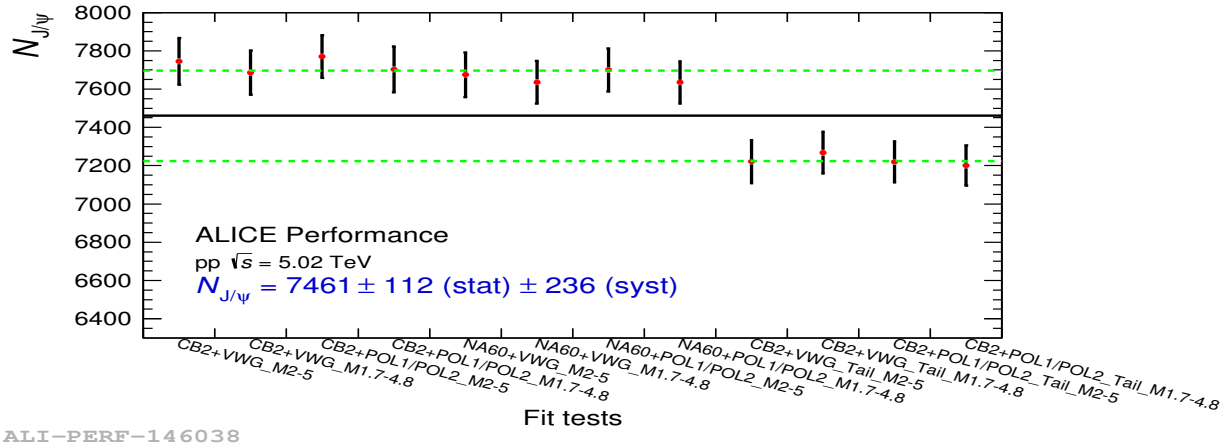

Figure 4-10: J/ψ signal extraction systematic uncertainty at $\sqrt{s}$ = 5.02 TeV.

The integrated numbers of J/ψ is calculated as $N_{J/\psi} = 7703 \pm 116(\mathrm{stat.}) \pm 45(\mathrm{syst.})$. After applying the weight for using tail parameters of 13 TeV the average integrated J/ψ which was used to compute the relative yield of J/ψ is $N_{J/\psi} = 7461 \pm 112(\mathrm{stat.})$

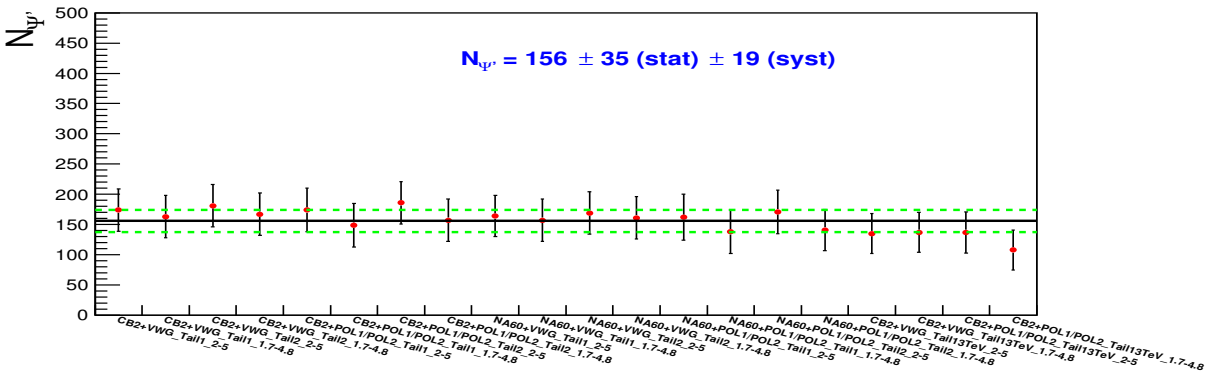

Figure 4-11: $\psi(2S)$ signal extraction systematic uncertainty at $\sqrt{s}$ = 5.02 TeV.

$\pm$ 236(syst.). The value of $\psi(2S)$ is also extracted for pp $\sqrt{s} = 5.02$ TeV as a function of multiplicity. The systematic of signal extraction was performed for $\psi(2S)$. The total number of integrated $\psi(2S)$ is obtained as $N_{\psi(2S)} = 156 \pm 35(\text{stat}) \pm 19(\text{syst.})$. The systematic uncertainties for signal extractions of $N_{J/\psi}$ and $\psi(2S)$ are shown in Figures 4-10 and 4-11.

The consistency of J/ψ results has been checked by taking the ratio of the number of J/ψ to the number of muon events. The calculated ratio (0.76%) is very close to the ratio that has been computed using inclusive J/ψ (0.75%) obtained in Section 4.2.3 and with the reported results of the independent J/ψ analysis (0.74%) [2].

The invariant mass of dimuons distributions were divided into six corrected tracklet bins and signal extraction was done in each multiplicity bin using the same fit procedure as mentioned above. The mass and width of J/ψ was fixed to that of integrated value while extracting signal in the multiplicity bins. The example of signal extraction in corrected tracklets bins is shown in Figure 4-12. The twelve fits for systematic uncertainty estimation were also applied for the multiplicity bin to estimate the signal extraction systematic uncertainties.

In a similar manner, the J/ψ signal extraction were performed for $\sqrt{s} = 2.76$ TeV. The combination of CB and CB2 as signal function and VWG, double exponential and ratio of polynomial 1 to polynomial 2 were considered as background functions. Three sets of tail parameters were used. Two sets were extracted from realistic MC

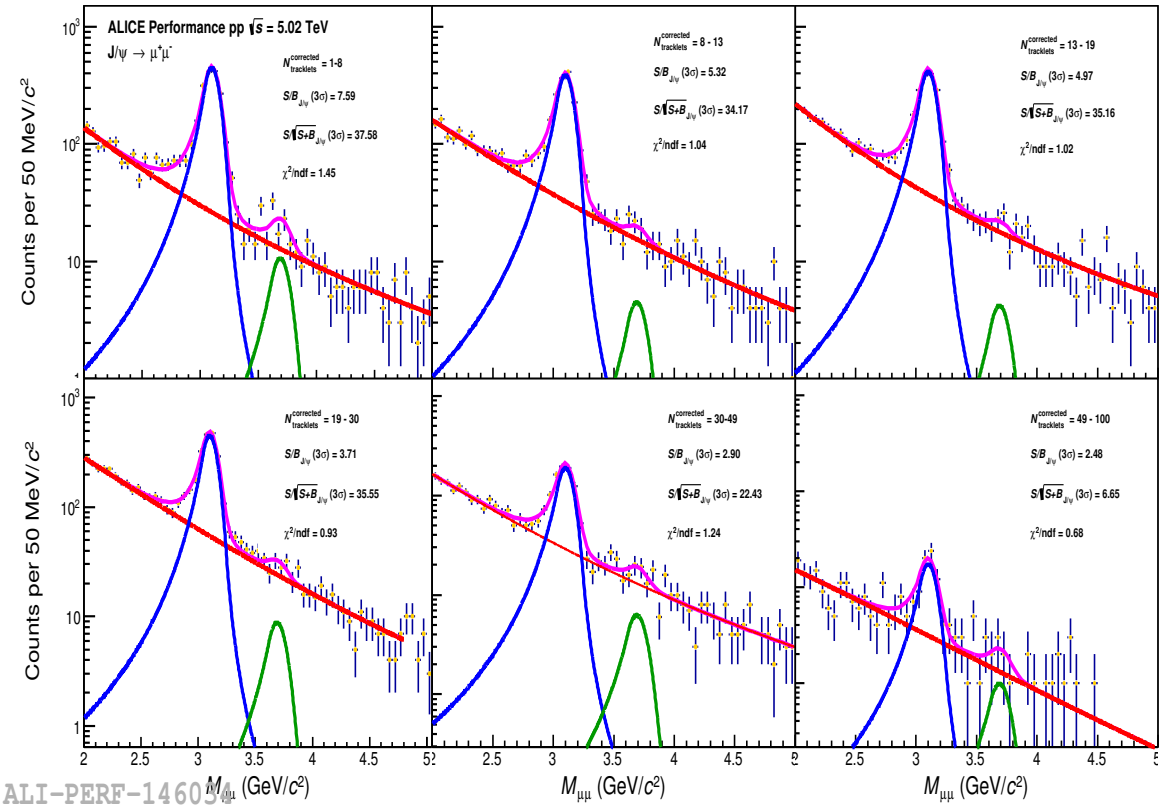

Figure 4-12: Example of signal extractions in multiplicity bins in pp collisions at $\sqrt{s}$ = 5.02 TeV.

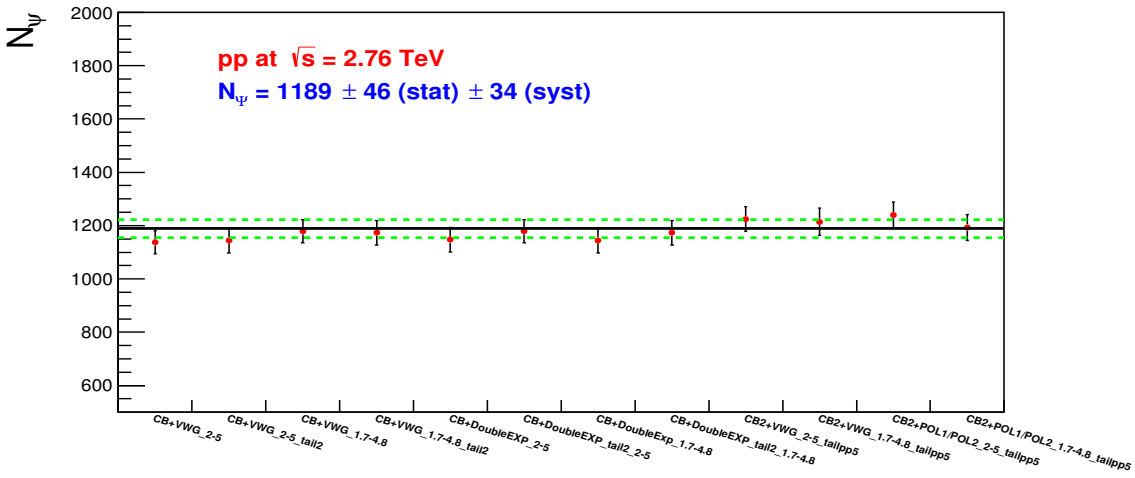

Figure 4-13: J/ψ signal extraction systematic uncertainty in pp collisions at $\sqrt{s}$ = 2.76 TeV.

simulation at $\sqrt{s} = 2.76$ TeV and one set from pp collisions at $\sqrt{s} = 5.02$ TeV data. The tail parameters with $\alpha = 0.953(1.20531)$ and n=4.44(3.58635) of CB function were taken from the reference [1]. The fittings were performed using log-likelihood method in ROOT software. The same fitting technique as mentioned in Section 4.1.1 was used. A weight of order two has been applied for using tail parameters of 5.02 TeV. Total twelve fits were performed and average value of J/ψ as well as systematic uncertainty were computed for $\sqrt{s} = 2.76$ TeV. After the systematic uncertainty calculations of signal extraction the total number of J/ψ obtained was $N_{J/\psi} = 1189 \pm 46(\text{stat}) \pm 34(\text{syst})$. The systematic uncertainty of signal extraction is shown in Figure 4-13 for integrated multiplicity, p_{T} and rapidity. The total number of $\psi(2S)$ in pp collisions at $\sqrt{s} = 2.76$ TeV was 20 and after the application of the multiplicity event selection conditions, the numbers reduced to 14. This count is too small to be considered in the analysis.

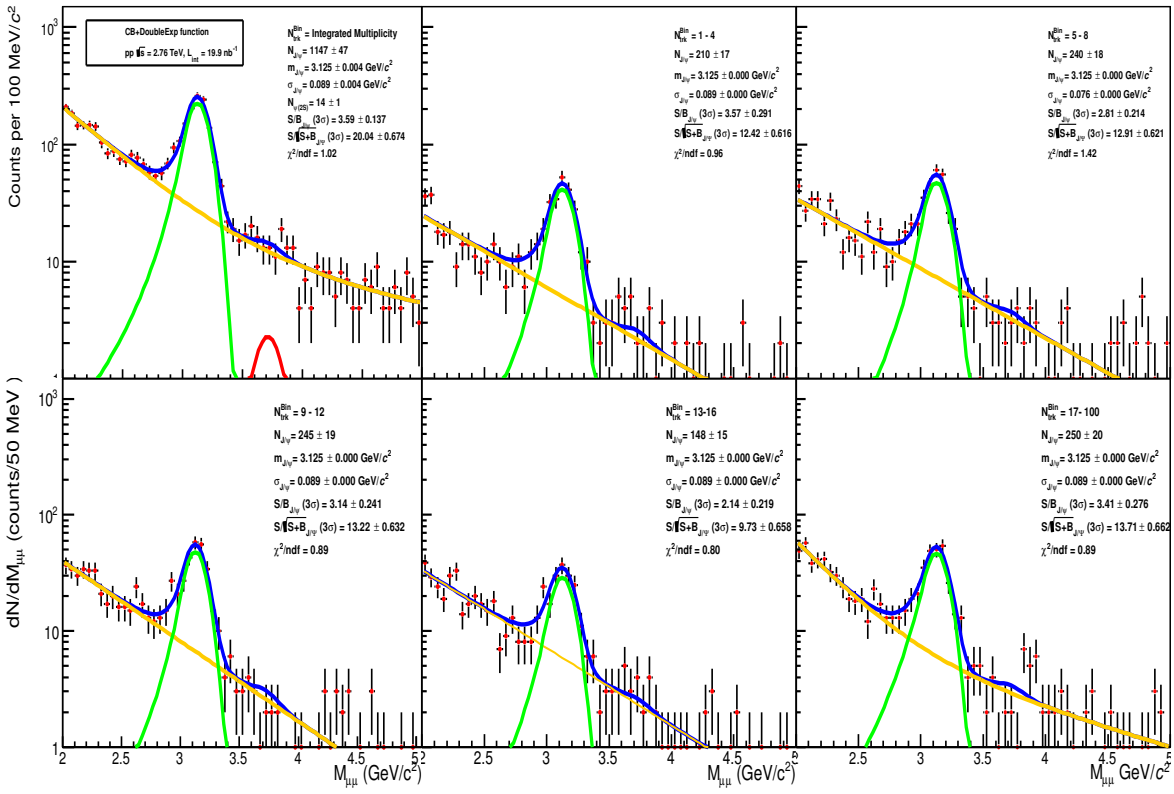

Figure 4-14: Example of signal extractions at different multiplicity bins at $\sqrt{s} = 2.76$ TeV.

The ratio of J/ψ to the number of MUON events (0.0161%) is consistent with published results (0.0155%) in the integrated multiplicity, p_{T} and rapidity [1]. After applying weight for using 5.02 TeV tail parameter the ratio of J/ψ to the number of MUON remained consistent with the reported value.

The data-set was divided into five multiplicity bins. The fits were performed in these tracklet bins exactly in the same manner as for the integrated multiplicity. The multiplicity differential J/ψ signals at 2.76 TeV at five N_{trk}^{corr} bins are shown in Figure 4-14.

$\sqrt{s}$ = 5.02 TeV		$\sqrt{s}$ = 2.76 TeV	
N_{trk}^{bin}	$N_{J/\psi}$	N_{trk}^{bin}	$N_{J/\psi}$
$1-7$	$1697 \pm 47(stat.) \pm 50(syst.)$	$1-4$	$229 \pm 18(stat.) \pm 12(syst.)$
$8-12$	$1523 \pm 47(stat.) \pm 50(syst.)$	$5-8$	$265 \pm 19(stat) \pm 14(syst.)$
$13-18$	$1629 \pm 49(stat.) \pm 54(syst.)$	$9-12$	$261 \pm 20(stat) \pm 13(syst.)$
$19-29$	$1758 \pm 52(stat.) \pm 59(syst.)$	$13-16$	$158 \pm 15(stat) \pm 6(syst.)$
$30-48$	$740 \pm 36(stat.) \pm 25(syst.)$	$17-100$	$244 \pm 20(stat) \pm 8(syst.)$
$49-100$	$68 \pm 11(stat.) \pm 3(syst.)$		
Integrated	$7461 \pm 112(stat.) \pm 236(syst.)$	*Integrated*	$1189 \pm 46(stat.) \pm 34(syst.)$

Table 4.1: $N_{J/\psi}^{i}$ counts in each multiplicity bins at the two CM energies.

The counts of J/ψ in multiplicity bins for both energies are summarised with their corresponding statistical and systematic uncertainties, in Table 4.1. It can be seen from the table that the total number of J/ψ obtained by summing up the number of J/ψ in the multiplicity bins is consistent with the integrated count. The use of the tail parameters of different centre of mass energies for a given set of data has the largest contribution in the systematic uncertainty. The weight factors increase the average value and enhance the systematics uncertainty in both the data sets. All the corresponding plots for systematic uncertainty of J/ψ due to signal extraction are listed in the Appendix B.3.

4.4.1 Normalization Factor in Multiplicity Bin (F_{Norm}^{i})

In this section, normalisation factor calculation as a function of multiplicity is discussed. In case of multiplicity analysis, the F_{Norm} was measured by offline method as the level 0 scalar input does not contain tracklet information. The integrated F_{Norm}

is re-calculated for multiplicity analysis applying the events selection mentioned in Section 3.2 using Equation 4.9. The pile-up selection tag was enabled from physics selection, hence the pile-up factor in Equation 4.9 was omitted to calculate F_{Norm} factor. As the whole minimum bias events were analysed instead of CINT7-B-MUFAST trigger events, there were sufficient statistics to compute F_{Norm} using one step offline method. The run by run F_{Norm} in each corrected tracklet bin is defined by the following equations :

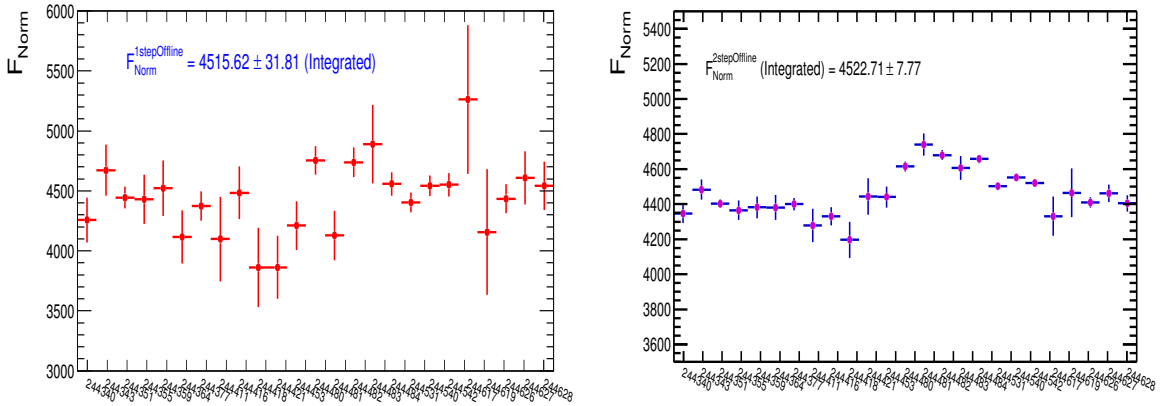

(a) (b)

Figure 4-15: Run by run One-step (a) and two-step (b) $F_{norm}^{offline}$ factors in pp at $\sqrt{s}$ = 5.02 TeV with multiplicity event cuts.

$$F_{norm}^{1stepOff,i,j} = \frac{MB^{i,j}}{MB\&0MUL^{i,j}} \tag{4.14}$$

$$F_{norm}^{2stepOff,i,j} = \frac{MSL^{i,j}}{MSL\&0MUL^{i,j}} \times \frac{MB^{i,j}}{MB\&0MSL^{i,j}} \tag{4.15}$$

where i and j denote the multiplicity bin and the run number respectively, as shown in Figure 4-17. The average F_{Norm}^{i} is calculated by taking the weighted average of muon events in multiplicity bin using the following definition :

$$F_{norm}^{i} = \frac{\sum_{i,j}^{n_{runs}} F_{norm}^{i,j}.N_{CMUL7}^{i,j}}{\sum_{i,j}^{n_{runs}} N_{CMUL7}^{i,j}} \tag{4.16}$$

Another method to compute F_{Norm}^{i} was tested, which may be called the re-scale

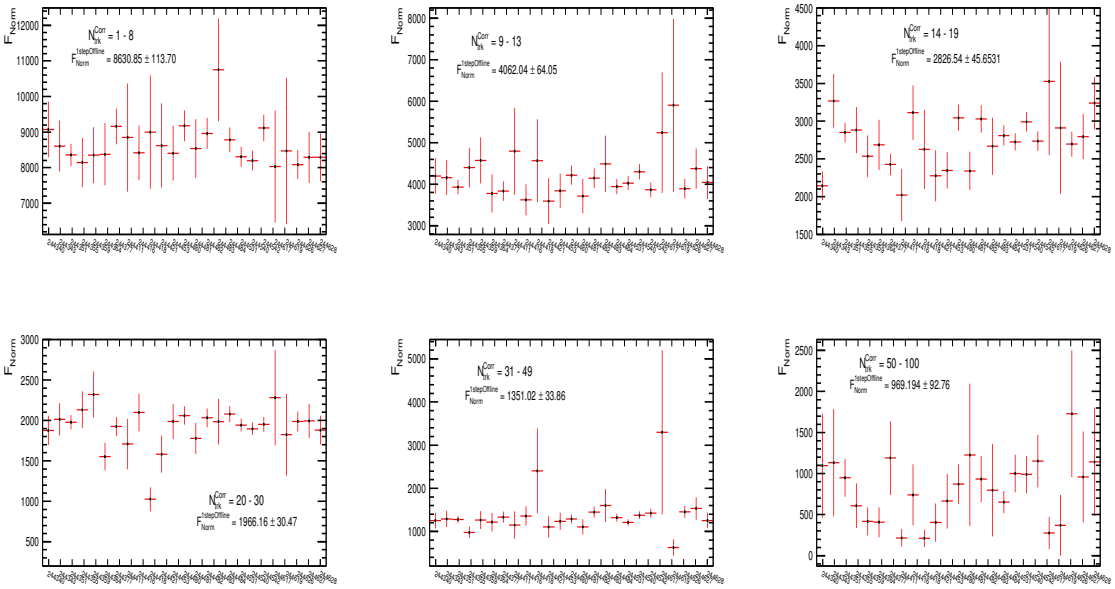

Figure 4-16: F_{norm}^{i} in six corrected tracklet bins calculated using one-step offline method (Equation 4.14).

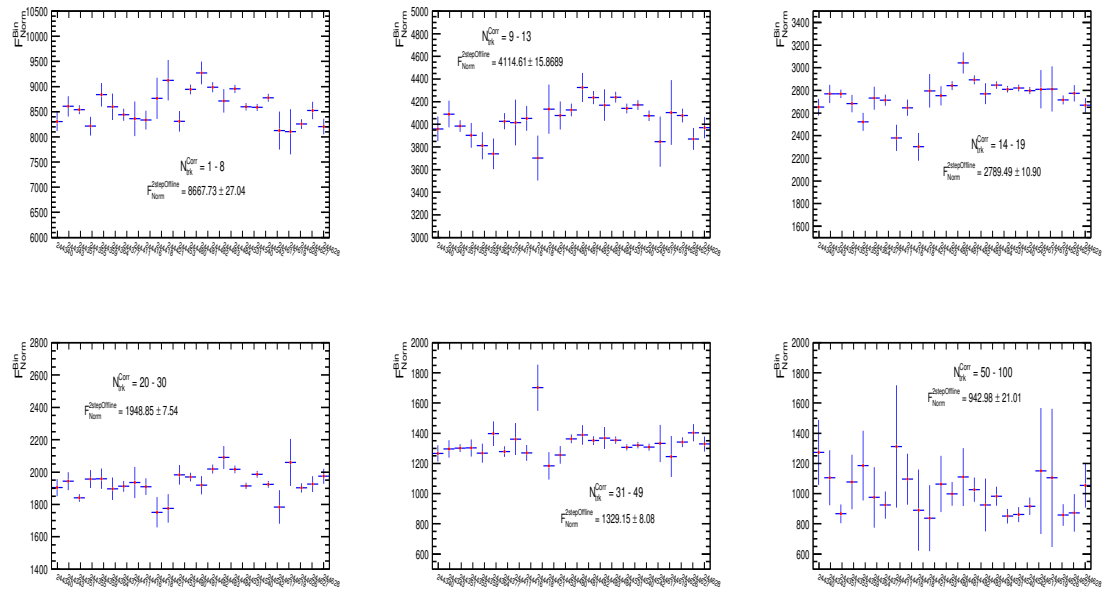

Figure 4-17: F_{norm}^{i} in six corrected tracklet bins calculated using two-step offline method (Equation 4.15).

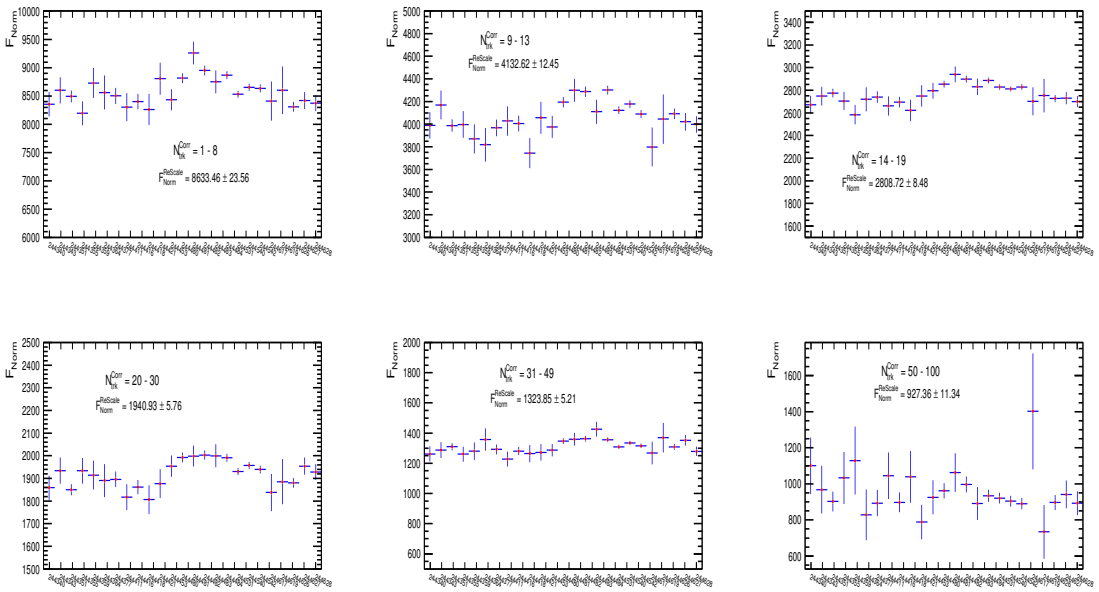

Figure 4-18: F^{i}_{norm} in six corrected tracklet bins calculated using re-scale method (Equation 4.17).

method. In this method the single muon trigger events do not come into play. This method uses the run by run $F^{offline}_{Norm}$, calculated by two-step offline formula and scaled with minimum bias events and the muon events in each run for every corrected tracklet bin. The run by run re-scale method is defined as follows:

$$F^{Rescale,i,j}_{norm} = F^{Offline,j}_{norm} \frac{N^{i,j}_{MB}/N^{j}_{MB}}{N^{i,j}_{CMUL7}/N^{j}_{CMUL7}} \tag{4.17}$$

Finally, taking sum over all the runs weighted by the muon events, the F^{i}_{Norm} factor are computed.

$$F^{Rescale,i}_{norm} = \frac{\sum_{j}^{n_{runs}} F^{j}_{norm}.N^{j}_{CMUL7}.N^{i,j}_{MB}/N^{j}_{MB}}{N^{i}_{CMUL7}} \tag{4.18}$$

Another technique to calculate F^{i}_{norm} is by taking the number of respective trigger events in the corrected tracklet bins integrated over all the runs instead of individual

run using the methods as follows:

$$F^{i}_{norm} = \frac{MB^{i}}{MB\&0MUL^{i}} \tag{4.19}$$

$$F^{i}_{norm} = \frac{MSL^{i}}{MSL\&0MUL^{i}} \times \frac{MB^{i}}{MB\&0MSL^{i}} \tag{4.20}$$

$$F^{i}_{norm} = F^{Offline}_{norm} \frac{N^{i}_{MB}/N_{MB}}{N^{i}_{CMUL7}/N_{CMUL7}} \tag{4.21}$$

The F^{i}_{norm} has been calculated in six multiplicity bins in pp collisions at $\sqrt{s} = 5.02$ TeV using the methods described above. The deviation in F^{i}_{norm} estimated by each method is included in the systematic uncertainty. The $F^{2stepOff}_{norm}$ for this period of data set was computed as 4522.71 ± 7.77554 (Figure 4-15). The values of F^{i}_{norm} are summarised in Tables 4.2 and 4.3.

$N^{corr}_{trk} bin$	$F^{1stepoff,i,j}_{norm}$	$F^{2stepoff,i,j}_{norm}$	$F^{Re-scale,i,j}_{norm}$
$1-7$	8630.85 ± 113.67	8667.73 ± 27.044	8633.46 ± 23.56
$8-12$	4062.04 ± 64.05	4114.61 ± 15.87	4132.62 ± 12.45
$13-18$	2826.54 ± 45.65	2789.49 ± 10.89	2808.72 ± 8.48
$19-29$	1966.16 ± 30.48	1948.85 ± 7.54	1940.93 ± 5.76
$30-48$	1351.02 ± 33.86	1329.15 ± 8.08	1323.85 ± 5.20
$49-100$	969.20 ± 92.76	942.97 ± 21.01	927.36 ± 11.34

Table 4.2: The F^{i}_{norm} is computed run by run in corrected tracklet bins. Here N^{corr}_{trk} corrected with $\langle N_{\rm trk} \rangle$ (z_v) reference maximum.

$N^{corr}_{trk} bin$	$F^{1stepoff,i}_{norm}$	$F^{2stepoff,i}_{norm}$	$F^{Re-scale,i}_{norm}$
$1-7$	8601.01 ± 104.74	8640.57 ± 25.66	8609.80 ± 18.24
$8-12$	4045.14 ± 58.94	4097.85 ± 15.02	4121.87 ± 10.18
$13-18$	2783.87 ± 40.87	2783.47 ± 10.36	2801.47 ± 6.94
$19-29$	1958.04 ± 28.01	1942.91 ± 7.13	1935.46 ± 4.67
$30-48$	1314.44 ± 28.56	1324.17 ± 7.61	1320.41 ± 4.65
$49-100$	932.03 ± 71.95	936.53 ± 19.41	922.96 ± 11.11

Table 4.3: F^{i}_{norm} is computed in corrected tracklet bins by taking integrated events.

F_{norm} calculated run by run method and with integrated number of events in multiplicity bins agree well with equivalent minimum bias events in case of Equations

4.17 and 4.21. It can be concluded from this observation that F^i_{norm} is stable over the runs of a different period. The calculated values of F^i_{norm} with each methods are in good agreement with each other. The values of F^i_{norm} computed with one-step offline method have large statistical errors as the fraction of minimum bias events with muons are very small. The results from one-step offline and re-scale methods are closer than that of two-step offline methods. The average F^i_{norm} and their systematic uncertainty are computed by taking into account the results from all these studies. These F^i_{norm} values are listed in Table 4.4.

$N^{corr}_{trk} bin$	F_{norm}
$1-7$	$8630.57 \pm 22.70(stat.) \pm 21.60(0.25\%)(syst)$
$8-12$	$4095.70 \pm 12.80(stat.) \pm 31.90(0.77\%)(syst.)$
$13-18$	$2798.93 \pm 8.80(stat.) \pm 15.40(0.54\%)(syst.)$
$19-29$	$1948.72 \pm 5.97(stat.) \pm 10.50(0.53\%)(syst.)$
$30-48$	$1327.17 \pm 5.60(stat.) \pm 11.55(0.87\%)(syst.)$
$49-100$	$938.51 \pm 14.41(stat.) \pm 15.13(1.61\%)(syst.)$
$Integrated$	$4477.46 \pm 6.23(stat.) \pm 48.14(1.07\%)(syst.)$

Table 4.4: The avergae F^i_{norm} in corrected tracklet bins.

The F^i_{norm} study was performed only in pp collisions at 5.02 TeV.

4.4.2 J/ψ yield measurement

The J/ψ yield in each multiplicity bin was calculated from

$$\langle dN_{J/\psi}/dy \rangle^{bin} = Y^{bin}_{J/\psi} = \frac{N^{bin}_{J/\psi}}{BR_{J/\psi\to\mu^+\mu^-} \times A \times \varepsilon \times N^{eq,i}_{\rm MB}} \tag{4.22}$$

where $N^{eq,i}_{MB}$ is the equivalent number of minimum bias events in each multiplicity bin selected within z-vertex 10 cm. $A \times \varepsilon$ is taken to be the same as the one for inclusive J/ψ yield.

Relative J/ψ yield is defined as,

$$\frac{Y^i_{J/\psi}}{Y^{tot}_{J/\psi}} = \frac{N^i_{J/\psi}}{N^{tot}_{J/\psi}} \times \frac{F_{norm}}{F^i_{norm}} \times \frac{N^{tot}_{\rm MUON}}{N^i_{\rm MUON}} \times \frac{\epsilon^i_{MB}}{\epsilon_{MB}} \times \frac{\epsilon_{J/\psi}}{\epsilon^i_{J/\psi}} \tag{4.23}$$

where,

- i is the multiplicity bin.
- N^i_{MUON} are the number of muon events in each respective multiplicity bin.
- F^i_{norm} is normalization factor in a multiplicity bin.
- ϵ_{MB} corresponds to the multiplicity integrated corrections for MB event.
- ϵ^i_{MB} corresponds to the corrections in multiplicity bin i for MB events.
- $\epsilon_{J/\psi}$ corresponds to the multiplicity integrated corrections for events with a J/ψ.
- $\epsilon^i_{J/\psi}$, i corresponds to the corrections in multiplicity bin i for events with a J/ψ.

Each of these four multiplicity terms have several contributions, namely:

- $\epsilon_{INEL>0}$ ($or \epsilon_{NSD}$), the minimum bias trigger efficiency for $INEL > 0$ (or NSD) events.
- $\epsilon_{vtxrange}$ the efficiency of the vertex range cuts.
- $\epsilon_{vtx,QA}$ the efficiency of the vertex QA cuts.
- ϵ_{pu} the efficiency of the pile-up rejection.

It has already been discussed that the efficiency correction factors in multiplicity bins are around unity except for the first multiplicity bin. The relative yield of J/ψ was calculated using minimum bias events, as the systematic uncertainty due to F_{Norm} is very small and the yield is almost constant. Hence the relative yield of J/ψ was computed by the expression:

$$\frac{Y^i_{J/\psi}}{Y^{tot}_{J/\psi}} = \frac{N^i_{J/\psi}}{N^{tot}_{J/\psi}} \times \frac{N_{MB}}{N^i_{MB}} \times \frac{\epsilon^i_{\mathrm{INEL}>0}}{\epsilon_{\mathrm{INEL}>0}} \times \frac{\epsilon^{J/\psi}_{vtx,QA}}{\epsilon^{MB}_{vtx,QA}} \times \frac{1}{\epsilon_{INEL==0}} \times \epsilon_{pu} \tag{4.24}$$

The same formula has been used to compute J/ψ yield at 2.76 TeV.

4.5 Systematic Uncertainty

4.5.1 Contribution from pile-up

In Section 4.2.1 the expected pile-up rate has been computed for two minimum bias trigger events coming from at least one collision using Poisson distributions. This pile-up rate is very small for the data period. The expected pile-up rate for the same minimum bias trigger was also calculated to see the probability of at least two collisions and average mean number of collisions per bunch crossing.

$Trigger$	$< \mu >$	$P(n \geq 1)$	$P(n \geq 2)$
$CINT7$	0.023	$1.005 \pm 0.006 \times 10^{-1}$	$4.80 \times 10^{-4} \pm 7.66 \times 10^{-7}$
$C0TVX$	0.009	$1.011 \pm 0.003 \times 10^{-1}$	$8.87 \times 10^{-5} \pm 5.87 \times 10^{-8}$

Table 4.5: The expected pile-up rate using Poisson distribution.

The pile-up tag in physics selection was used as the second argument (pileupfromPS). This removes most of the contamination. The pile-up events are defined by the occurrence of two interaction vertices reconstructed with the SPD. The 'IsPileUpfromSPD' is defined as events are rejected if the distance along the beam axis between the two vertices is larger than 0.8 cm, and if both vertices have at least three or five associated tracklets. The additional pile-up contamination were checked using tag 'IsPileUpfromSPD' with 3 contributors, 5 contributors and 'IsPileUpfrom SPD' multi-vertexer. The mean number of corrected tracklets with each pile-up tags were compared and events were rejected due this contaminations.

The corrected tracklet distribution with pile-up from physics selection tag and additional pile-up tests are shown in Figure 4-19. The long tail of tracklet is removed by the pile-up (PU) rejection. This observation shows Pile-up rejection cut from PS is mandatory. The ratio of pile-up tag from 'ISPileUpfromSPD' with 3, 5 and contributions from multi-vertexer to the 'pile-up from PS' is shown in Figure 4-20 for both minimum bias and muon events. It can be seen from the plots that except the 'pile-up from PS' the additional pile-up contaminations are almost removed by 'ISPileUpfromSPD' with 3 contributors because of the low multiplicity in pp collisions

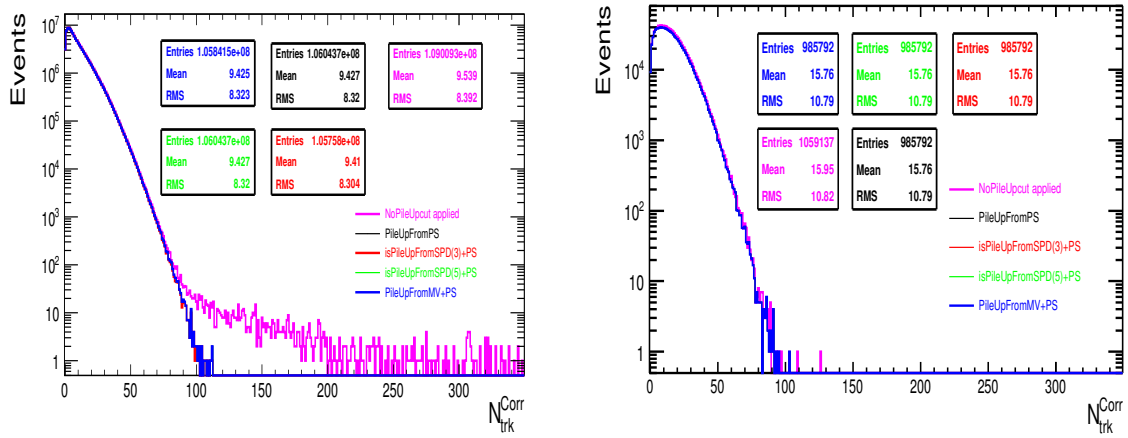

(a) (b)

Figure 4-19: Distribution of tracklets with various pile-up tests as a function of multiplicity for (a) CINT7 and (b) CMUL events.

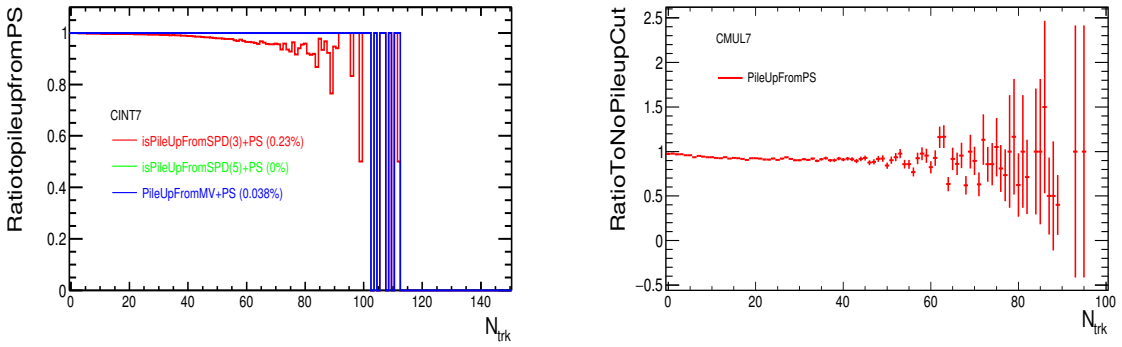

(a) (b)

Figure 4-20: Ratio of distribution of tracklets with various pile-up tests (a) to 'pile-up from PS' CINT7 and (b) to no pile-up test for CMUL events.

at $\sqrt{s} = 5.02$ TeV.

The verifications of these pile-up tags were studied in more details by checking the variation of mean corrected tracklets run by run (Figure 4-21). The 5 Runs 244411-244421 have large pile-up about 6.34% rejected by 'PU from PS' with 0.017% uncertainty. Additional pile-up contamination for the same runs is 0.38% with 0.001% uncertainty in case of CINT7. The overall 'PU from PS' rejected 1.12% contamination with 0.013% uncertainty. 'PS+SPD3' rejected $0.177\% \pm 0.002\%$ and 'PS+SPDMV' rejected $0.025\% \pm 0.080\%$ contamination. 'PS+SPD5' did not remove any additional

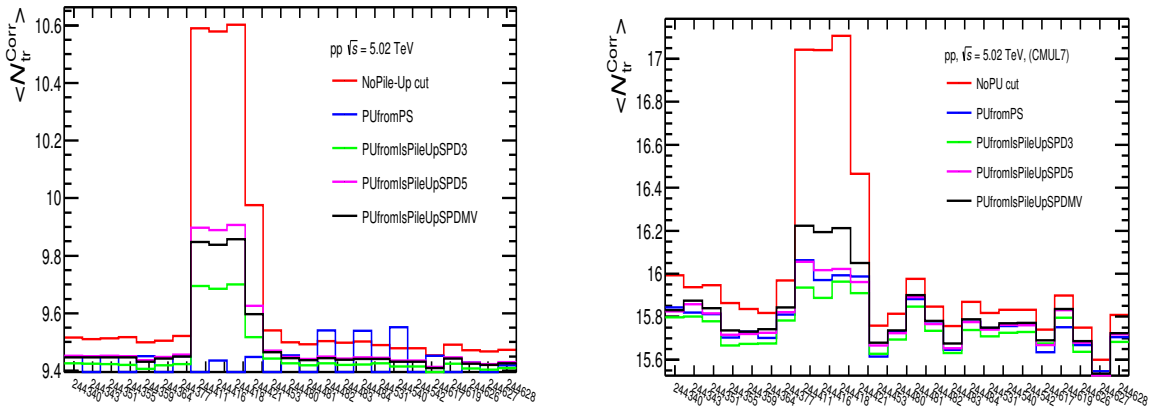

(a) (b)

Figure 4-21: Run by run various pile-up tests for (a) CINT7 and (b) CMUL events. x-axis label shows run numbers.

contamination. The similar results were obtained from muon events. In case of CMUL7, 'PU from PS' rejected 1.19% contamination with 0.05% uncertainty. In addition 'PS+SPD3' rejected 0.216% contamination with 0.0211% uncertainty. The muon events were not checked for 'ISpileUpfromSPD' multivertex and also for IsPile-Upfrom SPD with 5 contributors.

Some runs have higher pile-up rate as compared to others. Thus, the pile-up rate was not constant. To take into account this deviation in pile-up rate, two sub samples of high and low rate pile-up runs were compared.

The corrected tracklet distribution with 'PU from PS' in high and low PU rate runs are shown in Figure 4-22. Little fluctuation is observed towards high multiplicity bins. Overall fluctuation of pile-up rate between high and low PU runs was 0.75% for CINT7 and 0.27% for CMUL7. The PU contamination after applying PU from PS cut was negligible for all runs.

The ratio of $\langle N_{\rm trk} \rangle$ in each multiplicity bins between high and low PU rate runs are shown in Figure 4-23. The first bin has maximum deviation 0.44% and 0.33% with 'PS+SPD'. The ratio of $\langle N_{\rm trk} \rangle$ to the CINT7 event in each multiplicity bin are shown in Figure 4-24. The ratios are almost constant in 'pile-up from PS' and also after 'IsPileUpfromSPD' correction. The overall fluctuation in this case for minimum bias

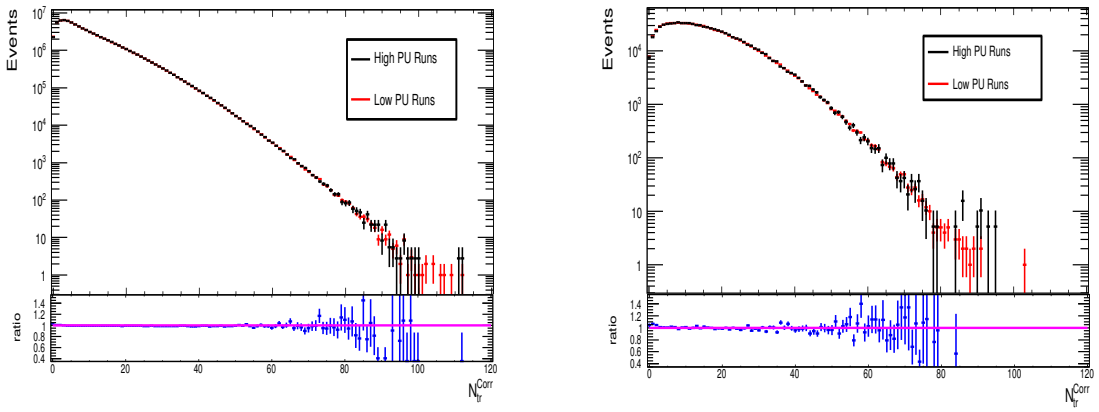

(a) (b)

Figure 4-22: The tracklet distribution of high and low pile-up rate runs for (a) CINT7 and (b) CMUL events. The lower pannel shows the ratio between the two observables.

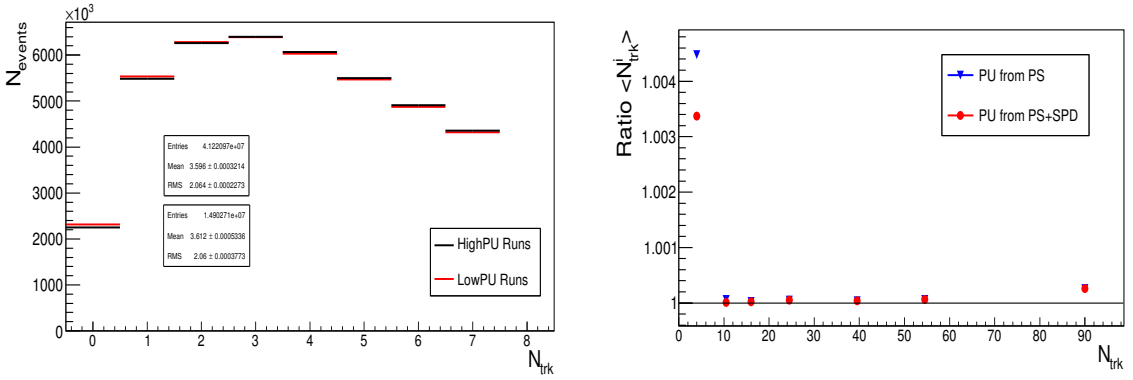

(a) (b)

Figure 4-23: (a) High vs. low pile-up rate runs distribution in first bin. (b) Ratio of $\langle N_{\rm trk} \rangle$ between 'PU from PS' and 'PU from PS+ all SPD tags' in multiplicity bins

$N_{trk}^{corr} bin$	$Pile-up fraction(\%)$	$Systematic(\%)$
$1-7$	0.047	0.311
$8-12$	0.003	0.067
$13-18$	0.002	0.057
$19-29$	0.008	0.053
$30-49$	0.034	0.135
$49-100$	0.067	1.035

Table 4.6: The fraction of pile-up and systematic uncertainty due to pile-up in multiplicity bins at 5.02 TeV.

events is 0.008% including 0.017% in first and 0.04% in last multiplicity bin. Total systematic uncertainty due to pile up is 1.8% for CINT7 and 2.65% for CMUL. The

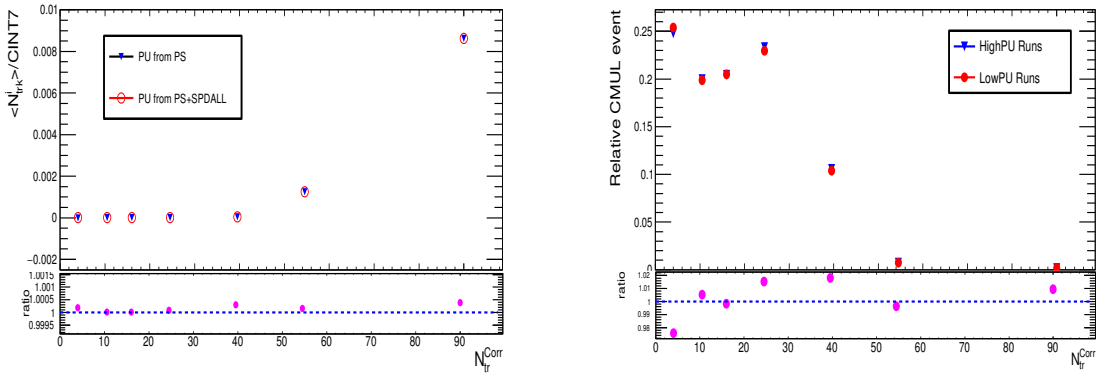

(a) (b)

Figure 4-24: (a) Ratio of $\langle N_{\rm trk} \rangle$ to the CINT7 event in each multiplicity bin for 'PU from PS' and 'PU from PS+ all SPD tags'. (b) Ratio of high and low PU runs for CMUL events in multiplicity bins.

systematic uncertainty due to contribution from pile-up is summarised in Table 4.6. From Table 4.6, it can be observed that the pile-up contamination has negligible effect in multiplicity study after applying the proper pile-up removal criteria selections. In pp collisions at $\sqrt{s} = 2.76$ TeV, the detailed pile-up study has not been performed as the 'IsPileUpfromSPD' tag is 99% efficient over all the multiplicity region. Therefore, the systematic uncertainty of 1% has been assigned due to contribution from pile-up.

4.5.2 Contribution from signal extraction

The main source of systematic uncertainty in J/ψ analysis is the uncertainty due to signal extraction. The signal extraction due to combination of fit functions, varying dimuon mass range and tail parameters are the sources of systematic uncertainty. In total 48 combinations were tested by varying background and mass range to estimate the uncertainty. The ratio of number of J/ψ in multiplicity bins ($N^{i}_{J/\psi}$) to the integrated number of J/ψ ($N^{\rm tot}_{\rm J/\psi}$) *i.e.* $N_{\rm J/\psi}/N^{\rm tot}_{\rm J/\psi}$ has been plotted by varying background and invariant mass-ranges are shown in Figure 4-25 to 4-30.

The results account for this systematic uncertainty are plotted bin by bin. The results of systematic uncertainty using 12 fits are shown in the Figure 4-31 (a). The systematic uncertainty for relative J/ψ yield was also computed by taking the quadrature of

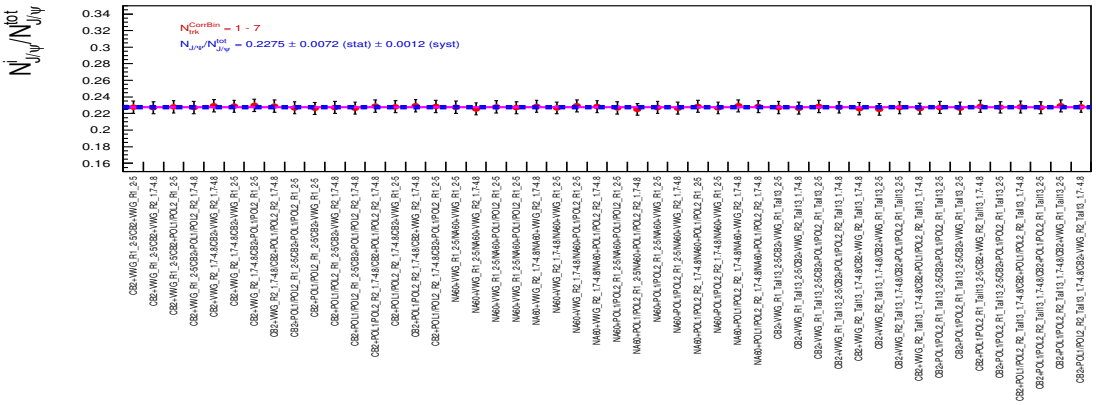

Figure 4-25: J/ψ yield systematic uncertainty in bin 1-7.

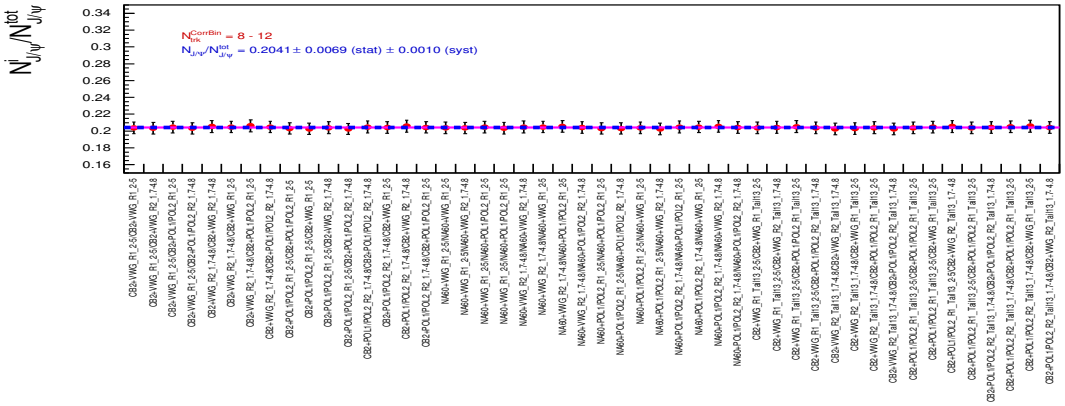

Figure 4-26: J/ψ yield systematic uncertainty in bin 8-12.

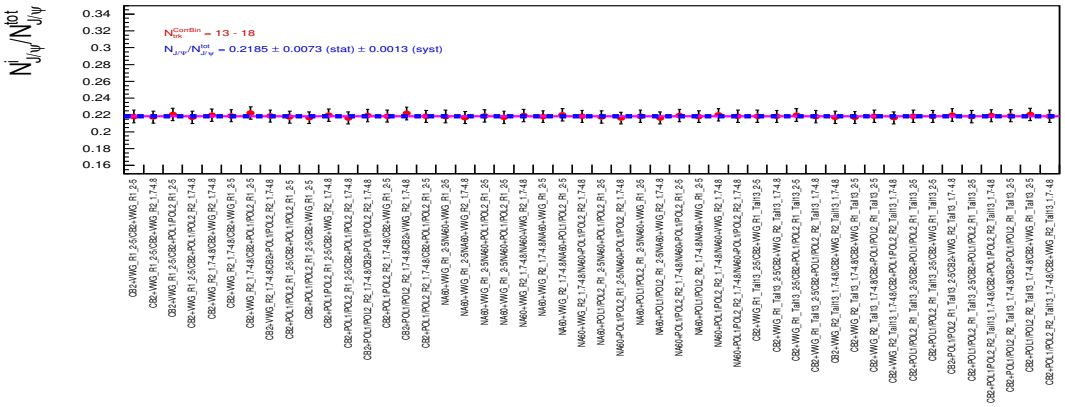

Figure 4-27: J/ψ yield systematic uncertainty in bin 13-18.

the systematic uncertainties of $N^{i}_{J/\psi}$ and $N_{J/\psi}$ directly without varying background and invariant mass ranges. This method gives higher values of systematic uncertainty due to signal extraction and the contamination due to background has to be taken

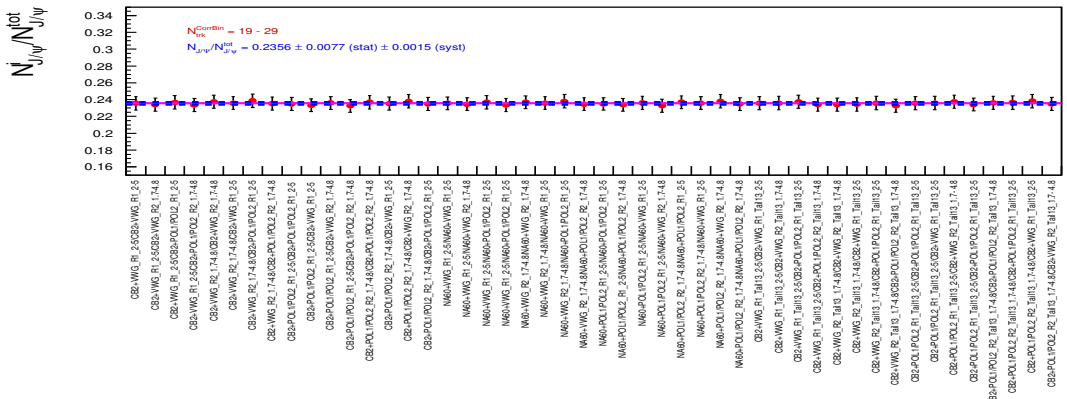

Figure 4-28: J/ψ yield systematic in bin 19-29.

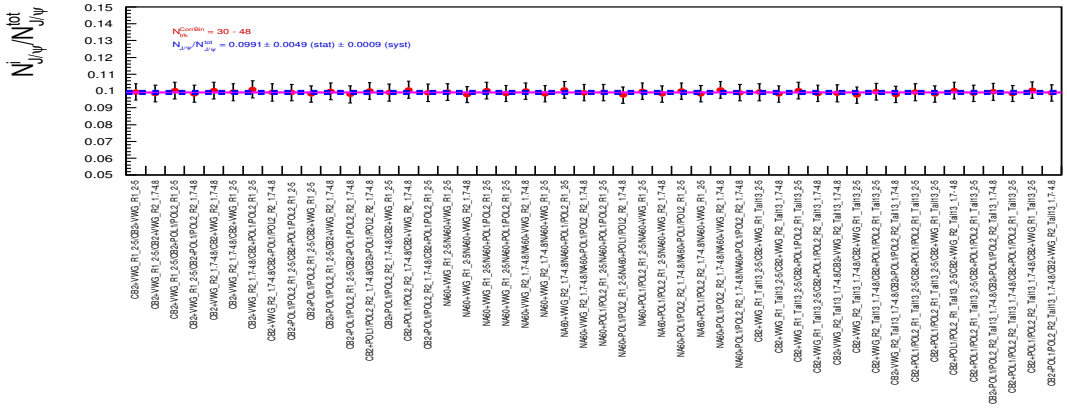

Figure 4-29: J/ψ yield systematic uncertainty in bin 30-48.

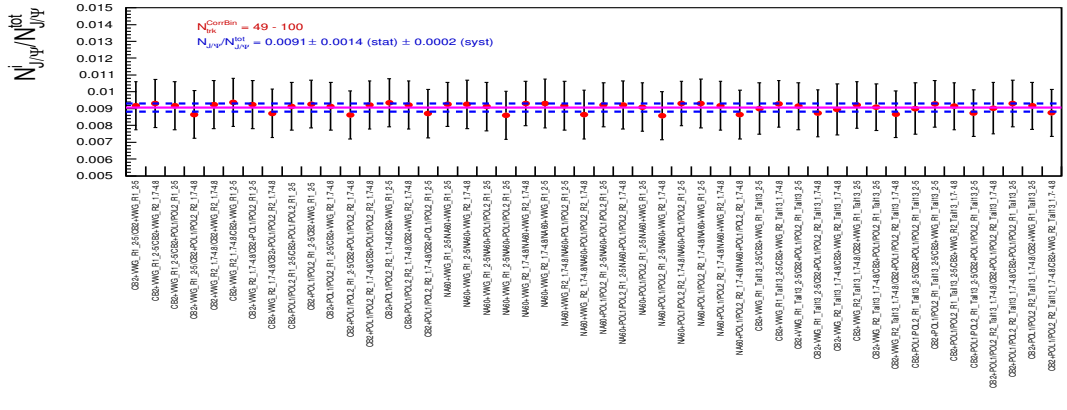

Figure 4-30: J/ψ yield systematic uncertainty in bin 49-100.

into account. Thus, the method mentioned above was opted for the estimation of uncertainty due to signal extraction. The results of systematic uncertainty due to 48 combination of tests are illustrated bin by bin in Figure 4-31 (b). Background func-

tion as well as invariant mass ranges were shuffled and weight was applied for 13 TeV tail parameter in this case. These value were taken as final systematic uncertainty from signal extraction on J/ψ yield. It gives results to a minimum of 0.523% and to a maximum of 2.622% systematic uncertainty in the last bin.

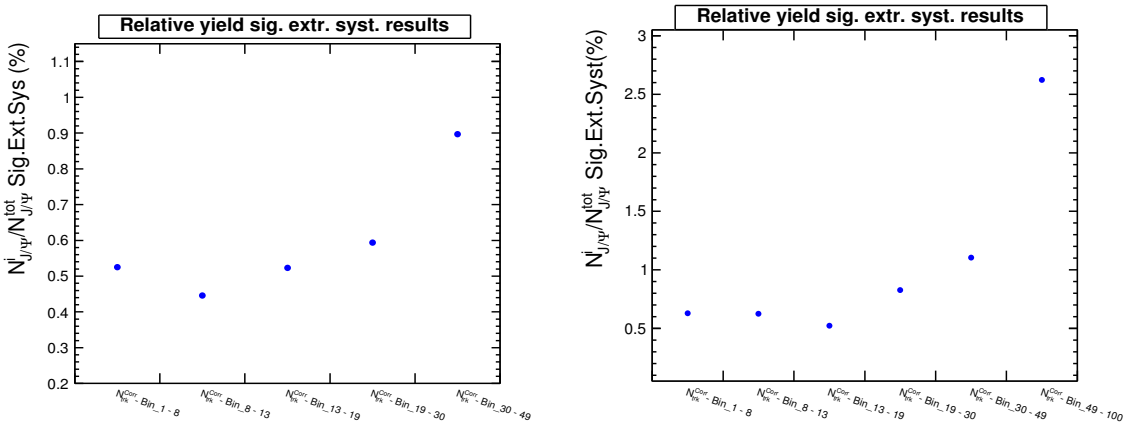

(a) (b)

Figure 4-31: (a) The J/ψ yields systematic uncertainty due to signal extraction. (b) Relative J/ψ yields systematic uncertainty due to signal extraction and background variation.

4.5.3 Contribution from F_{norm} factor

The self-normalised J/ψ yields in multiplicity bins were computed with F_{norm} calculated by several methods and compared with the relative J/ψ yields computed only with MB events. It can be seen from Figure 4-32 (a), that the values of relative J/ψ yield computed with different F_{norm} methods are consistent. Due to small statistics in the last multiplicity bin there is a fluctuation in F_{norm}. Thus, contribution of F_{norm} gives rise to very small systematic uncertainty $< 1\%$ except for the last multiplicity bin.

The results of systematic uncertainty due to F_{norm} factor are shown in Figure 4-33. The F_{norm} study was carried out independently to check whether it can be cancelled out in the ratio of the relative yield calculation, and assign a systematic uncertainty for that. It can be noted that F_{norm} is largely canceled out with only a

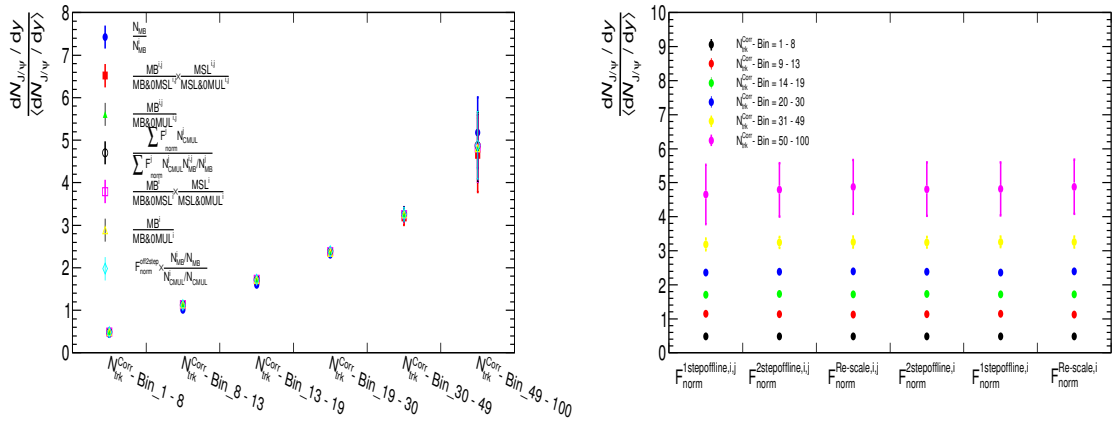

(a) (b)

Figure 4-32: (a) Relative J/ψ yields as a function of multiplicity bins calculated with different F_{norm} methods. (b) The values of relative J/ψ yield in multiplicity bins as function of various F_{norm}.

small systematic uncertainty. The relative J/ψ yield computed with the ratio of MB gives almost the same results as for F_{norm} methods. Therefore, for simplicity, MB events were used to compute relative yield of J/ψ and systematic uncertainty was assigned due to F_{norm} to the final results.

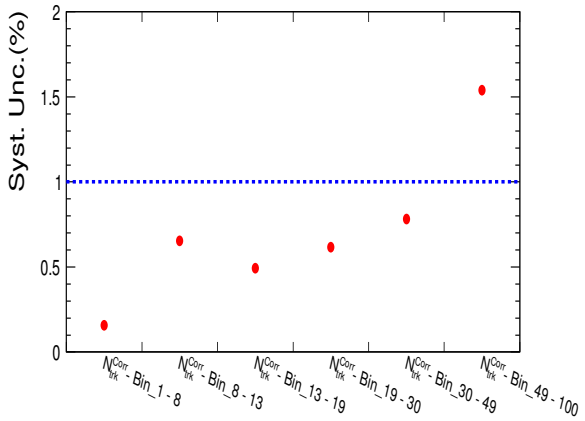

Figure 4-33: J/ψ yield systematic uncertainty due to F_{norm}.

4.5.4 Vertex QA efficiency for J/ψ

The J/ψ signal extracted from events which passes the vertex QA cuts and events with only Physics selection are cut shown in Figure 4-34. The vertex QA efficiency, $\epsilon^{J/\psi}_{vtx,QA}$ for J/ψ yield computed by the definition:

$$\epsilon^{J/\psi}_{vtx,QA} = \frac{IntegratedN_{J/\psi}(withvertexQA)}{IntegratedN_{J/\psi}(withoutvertexQA)} \tag{4.25}$$

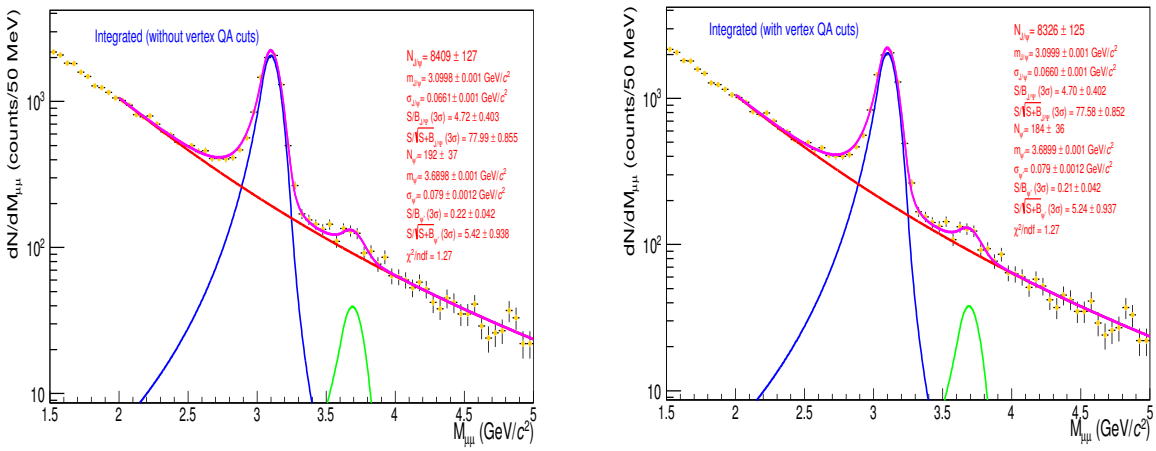

Figure 4-34: J/ψ signal without and with vertex QA cuts.

Similarly $\epsilon^{J/\psi}_{vtx,QA}$ has been computed for the first multiplicity bin. The obtained value for $\epsilon^{J/\psi}_{vtx,QA}$ is 0.99% independent of multiplicity. The ratio of minimum bias vertex corrections to the J/ψ corrections was computed as $\epsilon^{J/\psi}_{vtx,QA}/\epsilon^{MB}_{vtx,QA} = 1.03 \pm 0.02$. The $\epsilon^{J/\psi}_{vtx,QA}$ at 2.76 is 0.98% independent of the multiplicity, hence, at 2.76 TeV the value of $\epsilon^{J/\psi}_{vtx,QA}/\epsilon^{MB}_{vtx,QA}$ is 1.15 ± 0.06.

4.5.5 Summary of systematic uncertainties

Systematic uncertainty at both 2.76 and 5.02 TeV energies, due to various sources are summarised in Table 4.7. Systematic uncertainty due to event selection is described in the previous chapter. Systematic uncertainty due to acceptance and efficiency, trigger and tracking matching of muon spectrometer, are not essential for multiplic-

ity analysis, as these factors will cancel out in the self-normalisation process. It can be observed from the table that signal extraction gives major contribution in the systematic uncertainty at both energies for relative yield of J/ψ.

Source	Systematic Uncertainty	
	$\sqrt{s}$ = 5.02 TeV	$\sqrt{s}$ = 2.76 TeV
Signal extraction	0.47% − 2.76%	0.27% − 1.33%
F_{norm}	0.16% − 1.54%	1%
$Pile-up$	0.05% − 1.03%	1%
Events selection	1.53%	1%
$INEL == 0$	1.%	1.%
$N_{ch}(various\ sources)$	0.09% − 1.687%	0.270% − 3.162%
$\langle N_{ch}\rangle$ $(Integrated)*$	1.4%	8%
N_{ch} $non-linearity$	0.2% − 8%	0.67% − 8.11%
$\langle N_{ch}\rangle 1^{st} bin$	1.34%	1%

Table 4.7: The systematic uncertainties due to different sources.

In case of charged-particle multiplicity, the systematic uncertainty due to non-linearity is highest. In fact, it can be seen from Table 4.7 the systematic uncertainty due to non-linearity dominating over all other source of systematic uncertainty.[1]. It can also be concluded from the table that the measurements of relative yield of J/ψ as well as charged-particles multiplicity are more precise in pp collisions at $\sqrt{s}$ = 5.02 TeV than in $\sqrt{s}$ = 2.76 TeV.

4.6 Results and Discussions

The evolution of relative J/ψ yield as a function of relative charged-particle pseudo-rapidity density was investigated at $\sqrt{s}$ = 2.76 TeV and 5.02 TeV. The integrated pseudo-rapidity was measured for inelastic > 0 event class at both energies. The minimum bias efficiency correction factor was taken into account in the $dN_{ch}/d\eta$ calculation. The relative charged particle densities were normalised with integrated pseudo-rapidity taken from the references [4] and [5]. Hence, the value of charged-

[1] 1.4% and 8% are taken in this analysis from references [4] and [5].

particle density was corrected only in the first bin with efficiencies described in the Section 3.4.5 given that all the corrections were implemented in the integrated $dN_{ch}/d\eta$ and it has been observed that the values of the efficiencies are negligible in the higher multiplicity bins. The multiplicity dependence of the J/ψ yield is displayed for pp

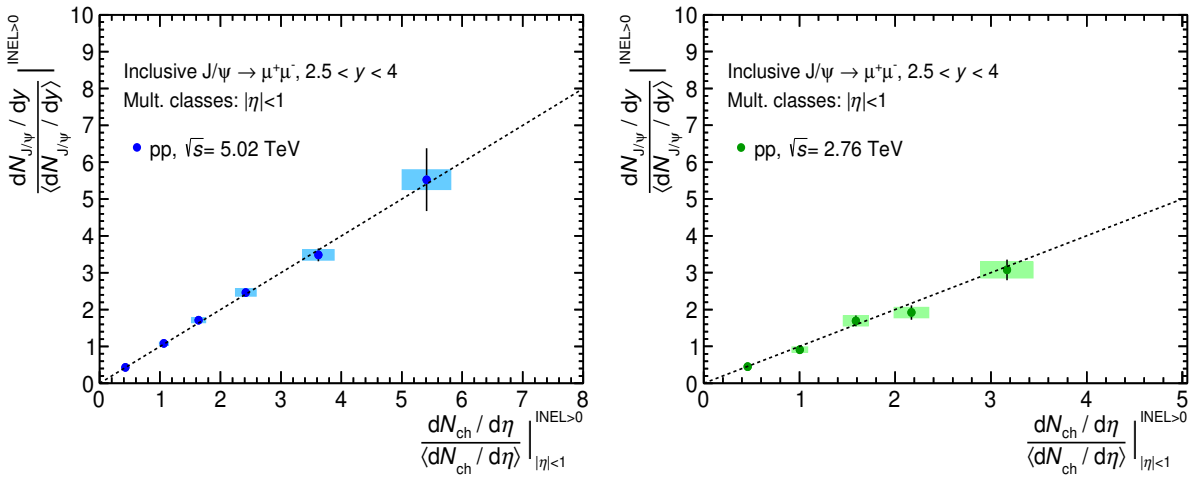

(a) (b)

Figure 4-35: Relative J/ψ yield as a function of relative charged-particle density in pp collisions at $\sqrt{s}$ = 5.02 (a) and 2.76 TeV (b).

collisions at $\sqrt{s}$ = 5.02 and 2.76 TeV in Figure 4-35 at forward rapidity. The increase in J/ψ production with the increase of multiplicity at forward rapidity is observed. The slope of the plot is fitted with x=y function to check the nature of increment and it is found to be around 1, and to check for the linear trend of d$N_{\rm ch}$/dη with relative J/ψ yield.

The correlation between multiplicity and J/ψ is compared to a linear function with a slope of 1 (y=x). The ratio of the relative J/ψ yield to this diagonal as a function of multiplicity is displayed in the bottom panel of Figure 4-36. The ratio shows no deviation from unity at forward rapidity. Since we observe similar trend at both the energies. It is interesting to note that the ratio is consistent with unity over the full multiplicity range. This, in turn, implies that the production of J/ψ scales linearly with the underlying event activity. It can be concluded from this observation that the evolution of J/ψ production increases linearly with charged-

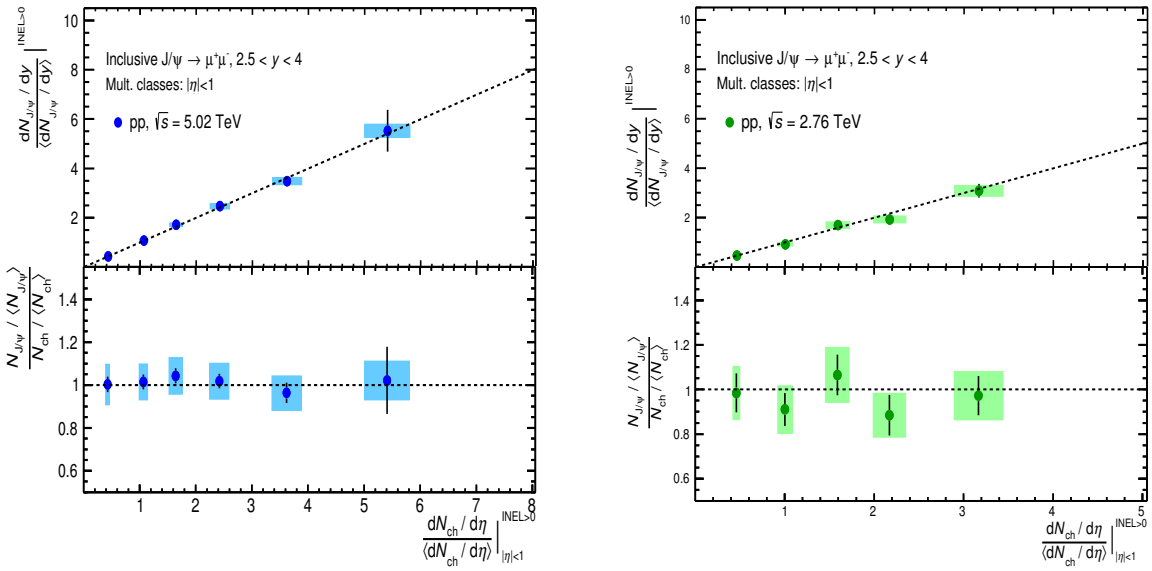

(a) $\sqrt{s}$ =5.02 TeV (b) $\sqrt{s}$ =2.76 TeV

Figure 4-36: The relative J/ψ yield as a function of the relative charged-particle density measured at forward rapidity in pp collisions at $\sqrt{s}$ = 5.02 and 2.76 TeV. Bottom panel: ratio of the relative J/ψ yield to the relative charged-particle density as a function of multiplicity at both the CM energies.

particle multiplicity. It can also be observed that the multiplicity dependence of J/ψ measurement is independent of the collision energy. To support our statement the results are compared with available ALICE results at forward and mid-rapidity.

4.6.1 Comparison with other ALICE results

The J/ψ yield observed at $\sqrt{s}$ = 5.02 and 2.76 TeV are compared with those reported for forward and mid-rapidity ALICE measurements in pp collisions at $\sqrt{s}$ = 7 TeV [6] and 13 TeV [7] and the results are displayed in Figure 4-37. It can be seen from Figure 4-37 (a), that the similar increasing trend of multiplicity dependence of J/ψ yield is observed as in pp collisions at $\sqrt{s}$ = 7 TeV and 13 TeV at forward rapidity. The comparison is not straight forward with the results of pp collisions at $\sqrt{s}$ = 7 TeV as the relative J/ψ yield is corrected for inelastic event class rather than INEL>0 event class. To get better understanding we fit the results for pp collisions at $\sqrt{s}$ = 7 TeV with first order polynomial function. The slope is 1.11 in case of pp collisions at $\sqrt{s}$ =

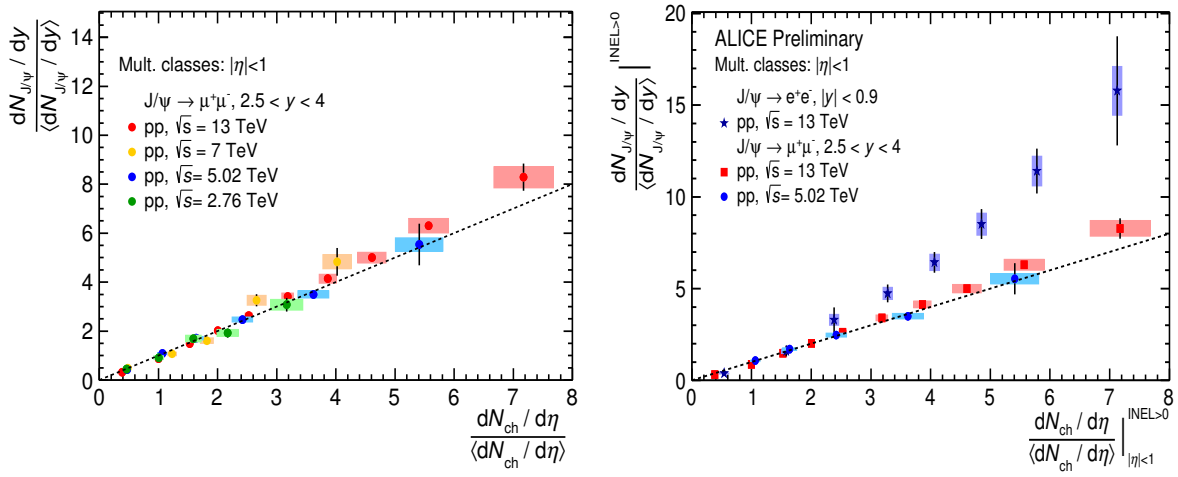

(a) (b)

Figure 4-37: (a) Comparison of J/ψ yield as a function of multiplicity with pp $\sqrt{s} = 7$ and 13 TeV at forward rapidity. (b) Comparison of multiplicity dependence of J/ψ production with pp at $\sqrt{s} = 13$ TeV results at mid and forward rapidity.

7 TeV. The measurement of self-normalised J/ψ yield as a function of multiplicity is carried out in the same process as mentioned in this thesis. Hence, ample comparison of results with 13 TeV analysis at forward rapidity is possible. It is evident from the figure that J/ψ yield estimated for different multiplicity bins are almost independent of the beam energy in the forward rapidity region.

These results are also compared with the similar ALICE analysis carried out in the mid-rapidity in pp collisions at 13 TeV [8]. The comparison with mid-rapidity shows a faster trend as compared to linear increment towards higher multiplicity region. At the mid-rapidity measurement, both multiplicity and J/ψ were measured in the same rapidity window *i.e.* no y-gap is provided. There might be a chance of double count of multiplicity which results in a serial correlation between hard probes and overall multiplicity measurement. Such a dependence may be attributed to the presence of auto-correlations between the J/ψ and the multiplicity measurements at mid-rapidity, which results in a stronger rather than linear increment at mid-rapidity. This effect can be reduced by introducing a rapidity gap between the J/ψ and the multiplicity estimator. Thus, the forward rapidity measurements show linear multiplicity dependence.

As we know 'jet' is a narrow cone of hadrons (it includes J/ψ as well) produced via hadronisation, travels in a forward direction. Here, J/ψ might decay into other particles which also add to the total charged-particle multiplicity. This effect is known as 'jet-bias' [9]. The effect of jet-bias could be very small unlike auto-correlation but it can not be removed by introducing a rapidity gap between observables. Hence, there might be possible contribution of jet-bias on the increase of J/ψ yield as a function of multiplicity at the mid- and forward rapidity.

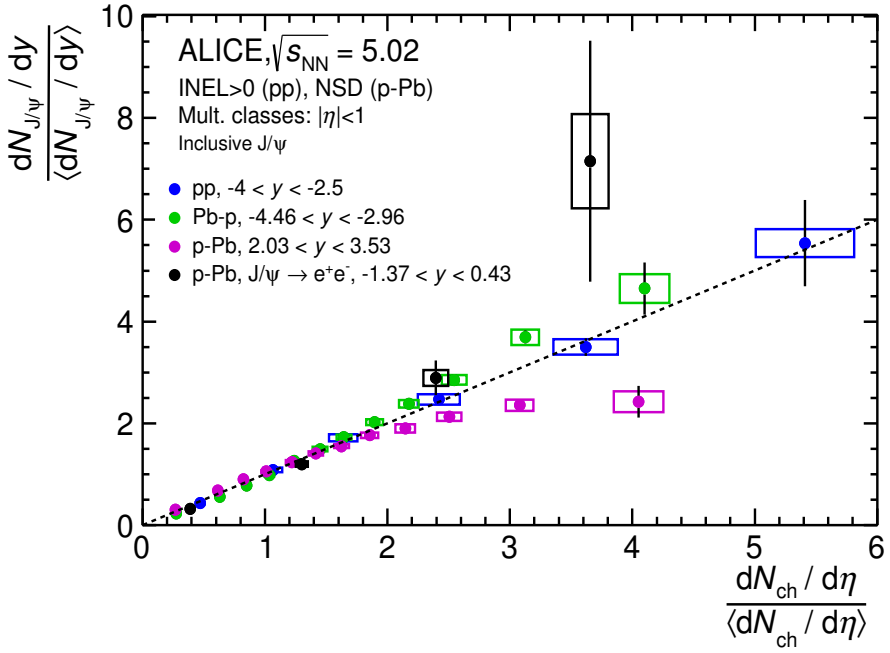

Figure 4-38: Comparison of J/ψ yield as a function of multiplicity in pp collisions at $\sqrt{s}$ = 5.02 TeV with p-Pb collision results at forward, backward and mid-rapidity regions.

Furthermore, the increasing trend of J/ψ production with multiplicity has also been investigated for collision systems like pp and p-Pb. The results of relative J/ψ yield in pp collisions at $\sqrt{s}$ = 5.02 TeV are compared with the results of p-Pb collisions at $\sqrt{s_{NN}}$ = 5.02 TeV as a function of relative charged-particle pseudo-rapidity density [10]. The evolution of J/ψ yield as a function of multiplicity is illustrated for different rapidity regions while the multiplicity is always measured at mid-rapidity. It can be observed from Figure 4-38 that the multiplicity dependence of J/ψ yield is sim-

ilar in pp collisions at forward rapidity and p-Pb collisions at backward rapidity(Pb going direction) at the same centre of mass energy. The mid-rapidity results show steeper increment similar to mid-rapidity results in pp collisions at 13 TeV. The similar increasing trend with multiplicity is observed in all rapidity regions and collision systems up to relative $\mathrm{d}N_{\mathrm{ch}}/\mathrm{d}\eta$ ~2,beyond which there are observed deviations.

4.6.2 Comparison with theoretical models

The results are compared with available theoretical model predictions for $\sqrt{s}$ =5.02 TeV at forward rapidity region and shown in Figure 4-39. The percolation model given by Ferreiro et. al., based on parton saturation or string interaction. This model showed deviation from linearity in pp collisions at $\sqrt{s}$ = 7 TeV at forward rapidity [11]. In pp collisions at $\sqrt{s}$ = 5.02 TeV, the percolation model shows linear behaviour at forward rapidity up to ~3 multiplicity. The quadratic increase at high multiplicity is observed similar to pp 7 TeV results. The Higher Fock states model by Kopeliovich et. al, also shows increment in J/ψ yield with multiplicity [12, 13]. The contribution of higher number of gluons in this model gives the best estimation of the data in pp collisions at $\sqrt{s}$ = 5.02 TeV. The calculation from EPOS3 model without the contribution of hydrodynamic evolution of the system seems to explain the data well up to the multiplicity ~3 [14]. The initial condition in this case was based on parton based 'Gribov-Regge' formalism which naturally includes the MPI [15].

Two new approaches based on CGC effective field theory have been used to explain the data. The CGC along with improved colour evaporation framework (CGC+ICEM) shows faster than linear increase of J/ψ as compared to the minimum bias events due to rapid growth in fragmentation of color-octet state [16]. Although it shows similar increasing trend, the multiplicity dependence of J/ψ shows much faster increment as compared to the data. The 3-gluon mechanism with CGC framework also gives linear increment of J/ψ yield but over estimates the data at higher multiplicities [17]. These observations imply that the CGC can be a good approach to explain the trend.

The comparison with PYTHIA8 model predictions are also shown in Figure 4-39.

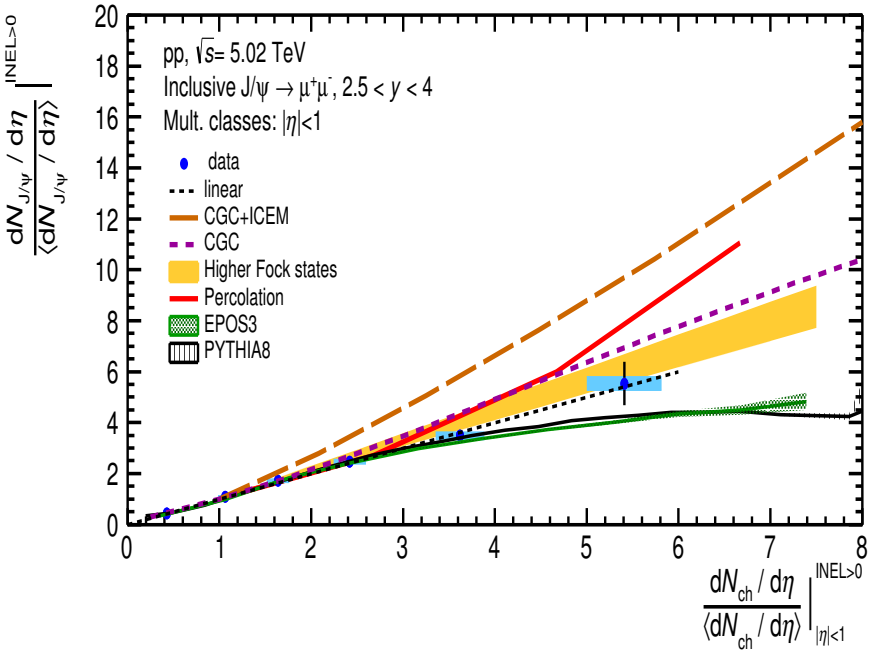

Figure 4-39: Comparison of data with theoretical model predictions in pp collisions at $\sqrt{s}$ = 5.02 TeV

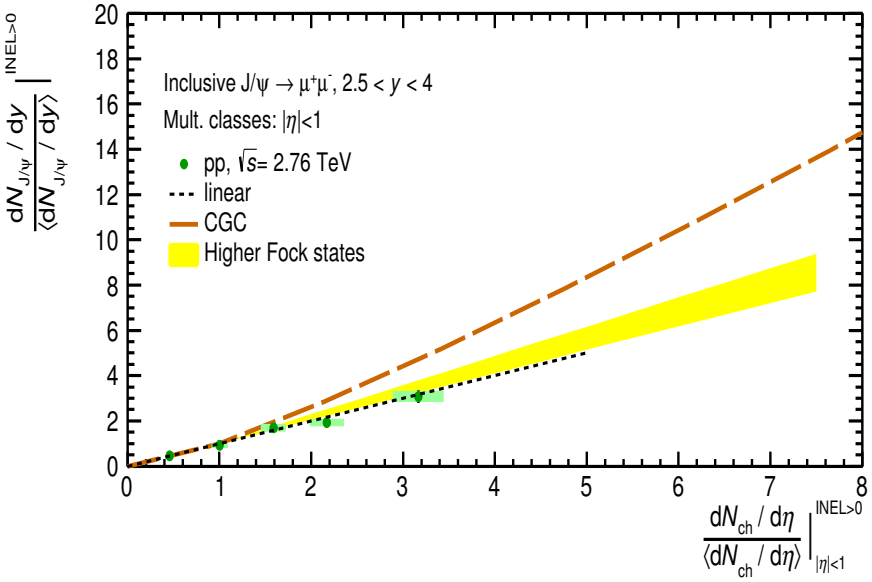

Figure 4-40: Comparison of data with theoretical model predictions in pp collisions at $\sqrt{s}$ = 2.76 TeV

The J/ψ yield is computed with two tunes of PYTHIA8 Monash the default tune and the 4C tune for inelastic >0 event class (4C tune results are in the Chapter 6). The hard processes in the MPI, gluon spitting, initial and final state radiation are the contributory factor in the increase of J/ψ yield as a function of multiplicity. The PYTHIA8 results are in good agreement with data at lower multiplicity region, but towards higher multiplicities it under estimates the data. In Figure 4-40, the comparison of available model predictions with pp collisions at $\sqrt{s}$ =2.76 TeV result is shown. The Higher Fock state model gives good description of the 2.76 TeV data as well. This model also shows no energy dependence of J/ψ production with multiplicity. However, the CGC with 3 gluon saturation model largely estimates the data at $\sqrt{s}$ = 2.76 TeV and here it can be seen from this model prediction at lower energy that the increase of relative J/ψ yield is enhanced as a function of multiplicity.

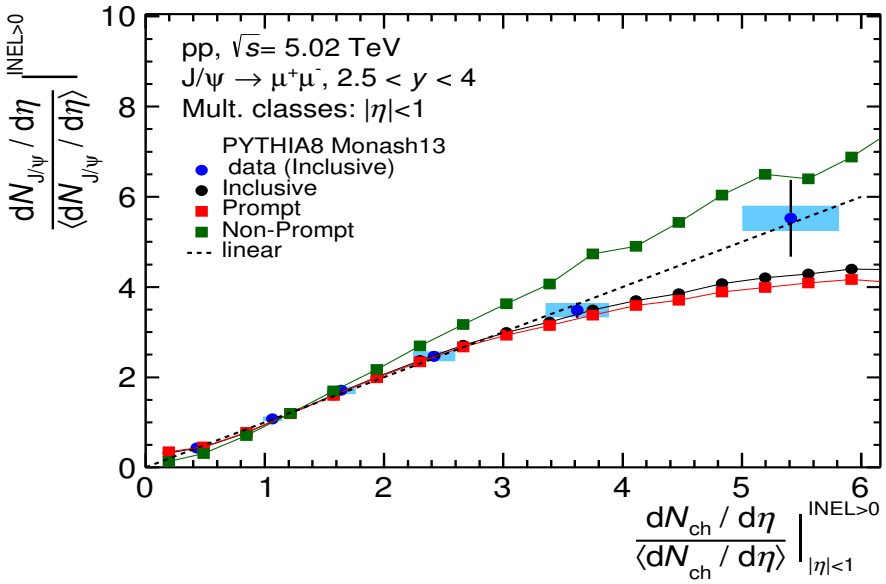

Figure 4-41: Comparison of data with PYTHIA8 prediction in pp collisions at $\sqrt{s}$ = 5.02 TeV

The contribution of prompt and non-prompt J/ψ yields as well as inclusive one are computed at 5.02 TeV in the same kinematic range [18]. It can be seen from Figure 4-41 that the inclusive and prompt J/ψ yields are similar and the same increasing trend is observed with deviation towards higher multiplicity. The non-prompt J/ψ yield

results over estimate the data and show faster increment. It can be seen from the figure that the J/ψ production from beauty feed-down increases faster than the prompt J/ψ yield. Since, all the J/ψ measurements were performed in the forward rapidity region, it can be assumed that the auto-correlation effect has very less contribution. The inclusive, prompt and non-prompt J/ψ yields are also computed as function of

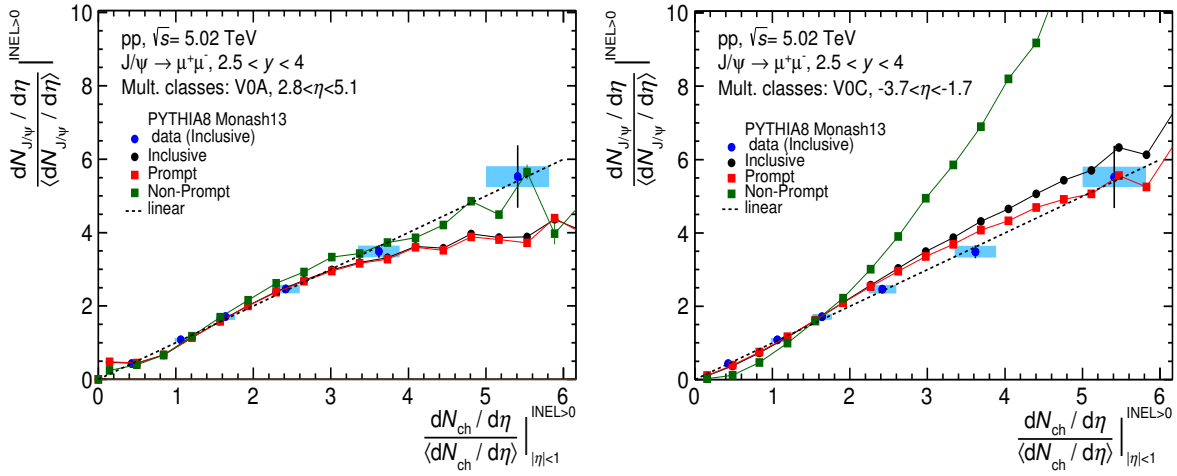

(a) V0A (b) V0C

Figure 4-42: (a) Comparison of data with J/ψ yield as a function of V0A multiplicity estimator in pp collisions at $\sqrt{s} = 5.02$ TeV. (b) A similar comparison with V0C multiplicity estimator.

V0A and V0C multiplicity estimator at two different rapidity regions. The V0A and V0C cover the rapidity ranges $2.8 < \eta < 5.1$ and $-3.7 < \eta < -1.7$ respectively. It can be observed from the Figure 4-42 that all the results with V0A estimator show increase of J/ψ similar to where multiplicity estimated from SPD. The J/ψ yield from non-prompt contribution as a function of V0C multiplicity shows faster than linear increment in pp collisions at $\sqrt{s} = 5.02$ TeV. The V0C and the Muon spectrometer covers almost similar rapidity region which may introduce the auto-correlation effect which results in enhancement of the J/ψ yield. The inclusive and prompt J/ψ yield also shows linear enhancement as a function of V0C multiplicity. On the other hand the J/ψ yield for three different cases shows similar increasing trend as function of V0A multiplicity.

It can be concluded from all the theoretical predictions and experimental obser-

vations that the J/ψ yield growing with multiplicity mostly depends on the rapidity range. The contribution from prompt and non-prompt J/ψ yield also plays an important role. The data is largely dominated with contribution from prompt J/ψ. The increasing trend of relative J/ψ yield with event activity does not depend on centre of mass energy or multiplicity estimator. All the models qualitatively describe the data irrespective of the different physics process involved.

Bibliography

[1] B. Abelev et al., ALICE Collaboration,"Inclusive J/ψ Production in pp Collisions at $\sqrt{s}$ = 2.76 TeV", Phys. Lett. B718 (2012) 295306..

[2] S. Acharya et al., ALICE Collaboration, "Energy Dependence of Forward-Rapidity J/ψ and ψ(2S) Production in pp Collisions at the LHC", Eur. Phys. J. C77 (2017) 392.

[3] M. Tanabashi et al., Particle Data Group Collaboration, "Review of Particle Physics", Phys. Rev. D98 (2018) 030001.

[4] S. Acharya et al., ALICE Collaboration,"Energy and Multiplicity Dependence Study of Charged-Particle Pseudorapidity-Density Distribution in pp Collisions at $\sqrt{s}$ = 5.02, 7 and 13 TeV", In preparation.

[5] J. Adam et al., ALICE Collaboration, "Charged-Particle Multiplicities in Proton-Proton Collisions at $\sqrt{s}$ = 0.9 to 8 TeV", Eur. Phys. J. C77 (2017) 33.

[6] B. Abelev et al., ALICE Collaboration, "J/ψ Production as a Function of Charged Particle Multiplicity in pp Collisions at $\sqrt{s}$ = 7 TeV", Phys. Lett. B712 (2012) 165.

[7] D. Thakur, ALICE Collaboration, "J/ψ Production as a Function of Charged-Particle Multiplicity with ALICE at the LHC" (2018), arXiv:1811.01535 [hep-ex].

[8] S. G. Weber, ALICE Collaboration,"Measurement of J/ψ Production as a Function of Event Multiplicity in pp Collisions at $\sqrt{s}$ =13 TeV with ALICE", Nucl. Phys. A967 (2017) 333.

[9] S. G. Weber et al., "Elucidating the Multiplicity Dependence of J/ψ Production in Proton-Proton Collisions with PYTHIA8", Eur. Phys. J. C79 (2019) 36.

[10] D. Adamová et al., ALICE Collaboration, "J/ψ Production as a Function of Charged-Particle Pseudorapidity Density in p-Pb Collisions at $\sqrt{s_{NN}}$ =5.02 TeV", Phys. Lett. B776 (2018) 91.

[11] E. G. Ferreiro et al., "High Multiplicity pp Events and J/ψ Production at LHC", Phys. Rev. C86 (2012) 034903.

[12] B. Z. Kopeliovich et al., "J/ψ in High-Multiplicity pp Collisions: Lessons from p-A", Phys. Rev. D88 (2013) 116002.

[13] B. Z.Kopeliovich et al., "Suppression Versus Enhancement of Heavy Quarkonia in pA Collisions", Phys. Rev. C95 (2017) 065203.

[14] K. Werner, Private Communication.

[15] H.J. Drescher et al., "Parton-Based Gribov-Regge Theory", Phys. Rept. 350 (2001) 93.

[16] Y. Q. Ma et al., "Event Engineering Studies for Heavy Flavor Production and hadronization in High Multiplicity Hadron-Hadron and Hadron-Nucleus Collisions", Phys. Rev. D98 (2018) 074025.

[17] M. Siddikov et al., "Multiplicity Distributions as Probes of Quarkonia Production Mechanisms", arXiv:1910.13579 [hep-ph].

[18] S. G. Weber, Private Communication.

Chapter 5

Mean transverse momentum of J/ψ as a function of multiplicity

In this chapter, the measurement of average transverse momentum of J/ψ, $\langle p_{\rm T}^{\rm J/\psi}\rangle$ as a function of charged-particle pseudo-rapidity density has been discussed. The first moment, $\langle p_{\rm T}\rangle$ of any particle, is an important observable which can provide information whether small systems like pp and p-Pb can exhibit collective behaviour like heavy-ion collisions. The $\langle p_{\rm T}^{\rm J/\psi}\rangle$ is estimated in pp collisions at $\sqrt{s}$ =5.02 TeV at forward-rapidity. The same data set has been analyzed as the one used for the J/ψ yield measurements. The events were selected for inelastic>0 class. All the events pass through the physics selection as well as multiplicity estimation criteria that were described in the previous chapters. The analysis procedure is described in references [1] and [2]. The procedure starts with signal extractions of $\langle p_{\rm T}^{\rm J/\psi}\rangle$ from raw dimuon-$p_{\rm T}$ invariant mass which is defined as follows:

$$\langle p_T^{\mu^+\mu^-}\rangle_i^{raw} = \frac{1}{n_i}\sum_{j=1}^{n_i} p_T^j \tag{5.1}$$

where n_i is number of dimuon pairs in i^{th} invariant mass bin and p_T^j is transverse momentum of j^{th} dimuon pair contributing to i^{th} bin. The $\langle p_{\rm T}^{\rm J/\psi}\rangle$ is extracted by

fitting Equation 5.1. The fit function is given below:

$$\begin{aligned}\langle p_T^{\mu^+\mu^-}\rangle(m_{\mu^+\mu^-}) &= \alpha^{J/\psi}(m_{\mu^+\mu^-}) \times \langle p_T^{J/\psi}\rangle \\ &+\alpha^{\psi(2S)}(m_{\mu^+\mu^-}) \times \langle p_T^{\psi(2S)}\rangle \\ +(1-\alpha^{J/\psi}(m_{\mu^+\mu^-}) &- \alpha^{\psi(2S)}(m_{\mu^+\mu^-})) \times \langle p_T^{bkg}\rangle\end{aligned} \tag{5.2}$$

$$\alpha^{J/\psi} = \mathrm{S_{J/\psi}}/(\mathrm{S_{J/\psi}} + \mathrm{S_{\psi(2S)}} + \mathrm{B}) \tag{5.3}$$

and

$$\alpha^{\psi(2S)} = \mathrm{S_{\psi(2S)}}/(\mathrm{S_{J/\psi}} + \mathrm{S_{\psi(2S)}} + \mathrm{B}) \tag{5.4}$$

where S and B represent signal and background for J/ψ and $\psi(2S)$, respectively. The signal and background parameters were fixed by fitting invariant mass of dimuon spectra. The α terms were fixed by these extracted parameters. The parameters related to $\langle p_{\mathrm{T}}\rangle$ were kept free.

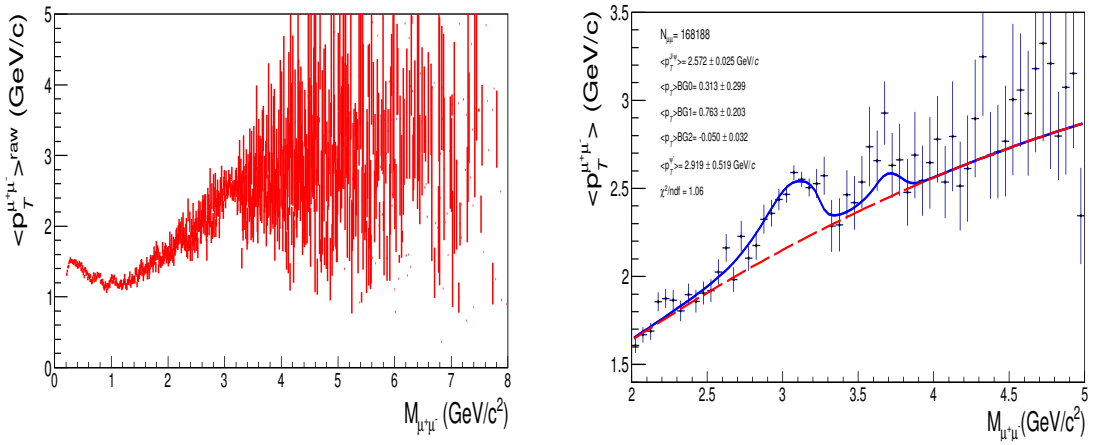

(a) (b)

Figure 5-1: (a) Raw $\langle p_{\mathrm{T}}^{\mathrm{J}/\psi}\rangle$ invariant mass of dimuon pairs in pp collisions at $\sqrt{s} = 5.02$ TeV. (b) Raw $\langle p_{\mathrm{T}}^{\mathrm{J}/\psi}\rangle$ signal at $\sqrt{s} = 5.02$ TeV.

An example of raw $\langle p_{\mathrm{T}}^{\mathrm{J}/\psi}\rangle$ signal extraction is shown in Figure 5-1 (b). The sig-

nal and backgrounds were fitted with combination of CB2 (Signal)+VWG (background)+polynomial2 (for $\langle p_{\rm T}^{{\rm J}/\psi}\rangle$ background). The $\langle p_{\rm T}^{{\rm J}/\psi}\rangle$ was corrected with Muon Spectrometer's acceptance and efficiency (A$\times\epsilon$) as transverse momentum strongly depends on A$\times\epsilon$ of the spectrometer. This can be achieved from realistic MC simulation of the dimuon triggered events. We use the MC data and input shape of $p_{\rm T}$ and y distributions that are used in reference [3] for the same data set. The J/ψ acceptance efficiency 2D-Map as function of $p_{\rm T}$ and y (A$\times\epsilon(p_{\rm T},y)$) were extracted from MC by taking the ratio of reconstructed to the generated $p_{\rm T}$ and y. The selected $p_{\rm T}$ limit of 12 GeV/c was to check consistency with the previous ALICE results. The acceptance efficiency was found to be 0.2443 $\pm$ 0.0003, consistent within uncertainty with the published results [3].

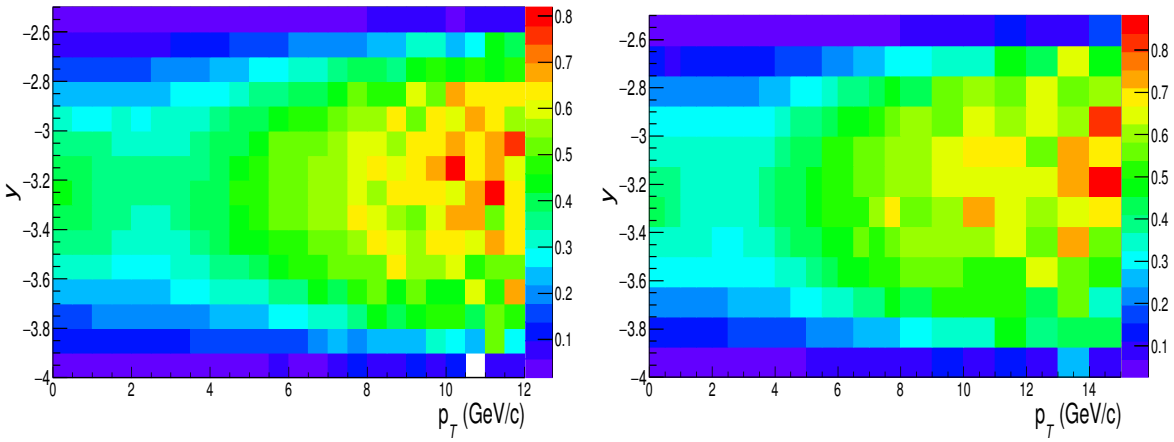

(a) (b)

Figure 5-2: J/ψ A$\times\epsilon$ 2D Map. (a) with $p_{\rm T}$ cut 12 GeV/c. (b) with p_T cut 15 GeV/c.

In the present analysis, the same event selection cuts have been used, which were used for J/ψ yield analysis. In addition, the upper $p_{\rm T}$ limit has been used to be consistent with data and MC. The dimuon invariant mass pairs were corrected by A$\times\epsilon(p_{\rm T},y)$ using the expression:

$$n_i^{corr} = \sum_{j=1}^{n_i} \frac{1}{A \times \epsilon(p_T^j, y^j)} \tag{5.5}$$

In the similar manner the mean-$p_{\rm T}$ invariant mass were corrected by the following

definition:

$$\langle p_T^{\mu^+\mu^-} \rangle_i^{A\times\epsilon corr.} = \frac{1}{n_i^{eff}} \sum_{j=1}^{n_i} \frac{p_T^j}{A \times \epsilon(p_T^j, y^j)} \tag{5.6}$$

The A×ϵ($p_{\rm T}$,y) corrected mean-$p_{\rm T}$ invariant mass was fitted with Equation 5.2. The $\langle p_{\rm T}^{\rm J/\psi} \rangle$ was extracted with $p_{\rm T}$ limit 12 GeV/c cut and 15 GeV/c cut. The deviation was negligible in these two cases. The example of corrected $\langle p_{\rm T}^{\rm J/\psi} \rangle$ extractions are shown in Figure 5-3.

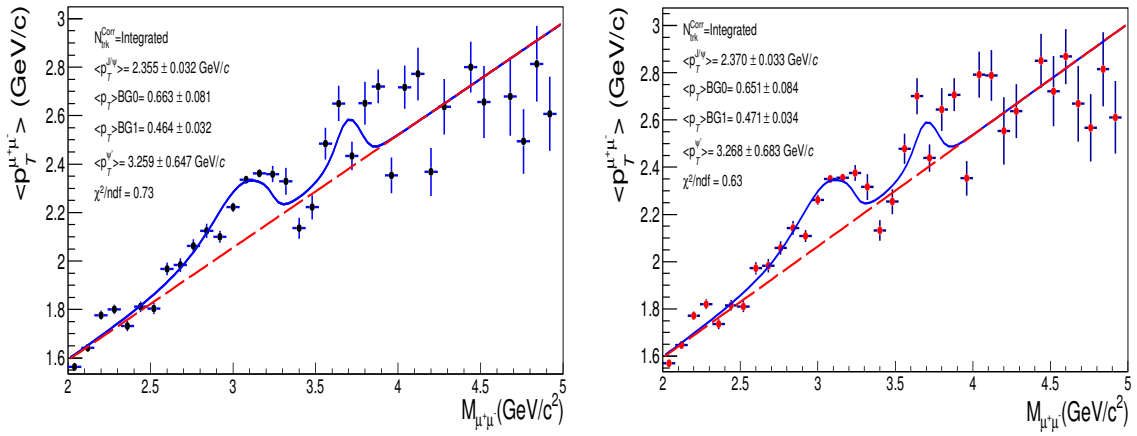

(a) (b)

Figure 5-3: A×ϵ corrected $\langle p_{\rm T}^{\rm J/\psi} \rangle$ signal (a) with $p_{\rm T}$ cut 12 GeV/c. (b) with p_T cut 15 GeV/c.

The corrected mean-$p_{\rm T}$ invariant mass has been divided into six multiplicity bins similar to that of J/ψ yield analysis. The invariant mass binning was chosen as 80 MeV/c^2 to control the small statistics in the multiplicity bins.

The example of $\langle p_{\rm T}^{\rm J/\psi} \rangle$ extraction in multiplicity bins are shown in Figure 5-4 and the corresponding A×ϵ corrected invariant mass fits are shown in the Appendix B.4. The fit in the last multiplicity bins (i.e. N_{trk}^{Corr} = 49-100) are not significant due to lack of statistics as seen in the Figures 5-5 (a) and 5-5 (b). More investigation on $\langle p_{\rm T}^{\rm J/\psi} \rangle$ extraction are done for the last multiplicity bin by fitting with various signal and background functions and from all the plots it can be concluded that background shapes of those fits are not reliable (Figure B-13). First order polynomial

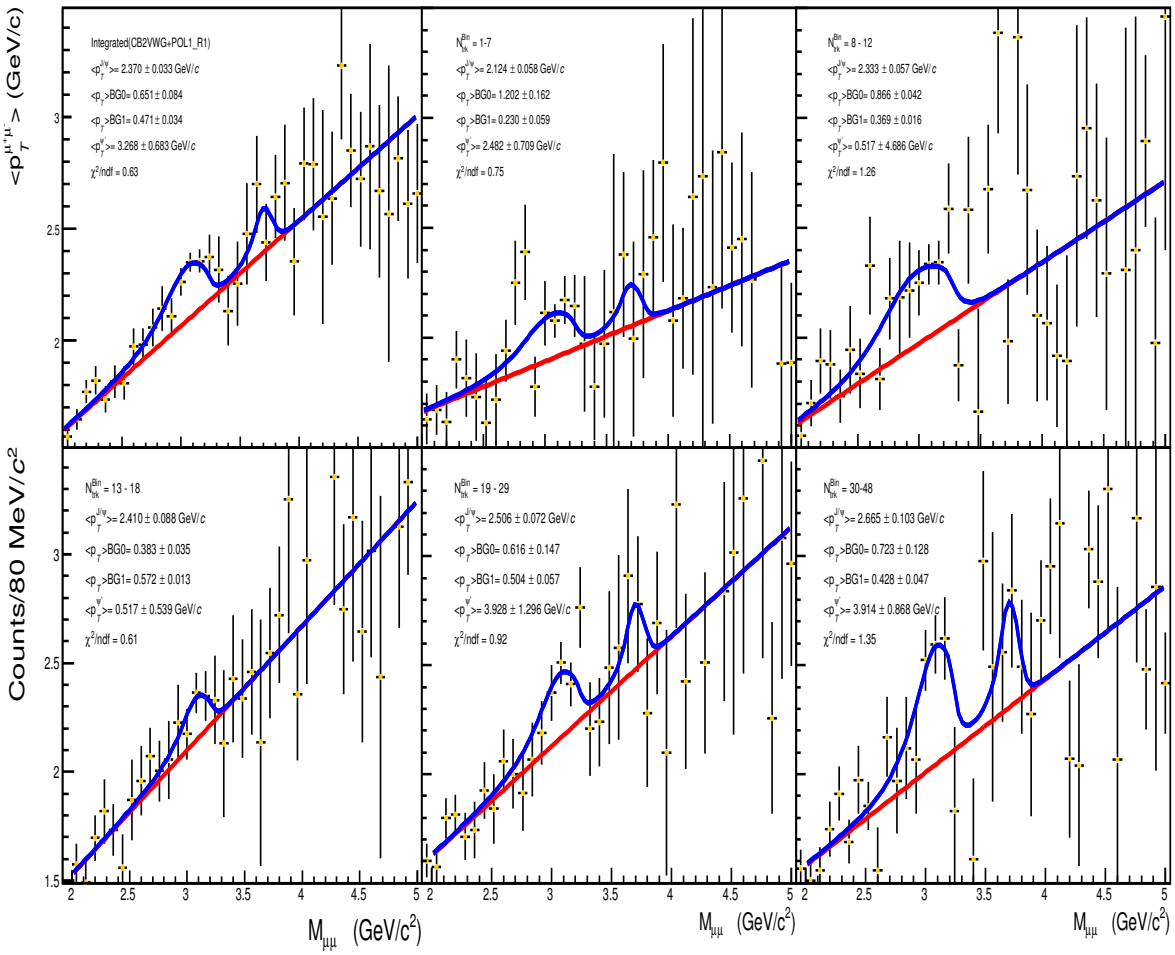

Figure 5-4: Corrected $\langle p_{\mathrm{T}}^{\mathrm{J}/\psi} \rangle$ in multiplicity bins.

and combination of exponential to second order polynomial functions give different background shapes (Figure B-14). Hence, the $\langle p_{\mathrm{T}}^{\mathrm{J}/\psi} \rangle$ for the N_{trk}^{Corr} = 49-100 bin was not to be included in the final results.

The $\langle p_{\mathrm{T}}^{\mathrm{J}/\psi} \rangle$ extraction has also been done for invariant mass binning count per 40 MeV/c^2 to check the consistency of the analysis (Figure B-15). It has been observed that the $\langle p_{\mathrm{T}}^{\mathrm{J}/\psi} \rangle$ value consistently increases as we go from low to high multiplicity bins. Different multiplicity binning were considered to see if the overall variation of dimuon-$\langle p_{\mathrm{T}} \rangle$ distribution depends on multiplicity ranges or the invariant mass ranges. The dimuon-$\langle p_{\mathrm{T}} \rangle$ distributions for different tracklets bin as compared to the present analysis are shown in Figure B-16.

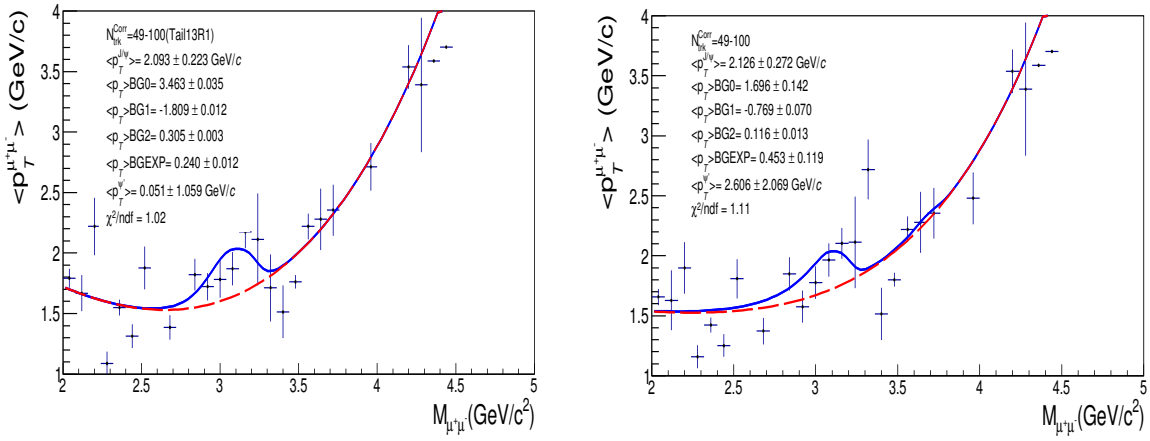

(a) (b)

Figure 5-5: $\langle p_{\mathrm{T}}^{\mathrm{J}/\psi} \rangle$ signal in multiplicity bin 49-100. (a) Fitted with tail parameter of $\sqrt{s}$ =13 TeV. (b) Fitted with tail parameter of 5.02 TeV.

5.1 Systematic uncertainty

In this section various sources of systematic uncertainty and their effect on $\langle p_{\mathrm{T}}^{\mathrm{J}/\psi} \rangle$ are discussed in detail. The systematic uncertainty for multiplicity differential $\langle p_{\mathrm{T}}^{\mathrm{J}/\psi} \rangle^i$ and integrated $\langle p_{\mathrm{T}}^{\mathrm{J}/\psi} \rangle$ has been estimated using the same method as has been used to extract the relative yield of J/ψ The absolute $\langle p_{\mathrm{T}}^{\mathrm{J}/\psi} \rangle$ and it's statistical and systematic uncertainties are computed using various signal and background functions. Apart from signal extractions other source of systematic uncertainties are acceptance efficiency, $\langle p_{\mathrm{T}}^{\mathrm{J}/\psi} \rangle$ variation with dimuon invariant mass and MC input mismatch. These have been studied in detail in following subsections. The systematic uncertainty due to trigger and event selection and pile-up contribution have already been studied for relative yield of J/ψ measurement.

5.1.1 $\langle p_{\mathrm{T}}^{\mathrm{J}/\psi} \rangle$ signal extraction systematic uncertainty

The $\langle p_{\mathrm{T}}^{\mathrm{J}/\psi} \rangle$ was extracted using the following fit combinations:

- CB2+VWG and NA60+VWG signal-background functions are taken to extract J/ψ from A×$\epsilon(p_{\mathrm{T}},y)$ corrected dimuon invariant mass.

- During invariant mass fit in the multiplicity bin the J/ψ peak and width are kept fixed to value of the one with the integrated multiplicity.
- First order polynomial, Second order polynomial and product of exponential times second order polynomial are taken as background to estimate $\langle p_{\rm T}^{\rm J/\psi} \rangle$.
- Two sets of tail parameters tuned in pp collisions at $\sqrt{s}$ = 5.02 TeV and at $\sqrt{s}$ = 13 TeV.
- MC tail from pp collisions at 5.02 TeV and data tail from pp collisions at $\sqrt{s}$ = 13 TeV are used (Appendix B.2).
- Two sets of invariant mass range 2.0-5.0 and 1.7-4.8 GeV/c^2.
- Same fit ranges were applied to extract $\langle p_{\rm T}^{\rm J/\psi} \rangle$.
- A weight factor is applied to compute the average $\langle p_{\rm T}^{\rm J/\psi} \rangle$ over all the tests for using the tail parameters of $\sqrt{s}$ = 13 TeV.

Total 18 combinations of tests were performed. The arithmetic mean of these tests was taken as average $\langle p_{\rm T}^{\rm J/\psi} \rangle$ and their root mean square (RMS) value was taken as systematic uncertainty. The average $\langle p_{\rm T}^{\rm J/\psi} \rangle$ and it's systematic uncertainty are shown in Figure 5-6 for the integrated multiplicity. The systematic uncertainty due to the extraction of $\langle p_{\rm T}^{\rm J/\psi} \rangle$ using various signal background functions, in different multiplicity bins are shown in Figures 5-7 to 5-11. It has been observed that weight factor corresponding to data tail parameter of $\sqrt{s}$ = 13 TeV has insignificant difference with respect to the one without the weight factor. The weighted values were taken as a final value for integrated as well as multiplicity differential $\langle p_{\rm T}^{\rm J/\psi} \rangle$.

The $\langle p_{\rm T}^{\rm J/\psi} \rangle$ for the present analysis has been measured as $2.368 \pm 0.033(stat.) \pm 0.009(syst.)$ GeV/c for integrated multiplicity and $p_{\rm T}$ and y. The integrated $\langle p_{\rm T}^{\rm J/\psi} \rangle$ result without weight factor for using tail parameter of $\sqrt{s}$ = 13 TeV has been found to be $2.367 \pm 0.033(stat.) \pm 0.008(syst.)$. The systematic uncertainty due to $\langle p_{\rm T}^{\rm J/\psi} \rangle^i$ extraction for the absolute measurement was found to be a minimum of 0.6% to a maximum of 0.97%.

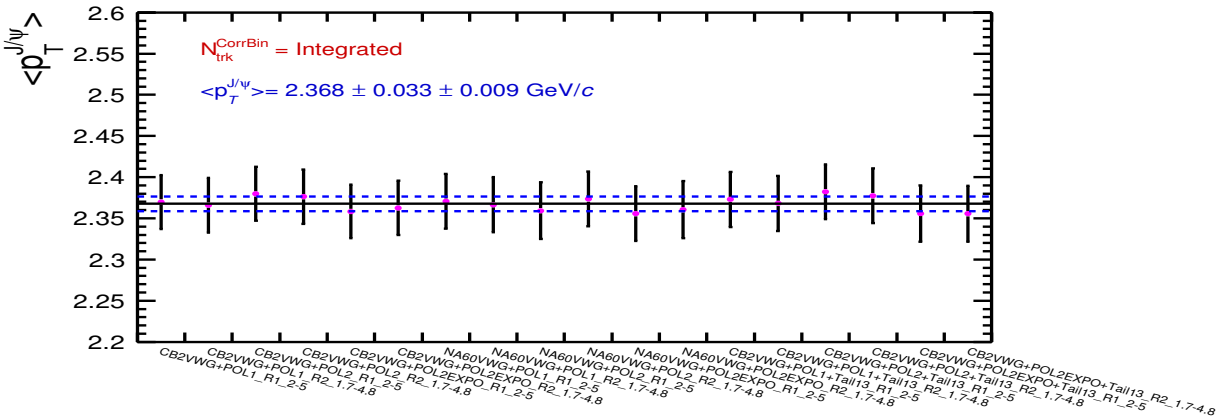

Figure 5-6: $\langle p_{\mathrm{T}}^{\mathrm{J}/\psi} \rangle$ systematic uncertainty integrated multiplicity.

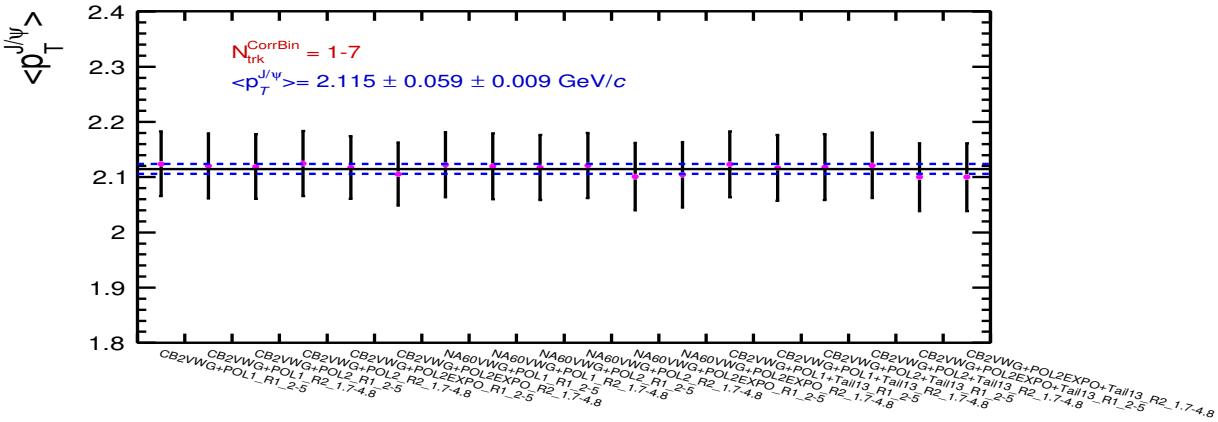

Figure 5-7: $\langle p_{\mathrm{T}}^{\mathrm{J}/\psi} \rangle$ systematic uncertainty for multiplicity bin 1-7.

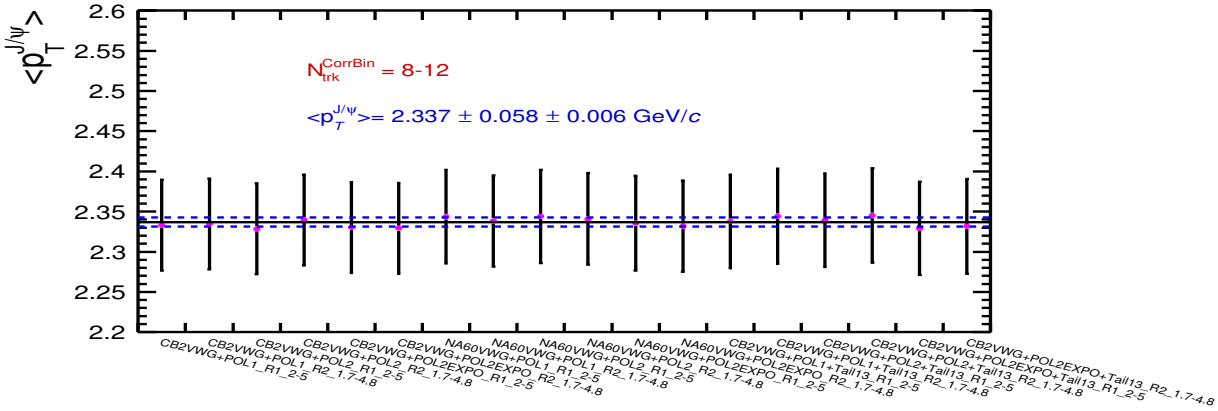

Figure 5-8: $\langle p_{\mathrm{T}}^{\mathrm{J}/\psi} \rangle$ systematic uncertainty for multiplicity bin 8-12.

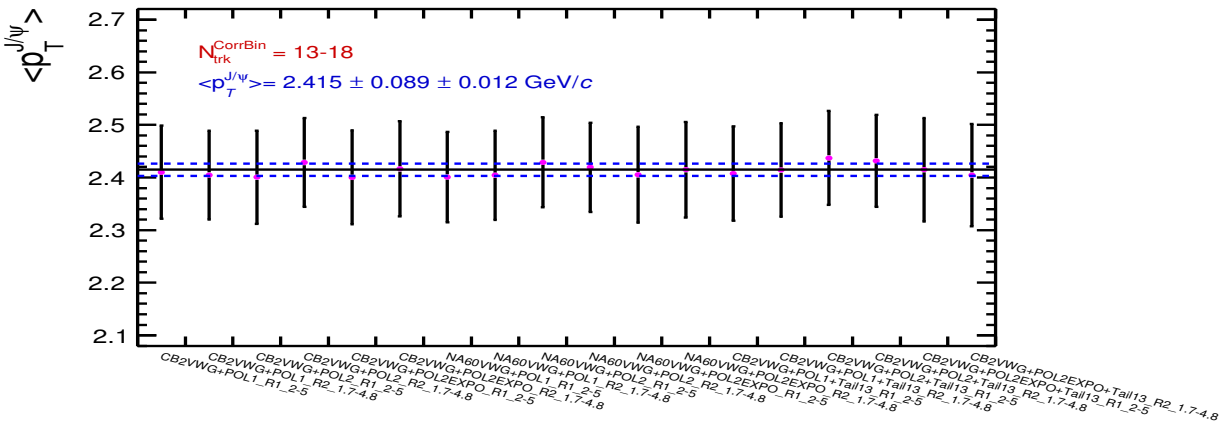

Figure 5-9: $\langle p_{\mathrm{T}}^{\mathrm{J}/\psi} \rangle$ systematic uncertainty for multiplicity bin 13-18.

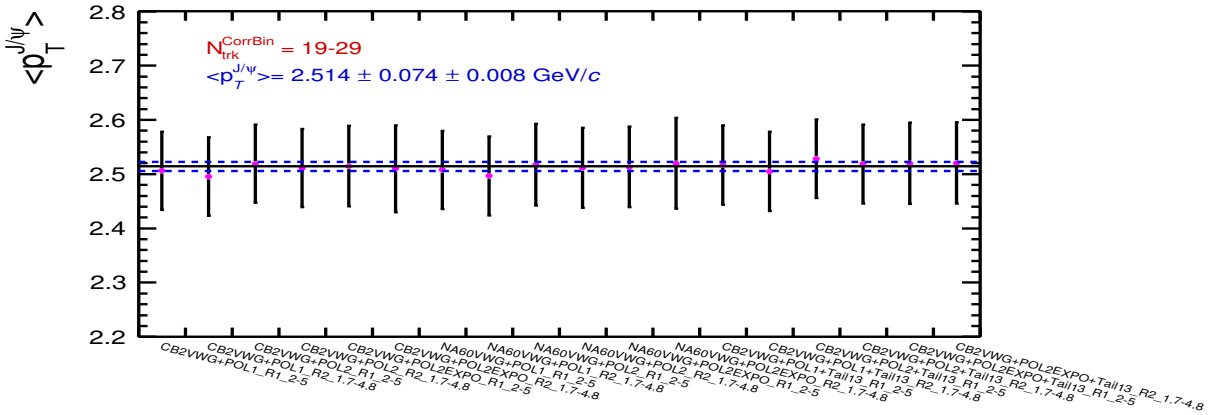

Figure 5-10: $\langle p_{\mathrm{T}}^{\mathrm{J}/\psi} \rangle$ systematic uncertainty for multiplicity bin 19-29.

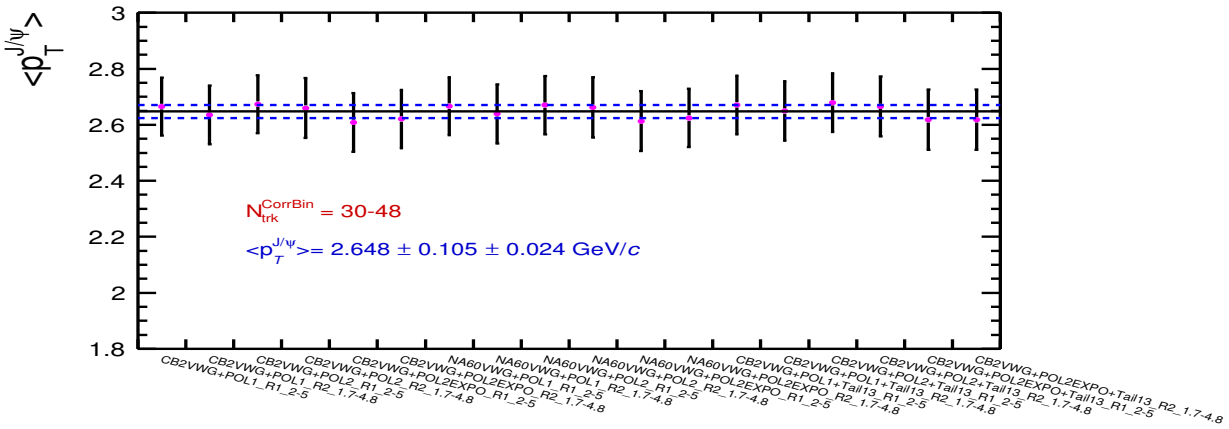

Figure 5-11: $\langle p_{\mathrm{T}}^{\mathrm{J}/\psi} \rangle$ systematic uncertainty for multiplicity bin 30-48.

5.1.2 Relative $\langle p_{\rm T}^{\rm J/\psi} \rangle$ signal extraction systematic uncertainty

The estimation of the relative $\langle p_{\rm T}^{\rm J/\psi} \rangle$ has been carried out using two approaches similar to the relative J/ψ yield analysis. In first method, the relative $\langle p_{\rm T}^{\rm J/\psi} \rangle^i$ were computed by taking the ratio of absolute $\langle p_{\rm T}^{\rm J/\psi} \rangle^i$ to the integrated $\langle p_{\rm T}^{\rm J/\psi} \rangle$ values. Here statistical and systematic uncertainties of relative $\langle p_{\rm T}^{\rm J/\psi} \rangle$ ($\langle p_{\rm T}^{\rm J/\psi} \rangle^R$) were computed by taking the quadrature sum of the respective errors.

Alternatively, to take into account the correlation between integrated and differential values of $\langle p_{\rm T}^{\rm J/\psi} \rangle$ while computing the average $\langle p_{\rm T}^{\rm J/\psi} \rangle^i / \langle p_{\rm T}^{\rm J/\psi} \rangle$, the background, dimuon mass combinations, tail parameters and invariant mass ranges were varied. In this method the signal function of integrated and differential $\langle p_{\rm T}^{\rm J/\psi} \rangle$ are taken as constant with multiplicity. Total 108 combination of tests are performed. The average $\langle p_{\rm T}^{\rm J/\psi} \rangle^i$ were computed in multiplicity bins using the equation:

$$\langle p_T^{J/\psi} \rangle_i^R = \left\langle \frac{\langle p_T^{J/\psi} \rangle^i}{\langle p_T^{J/\psi} \rangle^{int.}} \right\rangle = \frac{1}{n_{tests}} \sum_{j=1}^{n_{tests}} \left(\frac{\langle p_T^{J/\psi} \rangle^i}{\langle p_T^{J/\psi} \rangle^{int.}} \right)_j \tag{5.7}$$

where i represents the differential $\langle p_{\rm T}^{\rm J/\psi} \rangle$ and j index represents the possible combinations of the test. The arithmetic mean and square root of variance are taken as statistical and systematic uncertainties. The plots for these tests are shown in Figure 5-12 for the first multiplicity bin. Rest of the plots are listed in Figure B-17 - B-21. The result of systematic uncertainty due to relative $\langle p_{\rm T}^{\rm J/\psi} \rangle$ extraction is shown in Figure 5-13 and is found to be within 1% for all the multiplicity bins except the last one (which is not included in the final results). The systematic uncertainty varies between 0.56% to 0.967%.

The $\langle p_{\rm T}^{\rm J/\psi} \rangle$ and $\langle p_{\rm T}^{\rm J/\psi} \rangle^R$ values along with their respective uncertainties are listed in Table 5.1. The $\langle p_{\rm T}^{\rm J/\psi} \rangle^R$ measurement using the two methods, that are discussed above, gives consistent results with negligible variation in the statistical and the systematic uncertainties.

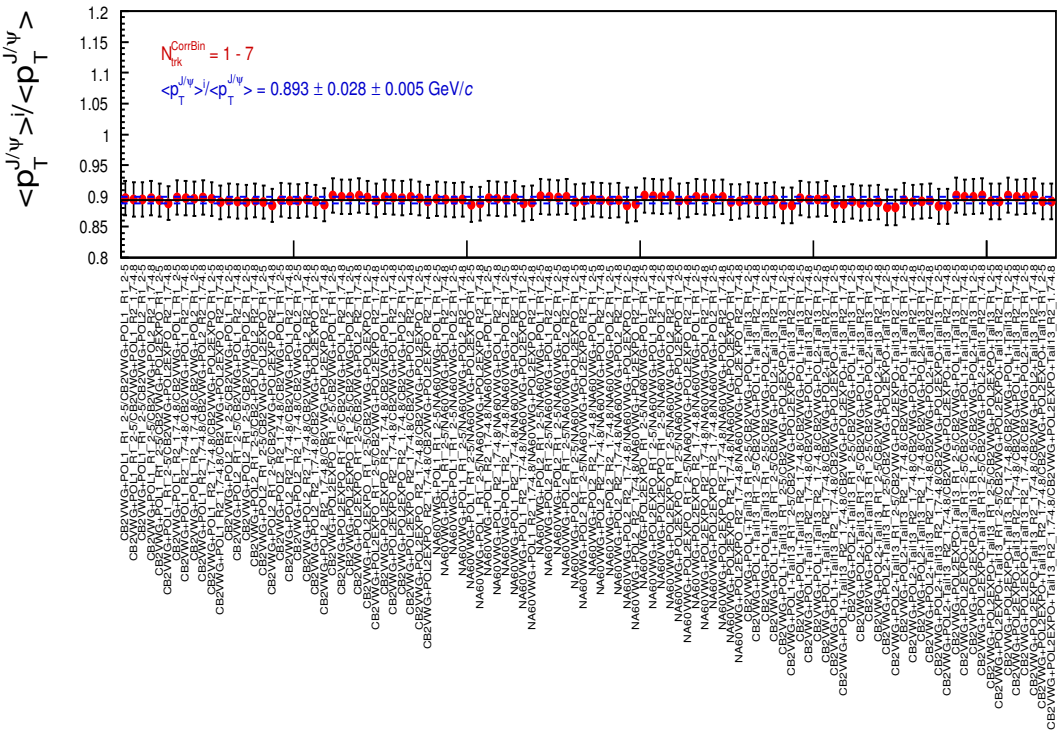

Figure 5-12: Relative $\langle p_{\mathrm{T}}^{\mathrm{J}/\psi} \rangle$ systematic uncertainty for multiplicity bin 1-7

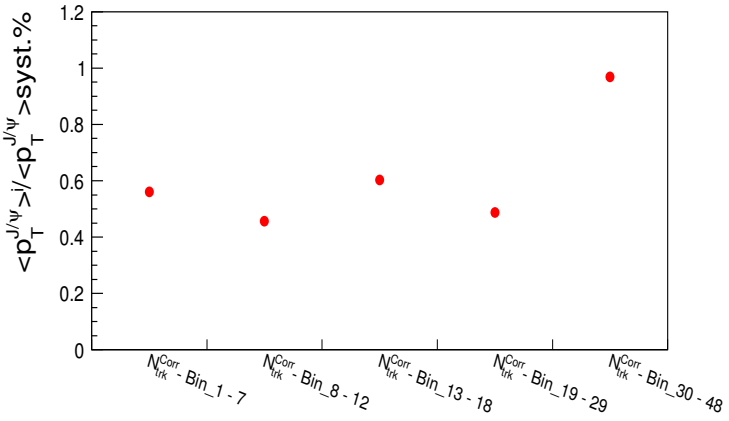

Figure 5-13: Results of relative $\langle p_{\mathrm{T}}^{\mathrm{J}/\psi} \rangle$ systematic uncertainty due to signal extraction.

5.1.3 Systematic uncertainty due to acceptance efficiency

The systematic uncertainty was computed for different input shapes to the MC simulation [4]. The study involve the following steps. First, the data was divided in low (N_{trk}^{Corr} <20) and high (N_{trk}^{Corr} >20) multiplicity sample. The J/ψ were extracted in

$N_{trk}^{corr} bin$	$\langle p_{\rm T}^{\rm J/\psi} \rangle$	$< p_T^{J/\psi} >^R$
$1-7$	$2.115 \pm 0.059 \pm 0.009$	$0.893 \pm 0.028 \pm 0.005$
$8-12$	$2.337 \pm 0.058 \pm 0.006$	$0.987 \pm 0.028 \pm 0.005$
$13-18$	$2.415 \pm 0.089 \pm 0.012$	$1.019 \pm 0.040 \pm 0.006$
$19-29$	$2.514 \pm 0.074 \pm 0.008$	$1.062 \pm 0.035 \pm 0.005$
$30-48$	$2.648 \pm 0.105 \pm 0.024$	$1.118 \pm 0.047 \pm 0.011$
$49-100$	$2.028 \pm 0.262 \pm 0.084$	$0.857 \pm 0.11 \pm 0.035$

Table 5.1: The $\langle p_{\rm T}^{\rm J/\psi} \rangle$ and $\langle p_{\rm T}^{\rm J/\psi} \rangle^R$ values with corresponding statistical and systematic uncertainties. Here systematic uncertainties are shown only due to signal extractions.

each $p_{\rm T}$ and y bins for 3 sets of data samples, as shown in Figure 5-14. These low and high multiplicity data sets were fitted using the functions given by Equations 5.8 and 5.9. The same procedure was repeated for the integrated multiplicity sample. The initial input parameters for $p_{\rm T}$ and y functions were taken from reference [3].

$$f(p_T) = p_0 \times \frac{p_T}{(p_1 + p_T^{p_2})^{p_3}} \tag{5.8}$$

$$f(y) = p_0 \times (1 + p_1 \times y^2) \tag{5.9}$$

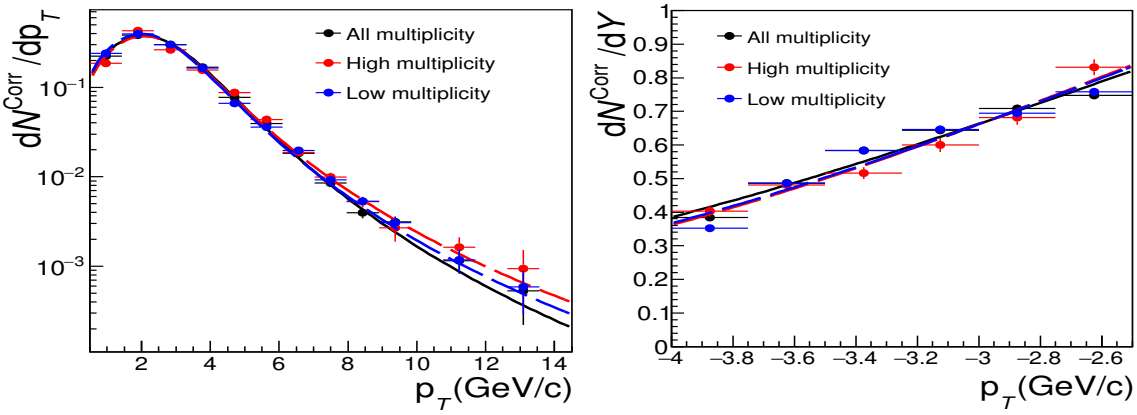

Figure 5-14: The J/ψ are plotted as a function of $p_{\rm T}$ and y for integrated, high and low multiplicity data samples.

A weight factor was estimated by normalizing the evaluated value of low and high multiplicity data samples with the integrated one. The four sets of A$\times\epsilon(p_{\rm T},y)$ 2D maps were created with these weight factors. The $\langle p_{\rm T} \rangle$ dimuon invariant mass dis-

tributions were corrected using newly created A×ϵ ($p_{\rm T}$,y) maps. The $\langle p_{\rm T}^{\rm J/\psi}\rangle$ were extracted in each case for integral and differential multiplicity. The ratio of these extracted $\langle p_{\rm T}^{\rm J/\psi}\rangle$ per multiplicity bin to the defaults results (computed using Equation 5.6) as a function of the multiplicity is shown in Figure 5-15. The relative error from the default $\langle p_{\rm T}^{\rm J/\psi}\rangle$ is taken as systematic uncertainty using the following equation:

$$\Delta R\langle p_T^{J/\psi}\rangle = \frac{\langle p_T^{J/\psi}\rangle^{default} - \langle p_T^{J/\psi}\rangle}{\langle p_T^{J/\psi}\rangle^{default}} \tag{5.10}$$

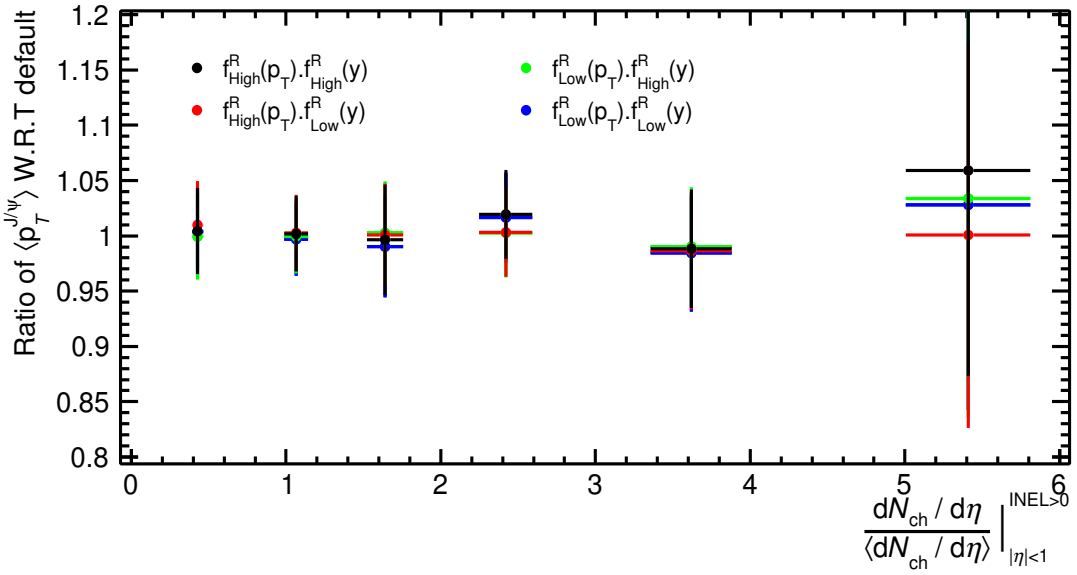

Figure 5-15: Ratio of $\langle p_{\rm T}^{\rm J/\psi}\rangle$ for each set of A×ϵ with respect to the default one as a function of relative charged-particle density.

where the systematic uncertainty is assumed to follow the Gaussian distribution and has been calculated as $\sigma = \Delta R/\sqrt{12}$. The per bin systematic uncertainty has been computed and it is found to vary from a minimum of 0.1% for the lowest multiplicity bin to a maximum of 2.1% corresponding to the multiplicity bin 49-100. The systematic uncertainty due to acceptance efficiency for integrated $\langle p_{\rm T}^{\rm J/\psi}\rangle$ is 0.33%. The total systematic uncertainty due to acceptance efficiency is taken as quadratic sum over all the multiplicity bins and is evaluated as ∼1%.

5.1.4 Systematic uncertainty due to $\langle p_{\mathrm{T}}^{\mathrm{J}/\psi} \rangle$ variation with invariant mass

The $\langle p_{\mathrm{T}}^{\mathrm{J}/\psi} \rangle$ signal extraction was done by considering $\langle p_{\mathrm{T}}^{\mathrm{J}/\psi} \rangle$ as a constant parameter and independent of invariant mass of J/ψ. This assumption may not be correct due the fact that the invariant mass of dimuon resolution depends on accurate estimation of the muon momentum and angle between the two muons. The mass resolution can be affected by several factors e.g. the event vertex determination, scatterings and energy-loss fluctuations in the muon absorber, and the precision of the tracking chambers etc. These effects may cause $\langle p_{\mathrm{T}}^{\mathrm{J}/\psi} \rangle$ variation as the function of dimuon invariant mass. The pure $\langle p_{\mathrm{T}}^{\mathrm{J}/\psi} \rangle$ signals from MC were studied to take into account these effects. The same reconstructed MC data was utilized, the one has been used for the $A \times \epsilon$ computation. The reconstructed dimuon-$\langle p_{\mathrm{T}} \rangle$ distributions are observed to have different shapes than that from the $A \times \epsilon$ corrected data as seen in Figure 5-16. In order to quantify this variation, the dimuon-$\langle p_{\mathrm{T}} \rangle$ distributions from MC was fitted with a polynomial 'piece-wise' function. The polynomial 'piece-wise' function has been defined as follows:

$$h(m_{\mu^+\mu^-}) = a_0 + \sum_{i=1}^{5} a_i (m_{\mu^+\mu^-} - m_{J/\psi}) \tag{5.11}$$

where,

$$\langle p_T^{J/\psi} \rangle (m_{\mu^+\mu^-}) = \begin{cases} h(2.79) + a_6(m_{\mu^+\mu^-} - 2.79) & m_{\mu^+\mu^-} \leq 2.79\ GeV/c^2 \\ h(m_{\mu^+\mu^-}) & 2.79\ GeV/c^2 < m_{\mu^+\mu^-} < 3.29\ GeV/c^2 \\ h(3.29) + a_7(m_{\mu^+\mu^-} - 3.29) & m_{\mu^+\mu^-} \geq 3.19\ GeV/c^2 \end{cases} \tag{5.12}$$

The Equation 5.12 gives $a_0 =< p_T^{J/\psi} >$, since the fitting function was evaluated at $m_{\mu^+\mu^-} - m_{J/\psi}$. The $\langle p_{\mathrm{T}}^{\mathrm{J}/\psi} \rangle$ extraction was done by fitting in the invariant mass range 2.75 to 3.7 GeV/c^2 and is found to be 2.368$\pm$0.005 GeV/c. The extraction of $\langle p_{\mathrm{T}}^{\mathrm{J}/\psi} \rangle$ from signal using 'piece-wise' function is shown in Figure 5-16.

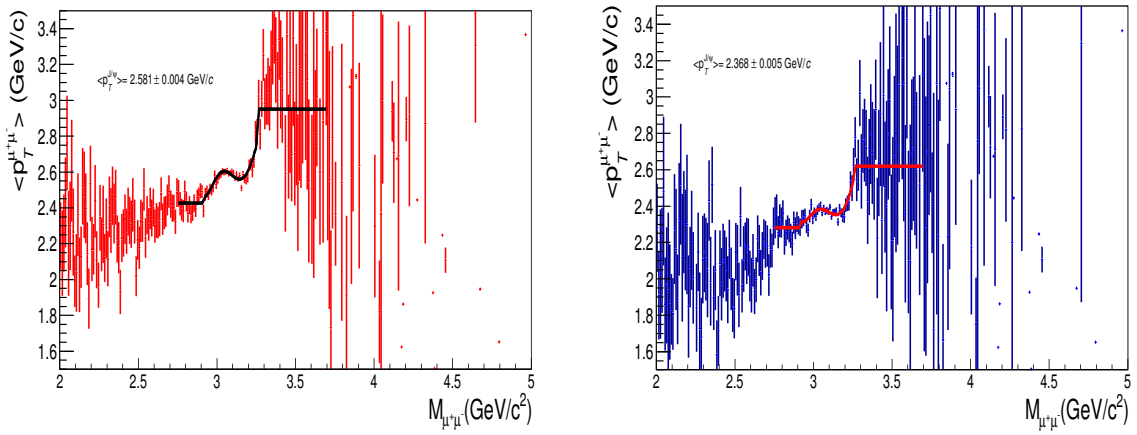

(a) (b)

Figure 5-16: (a) Pure $\langle p_{\mathrm{T}}^{\mathrm{J}/\psi} \rangle$ signal from MC. (b) A$\times\epsilon$ corrected pure $\langle p_{\mathrm{T}}^{\mathrm{J}/\psi} \rangle$ signal. Both spectra are fitted with the polynomial 'piece-wise' function.

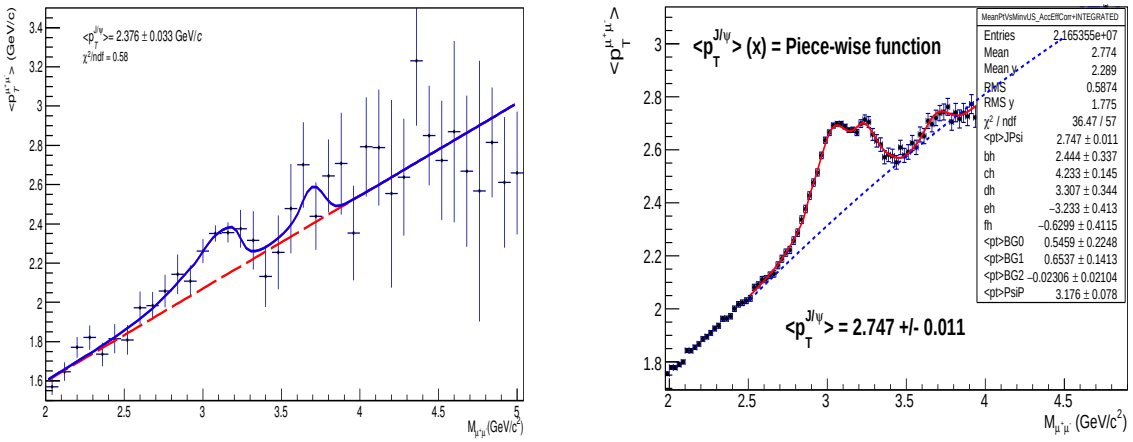

(a) (b)

Figure 5-17: The $\langle p_{\mathrm{T}}^{\mathrm{J}/\psi} \rangle$ signal from data fitted with the polynomial 'piece-wise' function with a linear background at (a) $\sqrt{s}$ =5.02 TeV and (b) $\sqrt{s}$ = 13 TeV

To test the variation of $\langle p_{\mathrm{T}}^{\mathrm{J}/\psi} \rangle$ as function of invariant mass, the data sample was fitted with the 'piece-wise' function along with a first order polynomial function which was used as the background function. The $\langle p_{\mathrm{T}}^{\mathrm{J}/\psi} \rangle$ parameter in Equation 5.2 was replaced by the 'piece-wise' function to consider $\langle p_{\mathrm{T}}^{\mathrm{J}/\psi} \rangle$ as a variable while fitting the data. The $\langle p_{\mathrm{T}}^{\mathrm{J}/\psi} \rangle$ value in this case is found to be 2.376±0.033 GeV/c and the corresponding fit is shown in Figure 5-17(a). This extracted $\langle p_{\mathrm{T}}^{\mathrm{J}/\psi} \rangle$ value is within statistical uncertainty

with the $\langle p_{\rm T}^{\rm J/\psi}\rangle$ while it is considered as constant parameter in MC calculation. It may be noted that a similar second peak on the right side tail (Figure 5-17(b)) has also been reported in references [1] and [5]. The double peak was not observed in pp collisions at 5.02 TeV unlike in pp collisions at $\sqrt{s}$ = 13 TeV. Thus, the mass variation effect on $\langle p_{\rm T}^{\rm J/\psi}\rangle$ can not be confirmed in the present analysis. The $\langle p_{\rm T}^{\rm J/\psi}\rangle$ values considering as constant parameter were extracted within one sigma confidence interval. The systematic uncertainty due to $\langle p_{\rm T}^{\rm J/\psi}\rangle$ mass variation was estimated as 0.4%. The mass variation effect is negligible in differential case which has been reported in reference [5]. Hence, in the present analysis the mass variation study is not done for the differential $\langle p_{\rm T}^{\rm J/\psi}\rangle$.

5.1.5 Difference from MC input

We can estimate the $\langle p_{\rm T}^{\rm J/\psi}\rangle$ value from the input $p_{\rm T}$ shape function 5.8 using the definition:

$$\langle p_T\rangle = \frac{\int p_T f(p_T)}{\int f p_T} \tag{5.13}$$

The value is found to be 2.353. This value is different from $\langle p_{\rm T}^{\rm J/\psi}\rangle$ extracted from the MC simulation of pure signal. Hence, the difference from MC input is assigned as systematic uncertainty which is 1.5%.

5.1.6 The $\langle p_{\rm T}^{\rm J/\psi}\rangle$ systematic uncertainty summary

The values of multiplicity integrated $\langle p_{\rm T}^{\rm J/\psi}\rangle$ are listed for the four cases in Table 5.2. The $\langle p_{\rm T}^{\rm J/\psi}\rangle$ as a constant parameter has been assumed to be the default value. A systematic uncertainty of 0.75%, due to difference with MC input (Table 5.2) and mass variation was added to the differential $\langle p_{\rm T}^{\rm J/\psi}\rangle$ in the multiplicity bins along with systematic uncertainty due to signal extraction and acceptance efficiency. The global uncertainty was computed by taking the statistical error of the multiplicity integrated $\langle p_{\rm T}^{\rm J/\psi}\rangle$ value as 0.033 and MC input mismatch value as 0.015, which were added in quadrature. The absolute global uncertainty has been estimated to be 3.62% and

relative global uncertainty is 1.52% for this analysis. The systematic uncertainties with their respective sources are listed in Table 5.3.

	$\langle p_T^{J/\psi} \rangle$ Integrated
$\langle p_{\mathrm{T}}^{\mathrm{J}/\psi} \rangle$ as constant parameter	2.368 ± 0.033
$\langle p_{\mathrm{T}}^{\mathrm{J}/\psi} \rangle$ with 'piece-wise' fit MC	2.368 ± 0.005
$\langle p_{\mathrm{T}}^{\mathrm{J}/\psi} \rangle$ with 'piece-wise' fit data	2.376 ± 0.033
$\langle p_{\mathrm{T}}^{\mathrm{J}/\psi} \rangle$ MC input	2.353

Table 5.2: The values of multiplicity integrated $\langle p_{\mathrm{T}}^{\mathrm{J}/\psi} \rangle$ calculated with different approaches.

Source	Systematic Uncertainty
Signal extraction	$0.56\% - 0.97\%$
$A \times \epsilon$	$\sim 1\%$
$\langle p_{\mathrm{T}}^{\mathrm{J}/\psi} \rangle$ variation with mass	0.4%
MC input mismatch	1.5%
Tracking efficiency*	1.%
Triggering efficiency*	1.8%
Matching efficiency*	1%

Table 5.3: The systematic uncertainties of $\langle p_{\mathrm{T}}^{\mathrm{J}/\psi} \rangle$ due to different sources.*Systematic uncertainties are taken from [3].

It can be seen from Table 5.3 that difference in the MC input to the data has large contribution in the systematic uncertainty along with the muon trigger efficiency. The muon trigger, tracking and matching of trigger with muon track efficiency has not been estimated in this analysis. These values are taken from independent analysis [3].

5.2 Results and discussions

The final results of multiplicity integrated and differential $\langle p_{\mathrm{T}}^{\mathrm{J}/\psi} \rangle$ with statistical and systematic uncertainties are listed in Table 5.4. These values have been plotted in Figure 5-18 (a). The data has been fitted with a function of the form $y = a-(b/c+x)$ in order to understand the pattern of the correlation between the traverse momentum of J/ψ and the multiplicity. The $\langle p_{\mathrm{T}}^{\mathrm{J}/\psi} \rangle$ increases towards low multiplicity and shows saturating trend towards high multiplicity bins.

$N_{trk}^{corr} bin$	$\langle p_{\mathrm{T}}^{\mathrm{J}/\psi} \rangle$	$< p_T^{J/\psi} >^R$
$1-7$	$2.115 \pm 0.059 \pm 0.018$	$0.893 \pm 0.025 \pm 0.008$
$8-12$	$2.337 \pm 0.058 \pm 0.019$	$0.987 \pm 0.024 \pm 0.009$
$13-18$	$2.415 \pm 0.089 \pm 0.022$	$1.019 \pm 0.038 \pm 0.010$
$19-29$	$2.514 \pm 0.074 \pm 0.022$	$1.062 \pm 0.031 \pm 0.010$
$30-48$	$2.648 \pm 0.105 \pm 0.032$	$1.118 \pm 0.044 \pm 0.014$
$\langle p_{\mathrm{T}}^{\mathrm{J}/\psi} \rangle$ Integrated $= 2.368 \pm 0.033 \pm 0.018$		

Table 5.4: The values of $\langle p_{\mathrm{T}}^{\mathrm{J}/\psi} \rangle$ and $\langle p_{\mathrm{T}}^{\mathrm{J}/\psi} \rangle^R$ with corresponding values of statistical and systematic uncertainties.

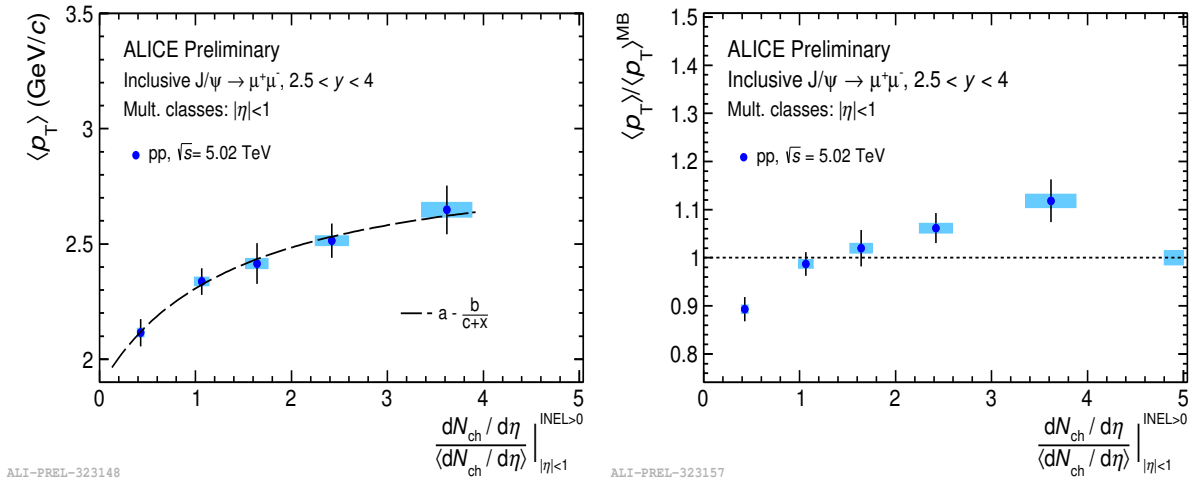

(a) (b)

Figure 5-18: The $\langle p_{\mathrm{T}}^{\mathrm{J}/\psi} \rangle$ (a) and relative $\langle p_{\mathrm{T}}^{\mathrm{J}/\psi} \rangle$ (b) as function of multiplicity in pp collisions at $\sqrt{s}$ =5.02 TeV.

The relative $\langle p_{\mathrm{T}}^{\mathrm{J}/\psi} \rangle$ values have been depicted as a function of charged-particle pseudo-rapidity density on Figure 5-18 (b). It also shows the similar trend as that exhibited by $\langle p_{\mathrm{T}}^{\mathrm{J}/\psi} \rangle$. The 1.52% global uncertainty on relative $\langle p_{\mathrm{T}}^{\mathrm{J}/\psi} \rangle$ has been shown around unity. The results of the last multiplicity bin have not been shown here following the discussion in previous section. It can be seen from the figure that the power-law function perfectly describes the trend of the $\langle p_{\mathrm{T}}^{\mathrm{J}/\psi} \rangle$ as a function of multiplicity. Although the constants a, b and c provide no meaningful information, but a different form of the power-law function (e.g. $Cm_{(T)}^{-P}$) might provide useful information about the system like energy, temperature, etc [6]. The scaling with this power-law behaviour will also be helpful to provide statistical description of

the experimental results. In this connection the evolution of $\langle p_{\mathrm{T}}^{\mathrm{J}/\psi} \rangle$ as function of underlying events might shed some light regarding the system produced in the collision irrespective of their initial condition.

5.2.1 Comparison with other analyses

These results have been compared to the similar analysis in pp collisions at $\sqrt{s} = 13$ TeV at forward rapidity [5]. It can be seen from Figure 5-19 (a) that both results show the identical behaviour at forward rapidity. The results are fitted with same function, $y = a - (\frac{b}{c+x})$ and shows increasing trend at low charged-particle density < 2, then a saturation trend follows towards higher multiplicity. The relative $\langle p_{\mathrm{T}}^{\mathrm{J}/\psi} \rangle$ as function of charged-particle multiplicity at forward rapidity for both the collision energies is shown in Figure 5-19 (b). The results at the two CM energies are consistent within the statistical uncertainties. The global uncertainties for relative $\langle p_{\mathrm{T}}^{\mathrm{J}/\psi} \rangle$ are 1.5% and 0.9%, respectively. Thus, the scaling of relative $\langle p_{\mathrm{T}}^{\mathrm{J}/\psi} \rangle$ with multiplicity has been observed as a function of $\sqrt{s}$.

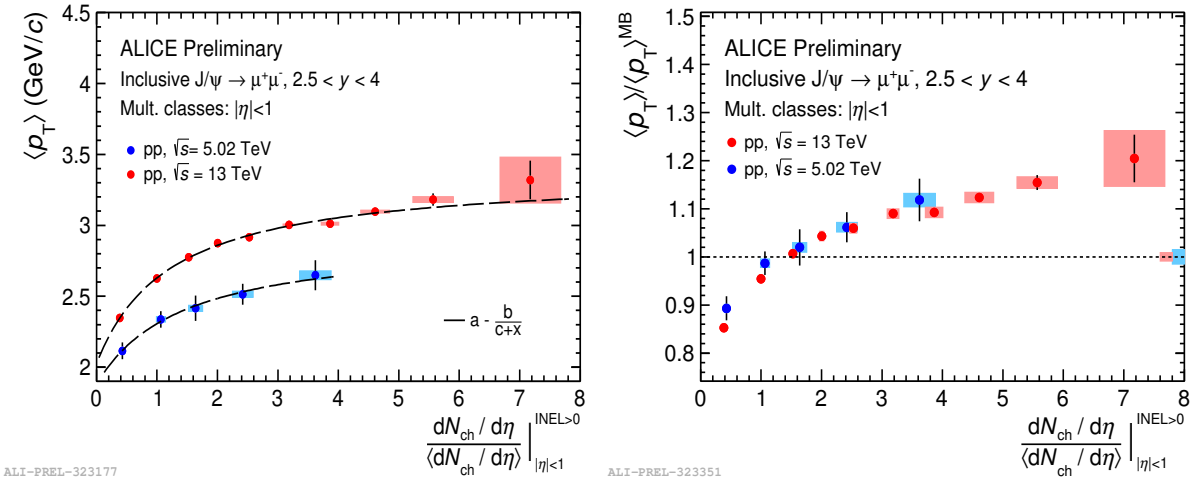

(a) (b)

Figure 5-19: The comparison of $\langle p_{\mathrm{T}}^{\mathrm{J}/\psi} \rangle$ (a) and relative $\langle p_{\mathrm{T}}^{\mathrm{J}/\psi} \rangle$ (b) as function of multiplicity in pp collisions at $\sqrt{s} = 5.02$ and 13 TeV at forward rapidity.

The multiplicity dependence of the relative $\langle p_{\mathrm{T}}^{\mathrm{J}/\psi} \rangle$ has been compared with the results from p-Pb collisions at identical energy $\sqrt{s_{\mathrm{NN}}} = 5.02$ TeV. Figure 5-20 (a) shows

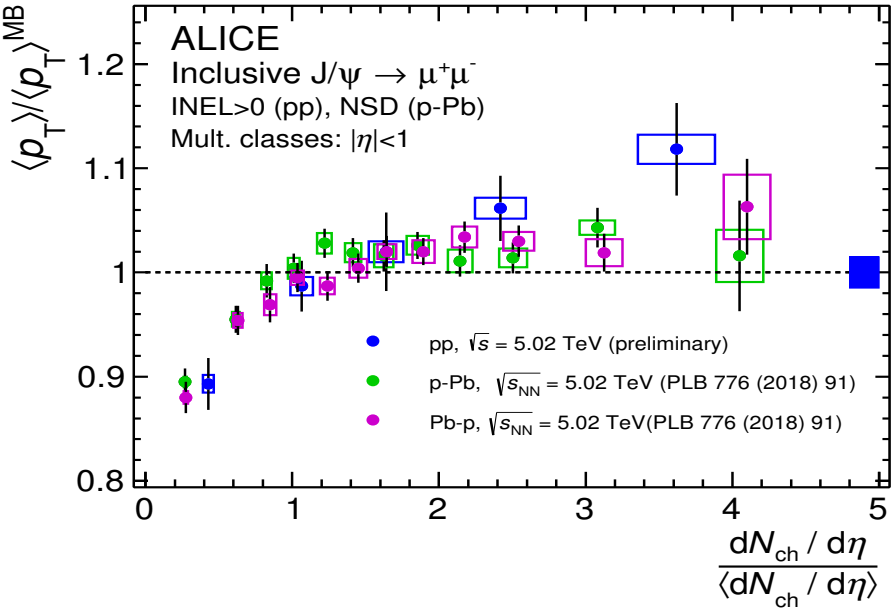

(a)

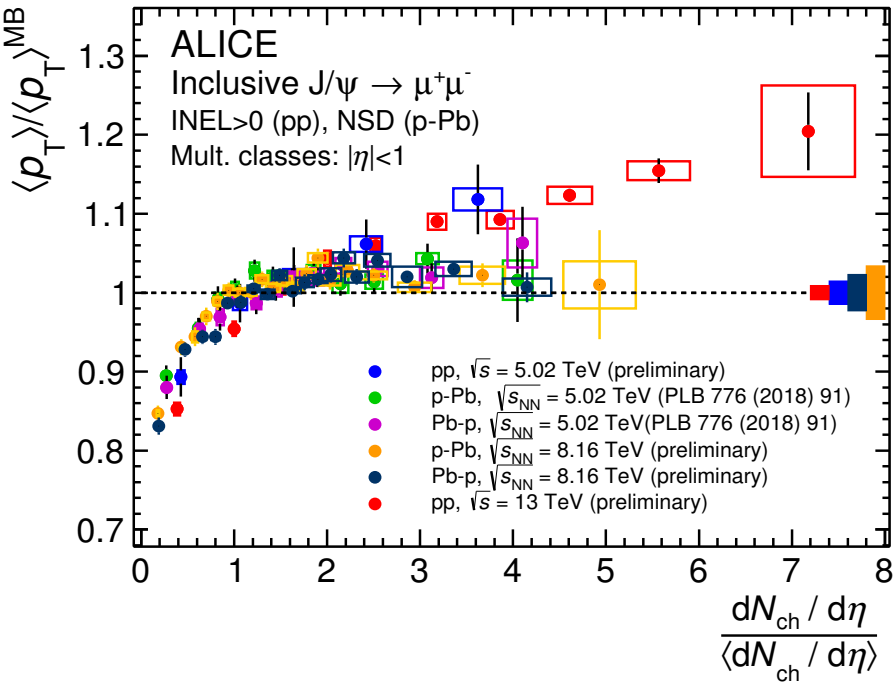

(b)

Figure 5-20: (a) The comparison of relative $\langle p_{\mathrm{T}}^{\mathrm{J}/\psi} \rangle$ as function of charged-particles multiplicity in pp and p-Pb collisions system at $\sqrt{s_{\mathrm{NN}}}$ = 5.02 TeV. (b) The comparison of relative $\langle p_{\mathrm{T}}^{\mathrm{J}/\psi} \rangle$ between all available ALICE results.

that the increase of relative $\langle p_{\rm T}^{\rm J/\psi}\rangle$ at lower multiplicities up to ∼1.5 and a saturating trend at higher multiplicity region. However, the increase in low multiplicity region seems to be faster in pp than p-Pb collisions for the same collision energy. Furthermore, a comparison of relative $\langle p_{\rm T}^{\rm J/\psi}\rangle$ as a function of $\mathrm{d}N_{\rm ch}^{R}/\mathrm{d}\eta$ has been illustrated in Figure 5-20 (b) for pp collisions $\sqrt{s}$ = 13 TeV [5] at forward rapidity and p-Pb collisions at $\sqrt{s_{\rm NN}}$ = 5.02 [1] and 8.16 TeV [4] at forward and backward rapidities, respectively. The $\langle p_{\rm T}^{\rm J/\psi}\rangle$ and $\mathrm{d}N_{\rm ch}^{R}/\mathrm{d}\eta$ were computed in p-Pb collisions for the non single diffractive events while in pp collisions $INEL > 0$ event class. The global uncertainties are shown to be around the unity. These errors are 1.5%, 0.9% for pp collisions at $\sqrt{s}$ = 5.02 and 13 TeV, respectively and for p-Pb and Pb-p collisions these are 3.4% and 2.3% at 8.16 TeV. It can be again concluded from the figure that the rise of $\langle p_{\rm T}^{\rm J/\psi}\rangle$ in pp collisions is faster than that in the p-Pb collisions.

The possible explanation for the observed saturation trend of relative $\langle p_{\rm T}^{\rm J/\psi}\rangle$ towards high multiplicity is as follows: At low multiplicity the number of interacting particles are less therefore, small number of particles carry most of the $p_{\rm T}$ in a given pseudo-rapidity range. At high multiplicity, number of particles increases so the J/ψ interacts with more number of particles which results in a decrease in $\langle p_{\rm T}^{\rm J/\psi}\rangle$ values. The purpose of normalization with total $\langle p_{\rm T}^{\rm J/\psi}\rangle$ is to check scaling behaviour, so that the observables become independent of the analysis, collision systems and collision energies.

5.2.2 Comparison with theory

The results of multiplicity dependence of $\langle p_{\rm T}^{\rm J/\psi}\rangle$ are compared with PYTHIA8 model calculation is shown in Figure 5-21. The PYTHIA8 Monash13 tune has been used for the purpose. The model predictions were provided in inelastic >0 event class for inclusive, prompt and non-prompt J/ψ at forward rapidity [7]. A trend similar to the one exhibiting from data is observed for inclusive and prompt $\langle p_{\rm T}^{\rm J/\psi}\rangle$ as a function of multiplicity. The contribution of $\langle p_{\rm T}^{\rm J/\psi}\rangle$ coming from beauty feed-down, is higher in the lower multiplicity region and saturates with increasing $\mathrm{d}N_{\rm ch}^{R}/\mathrm{d}\eta$.

The PYTHIA8 calculations further extended for V0A and V0C multiplicity esti-

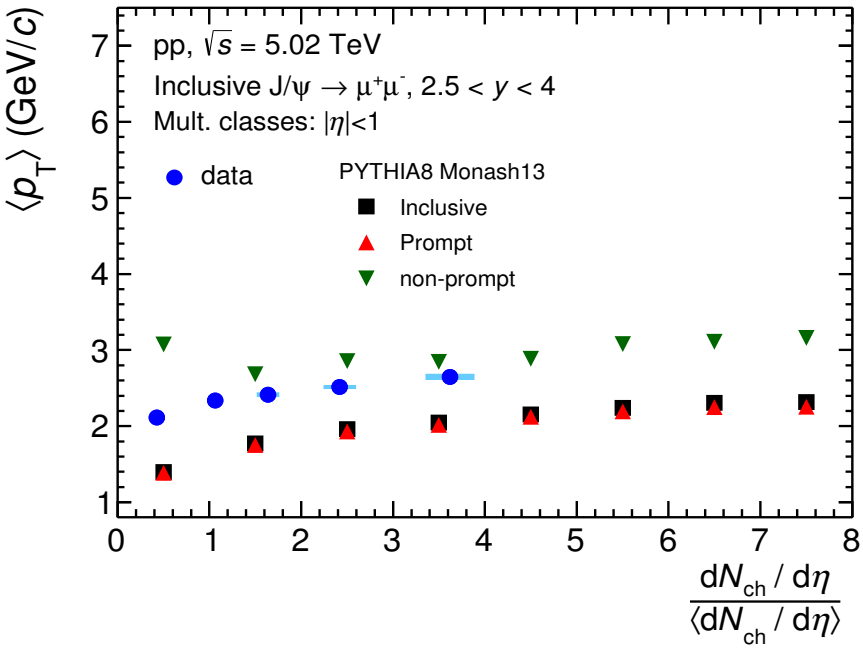

Figure 5-21: A comparison of $\langle p_{\mathrm{T}}^{\mathrm{J}/\psi} \rangle$ as function of multiplicity with PYTHIA8.

mator at forward and backward rapidity region, respectively (Figure 5-22). In both case of V0A and V0C, the inclusive and prompt $\langle p_{\mathrm{T}}^{\mathrm{J}/\psi} \rangle$ values show the same pattern as the one exhibited by data at 5.02 TeV. The non-prompt $\langle p_{\mathrm{T}}^{\mathrm{J}/\psi} \rangle$ values show fluctuations. The $\langle p_{\mathrm{T}}^{\mathrm{J}/\psi} \rangle$ grows faster in case of non-prompt J/ψ. It can be emphasized from these observations that the trend is independent of the multiplicity estimator and rapidity ranges. However, it depends on the nature of the J/ψ production.

Irrespective of the fluctuations in the multiplicity dependence of non-prompt $\langle p_{\mathrm{T}}^{\mathrm{J}/\psi} \rangle$ the data seems to be qualitatively described by the PYTHIA8. The multiplicity dependence of $\langle p_{\mathrm{T}}^{\mathrm{J}/\psi} \rangle$ is needed to be studied with higher precision. The data needs extensive theoretical model calculations with various approaches to understand the multiplicity dependence of $\langle p_{\mathrm{T}}^{\mathrm{J}/\psi} \rangle$.

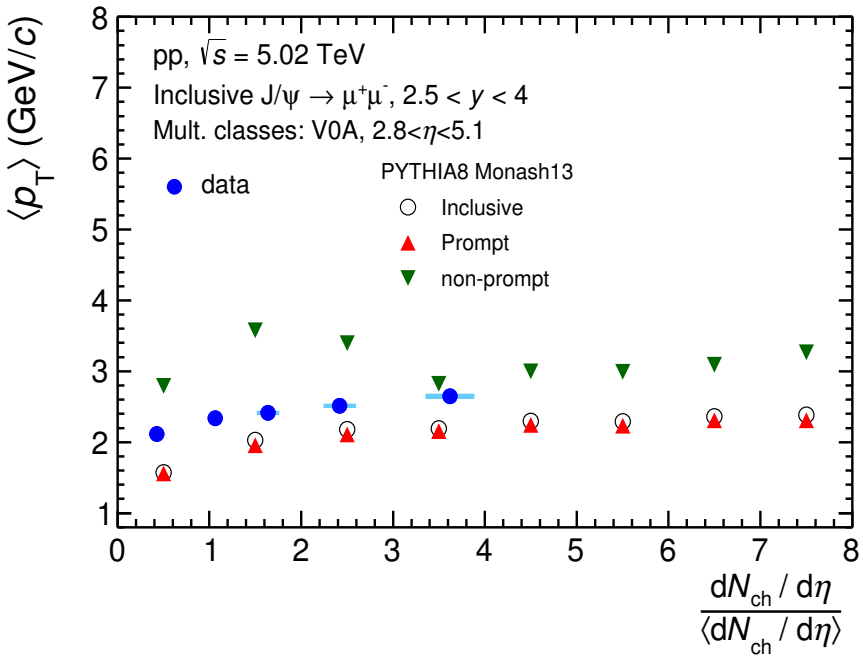

(a) V0A

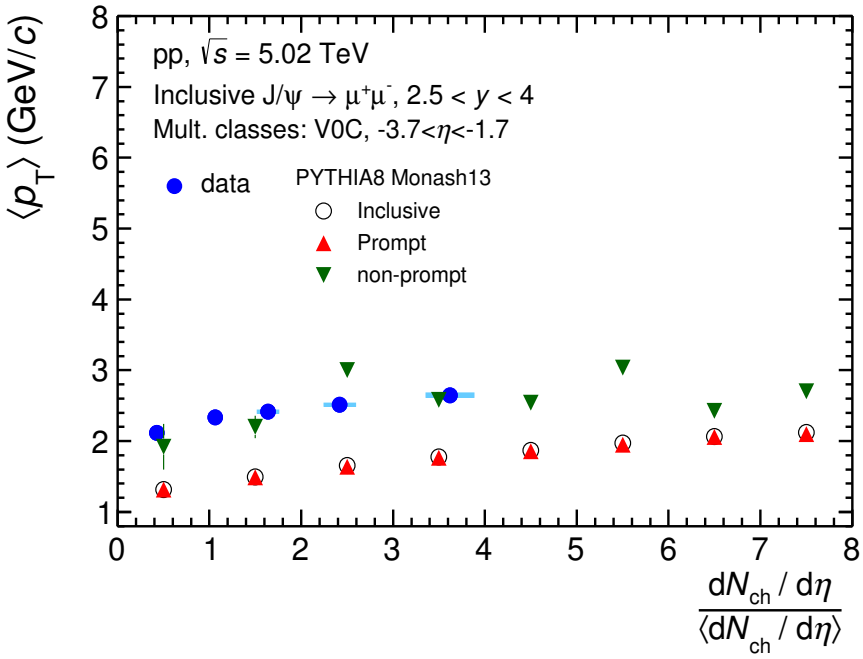

(b) V0C

Figure 5-22: A comparison of $\langle p_{\mathrm{T}}^{\mathrm{J}/\psi} \rangle$ as a function of different multiplicity estimator.

Bibliography

[1] D. Adamová et al., ALICE Collaboration, "J/ψ Production as a Function of Charged-Particle Pseudorapidity Density in p-Pb Collisions at $\sqrt{s_{NN}}$ = 5.02 TeV", Phys. Lett. B776 (2018) 91.

[2] J. M. Blanco, "Study of J/ψ Production Dependence with the Charged Particle Multiplicity in p-Pb Collisions at $\sqrt{s_{\rm NN}}$ = 5.02 TeV and pp Collisions at $\sqrt{s}$ = 8 TeV with the ALICE Experiment at the LHC", Ph.D. Thesis, CERN-THESIS-2016-070.pdf.

[3] S. Acharya et al., ALICE Collaboration, "Energy Dependence of Forward-Rapidity J/ψ and ψ(2S) Production in pp Collisions at the LHC", Eur. Phys. J. C77 (2017) 392.

[4] J. Crkovska, "Study of the J/ψ Production in pp Collisions at $\sqrt{s}$ = 5.02 TeV and of the J/ψ Production Multiplicity Dependence in p-Pb Collisions at $\sqrt{s_{\rm NN}}$ = 8.16 TeV with ALICE at the LHC", Ph.D. Thesis, CERN-THESIS-2018-281.pdf.

[5] D. Thakur, ALICE Collaboration, "J/ψ Production as a Function of Charged-Particle Multiplicity with ALICE at the LHC", (2018) arXiv:1811.01535 [hep-ex].

[6] M. Gaździcki et al., "Power Law in Hadron Production", Phys. Lett. B517 (2001) 250.

[7] S. G. Weber, Private Communication.

Chapter 6

Event shape analysis and thermodynamic aspect of J/ψ production with PYTHIA

The observation of QGP like effects in small systems (pp and p−A collisions) continues to generate considerable interest in the scientific community. For example, the discovery of collective-like phenomena [1, 2], strangeness enhancement [3], etc. in high-multiplicity pp and p−A collisions are a few among them. In this context, an important question arises whether the QGP-like phenomena involve all the particles in the system, or it is just the effect of contributions from the processes like resonance decays, jets, underlying events (UE) etc. Therefore, the small systems need to be re-investigated thoroughly. To observe similar effects and in particular, the effect of UE to J/ψ production, ALICE has performed the multiplicity dependence study of J/ψ at mid and forward-rapidities [4, 5]. A faster than linear and approximately linear behavior has been observed at mid and forward-rapidities, respectively [6]. The faster than linear increase of J/ψ yield with multiplicity questions the role of phenomena like collectivity, contribution of higher fock states, percolation, color reconnection etc., in addition to the multipartonic interaction (MPI) [7, 8, 9, 10, 11]. It has been speculated that different kinds of trend for multiplicity dependence of J/ψ at mid and forward rapidity might be due to auto-correlation and/or jet biases.

To understand the production dynamics in a better way, a differential analysis involving tools to separate jetty from isotropic events thus becomes evident. The event

shape analysis is a promising tool for controlling the jet biases in high multiplicity pp events. The collisions centrality, as well as the predominant reaction mechanisms at each centrality, can be inferred from the experimentally measured characteristics of the particle emission [12, 13, 14, 15, 16]. Therefore, event shapes measure the geometrical properties of the energy flow in QCD events. In the present work, the event shape analysis has been performed on the basis of transverse spherocity of mid-rapidity charged hadrons, applied to events generated with Pythia 8.2. This technique helps to isolate jetty-like (high-p_T jets) and isotropic (low-Q^2 partonic scatterings) events [17], which helps in studying the physical observables in jetty-like event and isotopic events separately. Hence, spherocity can be used to study the possibe soft and hard-QCD contributions to J/ψ production from both kinds of events. In this work, the spherocity evolution of J/ψ production with energy, multiplicity and rapidity has been investigated. This study may help in understanding the different kinds of trends for J/ψ as a function of multiplicity at mid and forward rapidities, particularly the jet biases in the J/ψ production. Therefore, the present work aims to explore the following aspects,

- Rapidity dependence of jet-bias to the multiplicity dependent J/ψ production.
- Energy dependence of jet-bias to the multiplicity dependent J/ψ production.
- Rapidity and energy dependence of production dynamics of J/ψ through the thermodynamic parameters on event shape and event multiplicity.

The analysis has been performed using pp collisions data at $\sqrt{s}$ = 5.02 and 13 TeV via the di-electron and di-muon decay channels of J/ψ at mid and forward rapidities, respectively. As the systems created in pp collisions are not fully thermalized and are more appropriate for J/ψ which is formed very early in the collisions, the Tsallis non-extensive statistics is a good approximation to draw inference about the thermodynamics of the small systems. The use of Tsallis distribution in describing particle spectra is also motivated by the spectral shape of identified particles in hadronic collisions as observed in RHIC and LHC experiments [18, 19, 20, 21, 22, 23].

Transverse spherocity:

For an event, transverse spherocity is defined for a unit vector $\hat{n}(n_T, 0)$ which minimizes the ratio given by the expression [15, 16, 17, 24]

$$S_0 = \frac{\pi^2}{4}\left(\frac{\Sigma_i\ \vec{p}_{T_i} \times \hat{n}}{\Sigma_i\ p_{T_i}}\right)^2. \tag{6.1}$$

By restricting it to the transverse plane, it avoids the biases from the boost along the beam direction. This variable ranges from *zero* for pencil-like events (di-jet events), to a maximum of *one* for circularly symmetric events (isotropic events), which corresponds to mainly hard events and soft events, respectively. A typical depiction of transverse spherocity distribution of a hadronic collision along with its jetty and isotropic events are shown in Figure 6-1.

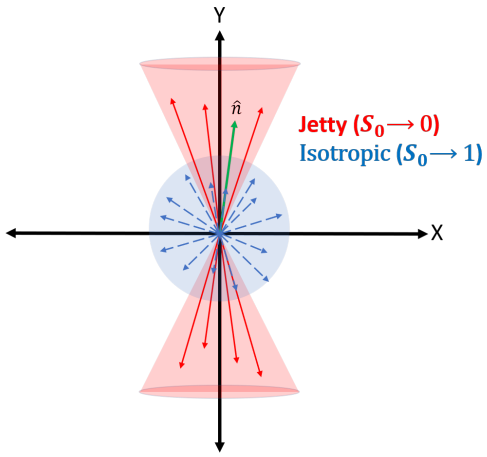

Figure 6-1: A schematic picture showing transverse spherocity distribution of a hadronic collision.

Tsallis non-extensive statistics:

The transverse momentum (p_T) spectra of final state particles produced in high-energy collisions has been proposed to follow a thermalized Boltzmann type of distribution as given by the Equation [25]

$$E\frac{d^3\sigma}{d^3p} \simeq C\exp\left(-\frac{p_T}{T_{exp}}\right). \tag{6.2}$$

To account for the high-p_{T} tail, a power-law in p_{T} distribution is proposed [26, 27], which empirically accounts for the possible QCD contributions. Hagedorn proposed a combination of both the aspects, which describes the experimental data over a wide p_{T} range [28] and is given by

$$\begin{aligned} E\frac{d^3\sigma}{d^3p} &= C\left(1+\frac{p_T}{p_0}\right)^{-n} \\ &\longrightarrow \begin{cases} \exp\left(-\frac{np_T}{p_0}\right) & \text{for } p_T \to 0, \\ \left(\frac{p_0}{p_T}\right)^n & \text{for } p_T \to \infty, \end{cases} \end{aligned} \tag{6.3}$$

where C, p_0, and n are mathematical parameters. A thermodynamically consistent non-extensive distribution function is given by [29, 30]

$$f(m_T) = C_q\left[1+(q-1)\frac{m_T}{T}\right]^{-\frac{1}{q-1}}. \tag{6.4}$$

Here, m_{T} is the transverse mass and q is called the non-extensive parameter: a measure of degree of deviation from equilibrium Equations 6.3 and 6.4 are related through the following transformations for large values of p_T:

$$n = \frac{1}{q-1}, \text{ and } \quad p_0 = \frac{T}{q-1}. \tag{6.5}$$

In the limit $q \to 1$, one arrives at the standard Boltzmann-Gibbs thermalized distribution (Equation 6.2) from the Tsallis distribution. The transverse momentum spectra of J/ψ is well described by a power-law function, shown in Equation 6.3 [31, 32]. In this work, through its thermodynamical connection, as given in Equation 6.5, the event shape as well as multiplicity dependence study of thermodynamic parameters of J/ψ has been performed using the Tsallis non-extensive statistics.

6.1 Event generation and analysis methodology

PYTHIA8 is the monte carlo based pQCD inspired event generator. It is an improved version of PYTHIA6 which includes the implementation of MPI based scenario, where $2 \rightarrow 2$ hard sub-processes can produce heavy quarks like charm (c) and beauty (b). Elaborate description of PYTHIA8.2 physics processes can be found in reference [33]. 4C tuned PYTHIA8.2 [34] is used in the present study. The same tune has been used in our previous works [11, 35]. Varying impact parameter (MultipartonInteractions:bProfile=3) is included in the present study to allow all incoming partons to undergo hard and semi-hard interactions. MPI-based scheme of Colour Reconnection (ColourReconnection:mode(0)) of PYTHIA8.2 is used. More details on various models of CR included in PYTHIA8.2 and their performances with respect to experimental data can be found elsewhere [36, 37].

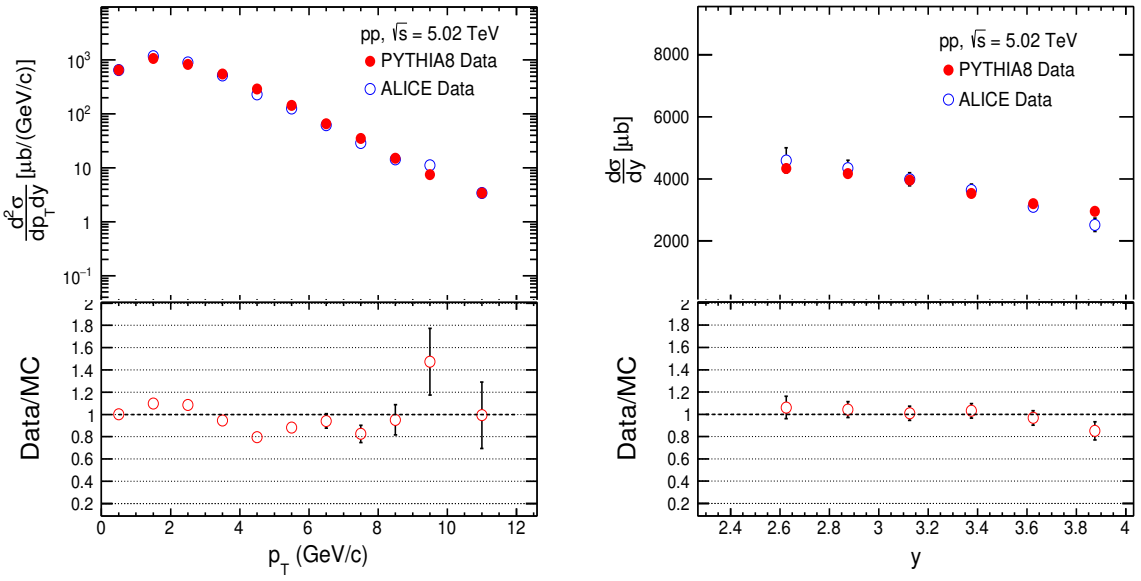

(a) (b)

Figure 6-2: (a) The comparison of ALICE data [4] and PYTHIA8 of J/ψ production cross-section as a function of transverse momentum for pp collisions at $\sqrt{s}$ = 5.02 TeV. (b) The comparison of ALICE data [4] and PYTHIA8 for of J/ψ production cross-section as a function of rapidity for pp collisions at $\sqrt{s}$ = 5.02 TeV. Bottom panels show the ratio between ALICE data and PYTHIA8.

In the present work, inelastic, non-diffractive component of the total cross-section for all hard QCD processes (HardQCD:all=on) are simulated, which includes the production of heavy quarks. A cut on $p_T = 0.5$ GeV/c (using PhaseSpace:pTHatMinDiverge) is imposed to avoid the divergences of QCD processes in the limit $p_T \to 0$. Two decay channels: (i) $J/\psi \to e^+ + e^-$ and (i) $J/\psi \to \mu^+ + \mu^-$ have been studied and the yields of the reconstructed J/ψ was measured by defining an external decay mode at forward and mid-rapidities, respectively. Figure 6-2 shows the comparison of experimental data with PYTHIA8. From these figures, it can be seen that PYTHIA8 well reproduces the ALICE measurements. For further studies of event shape analysis, these settings in PYTHIA8 have been used because of the agreement with experimental results.

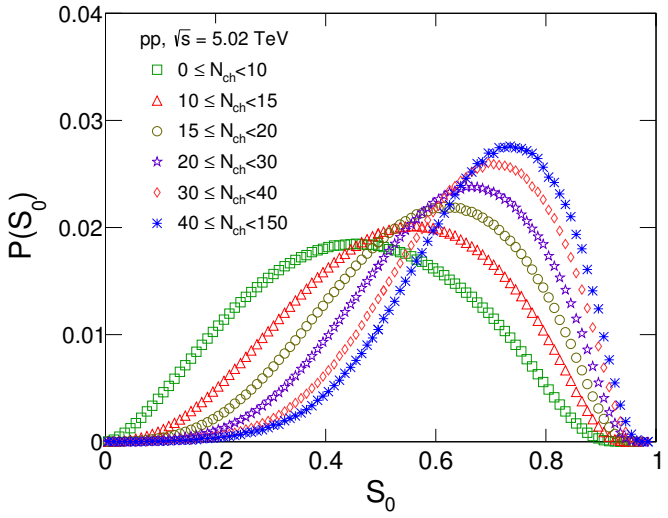

Figure 6-3: The spherocity distribution of minimum bias events as a function of charged-particle multiplicity in pp collisions at $\sqrt{s} = 5.02$ TeV.

We have generated (6.1×10^8, 1.22×10^8) and (9.6×10^8, 1.14×10^8) events for pp collisions at $\sqrt{s} = 5.02$ and 13 TeV at forward and mid-rapidities, respectively. The charged-particle multiplicity (N_{ch}) is measured at the mid-rapidity and the spherocity distributions are selected in the pseudo-rapidity range of $|\eta| < 0.8$ with a minimum constraint of 5 charged particles with p_T >0.15 GeV/c. The jetty events are those having $0 < S_0 < 0.37$ with lowest 20% and the isotropic events are those having

$0.71 < S_0 < 1$ with highest 20% of the total events. Figure 6-3 represents the spherocity distribution in different multiplicity intervals for pp collisions at $\sqrt{s} = 5.02$. Here it is observed that high-multiplicity events are more isotropic in nature. The process of isotropization in a multiparticle final state happens through multiple interactions between the quanta of the system. When the final state multiplicity in an event is higher, the probability of the event becoming isotropic is also higher.

6.2 Results and discussion

At the LHC energies, MPI is an important process which occurs at a substantial rate in hadronic collisions and is a very important ingredient in explaining the multiplicity dependence of various observables. MPI incorporated in PYTHIA8, is able to describe many of the experimentally observed features, such as multiplicity distribution and underlying events; light-flavour and heavy-flavor production; together with color-reconnection, it is able to reproduce flow-like patterns in pp collisions [38, 39, 40, 41, 42, 43]. Models containing MPI well describe the multiplicity dependence of J/ψ production and thus reveal that MPI is an important mechanism behind the production of J/ψ [7, 11]. In a given multiplicity interval, there are events originating from different number of MPIs, which make them different in nature. As discussed in the previous section, using the transverse spherocity, we can classify the events based on their jet content. Quarkonium production in the parton shower, which is able to explain the lack of observed polarization, predicts that J/ψ mesons are rarely produced in isolation in hadronic collisions [44, 45]. Further, the production cross-section of J/ψ at mid-rapidity is higher as compared to forward rapidity [32]. This indicates the difference in jet contribution at mid and forward rapidity J/ψ production. In this contribution, we have tried to quantify the jet content to the production of J/ψ by analyzing their p_{T} spectra in different jet environments.

First, we have calculated the relative J/ψ yield as a function of relative charged-particle pseudo-rapidity density, $\mathrm{d}N^{R}_{\mathrm{ch}}/\mathrm{d}\eta$ in pp collisions at $\sqrt{s} = 5.02$ TeV at forward rapidity. The multiplicity spherocity differential study of relative J/ψ yield is carried

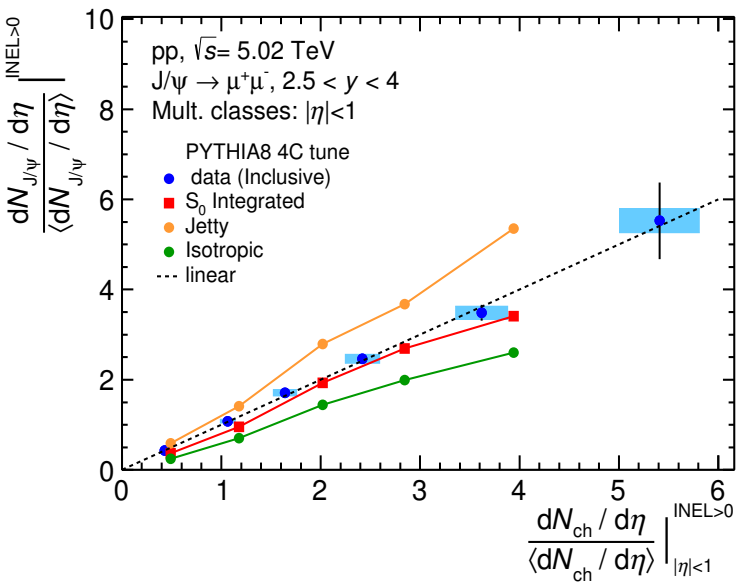

Figure 6-4: Comparison of multiplicity dependence of the relative J/ψ yield at inclusive, jetty and isotropic events with data in pp collisions at 5.02 TeV.

out for three spherocity class events. The results have been compared with the data, and are illustrated in Figure 6-4. It can be observed from the figure that the PYTHIA8 4C tune well describes the data at lower multiplicity in case of inclusive relative J/ψ yield. At higher multiplicity a slight deviation from the data is observed. The relative yield computed for jetty and isotropic events under and over estimate the data, respectively. A stronger than linear increment is observed in case of jetty events. Figure 6-5 exhibits the $\langle p_{\rm T}^{\rm J/\psi} \rangle$ variation as a function of $N_{\rm ch}$ computed at muon channel forward rapidity and electron channel mid-rapidity at $\sqrt{s} = 5.02$ TeV with PYTHIA8. At mid-rapidity the multiplicity and $\langle p_{\rm T}^{\rm J/\psi} \rangle$ are computed in the same rapidity interval. The increase of $\langle p_{\rm T}^{\rm J/\psi} \rangle$ with saturation towards higher multiplicity similar to the data (as shown in previous chapter) is observed at mid-rapidity for all the cases. The $\langle p_{\rm T}^{\rm J/\psi} \rangle$ values for jetty events dominates the one for integrated S_0 events. The muon channel results show that isotropic events dominates the other two event class results. The jetty and inclusive $\langle p_{\rm T}^{\rm J/\psi} \rangle$ shows a similar trend as observed earlier in most cases, whereas the isotropic events show opposite nature of the jetty results.

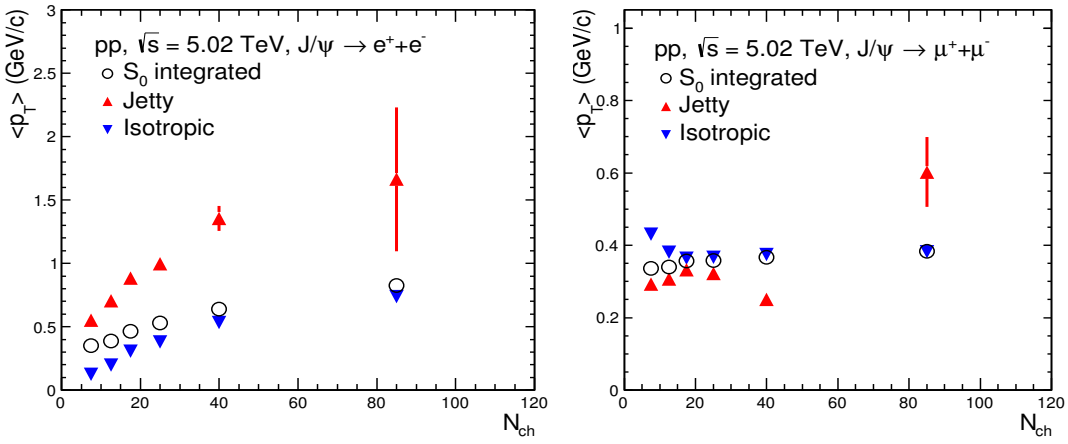

Figure 6-5: The event shape dependence of $\langle p_{\mathrm{T}}^{\mathrm{J}/\psi} \rangle$ as a function of multiplicity at forward and mid-rapidity.

6.2.1 Event shape dependence of J/ψ production at mid and forward rapidities

The event shape study is carried out using transverse spherocity in different charged-particle multiplicity classes (Table 6.1). Figure 6-6 shows the transverse momentum spectra of J/ψ at forward (left panel) and mid-rapidity (right panel) for integrated multiplicity (minimum bias) at $\sqrt{s}$ = 5.02 TeV for different spherocity classes. The lower panel of the same figure represents the ratio of p_{T}-spectra for isotropic and jetty events with respect to spherocity integrated (S_0) events. It can be seen that the lower p_T region is dominated by isotropic events over the jetty events. However, this scenario reverses as we move towards higher p_T. At a particular point, termed as 'crossing point', the jetty events dominate over the isotropic events. Therefore, the study of the 'crossing point' is of great interest as far as a feasible boundary for dominance of the event type and hence the associated particle production mechanisms are concerned.

From the previous studies of the light-flavor sector, it has been observed that the 'crossing point' largely depends on the multiplicity and the isotropic events are populated over jetty events as we move from lower to higher-multiplicities [16, 46, 47].

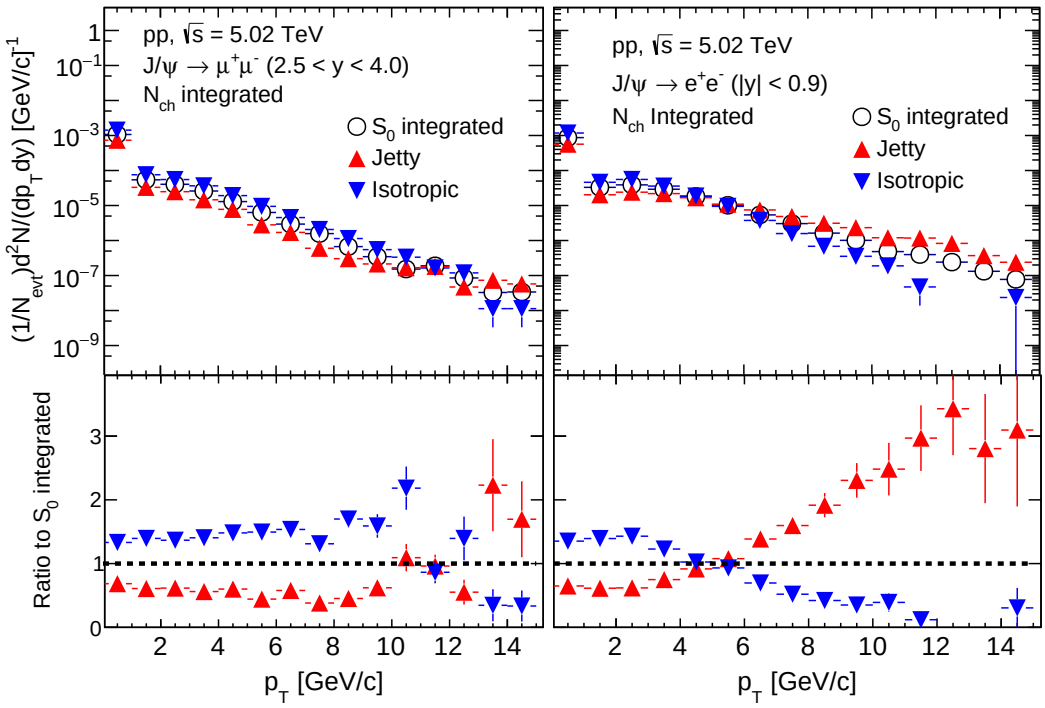

Figure 6-6: The upper Panel shows p_{T}-spectra of J/ψ for minimum bias pp collisions as a function of spherocity. Whereas, the lower panel shows the ratio of p_{T}-spectra for isotropic and jetty events with respect to S_0 integrated events.

These observations tend to suggest that the QGP-like effects seen in high-multiplicity pp collisions are not because of jet-bias effects rather may be due to a possible system formation, which should be explored further. In the present work, similar studies reveal that the speculation is valid in case of J/ψ as well. From the double differential study of J/ψ, we have found that isotropic events are dominant at high-multiplicities. A comparison of forward versus mid-rapidity reveals the shift of the 'crossing point' towards lower-p_T in case of mid-rapidity spherocity dependent J/ψ production. This means the contribution of jets in J/ψ production is higher at the mid-rapidity. Motivated from the recent results of multiplicity dependence of J/ψ production by ALICE [6], the analysis has been extended to look into the double differential study of rapidity dependence of J/ψ production at mid and forward rapidities. Figure 6-7 represents the rapidity and energy dependence of the 'crossing point'. This signifies how the contribution of jets to the production of J/ψ vary with rapidity and $\sqrt{s}$. For

completeness, we have also tabulated the values of transverse momentum in Table 6.1, after which the jetty events dominate over the isotropic events. From the Figure 6-7 as well as Table 6.1, one can easily notice the higher dominance of jetty events at the mid-rapidity compared to forward rapidity, irrespective of the event multiplicity, revealing the jet dominant contribution of J/ψ production at the mid-rapidity.

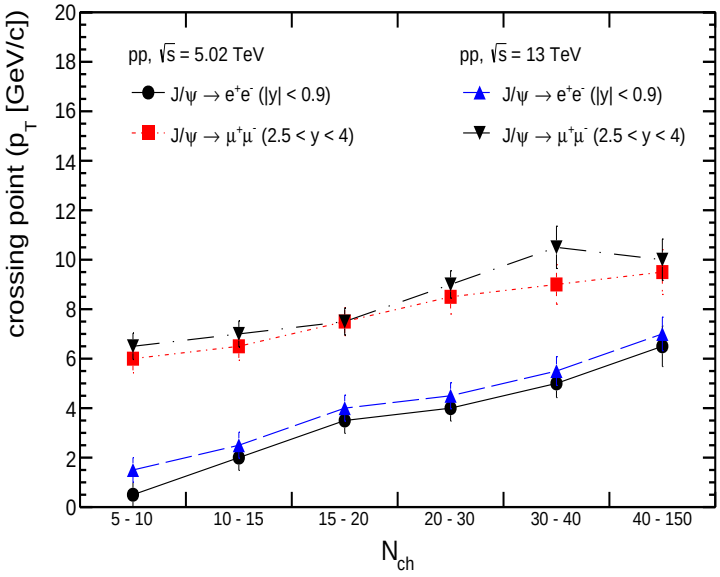

Figure 6-7: The rapidity and energy dependence of 'crossing point' (jet bias) to the J/ψ production as a function of multiplicity.

Furthermore, the dominance of jettiness in low-multiplicity events and isotropiness in high-multiplicity events in J/ψ production reveals apparent reduction and softening of the jet yields at high $N_{\rm ch}$ values [16, 48]. In QCD inspired models like PYTHIA8, the prime mechanism to produce high-multiplicity pp events is related to partonic interactions with large momentum transfer. Therefore, the reduction in jet contribution in the J/ψ production may indicate a reduced production of back-to-back jets [14]. Recently, in high-multiplicity pp collisions, away-side ridge in two-particle correlation has been observed, which is an indication of the presence of collectivity in the system [49].

Our current observations are in fair agreement with the one observed for populated isotropic events at high-multiplicities. Hence, the contribution of jets to the pro-

Multiplicity	$\sqrt{s}$ = 5.02 TeV		$\sqrt{s}$ = 13 TeV	
N_{ch} bin	$\|y\| < 0.9$	2.5< y <4.	$\|y\| < 0.9$	2.5< y <4.
5-10	0.50± 0.50	6.00±0.57	1.50±0.50	6.50±0.53
10-15	2.00± 0.52	6.50±0.57	2.50±0.52	7.00±0.53
15-20	3.50± 0.52	7.50±0.56	4.00±0.52	7.50±0.54
20-30	4.00± 0.52	8.50±0.69	4.50±0.53	9.00±0.55
30-40	5.00± 0.57	9.00±0.80	5.50±0.58	10.50±0.85
40-150	6.50± 0.82	9.50±0.90	7.00±0.68	10.00±0.69

Table 6.1: The crossing point (p_T in GeV/c) of jetty and isotropic events at forward and mid-rapidity for pp collisions at $\sqrt{s}$ = 5.02 and 13 TeV.

duction of J/ψ has very little but significant effect at high-multiplicities. But, still jet contribution in J/ψ production is significantly more at mid-rapidity compared to forward rapidity. High multiplicities are rich with isotropic events which may give rise to collective-like effects, but the difference in jet bias at both the rapidities might produce different multiplicity dependent trends in J/ψ production.

6.2.2 Energy dependence of J/ψ production in different event shapes

To investigate the possible dependence of jet effects on center-of-mass energy, we have performed the event activity dependence of double differential studies at $\sqrt{s}$ = 5.02 and 13 TeV. The Figure 6-7 and Table 6.1 represent the energy dependent contribution of jetty and isotropic events to the J/ψ production. This observation tends to show that although there is a large rapidity dependence of jet contribution to J/ψ production, it has very weak dependence on center-of-mass energy. From Table 6.1, at a particular center-of-mass energy and rapidity, one can see that the value of the 'crossing point' is the same within the uncertainty limits. This observation goes inline with the multiplicity dependence of J/ψ production as reported by ALICE experiment [6], where the J/ψ production as a function of multiplicity is found to be independent of $\sqrt{s}$ at a given rapidity. Therefore, the 'crossing point' depends on rapidity and is nearly independent of center-of-mass energy. This result supports the recent observation by ALICE, where no dependence of J/ψ production on $\sqrt{s}$ has

been observed [6].

6.2.3 Event shape dependence of system thermodynamics

As discussed in the previous sections, the production of J/ψ in jetty events are different from isotropic ones. When the former involves high-p_{T} phenomena and the latter is dominated by soft-particles. Tsallis non-extensive statistics is an appropriate model to describe all the three aspects of the event types, namely, S_0 integrated, jetty and isotropic events. The non-extensive parameter (q) gives the information about the degree of deviation of a system from thermodynamic equilibrium. Tsallis distribution function contains another parameter, "T", called Tsallis temperature, which gives the information about the temperature of the system [50]. To study the event shape and multiplicity dependence of "q" and "T", the transverse momentum spectra have been fitted in spherocity and multiplicity classes at $\sqrt{s}$ = 5.02 and 13 TeV.

The spectral description of Tsallis distribution function to J/ψ production as a function of p_T using PYTHIA8 are shown in Figure 6-8 for pp collisions at $\sqrt{s}$ = 5.02 TeV in the mid and forward rapidities for jetty, isotropic and S_0-integrated events. The data to fit ratio is computed and is shown at the lower panel of Figure 6-8, which shows that all the points fall around unity except for the high p_T bins where statistical fluctuation is larger. The analysis using Tsallis non-extensive statistics is repeated for different multiplicity classes and event shapes for pp collisions at $\sqrt{s}$ = 5.02 and 13 TeV. The "q" and "T" parameters have been studied as a function of multiplicity in three different event shape classes. Figures 6-9 and 6-10 show the variation of Tallis-temperature and Tsallis non-extensive q-parameter as a function of multiplicity, rapidity and center-of-mass energy for three different event classes.

A quantitative discussion of J/ψ production mechanism in non-extensive statistics is beyond the scope of the present work. We shall, therefore, only discuss about the difference in the thermodynamics of J/ψ production at mid and forward-rapidities in jetty and isotropic events via their transverse momenta spectra. Followings are the important observations from the current study:

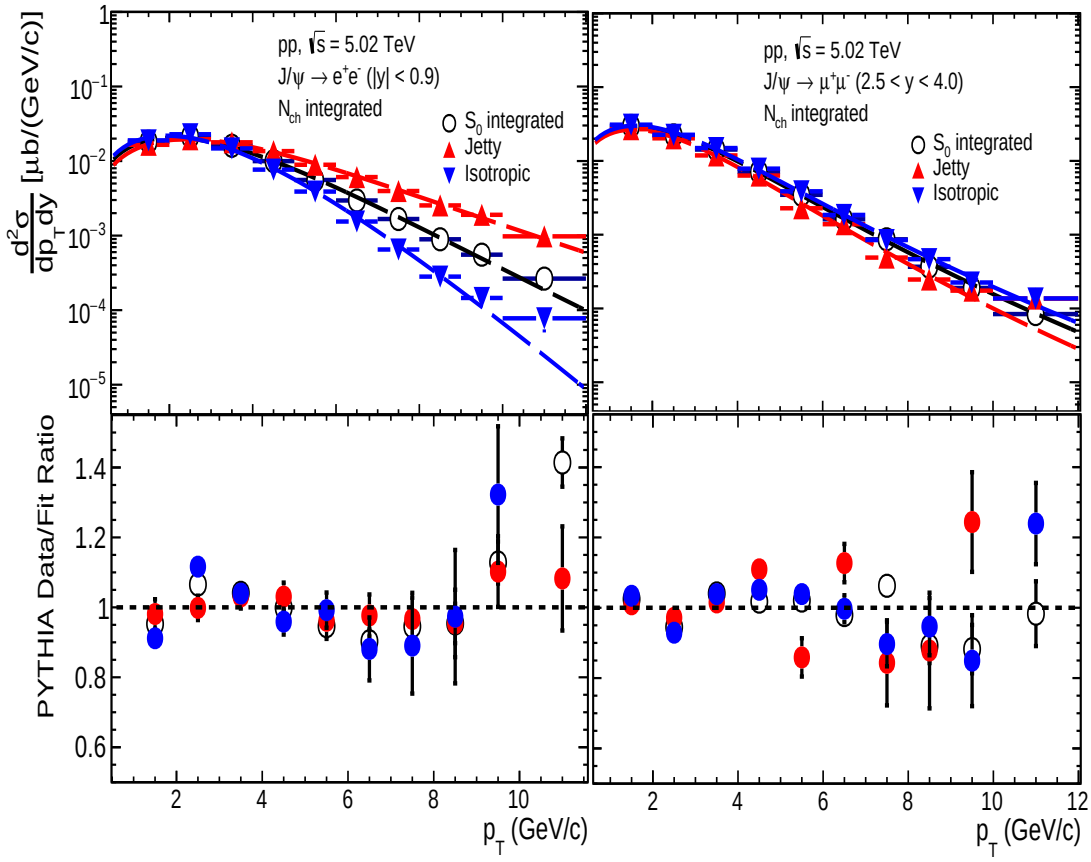

Figure 6-8: The J/ψ production cross-section as a function of p_T for minimum bias collisions in different event samples (jetty and isotropic) at mid (left panel) and forward rapidity (right panel). The spectra are described by Tsallis distribution function. The bottom panels show the data to fit ratios for the respective rapidities.

- Tsallis-temperature for jetty and isotropic events shows an increasing trend with multiplicity irrespective of the rapidity under investigation
- Tsallis-temperature for J/ψ is higher for higher center-of-energy ($T_{13} > T_{5.02}$)
- At the mid-rapidity, Tsallis-temperature of jetty events is higher than isotropic events whereas the behavior gets reversed at forward rapidity i.e $T_{isotropic} > T_{jetty}$
- Tsallis non-extensive q-parameter is consistent around 1.0−1.2, irrespective of center-of-mass energy, rapidity and multiplicity.

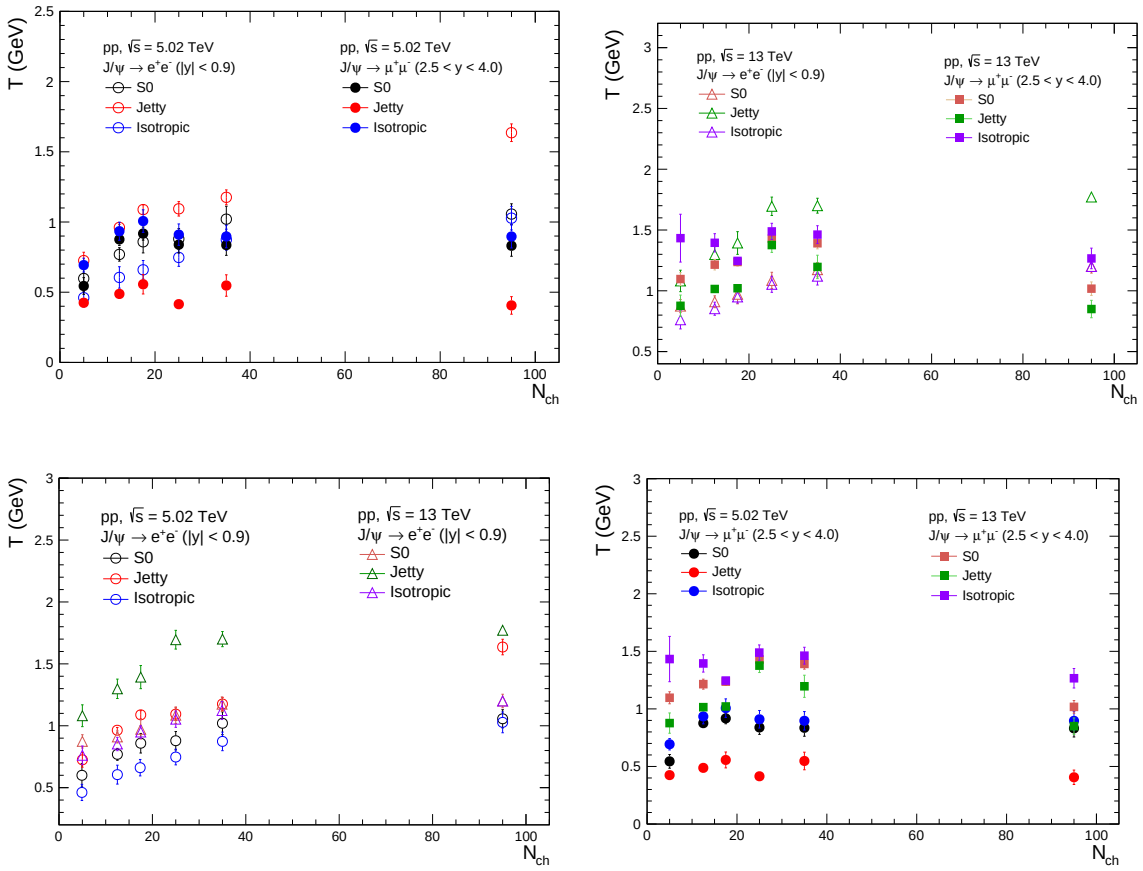

Figure 6-9: Multiplicity, rapidity and energy dependence of Tsallis temperature for J/ψ at mid and forward rapidity for pp collisions at $\sqrt{s}$ = 5.02 and 13 TeV. The upper two panels represent the rapidity dependence and the lower two panels show its energy dependent behavior.

As discussed in the introduction, the transverse momenta spectra of thermalized particles can be described by an exponentially decreasing behavior. But, at the higher momenta (at higher energies) the experimental data deviate from the usual Boltzmann function due to the dynamical effect of the system. The slope parameter represents the particle energy, which has both thermal (random) and collective contributions. The thermal motion gives the freeze out temperature (T_f), the temperature at which particles cease to interact with each other. In the presence of dynamical effect of a collective transverse flow, the increase of the slope parameter (T) at large m_T (m_T =

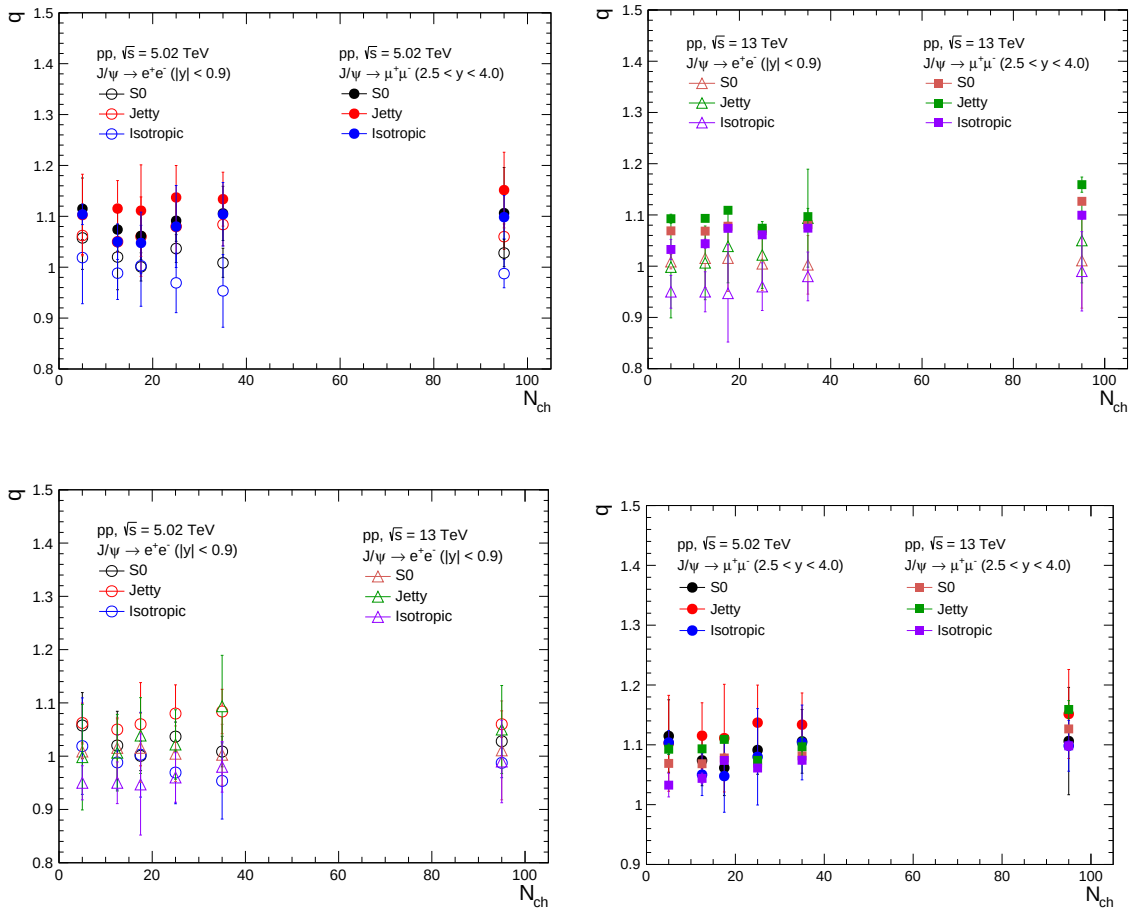

Figure 6-10: Multiplicity, rapidity and energy dependence of the non-extensive parameter (q) of the J/ψ at mid and forward rapidities for pp collisions at $\sqrt{s}$ = 5.02 and 13 TeV. The upper two panels represent the rapidity dependence and the lower two panels show its energy dependence behavior.

$\sqrt{m^2 + p_T^2}$) can be seen. Therefore, in the presence of collective transverse flow,

$$T = T_f + m\langle v_T \rangle^2. \tag{6.6}$$

where $\langle v_T \rangle$ is the average collective flow velocity and “m" is the mass of the detected particle [51]. The deviation from the Boltzmann slope at high-p_T can be explained by the presence of non-extensive statistical effects, which incorporate the effect of a collective flow. The “q" value extracted from the p_T spectra of J/ψ is not unity (Figure 6-10 and Table 6.3), which reveals that the system contains dynamical effects and hence the presence of collective behaviour.

At the mid-rapidity, we can see from the Figure 6-9 and Table 6.2 that the “T" parameter increases with an increase in multiplicity for both jetty and isotropic events. Further, the value of “T" parameter for jetty events is higher than that of isotropic events. These observations support the statements that the collective like effects increase from low to high-multiplicity irrespective of the effect of the event type in J/ψ production. The effect is more prominent for jetty events compared to isotropic events. The observation is in accord with our prediction from ‘crossing point’ study that the collective effect dominates towards higher multiplicities. When we look at the multiplicity dependent trend of ‘T’ parameter at forward rapidity (Figure 6-9), the values are almost the same for different event multiplicities irrespective of the event shapes. This states that if collectivity is present in the system, it has almost equal effect irrespective of the multiplicity under investigation. The higher value of “T" parameter in isotropic events with respect to the jetty events at forward rapidity might be due to the dominance of event type.

6.3 Summary

From the study of event shape, multiplicity and rapidity dependences of J/ψ production, the following important conclusions can be drawn:

Mid-rapidity:

- The jet contribution to the J/ψ production is more at mid-rapidity compared to forward rapidity, and is independent of $\sqrt{s}$.

- The system formed in pp collisions contain dynamical effects, which leads to collective-like behaviour. The collectivity increases from low to high-multiplicity at mid-rapidity, irrespective of the dominance of the event type in J/ψ production, and is more prominent for jetty events compared to isotropic events.

Forward rapidity:

- The dominance of isotropic events is found throughout all the multiplicity bins at forward rapidities with a very little contribution from jetty events, and is independent of $\sqrt{s}$.

- From the study of Tsallis "T" parameter at forward rapidity, it is found that the values are almost consistent with multiplicity for all the event types. Therefore, if collective effect is present in the system it has almost equal effect irrespective of the multiplicity under investigation.

The observation of completely different production dynamics of J/ψ with multiplicity at the mid-rapidity and forward rapidity but is independent of collision energy, supports the experimental results of ALICE.

Temperature (GeV) obtained in each multiplicity bin and event shape for $\sqrt{s}$ = 13 TeV						
	$\|y\| < 0.9$			2.5< y <4.		
Mult-Bin	S_0	**Jetty**	**Isotropy**	S_0	**Jetty**	**Isotropy**
0-10	0.874 ±0.054	1.081 ± 0.088	0.761 ± 0.075	1.097 ±0.052	0.876±0.090	1.433±0.197
10 - 15	0.910 ± 0.049	1.298 ± 0.078	0.853 ± 0.054	1.215± 0.043	1.015±0.010	1.395± 0.075
15 - 20	0.971 ± 0.078	1.393 ± 0.093	0.949 ± 0.050	1.237 ± 0.033	1.021 ±0.020	1.246± 0.012
20- 30	1.085 ± 0.067	1.695 ± 0.075	1.053 ± 0.065	1.430± 0.035	1.376± 0.061	1.488± 0.067
30 - 40	1.173 ±0.059	1.700 ± 0.061	1.120 ± 0.073	1.391± 0.046	1.196± 0.096	1.462± 0.073
40 - 150	1.200 ± 0.054	1.771 ± 0.038	1.200 ± 0.022	1.017± 0.055	0.850± 0.072	1.266± 0.085
Integrated	1.024 ± 0.095	1.072 ± 0.084	1.094 ± 0.097	1.181 ± 0.019	1.192± 0.053	1.270±0.035
Temperature (GeV) obtained in each multiplicity bin and event shape for $\sqrt{s}$ = 5.02 TeV						
0 - 10	0.597 ± 0.094	0.725±0.059	0.461± 0.065	0.544 ± 0.059	0.425±0.031	0.693 ± 0.049
10 - 15	0.769 ±0.047	0.961±0.022	0.605± 0.076	0.876 ± 0.043	0.488± 0.033	0.934 ± 0.064
15 - 20	0.859 ±0.079	1.088±0.033	0.659± 0.066	0.917 ± 0.047	0.556± 0.069	1.006 ± 0.080
20 - 30	0.879 ±0.074	1.093±0.051	0.747± 0.063	0.839± 0.060	0.415±0.036	0.910 ± 0.076
30 - 40	1.020 ±0.092	1.176±0.053	0.873± 0.075	0.836± 0.073	0.547± 0.076	0.897 ± 0.080
40 - 150	1.056 ±0.073	1.635±0.063	1.027± 0.084	0.831± 0.075	0.406± 0.062	0.896 ± 0.081
Integrated	0.799± 0.021	0.878± 0.067	0.715± 0.006	0.807± 0.021	0.797± 0.064	0.762± 0.043

Table 6.2: The extracted temperature parameter (T) from Tsallis distribution fitting (Equation 6.4) to the p_{T} spectra of J/ψ along with statistical uncertainty in different multiplicity bins for pp collisions at $\sqrt{s}$ = 5.02 and 13 TeV.

Tsallis-q parameter obtained in each multiplicity bin and event shape for $\sqrt{s}$ = 13 TeV						
	$\|y\| < 0.9$			2.5< y <4.		
Mult-Bin	S_0	**Jetty**	**Isotropy**	S_0	**Jetty**	**Isotropy**
0-10	1.010 ±0.013	0.998 ± 0.099	0.950 ± 0.032	1.069± 0.005	1.092± 0.008	1.033± 0.019
10 - 15	1.015 ±0.057	1.006 ± 0.072	0.950 ± 0.039	1.068± 0.004	1.093± 0.002	1.044± 0.008
15 - 20	1.016 ± 0.065	1.040 ± 0.071	0.947 ± 0.095	1.078± 0.007	1.109± 0.002	1.074± 0.002
20- 30	1.005 ± 0.052	1.023 ± 0.065	0.960 ± 0.046	1.069± 0.003	1.074± 0.002	1.061± 0.006
30 - 40	1.003 ± 0.057	1.094 ± 0.096	0.980 ± 0.048	1.081± 0.004	1.097± 0.016	1.074± 0.007
40 - 150	1.011 ± 0.093	1.050 ± 0.083	0.990 ± 0.077	1.127± 0.005	1.159± 0.015	1.098± 0.008
Integrated	1.018± 0.050	1.069± 0.084	0.974± 0.056	1.089 ±0.002	1.081±0.005	1.085±0.003
Tsallis-q parameter obtained in each multiplicity bin and event shape for $\sqrt{s}$ = 5.02 TeV						
0 - 10	1.057±0.062	1.062±0.037	1.019± 0.090	1.114 ±0.061	1.102± 0.080	1.104±0.020
10 - 15	1.020±0.064	1.050±0.020	0.988± 0.051	1.074 ±0.042	1.115 ± 0.055	1.050±0.035
15 - 20	1.000±0.028	1.060±0.078	1.003± 0.079	1.061 ± 0.046	1.111 ± 0.090	1.048±0.060
20 - 30	1.037± 0.027	1.080±0.054	0.969± 0.058	1.091± 0.040	1.137 ± 0.063	1.080±0.081
30 - 40	1.008±0.028	1.084±0.042	0.953± 0.071	1.106 ±0.053	1.133 ± 0.053	1.104± 0.062
40 - 150	1.028±0.027	1.060±0.025	0.987± 0.028	1.106±0.090	1.152 ± 0.074	1.098±0.042
Integrated	1.033± 0.004	1.073± 0.014	1.020± 0.001	1.089± 0.002	1.083± 0.006	1.097± 0.004

Table 6.3: The extracted non-extensive parameters (q) from Tsallis distribution fitting (Equation 6.4) to the p_{T} spectra of J/ψ along with statistical uncertainty in different multiplicity bins for pp collisions at $\sqrt{s}$ = 5.02 and 13 TeV.

Bibliography

[1] W. Li, CMS Collaboration, "Correlations and Fluctuations Measured by the CMS Experiment in pp and Pb-Pb", J. Phys. G38 (2011) 124027.

[2] V. Khachatryan et al., CMS Collaboration, "Observation of Long-Range Near-Side Angular Correlations in Proton-Proton Collisions at the LHC", J. High Energy Phys. 1006 (2010) 091.

[3] J. Adam et al., ALICE Collaboration, "Enhanced Production of Multi-Strange Hadrons in High-Multiplicity Proton-Proton Collisions", Nature Phys. 13 (2017) 535.

[4] B. Abelev et al., ALICE Collaboration, "J/ψ Production as a Function of Charged Particle Multiplicity in pp Collisions at $\sqrt{s} = 7$ TeV", Phys. Lett. B712 (2012) 165.

[5] D. Adamová et al., ALICE Collaboration, "J/ψ Production as a Function of Charged-Particle Pseudorapidity Density in p-Pb Collisions at $\sqrt{s_{\rm NN}} = 5.02$ TeV", Phys. Lett. B776 (2018) 91.

[6] D. Thakur, ALICE Collaboration, "Quarkonium Production as a Function of Charged Particles Multiplicity in pp and p-Pb Collisions Measured by ALICE at the LHC", PoS HardProbes2018 (2019) 164.

[7] S. G. Weber, ALICE Collaboration, "Measurement of J/ψ Production as a Function of Event Multiplicity in pp Collisions at $\sqrt{s} = 13\,\text{TeV}$ with ALICE", Nucl. Phys. A967 (2017) 333.

[8] T. Sjostrand et al., "A Brief Introduction to PYTHIA 8.1", Comput. Phys. Commun. 178 (2008) 852.

[9] E. G. Ferreiro et al., "High Multiplicity pp Events and J/ψ Production at LHC", Phys. Rev. C86 (2012) 034903.

[10] B. Z. Kopeliovich et al., "J/ψ in High-Multiplicity pp Collisions: Lessons from pA collisions", Phys. Rev. D88 (2013) 116002.

[11] D. Thakur et al., "Role of Multiparton Interactions on J/ψ Production in p+p Collisions at LHC Energies", Phys. Rev. D97 (2018) 094002.

[12] A. Banfi et al., "Phenomenology of Event Shapes at Hadron Colliders", J. High Energy Phys. (2010) 038.

[13] G. Aad et al., ATLAS Collaboration, "Measurement of Charged-Particle Event Shape Variables in $\sqrt{s}$ = 7 TeV Proton-Proton Interactions with the ATLAS detector", Phys. Rev. D88 (2013) 032004.

[14] A. Ortiz, "Experimental Results on Event Shapes at Hadron Colliders", Adv. Ser. Direct. High Energy Phys. 29 (2018) 343, ISBN: 978-981-3227-75-0.

[15] S. Tripathy et al., "Event Shape and Multiplicity Dependence of Freeze-out Scenario and System Thermodynamics in Proton+Proton Collisions at $\sqrt{s}$ = 13 TeV", arXiv:1905.07418 [hep-ph].

[16] A. Khuntia et al., "Event Shape Engineering and Multiplicity Dependent Study of Identified Particle Production in Proton+Proton Collisions at $\sqrt{s}$= 13 TeV using PYTHIA", arXiv:1811.04213 [hep-ph].

[17] E. Cuautle et al., "Mid-Rapidity Charged Hadron Transverse Spherocity in pp Collisions Simulated with PYTHIA" Nucl. Phys. A941 (2015) 78.

[18] B. I. Abelev et al., STAR Collaboration, "Strange Particle Production in p+p Collisions at $\sqrt{s}$ = 200 GeV", Phys. Rev. C75 (2007) 064901.

[19] A. Adare et al., PHENIX Collaboration, "Identified Charged Hadron Production in p+p Collisions at $\sqrt{s}$ = 200 and 62.4 GeV", Phys. Rev. C83 (2011) 064903.

[20] K. Aamodt et al., ALICE Collaboration, "Production of Pions, Kaons and Protons in pp Collisions at $\sqrt{s}$ = 900 GeV with ALICE at the LHC", Eur. Phys. J. C71 (2011) 1655.

[21] B. Abelev et al., ALICE Collaboration, "Neutral Pion and η Meson Production in Proton-Proton Collisions at $\sqrt{s}$ = 0.9 TeV and $\sqrt{s}$ =7 TeV", Phys. Lett. B717 (2012) 162.

[22] B. Abelev et al., ALICE Collaboration, "Multi-Strange Baryon Production in pp Collisions at $\sqrt{s}$ = 7 TeV with ALICE", Phys. Lett. B712 (2012) 309.

[23] A. Khuntia et al., "Multiplicity Dependence of Non-extensive Parameters for Strange and Multi-Strange Particles in Proton-Proton Collisions at $\sqrt{s}$ = 7 TeV at the LHC", Eur. Phys. J. A53 (2017) 103.

[24] B. Abelev et al., ALICE Collaboration, "Transverse Sphericity of Primary Charged Particles in Minimum Bias Proton-Proton Collisions at $\sqrt{s}$ = 0.9, 2.76 and 7 TeV", Eur. Phys. J. C72 (2012) 2124.

[25] R. Hagedorn, "Statistical Thermodynamics of Strong Interactions at High-Energies", Nuovo Cim. Suppl. 3 (1965) 147.

[26] C. Michael et al., "Consequences of Momentum Conservation for Particle Production at Large Transverse Momentum", J. Phys. G3 (1977) L151; C. Michael, "Large Transverse Momentum and Large Mass Production in Hadronic Interactions", Prog. Part. Nucl. Phys. 2 (1979) 1.

[27] G. Arnison et al., UA1 Collaboration, "Transverse Momentum Spectra for Charged Particles at the CERN Proton-Antiproton Collider", Phys. Lett. B118 (1982) 167.

[28] R. Hagedorn, "Multiplicities, p_T Distributions and the Expected Hadron $\rightarrow$ Quark - Gluon Phase Transition", Riv. Nuovo Cim. 6N10 (1983) 1.

[29] J. Cleymans et al., "The Tsallis Distribution in Proton-Proton Collisions at $\sqrt{s} = 0.9$ TeV at the LHC", J. Phys. G39 (2012) 025006.

[30] D. Thakur et al., "Indication of a Differential Freeze-out in Proton-Proton and Heavy-Ion Collisions at RHIC and LHC energies", Adv. High Energy Phys. 2016 (2016) 4149352.

[31] S. Acharya et al., ALICE Collaboration, "Energy Dependence of Forward-Rapidity J/ψ and ψ(2S) Production in pp Collisions at the LHC", Eur. Phys. J. C77 (2017) 392.

[32] S. Acharya et al., ALICE Collaboration, "Inclusive J/ψ Production at Mid-Rapidity in pp Collisions at $\sqrt{s} = 5.02$ TeV", J. High Ener. Phys. 10 (2019) 084, arXiv:1905.07211 [nucl-ex].

[33] Pythia8 Online Manual.
http://home.thep.lu.se/$\sim$torbjorn/pythia81html/Welcome.html

[34] R. Corke et al., "Interleaved Parton Showers and Tuning Prospects", J. High Energy Phys. 03 (2011) 032.

[35] S. Deb et al., "Multiplicity Dependence of J/ψ Production and QCD Dynamics in $p + p$ Collisions at $\sqrt{s} = 13$ TeV", arXiv:1808.01841 [hep-ph].

[36] C. Bierlich et al., "Effects of color Reconnection on Hadron Flavor Observables", Phys. Rev. D92 (2015) 094010.

[37] B. Abelev et al., ALICE Collaboration, "Multiplicity Dependence of the Average Transverse Momentum in pp, p-Pb, and Pb-Pb Collisions at the LHC", Phys. Lett. B727 (2013) 371.

[38] A. Ortiz et al., "Universality of the Underlying Event in pp Collisions", Phys. Rev. D96 (2017) 114019.

[39] S. Acharya et al., ALICE Collaboration, "Charged-Particle Multiplicity Distributions Over a Wide Pseudorapidity Range in Proton-Proton Collisions at $\sqrt{s} = 0.9$, 7, and 8 TeV", Eur. Phys. J. C77 (2017) 852.

[40] S. Acharya et al., ALICE Collaboration, "Multiplicity Dependence of Light-Flavor Hadron Production in pp Collisions at $\sqrt{s} = 7$ TeV", Phys. Rev. C99 (2019) 024906.

[41] J. Adam et al., ALICE Collaboration, "Measurement of Pion, Kaon and Proton Production in Proton-Proton Collisions at $\sqrt{s} = 7$ TeV", Eur. Phys. J. C75 (2015) 226.

[42] F. Colamaria et al., ALICE Collaboration, "Heavy-Flavor Correlations and Multiplicity Dependence in pp and p-Pb Collisions with ALICE", Nucl. Phys. A956 (2016) 497.

[43] A. O. Velasquez et al., "Color Reconnection and Flowlike Patterns in pp Collisions", Phys. Rev. Lett. 111 (2013) 042001.

[44] M. Baumgart et al., "Probing Quarkonium Production Mechanisms with Jet Substructure", J. High Energy Phys. 11 (2014) 003.

[45] R. Aaij et al., LHCb Collaboration, "Study of J/ψ Production in Jets", Phys. Rev. Lett. 118 (2017) 192001.

[46] G. Bencédi, ALICE Collaboration, "Event-shape- and Multiplicity-Dependent Identified Particle Production in pp Collisions at 13 TeV with ALICE at the LHC", Nucl. Phys. A982 (2019) 507.

[47] S. Acharya et al., ALICE Collaboration, "Event-Shape and Multiplicity Dependence of Freeze-out Radii in pp Collisions at $\sqrt{s}$ =7 TeV", J. High Ener. Phys. 09 (2019) 108.

[48] S. Chatrchyan et al., CMS Collaboration, "Jet and Underlying Event Properties as a Function of Charged-Particle Multiplicity in Proton-Proton Collisions at $\sqrt{s} = 7$ TeV", Eur. Phys. J. C73 (2013) 2674.

[49] V. Khachatryan et al., CMS Collaboration, "Evidence for Collectivity in pp Collisions at the LHC", Phys. Lett. B765 (2017) 193.

[50] L. Marques et al., "Description of High-Energy pp Collisions Using Tsallis Thermodynamics: Transverse Momentum and Rapidity Distributions", Phys. Rev. D91 (2015) 054025.

[51] W. M. Alberico et al., "Nonextensive Statistics, Fluctuations and Correlations in High-Energy Nuclear cCollisions", Eur. Phys. J. C12 (2000) 499.

Chapter 7

Correlations and event-by-event fluctuations in relativistic heavy-ion collisions

Any physical quantity measured in an experiment is subject to fluctuations. These fluctuations depend on the property of the system under study and are envisaged to provide useful information about nature of the system [1, 2, 3]. As regards the relativistic nucleus-nucleus (AA) collisions, the system so created is a dense and hot fireball consisting of hadronic and (or) partonic matter [1, 4]. One of the main aims of such a study is to investigate the existence of partonic matter in the early life of the fireball. Study involving fluctuations in relativistic AA collisions helps check the idea that fluctuations of a thermal system are directly related to the various susceptibilities [1, 2, 4, 5] and could usefully serve as an indicator of possible phase transitions. A key problem in search of dense partonic matter or qurak-gluon plasma (QGP) is to identify its signatures by studying the experimental observables. Besides the most likely signals, such as the direct production of dileptons, photons and flavour contents, correlation and non-statistical fluctuations are believed to be associated with the critical phenomena in the vicinity of phase transition and lead to local global differences in the events produced under similar initial conditions. Thus, the large event-by-event (ebe) fluctuations, if observed, might be a signal for the formation of a distinct class of events produced via formation of QGP [1, 5, 6, 7, 8], as under extreme conditions of energy density and temperature, a novel phase of matter, 'the QGP' is

expected to be formed. The search for occurrence of phase transition from hadronic matter to QGP in the collisions of sufficiently heavy nuclei at relativistic energies still remains a favorite topic of interest of high energy physicists [9, 10, 11, 12, 13]. Collisions of sufficiently heavier nuclei at extremely high energies are believed to be the best site to search for such a phase transition [1]. However, even if the conditions of QGP formation, are achieved, not all the events will be produced through QGP, because it is not yet known that how large will be the cross-section for QGP formation. Hence, to search for the QGP formation, one has to look for such special events of interest on the ebe basis [14].

A major contribution to the observed fluctuations results due to finite number of particles used to define an observable in a given event. These fluctuations are termed as the statistical fluctuations and can be evaluated by considering the independent emission of particles or by event mixing technique [15, 16]. The other fluctuations , if present will be of dynamical origin and may be classified into two categories: (i) fluctuations which do no change on ebe basis, such that, two particle correlations due to Bose-Einstein statistics or due to decays of resonances and (ii) fluctuations exhibiting variations on ebe basis, generally referred to as the ebe fluctuations. Examples are: fluctuations in charged to neutral particle multiplicity ratio due to creation of regions of disoriented chiral condensate (DCC) or creation of jets which contribute to the high transverse momentum (p_t) tail of p_t distribution. DCC is a region in space in which chiral order parameter points in a direction in isospin space, which is different from what is favoured by the true vacuum [17]. DCC formation may produce a spectacular event structure within a region of detector dominated by charged pions and the other by neutral pions. This behaviour may have been observed in Centauro events [17, 18, 19, 20]. It may be of interest to know whether there exist some mechanisms through which DCC creation in high energy AA collisions can be explained [1].

If these mechanisms involve the occurrence of QGP phase transition in an essential way, the DCC formation may help draw definite conclusions about the QGP formation [1, 17]. Occurrence of ebe fluctuations of dynamical origin have been reported by

several workers [21, 22, 23, 24, 25, 26, 27]. Various hadronic observables produced in central Pb-Pb collisions have been found [2, 26, 28] to exhibit qualitative changes in their energy dependence in the SPS energy range. A comparison of these observables with the prediction of hadronic transport or(and) statistical model(s) indicates that the experimental results are quite consistent with the expected signals of the onset of a phase transition in AA collisions at SPS energies [26, 28, 29]. However, most of these investigations are based on data collected using the detectors of limited acceptance. This not only reduces the particle multiplicity but may also distort some useful event characteristics. Needless to emphasize that experimental data collected using conventional nuclear emulsion technique has two main advantages over the data from other detectors : (i) its 4π solid angle coverage and (ii) data are free from biases due to full phase space coverage [1, 14]. Although the incident energies of the data used in the present study are not too high, yet it is expected that the findings based on the various aspects of ebe fluctuations and their comparisons with the theoretical models and correlation free Monte Carlo (MC) data samples might lead to make some interesting observations and help identify some baseline contribution to the ebe fluctuations .

Six samples of events used in the present study are taken from the series of emulsion experiments carried out by EMU01 collaboration [30, 31, 32, 33, 34, 35]. The following emulsion stacks were used in these experiments:

- $^{30-40}NIKFI$ BR-2 nuclear emulsion pellicles with dimensions $10 \times 20 \times 0.05$ cm^3, exposed to 4.5 A GeV ^{16}O beam from SF Dubna.
- $^{30}NIKFI$ BR-2 nuclear emulsion pellicles with dimensions $10 \times 20 \times 0.06$ cm^3 (10 stacks) or $10 \times 10 \times 0.06$ cm^3 (6 stacks) exposed to ^{16}O ion beams at AGS, BNL at 14.6A GeV and SPS, CERN at 60A and 200A GeV.
- $^{30}NIKFI$ 12 BR-2 nuclear emulsion with 30 pellicles with dimensions $10 \times 10 \times$ 0.06 cm^3 (6 stacks) exposed to ^{32}S ion beams at SPS, CERN at 200A GeV.
- A gold foil of 250 μm thickness, after 780 μm thick two sheets of polystyrene

coated with 220 μm thick emulsion layers on both sides, was used for the ^{32}S-Gold exposures.

In horizontally exposed pellicles, interaction were searched for by along-the-track scanning method. This method gives a reliable minimum bias event sample because of its high detection efficiency [16, 33]. Each track was picked up from the entry point and followed up to 6-7 cm. Interactions occurring within 2-5 cm from the edge of the plates were selected for measurements and analysis. Events found at distances $>$ 5 cm from the front edge were not considered because for such events measurement were difficult due to background of secondary particles. The tracks of the produced particles were identified [16, 30, 31, 36] on the basis of their ionization. The tracks having ionization, $I < 1.4I_0$, where I_0 is the minimum ionization produced by a singly charged relativistic particle, are termed as the shower tracks. These tracks are caused by newly created particles, mostly pions with a mixture of kaons, etc, and protons with $\beta > 0.7$ [37]. The number of such track in an event is denoted by n_s. The tracks with ionization in the range, $1.4I_0 \leq I \leq 10I_0$ are referred to as the grey tracks and their number in an event is represented by n_g. These are mostly knocked-out target protons with a mixture of low energy pions $0.3 < \beta < 0.7$ and having energy between 40-400 MeV. The tracks with ionization $I > 10I_0$ are called the black tracks and their number in an event is denoted by n_b. These tracks are produced due to the evaporation fragments from the target with relative velocity, $\beta < 0.3$ and energy $<$ 40 MeV. The grey and the black tracks are collectively called as the heavily ionizing tracks, and the number of these tracks in an event is denoted by $n_h = (n_b + n_g)$. Events having their n_h value greater than 7 are envisaged to be produced exclusively due to the interactions with AgBr group of nuclei whereas those having $n_h \leq 7$ are produced due to interaction with H or CNO group of nuclei or due to the peripheral collisions with AgBr group of nuclei [16, 38, 39]. The spectator projectile fragments (PFs) of charge $z = 1$, (protons) are usually produced within a narrow forward cone of angle $\theta < \theta_c = 0.2/\rho$. Complying these criteria, the data sample collected and available in our laboratory, which have been used for the present analysis and are listed in Table 7.1.

In order to compare the findings of the present work with the predictions of A Multi Phase Transport (AMPT) model, matching number of events equal to the experimental ones are simulated using the code, ampt-v1.21-v2.21 [40]. The events are simulated by taking into account the percentage of interactions which occur in collisions of the projectile with various targets in emulsion [16, 30]. Thus, the interactions with Ag and Br targets were set to occur in the proportion of 30.0 and 25.9, respectively. The value of impact parameter for each data sample was so set that the mean multiplicities of the relativistic charged particles, $< n_s >$ turn out to be nearly equal to those obtained for the real data. Furthermore, in order to search for the evidence of fluctuations of dynamical origin, if any, the results are compared with those obtained from the analysis of the data free from the dynamical correlations. The technique of event mixing gives such a reference data sample where dynamical correlations among the particles are completely destroyed. The mixed event samples corresponding to the real and AMPT data sets are simulated by adopting the standard procedure [16, 41], according to which a mixed event with 'n' number of particles is generated by randomly picking up one particle from each of the 'n' events selected randomly from the original sample. Thus, in a mixed event, there will be no two particles coming from the same event.

Energy (A GeV)	Type of Interaction	Events
4.5	^{16}O-AgBr	1200
14.5	^{16}S-AgBr	370
60	^{16}S-AgBr	422
200	^{32}O-AgBr	223
200	^{32}O-AgBr	452
200	^{32}S-Au	542

Table 7.1: Details of data sets used in the present analysis.

7.1 Event-by-event fluctuations

7.1.1 Presence of high density phase region

As mentioned earlier, even if the conditions for the QGP formations are achieved, not all the events would produce QGP. The search for such rare events from a large sample of events is, therefore, not an easy task and one has to find possible ways to characterize each event which, in turn, may lead to triggering of various classes of events and may help identify anomalous feature. A search is, therefore, to be carried out for the events having high density phase region, where a lot of entropy is confined within a narrow domain. These high density regions in one dimensional distributions are usually referred to as the 'hot regions' or spikes [1, 14, 42]. A parameter, d_{ik} has been introduced [14] for searching spikes or 'hot regions', if present in an event. d_{ik} measures local deviation from the average particle density in units of statistical errors. For a given distribution, d_{ik} for i^{th} bin of k^{th} event is defined as [14]:

$$d_{ik} = \left(n_{ik} - \frac{N_k}{< N >} < n_{ik} > \right) / \sigma_{ik} \tag{7.1}$$

where n_{ik} denotes the relativistic charged-particle multiplicity in i^{th} bin of k^{th} event, N_k represents the multiplicity of the k^{th} event, $\sigma_{ik}(= \sqrt{n}_{ik})$ is the statistical error and $< N >$ is the mean multiplicity of the sample.

d_{ik} distributions in the pseudorapidity, η , space for ^{32}S-AgBr and ^{32}S-Gold collisions at 200A GeV/c are compared with a reference distributions in Figure 7-1. These two data sets have been chosen from the available sets required for this type of analysis because of their high multiplicities. For the other data sets frequent occurrence of spikes is not expected as the particle multiplicities are not high enough. The reference distribution corresponding to the two real event samples are obtained by carrying out parallel analyses of the corresponding mixed events. The η-bin width is fixed to be 0.2. It may be noted from the figure that the d_{ik} distributions for the real

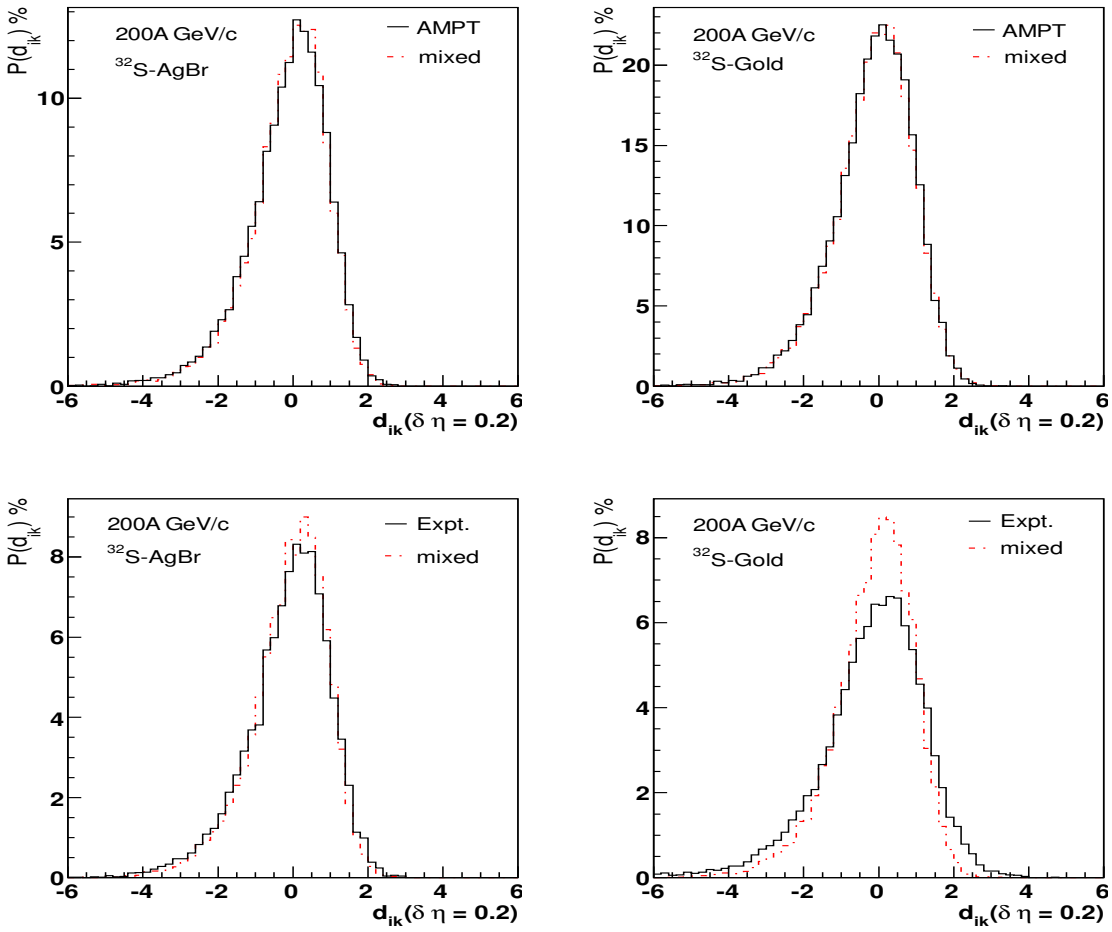

Figure 7-1: d_{ik} distributions for the experimental and AMPT events compared with the mixed events.

data have relatively longer tails in the region of high d_{ik} values. Such a tail is rather more prominent in the case of ^{32}S-Gold collisions. This fact is more prominently reflected in Figure 7-2, where the distributions of the differences of d_{ik} values of the real data and mixed events are plotted. This indicates that the real data might have some events with 'hot regions' or spikes in the η space. Spikes or 'hot regions' are defined as the regions having relatively larger d_{ik}. The value of d_{ik}, showing a spike has been taken as $d_{ik} \geq 2.5$ by Cherry et al [14, 42]. The same value of d_{ik} is also taken in the present study to identify a spike for ^{32}S-Gold collisions at 200 A GeV while for ^{32}S-AgBr collisions at the same incident energy, this value is taken to be 2.2. The reason for taking a somewhat smaller value of d_{ik} is to have a small percent

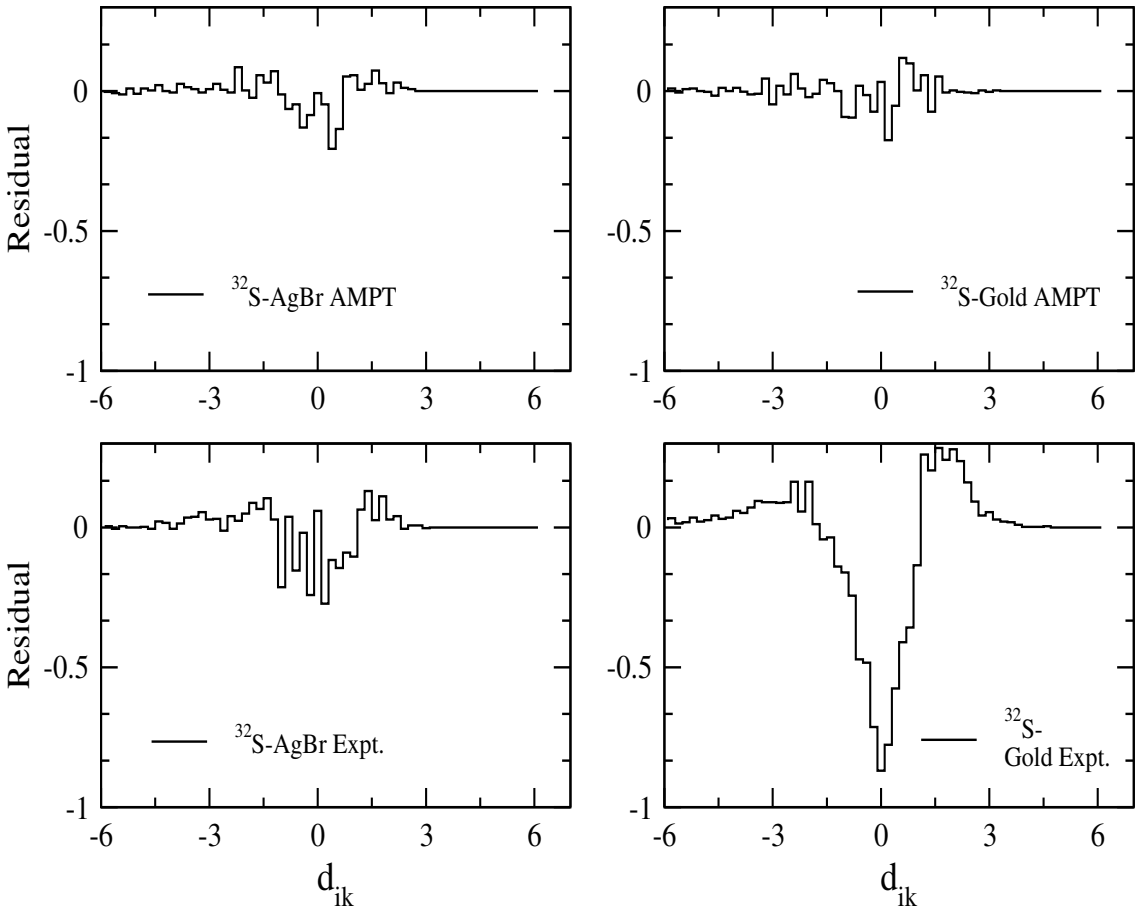

Figure 7-2: The residual distributions of differences between the real to AMPT data and corresponding mixed event d_{ik} spectra.

of the total events so that this sub-sample of events may have a reasonable statistics for further analysis. On taking $d_{ik} \geq 2.5$ for ^{32}S-AgBr collisions, only a few events are available and this number is too small to be considered as statistically reliable for further analysis. It has, however, been ensured before considering $d_{ik} \geq 2.2$ for ^{32}S-AgBr collisions that the values of various parameters linked with intermittency and clusterization, to be discussed in the coming section, are found to be almost identical for $d_{ik} = 2.2$ and 2.5. This fact is clearly reflected in Figure 7-3, in which $\ln F_2$ values are plotted against lnM values for the two data sets, taking $d_{ik} = 2.2$ for ^{32}S-AgBr and 2.5 for ^{32}S-Gold collisions. It is evident from the figure that the variations of $\ln F_2$ with lnM for the two d_{ik} cuts are essentially similar [1].

The probability of occurrence of spikes, $P(d_{ik})$ and the average sizes of the spikes,

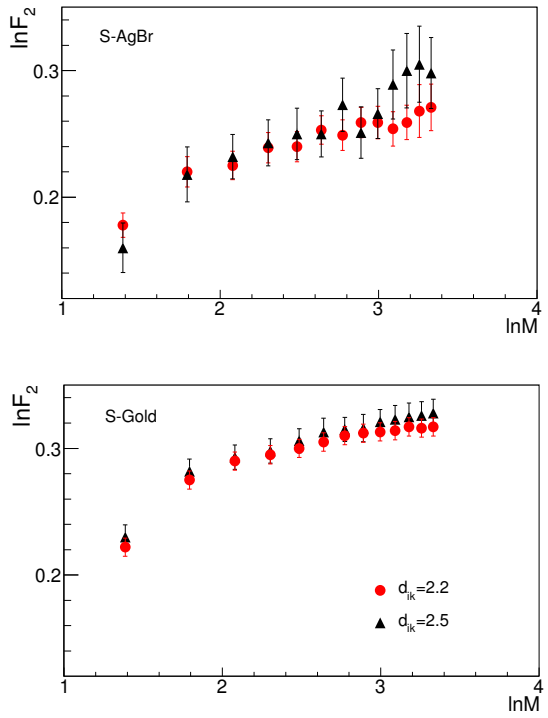

Figure 7-3: Variations of lnF_2 with lnM for ^{32}S-AgBr and ^{32}S-Gold collisions for d_{ik} cuts 2.2 and 2.5, respectively.

Type of interactions		Expt.		Mixed	
		$\Delta\eta = 0.1$	$\Delta\eta = 0.2$	$\Delta\eta = 0.1$	$\Delta\eta = 0.2$
^{32}S-AgBr	$P(d_{ik})$	0.19	0.39	0.15	0.27
	$< d_{ik} >$	2.41 $\pm$ 0.18	2.44 $\pm$ 0.22	2.34 $\pm$ 0.16	2.36 $\pm$ 0.17
^{32}S-Gold	$P(d_{ik})$	0.38	1.33	0.02	0.10
	$< d_{ik} >$	2.79 $\pm$ 0.25	2.98 $\pm$ 0.45	2.91	2.78 $\pm$ 0.23
		AMPT		Mixed	
^{32}S-AgBr	$P(d_{ik})$	0.11	0.20	0.06	0.08
	$< d_{ik} >$	2.37 $\pm$ 0.18	2.45 $\pm$ 0.20	2.28 $\pm$ 0.11	2.36 $\pm$ 0.12
^{32}S-Gold	$P(d_{ik})$	0.06	0.08	0.04	0.06
	$< d_{ik} >$	2.65 $\pm$ 0.11	2.76 $\pm$ 0.22	2.61 $\pm$ 0.08	2.65 $\pm$ 0.14

Table 7.2: Probability(%) of occurrence and mean values of $< d_{ik} >$ for spikes with $d_{ik} \geq 2.5$ for ^{32}S-Gold and with $d_{ik} \geq 2.2$ for ^{16}S-AgBr interactions

.

$< d_{ik} >$ with $d_{ik} \geq 2.5$ for ^{32}S-Gold and $d_{ik} \geq 2.2$ for ^{32}S-AgBr collisions are presented in Table 7.2 for various η bin widths. The distributions of d_{ik} for AMPT and corresponding mixed events are also shown in Figure 7-1, while the distributions of

differences of AMPT and mixed events are plotted in Figure 7-2. It may be noted from the figure that the d_{ik} distributions for the AMPT and the mixed events are almost identical in shapes, particularly in the regions of larger d_{ik} , i.e., $d_{ik} \geq 2.0$. The values of P(d_{ik}) and $< d_{ik} >$ for these data sets are also given in Table 7.2. The following useful inferences may be drawn from Figure 7-1 and 7-2 and Table 7.2:

- Occurrence of spikes is rare but their presence can not be ignored, especially in the case of experimental data.
- For the real data, average sizes of spikes are larger than those obtained for the mixed events. The difference in the d_{ik} values for the real and mixed events are rather more visible for larger η -bin widths.
- For the AMPT sample, d_{ik} values for the data and the corresponding mixed events are nearly the same.

Thus, by examining d_{ik} distributions, rare events having spikes may be separated from those having no 'hot regions' for further analysis.

7.1.2 Factorial Moments

The first investigation dealing with intermittent behaviour in multiparticle production at relativistic energies was based on the single JACEE event analysis [43, 44] in which unexpectedly large local multiplicity fluctuations were observed. However, it was soon realized that intermittency analysis can be carried out using events of any multiplicity provided a proper averaging procedure is adopted [45]. A power law growth of scaled factorial moments (SFMs), F_q , with decreasing phase space bin width, referred to as intermittency, emerged as a new tool to study the non-linear phenomena in high energy hadronic and ion-ion collisions [44, 46, 47, 48, 49].

This method of SFMs has been extensively used [50, 51, 52, 53, 54, 55, 56, 57, 58, 59, 60, 61] to search for the non-linear phenomena in hadron-hadron, hadron-nucleus and A-A collisions in a wide range of incident energies. Methods of SFMs have also been used to study various processes at SPS, RHIC [62] and LHC [60, 61] energies

with the aim to scan the phase diagram in a systematic search for the QCD critical point. Data on ^{12}C-^{12}C, ^{28}Si-^{28}Si and ^{207}Pb-^{207}Pb collisions at 158A GeV/c have been analyzed [62] to search for intermittent fluctuations in transverse dimensions. The investigations have also been carried out for $\pi^+\pi^-$ pairs having invariant mass very close to two pion threshold [62]. It has been reported that the power-law fluctuations in freeze out state of ^{28}Si-^{28}Si collisions approache in size as predicted by critical QCD, while for larger systems, like ^{207}Pb-^{207}Pb, this method can not be applied without entering into the invariant mass region with strong coulomb correlations because in such large systems, high multiplicity of the produced pions combined with the restrictions imposed by the necessity to exclude the coulomb correlations and the resolution of the experiment decrease the sensitivity to the sigma fluctuations near the two pion threshold [1, 62]. The value of intermittency index, ϕ_2, for such case is found to be vanishingly small. Such a small value of ϕ_2, whether due to the effect of high multiplicity or to a genuine non-critical nature of the freeze-out state of the system needs to be looked into. This can not be resolved without penetrating the coulomb region to cross $2m_\pi$.

It has also been pointed out [44, 63, 64, 65, 66, 67] that although there are advantages of the averaging procedure adopted in the intermittency analysis, yet it may not fully account for all the fluctuations a system may exhibit and there are chances that some interesting processes may be suppressed which might be present in the events, e.g., some unique properties due to the presence of QGP would manifest only in few events [68]. A few spiky events are, therefore separated to study intermittent fluctuations and compared with those obtained from the non-spiky event analysis. The distinct difference between the findings from the analyses of spiky and non-spiky events may lead to test each of the spiky events individually to separate out the events of interest. The event factorial moment of order q is defined as [1, 14, 42, 44]

$$F_q^{(e)} = \frac{< n(n-1)....(n-q+1) >_e}{< n >_e^q} \tag{7.2}$$

where 'n' represents particle multiplicity in a particular pseudorapidity bin, q is the

order of moments, while the quantities within angular brackets with subscript e denote the event averaged values.

Type of interaction	Type of events	$< n_s >_{expt.}$	$< n_s >_{AMPT}$
^{32}S-AgBr	all events	199.43 ± 6.20	205.65 ± 4.48
	(spiky)$_{\Delta\eta=0.2}$	309.32 ± 17.31	276.79 ± 18.75
	(non-spiky)$_{\Delta\eta=0.2}$	188.76 ± 6.35	204.21 ± 4.62
^{32}S-Gold	all events	363.28 ± 4.11	357.01 ± 3.51
	(spiky)$_{\Delta\eta=0.2}$	410.36 ± 7.94	368.00 ± 14.34
	(non-spiky)$_{\Delta\eta=0.2}$	350.12 ± 4.57	346.36 ± 3.54

Table 7.3: Values of mean multiplicities of relativistic charged particles for the experimental and AMPT generated events.

In order to estimate the values of F_2 , all the relativistic charged-particles having their η values in the range $\Delta\eta$ (= $y_c \pm$ 3.0) are considered, y_c being center of mass hadron-nucleon rapidity. This $\Delta\eta$ region is then divided into M cells, each of width $\delta\eta$ such that the number of cells are equal to $\Delta\eta/\delta\eta$. The values $F_q^{(e)}$ for q = 2, for the real, AMPT and mixed spiky and non-spiky events are calculated. Spiky and non-spiky events are sorted out by applying d_{ik} cut using Equation 7.2. Events having spikes with d_{ik} = 2.2 and 2.5 for ^{32}S-AgBr and ^{32}S-Gold collisions, respectively were grouped as spiky events, and the remaining ones were taken as non-spiky events. The values of the mean multiplicities of charged-particles $< n_s >$ for the spiky and non-spiky events are listed in Table 7.3. It may be noted from the table that the values of $< n_s >$ for the non-spiky events are closer to those obtained for all the events of the sample. However, for the spiky events, $< n_s >$ is found to be higher in comparison to the one obtained for all the events. This results suggests that spikes or high particle density regions occur more often in the high multiplicity events. Values of F_2 for various M values, by changing M from 2 to 20 in steps of 2 are compared. The trend of variations of F_2 with M, thus obtained for the real and corresponding mixed events are displayed in Figure 7-4. The spiky and non-spiky in the mixed events samples were sorted out by applying the same procedure; first the event mixing was done for each data set and then the d_{ik} cuts were applied. It may be noted from Figure

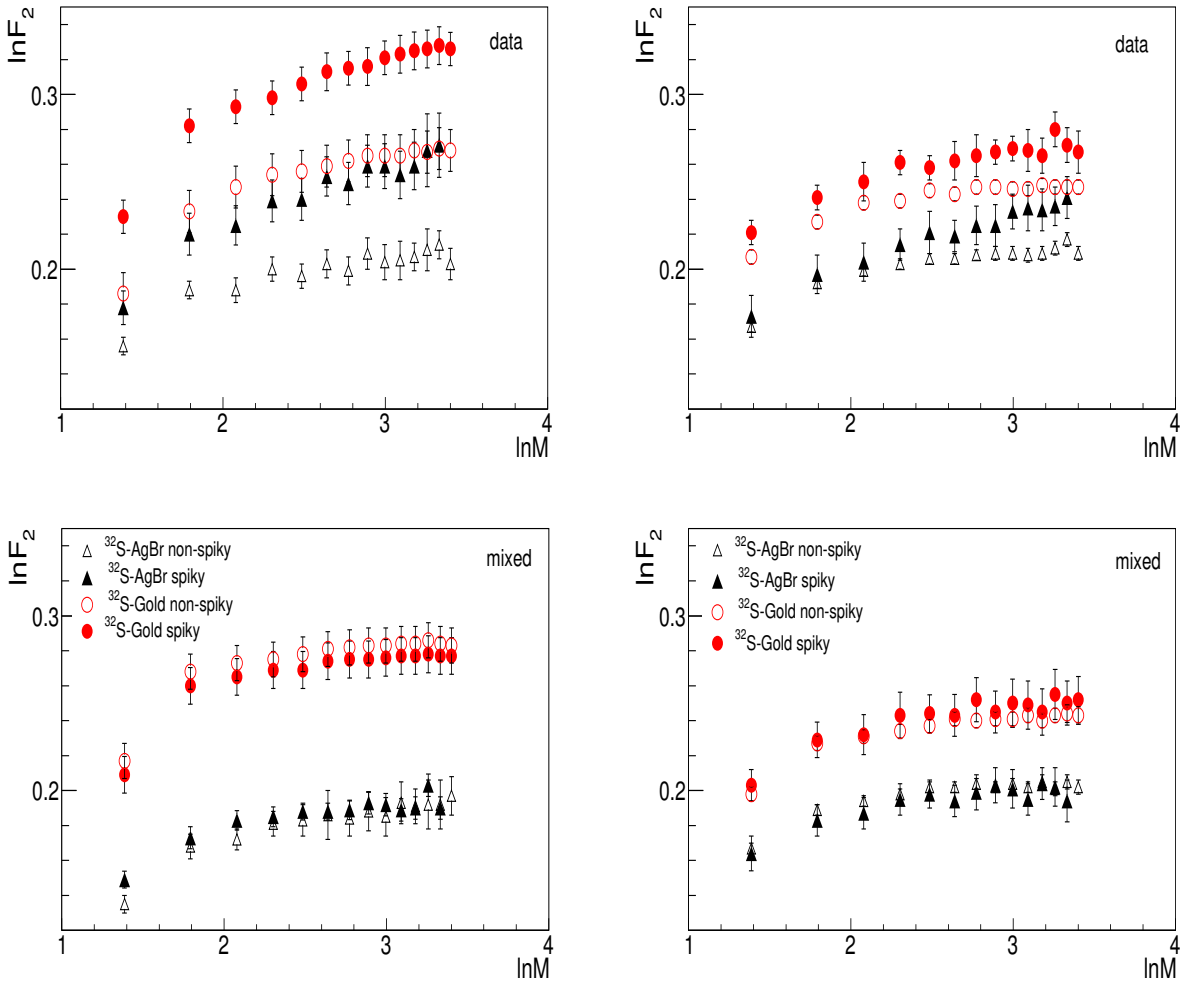

(a) (b)

Figure 7-4: (a) Variations of lnF_2 with lnM for the experimental and mixed event samples. (b) Variations of lnF_2 with lnM for the AMPT and corresponding mixed events.

7-4 that the values of F_2 for the spiky events are significantly larger than those for the non-spiky events. This difference, however, vanishes after mixing the events, i.e., the values of F_2 against M for the two categories of events become almost equal. Furthermore, the values of F_2 , for the AMPT events, plotted against the cell size, M, in Figure 7-4, are seen to be larger for the spiky events as compared to those obtained for the non-spiky ones. However, the difference between the F_2 values for the two types of events is somewhat smaller than those observed for the real events.

As mentioned earlier, intermittent pattern of the multiplicity fluctuations results

in the power law behaviour of the moments [44, 69] of the form:

$$< F_q^{(e)} >= M^{\phi_q}, \quad 0 < \phi_q < q - 1 \tag{7.3}$$

where ϕ_q characterizes strength of the intermittency signal. Hence, a linear dependence of $\ln F_q$ on lnM up to the limit of experimental resolution or the statistical limit is envisaged [69]. The physical significance of F_q is described [44] on the basis of self similar cascade model. The values of ϕ_2 for various data sets are calculated by performing linear fits to the data of the form:

$$ln < F_2 >= A - \phi_2 lnM \tag{7.4}$$

where A is some constant. The fits are performed in the linear regions of the plots. The values of ϕ_2, thus, obtained are listed in Table 7.4. The errors associated with the parameter are statistical ones, determined from the fitting procedure. It is evident from the table that the values of ϕ_2 for the spiky events are larger than those for the non-spiky events. Moreover, the values of ϕ_2 for ^{32}S-AgBr and ^{32}S-Gold collisions are almost the same for the spiky events. However, values of ϕ_2 for the spiky AMPT events are somewhat smaller in comparison to those for the real data, this indicates that the experimental data exhibits larger intermittent fluctuations than those predicted by the AMPT model. As far the non-spiky events are concerned, the values of ϕ_2 for the various data sets are essentially the same and match with those estimated from the mixed event data sets. It may, therefore, be remarked that the method of SFMs seems to be quite suitable for preliminary identification of a distinct class of events showing up significant fluctuations and thereafter more advanced triggering, like particle ratio, enhanced particle multiplicities in certain kinematical regions, etc, may be applied to the selected data sets. It may be noted that the method of SFMs may be successfully applied to the RHIC and LHC data because multiplicities of the particles produced in the central collisions at these energies are quite high, which may allow to apply suitable p_t cut to draw more meaningful conclusions. Also, due to high multiplicities, this method of SFMs may be applied to individual or small sample of rare events,

identified after applying d_{ik} cuts. The analysis of such individual high multiplicity events or smaller sample of events has been argued to be reliable [14, 70, 71] as the statistical fluctuations are treated as under control for such multiplicities.

Data type	^{32}S-AgBr		^{32}S-Gold	
	Spiky	Non-Spiky	Spiky	Non-Spiky
Expt.	0.031 ± 0.003	0.017 ± 0.002	0.030 ± 0.001	0.021 ± 0.002
Mixed	0.012 ± 0.002	0.015 ± 0.002	0.011 ± 0.001	0.011 ± 0.001
AMPT	0.027 ± 0.001	0.012 ± 0.001	0.019 ± 0.002	0.011 ± 0.002
Mixed	0.010 ± 0.001	0.010 ± 0.001	0.014 ± 0.002	0.010 ± 0.001

Table 7.4: Values of ϕ_2 for various data sets.

7.1.3 Clusterization

It is evident from the present study, that there are a few events present in the real data which have high particle density regions and somewhat fewer such events in the case of AMPT simulated data sets. Such regions of high particle density are envisaged to arise due to the decay of a heavier cluster or several clusters or jets of relatively smaller sizes [14, 72]. In order to ensure whether the high particle density regions or spikes present in the selected events are due to some dynamical reasons, presence of clusters or jet-like phenomena are looked into by following the algorithm applied to $p\overline{p}$ collisions [73]. This algorithm is somewhat different to that adopted by us earlier and described in references [74] and [75], where formation of clusters and determination of their sizes were investigated by histogramming the pseudorapidity differences between the n^{th} nearest neighbours. The present method of analysis is rather more suitable for searching the high particle density region in $\eta - \phi$ space, which provides a clear separation in the $\eta - \phi$ metric in the low multiplicity and low particle density final state [14]. In order to test how the jet algorithm works for high particle density data and to what degree of clustering in two dimensional space, analysis of the spiky and non-spiky events must be carried out separately. The method of clustering applied in the present investigation is envisaged to help estimate the cluster frequencies and the cluster multiplicities on ebe basis. Since the observables are very sensitive to the

total event multiplicities, a comparison of the findings from the real and mixed events (with matching multiplicities) may yield to some interesting results.

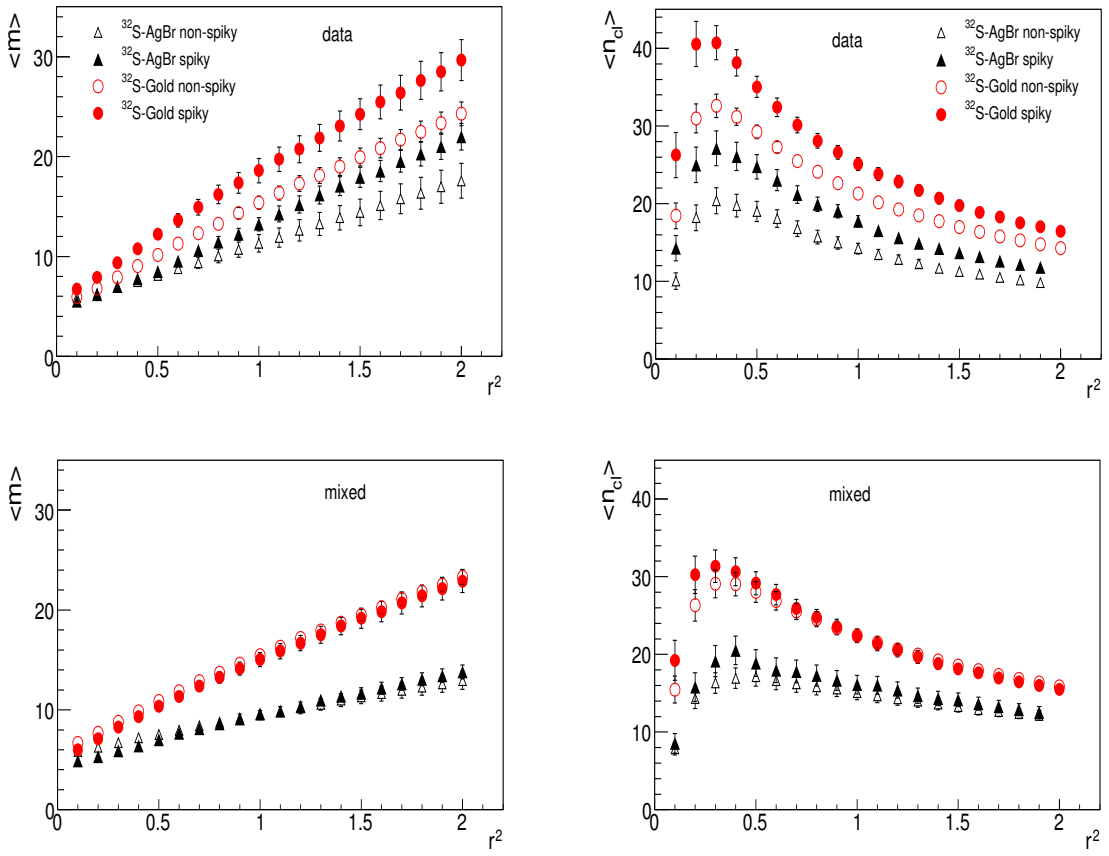

(a) (b)

Figure 7-5: (a) Variations of $< m >$ with r^2 for the experimental and mixed events. (b) $< n_{cl} >$ vs r^2 plots for the experimental and mixed events.

In order to check whether a particle of an event belongs to a certain cluster, we consider a particle i of an event with multiplicity 'n' and calculate its r_{ik} value with respect to the next particle k (k $\neq$ i) using the relation $r_{ik} = \sqrt{(}\delta\eta^2 + \delta\phi^2))$, where, $\delta\eta$ and $\delta\phi$ respectively denote the differences between the pseudorapidities and azimuthal angles of i^{th} and k^{th} particles. This gives a cone of radius r_{ik} which contains i^{th} and k^{th} particles [1, 14, 70, 71]. Thus, starting from 1^{st} particle, i.e., i=1, its r_{ik} value is calculated with respect to $(i+1)^{th}$ particle. If this value is less than a pre-fixed value r, the pair is treated as a cluster of two particles. Once a cluster is

obtained, another particle is added to it and checked whether it may also be grouped in the same cluster by calculating $r_{i,i+2}$ value and comparing with the pre-fixed value r. A cluster is considered to be genuine if it has at least 'm' particles with m≥2. Once a cluster is obtained, another cluster is searched for grouping the remaining particles of the event. It is, however ensured that once a particle is assigned to a particular cluster, it is not again considered while looking for the next cluster. Using this approach, one may conclude the following for a given value of r:

- Number of clusters in each event with each clusters having at least 'm' particles.
- Number of particles in a cluster.

It may be mentioned here that for a very small pre-fixed cone value, r, there may be no or only a few clusters in an event. However, for a very large value of r, almost all the particles of an event will fall into a single large cluster. The number of clusters in an event with (m≥5) and average number of particles in a cluster are determined for various data sets. Variations of mean cluster multiplicity $< m >$ and mean number of clusters $< n_{cl} >$ with r^2 are plotted in Figure 7-5 (a) and (b) for the real and mixed events, respectively. Similar plots for the AMPT events are displayed in Figures 7-6 (a) and (b). The following observations may be made from Figures 7-5 and 7-6.

1. For mixed events: In Figures 7-6 (a) and (b), mean cluster multiplicity, $< m >$ increases from $\sim$ 6 to 10 for ^{32}S-AgBr and 6 to 20 for ^{32}S-Gold collisions. The data points for spiky and non-spiky events overlap and have the same patterns of variations. Variations of $< n_{cl} >$ with r show almost the same ("quiet") pattern for the two categories of events, having broader maxima for r^2 between 0.2-0.3 and thereafter decreases slowly with increasing r^2 values. The maximum values of mean numbers of clusters are found to be 20 and 40 respectively for the collisions due to AgBr and Gold targets.

2. For real events: values of $< m >$ for the spiky events are much higher than those for the non-spiky events, indicating that clustering effects dominate in the case

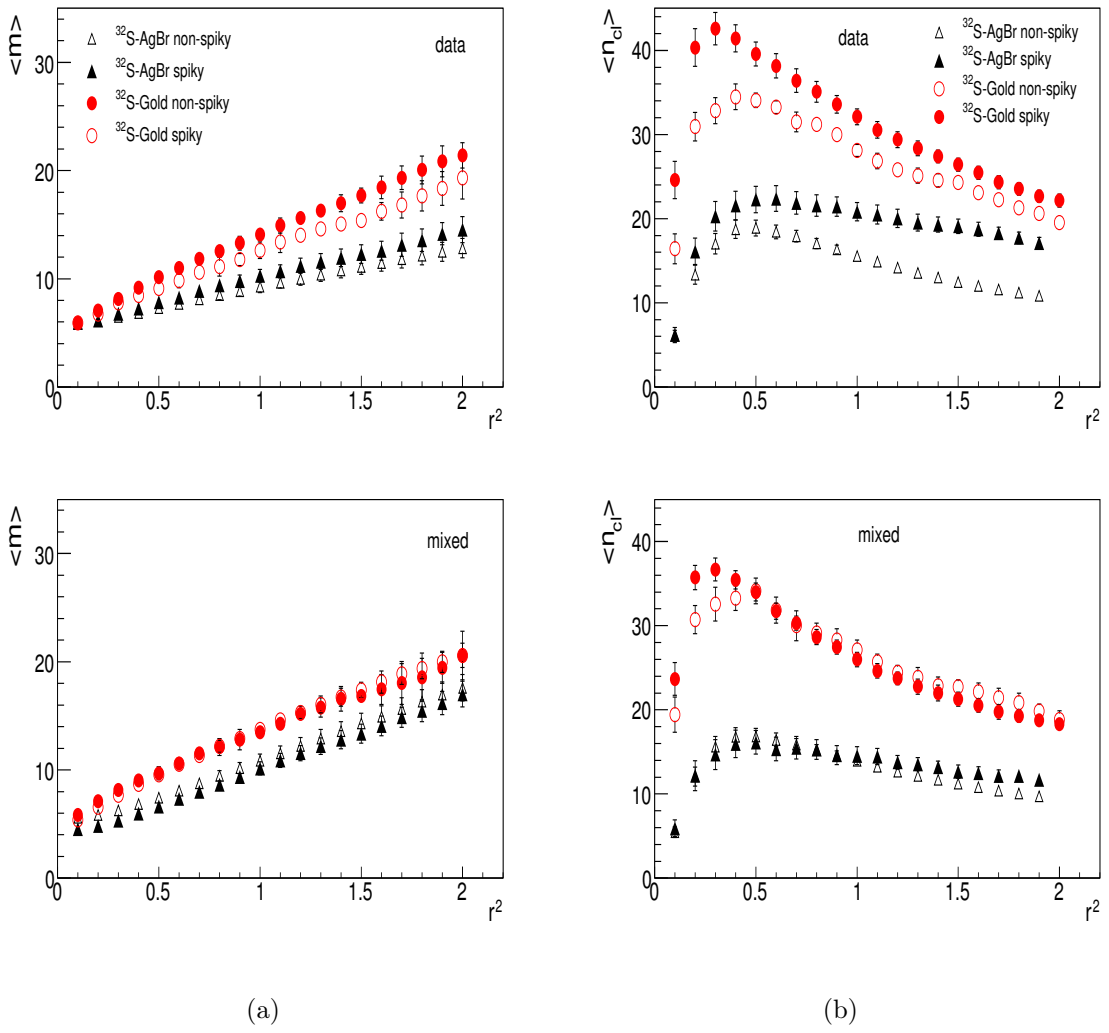

(a) (b)

Figure 7-6: (a) Variation of <m> with r^2 for the AMPT and mixed event samples. (b) $< n_{cl} >$ vs r^2 plots for the AMPT and corresponding mixed events.

of spiky events from $< n_{cl} >$ vs r^2 plots. It is observed that there are relatively more number of clusters present in spiky events as compared to the one present in the non-spiky events. This indicates that the dominant clustering effect in the spiky events is a distinct feature of the data which vanishes after events mixing.

3. For AMPT events: the trends of variations of $< m >$ and $< n_{cl} >$ with r^2 are essentially similar to that observed for the real data but with smaller magnitude. The finding, thus, suggests that AMPT model also predicts particle production through formation of clusters and more clusters of larger sizes are being formed

in the case of spiky events.

On the basis of these observations, it may be remarked that the algorithm used in the present study for investigating clusters or jet-like phenomena seems to be quite suitable to sort out the events having 'hot-regions' or spikes.

7.2 Search for long-range correlations

Studies involving correlations amongst the produced particles in η windows of varying widths are widely accepted as a method for searching the occurrence of phase transition in relativistic heavy-ion collisions [12, 76, 77, 78]. It has been reported [79, 80, 81] that inclusive two-particle correlations have two components: the short-range correlations (SRC) and the long range correlations (LRC). Presence of both SRC and LRC have been observed in hadronic and ion-ion collisions at SPS and RHIC energies [12, 77, 80, 81, 82, 83, 84, 85]. These observed correlations have been interpreted in terms of the concept of clustering [76, 86]; i.e., the particle production occurs via the formation of some intermediate states, commonly termed as 'clusters' which in turn decay isotropically in their centre-of-mass (CM) frame to real physical particles. Useful information about the properties of clusters, for example, size of clusters, mean number of clusters produced in an event and the 'width', i.e., the extent of phase space occupied etc., may be extracted by adopting the method, discussed in the previous section and (or) by studying the two-particle angular correlations [12, 87, 88, 89].

The short-range component of the two-particle correlations has been observed to remain confined within a region, $\eta \sim \pm 1$ unit around mid- rapidity, while the LRC , which arise due to ebe fluctuations of overall particle multiplicity, extend to a rather longer range (> 2 units of η) [76, 79, 80]. LRC have been observed at relatively higher beam energies [19, 76, 77, 79, 80, 90]. The magnitude of LRC , for hadron-hadron collisions, has been reported to increase with increasing beam energies as the non-singly diffractive inelastic cross-section increases with beam energy at $\sqrt{s} > 100$ GeV [91]. This effect has been successfully explained in terms of multiparton interactions [90]. In the case of AA collisions, the multiparton interactions are expected to give rise to

LRC , which would extend to relatively longer range as compared to those observed for hadron-hadron collision at the same beam energy [12, 76, 77, 92, 93]. The color glass condensate (CGC) picture of particle productions and the multiple scattering model also predicts the presence of LRC in AA collisions [77, 84, 92, 94, 95]. The analysis of experimental data on ^{16}O-AgBr collisions at 14.5A, 60A and 200A GeV reveals that the correlations present in the data are of short-range in nature and there is no evidence for the presence of LRC even in ^{16}O-AgBr collisions at 200A GeV/c [76].

After the availability of the data from RHIC and later from LHC , interest in the investigations on particle correlations increased manifolds: because of the idea that modifications of the cluster properties and (or) shortening of the correlation length in the pseudorapidity space, if observed, at these energies would be an indication for the QGP formation [16, 76, 78]. Numerous attempts have been made by experimental and theoretical physicists [6, 77, 81, 83, 89, 96, 97, 98, 99, 100, 101, 102, 103] to study forward-backward (F-B) multiplicity correlations at RHIC and LHC energies. It is, however, essential to identify some baseline contributions to the experimentally observed correlations which do not depend on new physics, for example, formation of some exotic states like DCC or QGP. An attempt is, therefore made to carry out a systematic study of F-B correlations in ^{16}O-AgBr and ^{32}S-AgBr collisions and comparing the findings with those obtained using the other data sets available in our laboratory [76]. It may be mentioned here that such studies would help understand the underlying physics at energies from AGS, SPS to RHIC , like dependence of correlation strength and correlation length on beam energy and system size. Once such dependence is understood, modification in the cluster characteristics or shortening of correlation length might be looked into to search for some new physics.

7.2.1 Formalism

F-B correlations are generally investigated by examining the linear dependence of mean charged particle multiplicity in the backward (B) region, $< n_b >$ on the multiplicity of charged-particles emitted in the forward (F) hemisphere, n_f of the form

$$< n_b >= a + bn_f \tag{7.5}$$

where a is intercept and b measures the slope. For symmetric F and B regions, b is often referred to as the correlation strength and is expressed in terms of expectation values [76, 77, 83, 84, 94]:

$$b = \frac{< n_f n_b > - < n_b >< n_f >}{< n_f^2 > - < n_f >^2} = \frac{D_{bf}^2}{D_{ff}^2} \tag{7.6}$$

where D_{ff} and D_{bf} denote the forward-forward and backward-forward dispersions respectively.

7.2.2 Results and discussion

Pseudorapidity, η distribution of relativistic charged-particles is divided into two parts with respect to its centre of symmetry, η_c. The region with $\eta < \eta_c$ is referred to as the backward (B) region while the region having values $\eta > \eta_c$ is termed as the forward (F) region. The number of relativistic charged-particles produced in F and B regions are counted on event-by-event (ebe) basis and the mean multiplicities in the two regions, $< n_f >$ and $< n_b >$ and dispersions D_{ff} and D_{bf} are calculated. Dependence of $< n_b >$ on n_f for ^{16}O- and ^{32}S-AgBr collisions are displayed in Figure 7-7. The straight lines in the figure are due to the best fits to data obtained using Equation 7.5 and the values of slope parameter, b, are presented in Table 7.5. Values of b for various data sets are also calculated using Equation 7.6 and are listed in the same table.

It may be noted from the table that the values of parameter b obtained from the linear fits match with the corresponding values estimated using Equation 7.6. F-B correlation strength, thus calculated from either way indicates the presence of F-B correlations in both real and simulated data sets. It may also be noted from Table 7.5 that the values of correlation strength b for the two data sets considered are nearly the same. However, the values of this parameter for ^{16}O-AgBr collisions at 14.5, 60,

Energy	b (linear fit)		b=$\frac{D_{bf}^2}{D_{ff}^2}$	
(GeV)	Expt.	AMPT	Expt.	AMPT
^{16}O-AgBr	1.21±0.06	1.08±0.06	1.20±0.03	1.07±0.05
^{32}S-AgBr	1.19±0.03	1.03±0.02	1.18±0.02	1.03±0.03
	Expt*.	HIJING*	Expt*.	HIJING*
14.5A	1.48 ± 0.08	1.01 ± 0.03	1.43 ± 0.05	0.98 ± 0.03
60A	1.30 ± 0.05	1.10 ± 0.03	1.33 ± 0.03	1.10 ± 0.03
200A	1.21 ±0.05	1.07 ± 0.05	1.20 ± 0.05	1.12 ± 0.06

Table 7.5: Values of correlation strength, b and χ^2/ndf for the experimental and AMPT event samples at different projectile energies. * values are taken from reference [76].

and 200A GeV reported earlier to decrease with increasing beam energy [76]. This result suggests that correlation strength in the case of AA collisions decreases with increasing beam energy but remains essentially unchanged with increasing projectile mass. The large values of b at lower energies observed might be due to the dominance of uncorrelated production for which F-B correlations depend on the mean multiplicity and multiplicity fluctuations in the combined F-B regions [12, 76, 79, 80, 101].

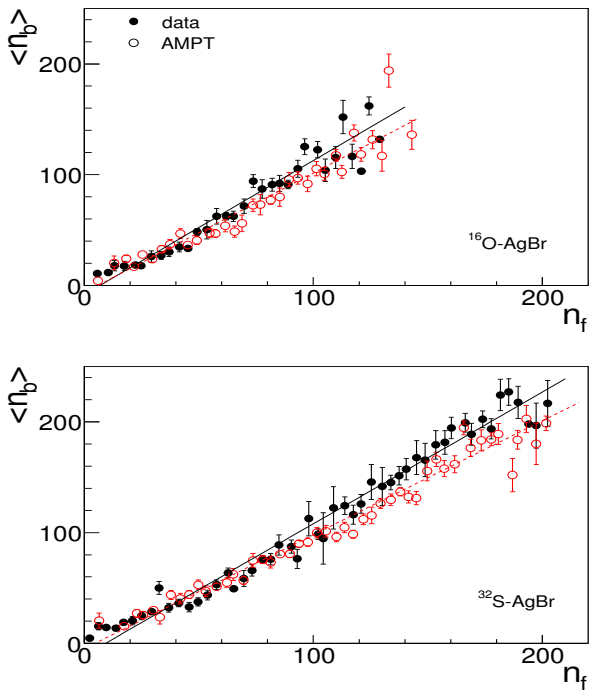

Figure 7-7: Variations of $< n_b >$ with n_f for ^{16}O- and ^{32}S-AgBr collisions. The straight lines represent the best fit to the data obtained using Equation 7.6.

Strong F-B correlations are observed when F and B regions are so chosen that there is no separation gap between the two regions. The reason for considering the F-B regions adjacent to each other is because of the fact that the clusters produced around η_c whose decay product would lie in both F- and B-regions, giving rise to strong SRC . The SRC are envisaged to be confined to a region of $\pm 1\eta$ units around η_c [76, 79, 80]. In order to reduce the contributions from SRC , a gap of $\Delta\eta$ from the centre of symmetry is introduced in both F-and B-regions such that the particles having η values $\eta_c < \eta < \eta_c + \Delta\eta$ in F-region and $\eta_c > \eta > \eta_c - \Delta\eta$ in B-region are not considered while evaluating n_f and n_b. The values of correlation strength b is then determined by evaluating D^2_{ff} and D^2_{bf} using Equation 7.6; the value of $\Delta\eta$ is taken to be 0.25 and then increased in steps of 0.25 until the region η_c+3.0 and η_c-3.0 is covered in F and B regions respectively. Variations of b, with $\Delta\eta$ thus obtained for the real and AMPT events are displayed in Figure 7-8.

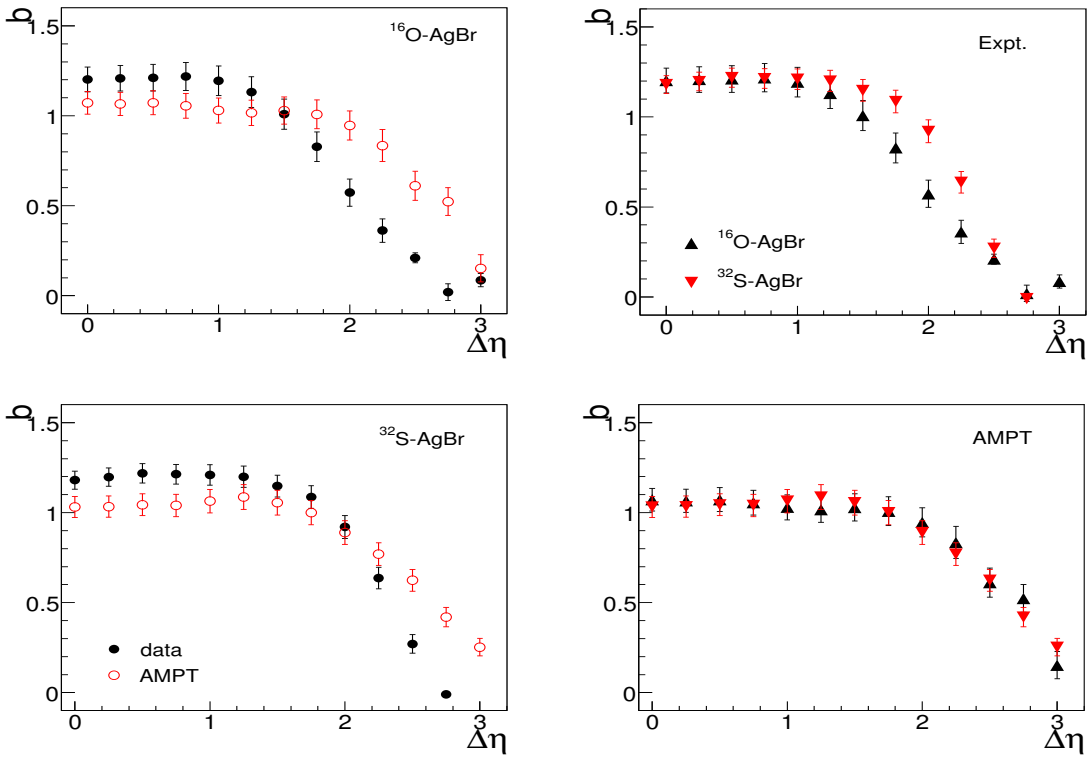

Figure 7-8: Variations of correlation strength b with pseudorapidity window width, $\Delta\eta$ for ^{16}O- and ^{32}S-AgBr collisions for real and AMPT events.

It is observed that the values of b, for both the data sets remain essentially constant up to $\Delta\eta \simeq 1.0$ and thereafter gradually decrease to 0 with increasing $\Delta\eta$. AMPT events too show almost similar trend of variations of b with $\Delta\eta$. But the model predicts somewhat lower values of b in the region of smaller $\Delta\eta$ ($\Delta\eta < 1.25$) and relatively larger values of b in the region of $\Delta\eta \geq 1.5$. The smaller values of b predicted by AMPT model in the region $\Delta\eta \leq 1.25$ might be due to the dominance of uncorrelated production in the AMPT model; the exact reason for uncorrelated production in the AMPT model can not be ascertained. Beyond this region, that is, $\Delta\eta \geq 1.5$, values of b are found to be higher for the AMPT data as compared to the real events. Thus, in the case of AMPT events, F-B correlations are observed to characteristically extend to longer range as compared to those obtained for experimental data. Moreover, nearly the same values of b for both ^{16}O and ^{32}S beams, as is evident from Figure 7-8, indicate that the correlation strength is independent of the mass of the colliding nuclei. This observation is nicely supported by the AMPT model. Some difference in the b values for ^{16}O-AgBr and ^{32}S-AgBr experimental events in the region $\Delta\eta \sim 2.0$ might be because of the fluctuations arising due to limited statistics.

It has been reported [12, 76, 101] that multiplicity distributions have different shapes in different η regions and exhibit large fluctuations in wider η-windows. In order to look for the F-B correlation strength in η windows of varying widths, two small windows of width $\eta_w = 0.25$ are placed adjacent to each other with respect to η_c such that the charged-particles of each event having their η values in the interval $\eta_c \leq \eta < \eta_c + \eta_w$ are counted as n_f while those having their η values lying in the range $\eta_c > \eta \geq \eta_c - \eta_w$ are counted as n_b. Using these value of n_f and n_b, D^2_{ff} and D^2_{bf} and hence correlation strength, b is estimated. The width of the η-windows η_w is then increased in step of 0.25 until entire η region is covered. Dependence of b and η_w for the real and AMPT events are displayed in Figure 7-9. It may be observed from the figure that the values of b first increases gradually as the window becomes wider (up to $\eta_w \sim 2.0$) and thereafter acquire nearly constant values. Similar trends of variations of b with η_w have also been observed in ^{16}O-AgBr collisions at 14.5A, 60A and 200A GeV/c (from the analysis of the data available in the laboratory). It

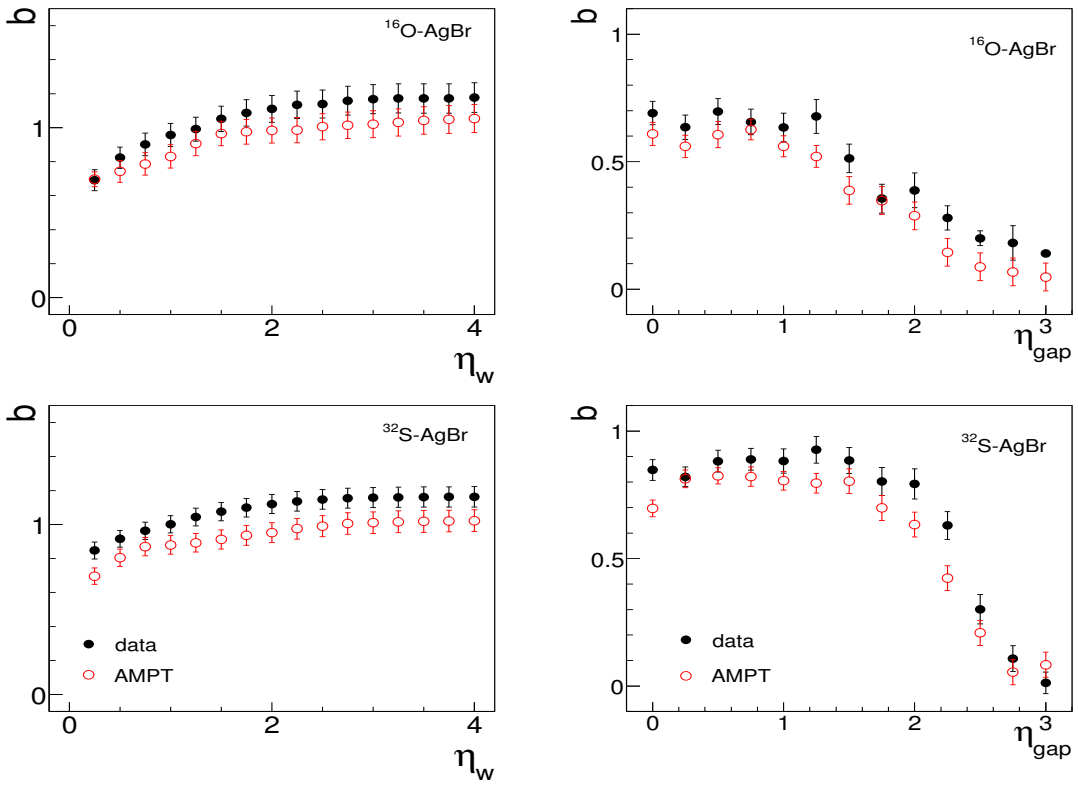

(a) (b)

Figure 7-9: (a) Dependence of b on rapidity window, η_w for ^{16}O- and ^{32}S-AgBr collisions. (b) Dependence of correlation strength, b on separation gap between two symmetric pseudorapidity windows, η_{gap} for various data sets.

may also be of interest to note in Figure 7-9 that although AMPT model predicts the similar trends of variations of b with η_w yet the values of b for any given η_w are somewhat smaller as compared to those obtained from the real data. However the values of b for any given η_w are observed to be independent of the mass of the colliding nuclei. It may be mentioned here that, in the saturation region, i.e., $\eta_w >$ 1.5 values of b, have been found to decrease with increasing beam energy as long as the system size remains the same [76]. Such a decrease is might be due to the increase in the ratio $< n_f > / < n_s >$ even in the limited phase space; $< n_f >$ denotes the average number of charged particles in the F region and while $< n_s >$ is the mean charged particle multiplicity in the considered phase space.

In order to examine the presence of LRC , if any, contribution from SRC is to be

eliminated. For this purpose F-B correlations are studied by adopting the method which has frequently been used, particularly at RHIC and LHC energies [77, 96, 97, 98, 99, 100, 101, 105, 106, 107]. According to this method, η windows of small but equal widths, η_w are placed in F and B regions in such a way that they are separated by equal distances (in η units), η_{gap} with respect to η_c. Thus, all the charged-particles having their η values in the interval $\eta_c + \eta_{gap} \leq \eta < \eta_c + \eta_{gap} + \eta_w$ are counted as n_f where as those having their η values in the range $\eta_c - \eta_{gap} \leq \eta < \eta_c - \eta_{gap} - \eta_w$ are counted as n_b. By varying the value of η_{gap} from 0 to 3.0 on each side of η_c, n_f and n_b are determined to estimate the values of b. Variations of b with η_{gap} for various data sets considered are displayed in Figure 7-9. It may be observed in the figure that the values of b acquire almost a constant value of $\sim$ 0.7 up to η_{gap} $\sim$1.25 for ^{16}O-beam and thereafter quickly falls to zero with increasing η gap values. However, for ^{32}S-beam the values of b are found to remain almost the same up to η_{gap} $\sim$1.75 and then decreases to zero. This indicates that with increasing projectile mass the F-B correlations extend to rather longer range. AMPT data, too, exhibit similar trends of variations of b with η_{gap} except that the values of b are somewhat smaller as compared to the one estimated for the real data. These observed correlation are envisaged to be due to formation of resonance or clusters in the central rapidity region, the decay products of which would lie in both F and B regions [19, 79, 80, 86]. This finding is, however, not conclusive enough to suggest the presence of some LRC but does suggest that the range of F-B correlations extends with increasing projectile mass. The range of F-B correlations has also been observed to increase with beam energy in ^{16}O-AgBr collisions in the incident energy range from 14.5A to 200A GeV/c [76]. It has been argued that the extended range of F-B correlations may be explained from simple statistical considerations of uncorrelated production of charged-particles [101]. Correlations in this range, if observed at higher energies or with heavier projectile might arise due to overall multiplicity fluctuations [19, 77, 79, 80, 101]; such fluctuations in AA collisions may show-up due to the fluctuations in nuclear geometry [101]. It has also been pointed out [34] that before making any conclusive remark about the presence of LRC due to dynamical reasons, it should be ascertained that the observed

F-B correlations are not arising due to overall multiplicity fluctuations by examining the features of multiplicity distributions and F-B correlations simultaneously in the same experiment.

7.3 Fluctuations of voids in relativistic ion-ion collisions

A system undergoing a second order phase transition is envisaged to exhibit large fluctuations and long-range correlations[13, 108]. If the symmetry of the quark system created in heavy-ion collisions is such that the quark-hadron phase transition is of second order then large fluctuations are expected in the multiplicity of hadrons not only from event-to-event but also from one region to the other in the geometrical space in which hadrons are emitted [13, 108]. Such a local hadron density fluctuations would form spatial patterns in which there would be cluster of hadrons in some regions along with the regions having no hadrons in between the adjacent clusters [108, 109]. The occurrence of non-hadronic regions between the regions of clusters, referred to as the voids, may provide a significant insight into the fluctuations associated with the critical behavior of QGP phase transition [109]. Hwa and Zhang [110] have proposed a method to study fluctuations of spatial patterns in terms of voids. However, only a few attempts [109, 111] have been made to study fluctuations of voids in hadronic and ion-ion collisions at high energies. It was, therefore, considered worthwhile to undertake a systematic study of fluctuations of voids by analyzing the experimental data on nucleus-nucleus collisions at different beam energies. Such study may help identify some baseline contributions to the fluctuations of voids.

7.3.1 Method of Analysis

In order to study the fluctuations of voids Hwa and Zhang [110] have proposed a method, whose details are presented elsewhere [109, 110]. According to this method non-flat single particle density distribution in η space is to be made flat in terms of

a cumulative variable, X(η), defined as [50, 112, 113, 114]:

$$X(\eta) = \frac{\int_{\eta_{min}}^{\eta} \rho(\eta) d(\eta)}{\int_{\eta_{min}}^{\eta_{max}} \rho(\eta) d(\eta)} \tag{7.7}$$

where, $\rho(\eta)$ represents single particle rapidity density, whereas η_{min} and η_{max} denote respectively the minimum and maximum values of η-range considered. The variable X(η), thus obtained, has a uniform distribution between 0 and 1. This one-dimensional X(η) space is divided into M bins of equal width, δ such that $\delta(= 1/\mathrm{M})$.

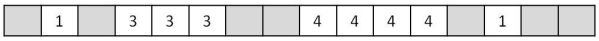

Figure 7-10: Schematic representation of a typical void pattern in one dimensional space.

The multiplicity of relativistic charged-particles produced in an event will vary from bin to bin and one may expect bins having a few or more hadrons along with some empty bins, i.e., bins with no hadrons or 'voids'. In case there are two or more empty bins adjacent to each other, then they are cumulatively added and treated as a single void [109, 114]. However, if there are one or more non-empty bins present between two empty bins, then these non-empty bins are treated as two different voids. The size of a void is simply the number of empty bins adjacent to one another constituting a void. A typical pattern of voids in a configuration generated for M = 16 is shown in Figure 7-10. The filled squares represent the non-empty bins, i.e., bins having hadron(s) while the open squares denotes the empty bins. The diagram hence show voids; the first, second and fourth voids are constituted only by a single bin where as each of the third and fifth voids are due to empty bins connected. If V_k is the sum of the empty bins constituting a void then the fraction of bins occupied by the k^{th} void is defined as [109, 111, 114];

$$x_k = V_k/M \tag{7.8}$$

For each event, therefore, there is a set $S_e(= x_1, x_2, x_3....)$ of void fractions that characterizes the spatial pattern. Since the pattern would vary from event to event, S_e

can not be used for comparing patterns in an efficient way. In order to compare these patterns, Hwa and Zhang [110] have proposed a moment g_q for each configuration as;

$$g_q = \frac{1}{m}\sum_{k=1}^{m} {x_k}^q \tag{7.9}$$

where, the sum runs over all voids in an event, m is the the total number of voids and q denotes the order of the moment. The normalized G moments of order q are written as:

$$G_q = \frac{g_q}{g_1^q} \tag{7.10}$$

G_q, thus, depends on q and M both. Hence, from the definition, $G_0 = G_1 = 1$. It should be mentioned here that G_q moments obtained from the above definition are quite different from those defined for studying the erraticity of rapidity gaps [50, 110, 113] because x_k do not satisfy the sum rule. The G_q moments defined above are also different from those used to investigate multifractal nature of multiparticle production [115]. G_q moment given by Equation 7.10 is a number for a given set of q and M obtained on ebe basis. Thus for a fixed M and q, G_q would fluctuate from event to event and give a distinct probability distribution, $P(G_q)$, for a given set of events, indicating that G_q is a measure of the void patterns. By using such a probability distribution, several moments may be estimated. The two lowest moments are defined as [110, 111];

$$< G_q >= \frac{1}{N_{ev}}\sum_{e=1}^{N_{ev}} G_q^{(e)} \tag{7.11}$$

and

$$S_q =< G_q ln G_q > \tag{7.12}$$

where, the superscript 'e' represents the e^{th} event and N_{ev} is the total number of events in the given sample. The moments, $< G_q >$ and S_q, are expected to follow a power-law behavior as;

$$< G_q > \propto M^{\gamma_q} \tag{7.13}$$

and

$$S_q \propto M^{\sigma_q} \tag{7.14}$$

Such a scaling behaviour, if observed, would indicate that voids of all sizes are formed at phase transition. As the moments of various orders are highly correlated, the scaling exponents γ_q and σ_q are visualized to depend on q as follows:

$$\gamma_q = c_0 + cq \tag{7.15}$$

$$\sigma_q = s_0 + sq \tag{7.16}$$

where c and s represent the slopes of slopes and characterize the fluctuations near the critical point.

7.3.2 Results and Discussion

Pseudorapidity values of the relativistic charged-particles produced in an event and lying in the η range, $\Delta\eta(= \eta_c \pm 3.0)$, are transformed into cumulative variable $X(\eta)$ using Equation 7.7: η_c being the centre of symmetry of the η distribution. The one dimensional $X(\eta)$ space is divided into M bins of equal width, $\delta(= 1/M)$. The occurrence of voids are searched for on ebe basis and the sizes of the voids are estimated by following the approach as discussed above. The values of void fractions, x_k, g_q moments and normalized G_q moments are computed using Equations 7.8-7.10. The values of G_q for q = 2-5 are obtained for various values of M, in the range M = 16 to 96 in steps of 8. Distributions of G_q moments for q = 2 and M = 16 & 64 for ^{16}O-AgBr interactions at 4.5A, 14.5A and 60A GeV/c are shown in Figure 7-11. Similar distribution for the AMPT events at three energies are displayed in the same figures. It is evident from these figures that G_q distributions exhibit fluctuation from event to event and are rather more pronounced for narrower bin width. It may also be noted from the figures that the shapes of G_q distributions are nicely reproduced by those obtained from the AMPT event samples. It is also evident from these figures that

mean value of G_q and the dispersions of their distributions change with M, for a fixed q value and also with q, for a fixed M (not shown). These observations, thus, tend to suggest that in order to look for simple irregularities in the nature of fluctuations of G_q, dependence of $< G_q >$ on M must be examined for all configuration [110].

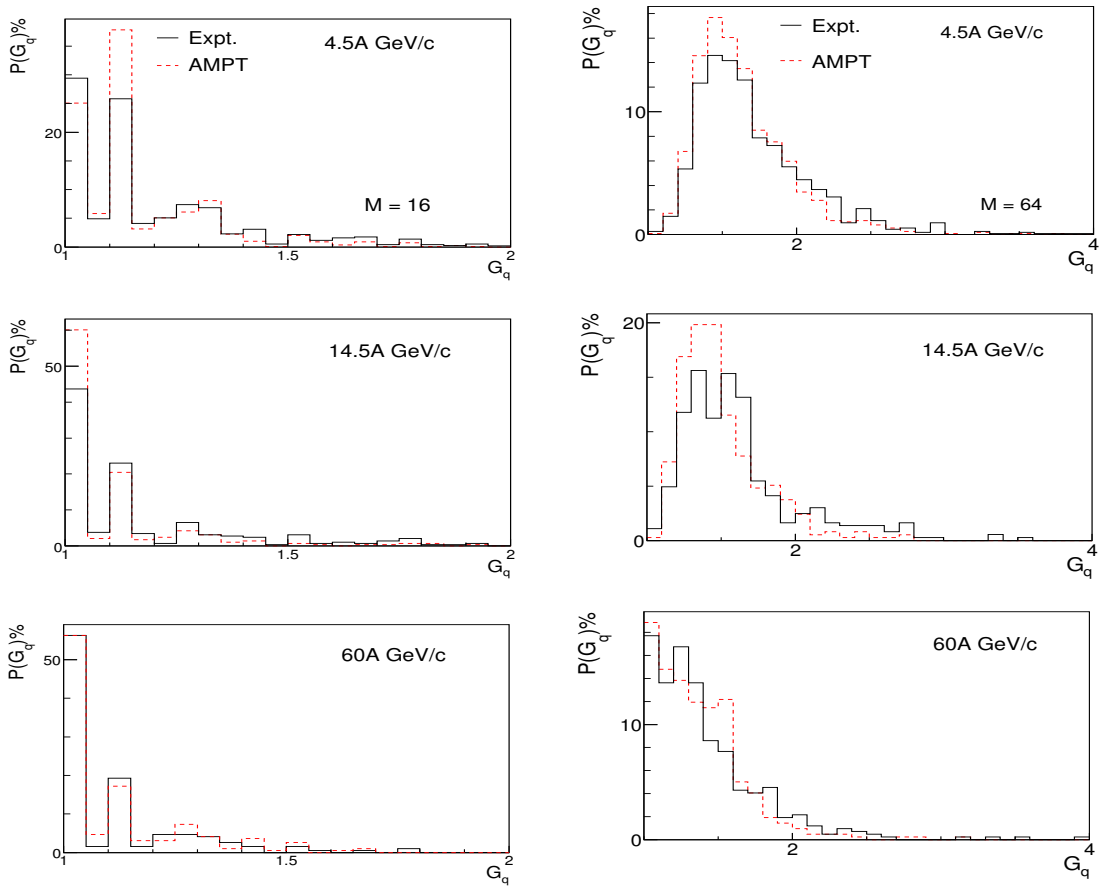

Figure 7-11: (a) G_q distributions for q = 2 and M = 16 for the real and AMPT data in 4.5, 14.5 and 60A GeV/c ^{32}S-AgBr interactions. (b) The same plot for M = 64.

Variations of $< G_q >$ with M on log-log scale for the data sets at the three energies are plotted in Figure 7-12 (a). Similar plots for corresponding AMPT event samples are also shown in Figure 7-12 (b). It may noted from the figures that $ln < G_q >$ increases with lnM. The lines in the figures are due to the best fits to the data of

the form:

$$ln < G_q >= a_1 + b_1 M + c_1 M^2 \tag{7.17}$$

	Energy (A GeV/c)	q	a_1	b_1	c_1
Expt.	4.5	2	-1.899 ± 0.073	1.039 ± 0.041	-0.108 ± 0.005
		3	-3.741 ± 0.120	2.109 ± 0.070	-0.209 ± 0.010
		4	-5.403 ± 0.166	3.144 ± 0.102	-0.299 ± 0.015
		5	-7.201 ± 0.228	4.298 ± 0.142	-0.403 ± 0.021
	14.5	2	-3.357 ± 0.210	1.675 ± 0.112	-0.179 ± 0.014
		3	-4.885 ± 0.315	2.486 ± 0.181	-0.237 ± 0.025
		4	-6.329 ± 0.425	3.305 ± 0.260	-0.286 ± 0.038
		5	-7.997 ± 0.569	4.292 ± 0.362	-0.352 ± 0.055
	60	2	-6.249 ± 0.310	2.893 ± 0.158	-0.313 ± 0.020
		3	-6.662 ± 0.444	3.0 ± 0.246	-0.278 ± 0.033
		4	-7.235 ± 0.595	3.234 ± 0.349	-0.242 ± 0.049
		5	-8.083 ± 0.768	3.643 ± 0.468	-0.221 ± 0.068
AMPT	4.5	2	-1.882 ± 0.061	1.027 ± 0.034	-0.109 ± 0.004
		3	-4.291 ± 0.112	2.4 ± 0.065	-0.253 ± 0.009
		4	-6.395 ± 0.149	3.662 ± 0.092	-0.375 ± 0.013
		5	-8.73 ± 0.196	5.095 ± 0.127	-0.517 ± 0.019
	14.5	2	-3.781 ± 0.219	1.851 ± 0.114	-0.201 ± 0.014
		3	-5.935 ± 0.358	2.945 ± 0.197	-0.297 ± 0.026
		4	-7.232 ± 0.511	3.637 ± 0.295	-0.334 ± 0.041
		5	-8.293 ± 0.703	4.262 ± 0.421	-0.357 ± 0.060
	60	2	-5.543 ± 0.287	2.529 ± 0.147	-0.269 ± 0.018
		3	-5.727 ± 0.404	2.574 ± 0.224	-0.233 ± 0.030
		4	-6.326 ± 0.551	2.893 ± 0.324	-0.224 ± 0.046
		5	-7.304 ± 0.741	3.477 ± 0.455	-0.245 ± 0.067

Table 7.6: Values of a_1, b_1, c_1 appearing in Equation 7.17

.

Values of constants a_1, b_1, c_1, appearing in the above expression are listed in Table 7.6. It is evident from Figures 7-12 (a) and (b) that dependence of $ln < G_q >$ with lnM is quadratic in nature for all data sets (real and simulated) considered. These findings are somewhat different from those reported earlier [109], where a linear dependence of $ln < G_q >$ with lnM has been observed for 350 GeV/c π^--AgBr and 200A GeV/c ^{32}S-AgBr collisions. It has also been suggested [110] that G_q moment should exhibit a linear dependence if plotted against number of phase space bins, M on log-log scale. In our case also the variations of $ln < G_q >$ and lnM displayed in Figure 7-12 (a) and 7-12 (b) show a linear behaviour for the data points corresponding to M = 32 and onwards. This, therefore, indicate a power-law behaviour expressible

by Equation 7.13. The values of indices γ_q for various order q are estimated by performing best fits to the data for M $\geq$ 32 and are presented in Table 7.3.2. It may be noted from the table that AMPT predicts slightly smaller values of γ_q as compared to those obtained for the corresponding real data. The scaling behaviour observed in the present study as well as by the other workers earlier may be interpreted as an indication for occurrence of voids of all sizes [110].

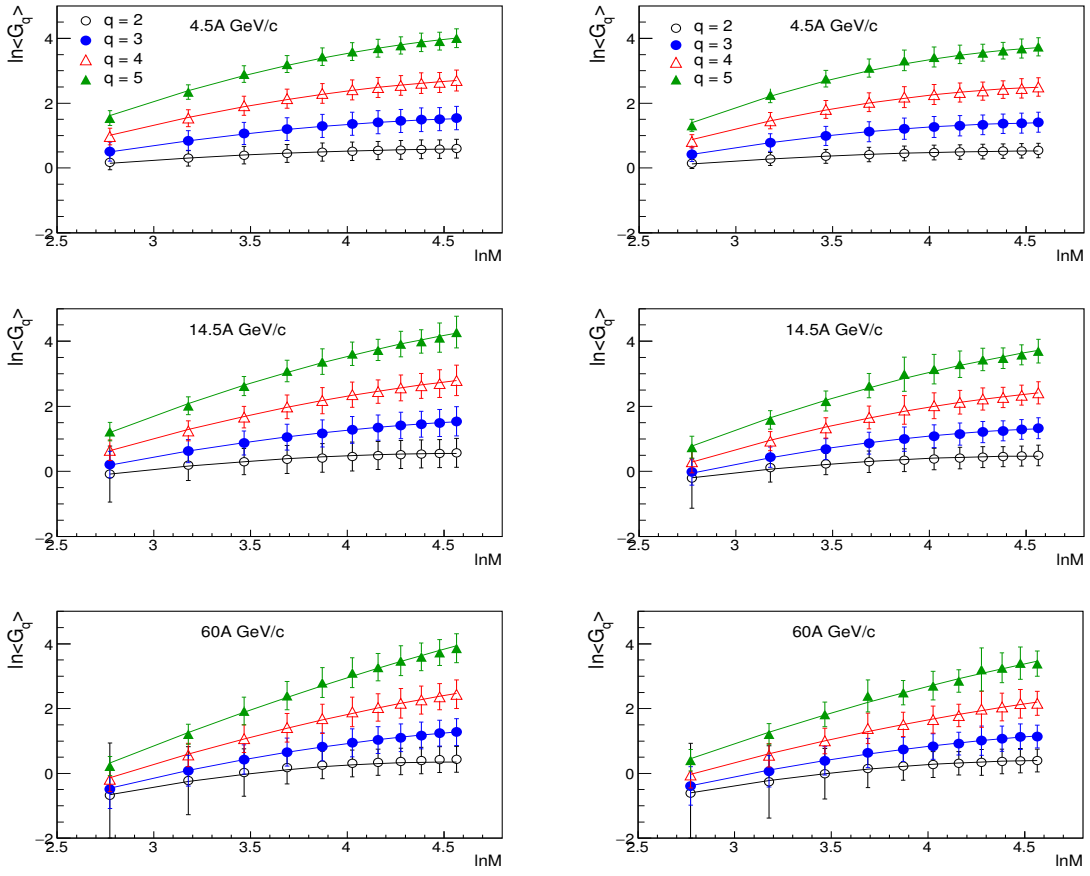

(a) (b)

Figure 7-12: (a) Dependence of $ln < G_q >$ on lnM for the experimental events at the three incident energies. (b) Variations of $ln < G_q >$ with lnM for the AMPT generated events at the three incident energies.

As the G_q moments of various orders are highly correlated, the scaling exponent γ_q is visualized to depend on the order number q in some simple ways. In order to look for this behaviour, variations of γ_q with q are plotted in Figure 7-13. The straight lines in the figure are obtained using Equation 7.15. The values of coefficient "c"

Type of events	q	Energy (A GeV/c)		
		4.5	14.5	60
Expt.	2	0.180 ± 0.006	0.250 ± 0.013	0.317 ± 0.015
	3	0.420 ± 0.016	0.598 ± 0.037	0.754 ± 0.040
	4	0.689 ± 0.028	1.006 ± 0.071	1.238 ± 0.081
	5	0.980 ± 0.042	1.455 ± 0.113	1.734 ± 0.136
AMPT	2	0.160 ± 0.005	0.232 ± 0.010	0.307 ± 0.016
	3	0.368 ± 0.014	0.569 ± 0.030	0.666 ± 0.038
	4	0.599 ± 0.027	0.947 ± 0.062	1.095 ± 0.077
	5	0.847 ± 0.043	1.249 ± 0.106	1.486 ± 0.132

Table 7.7: Values of slopes γ_q appearing in Equation 7.12 for various data sets at different energies.

occurring in Equation 7.15 are listed in Table 7.8. It has been suggested [110] that Equation 7.15 might be regarded as a convenient parameterization of γ_q which would permit to regard 'c' as a numeric description of the scaling behaviour of voids.

Energy	c		s	
(A GeV/c)	Expt.	AMPT	Expt.	AMPT
4.5	0.26±0.01	0.22±0.01	0.23±0.02	0.18±0.02
14.5	0.38±0.02	0.34±0.02	0.32±0.04	0.26±0.04
60	0.46±0.03	0.38±0.03	0.38±0.05	0.29±0.05

Table 7.8: Values of coefficients c and s estimated using Equation 7.14 and 7.15 respectively.

It is evidently clear from the G_q distributions, shown in Figures 7-11 (a) and (b), that only limited information from the distribution may be obtained. The shape of distributions, however, allows to characterize the nature of ebe fluctuations in the distribution. A moment which quantifies the degree of these fluctuations is expressed as;

$$C_{p,q} = \frac{1}{N}\sum_{e=1}^{N}(G_q^{(e)})^p = \int dG_q G_q^p P(G_q) \tag{7.18}$$

As $C_{1,q}(=< G_q >)$ provides no information about the extent of fluctuations but the derivative of $c_{p,q}$ at $p = 1$,

$$S_q = \frac{d}{dp}C_{p,q}\Big|_{p=1} =< G_q ln G_q > \tag{7.19}$$

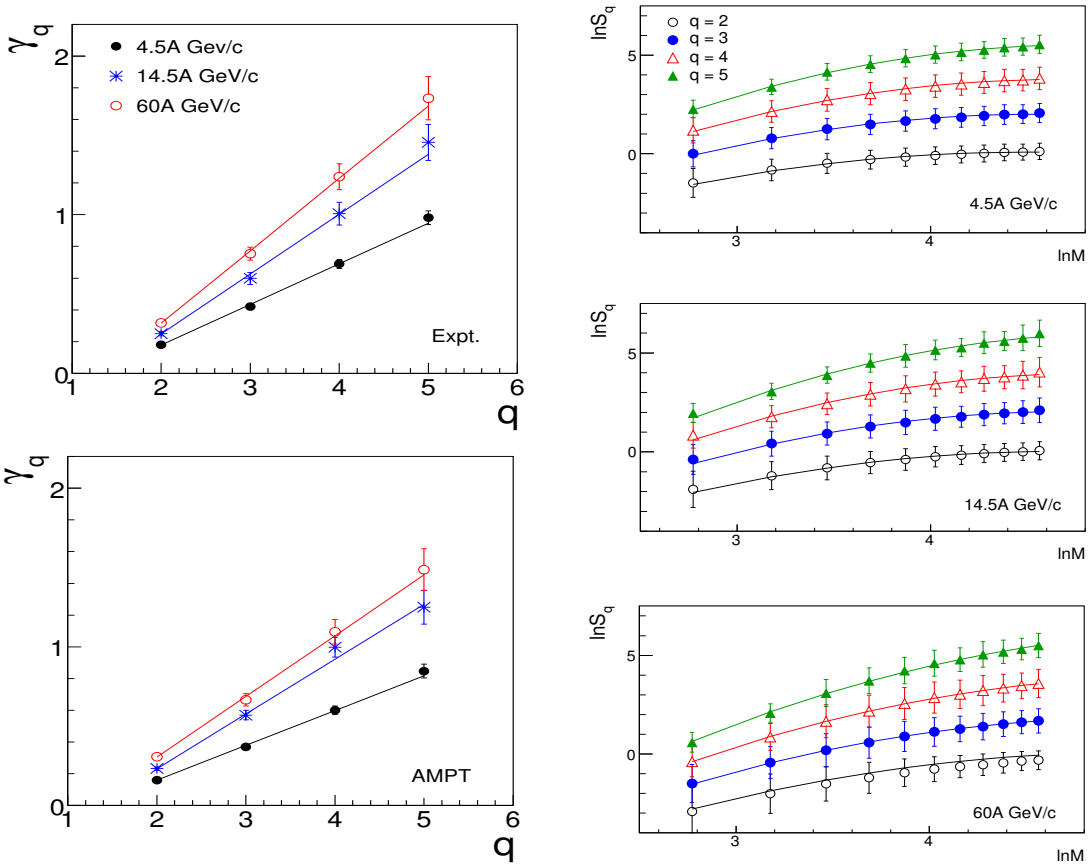

(a) (b)

Figure 7-13: (a) Variations of γ_q with q for the experimental and AMPT simulated events at the three incident energies. (b) Variations of lnS_q with lnM for the experimental 4.5, 14.5 and 60A GeV/c ^{32}S-AgBr interactions.

is envisaged to yield maximum information about the ebe fluctuations

Variations of S_q with lnM on log-log scale are shown in Figures 7-13 (a) and (b) for the experimental and AMPT events at the three beam energies considered. The lines in the figures are obtained by performing best fits to the data using the equation:

$$lnS_q = a_2 + b_2 M + c_2 M^2 \tag{7.20}$$

The values of the coefficients a_2, b_2, c_2, obtained are listed in Table 7.9. It is observed that the trend of variation of lnS_q with lnM can be nicely reproduced by a 2^{nd} order polynomial. Linear fits to the data for $M \geq 32$ are also performed to examine the

power-law behaviour given by Equation 7.14, as has been done in the case of G_q. The values of slopes, σ_q obtained are given in Table 7.10. It may be noted from the table that the values of σ_q predicted by AMPT model are relatively smaller in comparison to that estimated from the corresponding real data. Dependence of σ_q on order q is shown in Figure 7-14. The lines in the figure are due to Equation 7.12. The values of the "s" are listed in Table 7.8. It may be noted from the table that the values of "s" are somewhat larger for the real data as compared to those obtained from the AMPT events. It is can be seen from the table that the values of "c" and "s" increase with increasing beam energy. The values of "c" may be noticed to lie in the range, 0.26 - 0.46, while the values of "s" are found to lie in the range 0.23 - 0.38. The values of "c" and "s" for 200A GeV/c ^{32}S-AgBr interactions have been reported [109] to be 0.56 ± 0.01 and 0.43 ± 0.02 respectively. As a quantitative signature of 2^{nd} order quark-hadron phase transition, the values of "c" are predicted [110] to lie in the ranges 0.75-0.96, whereas those of "s" to lie in between 0.7 and 0.9. It should be mentioned here that the values of these two parameters obtained in the present study are much smaller than those expected for the 2^{nd} order quark-hadron phase transition. This tends to suggest that no such phase transition occurs at the energies considered in the present study.

The method of voids used in the present study is one of the various approaches proposed to study ebe fluctuations, e.g., multifractals [113, 115], normalized factorial moments [42, 44], intermittency [43], erraticity [64, 113], k-order rapidity spacing [14] and transverse momentum spectra [116], etc. Furthermore, fluctuations in the conserved quantities like baryon number [117], net charge and net proton number [118, 119], strangeness, particle ratios, etc., [120, 121] have emerged as new tools to estimate the degree of equilibration and criticality of the measured systems [121, 122]. Higher moments like variance, σ^2, skewness, S, kurtosis, k, etc, of conserved quantities such as net baryon, net charge and net strangeness multiplicity distributions are regarded as important tools to search for the QCD critical point at RHIC and LHC energies [123, 124, 125]. Dynamical development of hadronization of QGP have been looked into in a simple model envisaging critical fluctuations in the QGP to hadronic

matter and a first order phase transition in a small finite system [126]. Variations of skewness and kurtosis as a functions of temperature and volume abundance of hadronic matter are predicted which can be studied through a beam energy scan program using the data at RHIC . Dynamical fluctuations of higher order moment singularities of net proton distributions in Au-Au collisions at beam energies, $\sqrt{s_{NN}}$ =11.5-200 GeV have been investigated in the framework of PACIAE (parton and hadron cascade) model [123, 124, 125]. The energy dependence of various moments of net proton multiplicity distribution have been reported to be in nice agreement with those obtained from the real pp data analysis at RHIC and LHC energies [123].

	Energy (A GeV/c)	q	a_2	b_2	c_2
Expt.	4.5	2	-10.979 ± 0.295	4.910 ± 0.015	-0.545 ± 0.021
		3	-11.580 ± 0.355	5.920 ± 0.920	-0.648 ± 0.026
		4	-12.346 ± 0.415	6.912 ± 0.235	-0.741 ± 0.032
		5	-13.265 ± 0.475	7.871 ± 0.275	-0.825 ± 0.038
	14.5	2	-12.574 ± 0.741	5.361 ± 0.396	-0.573 ± 0.052
		3	-13.333 ± 0.931	6.510 ± 0.514	-0.689 ± 0.070
		4	-14.367 ± 1.128	7.569 ± 0.640	-0.781 ± 0.089
		5	-15.382 ± 1.324	8.509 ± 0.766	-0.850 ± 0.108
	60	2	-13.832 ± 0.741	5.465 ± 0.396	-0.536 ± 0.052
		3	-14.276 ± 1.168	6.306 ± 0.641	-0.616 ± 0.008
		4	-15.014 ± 1.393	7.137 ± 0.787	-0.612 ± 0.108
		5	-15.692 ± 1.601	7.817 ± 0.924	-0.695 ± 0.129
AMPT	4.5	2	-10.303 ± 0.351	4.910 ± 0.185	-0.493 ± 0.029
		3	-11.589 ± 0.502	5.900 ± 0.270	-0.650 ± 0.035
		4	-13.751 ± 0.696	7.611 ± 0.386	-0.841 ± 0.051
		5	-16.440 ± 0.928	9.529 ± 0.512	-1.052 ± 0.069
	14.5	2	-13.423 ± 0.794	5.550 ± 0.414	-0.581 ± 0.053
		3	-13.271 ± 1.018	6.172 ± 0.550	-0.634 ± 0.073
		4	-13.385 ± 1.252	6.738 ± 0.698	-0.669 ± 0.095
		5	-13.594 ± 1.477	7.27 ± 0.847	-0.691 ± 0.118
	60	2	-12.14 ± 0.859	4.606 ± 0.459	-0.448 ± 0.519
		3	-12.063 ± 1.054	5.270 ± 0.583	-0.507 ± 0.079
		4	-12.525 ± 1.283	6.022 ± 0.731	-0.567 ± 0.101
		5	-13.040 ± 1.516	6.72± 0.885	-0.611 ± 0.126

Table 7.9: Values of a_2, b_2, c_2 appearing in Equation 7.12.

As mentioned earlier, experimental data collected using nuclear emulsion technique have been analysed, where it was not possible to identify the charges of the produced particles and therefore, the net proton multiplicity distribution study was not possible. Hence, the method of voids have been opted to investigate the ebe fluctuations . It

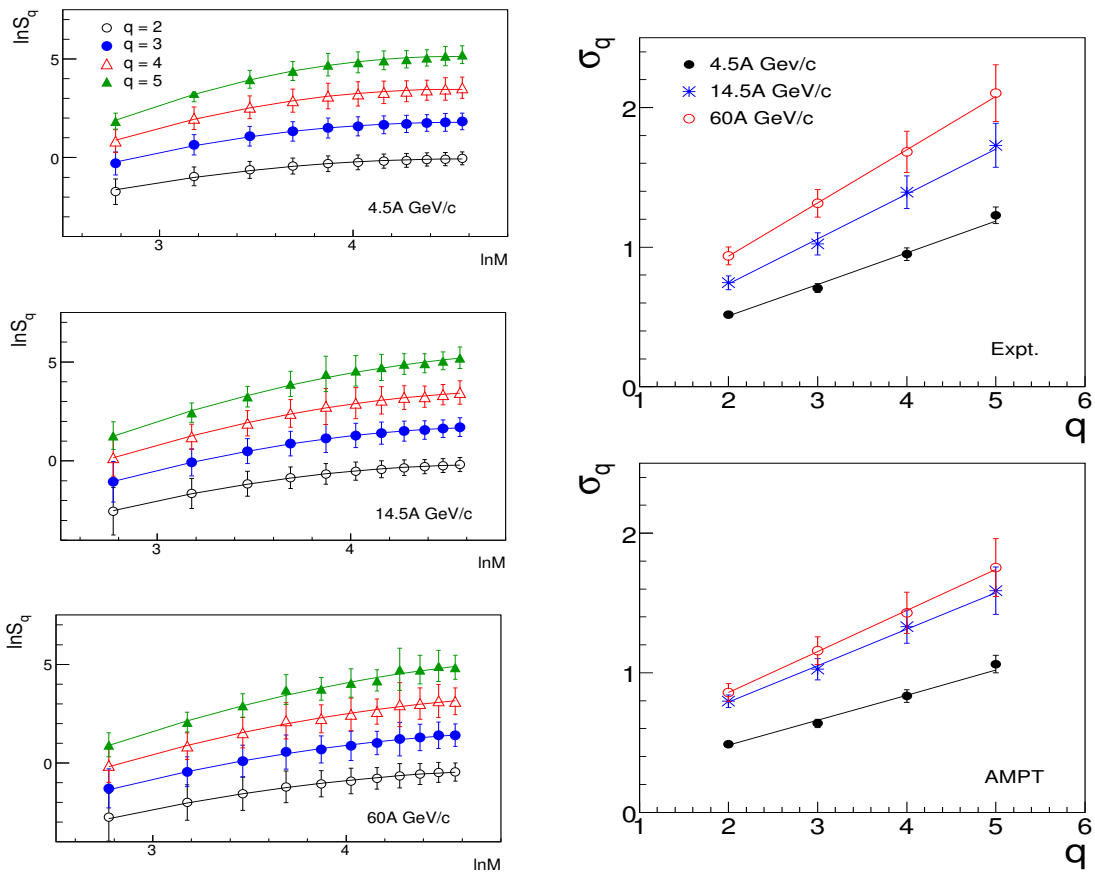

(a) (b)

Figure 7-14: (a) Variations of lnS_q with lnM for the AMPT generated 4.5, 14.5 and 60A GeV/c ^{32}S-AgBr collisions. (b) Variations of σ_q with q for the experimental and AMPT events at the three incident energies.

Type of events	q	Energy (A GeV/c) 4.5	14.5	60
Expt.	2	0.515 ± 0.021	0.744 ± 0.050	0.937 ± 0.063
	3	0.707 ± 0.032	1.023 ± 0.079	1.314 ± 0.098
	4	0.950 ± 0.044	1.392 ± 0.116	1.682 ± 0.147
	5	1.228 ± 0.059	1.730 ± 0.158	2.103 ± 0.203
AMPT	2	0.488 ± 0.018	0.795 ± 0.045	0.808 ± 0.062
	3	0.637 ± 0.029	1.025 ± 0.076	1.158 ± 0.098
	4	0.833 ± 0.044	1.331 ± 0.118	1.429 ± 0.148
	5	1.061 ± 0.062	1.588 ± 0.170	1.754 ± 0.207

Table 7.10: Values of slope σ_q for the experimental and AMPT events at different energies.

may be argued that this method is quite suitable for studying ebe fluctuations using the data at relatively lower energies (AGS and SPS) where particle multiplicities at

these energies are generally low and therefore the possibility of occurrence of voids are quite high in the phase space range. If the multiplicities of hadrons change significantly from one to other region, in the geometrical phase space, then having a detector capable of capturing the maximum phase space becomes important. Nuclear emulsion technique seems to be the most suited one of this kind of study because of its full phase space coverage. Thus, the findings based on the present study may help construct a baseline to the fluctuations arising from non-QGP critical point physics.

Bibliography

[1] S. Ahmad et al., "A Study of Event-by-Event Fluctuations in Relativistic Heavy-Ion Collisions", Int. J. Mod. Phys. E23 (2014) 1450065.

[2] B. Ali et al., "Event-by-Event Fluctuations Clusterization and Entropy Production in AA Collisions at AGS and SPS Energies", Int. J. Mod. Phys. E28 (2019) 1950018.

[3] V. Koch et al., "Event-by-Event Fluctuations and the QGP", Nucl. Phys. A702 (2002) 291.

[4] S. A. Voloshin et al., "Event-by-Event Fluctuations in Collective Quantities", Phys. Rev. C60 (1999) 024901.

[5] L. D. Landau and E. M. Lifschitz, "Statistical Physics, Part I", (1980) Pergamon Press, Oxford.

[6] J. L. Albacete et al., "The Initial State of Heavy-Ion Collisions", Int. J. Mod. Phys. A28 (2013) 1340010.

[7] M. Luzum et al., "Initial State Fluctuations and Final State Correlations in Relativistic Heavy-Ion Collisions", J. Phys. G41 (2014) 063102.

[8] C. Gale et al., "Hydrodynamic Modeling of Heavy-Ion Collisions", Int. J. Mod. Phys. A28 (2013) 1340011.

[9] E. Shuryak, "Quark-Gluon Plasma - New Frontiers", J. Phys. G35 (2008) 104044.

[10] H. Hess et al., "Heavy-Quark Probes of the Quark-Gluon Plasma and Interpretation of Recent data taken at the BNL Relativistic Heavy Ion Collider", Phys. Rev. C73 (2006) 034913.

[11] A. Sh. Gactinov et al., "Long-range and Short-Range Multiparticle Correlation in Collisions of $^{79}Au_{197}$ 10.7 A GeV with Photoemulsion Nuclei", arXiv:1310.7846 [nucl-th].

[12] S. Ahmad et al., "Search for Long-Range Correlations in Relativistic Heavy-Ion Collisions at SPS Energies", Adv. in High En. Phys. 2015 (2015) 615458.

[13] S. Ahmad et al., "A Study of Fluctuations of Voids in Relativistic Ion-Ion Collisions", Int. J. Mod. Phys. E24 (2015) 1550074.

[14] M. L. Cherry et al., KLM Collaboration, "Event-by-Event Analysis of High Multiplicity Pb (158-GeV/nucleon) Ag/Br Collisions", Acta Phys. Polon. B29 (1998) 2129.

[15] K. Adox et al., PHENIX Collaboration, "Event-by-Event Fluctuations in Mean p_T and Mean e_T in $\sqrt{s_{\rm NN}} = 130$ GeV Au+Au Collisions", Phy. Rev. C66 (2002) 024901.

[16] S. Ahmad et al., "Forward-Backward Multiplicity Fluctuations in 200A GeV/c ^{16}O-AgBr and ^{32}S-AgBr Collisions", Phys. Scr. 87 (2013) 045201.

[17] A. Gocksch, "Disoriented Chiral Condensates in Heavy-Ion Collisions", Nucl Phys. (Proc. Suppl.) B34 (1994) 113.

[18] C. M. G. Lattes et al., "Hadronic Interactions of High Energy Cosmic-ray Observed by Emulsion Chambers", Phys. Rep. 65 (1980) 151.

[19] G. J. Alner et al., "UA5: A General Study of Proton-antiproton Physics at $\sqrt{s_{\rm NN}} = 546$ GeV", Phys. Rep. 154 (1987) 247.

[20] J. R. Ren et al., "Properties of Hadron Families Observed with Thick-Type Emulsion Chambers at Mts. Kanbala and Fuji and Search for Centauro Events", Phys. Rev. D38 (1988) 1417.

[21] H. Sako et al., CERES/NA45 Collaboration, "Event-by-Event Fluctuations at 40A GeV/c, 80A GeV/c, and 158A GeV/c in Pb + Au Collisions", J. Phys. G30 (2004) S1371.

[22] S. S. Adler et al., PHENIX Collaboration, "Measurement of Non-Random Event-by-Event Fluctuations of Average Transverse Momentum in $\sqrt{s_{\rm NN}} =$ 200 GeV Au+Au and p+p Collisions", Phys. Rev. Lett. 93 (2004) 092301.

[23] D. Adamova et al., CERES Collaboration, "Event-by-Event Fluctuations of the Mean Transverse Momentum in 40, 80, and 158A GeV/c Pb-Au Collisions", Nucl. Phys. A727 (2003) 97.

[24] F. Jinghua et al., "Extracting Event Dynamics from Event-by-Event Analysis", Phys. Rev. C68 (2003) 064904.

[25] L. Lianshou et al., "A Comparison of Different Measures for Dynamical Event-mean Transverse Momentum Fluctuation", arXiv:0401129v1 [hep-ph].

[26] C. Alt et al., "Energy Dependence of Multiplicity Fluctuations in Heavy Ion Collisions at 20A to 158 A GeV", Phys. Rev. C78 (2008) 034914.

[27] S. Bhattacharya et al., "A Study of Pion Fluctuation and Correlation in Heavy-Ion Collisions", Eur. Phys. J. A52 (2016) 301.

[28] M. J. Tannenbaum, PHENIX Collaboration, "Event-by-Event Average p_T Fluctuations in PHENIX: Measurements and Jet Contribution Simulations", J. Phys. G30 (2004) S1367.

[29] M. Gazdzicki et al., "Fluctuations and Deconfinement Phase Transition in Nucleus Nucleus Collisions", Phys. Lett. B585 (2004) 115.

[30] M. I. Adamovich et al., EMU01 Collaboration, "Multiplicities and Rapidity Densities in 200A GeV ^{16}O Interactions With Emulsion Nuclei", Phys. Lett. B201 (1988) 397.

[31] M. I. Adamovich et al., EMU01 Collaboration, "Scaling Properties of Charged Particle Multiplicity Distributions in Oxygen Induced Emulsion Interactions at 14.6A GeV, 60A GeV and 200A GeV", Phys. Lett. B223 (1989) 262.

[32] M. I. Adamovich et al., EMU01 Collaboration, "Limiting Fragmentation in Oxygen Induced Emulsion Interactions at 14.6A GeV, 60A GeV and 200A GeV", Phys. Rev. Lett. 62 (1989) 2801.

[33] M. I. Adamovich et al., EMU01 Collaboration, "Rapidity Densities and Their Fluctuations in Central 200A GeV ^{32}S Interactions With Au and Ag, Br Nuclei", Phys. Lett. B227 (1989) 285.

[34] M. I. Adamovich et al., EMU01 Collaboration, "Scaled-factorial-moment Analysis of 200 A-GeV Sulfur+Gold Interactions", Phys. Rev. Lett. 65 (1990) 412.

[35] M. I. Adamovich et al., EMU01 Collaboration, "Produced Particle Multiplicity Dependence on Centrality in Nucleus-Nucleus Collisions", J. Phys. G22 (1996) 1469.

[36] G. I. Ordova et al, EMU01 Collaboration, Nucl. Phys. (Proc. Suppl.) B71 (1999) 33.

[37] P. L. Jain, "Characteristics of Charged Particle Multiplicities Distribution in Relativistic Heavy-Ion Interactions", Phys. Rev. C54 (1996) 1892.

[38] C. F. Powell et al., "Study of Elementary Particles by Photographic Method", (1959), Oxford: Pargmon.

[39] S. A. Azimov et al., "Multiplicity and Angular Distributions of Charged-Particles in Interactions of ^{56}Fe in Emulsion at 2.5A GeV/c", Nucl. Phys. A470 (1987) 653.

[40] L .W. Lin et al., "Multiphase Transport Model for Relativistic Heavy-Ion Collisions", Phys. Rev. C72 (2005) 064901.

[41] M. M Aggarwal et al., WA48 Collaboration, "Event-by-Event Charged-Neutral Fluctuations in Pb+Pb Collisions at 158A GeV", Phys. Lett. B701 (2011) 300.

[42] S. Ahmad et al., "Event-by-Event Analysis of High Multiplicity Events Produced in 158A GeV/c ^{208}Pb $-^{208}$ Pb Collisions", Euro. Phys. Lett. 112 (2015) 42001.

[43] T. H Brunett et al., "Extremely High Multiplicities in High-Energy Nucleus-Nucleus Collisions", Phys. Rev. Lett 50 (1983) 2062.

[44] A. Bialas et al., "Moments of Rapidity Distributions As a Measure of Short-Range Fluctuations in High-Energy Collisions", Nucl. Phys. B273 (1986) 703.

[45] P. Lipa et al., "From Strong to Weak Intermittency", Phys. Lett. B223 (1989) 465.

[46] A. Bialas et al., "Intermittency in a Single Event", Phys. Lett. B378 (1996) 319.

[47] I. V. Ajinenko et al., "Intermittency Patterns in π+p and K+p Collisions at 250-GeV/c", ESH/NA22 Collaboration, Phys. Lett. B222 (1989) 306.

[48] R. Holynski et al., KLM Collaboration, "Evidence for Intermittent Patterns of Fluctuations in Particle Production in High-Energy Interactions in Nuclear Emulsion", Phys. Rev. Lett. 62 (1989) 733.

[49] M. I. Adamovich et al., EMU01 Collaboration, "On the Systematic Behavior of the Intermittency Indices in Nuclear Interactions", Phys. Lett. B263 (1991) 539.

[50] S. Ahmad et al., "On Multifractality and Multifractal Specific Heat in Ion-Ion Collisions", Chaos Solitons and Fractals 42 (2009) 538.

[51] E. De-A. Wolf et al., "Scaling Laws for Density Correlations and Fluctuations in Multiparticle Dynamics", Phys. Rep. 270 (1996) 48.

[52] W. Bari et al., "Intermittency in 4.5A and 14.5A GeV/c ^{28}Si Nucleus Interactions", Int. J. Mod. Phys. E11 (2002) 131.

[53] R. Hasan et al., "Levy Stable Law of Intermittency and Multifractal Spectrum in ^{28}Si-AgBr collisions at 14.6A GeV", Chaos Solitions and Fractals 25 (2005) 1029.

[54] M. K. Ghosh et al., "Multifractal Moments of Particles Produced in ^{32}S-AgBr Interaction at 200A GeV/c", J. Phys. G22 (2006) 2293.

[55] D. Ghosh et al., "Fluctuation Of Pions in Relativistic and Ultra-Relativistic Nuclear Collisions-Scale Dependent or Not?", FIZIKA B16 (2007) 67.

[56] M. M. Khan et al., "Dynamical Fluctuations and Levy Stability in 14.5A GeV/c ^{28}Si Nucleus Interactions", Acta Phys. Pol B38 (2007) 2653.

[57] M. M. Khan et al., "A Study of Intermittency in Heavy-Ion Collisions at Relativistic Energies", Int. J. Mod. Phys. E23 (2014) 1450075.

[58] S. Ahmad et al., "Correlations and Event-by-Event Fluctuations in High Multiplicity Events Produced in ^{208}Pb $-^{208}$ Pb Collisions", Adv. in High Energy Phys. 2018 (2018) 694627.

[59] S. Ahmad et al., "Multifractal Characteristics of Multiparticle Production in Heavy-Ion Collisions at SPS Energies", Int. J. Mod. Phys. E27 (2018) 1850004.

[60] Ramni Gupta et al., "Intermittency Study of Charged-Particles Generated in Pb-Pb collisions at $\sqrt{s_{\rm NN}}$ = 2.76 TeV using EPOS3", arXiv:1911.13111 [hep-ex].

[61] Rohni Sharma et al., "Scaling Properties of Multiplicity Fluctuations in the AMPT Model", Adv. in High Energy Phys. 2018 (2018) 6283801.

[62] N. G. Antoniou, "Critical QCD in Nuclear Collisions", Nucl. Phys. A761 (2005) 149.

[63] R. A. Janik et al., "Improved Intermittency Analysis of Single Event Data", Acta Phys. Pol. B30 (1999) 259.

[64] R. C. Hwa, "Beyond Intermittency: Erraticity", Acta Phys.Pol. B 27 (1996) 1789.

[65] S. Ahmad et al., "Erraticity Behaviour in Relativistic Nucleus-Nucleus Collisions", J. Phys. G30 (2004) 1145.

[66] S. Ahmad et al., "Erratic Fluctuations in 14.5A GeV/c ^{28}Si-AgBr Collisions.", Acta Phys. Hung. A25 (2006) 105.

[67] M. M. Khan et al., "Analysis Beyond Intermittency in Multiparticle Production in Relativistic Nuclear Collisions", Int. J. Mod. Phys. E19 (2010) 2219.

[68] A. Bialas et al., "Intermittency Parameters As a Possible Signal for Quark-Gluon Plasma Formation", Phys. Lett. B253 (1991) 436.

[69] R. K. Shivpuri et al., "Target dependence of Intermittency and Multifractality of Multiplicity Fluctuations in 800 GeV Proton Emulsion-Nuclei Interactions", Phys. Rev. D47 (1993) 123.

[70] K. Fialkowski et al., "Event-by-Event Cluster Analysis of Final States from Heavy Ion Collisions", Acta Phys. Pol. B30 (1999) 2559.

[71] K. Fialkowski et al., "Entropy in cluster analysis of single events in heavy ion collisions", Acta Phys. Pol. B31 (2000) 681.

[72] I. M. Dremin et al., "Wavelet-Patterns in Nucleus-Nucleus Collisions at 158A GeV", Phys. Lett. B499 (2001) 97.

[73] F. Abe et al., CDF Collaboration, "Topology of Three-Jet Events in $\bar{p}$p Collisions at $\sqrt{s}$ = 1.8 TeV", Phys. Rev. D45 (1992) 1448.

[74] S. Ahmad et al., "Cluster Production in 14.5A GeV/c Si-Nucleus Collisions", Int. J. Mod. Phys. E8 (1999) 121.

[75] M. Irfan et al., "Determination of Cluster Size in Particle-Nucleus Interactions at 50 and 400 GeV", Phys. Rev. D30 (1984) 218.

[76] S. Ahmad et al., "Short and Long-Range Multiplicity Correlations in Relativistic Heavy-Ion Collisions", Int. J. Mod. Phys. E22 (2013) 1350066.

[77] B. I. Ablev et al.,"Growth of Long Range Forward-Backward Multiplicity Correlations with Centrality in Au+Au Collisions at $\sqrt{s_{\rm NN}}$ = 200âĂĽGeV", Phys. Rev. Lett. 103 (2009) 172301.

[78] V. P. Konchakovski et al., "Forward-Backward Correlations in Nucleus-Nucleus Collisions: Baseline Contributions from Geometrical Fluctuations", Phys. Rev. C79 (2009) 034910.

[79] R. E. Ansorge et al., Charged Particle Correlations in $\bar{p}$p Collisions at C.M. Energies of 200 GeV, 546 GeV and 900 GeV, Z. Phys. C37 (1988) 191.

[80] K. Alpgard et al., "Forward-Backward Multiplicity Correlations in p anti-p Collisions at 540 GeV", Phys. Lett. B123 (1983) 361-366.

[81] B. Alver et al., "Cluster Properties from Two-Particle Angular Correlations in p+p Collisions at $\sqrt{s}$ = 200 and 410 GeV", Phys. Rev. C75 (2007) 054913.

[82] J. Adam et al., ALICE Collaboration, "Forward-backward multiplicity correlations in pp collisions at $\sqrt{s}$ = 0.9, 2.76 and 7 TeV", J. High Energy Phys. 05 (2015) 097.

[83] T. J. Tarnowsky, "Probing the Quark-Gluon Phase Transition Using Energy and System-Size Dependence of Long-Range Multiplicity Correlations in Heavy-Ion Collisions from the STAR Experiment", Indian J. Phys. 85 (2011) 10911095.

[84] B. K. Srivastava et al., "Understanding the Particle Production Mechanism with Correlation Studies Using Long and Short Range Correlations", Int. J. Mod. Phys. E16 (2007) 2210.

[85] G. Singh et al., "Long-Range Correlations in Nucleus-Nucleus Interactions at Ultrahigh Energies", Phys. Rev. C39 (1989) 1835.

[86] E. L. Berger, "Rapidity Correlations at Fixed Multiplicity in Cluster Emission Models", Nucl. Phys. B85 (1975) 61.

[87] E. V. Shuryak, "Quantum Chromodynamics and The Theory of Superdense Matter", Phys. Rep. C61 (1980) 71.

[88] W. Li, "Two-Particle Angular Correlations in p+p and Cu+Cu Collisions at PHOBOS", J. Phys. G34 (2007) S1005.

[89] W. Li, "System Size Dependence of Two-Particle Angular Correlations in p+p, Cu+Cu and Au+Au Collisions", J. Phys. G35 (2008) 104142.

[90] T. Alexopoulos et al., "Charged-Particle Multiplicity Correlations in p$\bar{p}$ Collisions at $\sqrt{s}$ = 0.3 - 1.8 TeV", Phys. Lett. B353 (1995) 155.

[91] W. D. Walker, "Multiparton Interactions and Hadron Structure", Phys. Rev. D69 (2004) 034007.

[92] A. Capella et al., "Dual Parton Model", Phys. Rep. 236 (1994) 329.

[93] Y. V. Kovchegov et al., "Large Scale Rapidity Correlations in Heavy-Ion Collisions", Phys. Rev. C63 (2001) 024903.

[94] B. K. Srivastava, "Fluctuations and Correlations in STAR", Eur. Phys. J. A 31 (2007) 862.

[95] A. Bzdak, "Forward-Backward Multiplicity Correlations in Au-Au Collisions", Acta Phys. Pol. B40 (2009) 2029.

[96] M. Skoby, "Forward-Backward Multiplicity Correlations at STAR", Nucl. Phys. A854 (2011) 113.

[97] A. K. Dash et al.,"Expectation of Forward-Backward Rapidity Correlations in p+p Collisions at the LHC Energies", Int. J. Mod. Phys. A27 (2012) 1250079.

[98] Y. L. Yan et al., "Centrality Dependence of Forward-Backward Multiplicity Correlation in Au+Au Collisions at $\sqrt{s_{\rm NN}}$ = 200 GeV", Phys. Rev. C81 (2010) 044914.

[99] Y. L. Yan et al., "Forward-backward multiplicity correlations in pp, p$\bar{p}$ and Au+Au collisions at RHIC energy", Nucl. Phys. A 834 (2010) 320c.

[100] A. Abdelsalam et al., " Study of Relativistic Forward-Backward Hadron Production in the Interactions of He-3 and He-4 with Emulsion Nuclei at Dubna Energy", Fizika B15 (2006) 9.

[101] J. Fu, "Statistical Interpretation of Multiplicity Distributions and Forward-Backward Multiplicity Correlations in Relativistic Heavy-Ion Collisions", Phys. Rev. C77 (2008) 027902.

[102] A. Korner et al., "Angular and Long Range Rapidity Correlations in Particle Production at High Energy", Int. J. Mod. Phys. E22 (2013) 1330001.

[103] P. L. Jain et al., "Short and Long-Range Correlations of Produced Particles at Very High Energies", Phys. Rev. D34 (1986) 2886.

[104] A. Capella et al., "Unitarity Corrections to Short-Range Order: Long-Range Rapidity Correlations", Phys. Rev. D18 (1978) 4120.

[105] B. Alver et al., "System Size Dependence of Cluster Properties from Two-Particle Angular Correlations in Cu+Cu and Au+Au Collisions at $\sqrt{s_{\rm NN}}$ = 200 GeV", Phys. Rev. C81 (2010) 024904.

[106] T. J. Tarnowski, "Recent Results of Fluctuation and Correlation Studies from the STAR Experiment", J. Phys. Conf. Ser. 230 (2010) 012025.

[107] B. Alver et al., "Multiplicity Fluctuations in Au+Au Collisions at RHIC", Int. J. Mod. Phys. E16 (2007) 2187.

[108] R. C. Hwa et al., "Void Analysis of Hadronic Density Fluctuations at the Quark-Hadron Phase Transition", Phys. Rev. C64 (2001) 054904.

[109] M. Mondal et al., "Multidimensional Void Fluctuation: A Search for Quark-Hadron Phase Transition", Astropart. Phys. 55 (2014) 26.

[110] R. C. Hwa et al., "Fluctuation of Voids in Hadronization at Phase Transition", Phys. Rev. C62 (2000) 05902.

[111] D. Ghosh et al., "Void Fluctuation Study of Compound Hadrons: Signatures of Quark-Hadron Phase Transition", Phys. Part. Nuclei Lett. 12 (2015) 246.

[112] A. Bialas et al., "A New Variable to Study Intermittency", Phys. Lett. B252 (1990) 483.

[113] S. Ahmad et al., "Erratic Fluctuations in Rapidity Gaps in Relativistic Nucleus-Nucleus Collisions", Acta Phys. Pol. B35 (2004) 809.

[114] R. C. Hwa et al., "Erraticity of Rapidity Gaps", Phys. Rev. D62 (2000) 014003.

[115] R. C. Hwa, "Fractal Measures in Multiparticle Production", Phys. Rev. D41 (1990) 1456.

[116] J.G. Ried et al., STAR Collaboration, "STAR Event-by-Event Fluctuations", Nucl. Phys. A 698 (2002) 611.

[117] S. Acharya et al., ALICE Collaboration, "Global Baryon Number Conservation Encoded in Net-Proton Fluctuations Measured in Pb-Pb Collisions at $\sqrt{s_{\rm NN}}$ = 2.76 TeV", arXiv:1910.14396 [nucl-ex].

[118] S. Acharya et al., ALICE Collaboration, "Transverse Momentum Spectra and Nuclear Modification Factors of Charged Particles in pp, p-Pb and Pb-Pb Collisions at the LHC", J. High Energy Phys. 1811 (2018) 013.

[119] B. Abelev et al., ALICE Collaboration, "Net-Charge Fluctuations in Pb-Pb Collisions at $\sqrt{s_{\rm NN}}$ = 2.76 TeV", Phys. Rev. Lett. 110 (2013) 152301.

[120] Mesut Arslandok, ALICE Collaboration, "Event-by-Event Identified Particle Ratio Fluctuations in Pb-Pb Collisions with ALICE using the Identity Method", Nucl. Phys. A956 (2016) 870.

[121] S. Jena, ALICE Collaboration, "Recent Results on Event-by-Event Fluctuations in ALICE at the LHC", J. Phys. Conf. Ser. 612 (2015) 012047.

[122] N. M. Abdelwahab et al., STAR Collaboration, "Energy Dependence of K/π, p/π, and K/p Fluctuations in Au+Au Collisions from $\sqrt{s_{\rm NN}}$ = 7.7 to 200 GeV", Phys. Rev. C92 (2015) 021901.

[123] A. Limphirat et al., "PACIAE Model Capability in Describing Net Proton Moments", Cent. Eur. J. Phys. 10 (2012) 1388.

[124] D. M. Zhou et al., "Higher Moment Singularities Explored by the Net Proton Non-Statistical Fluctuations", Phys. Rev. C85 (2012) 064916.

[125] D. M. Zhou et al., "Comparative Study for Non-Statistical Fluctuation of Net Proton, Baryon, and Charge Multiplicities", J. Phys. G41 (2014) 065103.

[126] L.P. Csernai et al., "Fluctuations in Hadronizing QGP", Phys. Rev. C85 (2012) 068201.

Chapter 8

Summary and Future Direction

In this thesis, the hard probes (J/ψ production), the soft probes (correlations, fluctuations and multiplicity) and the hard probes as a function of soft probe have been studied. The self-normalized J/ψ production and first moment of p_{T} of J/ψ have been measured as a function of charged-particle multiplicity in pp collisions at $\sqrt{s}$ = 2.76 and 5.02 TeV using ALICE detector. The J/ψ were measured at forward rapidity ($2.5 < y < 4.0$) through dimuon decay using the Muon Spectrometer and the charged-particles were detected at mid-rapidity ($|\eta| < 1$) by the silicon pixel detector of the ITS of the ALICE. The extensive study of J/ψ production using two observables, multiplicity and spherocity, were also reported using PYTHIA8 simulation. The study of charged-particle correlations and event by event fluctuations have been carried out in heavy-ions collisions using emulsion data from EMU01 collaboration. The results obtained in the present work were compared with theoretical model predictions as well. In this chapter, all the main aspects of the reported analyses are summarized.

The inclusive J/ψ production cross-section was calculated in pp collisions at $\sqrt{s}$ = 2.76 and 5.02 TeV at forward rapidity using data collected from ALICE detector. The measurements of inclusive J/ψ production cross-section was carried out for cross-checking with the reported values. Various trigger events were checked and finally the results of inclusive number of muon events as well as J/ψ count and production cross-section were found to be in good agreement with the previous study. An extensive

cross-check of inclusive J/ψ production cross-section was carried out in pp collisions at $\sqrt{s}$ =5.02 TeV. The MC study was also performed at $\sqrt{s}$ = 5.02 TeV to estimate the tail parameters and the acceptance and efficiency corrections of the Muon Spectrometer. The obtained results were found to be consistent with the ALICE results within the statistical and systematic uncertainties.

The evolution of the J/ψ production as a function of charged-particle multiplicity was investigated in detail in pp collisions at $\sqrt{s}$ = 2.76 and 5.02 TeV at forward rapidity. A similar approach of analysis has been adopted for both the CM energies. The measurement of the charged-particle multiplicity has been performed using three different methods. The method which gave lowest systematic uncertainty was adopted for the final results. The calculation of charged-particle multiplicity using ad-hoc polynomial technique has been used for the first time for the present work. The estimation of various efficiency correction factors are reported in this research work. The multiplicity dependence of J/ψ yield has been measured for inelastic $>$ 0 event class at forward rapidity. The increase of J/ψ yield with the event multiplicity has been found to be linear at forward rapidity at both the CM energies. The obtained results have been compared with similar study performed at ALICE at various collision energies and rapidity ranges. The multiplicity dependence of J/ψ yield is observed to be independent of the $\sqrt{s}$. A strong dependence on the choice of rapidity region has been observed. If both J/ψ and the charged-particles are chosen in the same phase space (here the rapidity range) the increment of J/ψ as a function of multiplicity enhanced due to auto-correlation effect. Further contribution to the increase of J/ψ production might originate from the jet biases. The effect of auto-correlation can be removed by introducing a rapidity gap between the J/ψ yield and charged-particles pseudo-rapidity density which lead to the linear increment at forward rapidity.

Theoretical model calculations from PYTHIA8, percolation, higher fock state and EPOS3 have been used to understand the experimental data at $\sqrt{s}$ = 5.02 TeV. The data is being well explained by the theoretical models at low multiplicity region. The higher fock state model gives the best description of the data at its lower limit in both the CM energies. The percolation model overestimate the data at high multiplicity

while the PYTHIA8 and EPOS3 underestimate the data at the high multiplicity. Along with that the experimental results have also been compared with two new model predictions i.e. CGC with three gluon saturation and combination of CGC with ICEM. The CGC model with three gluon fusion mechanism overestimate the data at both 2.76 and 5.02 TeV. A good description of the data points are given by the CGC with ICEM model.

The relative $\langle p_{\mathrm{T}}^{\mathrm{J}/\psi} \rangle$ as a function of charged-particles pseudo-rapidity density was also computed in pp collisions at $\sqrt{s} = 5.02$ TeV at forward rapidity. The first moment of p_{T} of J/ψ as well as self-normalized $\langle p_{\mathrm{T}}^{\mathrm{J}/\psi} \rangle$ shows increasing trend up to relative charged-particles density up to ∼2, then tends to saturate towards higher multiplicity. A fit with power-law function describes well the saturating trend of $\langle p_{\mathrm{T}}^{\mathrm{J}/\psi} \rangle$ at high multiplicity. The obtained results are put into perspective of the other results from ALICE such as pp collisions at $\sqrt{s} = 13$ TeV at forward rapidity as well as with p-Pb collisions at $\sqrt{s_{\mathrm{NN}}} = 5.02$ and 8.16 TeV at the both forward and backward rapidity regions. The comparison study shows that the multiplicity dependence of $\langle p_{\mathrm{T}}^{\mathrm{J}/\psi} \rangle$ is independent of the $\sqrt{s}$ at the same rapidity interval. The saturating trend of $\langle p_{\mathrm{T}}^{\mathrm{J}/\psi} \rangle$ towards high multiplicity is independent of the collision system although the saturation is achieved faster in the p-Pb collision system due to large number of charged-particles.

The J/ψ production mechanism was also reported in terms of event shape obeservables using PYTHIA8 at forward and mid-rapidity for $\sqrt{s} = 5.02$ and 13 TeV. The multiplicity dependence of J/ψ yield and $\langle p_{\mathrm{T}}^{\mathrm{J}/\psi} \rangle$ were studied in two spherocity classes i.e. for isotropic and jetty events. The thermodynamic properties of J/ψ production were also investigated by means of non-extensive Tsallis distribution. It can be concluded from the double differential study of event shape and multiplicity that the self-normalized J/ψ production as a function of multiplicity is independent of $\sqrt{s}$. The contribution of jet to the J/ψ production is more at mid-rapidity while at forward rapidity, isotropic events dominate. The presence of dynamical effects might be the results of collective behaviour in pp collisions.

Five data sets, reconstructed in experiments from EMU01 collaboration have been

analyzed to study the event by event correlation and fluctuations in relativistic heavy-ion collisions at SPS, RHIC and LHC energies. Experimental finding were compared with different theoretical models such as AMPT. The study shows that the observed forward-backward (F-B) multiplicity correlations are mainly of short-range in nature. The particle density fluctuations, in terms of scaled factorial moments and searched for dominant cluster or jet-like phenomenon in two dimensional $\eta-\phi$ space have been shown. Fluctuations in hadronic matter were also investigated in terms of voids which reveals scaling exponent estimated from the power-law behavior of the voids. The investigation of fluctuation voids may be helpful to characterize the various properties of hadronic phase transition. The results also rule out occurrence of second-order quark-hadron phase transition at the projectile energies.

8.1 Further directions

The study of the production ratio of $\psi(2S)/J/\psi$ as a function of charged-particle multiplicity in small systems will be a promising extension of the present analysis. A corresponding analysis in pp collisions at $\sqrt{s}$ =13 TeV has been taken up in ALICE collaboration during the stage of this thesis writing. The computation of nuclear modification factor in terms of event activity in small systems may lead to the collectivity that are under investigation. The forward rapidity measurements will be more precise since there will be no auto-correlation effects. It will be interesting to study theses observable particularly for high and low multiplicity events. The study of ratio between various quarkonium states and comparison of the results in different kinematics such as rapidity, p_{T}, multiplicity and spherocity in small systems may shed more light in this direction. The multiplicity dependence study of hard-probes in various phase space $(\eta-\phi)$ is worth of investigation. The $\langle p_{\mathrm{T}}\rangle$ of J/ψ is an important observable which gives direct link to the temperature of the nuclear medium under study.

There are many open issues related to quarkonium study at the LHC. There are various aspects from spectroscopic point of view, to production mechanism, to J/ψ

hadron interaction in the medium, and J/ψ rare decay modes etc which are interesting topics that can be studied. As we know that in pp, p-Pb and Pb-Pb collisions quarkonium production mechanism is not fully understood and we have mostly studied inclusive J/ψ at forward rapidity, it will be nice to explore the contribution of prompt, non-prompt J/ψ at forward rapidity.

At present, ALICE detector is going through upgradation process after LHC Run phase 2 was completed in November 2018. This major upgradation procedure during Long Shutdown (LS2) will be continued till 2021. The upgradation of the two main detectors relevant to this thesis is worth mentioning here.

ITS upgrade : The present ITS is being replaced by a new tracker based on monolithic silicon pixel sensors. The material budget is less due to the use of monolithic pixel sensors. The accuracy of primary vertex measurement will be improved. The feed-down contribution from beauty to charm measurements will be estimated directly from the data with the upgradation of ITS. The precise measurement of the nuclear modification factor and elliptic flow measurement of J/ψ (D and B mesons), study of heavy flavour baryons, baryon to meson ratio and low momentum di-electrons in higher CM energies in p-Pb and Pb-Pb collisions will be possible with ITS upgrade.

The Muon Forward Tracker (**MFT**) : The new MFT for the ALICE Muon Arm is being installed as part of ALICE upgrade. The current muon physics program suffers from few limitations despite of the remarkable results already obtained from the MS data. The main draw backs were the multiple scattering induced on the muon tracks by the forward absorber and limited possibility to prevent muons coming from semi-muonic decays of pions and kaons which are the main source of the background. The addition of MFT will help to overcome these limitations. In particular the uncertainties related to $\psi(2S)$ measurements will be improved due to the enhanced rejection of the combinatorial background. The measurement of the J/ψ production from beauty mesons will be possible with the upgradation of MFT. The MFT will allow a reliable disentanglement between prompt and non prompt charmo-

nia production in the forward rapidity. The low mass dimuon measurements will also benefit from much better mass resolution.

Appendix A

Additional information related to charged-particle multiplicity

A.1 Runlist

p-p $\sqrt{s}$ = 2.76 TeV

Run list : 146860, 146859, 146858, 146856, 146824, 146817, 146807, 146806, 146805, 146804, 146803, 146802, 146801, 146748, 146747, 146746, 146689, 146688

p-p$\sqrt{s}$ = 5.02 TeV

Run list : 244628, 244627, 244626, 244619, 244617, 244542, 244540, 244531, 244484, 244483, 244482, 244481, 244480, 244453, 244421, 244418, 244416, 244411, 244377, 244364, 244359, 244355, 244351, 244343, 244340

A.2 Charged-particle multiplicity

A.2.1 Systematics uncertainty for α in pp at $\sqrt{s} = 5.02$ TeV

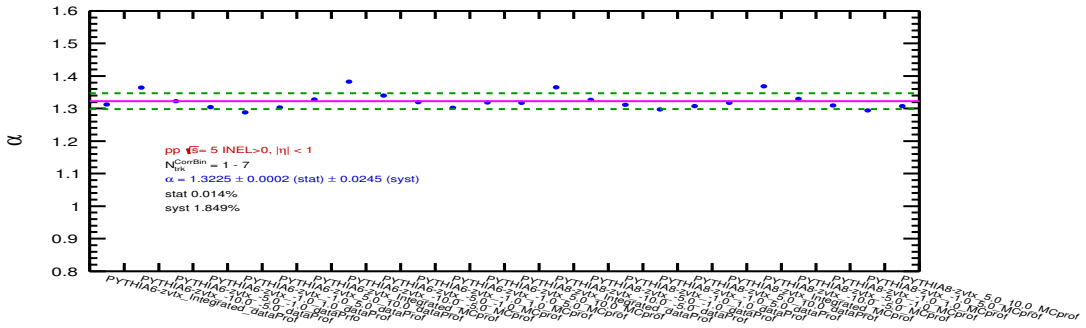

Figure A-1: α systematic uncertainty tracklets bin 1-7.

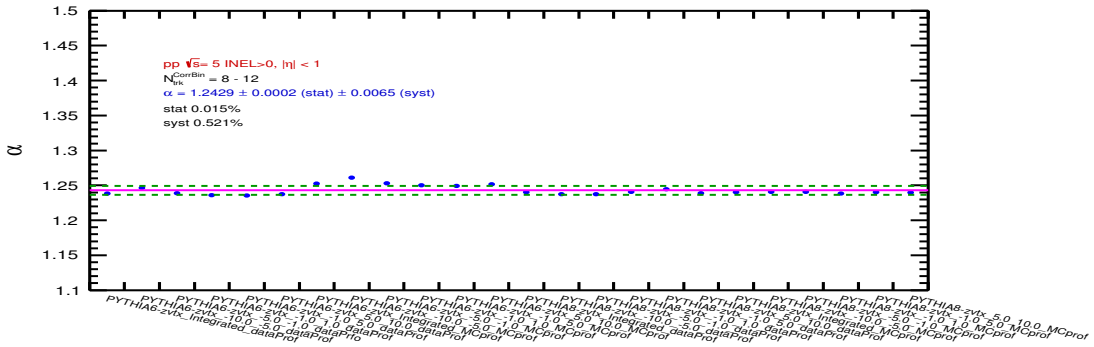

Figure A-2: α systematic uncertainty for tracklets bin 8-12.

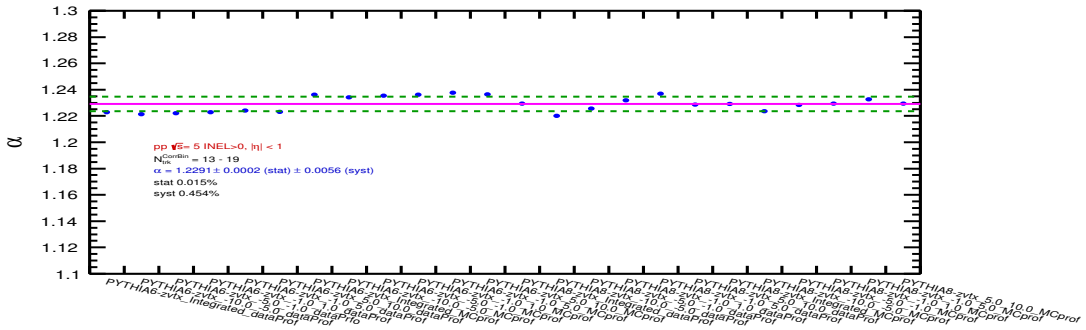

Figure A-3: α systematic uncertainty for tracklets bin 13-18.

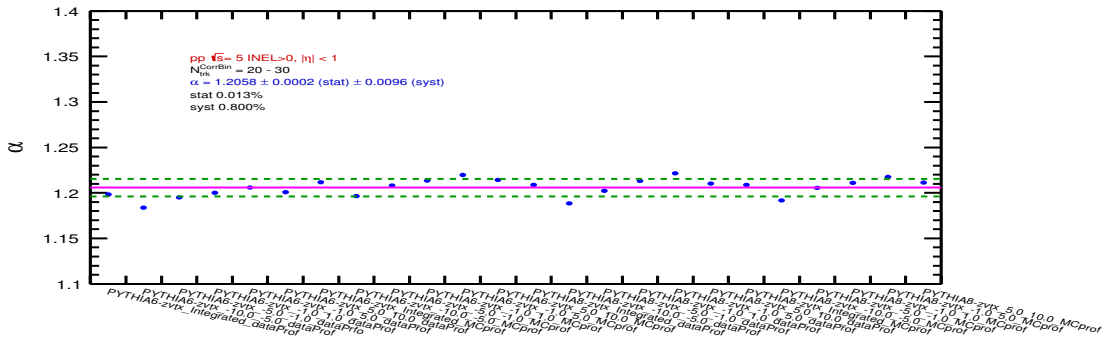

Figure A-4: α systematic uncertainty for tracklets bin 19-30.

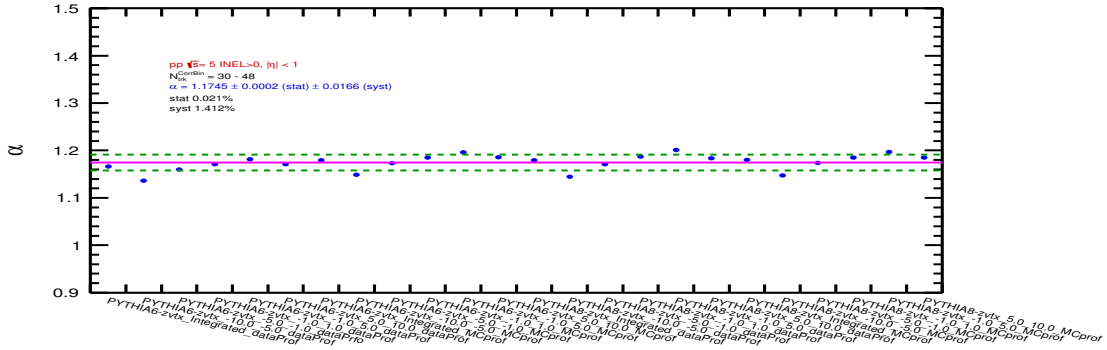

Figure A-5: α systematic uncertainty for tracklets bin 30-48.

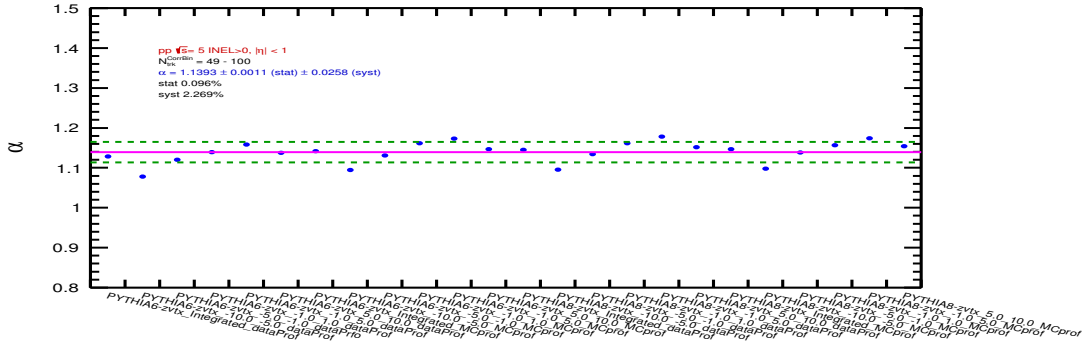

Figure A-6: α systematic uncertainty for tracklets bin 49-100.

A.2.2 α systematics in pp at $\sqrt{s} = 2.76$ TeV

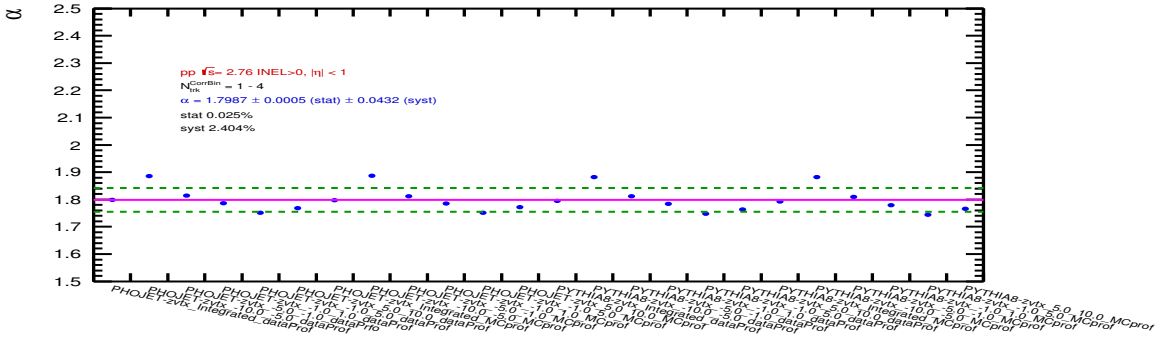

Figure A-7: α systematic uncertainty for tracklets bin 1-4.

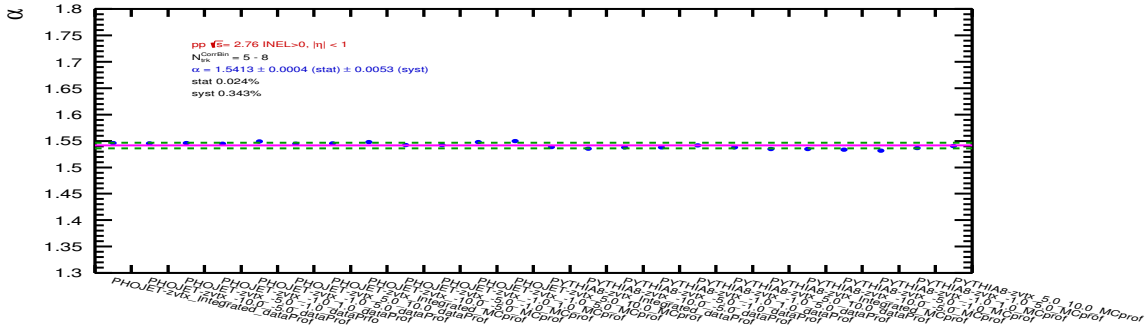

Figure A-8: α systematic uncertainty for tracklets bin 5-8.

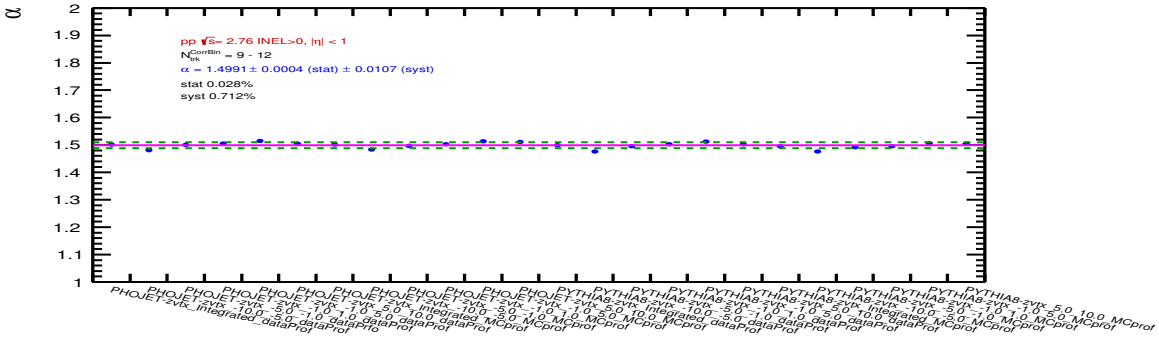

Figure A-9: α systematic uncertainty for tracklets bin 9-12.

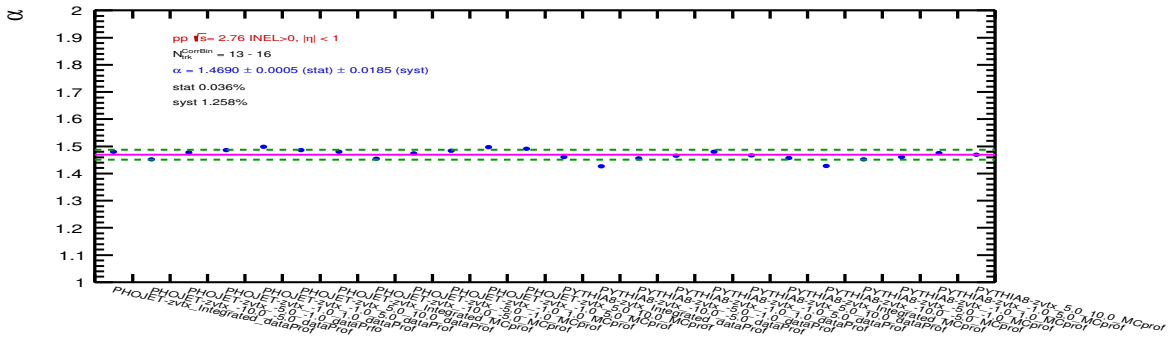

Figure A-10: α systematic uncertainty for tracklets bin 13-16.

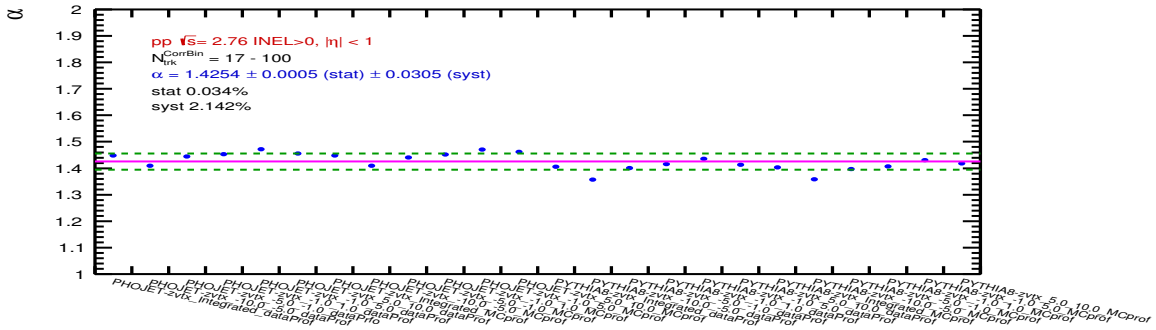

Figure A-11: α systematic uncertainty for tracklets bin 17-100.

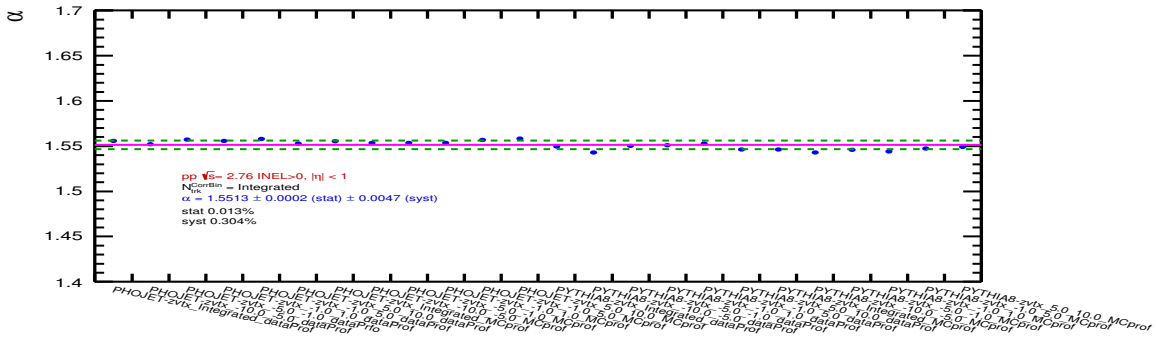

Figure A-12: α systematic uncertainty for integrated multiplicity at 2.76 TeV.

A.2.3 Ad-hoc polynomial method control plots

The $N_{ch} - N_{trk}^{corr}$ correlations fitted with ad-hoc polynomial as well second-order polynomial functions.

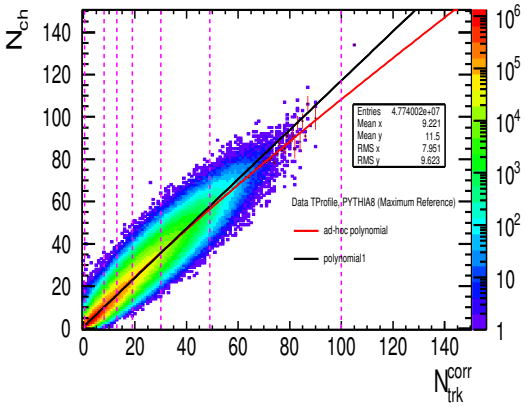

(a) PYTHIA8

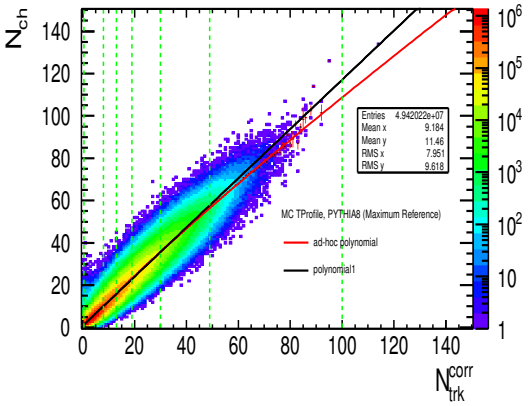

(b) PYTHIA8

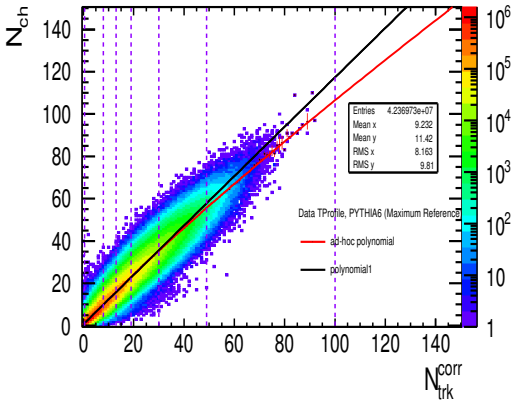

(c) PYTHIA6

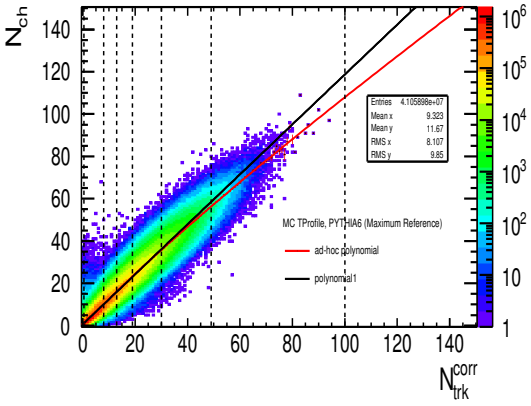

(d) PYTHIA6

Figure A-13: The $N_{ch} - N_{trk}^{corr}$ correlations fits at 5.02 TeV

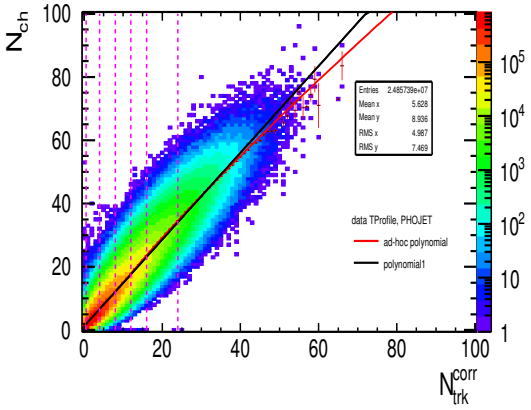

(a) PHOJET

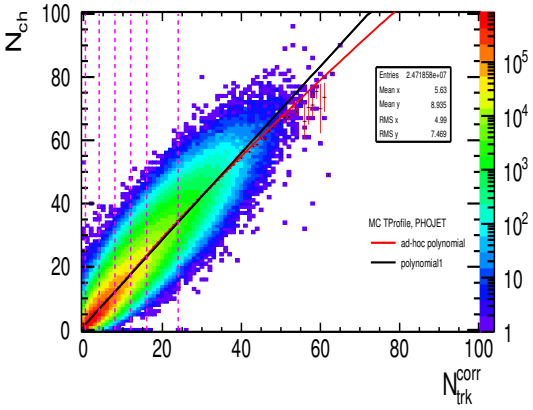

(b) PHOJET

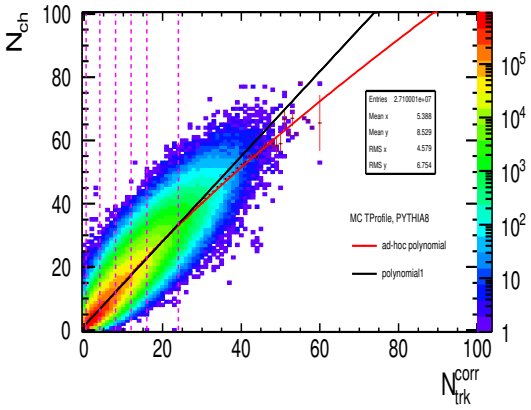

(c) PYTHIA8

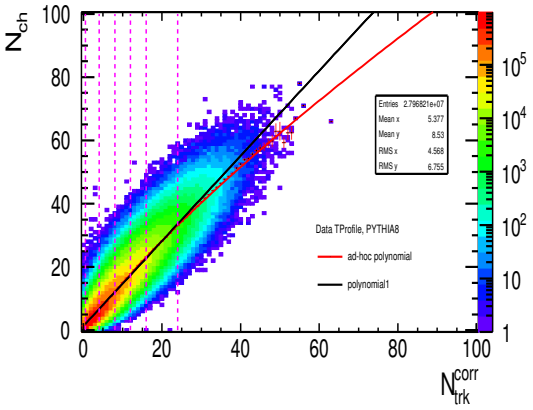

(d) PYTHIA8

Figure A-14: The $N_{ch} - N_{trk}^{corr}$ correlations fits at 2.76 TeV

A.2.4 Systematic uncertainty using ad-hoc polynomial method at 5.02 TeV

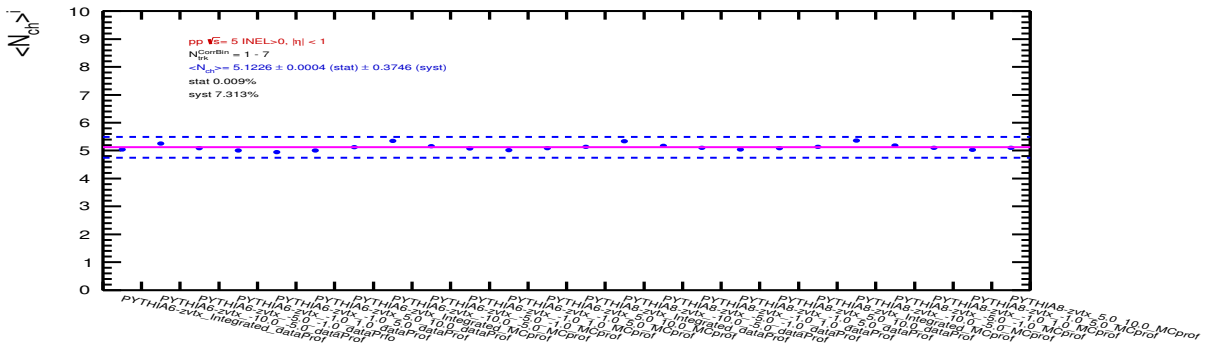

Figure A-15: Mean charged-particle systematic for tracklets bin 1-7.

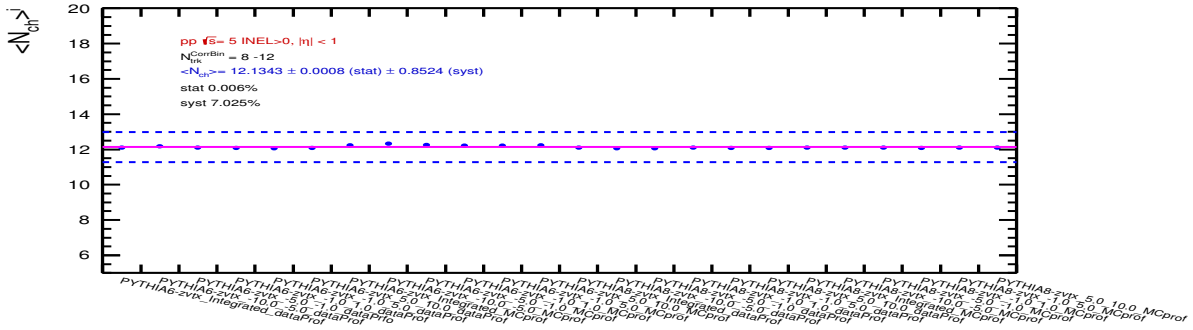

Figure A-16: Mean charged-particle systematic for tracklets bin 8-12.

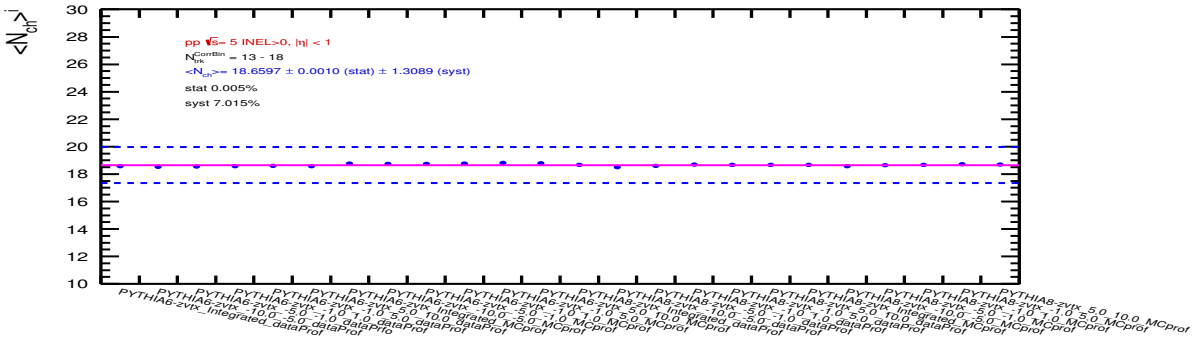

Figure A-17: Mean charged-particle systematic for tracklets bin 13-18.

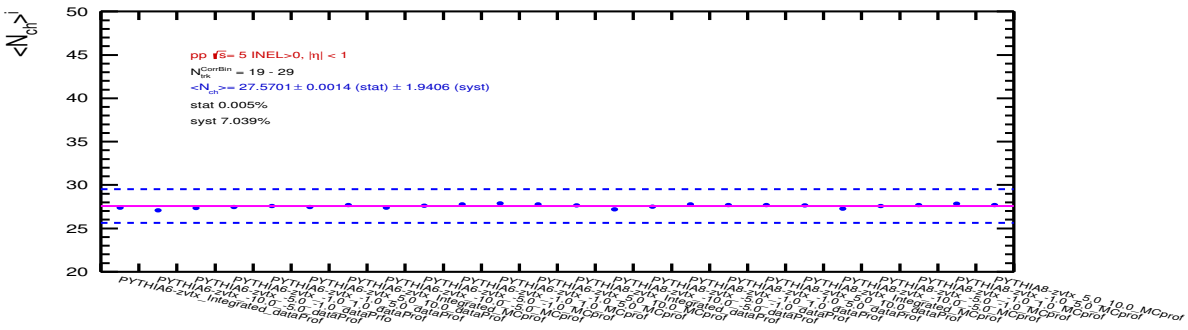

Figure A-18: Mean charged-particle systematic for tracklets bin 19-29.

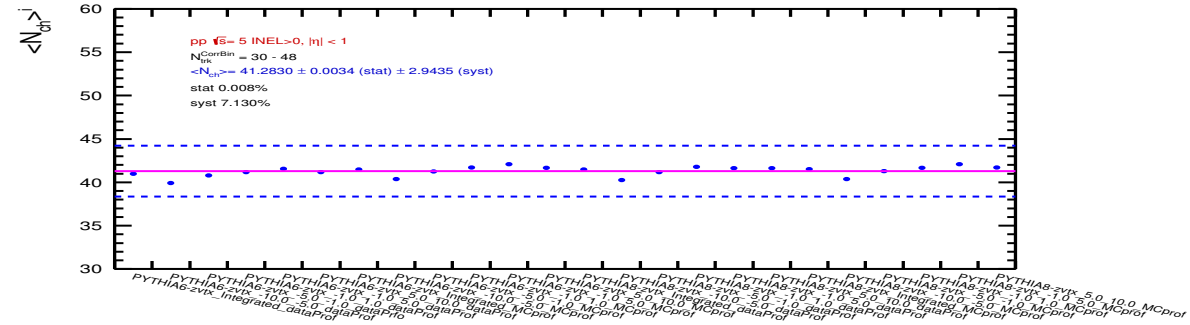

Figure A-19: Mean charged-particle systematic for tracklets bin 30-48.

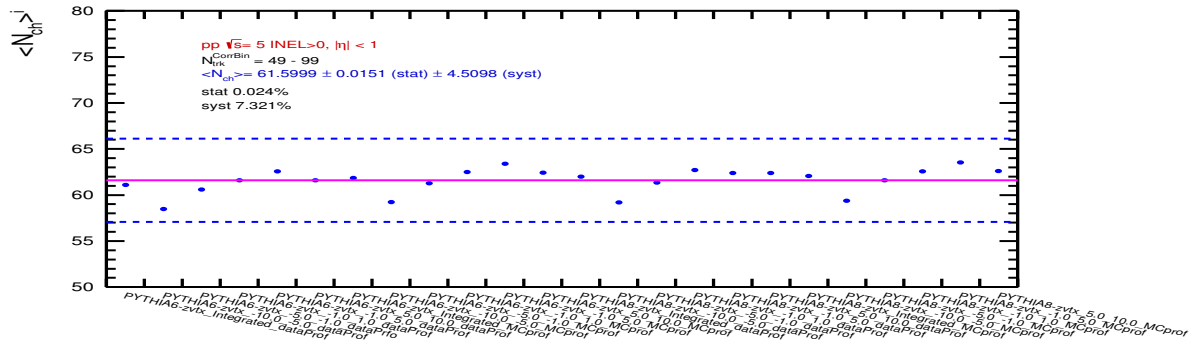

Figure A-20: Mean charged-particle systematic for tracklets bin 49-100.

A.2.5 Systematic uncertainty using ad-hoc polynomial method at 2.76 TeV

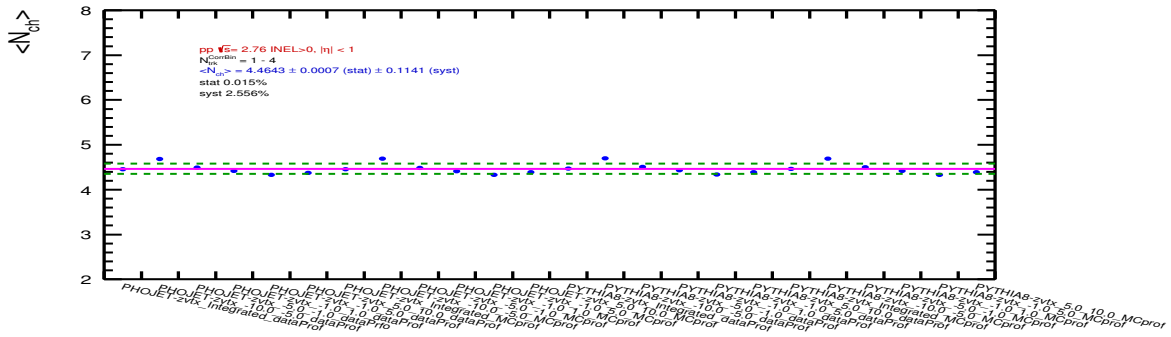

Figure A-21: Mean charged-particle systematic for tracklets bin 1-4.

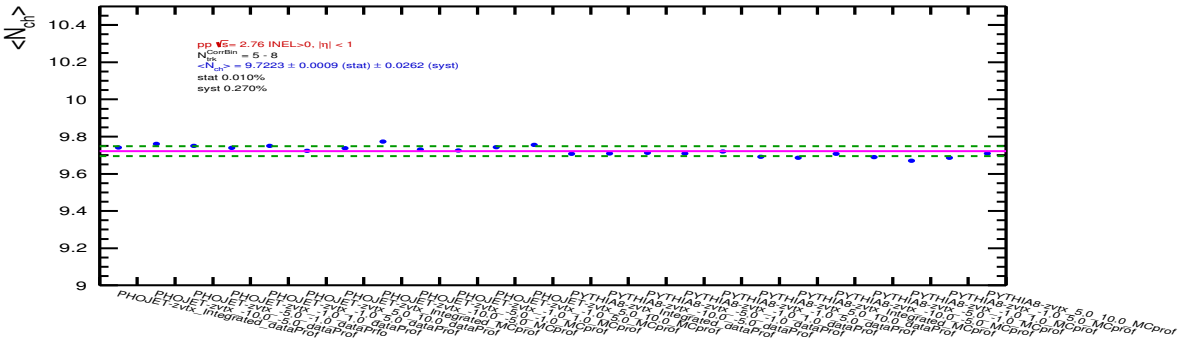

Figure A-22: Mean charged-particle systematic for tracklets bin 5-8.

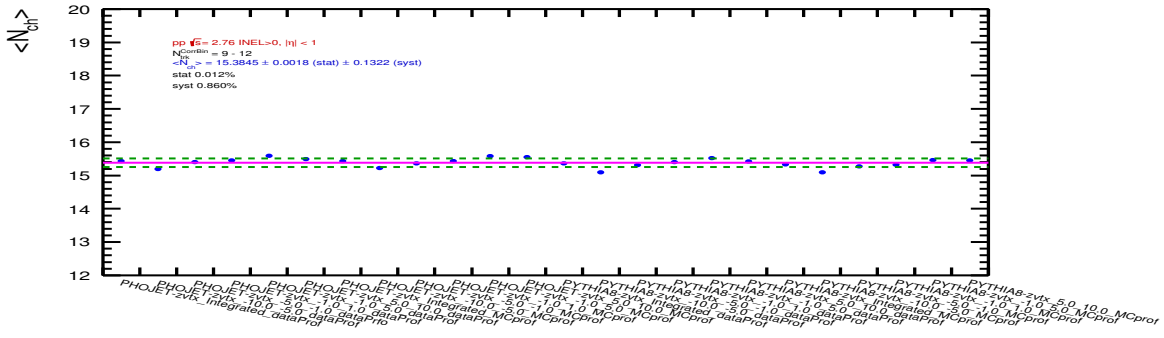

Figure A-23: Mean charged-particle systematic for tracklets bin 9-12.

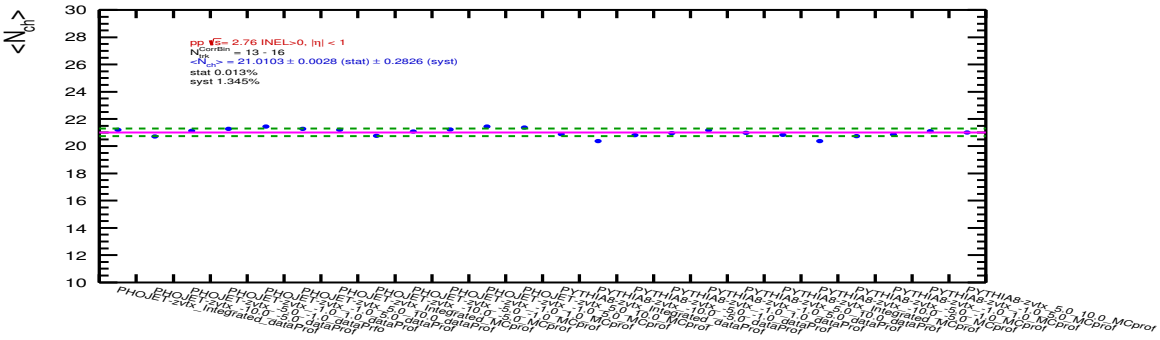

Figure A-24: Mean charged-particle systematic for tracklets bin 13-16.

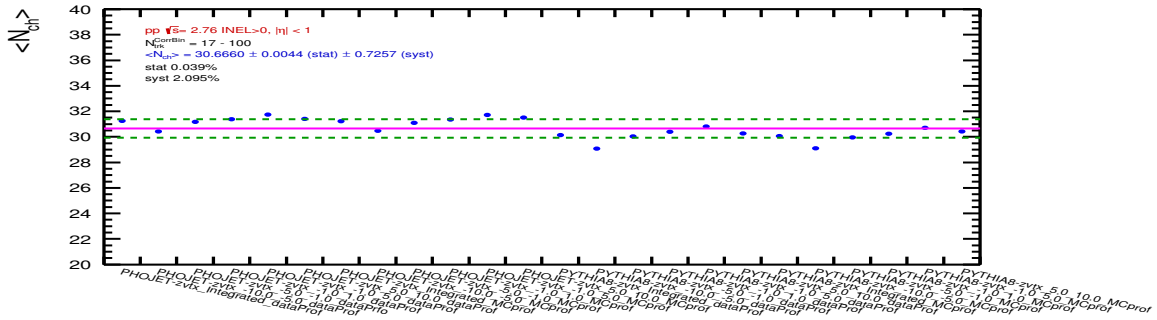

Figure A-25: Mean charged-particle systematic for tracklets bin 17-100.

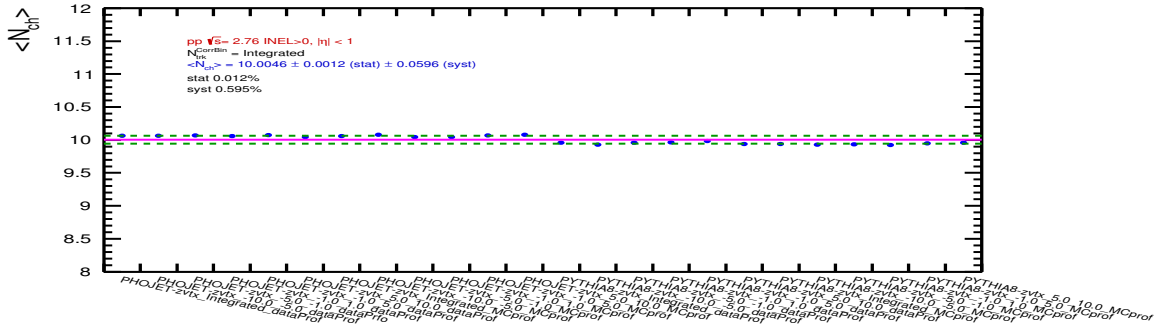

Figure A-26: Mean charged-particle systematic uncertainty for integrated multiplicity at 2.76 TeV.

Appendix B

Extras related to J/ψ yield measurements

B.1 Fit functions

1. Crystal Ball (CB) : It consists of a Gaussian core portion and a power-law tail at low mass defined by the parameters α and n. The power-law part reproduces non Gaussian fluctuations due to energy loss processes.

$$f(x;\mu,\sigma,\alpha,n) = N.\begin{cases} \exp(-\frac{(x-\mu)^2}{2\sigma^2}) & \text{for } \frac{x-\mu}{\sigma} > -\alpha \\ A.(B-\frac{x-\mu}{\sigma})^{-n} & \text{for } \frac{x-\mu}{\sigma} \leq -\alpha \end{cases} \tag{B.1}$$

$$A = \left(\frac{n}{|\alpha|}\right)^n .\exp\left(-\frac{|\alpha|^2}{2}\right)$$

$$B = \frac{n}{|\alpha|} - |\alpha|$$

2. Extended Crystal Ball(CB2) : A Gaussian core convoluted with two power-law

tails. The function has 7 parameters.

$$f(x;\mu,\sigma,\alpha,n,\alpha',n') = N.\begin{cases} \exp(-\frac{(\mathrm{x}-\mu)^2}{2\sigma^2}) & \text{for } \alpha' > \frac{x-\mu}{\sigma} > -\alpha \\ A.(B-\frac{x-\mu}{\sigma})^{-n} & \text{for } \frac{x-\mu}{\sigma} \leq -\alpha \\ C.(D+\frac{x-\mu}{\sigma})^{-n'} & \text{for } \frac{x-\mu}{\sigma} \geq \alpha' \end{cases} \tag{B.2}$$

$$A = \left(\frac{n}{|\alpha|}\right)^n .\exp\left(-\frac{|\alpha|^2}{2}\right)$$

$$B = \frac{n}{|\alpha|} - |\alpha|$$

$$C = \left(\frac{n'}{|\alpha'|}\right)^{n'} .\exp\left(-\frac{|\alpha'|^2}{2}\right)$$

$$B = \frac{n'}{|\alpha'|} - |\alpha'|$$

3. NA60 function : This is a function adopted for charmonia in NA50 and NA60 experiments. New parameter NA60 function is used. It has eight tail parameters (α^L, P_1^L, P_2^L, P_3^L, α^L, P_1^R, P_2^R,P_3^R) and two Gaussian core ($\bar{x}$, σ).

$$f(x) = N.\exp\left(-0.5\left(\frac{\mathrm{t}}{\mathrm{t}_0}\right)^2\right) \text{with t} = \frac{\mathrm{x}-\bar{\mathrm{x}}}{\sigma} \tag{B.3}$$

$$\begin{cases} t_0 = 1 + p_1^L(\alpha^L - t)^{(p_2^L - p_3^L\sqrt{\alpha^L - t})} & \text{for} \quad t < \alpha^L \\ t_0 = 1 & \text{for } \alpha^L < t < \alpha^R \\ t_0 = 1 + p_1^R(\alpha^R - t)^{(p_2^R - p_3^R\sqrt{\alpha^R - t})} & \text{for} \quad t > \alpha^R \end{cases} \tag{B.4}$$

Right and left asymmetric tails are allowed. The function has 11 parameters. NA60 function better describes both right and left sides of the MC spectrum.

4. Double Exponential function : Simple addition of two exponential functions. This function has 4 parameters.

$$f(x) = e^{(a+bx)} + e^{(c+dx)} \tag{B.5}$$

5. Variable Width Gaussian (VWG) : A Gaussian function with a width (σ) which varies as a function of the mass values has been adopted for background :

$$\sigma = \beta + \gamma \times ((x - \alpha)/\alpha) \tag{B.6}$$

$$f(x) = N.\exp(-\frac{(\mathrm{x} - \alpha)^2}{2\sigma^2}) \tag{B.7}$$

6. Ratio of the polynomial 1 to the polynomial 2 : This function has 5 parameters.

$$f(x) = f(x1)/f(x2) \tag{B.8}$$

where

$$f(x1) = a + bx \ and \ f(x2) = c + dx + ex^2 \tag{B.9}$$

B.2 Tail Parameters

$CB2$		
$Parameters$	$PresentAnalysis$	$ANA-3151$
α_L	0.9757 ± 0.0036	0.9427 ± 0.0028
n_L	3.083 ± 0.014	3.151 ± 0.012
α_R	2.201 ± 0.011	2.235 ± 0.009
n_R	2.585 ± 0.036	3.038 ± 0.037

Table B.1: Tail parameters for CB2 used in this analysis for pp collisions at $\sqrt{s}$ = 5.02 TeV.

$NA60$		
$Parameters$	$PresentAnalysis$	$ANA-3151$
α^L	-0.8498 ± 0.002	-0.9501 ± 0.0023
p_1^L	0.002499 ± 0.000005	0.002695 ± 0.000003
p_2^L	0.4247 ± 0.0003	0.4256 ± 0.0002
p_3^L	0.2142 ± 0.0001	0.2177 ± 0.0001
α^R	2.014 ± 0.010	2.306 ± 0.007
p_1^R	0.1879 ± 0.0004	0.1878 ± 0.00004
p_2^R	1.297 ± 0.003	1.193 ± 0.003
p_3^R	0.05606 ± 0.00085	0.04054 ± 0.00079

Table B.2: Tail parameters for NA60 used in this analysis for pp collisions $\sqrt{s}$ = 5.02 TeV.

B.3 Signal extraction systematic uncertainty

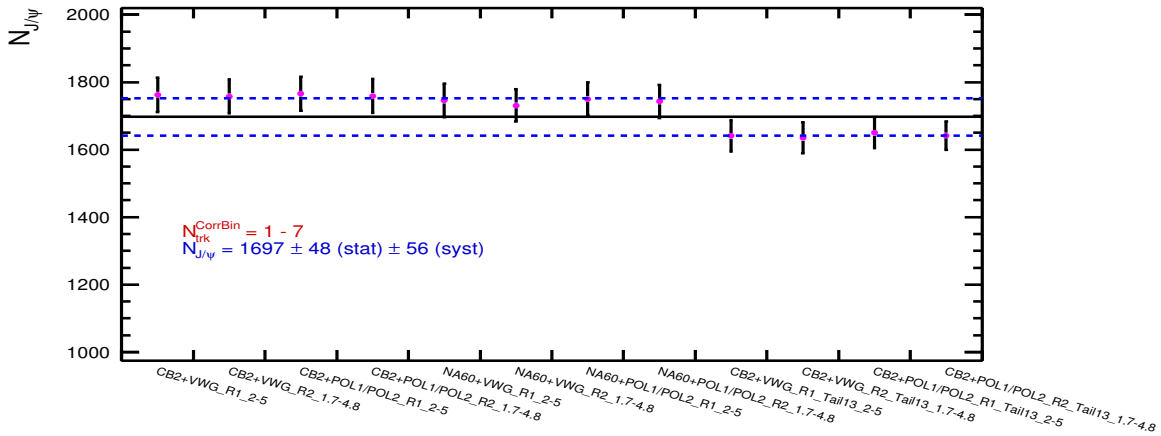

Figure B-1: J/ψ systematic uncertainty in multiplicity bin 1-7 at $\sqrt{s}$ =5.02 TeV.

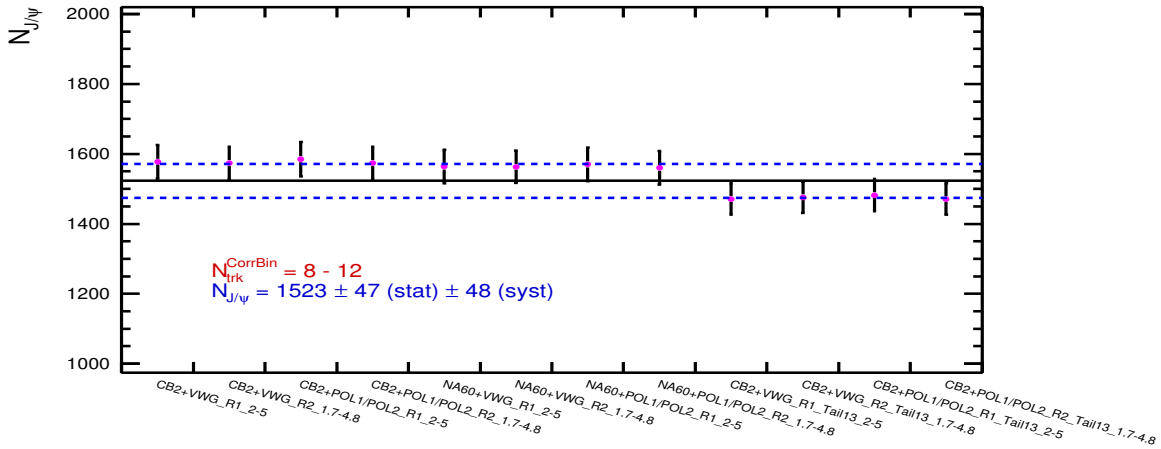

Figure B-2: J/ψ systematic uncertainty in multiplicity bin 8-12 at $\sqrt{s}$ =5.02 TeV.

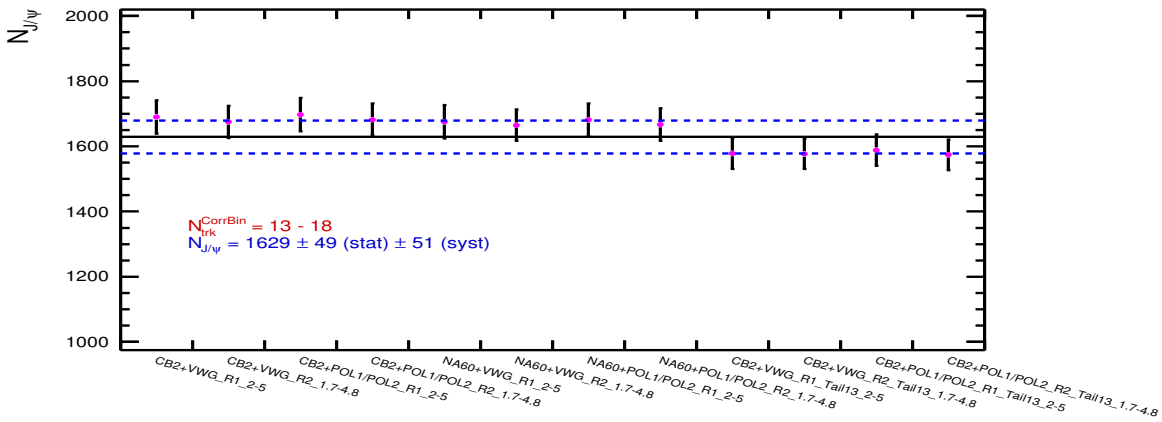

Figure B-3: J/ψ systematic uncertainty in multiplicity bin 13-18 at $\sqrt{s}$ =5.02 TeV.

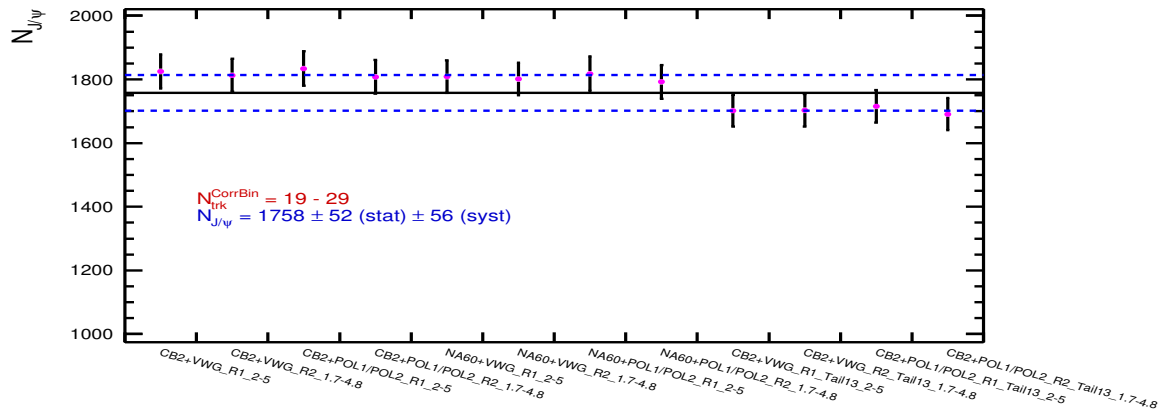

Figure B-4: J/ψ systematic uncertainty in each multiplicity bin 19-29 at $\sqrt{s}$ =5.02 TeV.

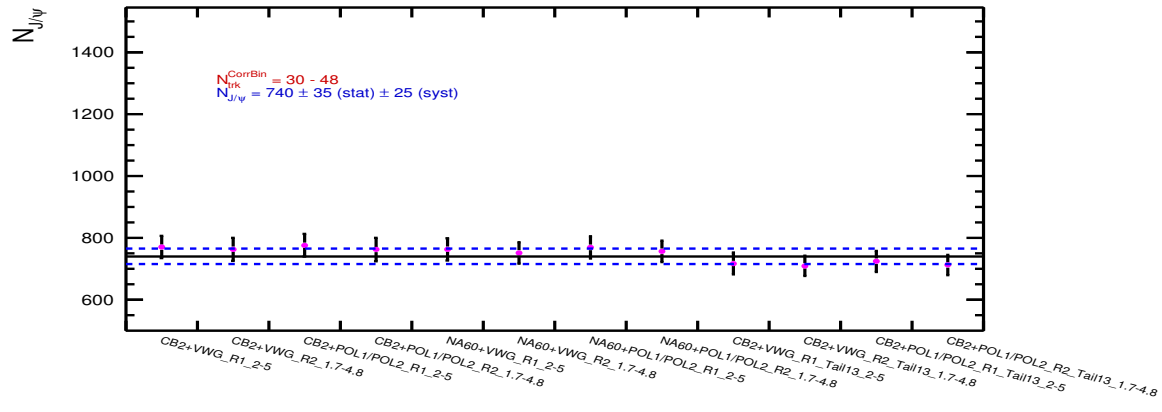

Figure B-5: J/ψ systematic uncertainty in multiplicity bin 30-48 at $\sqrt{s}$ =5.02 TeV.

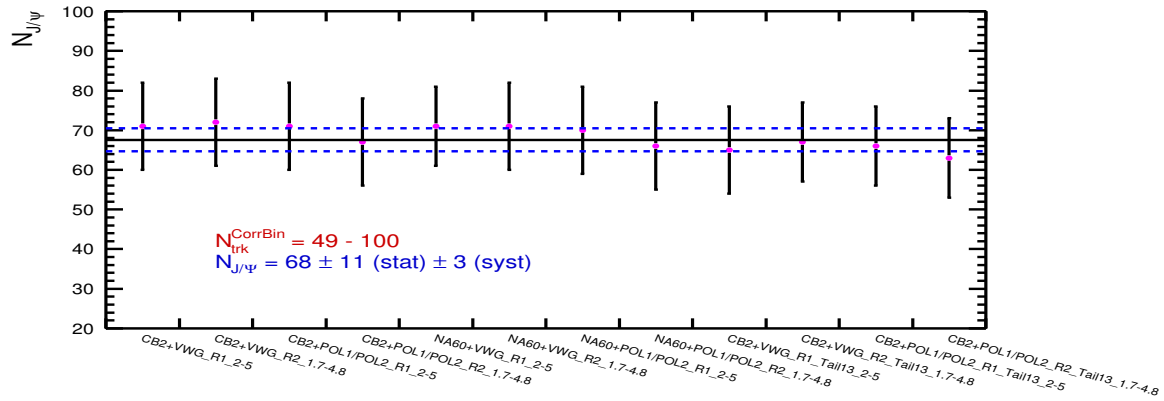

Figure B-6: J/ψ systematic uncertainty in multiplicity bin 49-100 at $\sqrt{s}$ =5.02 TeV.

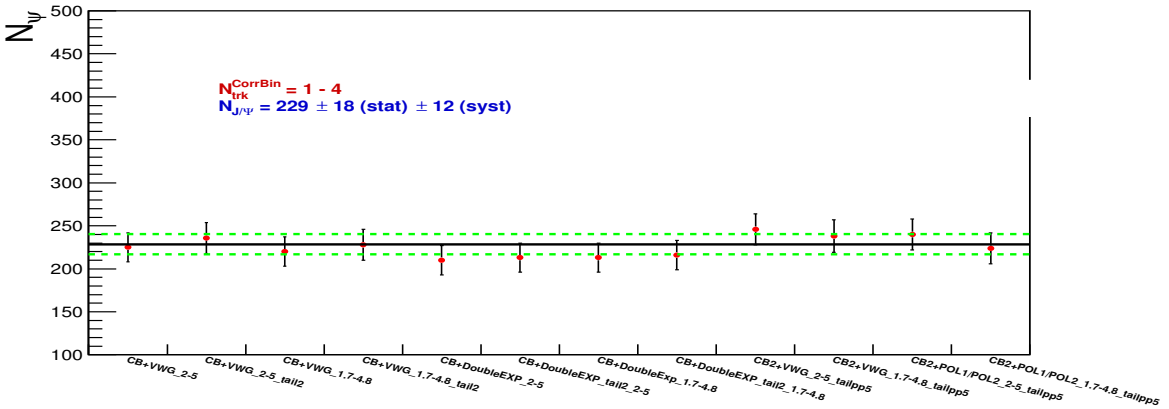

Figure B-7: J/ψ systematic uncertainty in multiplicity bin 1-4 at $\sqrt{s}$ = 2.76 TeV.

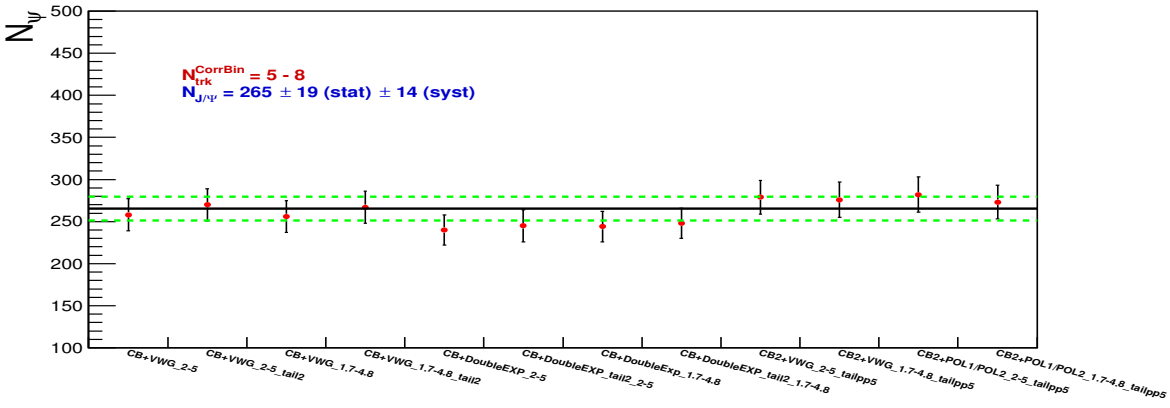

Figure B-8: J/ψ systematic uncertainty in multiplicity bin 5-8 at $\sqrt{s}$ = 2.76 TeV.

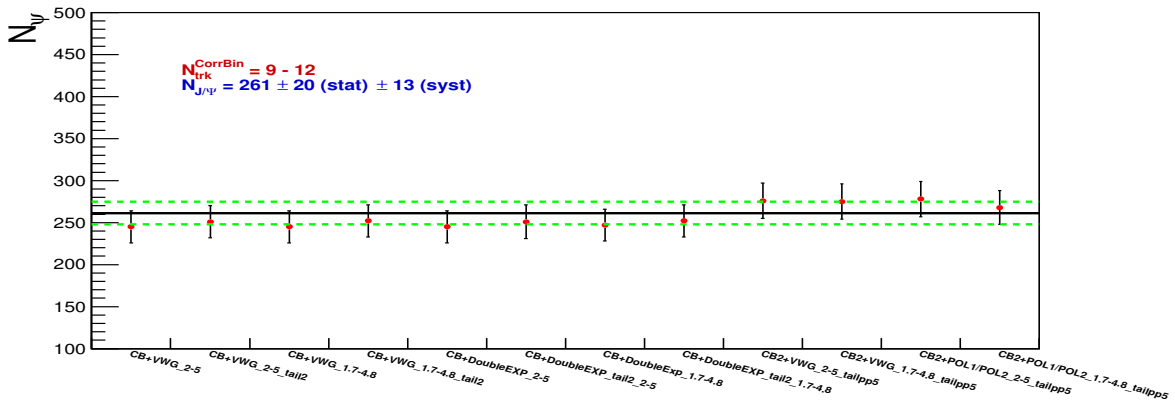

Figure B-9: J/ψ systematic uncertainty in multiplicity bin 9-12 at $\sqrt{s}$ = 2.76 TeV.

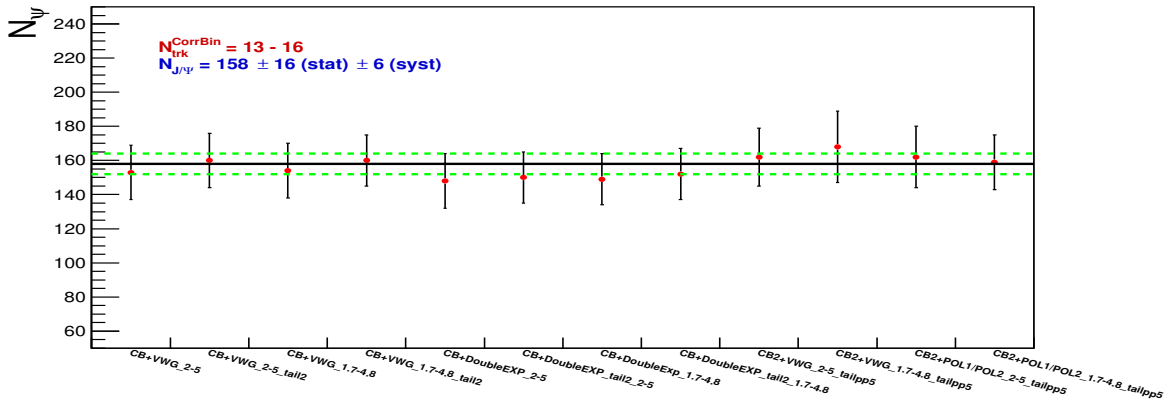

Figure B-10: J/ψ systematic uncertainty in multiplicity bin 13-16 at $\sqrt{s}$ = 2.76 TeV.

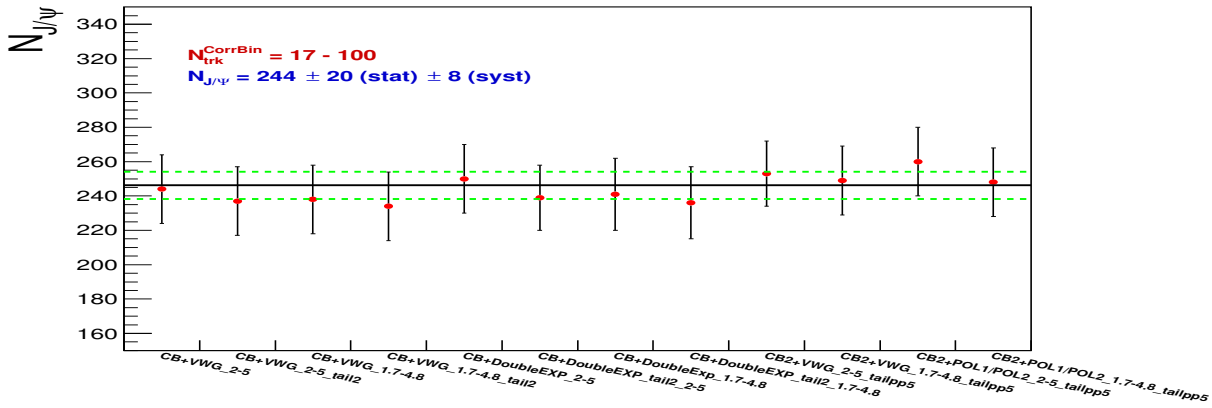

Figure B-11: J/ψ systematic uncertainty in multiplicity bin 17-100 at $\sqrt{s}$ = 2.76 TeV.

B.4 Control plots for mean tranverse momentum of $\mathbf{J/\psi}$ at $\sqrt{s} = 5.02$ TeV

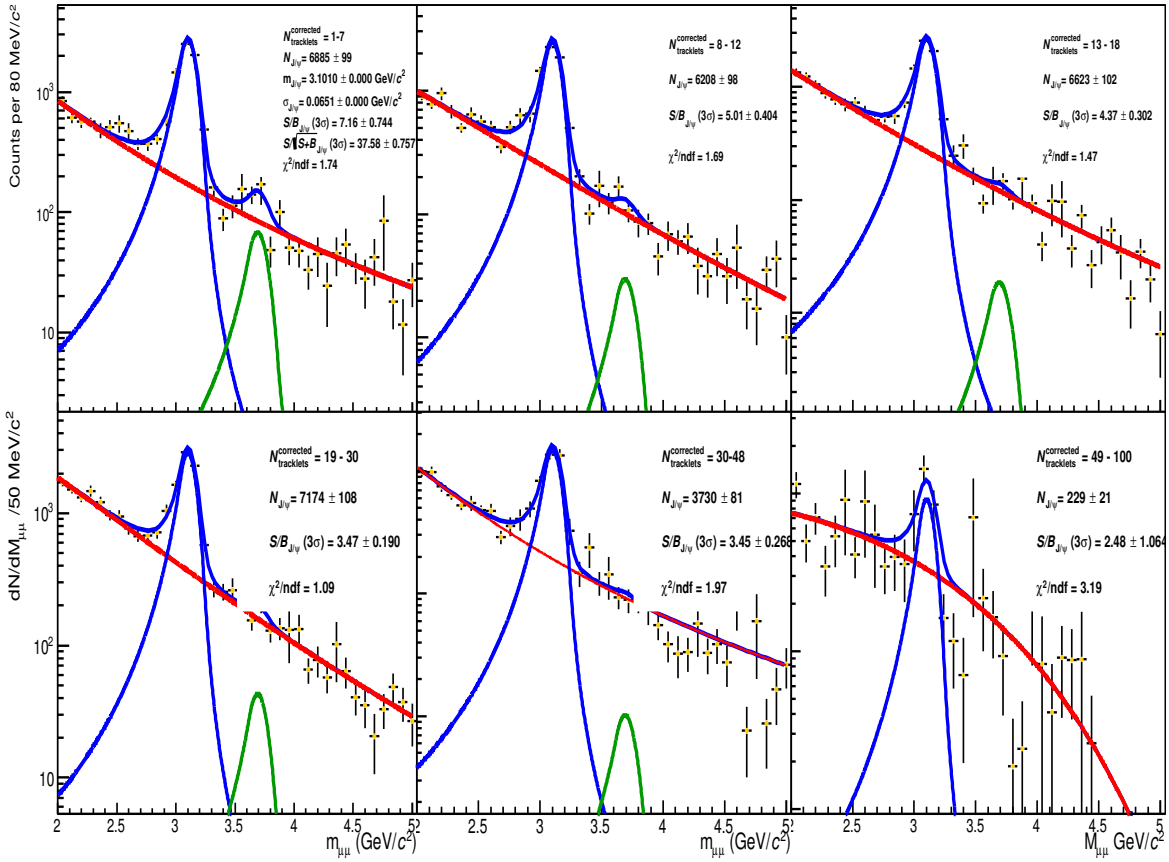

Figure B-12: Acceptance efficiency corrected J/ψ in multiplicity bins fitted with CB2+VWG.

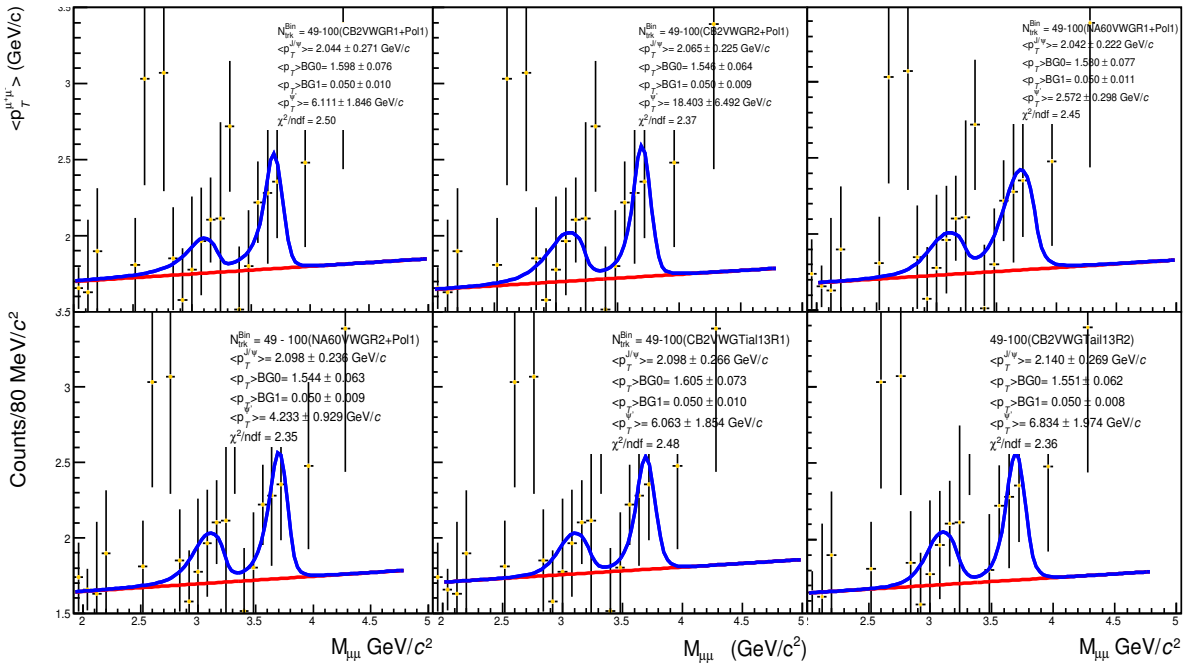

Figure B-13: Corrected $\langle p_T^{J/\psi} \rangle$ in multiplicity bin 49-100, fitted by first order polynomial function as background.

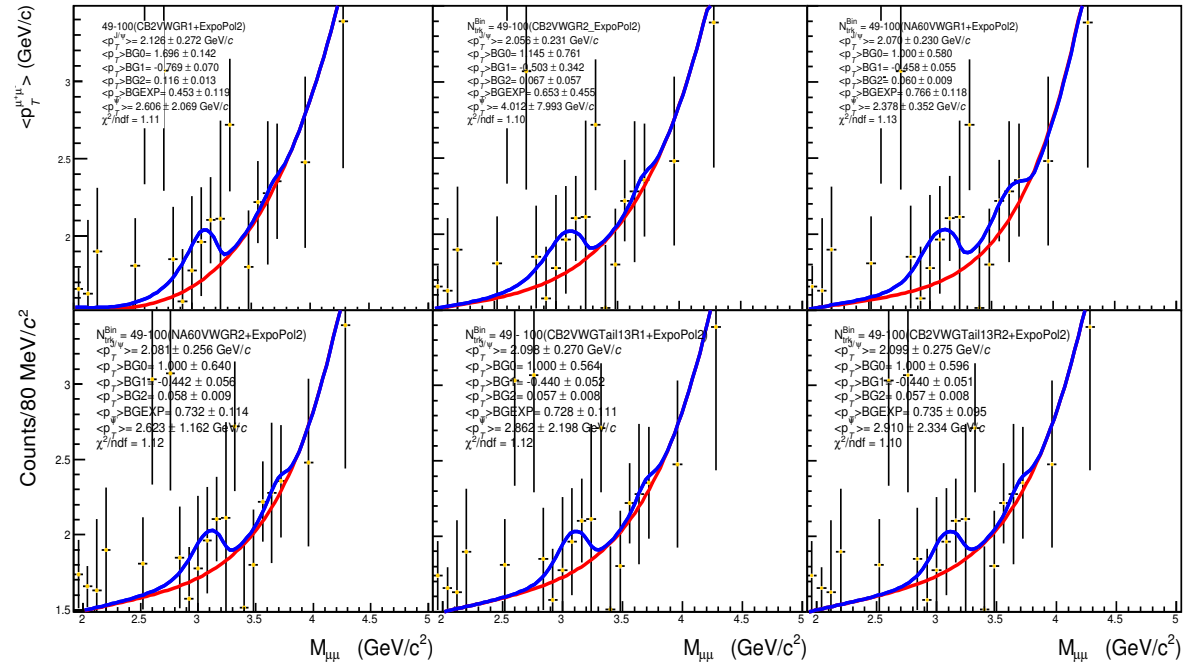

Figure B-14: Corrected $\langle p_T^{J/\psi} \rangle$ in multiplicity bin 49-100, fitted by exponential and second order polynomial product as background.

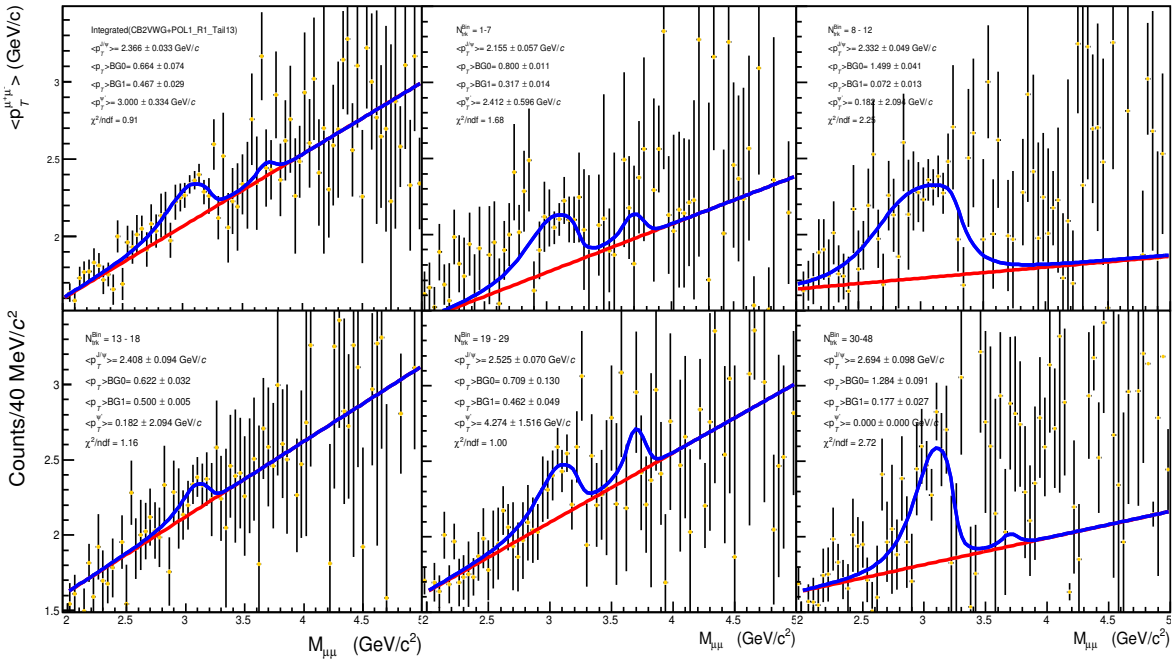

Figure B-15: Example of $\langle p_T^{J/\psi} \rangle$ in multiplicity bins fitted by taking invariant mass bin count per 40 GeV/c^2.

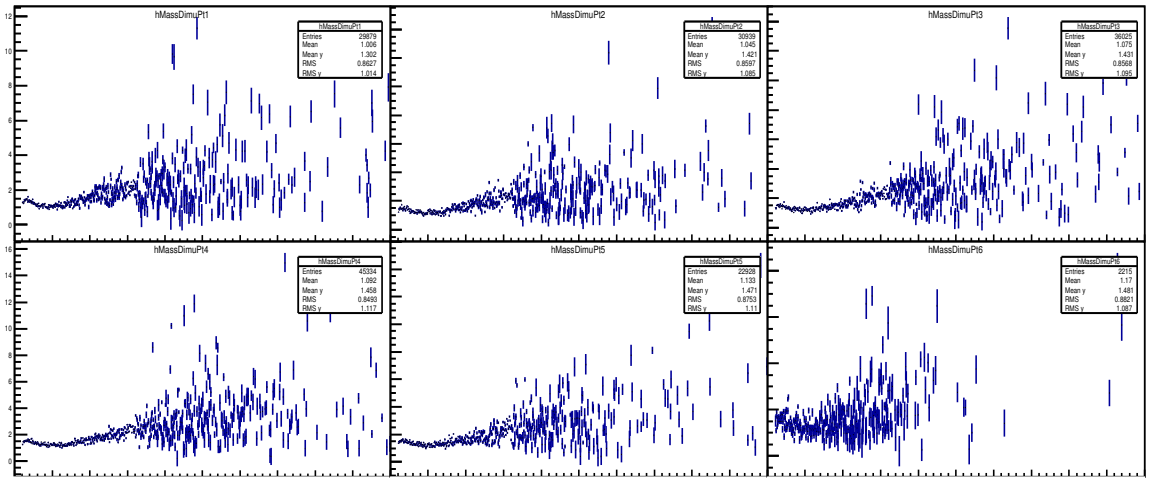

Figure B-16: Corrected $\langle p_T^{J/\psi} \rangle$ dimuon invariant mass distribution in new multiplicity bins different from that are used in analysis.

B.5 Signal extraction systematic uncertainty for relative $\langle p_T^{J/\psi} \rangle$

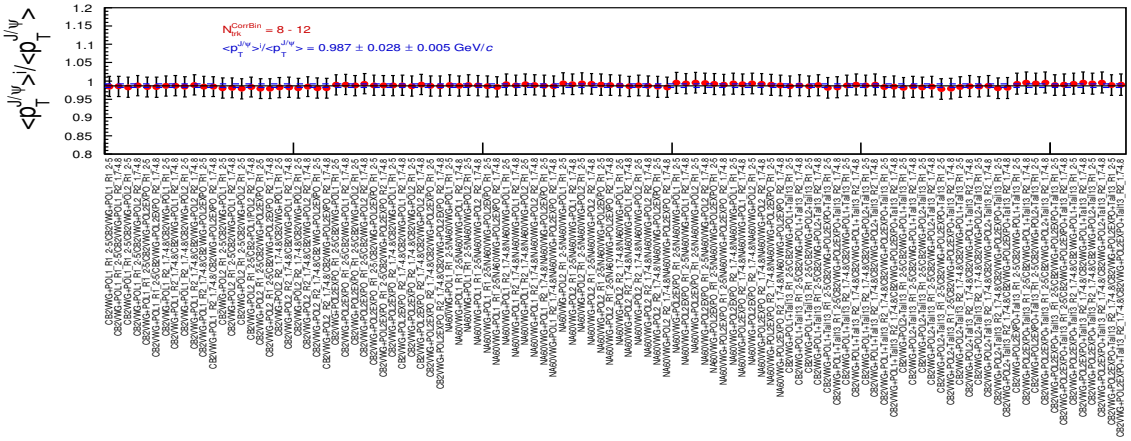

Figure B-17: Relative $\langle p_T^{J/\psi} \rangle$ systematic uncertainty for multiplicity bin 8-12.

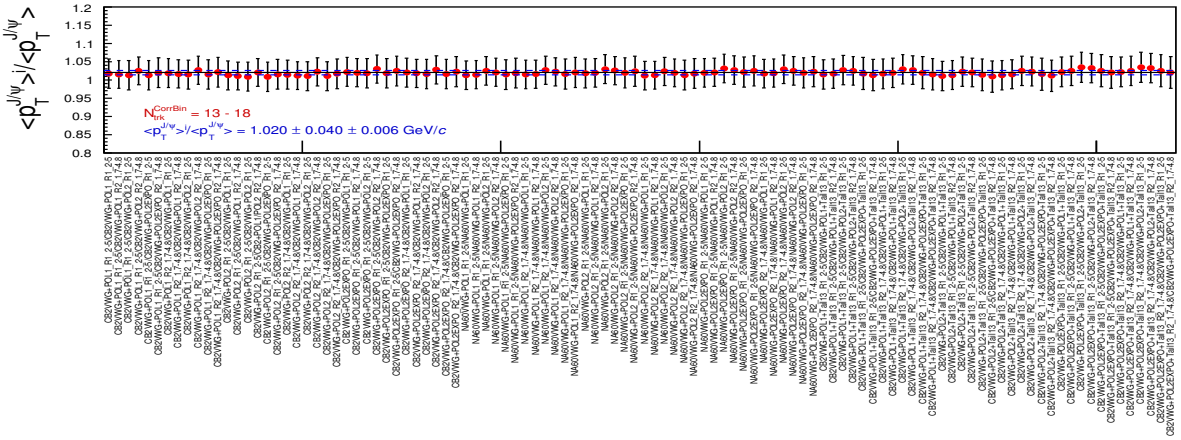

Figure B-18: Relative $\langle p_T^{J/\psi} \rangle$ systematic uncertainty for multiplicity bin 13-18.

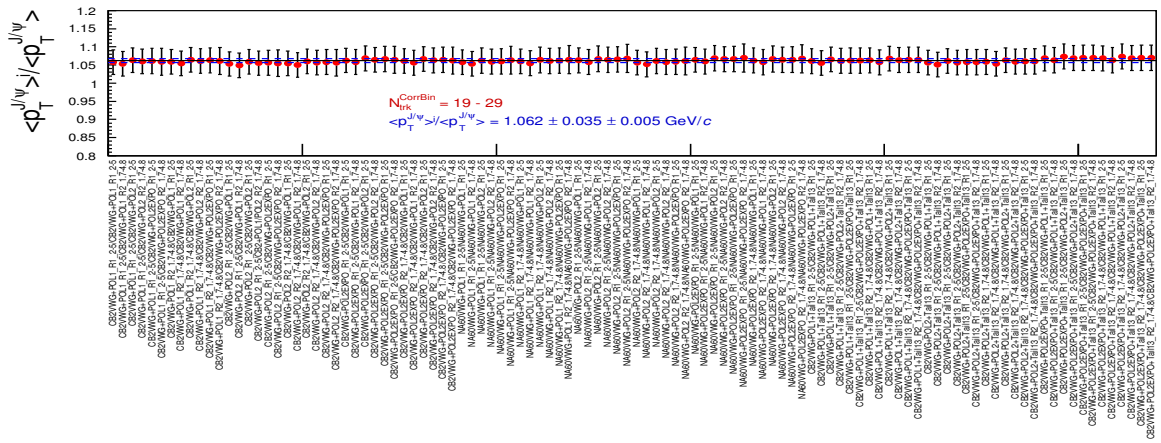

Figure B-19: Relative $\langle p_T^{J/\psi} \rangle$ systematic uncertainty for multiplicity bin 19-29.

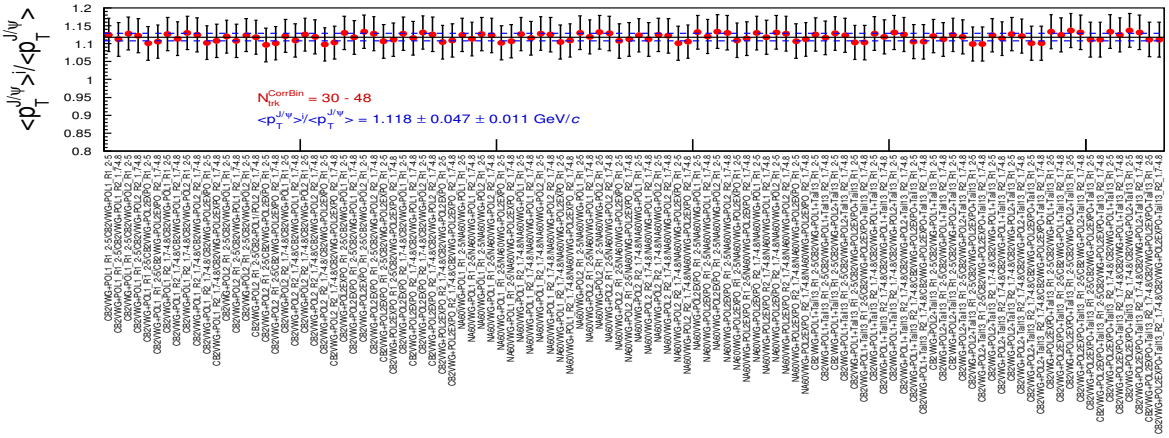

Figure B-20: Relative $\langle p_T^{J/\psi} \rangle$ systematic uncertainty for multiplicity bin 30-48.

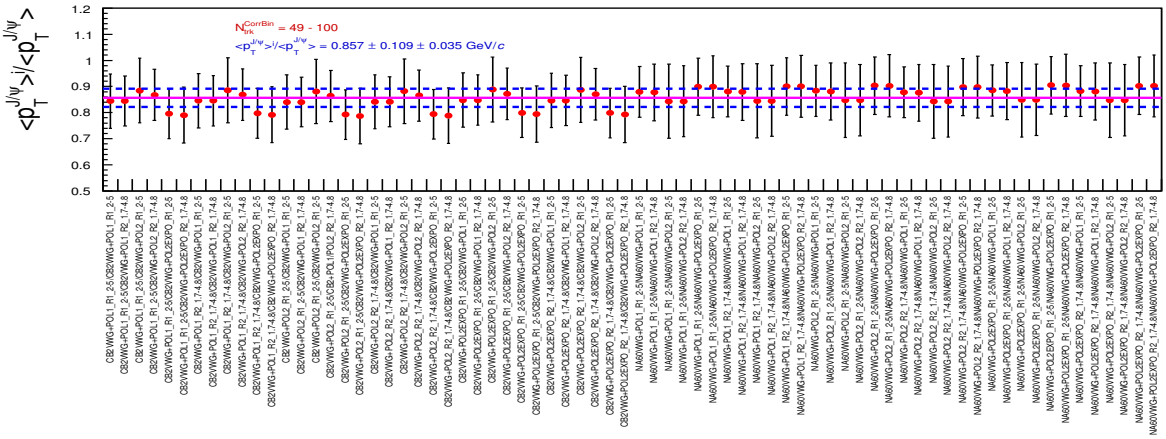

Figure B-21: Relative $\langle p_T^{J/\psi} \rangle$ systematic uncertainty for multiplicity bin 49-100.

Appendix C

List of Publication

ALICE collaboartion

More than 100 publications inside ALICE collaboration: Among them primarily contributed to:

1. ALICE Collaboration, "Forward-rapidity J/ψ production as a function of charged particle multiplicity in pp collisions at $\sqrt{s}$ = 5.02 and 13 TeV with ALICE", In preparation.

2. ALICE Collaboration, "Energy dependence of forward-rapidity J/ψ and ψ(2S) production in pp collisions at the LHC", Eur. Phys. J. C 77 (2017) 392.

3. ALICE Collaboration, "J/ψ suppression at forward rapidity in Pb-Pb collisions at $\sqrt{s}_{NN}$ = 5.02 TeV", Phys. Lett. B 766 (2017) 212-224.

Other than ALICE collaboration:

1. Anisa Khatun, Dhananjaya Thakur, Suman Deb, Raghunath Sahoo, "J/ψ Production Dynamics: Event shape, Multiplicity and Rapidity dependence in Proton+Proton Collisions at LHC energies using PYTHIA8", J. Phys. G, accepted manuscript DOI: 10.1088/1361-6471/ab7a0e, arXiv:1909.03911 [hep-ph].

2. Shakeel Ahmad, M.M. Khan, Shaista Khan, A. Khatun and M. Irfan, "A study of fluctuations of voids in relativistic ion-ion collisions", Int. J. Mod. Phys. E24 (2015) 1550074.

3. Shakeel Ahmad, Anisa Khatun, Shaista Khan, A. Ahmad and M. Irfan, "Search for long-range correlations in relativistic heavy-ion collisions at SPS energies", Adv. in High Energy Phys. vol.2015 (2015), 615458.

4. Shakeel Ahmad, M.M. Khan, Shaista Khan, A. Khatun and M. Irfan, "A study of event-by-event fluctuations in relativistic heavy-ion collisions", Int. J. Mod. Phys. E23 (2014) 1450065.

Papers Contributed in International/National Symposia/Conferences:

1. Anisa Khatun, Dhananjaya Thakur, Suman Deb, Raghunath Sahoo, "Energy and rapidity dependence of J/ψ production as function of charged-particle multiplicity in different event shapes", DAE-BRNS Symposium on Nuclear Physics, Lucknow, India, Dec. 23-27, 2019.

2. Anisa Khatun (for the ALICE Collaboration), "J/ψ production as a function of charged-particle multiplicity in pp collisions at $\sqrt{s} = 5.02$ TeV with ALICE", Conference Proceeding 23^{rd} DAE-HEP 2018 symposium (2018), arXiv:1906.09877.

3. Anisa Khatun (for the ALICE Collaboration), "Measurement of J/ψ production as a function of multiplicity in pp and p-Pb collisions with ALICE", EPJ Web Conf. Volume 182 (2018) 02064, arXiv:1711.09865.

4. Shakeel Ahmad, Shaista Khan and Anisa Khatun, "Fluctuations of Voids in pp Collisions at LHC Energies", 61^{st} DAE Symposium on Nuclear Physics, Kolkata, Dec. 05-09, 2016.

5. Shakeel Ahmad, A. Khatun, Shaista Khan, T. Ahmad and A. Ahmad, "Entropy analysis in relativistic ion-ion collisions", DAE Symposium on Nuclear Physics, Varanasi, Dec. 07-12, 2014.

Appendix D

List of Abbreviations

- RHIC : Relativistic Heavy Ion Collider
- BNL : Brookhaven National Laboratory
- LHC : Large Hadron Collider
- CERN : Conseil Europeen pour la Recherche Nucleaire
- ATLAS : A ToroidaL AparatuS
- CMS : Compact Muon Solenoid
- ALICE : A Large Ion Collider Experiment
- LHCb : Large Hadron Collider beauty
- STAR : for Solenoidal Tracker at RHIC
- HERA : Hadron-Electron Ring Accelerator
- CDF : Collider Detector at Fermilab
- SPEAR : Stanford Positron Electron Asymmetric Rings
- EMCAL : Electro Magnetic CALorimeter